[redacted]

C\ 5
Copy
RM E56B03b

NACA RM E56B03b

FOR REFE[redacted]
NOT TO BE TAKEN FROM THIS ROOM

RESEARCH MEMORANDUM

AERODYNAMIC DESIGN OF AXIAL-FLOW COMPRESSORS

VOLUME III

By Members of the Compressor and Turbine Research Division

Lewis Flight Propulsion Laboratory
Cleveland, Ohio

CLASSIFICATION CHANGED

To UNCLASSIFIED

By authority of NACA Res abs + RN-130 Date effective Sept 30, 1958
Amt 10 6 58

CLASSIFIED DOCUMENT

This material contains information affecting the National Defense of the United States within the meaning of the espionage laws, Title 18, U.S.C., Secs. 793 and 794, the transmission or revelation of which in any manner to an unauthorized person is prohibited by law.

NATIONAL ADVISORY COMMITTEE
FOR AERONAUTICS
WASHINGTON
August 1, 1956

[redacted]

NASA Technical Library
3 1176 01435 4774

AERODYNAMIC DESIGN OF AXIAL-FLOW COMPRESSORS

VOLUME III

By Members of the Compressor and Turbine Research Division
Lewis Flight Propulsion Laboratory
Cleveland, Ohio

Edited by
Irving A. Johnsen and Robert O. Bullock

[redacted]

3309

TABLE OF CONTENTS

AERODYNAMIC DESIGN OF AXIAL-FLOW COMPRESSORS

VOLUME I

FOREWORD

CHAPTER

I - OBJECTIVES AND SCOPE

II - COMPRESSOR DESIGN REQUIREMENTS

III - COMPRESSOR DESIGN SYSTEM

IV - POTENTIAL FLOW IN TWO-DIMENSIONAL CASCADES

V - VISCOUS FLOW IN TWO-DIMENSIONAL CASCADES

VOLUME II

CHAPTER

VI - EXPERIMENTAL FLOW IN TWO-DIMENSIONAL CASCADES

VII - BLADE-ELEMENT FLOW IN ANNULAR CASCADES

VIII - DESIGN VELOCITY DISTRIBUTION IN MERIDIONAL PLANE

IX - CHART PROCEDURES FOR DESIGN VELOCITY DISTRIBUTION

X - PREDICTION OF OFF-DESIGN PERFORMANCE OF MULTISTAGE COMPRESSORS

VOLUME III

CHAPTER

XI - COMPRESSOR STALL AND BLADE VIBRATION

XII - COMPRESSOR SURGE

XIII - COMPRESSOR OPERATION WITH ONE OR MORE BLADE ROWS STALLED

XIV - THREE-DIMENSIONAL COMPRESSOR FLOW THEORY AND REAL FLOW EFFECTS

XV - SECONDARY FLOWS AND THREE-DIMENSIONAL BOUNDARY-LAYER EFFECTS

XVI - EFFECTS OF DESIGN AND MEASUREMENT ERRORS ON COMPRESSOR PERFORMANCE

XVII - COMPRESSOR AND TURBINE MATCHING

3309

TABLE OF CONTENTS

VOLUME III

Chapter Page

XI - COMPRESSOR STALL AND BLADE VIBRATION, by Robert W. Graham and Eleanor L. Costilow 1

SUMMARY 1

INTRODUCTION 1
Off-Design Operation 2
Inlet-stage stall 2
Stall-limit or surge line 2
Stall Phenomena 3

SYMBOLS 4

ROTATING STALL 4
Mechanism of Stall Propagation 4
Experimental Detection of Rotating Stall 5
Characteristics of experimentally observed stall patterns 6
Single- and multistage stall data summary 6
Classification of Stall 7
Progressive or abrupt stall 7
Partial- or total-span stall 7
Steady or intermittent stall 8
General Observations on Rotating-Stall Phenomena . . . 8
Hysteresis effect 8
Stall-propagation rates 8
Flow and pressure fluctuations 9
Multistaging effect 9
Variation in stall patterns 10
Effect of inlet temperature 10
Blade Vibration Incurred during Rotating Stall 11
Single-stage compressors 11
Multistage compressors 12
Methods of alleviating blade vibration 12
Theories of Rotating Stall 13
Emmons theory 13
Stenning theory 14
Sears airfoil theory 16
Sears channel theory 17
Marble theory 19
Remarks on stall theories 22

3309

Chapter Page

INDIVIDUAL BLADE STALL 23

STALL FLUTTER 23
Distinction between Stall and Classical Flutter 23
Mechanism of Stall Flutter 23
Brief literature survey 24
Experimental evidence 25

CONCLUSIONS 25
Aerodynamic Aspect 25
Vibration Aspect 26

REFERENCES 27

TABLE I - SUMMARY OF ROTATING-STALL DATA 30

TABLE II - SINGLE-STAGE-COMPRESSOR DESIGN DATA 32

FIGURES 33

XII - COMPRESSOR SURGE, by Merle C. Huppert 53

SUMMARY 53

INTRODUCTION 53

SYMBOLS 54

STEADY-STATE COMPRESSOR CHARACTERISTIC 55

EXPERIMENTAL INVESTIGATIONS OF SURGE 55
Surge Due to Abrupt Stall 56
10-Stage subsonic axial-flow research compressor . . 56
16-Stage subsonic axial-flow compressor 57
Surge in jet engines 59
Surge Due to Progressive Stall 59

THEORETICAL INVESTIGATIONS OF SURGE 60
Surge Due to Abrupt Stall 61
Surge Due to Progressive Stall 62
Comparison of Compressor Surge with Other Oscillatory Phenomena 63

SUMMARY OF RESULTS 64

Chapter Page

REFERENCES 64

FIGURES 66

XIII - COMPRESSOR OPERATION WITH ONE OR MORE BLADE ROWS STALLED, by William A. Benser 77

SUMMARY 77

INTRODUCTION 78

GENERAL CONSIDERATIONS 80
Single-Stage Stall Characteristics 80
Stage Interactions 80
Radial maldistribution of flow 80
Unsteady flow 81
Complete Compressor Stall and Surge 81

STAGE STACKING 82
Hypothetical Compressor, Cases I, II, and III 83
Hypothetical Compressor, Cases IV and V 84
Range of Calculations 84

DISCUSSION OF COMPUTED PERFORMANCE 85
Case I 85
Computed over-all performance 85
Variation of stage flow coefficients 86
Case II 88
Performance with front stages unstalled 88
Performance with first stage stalled 88
Complete performance map 89
Transition from stalled to unstalled operation of inlet stage 89
Complete-compressor-stall limit 90
Effect of unstalling hysteresis 92
Part-speed efficiency 92
Case III 92
Complete performance map 93
Transition from stalled to unstalled operation of inlet stage 93
Complete-compressor-stall limit 93
Effect of unstalling hysteresis 94
Part-speed efficiency 94
Multiple-valued performance characteristics 94

Chapter Page

Case IV 94
Computed over-all performance 95
Stage progressive-stall limits 95
Comparison of cases I and IV 96
Case V 97
Computed over-all performance 97
Stage progressive-stall limits 97
Comparison of cases I and V 97

CONCLUDING REMARKS 98
Part-Speed Performance Problems 98
Stage-Matching Compromises 100
Variable Geometry 101
Inlet baffles 101
Adjustable blading 101
Compressor air bleed 102

REFERENCES 102

TABLE I - REFERENCE-POINT VALUES 104

FIGURES 105

XIV - THREE-DIMENSIONAL COMPRESSOR FLOW THEORY AND REAL FLOW EFFECTS, by Howard Z. Herzig and Arthur G. Hansen 127

SUMMARY 127

INTRODUCTION 127

SYMBOLS 129

DESIGN ASSUMPTIONS 131
Axial Symmetry 131
Simple radial equilibrium 132
Constant entropy radially 132
Blade-Element Flow 133
Improved Design Theories 134

COMPRESSOR DESIGN THEORIES 135
Basic Equations 135
Equilibrium equation 136
Energy equation 137
Entropy equation 138
Continuity equation 139

Chapter Page

Axisymmetric-Flow Theory 139
Equilibrium equation 139
Energy equation 140
Entropy equation 140
Continuity equation 141
Improved Flow Theories 141
Radial-equilibrium condition 141
Finite blade spacing 143
Through-flow theory 144
Blade thickness 145
Three-Dimensional Theory 146
Analysis 146
Initial approximations 148
Solutions on flow surfaces S_1 and S_2 148
Evaluation and relation to previous methods 149

SOME ASPECTS OF THREE-DIMENSIONAL FLOWS 150
Radial-Flow Variations 150
Radial-flow shifts 151
Flow near blade rows 152
Radial adjustment and blade-row interference 154
Secondary-Flow Effects 154
General discussion 154
Commentary 155

TIME-UNSTEADY FLOW 156

REFERENCES 160

FIGURES 163

XV - SECONDARY FLOWS AND THREE-DIMENSIONAL BOUNDARY-LAYER EFFECTS, by Arthur G. Hansen and Howard Z. Herzig 165

SUMMARY 165

INTRODUCTION 165

EXPERIMENTAL INVESTIGATION OF SECONDARY FLOWS 167
Cross-Channel Flows and Passage Vortex Formation . . . 167
Apparatus and procedure 167
Passage vortex formation 168
Passage vortex behavior and effects 169

Chapter Page

Radial Secondary Flows in Stators 169
Apparatus and procedure 169
Indications of radial flows based on downstream measurements 170
Visual indications of radial flows 171
Evaluation of radial components of secondary flow . . 171
Loss accumulations and passage vortices 171
Flow in Blade End Regions with Clearance 174
Tip clearance 174
Relative motion between blades and wall 174
Rotor-Stator Interaction Effects 175
A Model of Secondary Flow in Compressor Blade Rows . . 175
Flow in shrouded stators 176
Flow in unshrouded stators 177
Flow in rotors 177

THEORETICAL INVESTIGATION OF SECONDARY FLOWS 177
Discussion of Methods 178
Nonviscous-Secondary-Flow Theory 181
Flows in channels and two-dimensional cascades . . . 181
Evaluation and conclusions 184
Three-Dimensional Boundary-Layer Flows 186
Investigations of three-dimensional boundary-layer equations 187
Boundary-layer crossflow over flat plate with leading edge 188
Flow over flat plate with thick boundary layer . . . 192
Boundary-layer flow in corners 193
Evaluation and conclusions 194

CONCLUDING REMARKS 195

REFERENCES 196

FIGURES 199

XVI - EFFECTS OF DESIGN AND MEASUREMENT ERRORS ON COMPRESSOR PERFORMANCE, by Robert J. Jackson and Peggy L. Yohner . . . 229

SUMMARY 229

INTRODUCTION 229

SYMBOLS 230

Chapter Page

ANALYTICAL APPROACH 232
Design Errors 232
Measurement Errors 238

CALCULATION AND PRESENTATION OF FORMULAS 239
Design-Error Formulas 240
Measurement-Error Formulas 247
Reading of Carpet Plots 252

DISCUSSION OF FORMULAS AND CHARTS 253
Sample Design and Measurement Errors 254
Interpretation of numerical values 257
Trends exhibited by sample design errors 257
Trends exhibited by sample measurement errors 258
Use of Design-Error Charts 258
Estimation of uncertainty intervals 260
Calculation of uncertainty intervals in performance . 261
Use of Measurement-Error Charts 261
Uncertainty intervals in performance 261
Evaluation of data 261
Instrumentation 262

CONCLUDING REMARKS 262

APPENDIX A - ACCURACY OF FORMULAS 264
Design-Error Formulas 264
Measurement-Error Formulas 266
Local specific mass flow 266
Relative air angle 267

APPENDIX B - DERIVATION OF FORMULAS 268
Design-Error Formulas 268
Measurement-Error Formulas 271

REFERENCES 272

FIGURES 273

XVII - COMPRESSOR AND TURBINE MATCHING, by James F. Dugan, Jr. . . 311

SUMMARY 311

INTRODUCTION 312

SYMBOLS 314

Chapter Page

GENERAL DISCUSSION 316

GENERAL METHODS FOR EQUILIBRIUM OPERATION 317
One-Spool Gas Generator 318
Matching relations 318
Matching maps and their superposition 319
Component parameters 321
Compressor operation from gas-generator performance . 322
Two-Spool Gas Generator 322
Direct method of matching outer and inner spools . . 323
Iterative method of matching outer and inner spools . 324
Variable pressure losses in primary combustor 325
Component parameters 326
Compressor operation from gas-generator performance . 326
Matching Gas Generator with Other Engine Components . . 327
Simple turbojet 327
Afterburning turbojet 328
Turboprop with coupled power turbine 328
Turboprop with free-wheeling power turbine 328
Turbojet- and turboprop-engine performance 330

SIMPLIFIED METHODS FOR EQUILIBRIUM OPERATION 331
One-Spool Gas Generator 332
Design point 332
Off-design points 332
Two-Spool Gas Generator 333
Inner-spool matching 334
Outer-spool matching 334

EQUILIBRIUM OPERATING LINE OF ONE-SPOOL TURBOJET 335
Use of Charts for Design Point 337
Use of Charts for Off-Design Points 338

METHODS FOR TRANSIENT OPERATION 339
One-Spool Turbojet 339
Compressor operation 340
Turbine operation 340
Time to accelerate 342
Two-Spool Turbojet 342
Compressor operation 343
Turbine operation 344
Time to accelerate 345

REFERENCES 346

FIGURES 350

3309

CH-1

CHAPTER XI

COMPRESSOR STALL AND BLADE VIBRATION

By Robert W. Graham and Eleanor L. Costilow

SUMMARY

The extent of the useful operating range of the multistage axial-flow compressor is greatly influenced by its stalling characteristics. Over the entire range of possible compressor speeds there is a minimum flow point for each speed where the compressor will either surge or stall, depending upon the geometry of the compressor receiver. If surge does not occur, the efficiency will be so poor in the stalled condition that the compressor will limit the useful operation of a turbojet engine. These surge or stall points define the familiar surge or stall-limit line. In addition to this stall line, stall of the front and rear stages occurs at part-speed and overspeed operation, respectively. Serious blade vibrations may occur for either of these conditions as a result of stall.

Compressor stall may be manifested as rotating stall, individual stall of each blade, or stall flutter. From experimental evidence, the first of these seems the most prevalent.

Several theories of rotating stall in single-stage compressors appear in the literature, none of which can be used to predict propagation rates with any appreciable degree of reliability. However, these theories are useful in evaluating the significance of parameters pertinent to the stall-propagation mechanism and thus in planning experimental research programs. The prediction of rotating-stall data for multistage compressors is even more complicated, because of interaction effects among the stages.

INTRODUCTION

Historically, it is interesting that one of the earliest references to rotating stall appeared in 1945 in a British report on the performance of a centrifugal compressor (ref. 1). In 1950 an NACA publication (ref. 2) reported the occurrence of an asymmetric flow pattern in an impulse axial-flow compressor. In both of these early investigations, flow

patterns were detected by means of wool tufts. This asymmetric flow phenomenon was labeled as a propagating stall in reference 3 (1951), which presented the stalling characteristics of an axial-flow compressor. The rotating-stall patterns found in that investigation were detected with high-frequency-response hot-wire anemometers. During the past three years, much research effort has been devoted to the study of rotating stall in both single- and multistage compressors.

Off-Design Operation

3309

With the use of aerodynamic theory, the design-point performance of a multistage compressor can be predicted with reasonable accuracy. However, as is pointed out in chapter X (ref. 4), current design techniques cannot be used to predict compressor operation that deviates markedly from design. Since the compressor of a turbojet engine must operate at part design speed during acceleration of the engine and also at high flight Mach numbers, analytical methods for accurately predicting part-speed operation are desired by compressor designers. In addition, designers are concerned with blade vibrations that occur during operation in stall.

The internal aerodynamics of the compressor must be thoroughly understood at off-design conditions before design techniques applicable to this region of operation can be developed. During compressor off-design operation, degeneration of the performance of a stage is accompanied by a serious flow separation in the blade passages. This unfavorable operating condition is termed stall. Two significant areas of off-design performance are labeled in figure 1, which is a representative multistage compressor map: (1) inlet-stage stall and (2) the stall-limit or surge line. These conditions result from stall of some of the compressor blade elements. The occurrence of separated flow at each of these regions can be explained without an elaborate analysis.

Inlet-stage stall. - At low speeds, insufficient pressure rise in the stages causes the density level of the fluid to be too low in the rear stages. The resulting high relative velocities and incidence angles cause choking in the rear stages. This choking limits the flow through the front stages and causes excessively high angles of attack or stall.

Stall-limit or surge line. - The stall-limit line represents the locus of minimum-flow points just before the performance of the compressor deteriorates abruptly. This deterioration in performance, which is attributed to the operation of one or more of the stages in severe stall, is sometimes called "complete compressor stall." In chapter XIII, the stages instigating the stall limit are analyzed and the significance of the shape of the stall-limit line and its relative position on the compressor map is discussed. The stall-limit line is often referred to as

the surge line, since surge may occur, depending on the geometry of the compressor receiver. An analysis of surge in the multistage compressor is presented in chapter XII.

In addition to the part-speed stalling conditions discussed earlier, the possibility of rear-stage stall at near-design and overspeed operation of the compressor must be admitted. Experimental evidence for overspeed stall is lacking, but such a stalling condition seems possible. At these conditions, continuity requirements in the rear stages cause some of the blade elements to operate at stalled angles of attack. Chapter XIII concludes that stall of the rear stages determines the stall-limit line at high part-speed and overspeed operation.

Stall Phenomena

Experimental data and analyses give credibility to the existence of at least three distinct phenomena during stall operation, the first two being aerodynamic phenomena, and the last an aeroelastic phenomenon:

(1) Rotating or propagating stall, which consists of large stall zones covering several blade passages and propagating at some fraction of rotor speed in the absolute direction of rotor rotation. These stall zones can produce resonant blade vibrations. The number of stall zones and the propagation rate vary considerably. Compressor investigation has shown rotating stall to be the most prevalent type of stall phenomenon.

(2) Individual blade stall, which is characterized by the development of large separated-flow regions or zones of low flow in the wake of each blade.

(3) Stall flutter, which is a self-excited blade oscillation that must be distinguished from the more familiar classical flutter. The latter, which is a self-sustained oscillation caused by the coupling of the inertia, damping, elastic, and aerodynamic forces on a wing section, takes place at low angles of attack (unstalled flow) when a certain critical velocity that is a function of the wing design is reached. In contrast, stall flutter takes place at high angles of attack and is associated with individual blade stall.

The present report summarizes the pertinent experimental and theoretical work that has been done on these three stall phenomena. The assumptions and analytical techniques are emphasized in presenting the theories. Wherever possible, theoretical results are compared with experimental data. The discussion includes experimental data on blade vibration incurred during rotating stall.

CH-1 back

SYMBOLS

The following symbols are used in this chapter:

N	rotational speed, rpm
U	rotor speed, ft/sec
V	air velocity, ft/sec
β	air angle, angle between air velocity and axial direction, deg
θ	ratio of total temperature to NACA standard sea-level temperature of 518.7° R
ρ	density, lb-sec^2/ft^4
$\Delta\rho V/\overline{\rho V}$	amplitude of ρV fluctuation divided by average ρV based on average anemometer current

Subscripts:

t	tip
z	axial direction
1	station at exit of guide vanes
2	station at rotor exit
3	station at stator exit

Superscript:

'	relative to rotor

ROTATING STALL

Mechanism of Stall Propagation

Rotating stall has been depicted as the propagation of large stall zones relative to the blade row. The propagation mechanism can be described by considering the blade row to be a cascade of blades similar to that shown in figure 2. Assuming that some flow perturbation has caused blade 2 to reach a stalled condition before the other blades in the cascade, then this stalled blade does not produce sufficient pressure rise to maintain the flow around it. Consequently, effective flow blockage or a zone of reduced flow develops. This retarded flow (shaded in fig. 2) diverts the flow around it so that the angle of attack increases on blade

3 and decreases on blade 1. The stall propagates downward relative to the blade row; the diverted flow stalls the blades below the retarded-flow zone and unstalls the blades above it. The retarded-flow or stall zone moves from the pressure side to the suction side of each blade (the opposite direction of rotor rotation). The stall zone may cover several blade passages. From compressor tests, the relative speed of propagation has been observed to be less than absolute rotor speed. Consequently, as observed from an absolute frame of reference, the stall zones appear to be moving in the direction of rotor rotation.

3309

Experimental Detection of Rotating Stall

At present, the hot-wire anemometer is generally used at the NACA Lewis laboratory to detect and measure the flow fluctuation of stall. However, since a pressure change accompanies these flow fluctuations, a high-frequency-response electronic pressure pickup is also a suitable detection device. The hot-wire-anemometer probe and two types of hot-wire-anemometer amplifying systems, the constant-current and the constant-temperature, are discussed in references 5 to 7. A method of determining from hot-wire-anemometer data the number of stall zones in a given pattern and the magnitude of the flow fluctuation in the stall zones with respect to some mean flow value is given in reference 8.

The testing procedure generally followed in determining the rotating-stall characteristics of a compressor is to operate the compressor at a constant speed and gradually decrease the weight flow while observing the resulting changes in the hot-wire-anemometer output. The hot-wire-anemometer signal, usually observed on an oscilloscope, follows a definite evolutionary process as the weight flow is decreased. As an illustration, this process is described in conjunction with the performance characteristic of a single-stage axial-flow compressor (fig. 3).

When the test is begun, at high weight flows near the best operating point of the compressor, the hot-wire signal viewed on the oscilloscope indicates sharply defined blade wakes in region A. Typical oscillograms showing these blade wakes are given in figure 4. As the weight flow is reduced below the peak-pressure-ratio weight flow denoted by region B of figure 3, the blade wakes become wider and less well defined, indicating flow separation and the possibility of stall somewhere along the blade. A momentary or unstable stall zone covering several blade passages is occasionally observed on the oscilloscope. The sporadic stall zone is often the herald of a periodic rotating-stall pattern that develops at lower weight flows. Periodic rotating-stall zones are observed as the weight flow is further reduced to region C of figure 3. A typical rotating-stall pattern for this area is shown by the oscillogram of figure 5. Further throttling of the compressor weight flow may promote changes in the rotating-stall patterns with respect to the number and

size of the stall zones. If the weight flow is gradually increased, generally the same rotating-stall patterns will appear; however, the stall pattern will be instigated at higher weight flow, as shown in figure 3. This behavior of stall instigation is called hysteresis.

Characteristics of experimentally observed stall patterns. - Single-stage compressors: Rotating-stall characteristics have been investigated in a considerable number of single-stage experimental compressors, with symmetrical, solid-body, or free-vortex velocity diagrams and a variety of blade shapes. The rotating-stall data obtained embrace a wide range of stall-propagation rates and number of zones in each stall pattern. The number of zones varies from 1 to 12, and the absolute propagation rate varies from approximately 10 to 85 percent of rotor speed. Generally, more than one stall pattern occurs; that is, the number of zones and the geometric configuration of the stall-zone region change as the flow is varied in a given compressor. Figure 6 is a typical single-stage-compressor performance map with the stall patterns observed and the weight-flow range of each pattern indicated on the figure. Generally, as in the example used in the figure, the propagation rate remained essentially constant over the entire stall region, notwithstanding changes in the number of stall zones. Some exceptions to the consistency of the stall-propagation rate have been observed when appreciable changes in the radial extent of the stall zone take place.

3309

Multistage compressors: Multistage compressors exhibit stall characteristics similar to those of the single-stage units. The stall zones appear to extend axially through the compressor, that is, with little or no spiraling. As the weight flow was throttled at a constant speed, the number of stall zones in the annulus varied from 1 to 7 among the several compressors investigated. Rotating stall in multistage compressors may exist from choked flow to surge at low speeds. The rotational speed of the stall zones ranged from 43 to 57 percent of the rotor speed, and the stall propagated in the direction of the rotor rotation (absolute frame of reference) for all compressors investigated.

Rotating-stall characteristics are superimposed on a typical multistage-compressor performance map in figure 7. For this compressor, stall existed throughout the compressor in the intermediate-speed range. The number of stall zones increased with a decrease in the weight flow at a given speed.

Single- and multistage stall data summary. - Tables I(a) and (b) give a general summary of the stall data from single- and multistage compressors, respectively. More information regarding stall has been taken for single-stage units than for multistage compressors. Single-stage-compressor design data are given in table II.

Classification of Stall

Rotating stall may be classified as progressive or abrupt, according to the performance characteristic of the compressor. In addition, the stall pattern is described as partial or total span and steady or intermittent, according to the geometry of the stall zone and the periodicity.

3309

Progressive or abrupt stall. - Classifying rotating stall by the type of stage performance characteristic associated with it is probably the most important way to denote stall types. A smooth, continuous stage performance characteristic in the stall region similar to that shown in figure 6 indicates the gradual increase in blocked annulus area due to stall. Appropriately, this type is called "progressive" stall. In contrast, a discontinuous stage performance characteristic like that shown in figure 3 has also been observed during stall. Generally, for this type of performance curve a single stall zone covering as much as half the annulus area and extending over the entire blade span has been observed. Because of the discontinuity in the pressure curve, this type of stall is called "abrupt."

The term "complete compressor stall" is applied to multistage compressors to describe a discontinuous performance curve similar to that for abrupt stall of single-stage compressors. The complete-compressor-stall points on the performance map define the stall-limit line.

The magnitude of the pressure drop at the discontinuous point of the performance characteristic is shown in figure 8 for abrupt stall of blade elements. Here the pressure drop due to stall divided by the pressure rise immediately before encountering stall is plotted against the compressor pressure ratio measured just before compressor stall. Both single- and multistage data are included; that is, both abrupt and complete-compressor-stall data are plotted. Evidently, abrupt stall of some blade elements and complete compressor stall are similar. From this figure it is apparent that the pressure drop accompanying complete compressor stall is severe and will result in appreciable penalties in compressor efficiency.

Partial- or total-span stall. - The radial extent of the stall zone along a blade is another convenient characteristic for classifying rotating stall. In addition to extending circumferentially over several blade passages, the stall zone also covers part or all of the blade span. Thus, the term partial-span stall is used to denote stall covering part of the blade span, and total-span refers to stall covering the whole blade length. Figure 9 shows the type of oscillogram obtained during a radial traverse with a hot-wire-anemometer probe. The large-amplitude pulsations from hub to tip (fig. 9(a)) are typical for total-span stall. Figure 9(b) shows a partial-span stall concentrated at the tip, as shown by the disappearance of the stall "blip" from the anemometer trace at the hub.

Steady or intermittent stall. - It has been observed that compressors may also have an intermittent type of stall pattern for a given operating point. In this case one stall pattern exists for an instant, then changes to a new stall pattern. Intermittent changing among three different stall patterns has been observed in one multistage compressor.

General Observations on Rotating-Stall Phenomena

3309

The following general observations concerning rotating-stall phenomena are made from examination of the existing data. The remarks apply to both single- and multistage compressors. Exceptions to the generalizations are also discussed.

Hysteresis effect. - When a compressor is being run at a constant aerodynamic speed and a rotating-stall pattern is encountered during a throttling of the weight flow, usually that same stall pattern will be observed for subsequent repeated tests. In fact, for single-stage tests over a range of speeds the stall pattern will be repeated for all speeds if the compressor is operated at the same flow coefficient in each case. However, it is interesting that, once a stall pattern has been established during a throttling process, if the flow is allowed to increase the pattern will persist above the value of the throttled weight flow (or flow coefficient for single-stage compressors) to a higher weight flow before disappearing. A graphical superposition of this apparent reluctance of the stall pattern to change on a compressor performance curve resembles the well-known hysteresis loop of other physical phenomena. Consequently, it has been labeled "hysteresis," although no time-dependency is involved. The resemblance is most striking for abrupt stall, because a distinct loop is formed.

This so-called hysteresis effect is also present when a change in the stall pattern occurs. The weight flow marking the inception of a pattern during the throttling process is lower than that marking the disappearance of the pattern when the flow is increased.

Stall-propagation rates. - Single-stage compressors exhibit a wider range of stall-propagation rate than multistage compressors. Most multistage compressors have stall patterns with propagation rates of about half the rotor speed; whereas, single-stage-compressor stall patterns range from approximately 10 to 85 percent of rotor speed. Both multistage and single-stage compressors usually exhibit one stall-propagation rate for all stall patterns, if the geometry of the stall pattern does not change. Exceptions to this generality have been mentioned in the discussion of single-stage stall data. No exceptions have been observed for multistage compressors.

Flow and pressure fluctuations. - Table 1(a) includes a column in which the flow fluctuation accompanying rotating stall in a single-stage compressor is listed in terms of the parameter $\Delta\rho V/\overline{\rho V}$. The magnitude of $\Delta\rho V/\overline{\rho V}$ varies from 0.6 to 2.14. No apparent correlation of the magnitude of the parameter with the size or number of stall zones can be obtained from the existing data on single-stage compressors.

The magnitude of $\Delta\rho V/\overline{\rho V}$ for blade wakes measured during design flow conditions may range from approximately 0.1 to 0.2. By comparison, the stall disturbance is rather severe.

3309

The magnitude of the parameter $\Delta\rho V/\overline{\rho V}$ in the inlet stage of a 10-stage research compressor was found to be similar to that observed in single-stage compressors. The stall data reported in reference 9 were obtained at 50, 60, and 70 percent of design speed. This operating region is the inlet-stage stall region indicated in figure 1. By locating hot-wire anemometers at various axial stages, the magnitude of the flow fluctuation throughout the entire compressor was measured. The data of figure 10 (ref. 9) show that the intensity of the flow-fluctuation level diminished appreciably after the fourth or fifth stage of the compressor.

CH-2

The pressure fluctuations peculiar to the abrupt stall that occurs along the stall-limit or surge line of multistage compressors are significant, because the attendant efficiency drop limits the useful engine operating range. In discussing figure 8, it was pointed out that an abrupt (40- or 50-percent) drop in pressure rise may occur when the compressor operating point reaches the stall-limit line. In reference 10 the drop in the discharge pressure and the pressure fluctuation accompanying abrupt stall were measured during stalled operation. At 82-percent design speed, when the compressor reached the stall-limit line, the mean level of the discharge pressure dropped 50 percent and the discharge pressure fluctuated 25 percent above and below the mean pressure level of the stalled operation.

Usually, the rotating-stall pattern observed when the stall-limit line is reached is a single-zone total-span stall. Because of the discontinuity in the performance curve, the stall is classified as abrupt.

Multistaging effect. - Experimental evidence has shown that data on propagation rate or number of stall zones in single-stage compressors do not apply to the rotating-stall characteristics of multistage units composed of these stages. In reference 11, the single-stage stall data for three identical stages composing a multistage compressor are compared with the multistage stall data. In order to explain the difference in the stall of stages tested individually and as a part of a multistage compressor, multistaging or interaction effects must be considered.

In multistage compressors, each stage operates in an aerodynamic environment determined to some extent by all the compressor stages. This environment comprises two multistaging or interaction effects:

(1) The radial gradients in axial velocity emanating from a stage at off-design operation, which may be sufficiently severe to cause a stall angle of attack over a part of the blade span of some downstream blade row

(2) The influence of low-flow or stall zones emanating from other stages of the compressor

3309

The result of the radial gradient in axial velocity might well be the development of a rotating-stall pattern considerably different from anything expected from single-stage stall data alone. In a series of tests conducted at the NACA Lewis laboratory on a production turbojet engine, it was observed that the stall characteristics of the compressor could be changed by altering the velocity profile entering the first blade row. Wire screens were used to partially block the flow into the compressor inlet. When the screens were arranged to produce circumferential variation in the flow, no appreciable changes in the stalling characteristics were evident. However, when radial gradients in the flow were achieved by partial blockage of the whole annulus of the inlet passage, the stalling characteristic of the compressor was altered significantly.

It was previously pointed out that, when rotating stall occurs in multistage compressors, the stall zones extend throughout the entire axial length of the compressor, as shown in figure 10. This means that each stage in the compressor will experience periodically recurring low-flow zones. If a stage or stages operate sufficiently near the stall point, the presence of the low-flow zones may cause stall angles of attack to occur when the blades pass through the stall zones.

Variation in stall patterns. - One of the objectives in presenting table I is to emphasize the great variety of stall patterns that have been observed. At present, there appears to be no way of cataloging the stall with respect to any type of compressor design. Among several commercial engines of one type, each of which was installed in the same test facility, the stall patterns were different, although the propagation rate remained essentially the same. Apparently, in this case the stall pattern was sensitive to such small changes in compressor geometry as would result from production tolerances. Such minute differences in geometry would be difficult to include in a theory that would predict the stall pattern from design data.

Effect of inlet temperature. - Stall frequency for a given stall pattern is proportional to actual engine speed and is independent of inlet temperature. The speed range over which a given stall pattern is

observed is a function of equivalent speed and, therefore, varies with inlet temperature. If the mechanical speed is changed to accommodate inlet temperature changes, so that the corrected speed $N/\sqrt{\theta}$ is constant, the stall frequency will vary with the mechanical speed. Consequently, it will be impossible to tune the natural frequency of the compressor blades to avoid a resonance with the fundamental stall disturbance or its harmonics over a range of compressor-inlet temperatures.

Blade Vibration Incurred during Rotating Stall

3309

Since rotating stall consists of one or more low-flow zones that rotate in the compressor annulus, usually at constant speed, the blade rows experience periodic aerodynamic forces as the low- and high-flow zones go by the blades. In reference 12 the fluctuating forces due to rotating stall were measured on the guide vanes and stators of a single-stage compressor. The blade-force fluctuations during rotating stall were comparable to the steady-state blade force measured during unstalled operation. This periodic force can therefore be a source of resonant blade vibration, where the frequency of the stall relative to the blades excites the blades. From current evidence, the compressor designer must always be concerned with the possibility of blade failure due to resonance between the blade frequency and the stall frequency.

CH-2 back

Single-stage compressors. - When the high stresses accompanying rotating stall are investigated, it is necessary first to determine the magnitude of the blade stresses when accompanied by rotating stall. An investigation of the effect of rotating stall on the blading of a single-stage compressor with a hub-tip radius ratio of 0.5 is reported in reference 13. The experimental results show that stall zones can excite blade vibration with resultant bending stresses sufficiently severe to cause blade failure. Fatigue cracks were observed in the aluminum stator blades. The blades were in resonance with the first two harmonics, as shown in figure 11, which is a plot of the ratio of the stall frequency to the natural bending frequency of the blade against rotor speed. Resonant vibrations occur at compressor speeds corresponding to the intersection of the stall-frequency line with horizontal lines representing resonance with the fundamental stall frequency and the first two harmonics.

Other fatigue failures of experimental single-stage compressors have been attributed to rotating stall. Stall data were not obtained for all the compressors that failed, but each compressor had been operated in the stalled region. Most of these compressors were stages of 0.5 hub-tip ratio. A fatigue failure with much shorter blades, where the hub-tip ratio was 0.72, was attributed to resonance between the relative fundamental stall frequency and the natural bending frequency of the blades (see ref. 14).

Multistage compressors. - Although several multistage-compressor failures at the NACA might be attributable to rotating stall, only one was sufficiently instrumented with strain gages and hot-wire anemometers to trace the failure directly to rotating stall. This investigation is reported in reference 15, in which a resonant-vibration condition was found in the first-stage rotor at approximately 62- and 70-percent design speed, as shown in figure 12. The strain-gage data indicated vibratory stresses of approximately ±13,500 and ±34,800 pounds per square inch, respectively, at these operating points, which were sufficient to cause fatigue failure of the aluminum blades. Typical high-stress vibration bursts caused by rotating stall as recorded from the strain gages are shown in figure 13 for 62-percent design speed.

3309

Methods of alleviating blade vibration. - To the axial-flow-compressor designer, the most serious result of rotating stall is blade failure. The theory of rotating stall developed thus far does not provide a method for predicting stall frequency for new designs and thus "tuning" blades out of dangerous blade-vibration frequencies. Furthermore, as mentioned in the discussion of the effect of inlet temperature on the stall frequency, it appears impossible to tune the blades for all the troublesome stall frequencies over the range of inlet temperature encountered in flight.

Inasmuch as it appears impossible to tune blades to avoid critical stall frequencies, other possible means of circumventing the blade-vibration problem must be considered. These include: (1) increasing the damping of the blades, (2) preventing the operation of any compressor blade row in a stalled attitude, and (3) disrupting the periodicity of the stall patterns so that a resonant condition between the blade frequency and the stall frequency cannot exist.

Increasing blade damping: The vibration-damping properties of a blade may be changed markedly by changing the blade material. Some materials exhibit greater damping properties than others; for example, stainless steel has better damping properties than aluminum. Blades fabricated from plastics are currently being investigated for their damping qualities. Obviously, the damping properties of a blade may also be improved by changing the mechanical design of the blade. Such modifications as altering the thickness-chord ratio, the aspect ratio, or the fillet radius may substantially increase the stiffness of blades. In addition, the method of blade attachment or blade support is a design variable that can alter the damping.

Preventing stalled attitude: As was mentioned in the INTRODUCTION, part-speed operation of multistage compressors causes the exit stages to choke, which limits the flow in the inlet stages and causes them to stall. Any bleed-off system that unchokes the rear stages will alleviate the stalling condition in the inlet stages and consequently will increase the stall-free range of the compressor.

Another possible method of increasing the stall-free range of a compressor is the use of adjustable guide vanes and stators. By this method, the angle of attack on the inlet rotors is diminished so that stall of the early stages is delayed. By increasing the angle of attack in the latter stages, the situation there is improved. This device is currently being used in one commercial multistage compressor as a means of improving the part-speed operation.

3309

Disrupting periodicity of stall: As a means of controlling the stalling characteristics of multistage compressors, adjustable inlet ramps or baffles have been used. Reference 16 reports the successful application of ramps at the hub that appreciably reduced the range of inlet-stage stall. The effect of the ramps or baffles is to reduce the inlet flow area. In engines tested with the baffles, rotating-stall patterns were no longer periodic, and the danger of blade failure due to resonant vibration was eliminated.

Theories of Rotating Stall

Several theoretical analyses have been proposed to predict the propagation rate of rotating stall. In order to identify the theories for discussion, each is referred to by the name of the first author. The notation is that used in the original references.

Emmons theory. - In the presentation of the Emmons theory in reference 17, the authors did not produce a result involving the prediction of stall-propagation rates. The purpose of the analysis was to establish the necessary conditions for the amplification of small disturbances of asymmetric flow corresponding to those observed in stall propagation.

The physical model analyzed was a cascade in which total-pressure losses were considered by introducing a parameter α, which consisted of the ratio of an isentropic flow area required to carry the inlet flow to the actual exit flow area. A linear dependence between this parameter and the tangent of the inlet flow angle of the cascade was assumed, and

the static pressure behind the blade row was considered constant. [NACA data (ref. 18) show that the static pressure behind the blade row varies appreciably.] Under certain circumstances, with the assumption of an initial small asymmetric disturbance at the cascade entrance, the analysis showed emphatically that the asymmetric flow will develop into a large disturbance.

As a result of the small-perturbation analysis, the authors of the Emmons theory concluded that the velocity of propagation is proportional to the wavelength. The Emmons theory suggests that an analysis involving finite disturbances will yield an answer to the size of the stall zones.

3309

Stenning theory. - The Stenning theory (ref. 19) extends the work of Emmons by more precisely defining the time-delay mechanisms on which the velocity or propagation of rotating stall depends. The principal time delays considered are the inertia of the fluid between the airfoils and the response of the boundary layer.

Theory: The author bases his analysis on the same model setup used by Emmons, where it was assumed that the effective outlet area of a channel representing the blade passage is reduced as a result of stall and that the static pressure remains constant behind the cascade. By considering small perturbations in velocity from the steady flow, a solution is obtained from momentum considerations within the cascade for the velocity of stall propagation in terms of inlet and exit angle, chord to wavelength ratio, and effective-area to inlet-area ratio.

Results and conclusions: According to Stenning, the equation for stall-propagation rate is

$$\frac{U_m}{c_x} = \frac{\cot \beta_1}{\alpha^2 \cos \beta_2 \left(\frac{L n \pi}{b} + \cos \beta_2\right)} \tag{1}$$

where

U_m stall-zone velocity relative to blade row

c_x axial velocity

β_1 relative inlet-air angle

α ratio of effective exit area to inlet area

β_2 relative outlet-air angle

L blade chord

n integers giving harmonics

b one-half wavelength of disturbance

3309

A carpet plot of equation (1) is shown in figure 14. The inlet-air angle β_1 and the outlet-air angle β_2 are treated as variables in the plot, and the ratio L/b is considered as a parameter. The ordinate of the graph is the stall-propagation parameter (ratio of relative stall speed U to rotor speed at mean blade height ωR) multiplied by the square of the area-ratio parameter α. Data from table I(a) are presented for comparison with the values predicted by theory. It should be pointed out that the configuration of the compressors did not closely correspond to Stenning's model. Because it is impossible to obtain reliable measurements of flow angles during stall, the inlet angle was calculated from the weight-flow data, and outlet angle could only be estimated. In addition, the ratio α is not a measurable quantity and could only be estimated as some value less than unity. (Stenning considers it to be 0.75.) Thus, only the inlet-air angle, the propagation-rate parameter, and the value of L/b could be considered to be "data" in the comparison. The carpet surfaces were drawn to extend over a wide range of possible exit and inlet flow angles. Assuming α to be 0.5, most experimental data of table I(a) are within the values predicted by the Stenning theory. These points are plotted on the interpolated L/b carpet plots indicated by the dashed lines. If α is taken as 0.75 as Stenning suggests, the data do not agree well with the theoretical values. These points do not appear in figure 14: It is not clear whether the inconsistency of the predicted values as compared with the data should be attributed to the limitations of the theory or to inappropriate application of the theory to compressors not similar to the model used by Stenning.

The theoretical results show that the velocity of stall propagation relative to the rotor increases with the size of the stall zone. A comparison with the test results of Emmons also shows this to be true; however, stall data taken from the compressors of table I(a) indicate this may not always be the case. The inclusion of a boundary-layer time delay in the analysis had the effect of decreasing the velocity of propagation of the stall zone and indicated that rotating stall is possible for a range of inlet angles.

Sears airfoil theory. - Sears has published two papers on the subject of stall propagation. The first paper (ref. 20) demonstrates that asymmetric flow can exist in a cascade. It also presents a picture of the model used by Sears for the second paper.

Theory: To represent a blade row in a compressor, an annulus of infinitely many blades of small chord was chosen. This configuration amounts to an actuator disk or vortex sheet simulating the blade row, as shown in figure 15. The flow pattern was considered steady with respect to a rotating coordinate system (rotating slower than rotor speed), so that the circulation distribution in the disk could be assumed to be a function of the y-coordinate of figure 15. An incompressible flow field was assumed, and small-perturbation theory was applied in the analysis. Since the blades of this rotor move relative to a fixed circulation distribution, they experience unsteady flow. Unsteady-flow theory states that airfoils will shed wakes at their trailing edges. The complete model, then, consists of a vortex sheet representing the rotor, an irrotational flow field representing the flow entering the rotor, and a rotational flow representing the wake leaving the rotor disk.

The model proposed by Sears differs from that used by Emmons in the following respects: Sears uses an actuator disk where Emmons used a cascade of finite length; and, while Emmons assumed constant static pressure at the exit of the cascade, Sears considers the vorticity following the blade row to be uniformly distributed and does not impose any restrictions on the pressure field.

The principal object of Sears in reference 20 was to develop the relation between the induced velocities at the rotor disk and the circulation distribution. Briefly, the manner of solving the problem was to divide the flow field into two parts, an irrotational part and a rotational part, and then to devise relations between the x and y velocity components in each type of flow (see fig. 15). The next step was to develop expressions for the circulation in terms of the velocity distribution. The induced inflow velocities at the actuator disk could then be calculated when the circulation distribution was known. To complete the solution, airfoil theory was used to relate the circulation function to the incidence angle of the blade row. This type of solution is called the "airfoil theory" to distinguish it from another analysis in which Sears substituted a so-called "channel theory."

Results and conclusions: Assuming a sinusoidal variation in the circulation distribution, Sears found that no solution could be obtained for a lift function that was linear with incidence angle, whether the airfoil is stalled or unstalled. However, when a phase angle was introduced between the lift and angle of attack so that the lift lagged the

angle of attack, a solution was found, which means that a permanent asymmetric flow pattern exists. The phase-angle concept used by Sears was based on the work presented in reference 21.

Emmons and Stenning studied the stability of an asymmetric pattern imposed on the flow field; Sears did not employ a stability study to show that an asymmetric flow could initiate itself under the conditions mentioned in the preceding paragraph.

3309

Sears channel theory. - Theory: The second paper by Sears (ref. 22) presents an extension of the first theory. The analysis involving the airfoil relations is repeated, but the final results are presented in a somewhat different manner. The phase angle Δ is related to the asymmetric-flow propagation rate and the properties of the cascade by the following formula:

$$\tan \Delta = b + \left(\frac{2k + b}{k^2}\right)(1 + b^2) \tag{2}$$

CH-3

where

b $\quad \frac{1}{\Phi}\left(\frac{h}{N} - \Phi \tan \beta\right)$

k $\quad \left(1 - \frac{h}{N}\right) \Big/ \Phi$

Φ flow coefficient

h/N ratio of stall-propagation rate to rotor speed, absolute frame of reference

β absolute inlet-air angle

The analysis also presents an equation that relates the slope of the lift curve m to the variables appearing in equation (2):

$$\frac{-m\sigma}{4} = \frac{1 + b^2}{k^2} \sqrt{1 + (b + k)^2} \cos \Delta \tag{3}$$

where σ is the solidity. The curves of the predicted asymmetric flow patterns for the airfoil theory (fig. 16(a)) result from the simultaneous solution of equations (2) and (3). It should be noted that the parameter k used by Sears is the ratio of the stall-propagation speed to the axial velocity.

In this theory, an analysis involving channel relations is substituted for the airfoil analysis. The so-called channel theory is based on empirical relations derived from cascade tests. The two principal relations of the channel theory state that the relative outlet-air angle is a function of the inlet angle and that the pressure rise across the blade row is independent of the inlet-air angle. The principal distinction between the airfoil theory and the channel theory is an inclusion of the total-pressure loss in the latter. Since stall implies large losses, it would seem at the outset that the channel theory would conform more nearly to the physics of the actual flow. The procedure of the analysis involving channel theory is similar to that of the airfoil theory previously outlined. Also, a phase angle δ comparable to the phase angle Δ of airfoil theory is introduced.

3309

Results and conclusions: Solutions for asymmetric flows satisfying the conditions of the problem were found for both types of analysis. The results of both airfoil and channel analyses are presented in reference 22 in graphical form and are reproduced here in figure 16. The ordinate and abscissa are labeled with Sears' notation and in terms of the vector-diagram terminology. The ordinate is the rotor tangential velocity relative to the tangential velocity of the stall propagation divided by the axial velocity, and the abscissa is simply the tangent of the mean relative inlet-air angle β'. The ordinate may also be expressed as the tangent of the swirl angle of the asymmetric flow pattern relative to the rotor.

For the airfoil analysis, solutions were found for a considerable range of phase angles including zero. In reference 20 Sears assumed a small swirl angle and did not obtain a solution for zero phase angle; but in reference 22 the swirl angle considered was larger, and a solution resulted for zero phase angle. However, the zero-phase-angle solutions do seem out of the range of the compressor data and consequently are of little interest.

The channel-analysis solution shown in figure 16(b) indicates that asymmetric flow patterns are possible for a wider range of conditions than was evident from the airfoil analysis. For flow conditions comparable to actual compressor data, asymmetric flow solutions are possible with zero phase lag. The equation for the phase angle δ used in the channel analysis is

$$\tan \delta = \frac{1 + b^2 - k^2}{b(b + k)^2 + 2k + b} \tag{4}$$

where k and b are the same parameters used in the airfoil analysis. In the channel-theory analysis, the slope of the pressure-rise curve plays a role analogous to that of the slope of the lift curve in the

airfoil theory. The expression for the slope m of the pressure-rise curve is

$$\frac{m}{\sqrt{1 + b^2}} = 1 + (b + k)^2 \tag{5}$$

The curves of the asymmetric flow patterns for the channel theory shown in figure 16(b) result from simultaneous solution of equations (4) and (5).

3309

Experimental comparison: In reference 23, experimental rotating-stall data from several single-stage compressors are compared with the results of Sears' theory. Both the airfoil and channel analyses were tried; however, it was found that, in using the channel analysis, the phase angle δ was consistently negative. To the authors of reference 23, a negative phase angle seemed inconsistent with physical interpretation, and for this reason the comparison was limited to the airfoil analysis, where the computed phase angle Δ was positive for all the data used.

CH-3 back

The points in figure 17 represent experimental data superimposed on the theoretically derived curves. The data points for each stall-propagation rate lie along curves of approximately constant phase angle. Furthermore, if the phase angle is plotted as a function of the stall-propagation rate, a correlation exists, as shown by figure 18. The stall-propagation rate diminishes as the phase angle increases, which seems to be in accord with the generally accepted mechanism of stall propagation. Also apparently involved in the process of stall propagation is a time constant that governs the propagation rate. The greater the time constant, the slower the propagation rate. The correlation of phase angle and stall-propagation rate of figure 18 does not permit the prediction of stall-propagation rates, since the phase angle cannot be determined from design data.

Marble theory. - A recent analysis of rotating stall is presented by Marble in reference 24. In this theory, an expression for the stall-propagation rate and the peripheral extent of the stall zone is developed.

Theory: The model employed in the analysis is similar to that used by Sears in his channel theory, in that the blade row is simulated by means of an actuator disk across which pressure and fluid velocity change discontinuously. Using an actuator disk to represent the blade row without the introduction of a phase angle prohibits Marble from introducing inertia effects within the blade row. The Stenning analysis demonstrated

the significance of inertia in the blade passage and its effect on stall-propagation velocity. Experimental characteristics of a cascade were utilized to prescribe the change in pressure and velocity across the actuator disk. The pressure-rise curve across the disk (based on experimental evidence) was assumed to be a linear function of the air inlet angle for unstalled flow, but for stalled flow the pressure rise was assumed to drop discontinuously to zero. In choosing this discontinuous lift curve, Marble more fully described the performance of the channel in comparison with the Sears linearized lift curve. Consequently, Marble was able to obtain solutions for the peripheral extent of the stall zone as well as the stall-propagation rate. 3309

The expression for stall-propagation rate differs from that of Sears, in that a phase angle was not included in Marble's equation. By considering the pressure-rise parameter to be a function of the air inlet angle and to behave as described, the increased losses attending stall were included in the analysis. Marble simulated the asymmetric flow in his model by considering a stall zone of variable circumferential width to exist in the actuator disk. It was assumed that small-perturbation theory could be applied to describe the influence of rotating stall on the velocity and pressure. The coordinate system used in the analysis was selected to rotate at stall frequency so that the steady-flow equations would apply.

In order to describe the flow field upstream and downstream of the actuator disk, it was assumed that the pressure and angle perturbations vanished far upstream and were at most a constant value far downstream. When these upstream and downstream conditions were known, as well as the pressure rise and flow angle for both the stalled and unstalled region of the actuator disk, the problem was to find a stall zone of suitable size and propagation rate to satisfy these flow conditions. First of all, Marble solved the problem for a "simple cascade," one in which deviation angle remained constant for all values of incidence angle. A very simple expression for stall-propagation rate and circumferential extent of the stall zone was obtained.

The equation for stall-propagation speed is

$$\frac{\omega R}{u} = \csc 2\beta_1 \tag{6}$$

where

ωR stall-propagation speed

u axial velocity

β_1 relative inlet-air angle

The peripheral extent of the stall zone α is given by the following expression:

$$\alpha = \frac{1}{2} - 4(\beta_1^* - \beta_1) \csc 2\beta_1 \left(\frac{\frac{1}{2}\rho u^2}{\Delta p^*}\right) \tag{7}$$

where

3309

β_1^* relative inlet-air angle at stall

ρ density

Δp^* static-pressure rise at stall

After solving the problem for the simple cascade, a solution was completed with "general cascade characteristics." For the general characteristics the pressure rise across the cascade and the deviation angle are considered functions of the incidence angle. This is a more realistic representation of an actual cascade. Expressions were developed for the stall-propagation rate and the circumferential extent of the stall zone that were more complicated than for the simple case. The expression for the stall-propagation rate based on general cascade characteristics is

$$\frac{\omega R}{u} = \left(1 + a \frac{\cos^2\beta_1}{\cos^2\beta_2}\right) \csc 2\beta_1 \tag{8}$$

where a is the ratio of outlet-angle perturbation to inlet-angle perturbation, and β_2 is the relative outlet-air angle.

The peripheral extent of the stall zone α for the more general cascade model is given by

$$\alpha = \frac{1}{2} - 4(\beta_1^* - \beta_1) \frac{\frac{1}{2}\rho u^2}{\Delta p^*} \left[\left(1 + a \frac{\cos^2\beta_1}{\cos^2\beta_2}\right) \csc 2\beta_1 + \frac{b}{8}\right] \tag{9}$$

where b is a constant in the expression for pressure rise across the cascade.

Marble concluded that the ratio a is generally a small positive quantity, and that variations in the deviation angle prescribed by the "general cascade characteristics" would not alter the stall-propagation

rate predicted from the simple-cascade equation. Consequently, variations in the deviation angle do not influence the stall-propagation rate. This conclusion agrees with most experimental evidence. As has been pointed out in the general discussion of rotating-stall characteristics, stall-propagation rate remains constant over a wide range of weight-flow conditions in the stall region.

Experimental comparison: Because of the lack of unclassified experimental rotating-stall data, Marble was able to use the data from only one compressor to compare the experimental stall-propagation rates with predictions from his theory. Stall data from several NACA single-stage compressors were compared with propagation rates predicted by Marble. Included in the comparison were data on total-span rotating-stall patterns in order to resemble more closely the geometry of the stall zone used in Marble's model. Equation (6), which is the solution for the simple cascade, was used to calculate the propagation rates. The equation was modified so that the guide-vane turning and the stall-propagation-rate parameter of table I could be used. 3309

The ordinate of figure 19 is the absolute stall-propagation-rate parameter, and the abscissa is the inlet-air-flow angle computed at the mid-radius station. Good agreement was obtained between Marble's predicted propagation rate and the data from compressor 4 of table I(a), but the comparison with the other data on the curve was poor.

As is shown in figure 19, Marble's theory predicts that, for proper inlet angle and counterrotating guide-vane turning, the stall zones should rotate in the opposite direction (absolute coordinate system) to rotor rotation. Experimental evidence has shown that this does not occur. The sense of the stall-zone rotation is the same for counterrotating guide-vane turning as for conventional guide vanes.

Remarks on stall theories. - In order to compare the results of the Stenning, Sears, and Marble theories, the phase angle introduced by Sears in the channel theory is considered to be zero. For this condition the results show that the Sears and Marble theories are identical in their expression of propagation rate. A comparable result from Stenning's analysis indicates that his predicted propagation rate is twice that of the other two investigators.

Experimental evidence shows that the radial extent of the stall zones varies considerably, but none of the existing theories include radial effects. All the theories apply to a single blade row. There is considerable doubt whether the theories can be applied to a single stage including guide vanes, rotor, and stators, or whether the theories can be further extended to the more complicated case of the multistage compressor.

INDIVIDUAL BLADE STALL

A type of stall in which all the blades around the compressor annulus stall simultaneously, without the occurrence of a stall-propagation mechanism, has been observed. The circumstances under which individual blade stall is established rather than rotating stall are unknown at present. It appears that the stalling of a blade row generally manifests itself in some type of propagating stall and that individual blade stall is an exception.

3309

STALL FLUTTER

Distinction between Stall and Classical Flutter

Before discussing flutter, the distinction between classical flutter and stall flutter should be made clear. Classical flutter is a coupled torsional-flexural vibration that occurs when the free-stream velocity over a wing or airfoil section reaches a certain critical velocity. For wings of low frequency, this critical velocity can be calculated. According to reference 25, classical flutter cannot occur with compressor or turbine blades, because the critical velocity required would be unreasonably high. Stall flutter, on the other hand, is a phenomenon that has been explained on the basis of the behavior of the lift characteristic at stall.

Mechanism of Stall Flutter

At stall the lift may decrease sharply as shown in figure 20, where a typical lift characteristic is plotted as a function of angle of attack. According to reference 25, the aerodynamic damping of a blade is a function of the partial derivative of lift with respect to angle of attack. When this derivative becomes negative, stall flutter is likely to take place. That is, a reduction in the aerodynamic damping allows the airstream to feed energy into the blades and produce a self-excited oscillation.

Another explanation for stall flutter is presented in reference 26, in which the airfoil vibration is considered to result from a system of Kármán vortices in the airfoil wake. Whenever the frequency of these vortices coincides with a natural frequency of the airfoil, flutter will occur.

The concept of an aerodynamic hysteresis was developed by Studer to show that energy could be absorbed from the airstream to promote blade vibration (ref. 21). It was hypothesized in this explanation of stall flutter that separation at the stall point was delayed until the oscillating blade reached its position of maximum angle of attack, and then the nonseparated flow was not established until the blade reached its minimum angle of attack. The maximum and minimum angles of attack were considered to be above and below the stalling angle of attack, respectively, giving rise to the hysteresis effect.

Brief literature survey. - The general theory of flutter, even for an isolated airfoil in a potential flow, is not a very elementary mathematical problem. The problem becomes much more complicated when flutter in a cascade of airfoils is considered, because the effects of the geometry of the cascade must be included in the theory in order to account for the interference effects between the blades. Much of the early work on flutter theory was devoted to airfoils with but one degree of freedom, a torsional oscillation or vibration.

However, in the type of cascade that more accurately represents conditions in a turbine or compressor, according to reference 27, the stall-flutter oscillations may have at least two degrees of freedom, torsional oscillation and flexural bending. This latter type of flutter is treated in reference 28. The experimental observations of such a cascade showed that either torsional or flexural vibrations were obtained, depending upon the velocity of the airstream; and the frequencies of each mode were practically identical. The two modes of vibration were not coupled as in the case of the classical flutter for wings. The flutter or bending self-excited vibrations were explained as the result of variations in the angle of incidence, which in turn caused the lift force to vary. However, the lift force always lags the elastic force by a phase angle. The forces acting on a blade are shown in figure 21. Whenever the component of the force parallel to the damping force exceeds the damping force, a self-excited vibration of the blade takes place.

The authors of reference 28 observed that self-induced vibrations occurred whenever the free-stream velocity entering the cascade reached a critical value. They found that the critical velocity could be determined from a dimensionless velocity coefficient that was shown to be a function of the geometry of the cascade (stagger angle and angle of incidence) and the angle between the direction of the blade displacement and the blade chord.

In a more recent paper (ref. 29) only one degree of freedom, a flexural oscillation, is admitted as a possible mode of stall-flutter

vibration in a two-dimensional cascade representing compressor blades. A different interpretation of the mechanism of flexural vibration is also presented in this paper. After rather extensive experimental observations, it was concluded that no appreciable changes in lift were observed for varying positions of the cascade in a separated-flow field; consequently, no self-excited flexural vibrations could be established by this mechanism as proposed in reference 28. However, it was observed that, when an airfoil is translated in separated flow, the lift force will feed energy into the blade and thus sustain a self-excited motion.

3309

Other more mathematically complicated treatments of flutter in cascades have been considered in papers such as reference 30. Phase differences in the mode of the vibration between the blades in the cascade are considered mathematically in this paper.

Extension of flutter theory to compressor blades brings up a most complicated problem, because not only cascading effects but also centrifugal effects must be considered. The cascading or interference effects on flutter are not well understood for the compressor.

CH-4

Experimental evidence. - Although stall flutter has been considered to be a cause of compressor blade failure, there is insufficient experimental evidence to support this view. According to reference 27, conditions where flutter exists do not correspond to operation at high angles of incidence and low speed, the mode of operation that has caused compressor blades to fail. The measurements required of rotating rigs in order to investigate the possibility of stall flutter are almost impossible to make with current research techniques.

CONCLUSIONS

Aerodynamic Aspect

The stalled operation of a compressor may be described as the degeneration of compressor performance accompanied by serious flow separation in the flow passages. Three distinctively different phenomena may occur during stalled operation: (1) rotating stall, (2) individual blade stall, or (3) stall flutter. The first two are aerodynamic effects and the third an aeroelastic effect. Rotating stall has been found to be the most prevalent type of stall phenomenon. A large amount of data is available which demonstrates that poor performance of compressors may be directly attributable to the occurrence of rotating stall.

In this chapter, rotating-stall patterns are cataloged according to their effect on the performance characteristic of single-stage compressors. A progressive rotating stall is associated with a smooth continuous performance characteristic; and an abrupt rotating-stall pattern, with a discontinuous performance characteristic that is coincident with an abrupt drop in compressor pressure. Similar types of stall are observed in multistage compressors; however, the discontinuous performance characteristic for a multistage unit is defined here as complete compressor stall. The pressure rise across a multistage compressor may drop as much as 50 percent after complete compressor stall is initiated. This stalling condition is particularly important, because it determines the limit of useful operation of the compressor (the surge limit or stall limit shown in fig. 1). 3309

With a single blade row as a model, several theories have been developed showing the existence of asymmetric flow and in some cases predicting the rotative speed and the size of the pattern. The results of the theories are in poor agreement with experimental data.

Vibration Aspect

Although rotating stall seems to be the most significant cause of blade vibration in compressors, it must be recognized from cascade data that stall flutter may be a possible cause of blade vibration. No experimental evidence is presently available to show that stall flutter has been the cause of compressor blade excitation. If the rotating-stall frequency coincides with the natural bending frequency of the blade or a harmonic thereof, a resonant condition will result that may cause blade failure. Other possible causes of blade vibration include: (1) resonance of the rotor blade frequency with the frequency of wakes from stators or supporting struts, and (2) mechanical failures resulting from a resonance between the natural bending frequency of the blade and transmitted vibrations emanating from the gearing or shafts. These effects are considered unimportant compared with the problem of rotating stall.

REFERENCES

1. Cheshire, L. J.: The Design and Development of Centrifugal Compressors for Aircraft Gas Turbines. War Emergency Issue No. 12 pub. by Inst. Mech. Eng. (London), 1945. (Reprinted in U.S. by A.S.M.E., Jan. 1947, p. 438.)

2. Schulze, Wallace M., Erwin, John R., and Westphal, Willard R.: Investigation of an Impulse Axial-Flow Compressor Rotor over a Range of Blade Angles. NACA RM L50F27a, 1950.

3. Grant, Howard P.: Hot Wire Measurements of Stall Propagation and Pulsating Flow in an Axial Flow Inducer-Centrifugal Impeller System. Pratt and Whitney Res. Rep. No. 133, June 1951.

4. Compressor and Turbine Research Division: Aerodynamic Design of Axial-Flow Compressors. Vol. II. NACA RM E56B03a, 1956.

5. Ossofsky, Eli: Constant Temperature Operation of the Hot-Wire Anemometer at High Frequency. Rev. Sci. Instr., vol. 19, no. 12, Dec. 1948, pp. 881-889.

6. Laurence, James C., and Landes, L. Gene: Auxiliary Equipment and Techniques for Adapting the Constant-Temperature Hot-Wire Anemometer to Specific Problems in Air-Flow Measurements. NACA TN 2843, 1952.

7. Lowell, Herman H.: Design and Application of Hot-Wire Anemometers for Steady-State Measurements at Transonic and Supersonic Airspeeds. NACA TN 2117, 1950.

8. Huppert, Merle C.: Preliminary Investigation of Flow Fluctuations during Surge and Blade Row Stall in Axial-Flow Compressors. NACA RM E52E28, 1952.

9. Huppert, Merle C., Costilow, Eleanor L., and Budinger, Ray E.: Investigation of a 10-Stage Subsonic Axial-Flow Research Compressor. III - Investigation of Rotating Stall, Blade Vibration, and Surge at Low and Intermediate Compressor Speeds. NACA RM E53C19, 1953.

10. Delio, G. J., and Stiglic, P. M.: Experimental Investigation of Control Signals and the Nature of Stall and Surge Behavior in a Turbojet Engine. NACA RM E54I15, 1954.

11. Iura, T., and Rannie, W. D.: Observations of Propagating Stall in Axial-Flow Compressors. Rep. No. 4, Mech. Eng. Lab., C.I.T., Apr. 1953. (Navy Contract N6-ORI-102, Task Order 4.)

12. Johnson, Donald F., and Costilow, Eleanor L.: Experimental Determination of Aerodynamic Forces Normal to the Chord Due to Rotating Stall Acting on Compressor Blading. NACA RM E54F14, 1954.

13. Huppert, Merle C., Johnson, Donald F., and Costilow, Eleanor L.: Preliminary Investigation of Compressor Blade Vibration Excited by Rotating Stall. NACA RM E52J15, 1952.

14. Graham, Robert W., and Prian, Vasily D.: Rotating Stall Investigation of 0.72 Hub-Tip Ratio Single-Stage Compressor. NACA RM E53L17a, 1954.

15. Huppert, Merle C., Calvert, Howard F., and Meyer, André J.: Experimental Investigation of Rotating Stall and Blade Vibration in the Axial-Flow Compressor of a Turbojet Engine. NACA RM E54A08, 1954.

16. Lucas, James G., Finger, Harold B., and Filippi, Richard E.: Effect of Inlet-Annulus Area Blockage on Over-All Performance and Stall Characteristics of an Experimental 15-Stage Axial-Flow Compressor. NACA RM E53L28, 1954.

17. Emmons, H. W., Pearson, C. E., and Grant, H. P.: Compressor Surge and Stall Propagation. Trans. A.S.M.E., vol. 77, no. 4, May 1955, pp. 455-467; discussion, pp. 467-469.

18. Costilow, Eleanor L., and Huppert, Merle C.: Rotating-Stall Characteristics of a Rotor with High Hub-Tip Radius Ratio. NACA TN 3518, 1955.

19. Stenning, Alan H., Kriebel, Anthony R., and Montgomery, Stephen R.: Stall Propagation in Axial-Flow Compressors. NACA TN 3580, 1956.

20. Sears, W. R.: On Asymmetric Flow in an Axial-Flow Compressor Stage. Jour. Appl. Mech., vol. 20, no. 3, Sept. 1953, pp. 442-443.

21. Mendelson, Alexander: Effect of Aerodynamic Hysteresis on Critical Flutter Speed at Stall. NACA RM E8B04, 1948.

22. Sears, W. R.: A Theory of "Rotating Stall" in Axial Flow Compressors. Grad. School Aero. Eng., Cornell Univ., Ithaca (N.Y.). (Contract No. AF 33 (038)-21406.)

23. Graham, Robert W., and Prian, Vasily D.: Experimental and Theoretical Investigation of Rotating-Stall Characteristics of Single-Stage Axial-Flow Compressor with Hub-Tip Ratio of 0.76. NACA RM E53I09, 1953.

3307

24. Marble, Frank E.: Propagation of Stall in a Compressor Blade Row. Tech. Rep. No. 4, GALCIT, Jan. 1954. (Office Sci. Res., Air Res. and Dev. Command Contract AF 18(600)-178.)

25. Pearson, H.: The Aerodynamics of Compressor Blade Vibration. Fourth Anglo-American Aero. Conf. (London), Sept. 15-17, 1953, pp. 127-162; discussion, pp. 162A-162J. (Publ. by Roy. Aero. Soc. (London).) (Summarized in The Engineer, Oct. 9, 1953, pp. 473-476.)

26. Bollay, William, and Brown, Charles D.: Some Experimental Results on Wing Flutter. Jour. Aero. Sci., vol. 8, no. 8, June 1941, pp. 313-318.

27. Howell, A. R., and Carter, A. D. S.: Note on Stalling Flutter of Compressor Blades. Memo. No. 131, British N.G.T.E., Oct. 1951.

28. Bellenot, C., and D'Epinay, J. Laline: Self-Induced Vibrations of Turbo-Machine Blades. Brown-Boveri Rev., vol. XXXVII, no. 10, Oct. 1950, pp. 368-376.

29. Schnittger, Jan R.: Single Degree of Freedom Flutter of Compressor Blades in Separated Flow. Jour. Aero. Sci., vol. 21, no. 1, Jan. 1954, pp. 27-36.

30. Sisto, F.: Stall-Flutter in Cascades. Jour. Aero. Sci., vol. 20, no. 9, Sept. 1953, pp. 598-604.

31. Lewis, George W., Jr., Schwenk, Francis C., and Serovy, George K.: Experimental Investigation of a Transonic Axial-Flow-Compressor Rotor with Double-Circular-Arc Airfoil Blade Sections. I - Design, Over-All Performance, and Stall Characteristics. NACA RM E53L21a, 1954.

32. Serovy, George K., Robbins, William H., and Glaser, Frederick W.: Experimental Investigation of a 0.4 Hub-Tip Diameter Ratio Axial-Flow Compressor Inlet Stage at Transonic Inlet Relative Mach Numbers. I - Rotor Design and Over-All Performance at Tip Speeds from 60 to 100 Percent of Design. NACA RM E53I11, 1953.

3309

TABLE I. - SUMMARY OF ROTATING-STALL DATA

(a) Single-stage compressors

Type of velocity diagram	Compressor number	Hub-tip radius ratio	Number of stall zones	Propagation rate, $\frac{\text{Stall speed, abs}}{\text{Rotor speed}}$	Weight-flow fluctuation during stall, $\Delta\rho V/\overline{\rho V}$	Radial extent of stall zone	Type of stall	Reference
Symmetrical	1	0.50	3 4 5	0.420 .475 .523	1.39 2.14 1.66	Partial	Progressive	8
	2	0.90	1	0.305	1.2	Total	Abrupt	
	3	0.80	8 1	0.87 .36	0.76 1.30	Partial Total	Progressive Abrupt	
	4	0.76	7 8 5 3 4 3 2	0.25 .25 .25 .23 .48 .48 .49	2.14 1.10 1.10 2.02 1.47 2.02 1.71	Partial Total	Progressive	23
	5	0.72	6,8	0.245	0.71 to 1.33	Total	Progressive	14
Free vortex	6	0.60	1 2 1	0.48 .36 .10	0.60 .60 .68	Partial Partial Total	Progressive Progressive Abrupt	11
Solid body	7	0.60	1 1	0.45 .12	0.60 .65	Partial Total	Progressive Abrupt	
Vortex transonic	8	0.50	3 2	0.816 .634	---- ----	Partial Total	Progressive Progressive	31
	9	0.50	1	0.565	----	Total	Abrupt	--
	10	0.40	2	-----	----	Partial	Progressive	32

3309

TABLE I. - Concluded. SUMMARY OF ROTATING-STALL DATA

(b) Multistage compressors

Compressor number	Number of stall zones	Propagation rate, $\frac{\text{Stall speed, abs}}{\text{Rotor speed}}$	Radial extent of stall zone	Periodicity	Type of stall	Reference
1	3 4 5 6 7	0.57	Partial	Steady	Progressive	Unpublished data
2	4 5 6	0.55	Partial	Intermittent	Progressive	15
3	1	0.48	Partial	Steady	Progressive	Unpublished data
4	1 2 3 4	0.57	Partial	Steady	Progressive	
5	1 2 3 4 5	0.57	Partial	Intermittent	Progressive	16
6	1	0.47	Total	Steady	Abrupt	Unpublished data
7	1	0.43	Total	Steady	Abrupt	10
8	1	0.53	Total	Steady	Abrupt	16

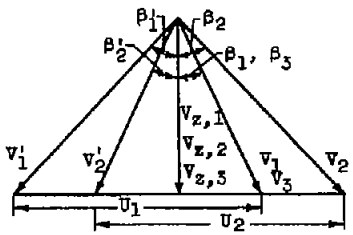

Compressors 2, 4, 5, and 10

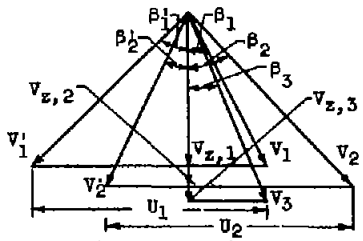

Compressors 1 and 3

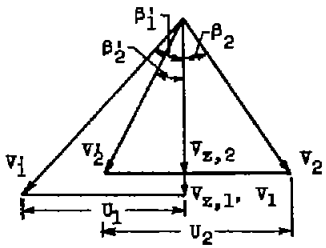

Compressor 8

TABLE II. - SINGLE-STAGE-COMPRESSOR DESIGN DATA

Compressor (table I(a))	Hub-tip ratio	O.D., in.	I.D., in.	Design tip speed, ft/sec	V_1/U_t	V_1'/U_t	V_2/U_t	V_2'/U_t	V_3/U_t	$\frac{V_{z,1}}{U_t}$	$\frac{V_{z,2}}{U_t}$	$\frac{V_{z,3}}{U_t}$	U_1/U_t	U_2/U_t	β_1, deg	β_1', deg	β_2, deg	β_2', deg	β_3, deg
1	0.50	14	7	777.5	0.706	0.846	0.856	0.740	0.745	0.669	0.694	0.718	0.749	0.763	18.9	37.9	36.0	20.48	15.9
2	.90	14	12.6	------	.725	.9475	.9475	.725	.725	.670	.670	.670	.950	.950	22.88	45	45	22.68	22.68
3	.80	14	11.2	826	.635	.915	.941	.670	.701	.600	.637	.670	.898	.898	18.95	49.12	47.38	17.92	17.1
4	.76	14	10.62	790	.9471	.9585	.9585	.9471	.9471	.7328	.7328	.7328	.8807	.8807	20.30	39.70	39.70	20.30	20.30
5	.72	14	10.09	790	.8273	.9363	.9363	.9273	.9273	.7213	.7213	.9213	.8594	.8594	20.49	39.25	39.25	20.49	20.49
6	.60	--	-----	------	------	------	------	------	------	------	------	------	------	------	-----	-----	-----	-----	-----
7	.60	--	-----	------	------	------	------	------	------	------	------	------	------	------	-----	-----	-----	-----	-----
8	.50	14	7	1000	.60	.92	.65	.67	------	.80	.858	------	.698	.698	0	49.30	30.67	33.40	-----
9	.50	18	9	1000	------	------	------	------	------	------	------	------	------	------	-----	-----	-----	-----	-----
10	.40	14	5.6	1000	.647	.953	.782	.743	------	.647	.647	------	.7597	.7597	0	47.3	31.9	28.9	-----

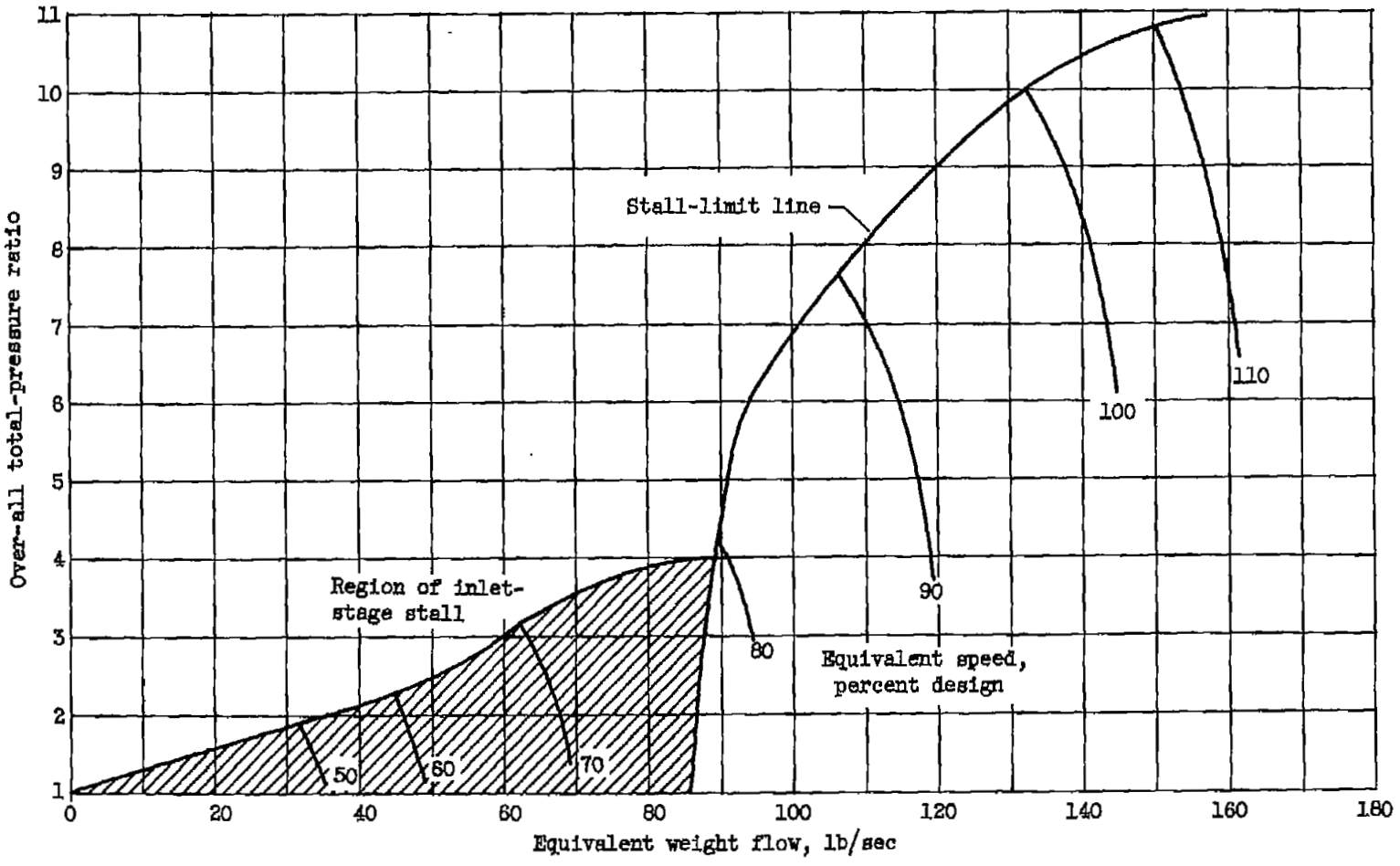

Figure 1. - Over-all performance of a multistage compressor.

3309

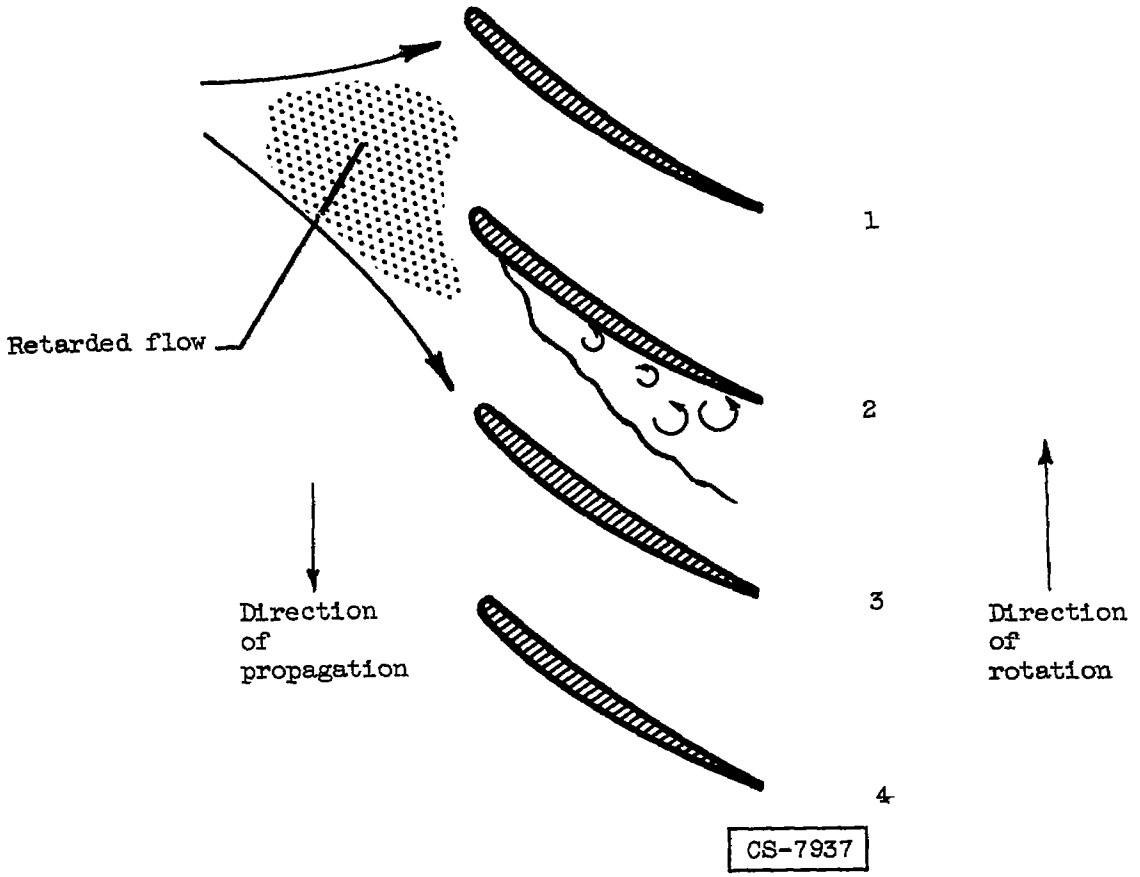

Figure 2. - Propagating stall in a cascade.

3309

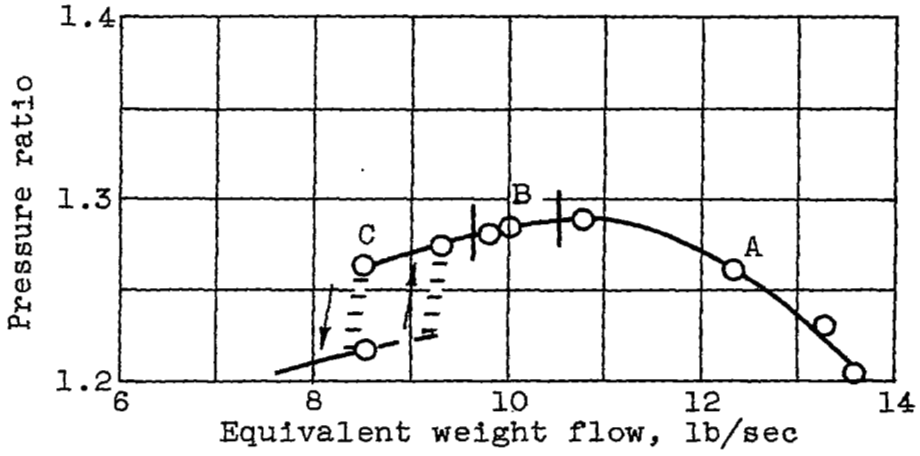

Figure 3. - Performance of compressor as operation point varies from unstalled to stalled.

CH-5 back

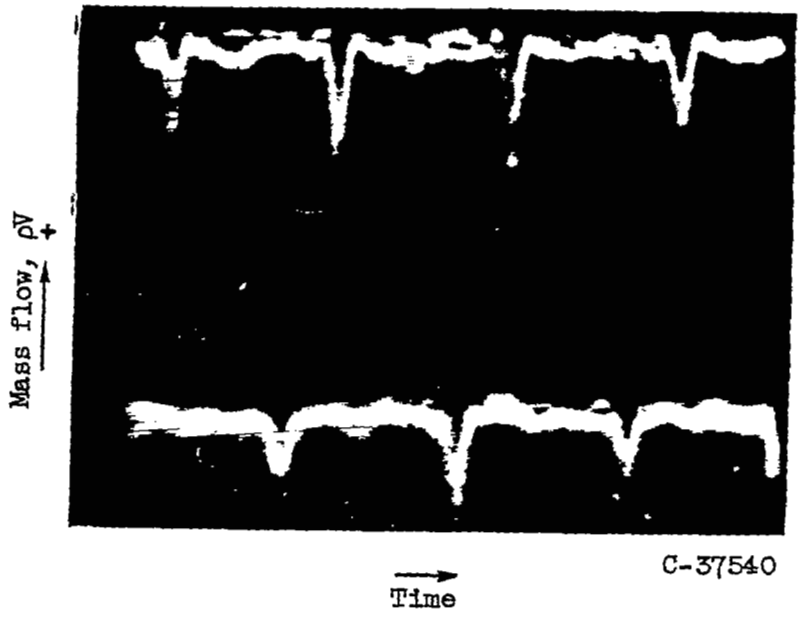

Figure 4. - Oscillograms of blade wakes.

[redacted]

3309

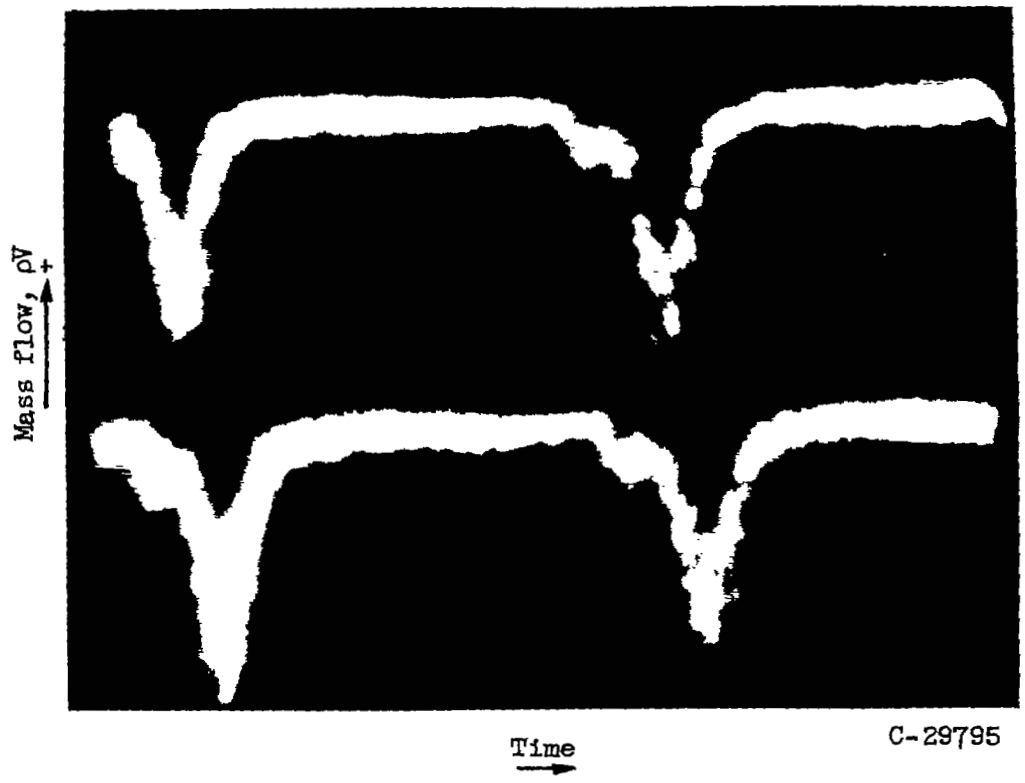

Figure 5. - Typical rotating-stall oscillogram

[redacted]

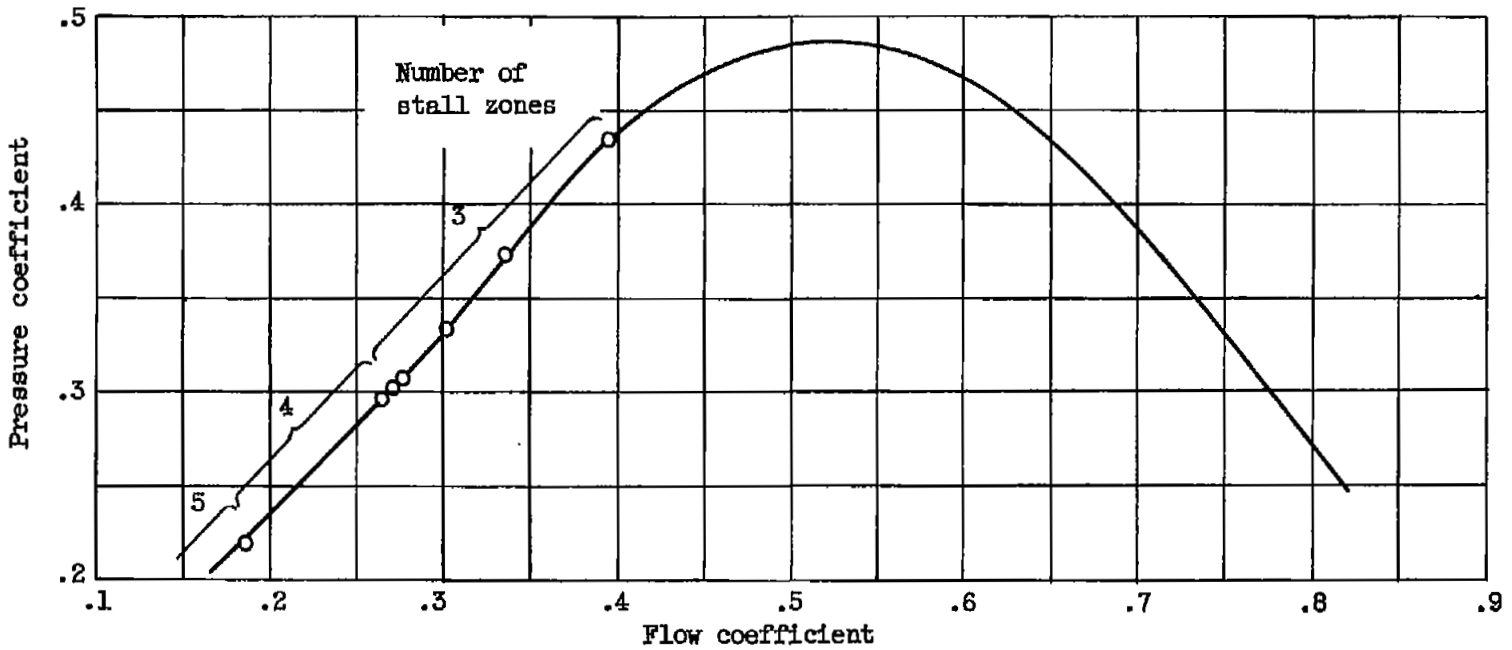

Figure 6. - Performance of single-stage compressor showing conditions at which rotating stall occurs.

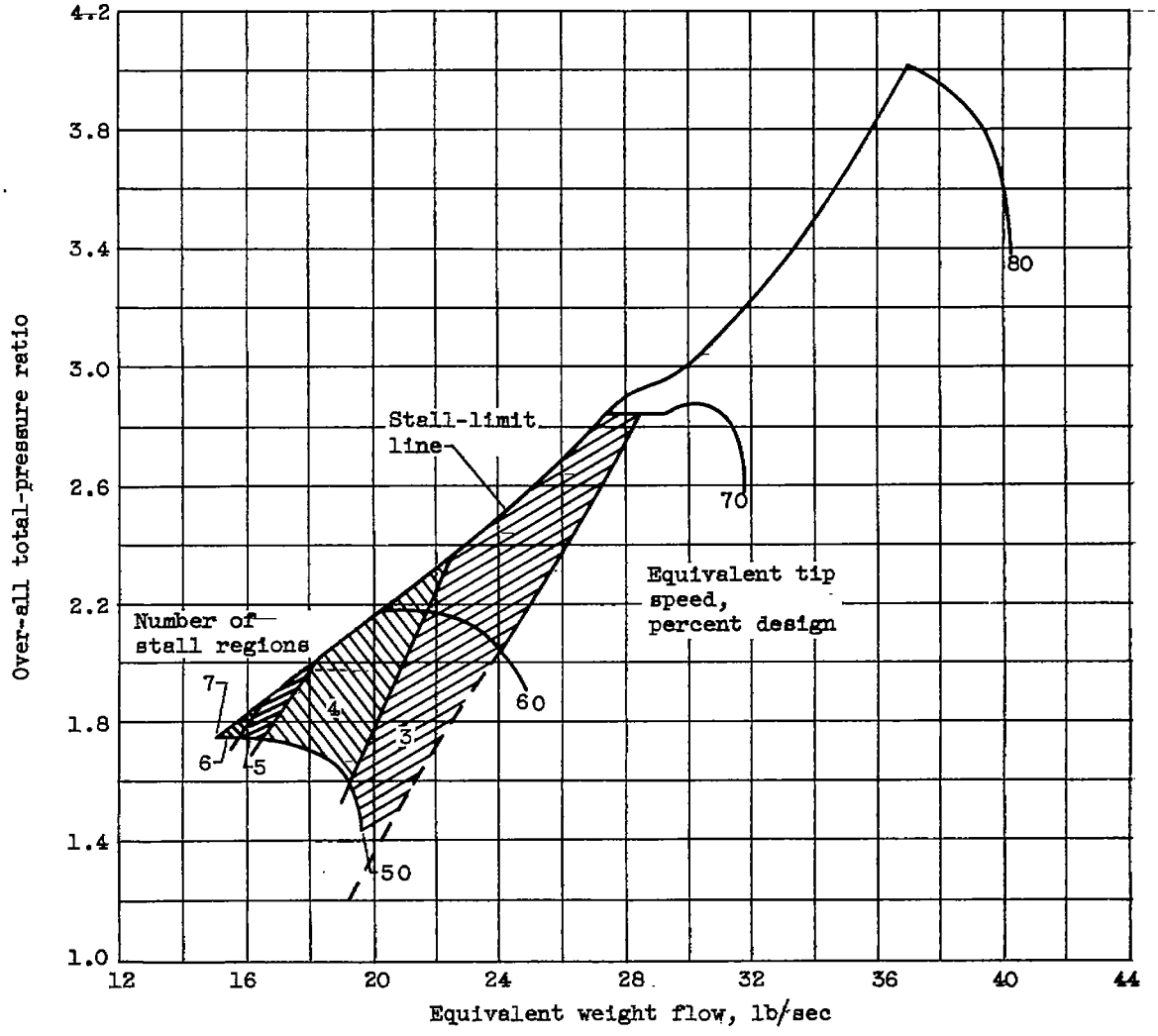

Figure 7. - Performance of multistage compressor showing conditions at which rotating stall occurs.

3309

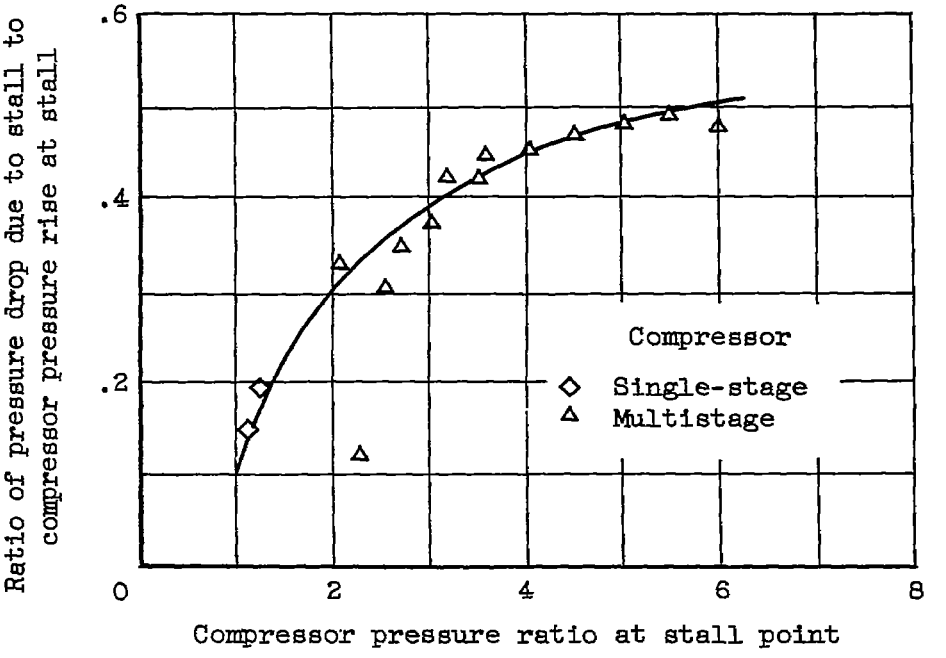

Figure 8. - Correlation of pressure drop at stall with compressor pressure ratio at stall.

3309

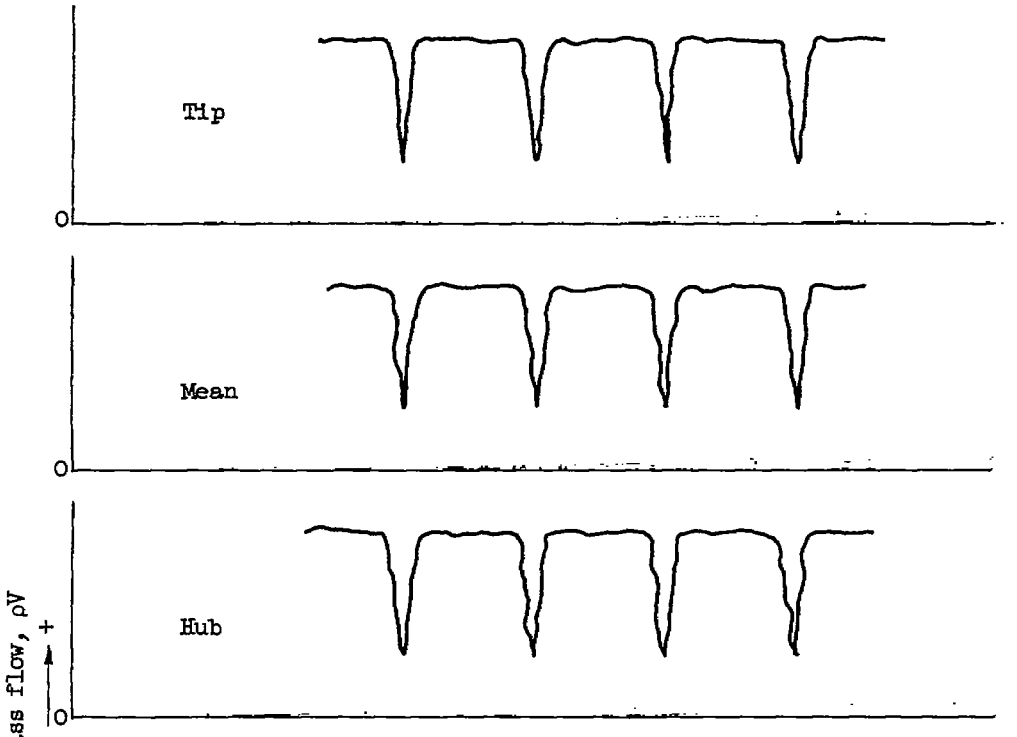

(a) Total-span stall.

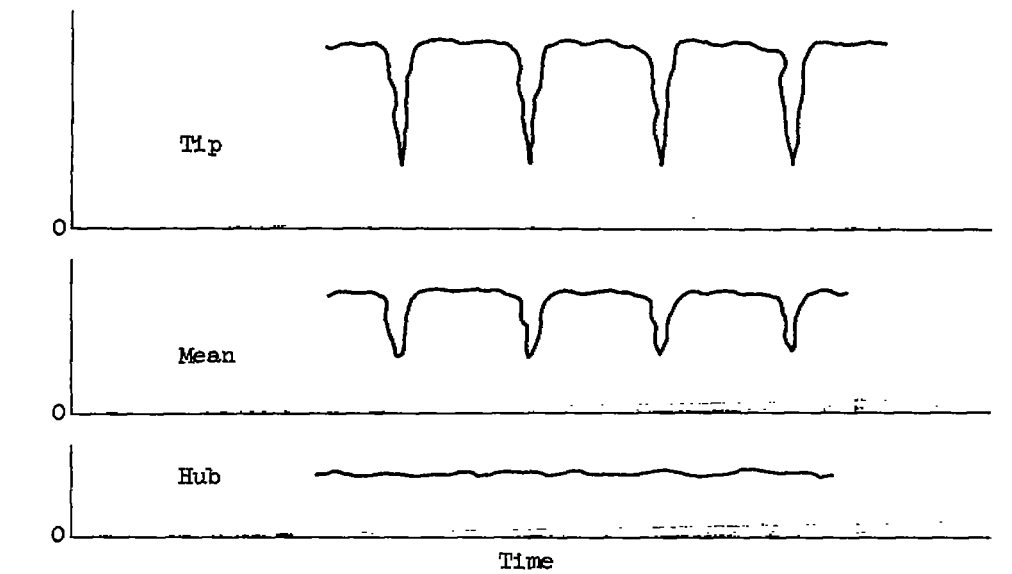

(b) Partial-span stall.

Figure 9. - Sketches of typical oscilloscope traces of total- and partial-span rotating stall.

3309

CH-6

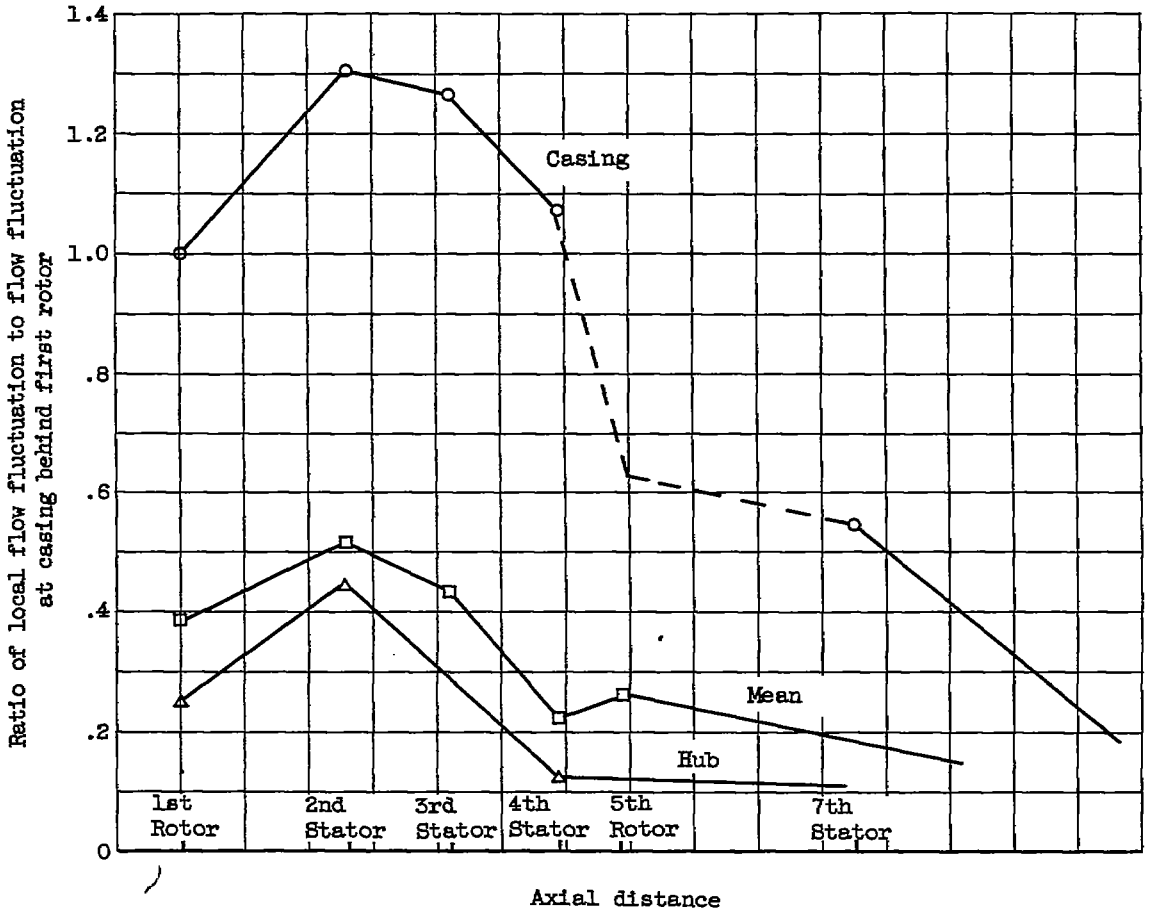

Figure 10. - Variation of flow fluctuation with axial distance in compressor at three radii at 50-percent design speed (ref. 9).

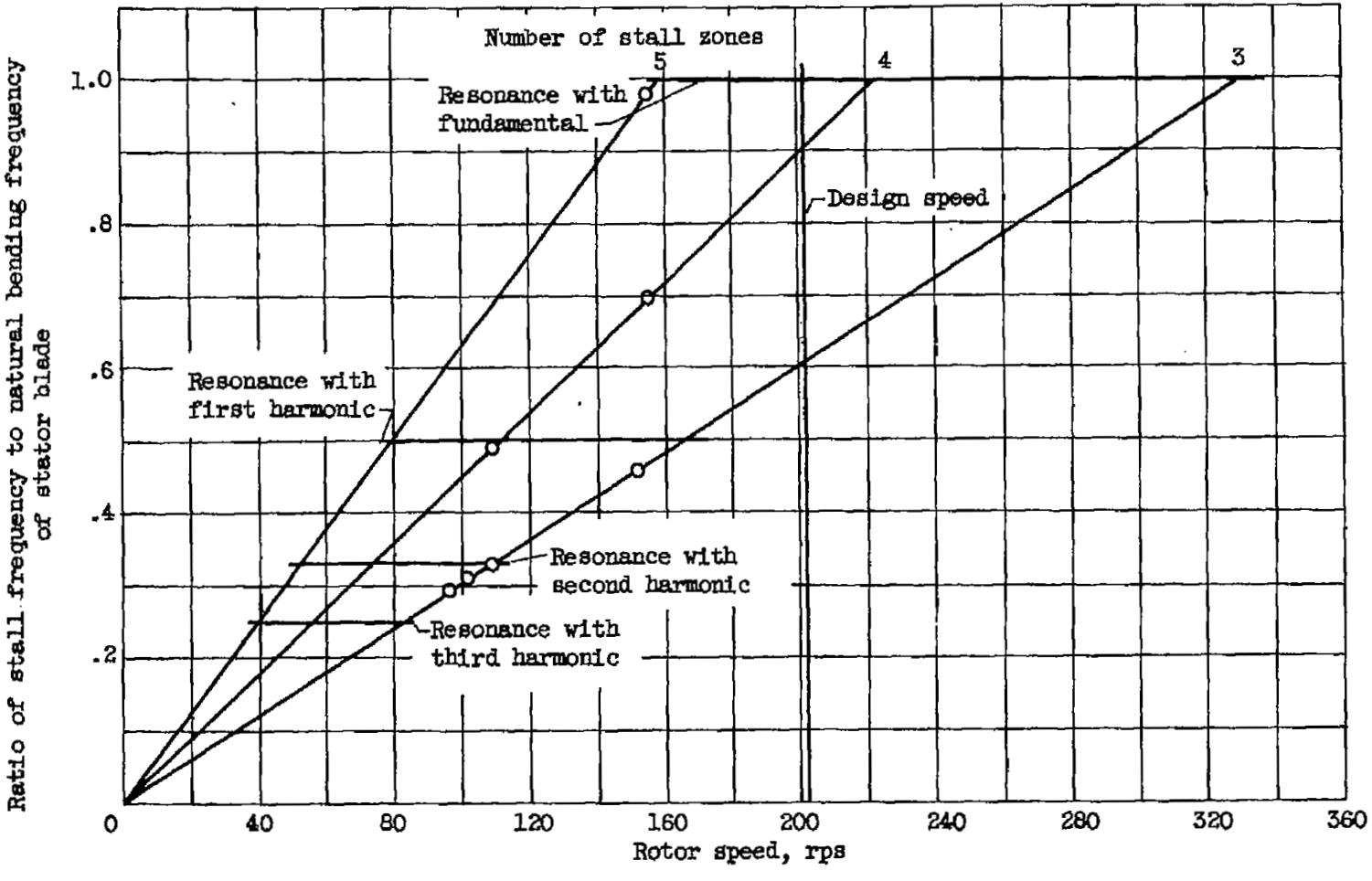

Figure 11. - Variation of stall frequency with rotor speed for three stall patterns in a single-stage compressor.

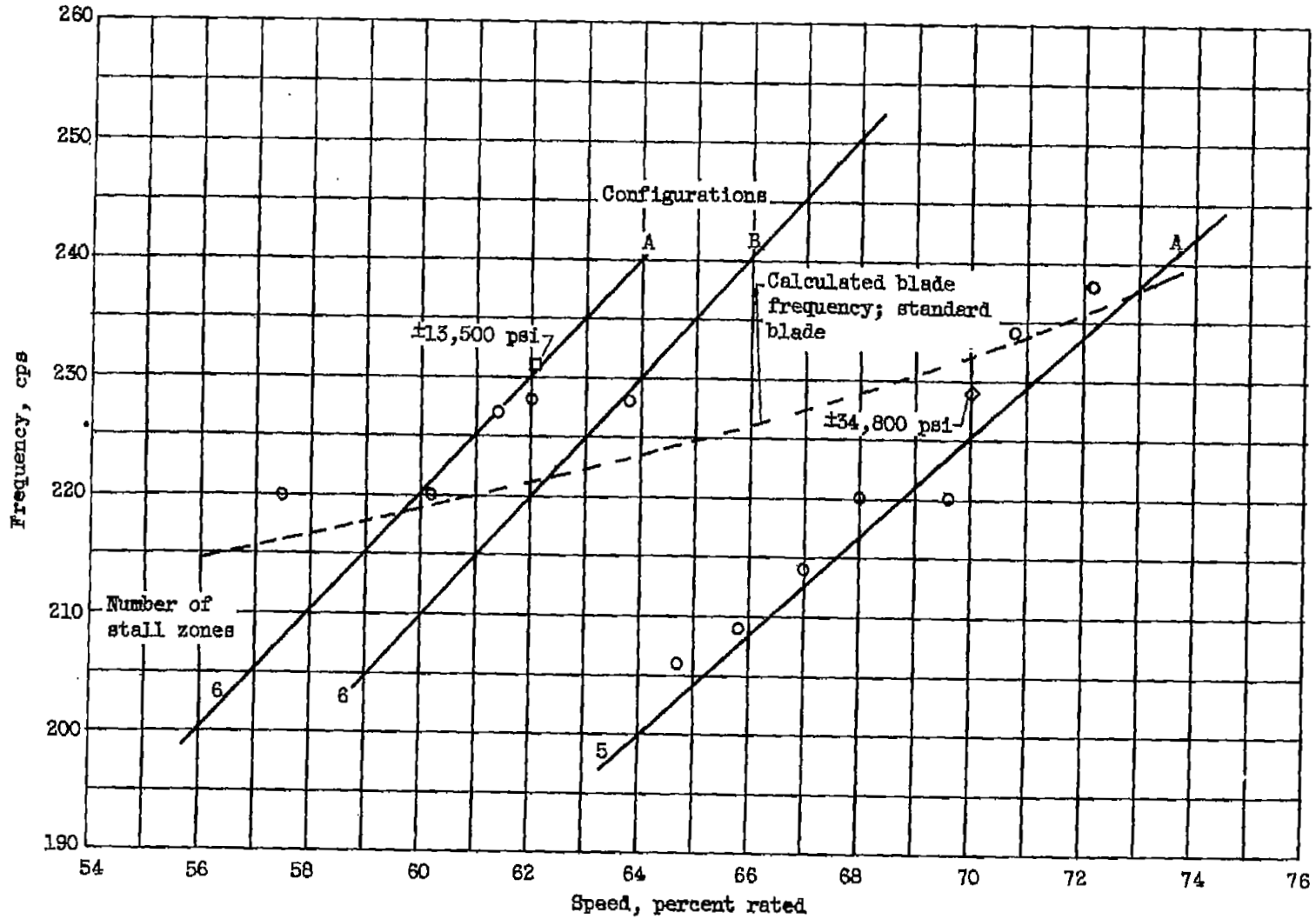

Figure 12. - Correlation of relative stall frequency with rotor blade-vibration frequency for a multistage compressor (ref. 15).

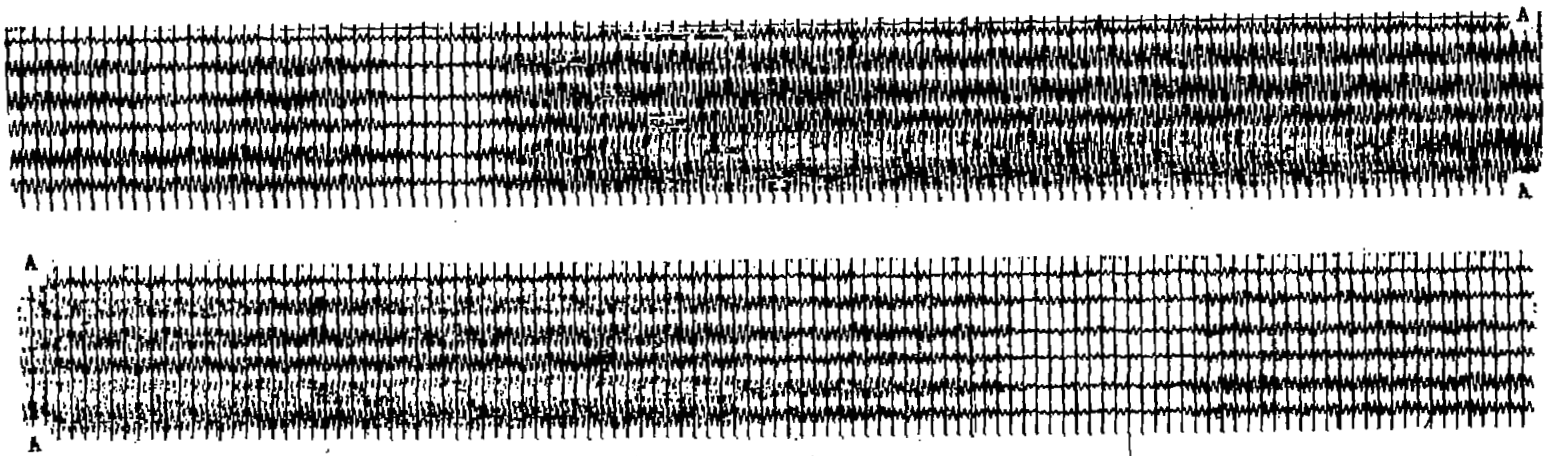

Figure 13. - Oscillogram of vibration burst caused by six-zone stall pattern. Engine speed, 62 percent design; blade-vibration frequency, 819 cycles per second (ref. 15).

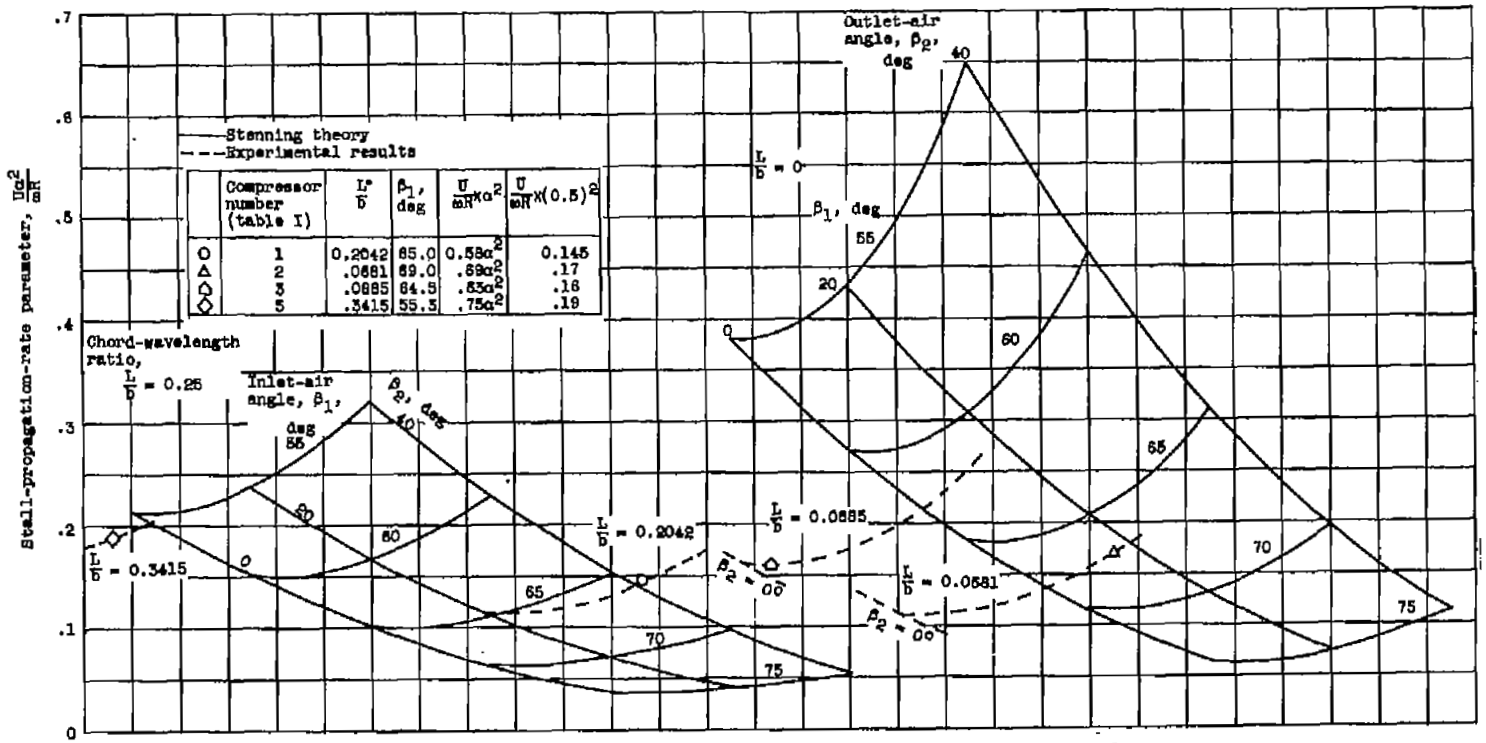

	Compressor number (table I)	$\frac{L}{b}$	β_1, deg	$\frac{U}{\omega R}\times\alpha^2$	$\frac{U}{\omega R}\times(0.5)^2$
○	1	0.2042	65.0	$.58\alpha^2$	0.145
△	2	.0581	69.0	$.69\alpha^2$	.17
⬡	3	.0885	64.5	$.63\alpha^2$	.16
◇	5	.3415	55.3	$.75\alpha^2$	.19

Figure 14. - Carpet plot of Stenning's results. $0^\circ < \beta_2 < 40^\circ$.

3309

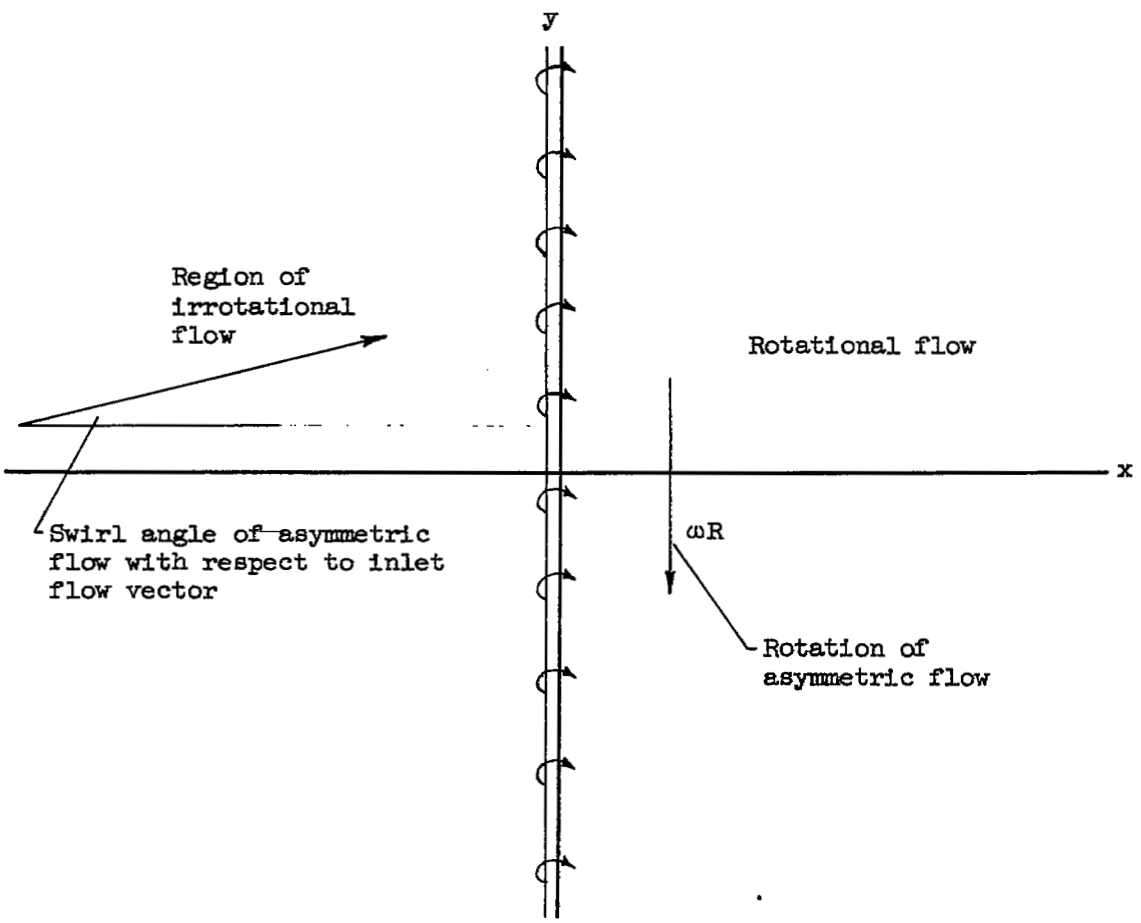

Figure 15. - Actuator disk employed by Sears.

3309

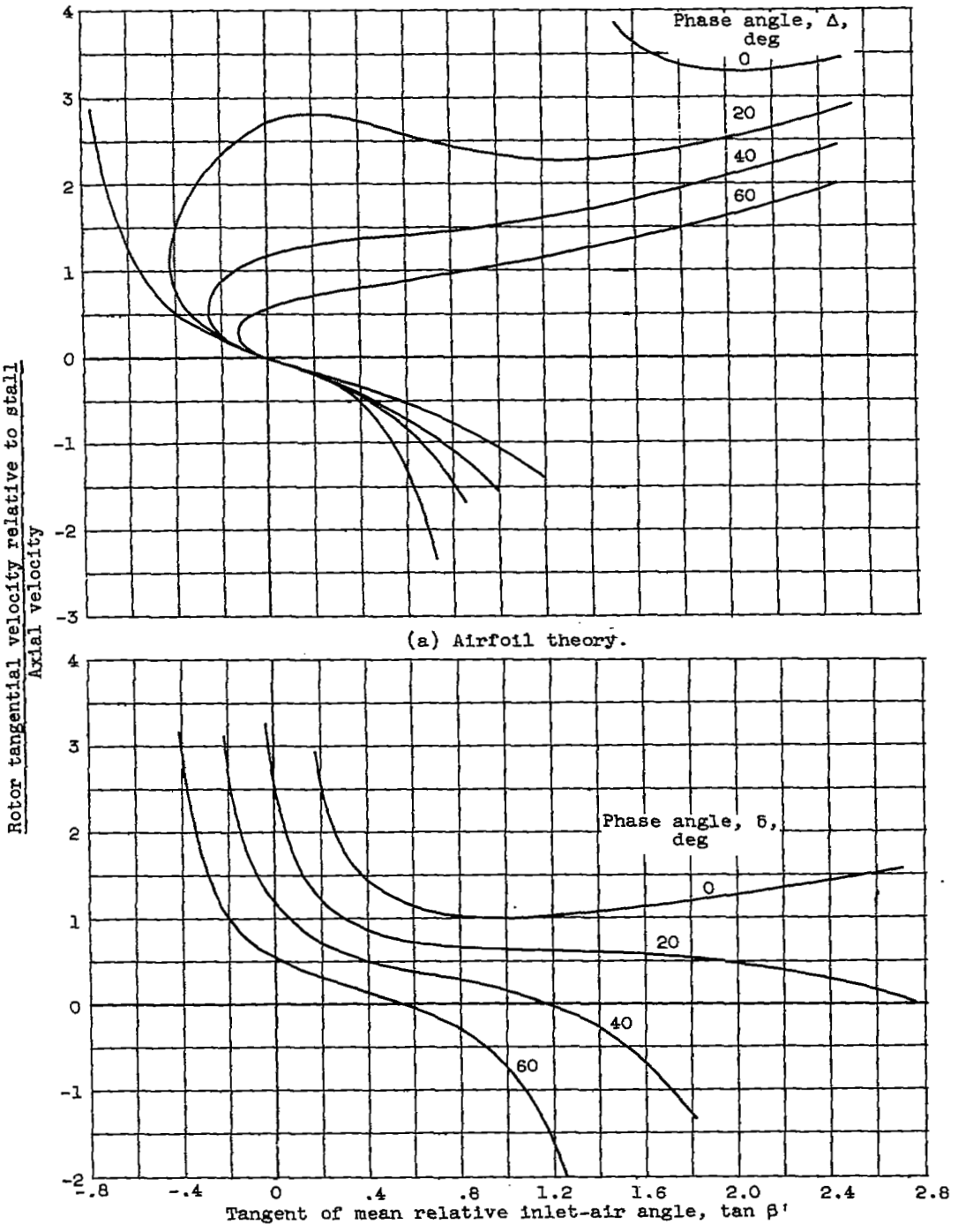

(b) Channel theory.

Figure 16. - Predicted asymmetric flow patterns obtained from Sears theory of rotating stall.

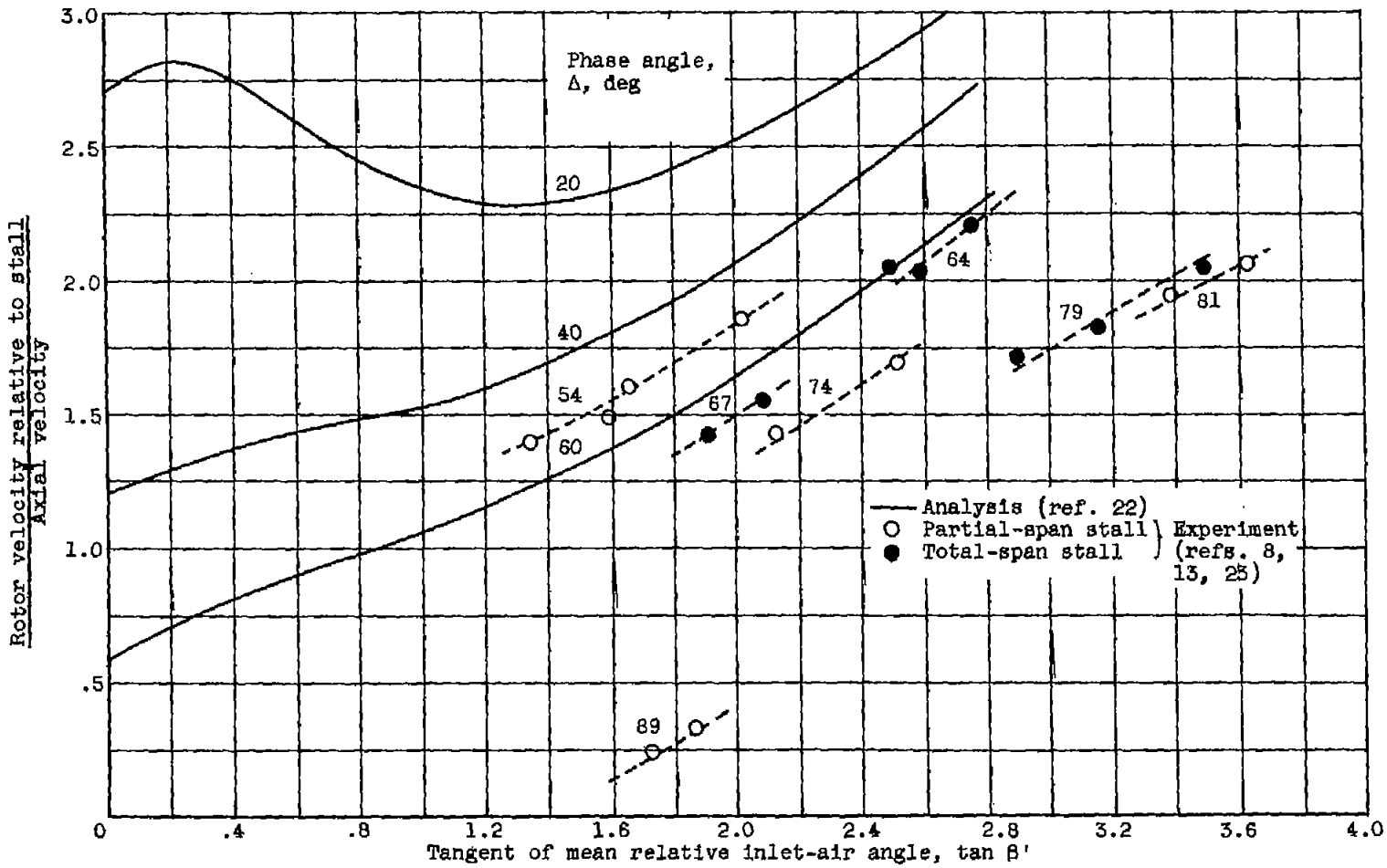

Figure 17. - Correlation of stall data with analytically derived phase angle (Sears theory).

3309

CH-7

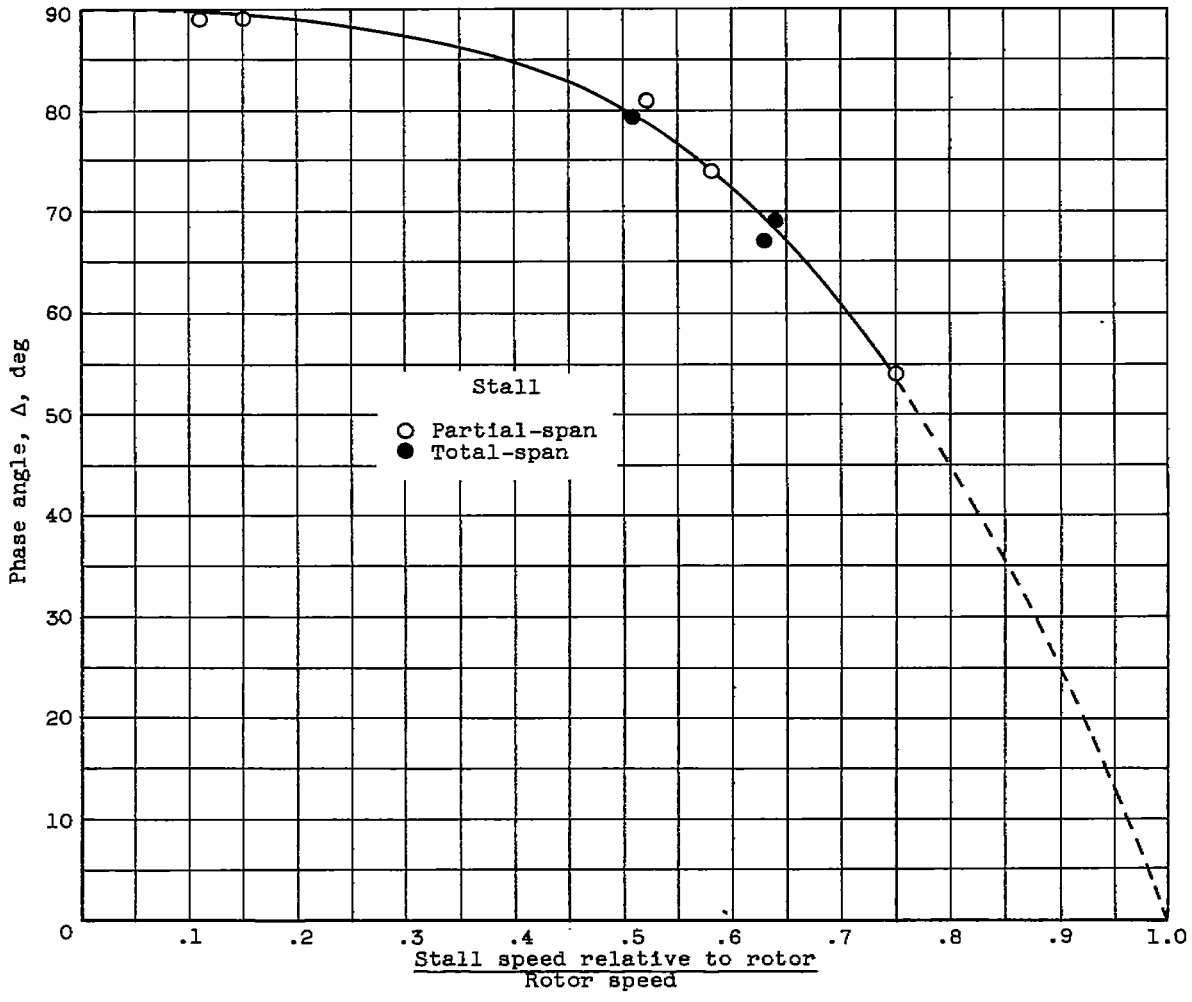

Figure 18. - Relation between stall rotational speed relative to rotor and phase angle (ref. 23).

[redacted]

3309

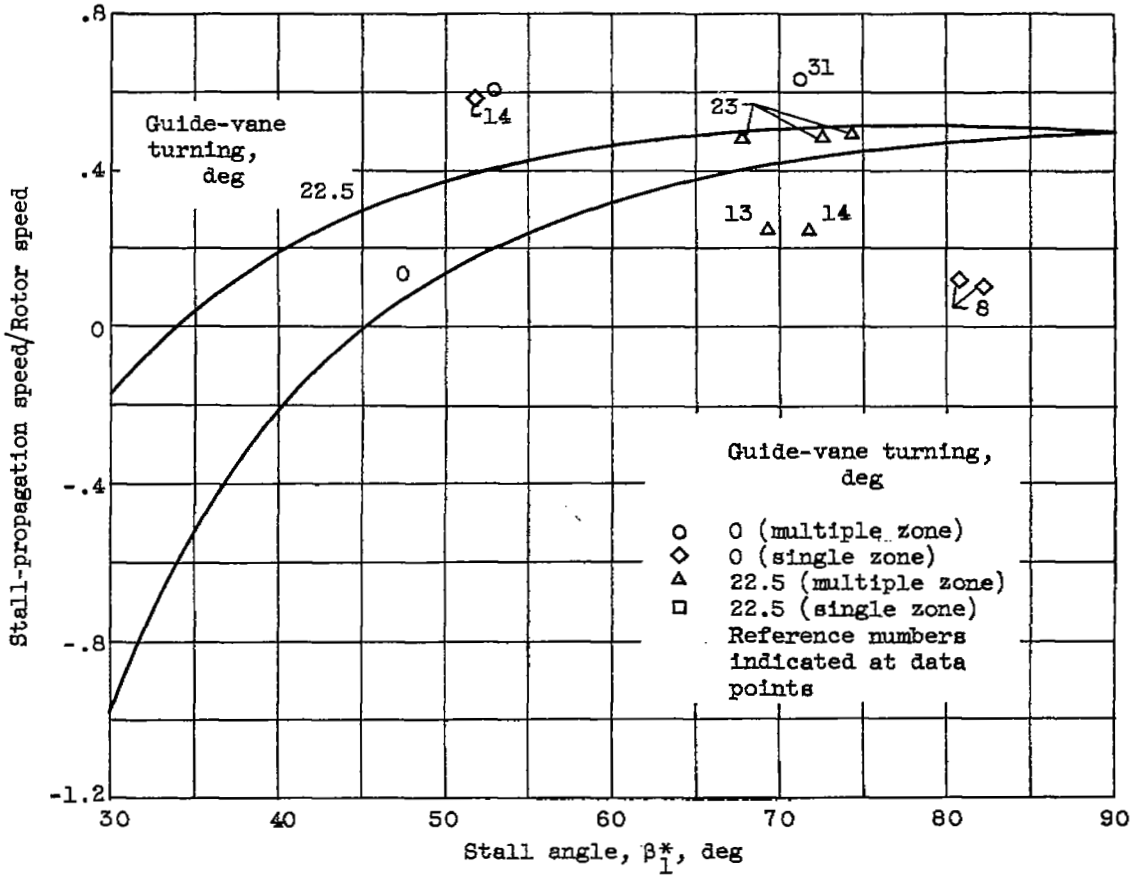

Figure 19. - Comparison of single-stage stall data with Marble's theory.

3309

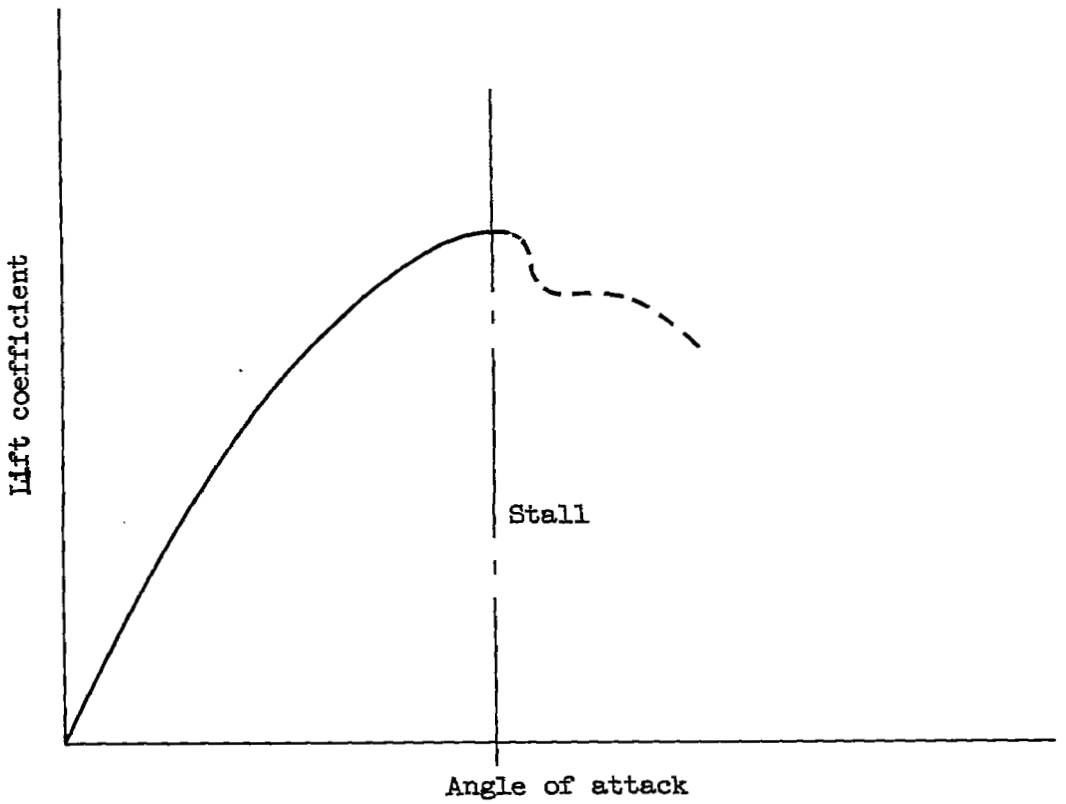

Figure 20. - Lift characteristic of an airfoil.

CH-7 back

3309

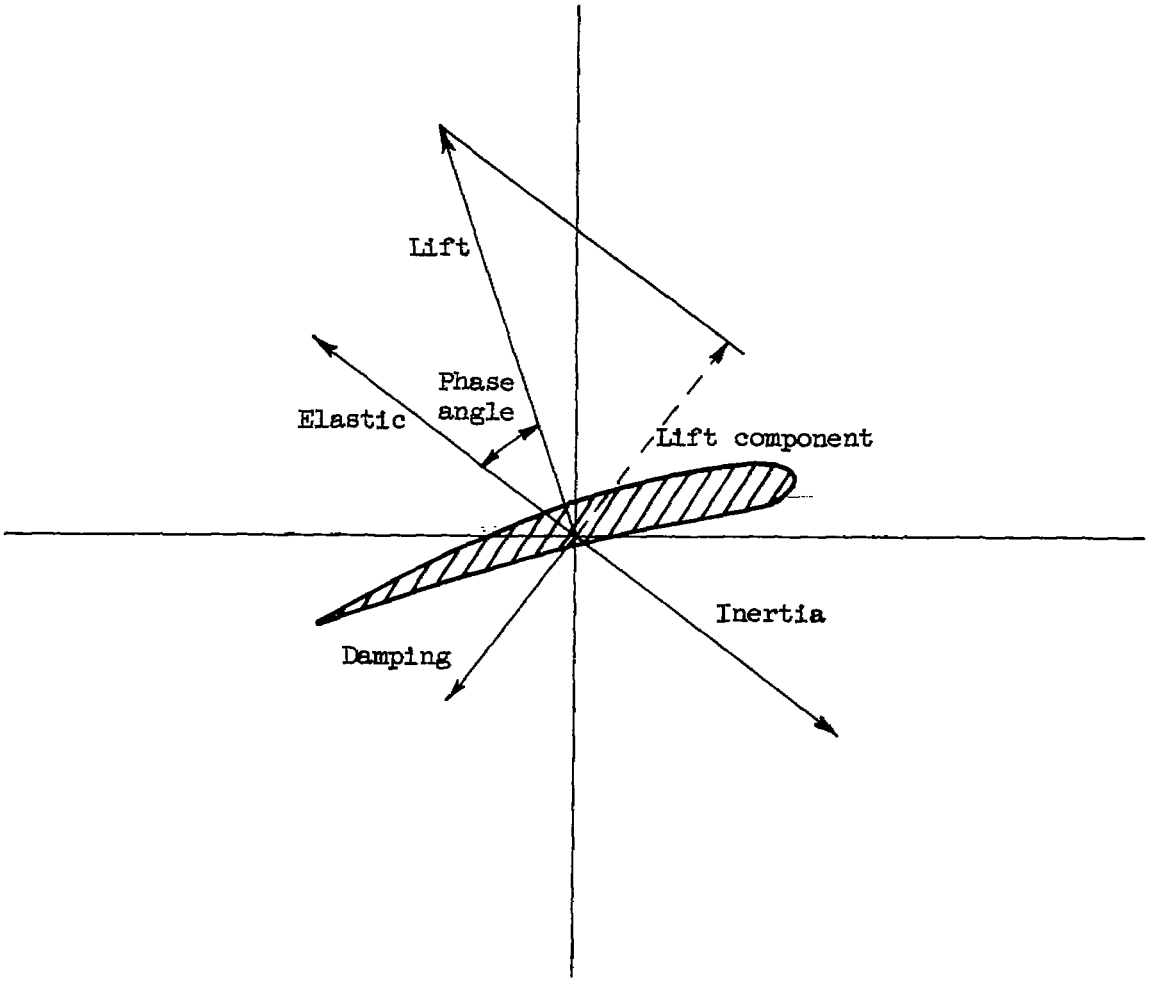

Figure 21. - Diagram of forces on blade.

CHAPTER XII

COMPRESSOR SURGE

By Merle C. Huppert

SUMMARY

Experimental data indicate that there are two principal types of surge in compressors: (1) surge due to an abrupt stall, and (2) surge due to progressive stall. Surge due to abrupt stall is generally violent and audible, whereas that occurring with progressive stall is generally mild and inaudible. The violent surge obtained in jet engines during engine acceleration is identified as surge due to abrupt stall.

INTRODUCTION

The effect of unsteady flows on compressor performance and life expectancy has become of considerable interest and importance in the application of axial-flow compressors to jet engines. Perhaps the most significant flow fluctuations are those associated with stall of blade elements within the compressor. In the past, any audible flow fluctuation or rumbling noise emanating from a compressor was loosely defined as surge. Comparatively recent investigations show that certain flow fluctuations are not due to surge in a strict sense, but are due to a phenomenon called propagating or rotating stall. Rotating stall, which is discussed in detail in chapter XI, consists of zones of low flow that revolve about the compressor axis.

The term surge, as used herein, defines flow fluctuations distinctly different from those due to rotating stall. Surge involves fluctuations in the net flow through the compressor; whereas rotating stall consists of low-flow zones revolving about the compressor axis, but with a constant net or average flow through the compressor.

This chapter presents a discussion of surge in axial-flow compressors. Pressure- and flow-fluctuation data obtained from surging compressors are presented and discussed. Data obtained from both compressor test facilities and jet engines are included. Some theoretical aspects of surge are discussed, and a distinction is made between surge due to abrupt stall and surge due to progressive stall. The surging compressor is compared with other types of oscillators.

SYMBOLS

The following symbols are used in this chapter:

f_{stall}	frequency of flow fluctuations due to rotating stall, cps
f_{surge}	frequency of flow fluctuations due to surge, cps
P	total or stagnation pressure, lb/sq ft
ΔP_C	compressor total-pressure rise at stall point, lb/sq ft
ΔP_{stall}	decrease in compressor-discharge total pressure due to abrupt stall, lb/sq ft
ΔP_{surge}	amplitude of total-pressure fluctuation due to surge, lb/sq ft
V	air velocity, ft/sec
w	weight flow, lb/sec
$w\sqrt{\theta}/\delta$	equivalent weight flow, lb/sec
α	angular spacing of hot-wire-anemometer probes, deg
δ	ratio of total pressure to NACA standard sea-level pressure of 2116 lb/sq ft
θ	ratio of total temperature to NACA standard sea-level temperature of 518.7° R
λ	number of stall zones in stall pattern
ρ	density, lb/cu ft
$\Delta\rho V/\overline{\rho V}$	amplitude of ρV fluctuation divided by average ρV based on average anemometer current (see ch. XI)

Subscripts:

1	station at compressor inlet
2	compressor-discharge station

3325

STEADY-STATE COMPRESSOR CHARACTERISTIC

Before considering the phenomenon of surge, "steady-state" or "surge-free" compressor operation should be discussed. Steady-state operation (sometimes called static operation) is operation under conditions in which the net flow through the compressor and the torque required to drive the compressor are constant for any given operating point. From this definition, operation with rotating stall is considered a steady-state condition. (Rotating stall is discussed in detail in ch. XI.) Figure 1 shows the range of flow for each of several compressor speeds over which steady-state operation occurred in a 10-stage axial-flow research compressor. The shaded areas indicate the flow range where rotating stall existed. At 50 percent of design speed, rotating stall occurred over the entire range of flow from the surge point to the maximum flow obtainable. The number of zones in the stall pattern, however, varies from 3 at the highest flow attainable to 7 at the surge point. At higher values of rotational speed, rotating stall existed over only a part or none of the flow range between maximum flow and the surge line. The surging obtained was due to abrupt stall of the compressor, as will be discussed later.

3325

Stall may, in most cases, be classified as either progressive or abrupt (ch. XI). Progressive stall results in a gradual reduction in stage pressure ratio and efficiency as the flow is decreased and generally results in the formation of a rotating-stall pattern consisting of more than one stall zone. The shaded area of figure 1 represents the condition of progressive stall in the inlet stages. Abrupt stall in single- or multistage compressors results in an abrupt or apparently discontinuous drop in compressor pressure rise and efficiency and a "hysteresis" loop between stall and stall recovery. A single-zone stall pattern is associated with abrupt stall.

In the intermediate-speed range, the steady-state performance at a given compressor speed is not always unique. As discussed in chapter XIII, several steady-state performance characteristics may be obtained at a single compressor speed.

EXPERIMENTAL INVESTIGATIONS OF SURGE

On the basis of experimental evidence, two types of surge may be distinguished as follows:

(1) Surge associated with discontinuous compressor characteristics due to abrupt stall

(2) Surge associated with apparently continuous compressor characteristics where blade-row stall is progressive rather than abrupt

Surge Due to Abrupt Stall

In order to describe the flow fluctuations due to surge associated with abrupt stall, the results of recent investigations in which fast-response pressure and flow instrumentation were used will be reviewed.

10-Stage subsonic axial-flow research compressor. - The investigation reported in reference 1 was conducted with a 10-stage subsonic axial-flow research compressor. The test facility incorporated a large inlet tank and a large receiver at the compressor discharge. The overall compressor performance map showing the speed and flow range where rotating stall occurred is presented in figure 1. At all rotational speeds investigated, the useful operating flow range was terminated at low flows by a violent surge. 3325

The flow fluctuations associated with surge at 50 percent of design speed were investigated in some detail; the variation in compressor-inlet and -discharge total pressure and the variation in flow rate measured behind the first rotor due to surge are shown in figure 2. The amplitude of the compressor-discharge total-pressure variation (fig. 2(a)) was 75 percent of the compressor pressure rise at the surge point. The variation in compressor-inlet stagnation pressure was somewhat smaller. The compressor-discharge pressure recovered to the value at the surge point at the end of each surge pulse. The hot-wire-anemometer signal (flow fluctuations, fig. 2) indicates that the initial drop in compressor-discharge pressure was coincident with a sharp drop in flow. As the compressor-discharge pressure continued to decrease, however, the flow increased and exceeded its value at the beginning of the surge pulse.

The flow is maximum when the compressor-discharge pressure is minimum. The recording oscillograph used to obtain the oscillogram reproduced in figure 2 was not capable of recording frequencies greater than about 90 cps. Consequently, these oscillograms indicate only the low-frequency components of the variation in flow and pressure during surging operation.

The flow fluctuations that occurred during a surge pulse are shown in much greater detail in figure 3. The oscillograms shown (film strips) were obtained from hot-wire-anemometer signals recorded from a dual-beam direct-coupled cathode-ray oscilloscope (signal filtered to pass frequencies from 0 to 10,000 cps). Signals from anemometer probes installed behind the third, seventh, and tenth stators are shown along with the signal from an anemometer probe installed behind the first rotor. A rotating-stall pattern with a single stall zone is shown at all four axial stations at the beginning of the surge pulse. As pointed out in chapter XI, single-zone rotating stall is typical of abrupt stall. As the flow was reduced following the formation of the single-zone stall pattern, the stall zone evidently spread to cover the complete annulus of

the compressor. Stall-zone spreading to cover the complete annulus during surge, as noted in this investigation, is not typical. Surge data obtained from several jet engines and from other compressors operating in compressor test facilities indicate that the single-zone rotating-stall pattern usually exists up to the time of stall recovery. Stall recovery resulted in a marked increase in flow followed by a comparatively gradual reduction. As the flow was reduced following stall recovery, the first stall pattern indicated on the oscillogram was the one consisting of three stall zones. Although not shown in figure 3, the stall patterns with four, five, and six stall zones appeared in succession as the flow was further reduced. Just before abrupt stall (end of one surge pulse and beginning of next), the stall pattern with seven stall zones was indicated (fig. 3). The stall patterns obtained after stall recovery (weight flow decreasing) were the same as those obtained during steady-state operation (fig. 1). Abrupt stall without surge was not obtained during this investigation.

3325

16-Stage subsonic axial-flow compressor. - The test facility used for the investigation of the 16-stage subsonic axial-flow compressor was similar to that used for the 10-stage compressor. A large inlet tank was used at the compressor inlet. The construction of the receiver at the compressor discharge permitted the installation of flow-control devices (throttles) at two stations. The throttle close to the compressor permitted operation with a small receiver volume, and the throttle somewhat downstream of the compressor permitted operation with a much larger effective receiver volume. The large receiver volume was approximately 9 times that of the small receiver volume.

CH-9

A violent audible surge was obtained at all compressor speeds from 30-percent design to design speed when the large receiver volume was used. Figure 4 is an oscillogram showing the variation in total pressure at the compressor inlet and discharge during surging operation with the large receiver volume at 50 percent of design speed. The surge frequency was about 1 cps. The compressor-discharge pressure reduction during the surge was about 40 percent of the compressor pressure rise at the surge point. The inlet pressure increased about 8 percent during a surge pulse. Rotating stall is indicated on the oscillograms during the time interval in which the compressor-discharge pressure is decreasing. The rotating stall is, however, shown much better by the hot-wire-anemometer trace in figure 5. The oscillogram shown in figure 5 was also obtained during surging operation at 50 percent of design speed. The surge frequency, however, was 1.6 cps at the time the oscillogram was obtained. The rotating-stall pattern contained one stall zone and was rotating about the compressor axis in the direction of rotor rotation (absolute frame of reference) at about 45 percent of compressor speed.

The pressure and flow fluctuations due to surge obtained with the 16-stage axial-flow compressor are quite similar to those obtained with the 10-stage compressor. The surge pulse was initiated by the formation

of a single-zone rotating-stall pattern; but, unlike that of the 10-stage compressor, the stall pattern persisted until stall recovery was effected. Actually, the persistence of the single-zone rotating-stall pattern, until stall recovery occurs, is fairly typical of compressors surging in jet engines.

When the compressor was operated with the small receiver volume, audible surge was not obtained at 50 percent of design speed. Instead, abrupt stall was obtained as shown by the oscillogram in figure 6. The rotating-stall pattern obtained is the same as that indicated during the surging operation when the large receiver volume was used. The decrease in compressor-discharge pressure due to abrupt stall was approximately the same as the amplitude of the compressor-discharge pressure oscillation due to surge (fig. 4). The compressor-inlet and -discharge pressures increased gradually following stall because of the flow reduction through the inlet throttle. The compressor pressure ratio following abrupt stall was essentially constant. Audible surge was not obtained when the small receiver volume was used, presumably because stall recovery did not occur during the flow transient caused by abrupt stall. The reduced receiver volume resulted in a more rapid adjustment in receiver pressure following stall and consequently smaller oscillations in net flow. It is of interest to note that, although audible surge due to cyclic stall and stall recovery was not obtained when the small receiver volume was used, stalled operation was not completely stable. A mild inaudible surge with a frequency of approximately 5 cps was indicated (fig. 6). The amplitude of these mild surge oscillations appeared to vary in a somewhat random fashion.

Operation at 30 percent of design speed with the large receiver volume resulted in intermittent abrupt stall and surge, as shown in figure 7. The oscillogram was obtained with a fixed setting of both the inlet and discharge throttles. While the compressor remained stalled, a single-zone rotating stall with a frequency of about 14 cps was indicated. The stall zone was rotating at approximately 45 percent of compressor speed. Also, during stalled operation a mild inaudible surge was indicated on the oscillogram. The mild surge frequency, about 2 cps, was somewhat less than that obtained with stalled operation at 50 percent of design speed (fig. 6), where the mild-surge frequency was about 5 cps.

According to reference 2, the frequency of surge should be proportional to the reciprocal of the square root of the receiver volume. The large receiver volume was approximately 9 times that of the small receiver volume. Then, according to reference 2, the surge frequency with the small receiver volume would be approximately 3 times that with the large receiver volume. This is in agreement with mild-surge data. The surge data obtained for the 16-stage axial-flow compressor demonstrate that surge may or may not result from abrupt stall, depending on the volume of the receiver into which the compressor is discharging. In

addition, the data demonstrate that, with a given receiver volume, surge due to abrupt stall is more likely to occur at high than at low compressor speeds. In many cases, abrupt stall is obtained without surge as defined herein (e.g., refs. 3 and 4). But, for high-pressure-ratio compressors, surge due to abrupt stall is common in compressor test facilities and in jet engines.

3325

Surge in jet engines. - Surge in the compressor component of a jet engine is much the same as surge obtained with the 16-stage axial-flow compressor operating in a test facility. The principal difference is that the surge frequency in a jet engine is generally somewhat greater (5 to 15 cps) than that for the same compressor operating in a test facility. The surge frequency in a jet engine is increased mainly because the volume of jet-engine combustors is somewhat smaller than that of the receivers used in compressor test facilities.

CH-8 back

An experimental investigation of stall and surge in a jet engine is reported in reference 5. Surge was obtained by subjecting the engine to a step increase in fuel flow. For the particular jet engine used in the investigation, surge occurred as a result of abrupt stall at compressor rotational speeds where the pressure drop due to stall was greater than 16 percent of the pressure rise at the stall point. The pressure ratio at which stall occurred is referred to as the critical pressure in reference 5. Figure 8, taken from reference 5, shows the pressure-ratio oscillations due to surge obtained by step increases in fuel flow at compressor speeds of 72.8 and 78 percent of design speed. Also shown are the pressure ratio at the stall point, the pressure ratio after stall, and the steady-state or equilibrium operating line. The sequence of events following the increase in fuel flow was as follows: The compressor-discharge pressure increased until the stall point was reached. Several cycles of surge occurred, and then surging ceased and the compressor remained stalled. The engine speed increased even though surging occurred. When the compressor quit surging and was operating stalled, the rate of speed increase (acceleration) was markedly reduced.

During surge investigations in jet engines it has been noted that surge does not, in all cases, begin immediately after the stall point is reached. In some cases, surging does not begin until after the compressor has operated in a stalled condition (abrupt stall) for a short time and the engine speed has increased somewhat.

Surge Due to Progressive Stall

Surge due to progressive stall involves flow fluctuations in the flow range of the compressor map where there are no apparent abrupt changes in pressure ratio due to stall. Progressive stall may occur at flows greater or less than that at which abrupt stall occurs. Surge

associated with progressive stall is generally quite mild compared with surge caused by abrupt stall. Mild surge obtained during stalled operation of the 16-stage axial-flow compressor is shown in figures 6 and 7. The amplitude of the compressor-discharge total-pressure fluctuations that occurred during mild surge is from 15 to 20 percent of that for surge due to abrupt stall.

Mild inaudible surge is sometimes observed in single-stage compressors operating near the peak of the characteristic curve. In these cases, a partial-span rotating-stall pattern is generally associated with the surge. The amplitude of the flow fluctuation due to rotating stall varies as the net flow rate varies. An example of this type of surge obtained with a single-stage compressor is shown in figure 9 (taken from ref. 6). The stall pattern obtained contained eight stall zones, and the flow-fluctuation frequency due to the stall pattern was 1420 cps. The surge frequency was from 10 to 15 cps. The amplitude of the flow fluctuations of rotating stall is greatest when the net flow is minimum and smallest when the net flow rate is maximum. The amplitude of the net flow variation due to surge shown in figure 9 was estimated to be 10 percent of the average flow rate. The amplitude of the surge fluctuations, however, increased and decreased in a somewhat random fashion similar to the mild surge shown in figures 6 and 7.

Although a rotating-stall pattern is generally present during all or part of the surge cycle, mild inaudible surge without rotating stall has been observed in single-stage compressors. Presumably, individual blade stall had occurred without rotating stall. (See ch. XI for discussion of individual blade stall.) Other examples of mild surge are reported in references 2 and 7.

THEORETICAL INVESTIGATIONS OF SURGE

Theories of surge have been primarily concerned with the question of the stability of the flow through the compressor and the system in which it is operating. The complexity of the flow system associated with the compressor considered in the theories has varied considerably. The analysis in reference 8 involves a relatively simple system consisting of an inlet throttle for controlling the flow and an inlet duct or tank followed by the compressor. Reference 2 considers a somewhat more complete system consisting of an inlet duct and an inlet tank followed by the compressor, which discharges into a discharge tank or receiver connected to an exit duct. The analysis presented in reference 9 is somewhat more complex than those presented in references 2 or 8, in that the inertia and capacitance effects of each stage of a multistage compressor are considered.

The analysis of the stability of an operating point of the compressor in equilibrium with a flow system involves setting up linear differential equations in an approximate way to describe the dynamics of the system. The stability of the system may be determined without actually solving the differential equations by use of the method of Routh (see ref. 10 or 11, e.g.).

3325

In general, the conclusions drawn as a result of all surge analyses are essentially the same: The system becomes unstable at compressor operating points where the slope of the compressor characteristic is zero or slightly positive. When the system is unstable, the system damping is negative, so that any small disturbances will grow in amplitude. A point of critical stability has no damping. As the flow varies, however, the system damping also varies. That is, the system damping depends on the slope of the compressor characteristic at the instantaneous operating point during the flow fluctuation. As a consequence, the linear theory used to determine the stability no longer applies after the amplitude of the flow fluctuations becomes finite. Surge occurs as a result of the instability if the nonlinearities of the system are such as cause oscillations to grow in amplitude until some limiting stable value of steady-state oscillations occurs. The resulting cycle of oscillations is called the "limit cycle" (e.g., ref. 11). So far as is known, there are no published analyses of surge that consider the nonlinear aspects of the problem. It seems evident, however, that the flow oscillations that result from an instability will depend to a great extent on the shape of the compressor characteristic. That is, the variation in the slope of the compressor characteristic with flow, at flows greater and less than that at an unstable operating point, probably constitutes the principal nonlinearity of the system.

In chapter XI compressor characteristics are classified as either continuous or discontinuous, depending on whether stall occurred in a gradual or progressive manner or abruptly. It seems appropriate to classify surge in a similar way. That is, surge may occur because of the discontinuous decrease in pressure ratio due to abrupt stall, or because of an instability resulting from a gradual reduction in compressor pressure ratio due to progressive stall.

Surge Due to Abrupt Stall

Surge due to abrupt stall may be described in a qualitative manner with the aid of figure 10. The compressor static or steady-state characteristic is represented by the solid line. The throttle characteristic is represented by the dashed line which crosses the compressor characteristic curve at points A and B. Point C is the stall recovery point. The compressor is operating at point A (the stall point). Point B is a possible stable operating point. Point A is unstable, because a small

reduction in flow will cause the compressor to stall and immediately become incapable of producing a discharge pressure equal to that in the receiver. If the receiver volume were infinite, the direction of flow through the compressor would reverse after stall, and steady backflow would occur with operation at point D. If the receiver volume were very small, its pressure would adjust very quickly after stall to that which the compressor is capable of producing, and operation would instantaneously come to equilibrium at point B.

In any compressor installation the receiver volume would be neither large enough to permit steady operation at point D nor small enough to cause equilibrium to be established instantaneously at point B. In the practical case, then, the pressure and flow fluctuations may follow paths depicted in figure 10 as surge or abrupt stall. For the case of abrupt stall, the receiver pressure and flow may follow the path indicated. After a few damped oscillations in pressure and flow (indicated by the spiral path), the system comes to equilibrium at point B. If, however, the flow oscillations are sufficiently large to exceed the value required for stall recovery (point C), equilibrium will not be established at point B. Instead, stall recovery will occur and result in an increase in flow followed by a gradual increase in receiver pressure and decrease in flow. Following stall recovery, the system tends toward equilibrium at point A. Stall will occur again, and the cycle (called the limit cycle) will be repeated as indicated in figure 10. Surging will cease if the throttle is opened (throttle curve moved to the right in fig. 10) sufficiently to prevent stall from occurring during the flow transient following stall recovery. Similarly, surging will cease if the throttle is closed (throttle curve moved to the left in fig. 10) sufficiently so that stall recovery does not occur during the flow transient following stall. If equilibrium is established on the stalled branch of the compressor characteristic and the throttle is then opened so that the throttle characteristic passes through the stall recovery point C, the situation is quite similar to that with operation at the stall point. A small disturbance in the flow may cause stall recovery, and a surge cycle may be established similar to that which occurs with the throttle characteristic passing through the stall point. Equilibrium operation after stall is not always completely stable. Mild surge may occur after abrupt stall has occurred (figs. 6 and 7). The flow fluctuations of mild surge may, in some cases, become sufficiently large to cause stall recovery, as indicated by the oscillogram shown in figure 7.

3325

Surge Due to Progressive Stall

Mild surge due to progressive stall will be discussed in conjunction with figure 11. The solid curve is the compressor characteristic, and the dashed curve is the throttle characteristic, which crosses the compressor characteristic at the highest flow at which the system is critically

stable. That is, small oscillations about the intersection point are undamped. Inasmuch as the slope of the compressor characteristic becomes larger positively at flows less than point A, the damping becomes larger negatively if the flow is reduced a finite amount. If the flow increases to a value greater than that at point A, the slope of the compressor characteristic becomes negative and the system damping becomes positive. As a consequence of the variation of the system damping with compressor flow, any small disturbance will grow in amplitude, as indicated by the spiral path from point A, until the effective or average damping of the cycle vanishes (see ref. 11). The resulting cycle of oscillation is the limit cycle. Rotating stall may exist during all or part of the surge cycle (fig. 9). Presumably, surge could occur at any compressor operating point where the system damping is negative, since the flow is unstable there.

3325

As pointed out in the section on experimental investigations, most data obtained with surge associated with progressive stall indicate a mild inaudible surge. Although the relation between the shape of the compressor characteristic and the amplitude of the flow fluctuations of surge has not been established, it seems quite likely that surge with progressive stall may, in some cases, become quite violent. In fact, if the damping is sufficiently negative, the situation is not unlike that for abrupt stall.

Comparison of Compressor Surge with Other Oscillatory Phenomena

Although surge in compressors is very undesirable, there are many technologically useful devices that utilize oscillatory phenomena. Since much of the theory of nonlinear effects has been developed through the study of oscillators, it seems appropriate to apply some of concepts and terminology used in oscillator theory to explain compressor surge.

According to reference 11, there are two principal kinds of oscillators, feedback and relaxation oscillators. All oscillators depend for their operation on some nonlinear action, and feedback and relaxation oscillators are distinguished by the type of nonlinearity utilized to control the amplitude of the oscillations. Relaxation oscillators operate by virtue of some discontinuous or quasi-discontinuous effect. Certain trigger circuits used with relaxation oscillators are discussed in reference 12. The effects of the discontinuous steady-state compressor characteristic are evidently analogous to those of the trigger circuits used with relaxation oscillators. Consequently, it seems justifiable to refer to surge associated with abrupt stall as a relaxation oscillation. Similarly, it seems justifiable to refer to surge associated with progressive stall as feedback-type oscillations. Progressive stall results in a progressive nonlinearity. The theoretical treatment of compressor surge could undoubtedly be enhanced by use of the theory of nonlinear systems.

SUMMARY OF RESULTS

A survey of available data obtained from surging compressors indicates that there are two principal types of surge: (1) surge due to abrupt stall, which is generally a violent audible surge, and (2) surge due to progressive stall, which is generally a mild inaudible surge detectable by use of fast-response instrumentation. The violent surge obtained in jet engines during engine acceleration is identified as surge due to abrupt stall.

3325

REFERENCES

1. Huppert, Merle C., Costilow, Eleanor L., and Budinger, Ray E.: Investigation of a 10-Stage Subsonic Axial-Flow Research Compressor. III - Investigation of Rotating Stall, Blade Vibration, and Surge at Low and Intermediate Compressor Speeds. NACA RM E53C19, 1953.

2. Emmons, H. W., Pearson, C. E., and Grant, H. P.: Compressor Surge and Stall Propagation. Trans. A.S.M.E., vol. 77, no. 4, May 1955, pp. 455-467; discussion, pp. 467-469.

3. Smith, A. G., and Fletcher, P. J.: Observations on the Surging of Various Low-Speed Fans and Compressors. Memo. No. M.219, British N.G.T.E., July 1954.

4. Schulze, Wallace M., Erwin, John R., and Westphal, Willard R.: Investigation of an Impulse Axial-Flow Compressor Rotor over a Range of Blade Angles. NACA RM L50F27a, 1950.

5. Delio, G. J., and Stiglic, P. M.: Experimental Investigation of Control Signals and the Nature of Stall and Surge Behavior in a Turbojet Engine. NACA RM E54I15, 1954.

6. Huppert, Merle C.: Preliminary Investigation of Flow Fluctuations during Surge and Blade Row Stall in Axial-Flow Compressors. NACA RM E52E28, 1952.

7. Lewis, George W., Jr., Schwenk, Francis C., and Serovy, George K.: Experimental Investigation of a Transonic Axial-Flow-Compressor Rotor with Double-Circular-Arc Airfoil Blade Sections. I - Design, Over-All Performance, and Stall Characteristics. NACA RM E53L21a, 1954.

8. Bullock, Robert O., Wilcox, Ward W., and Moses, Jason J.: Experimental and Theoritical Studies of Surging in Continuous-Flow Compressors. NACA Rep. 861, 1946. (Supersedes NACA TN 1213.)

9. Pearson, H., and Bower, T.: Surging of Axial Compressors. The Aero. Quarterly, vol. 1, pt. III, Nov. 1949. (Pub. by Roy. Aero. Soc. (London).)

10. Doherty, Robert E., and Keller, Ernest G.: Mathematics of Modern Engineering. Vol. I. John Wiley & Sons, Inc., 1936.

11. Trimmer, John Dezendorf: Response of Physical Systems. John Wiley & Sons, Inc., 1950.

12. Brainerd, J. G., Koehler, Glenn, Reich, Herbert J., and Woodruff, L. L.: Ultra High Frequency Techniques. D. Van Nostrand Co., Inc., 1942.

3325

CH-9

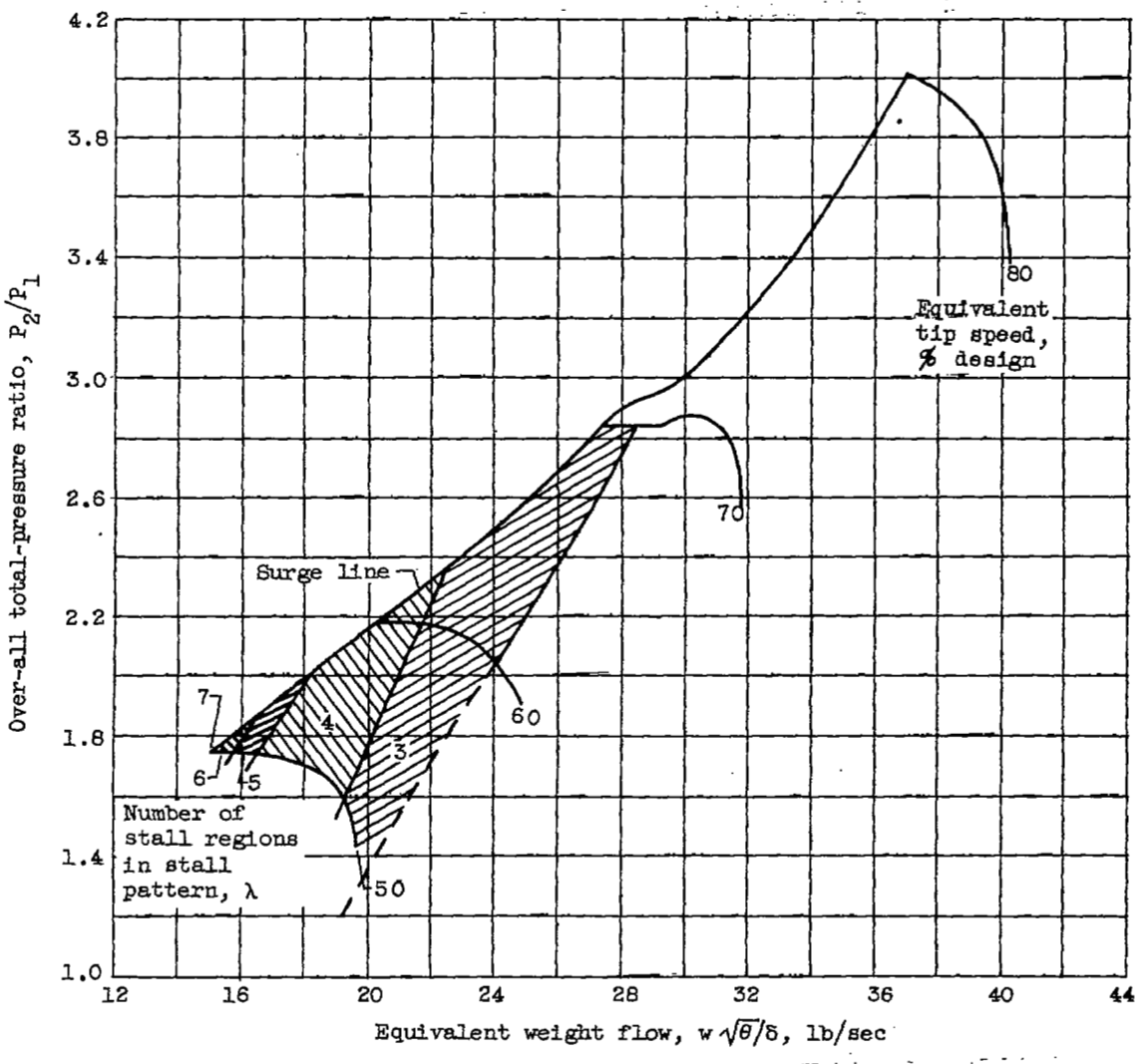

Figure 1. - Over-all compressor performance map showing conditions at which rotating stall occurred in 10-stage subsonic axial-flow research compressor (ref. 1).

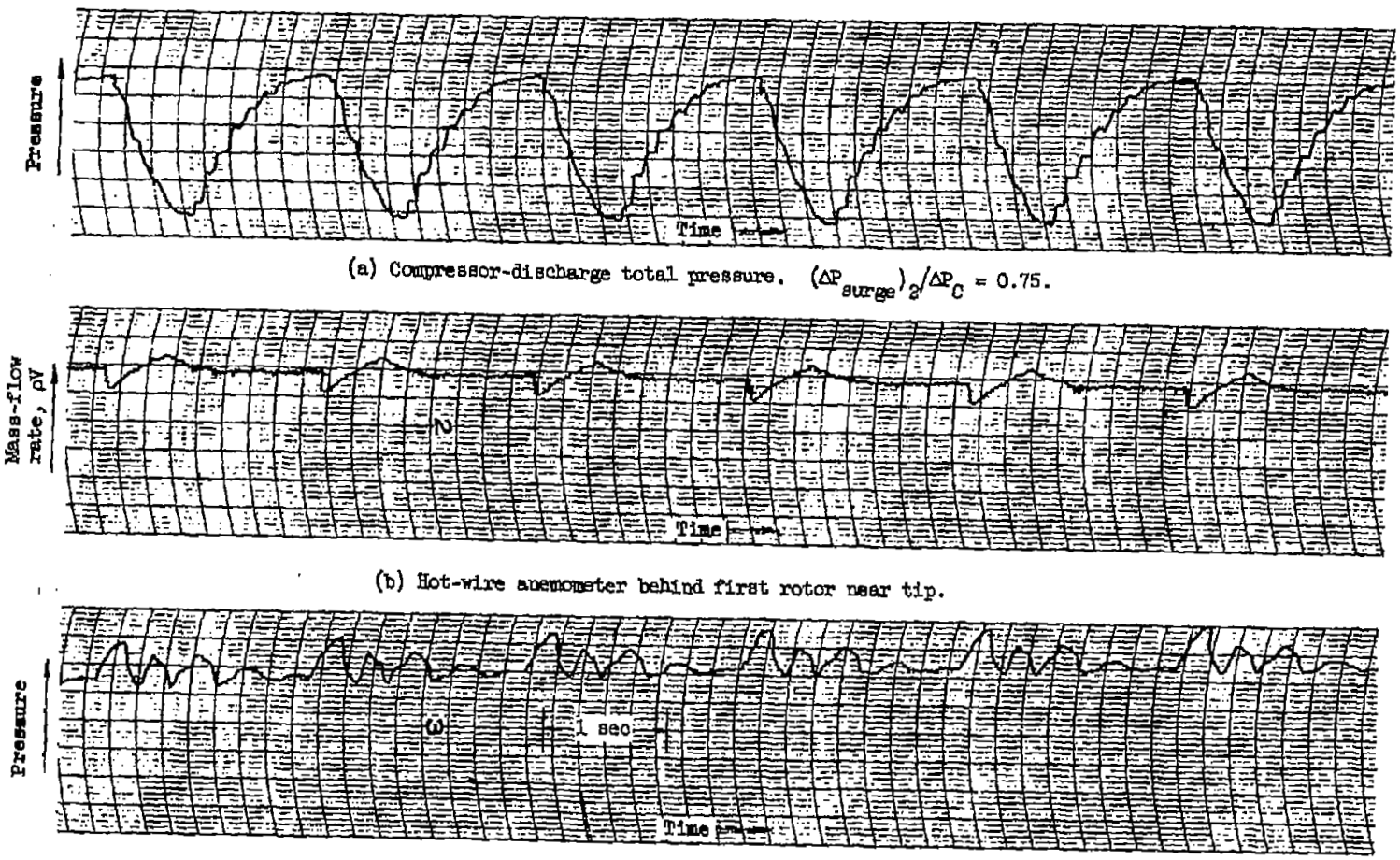

(a) Compressor-discharge total pressure. $(\Delta P_{surge})_2/\Delta P_C = 0.75$.

(b) Hot-wire anemometer behind first rotor near tip.

(c) Compressor-inlet total pressure. $(\Delta P_{surge})_1/P_1 = 0.1$.

Figure 2. - Variation of compressor-inlet and -discharge total pressures and mass-flow rate during surge of 10-stage axial-flow compressor at 50 percent of design speed. Surge frequency, 0.57 cps (ref. 1).

3325
CH-9 back

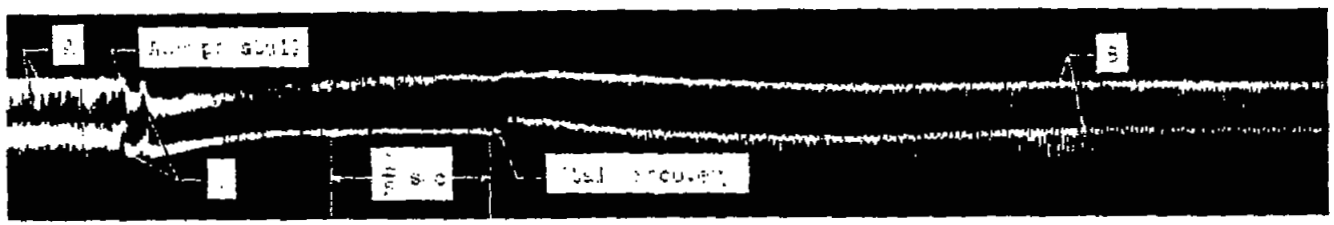

(a) Upper trace behind first rotor; lower trace behind third stator. Angle between probes, 64.6°.

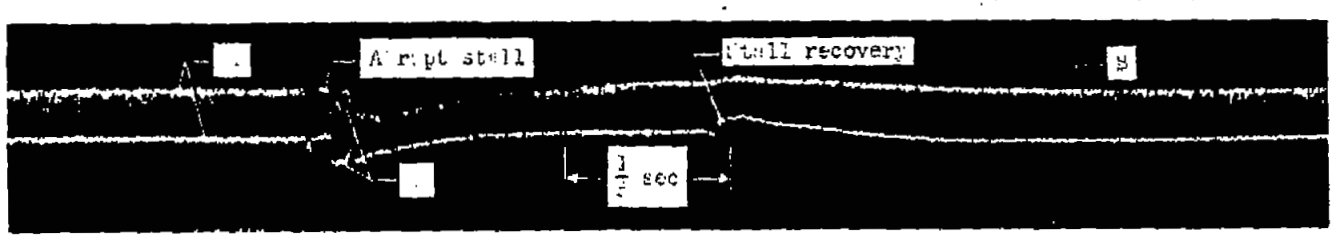

(b) Upper trace behind first rotor; lower trace behind seventh stator. Angle between probes, 104.1°.

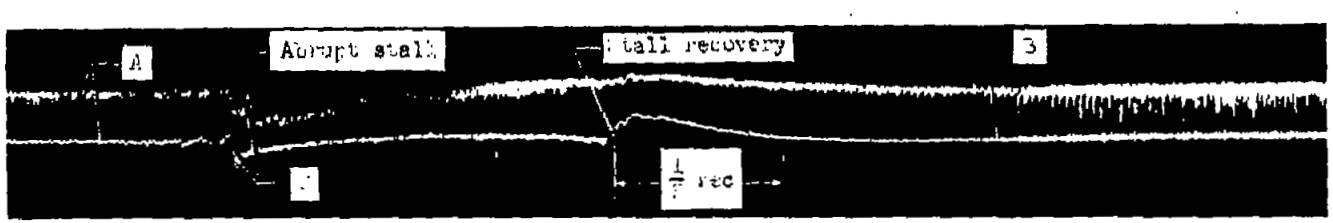

Mass-flow rate, cV

Time

C-32515

(c) Upper trace behind first rotor; lower trace behind tenth stator. Angle between probes, 104.9°.

Figure 3. - Oscillogram of surge at various axial stations in 10-stage axial-flow compressor at 50 percent of design speed. Anemometer probes near casing; surge frequency, 0.57 cps (ref. 1). (A indicates λ of 7, f_{stall} of 340 cps; B indicates λ of 3, f_{stall} of 140 cps; C indicates λ of 1, f_{stall} of 30 cps.)

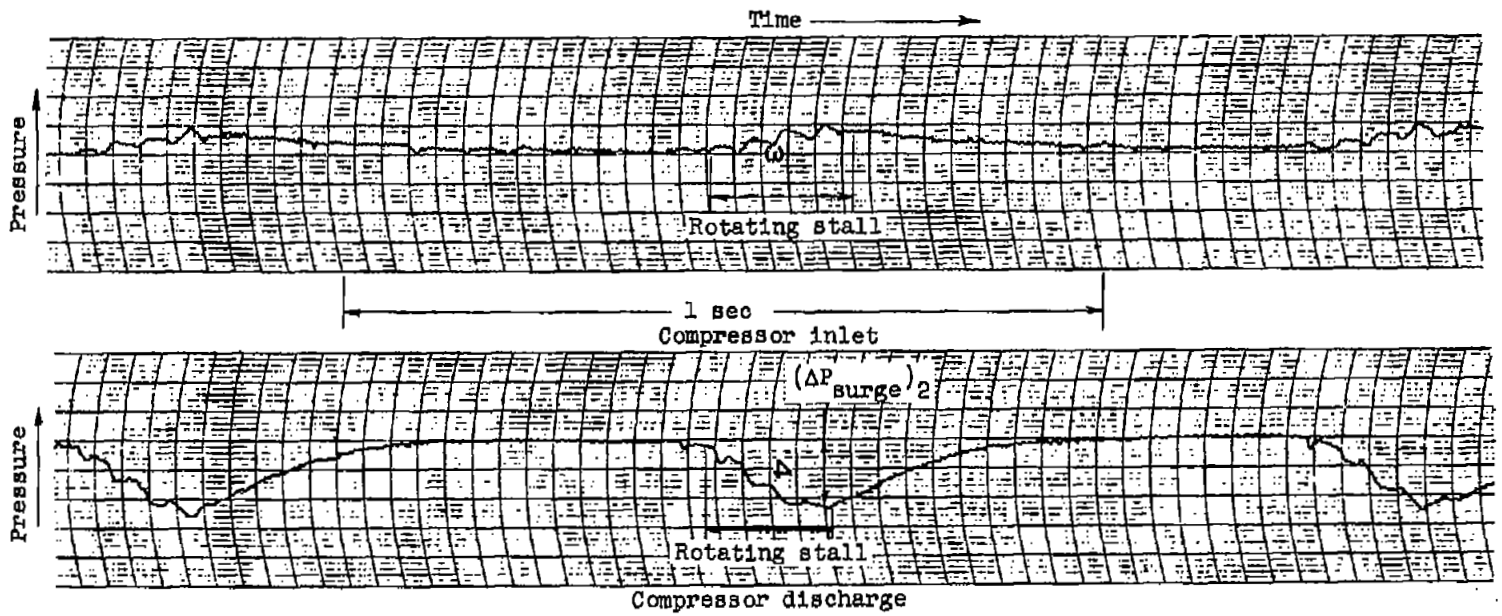

Figure 4. - Variation of compressor-inlet and -discharge total pressures during surge of 16-stage axial-flow compressor at 50 percent of design speed. Large receiver volume; $(\Delta P_{surge})_2/\Delta P_C$, 0.41; $(\Delta P_{surge})_1/P_1$, 0.085 (ref. 6).

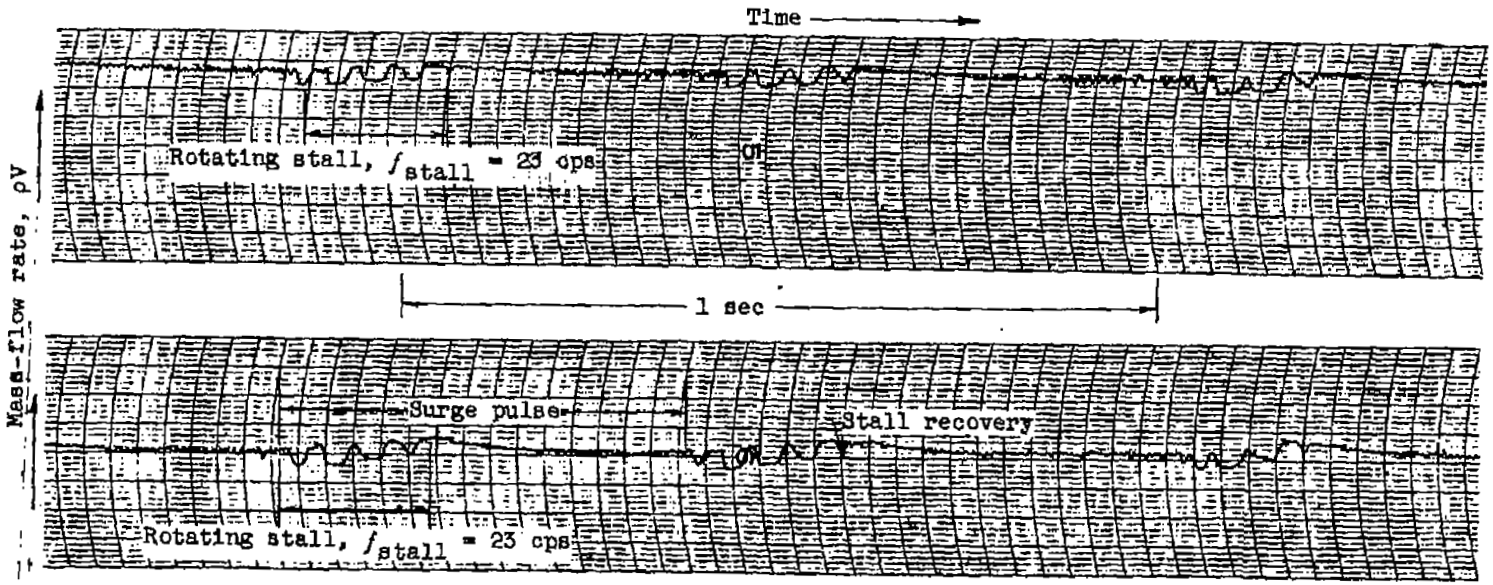

Figure 5. - Hot-wire-anemometer output during surge of 16-stage axial-flow compressor at 50 percent of design speed. Anemometer in seventh-stage stator; large receiver volume; probe spacing, 105°; surge amplitude, $\Delta\rho V/\overline{\rho V}$, ±0.3; rotating-stall amplitude, $\Delta\rho V/\overline{\rho V}$, 1.2 (ref. 6).

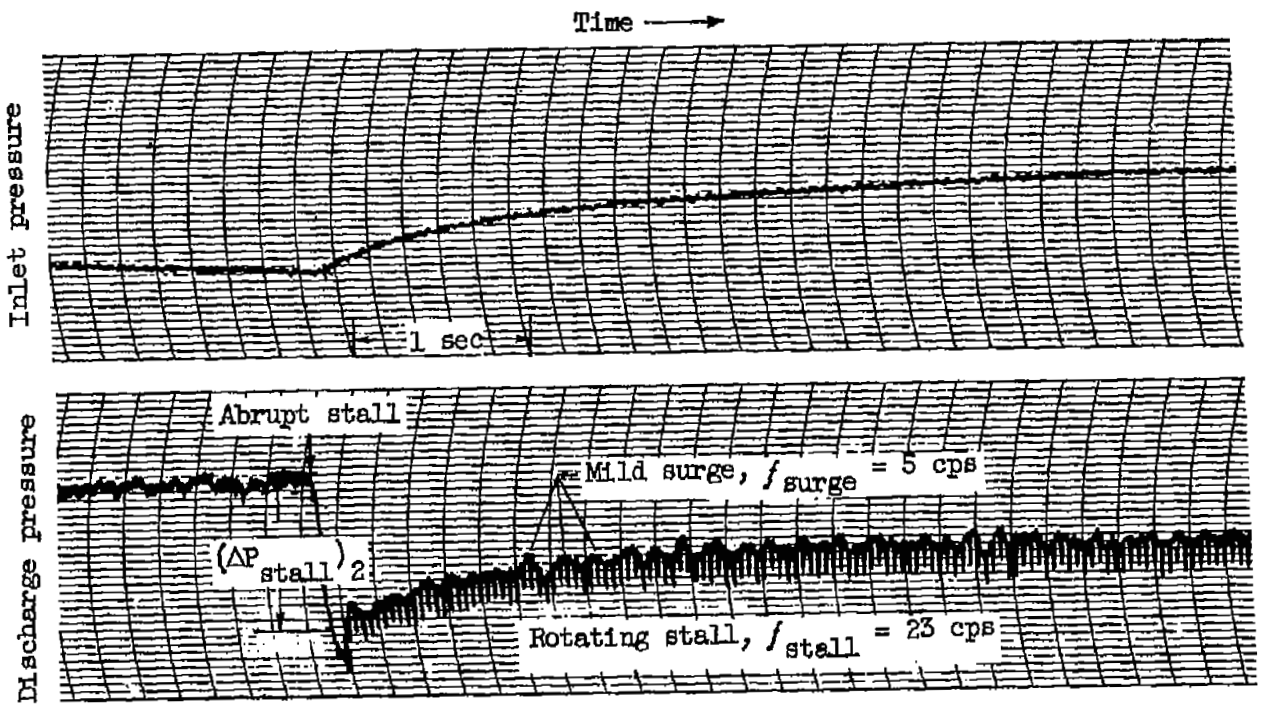

Figure 6. - Abrupt stall of 16-stage axial-flow compressor at 52 percent of design speed. Small receiver volume; $(\Delta P_{stall})_2/\Delta P_C$, 0.41; compressor pressure ratio at stall point, 1.7.

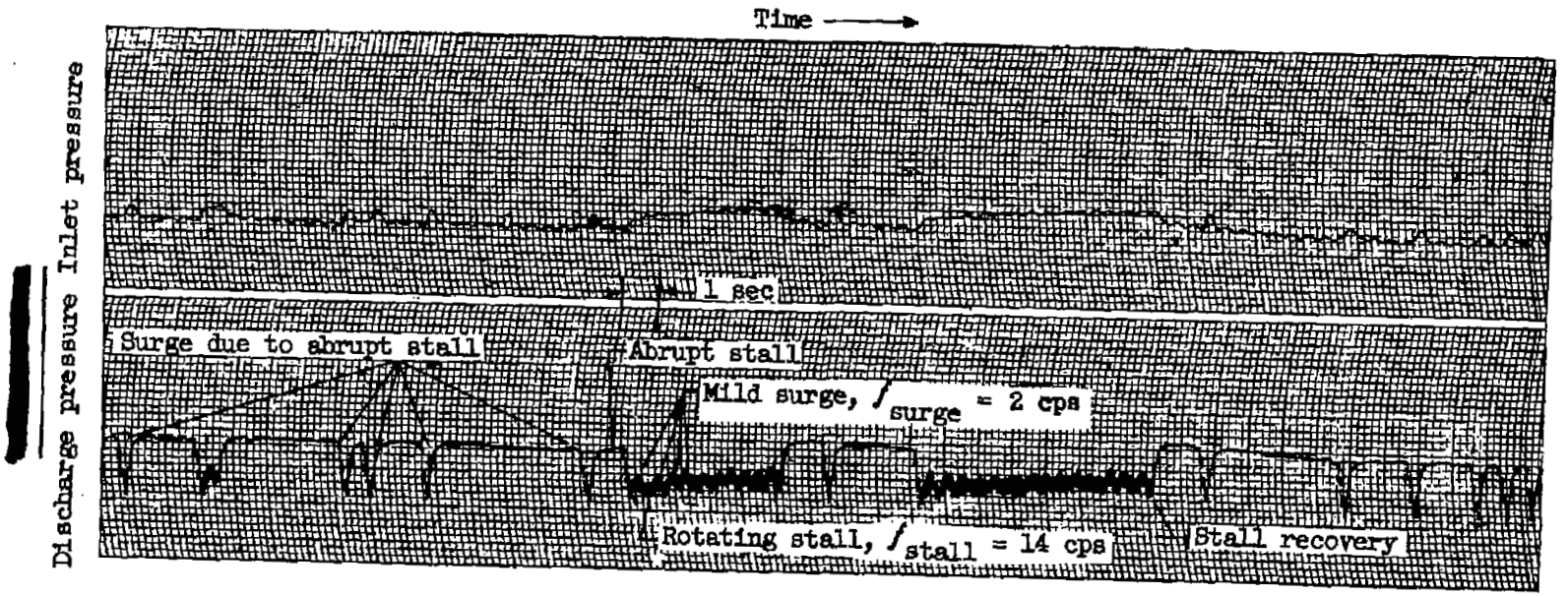

Figure 7. - Intermittent abrupt stall and surge of 16-stage axial-flow compressor at 30 percent of design speed. Large receiver volume; $(\Delta P_{stall})_2/\Delta P_C$, 0.30; compressor pressure ratio at stall point, 1.25.

3325

CH-1D

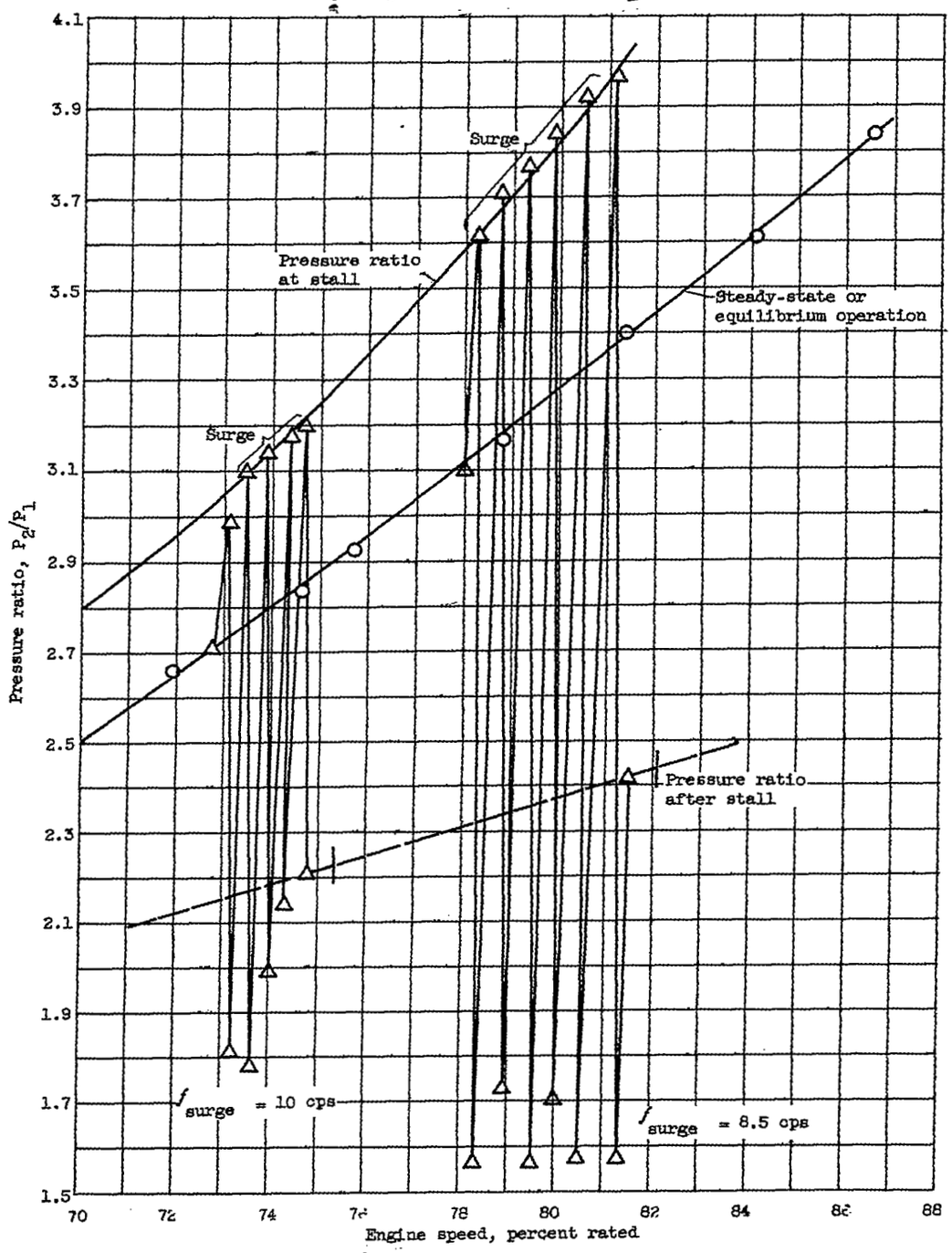

Figure 8. - Behavior of compressor total-pressure ratio in surge encountered during engine acceleration from initial speeds of 72.8 and 78 percent of rated speed (ref. 5).

[redacted]

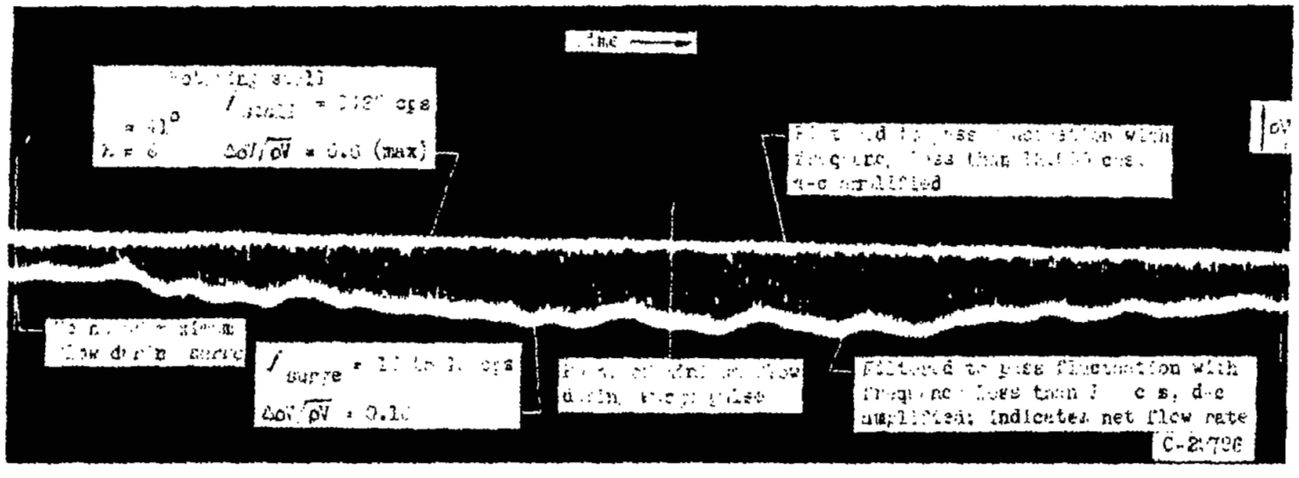

Figure 9. - Hot-wire-anemometer oscillogram of flow fluctuations during mild inaudible surge of single-stage compressor with hub-tip ratio of 0.8 at 70 percent of design speed (ref. 6).

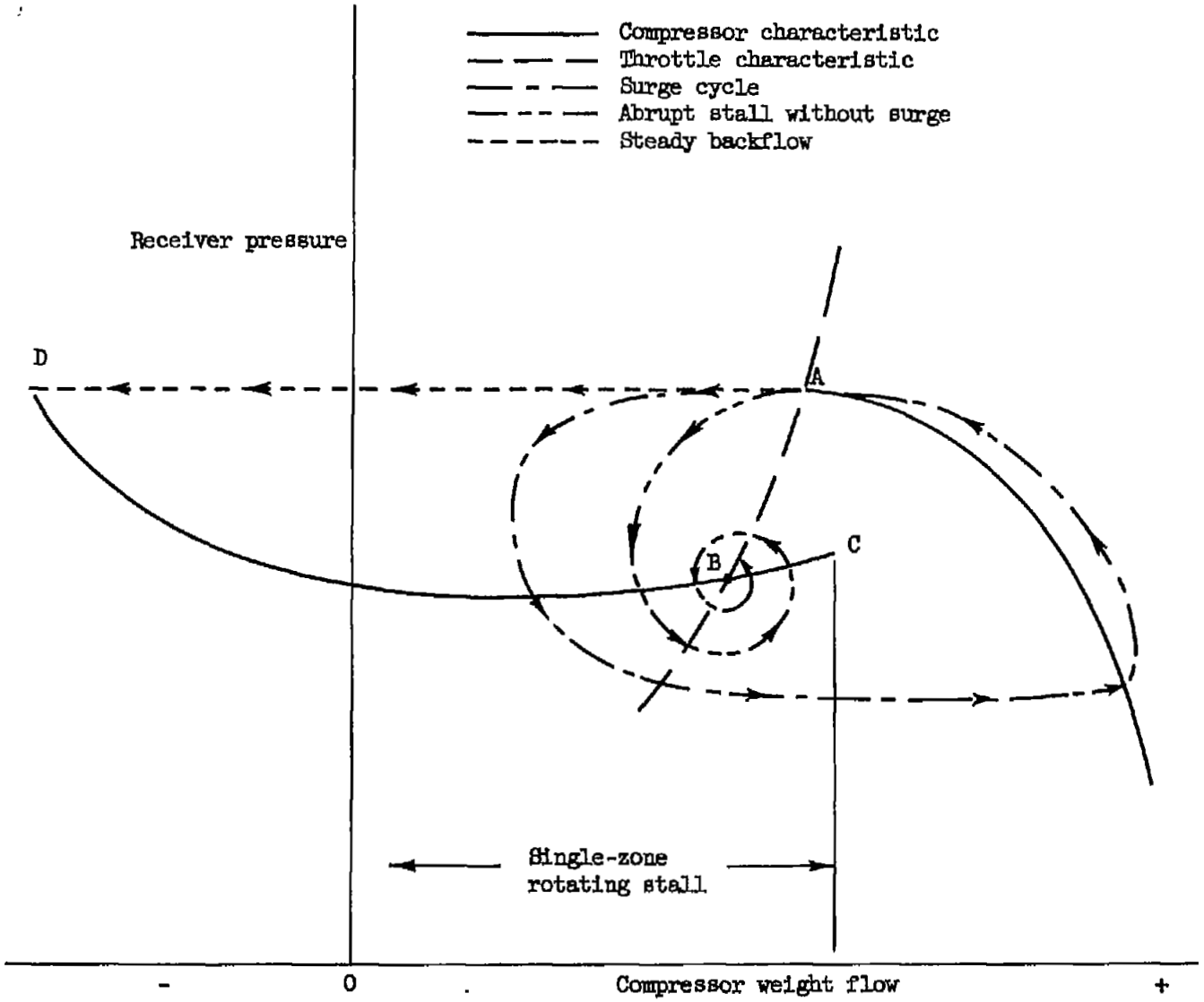

Figure 10. - Flow and pressure oscillations due to abrupt stall.

3325

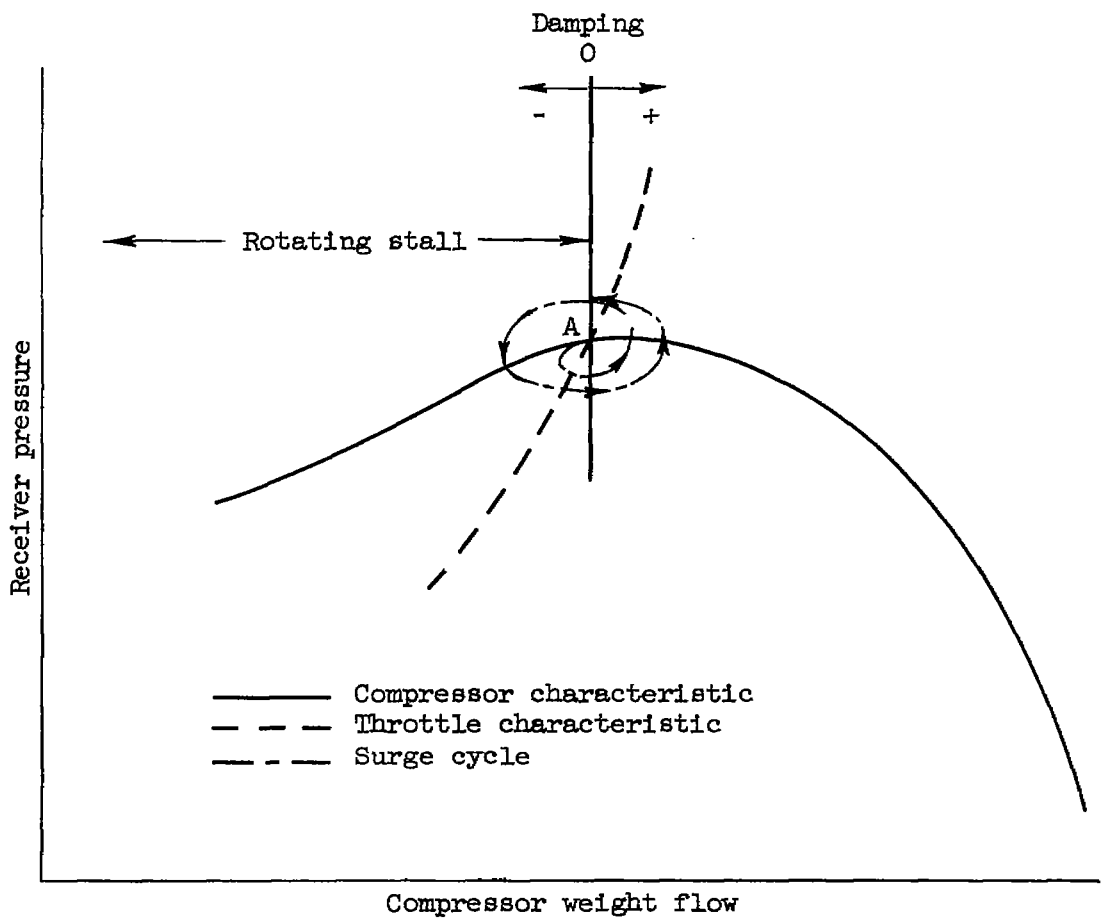

Figure 11. - Flow and pressure fluctuations due to surge associated with progressive stall.

3357

CHAPTER XIII

COMPRESSOR OPERATION WITH ONE OR MORE BLADE ROWS STALLED

By William A. Benser

SUMMARY

An analysis of the part-speed operating problems of high-pressure-ratio multistage axial-flow compressors was made by means of a simplified stage-stacking study. The principal problems considered were poor low-speed efficiency, multiple-valued performance characteristics at intermediate speeds, and poor intermediate-speed compressor surge or stall-limit characteristics. The analysis indicated that all these problems could be attributed to discontinuities in the performance characteristics of the front stages. Such discontinuities can be due to the type of stage stall or to a deterioration of stage performance resulting from stall of adjacent stages.

The effects of compromises of stage matching to favor part-speed operation were also considered. This phase of the study indicated that such compromises would severely reduce the complete-compressor-stall margin. Furthermore, the low-speed stage stall problem is transferred from the inlet stages to the middle stages, which are more susceptible to abrupt-stall characteristics.

The analysis indicates that inlet stages having continuous performance characteristics at their stall points are desirable with respect to part-speed compressor performance. These characteristics must, however, be obtained when the stages are operating in the flow environment of the multistage compressor. Alleviation of part-speed operational problems may also be obtained by improvement in either stage flow range or stage-loading margin.

The results of this analysis are only qualitative. The trends obtained, however, are in agreement with those obtained from experimental studies of high-pressure-ratio multistage axial-flow compressors, and the results are valuable in developing an understanding of the off-design problem. In addition to these stage-matching studies, a general discussion of variable-geometry features such as air bleed and adjustable blades is included.

INTRODUCTION

High-pressure-ratio multistage axial-flow compressors frequently exhibit extremely low efficiencies and severe blade-vibration problems at intermediate and low rotational speeds. In addition, such compressors may exhibit a sharp dip or kink in the surge or stall-limit line at intermediate rotational speeds, so that the attainable pressure ratios in this speed range are severely limited. Multiple performance characteristics have also been observed in this intermediate-speed range. Operation such as engine acceleration and high Mach number flight requires that the compressor component of the engine operate satisfactorily in the low- and intermediate-speed ranges. In order to alleviate these part-speed compressor problems, an understanding of the flow mechanism that causes poor part-speed performance is required. Such variable-geometry features as adjustable guide vanes or compressor air bleed may solve some part-speed operating problems, but satisfactory application of such features also depends on a knowledge of the flow mechanism. 3357

As indicated by the stage-matching analysis of reference 1, the fundamental difficulty of low-speed operation results from stalling of the front stages of the compressor. As compressor speed is decreased, the density ratio across the compressor decreases rapidly; and at low values of density ratio the small flow area of the rear stages seriously limits the flow through the compressor. Thus, the inlet stages are forced to operate at flows well below their stall limits. These trends have been verified experimentally. For example, reference 2 indicated first-stage stall for speeds below 80 percent of design speed, and reference 3 indicated first-stage stall for speeds below 70 percent of design speed. It should be noted that this mismatching of the front and rear stages of the compressor at low speeds will, in general, be more severe for high-pressure-ratio than for low-pressure-ratio compressors. A further indication as to the source of the part-speed problem can be obtained from chapter XI, which shows that rotating stall is the prevalent type of stage stall, and that rotating stall originating in the first stage of a multistage compressor results in flow fluctuations that extend completely through the compressor. The flow fluctuations of rotating stall are also a serious source of compressor blade vibrations (ch. XI).

As pointed out in chapter XII, serious compressor surge is a result of a discontinuity in the compressor performance characteristics. This discontinuity of performance may result from the abrupt type of stage stall discussed in chapter XI or from a deterioration of the performance of several stages as a result of the flow fluctuations imposed by the instigation of rotating stall in the inlet stage. The dip or kink in the surge-limit line of a 16-stage research compressor (ref. 2) was attributed to these interaction effects or to deterioration of performance of several stages as a result of stall of the inlet stage.

The existence of multiple-valued performance characteristics is shown in reference 4, which presents data showing three separate and distinct performance curves for a three-stage axial-flow compressor operating at a constant value of rotational speed. Tests of a high-pressure-ratio multistage compressor (ref. 5) show the existence of six separate performance characteristic curves for a rotational speed of approximately 75 percent of the design value. Hot-wire-anemometer data taken during this investigation indicate a correlation between compressor performance and the number of stall zones in the rotating-stall pattern.

3357

It is evident that the problems of poor part-speed efficiency, compressor blade vibration, intermediate-speed surge or stall limit, and multiple-valued performance characteristics of high-pressure-ratio multistage axial-flow compressors are all related to rotating stall and the attendant interactions or deteriorations of stage performance due to unsteady flow. The experimental approach does not yield a complete understanding of the general part-speed performance problem, because the inherent performance of each stage is not easily obtained, particularly in the range of speeds and flows where rotating stall exists in the compressor. Furthermore, the range of stage operation that can be studied experimentally is limited because of compressor surge. Therefore, to obtain a qualitative evaluation of the effects of stage stalling characteristics and of stage interactions on the general part-speed compressor performance problem, a simplified stage-stacking study was made. The basic hypothetical compressor considered was a 12-stage unit with an overall pressure ratio of 7.75. The stage performance characteristics used in the computation of multistage performance were assumed to be similar to those obtained from single-stage compressors. Interaction effects were evaluated by arbitrary modification of the assumed stage performance curves. The first three cases considered herein (repeated from refs. 6 and 7) concern various severities of interaction effects. The last two cases considered evaluate the effect of compromises of stage matching to favor part-speed performance as suggested in reference 1. When possible, the results of these studies are compared with experimental data.

Because of the assumptions made in regard to stage performance characteristics and stage interaction effects and because of the simplified stacking technique used, the computed values of compressor performance must be considered only as qualitative values. The general trends, however, are valuable in obtaining an understanding of the part-speed efficiency problem, the intermediate-speed surge or stall problem, and the multiple-valued performance characteristic problem of high-pressure-ratio axial-flow compressors. An indication of desirable types of stage performance characteristics is obtained; and, in addition, this analysis indicates some of the factors that must be evaluated if accurate performance predictions are to be obtained for the range of compressor operation where one or more of the elements are stalled. This analysis, however, does not consider the adverse effects of inlet flow distortion on the compressor stall limit.

GENERAL CONSIDERATIONS

Single-Stage Stall Characteristics

As discussed in chapter XI, stage stall may be divided into two types: (1) progressive stall, characterized by a gradual but continuous decrease in stage performance as the flow coefficient is decreased below the stalling value, and (2) abrupt stall, characterized by a sudden or abrupt drop in stage performance at the stalling value of flow coefficient. Either type of stage stall normally results in the formation of one or more low-flow or stalled zones that rotate about the compressor axis and are thus defined as rotating stall. Progressive stall is normally associated with rotating-stall zones that start at one end of the blade and grow radially and circumferentially as the flow coefficient is decreased. The stall pattern for this type of stall may consist of from one to twelve stall zones, and the number of stall zones generally increases as flow coefficient is decreased. Abrupt stall is normally associated with a simultaneous stall of all radial elements of the blade, and the stall pattern generally consists of a single stall zone. 3357

Progressive stall is prevalent in low hub-tip ratio or inlet stages, whereas abrupt stall is prevalent in high hub-tip ratio or exit stages. Typical middle stages of a multistage compressor or intermediate hub-tip ratio stages may exhibit a progressive stall followed by an abrupt stall as flow is further reduced. Both progressive and abrupt stalls exhibit a hysteresis effect, in that the flow coefficient at which stall recovery is achieved is higher than that at which stall was first encountered as the flow was decreased. This hysteresis effect is also discussed in chapter XI.

Stage Interactions

The performance and stalling characteristics may be appreciably different when a stage is operated as a single stage and when it is operated as a stage of a multistage compressor. These differences of performance, which may be designated as interaction effects, result from the radial and circumferential variations of stage-inlet conditions that may exist in the multistage compressor. As pointed out in chapter XI, interaction effects may be attributed to two main sources: (1) radial maldistribution of flow due to off-design performance of adjacent stages, and (2) circumferential maldistribution of flow or unsteady flow due to rotating stall originating in adjacent stages.

Radial maldistribution of flow. - Radial maldistribution may be defined as large variations from the design radial distribution of flow. For any stage other than the first stage of a multistage compressor, these radial maldistributions of flow result from off-design performance of preceding stages. For example, as the flow coefficient of the first stage is decreased, the energy addition at the tip of this stage usually increases

more rapidly than that at the root. Requirements of radial equilibrium of static pressure at the exit of the first-stage stator, therefore, may lead to a ratio of axial velocity at the blade tip to that at the blade root that is larger than the design value. This radial variation from design flow may be aggravated through the first few stages of the compressor and may alter the relative rate of approach to stall for the tip and root sections of subsequent stages. Thus, a stage that exhibits a partial-span progressive stall when tested as a single stage may exhibit an abrupt total-span stall when operated as a stage of a multistage compressor. Furthermore, radial maldistribution of flow can result in appreciable variations in average stage-work input for a given value of flow coefficient as well as in variations in the stalling value of flow coefficient for any stage.

3357

Unsteady flow. - When rotating stall exists in a multistage compressor, the resulting flow fluctuations extend through all stages (ch. XI). These flow fluctuations of rotating stall impose a time-unsteady circumferential velocity variation on all stages, and the instantaneous loading of the blades is certainly altered from that for steady flow at the same mean value of flow coefficient. Thus, when rotating stall is instigated by an inlet stage, the performance of all subsequent stages may be altered because of the resulting variations in circumferential flow distribution.

CH-11

Imposition of flow fluctuations of rotating stall on any stage that is operating near its stall point may result in stall of that stage. Thus, the flow fluctuations may be increased in magnitude, as was the case for the 10-stage compressor discussed in chapter XI. In addition to premature incurrence of stall in a given stage due to stall of an adjacent stage, the resulting stall pattern and performance of the given stage may be appreciably different from those predicted by single-stage tests. Stages operating at flow coefficients appreciably above the value for stall or near their choke limit, however, tend to decrease the amplitude of flow fluctuations resulting from rotating stall originating in preceding stages. The effects of flow fluctuations on the performance of such stages may, therefore, be small.

Complete Compressor Stall and Surge

Abrupt stall of one or more stages and progressive stall of the inlet stage, which result in deterioration of the performance of several subsequent stages, will both result in discontinuities in over-all performance of a multistage compressor. For the purposes of this analysis, discontinuity points in the over-all compressor performance characteristic at a given speed are designated as complete compressor stall to differentiate between stall of the over-all compressor and stall of the individual stages. As discussed in chapter XII, discontinuities in over-all compressor performance may result in compressor surge. The occurrence of

surge will, of course, depend on the external system characteristics as well as the compressor characteristics. If surge does not occur, stable performance at a lower level of pressure ratio and efficiency will be obtained. During component tests of a multistage compressor, these discontinuities in performance are not often observed, because compressor surge is encountered. Complete compressor stall and surge, however, represent the same limit of compressor operation.

STAGE STACKING

3357

As pointed out in chapter X (ref. 8), the off-design performance of a multistage axial-flow compressor may be approximated by a simplified stage-stacking technique if the generalized stage performance characteristics are known. The main purpose of the analysis reported herein is to study qualitatively the effects of various stage stall characteristics and stage interactions on the part-speed operating characteristics of multistage axial-flow compressors. In order to simplify the computations, effects of radial maldistribution of flow and effects of Mach number on stage flow range and efficiency were ignored. The detailed stacking procedure used for these computations is given in appendix B of reference 6 and is similar to that outlined in chapter X (ref. 8).

For this analysis the stage curves are assumed in terms of adiabatic efficiency and pressure coefficient as functions of flow coefficient. The adiabatic efficiency is the ratio of useful or isentropic work input to actual work input; the pressure coefficient is a function of useful work input divided by the square of the mean-radius wheel speed; and the flow coefficient is the ratio of the average inlet axial velocity to the wheel speed at the mean radius. Study of the performance of numerous stages indicates that stage performance for a range of speeds can be generalized to a single curve on the basis of these parameters. The effectiveness of this manner of generalization of data is illustrated in figure 1, which is a plot of the performance of the first, fifth, and tenth stages of the compressor reported in reference 3. Some random variations exist because of the difficulty of obtaining accurate stage performance data in the multistage compressor. The stage data, however, can be well approximated by a single curve for all speeds except for the maximum-flow points in the tenth or last stage of the compressor. In this case the effect of stage-inlet Mach number on the negative-incidence stalling angle tends to decrease the choking value of flow coefficient as compressor speed is increased. Similar Mach number effects may exist in the inlet stage. At any given speed, however, the inlet stage covers only a small part of its total range. Therefore, the Mach number effect is not noted on such a plot of experimental data. The fifth stage does not cover an appreciable flow range and, thus, does not exhibit a noticeable Mach number effect. Inasmuch as the inclusion of Mach number effects would not appreciably alter the trend obtained from the stage-stacking analysis, these effects were not considered in the computation of compressor performance.

Interaction effects were small for the compressor of reference 3, as indicated by the measured stage performance characteristics. For the compressor of reference 2, however, appreciable interaction effects were noted. For the computations reported herein, interaction effects due to unsteady flow resulting from stall in the inlet stage were estimated by altering the individual stage performance curves of several succeeding stages for those conditions where stall existed in the inlet stage. Estimated hysteresis effects in the unstalling characteristics were also incorporated in the stage curves.

For cases I to III, three combinations of stage stall, interaction effects, and unstalling hysteresis were considered. In cases IV and V, stage matching was compromised to favor part-speed operation. No effects of interaction or unstalling hysteresis were evaluated for cases IV and V.

Hypothetical Compressor, Cases I, II, and III

The basic hypothetical compressor was identical for the first three cases considered and was the same as that presented in references 6 and 7. The compressor had 12 stages of constant tip diameter. All stages had identical performance in terms of pressure coefficient and efficiency against flow coefficient, except for the stalling characteristics. Pertinent reference-point details of the compressor are as follows:

Over-all total-pressure ratio	7.75
Inlet specific weight flow, equivalent flow per sq ft annulus area	33.5
Inlet corrected tip speed, ft/sec	950
Absolute inlet-air angle at pitch radius of each stage, deg	$22\frac{1}{2}$
Flow coefficient for each stage	0.69
Pressure coefficient for each stage	0.3

Individual stage hub-tip radius ratios, area ratios, mean-radius ratios and reference-point pressure ratios are listed in table I(a).

The assumptions of stall type, interactions, and hysteresis effects for cases I to III are as follows:

Case	Type of stall			Interactions	Hysteresis effects
	Stages 1 to 4	Stages 5 to 8	Stages 9 to 12		
I	Progressive	Progressive and abrupt	Abrupt	None	None
II	Progressive	Progressive and abrupt	Abrupt	Stages 1 to 4	Stage 1
III	Progressive	Progressive and abrupt	Abrupt	Stages 1 to 8	Stage 1

3357

CH-11 back

The individual stage curves assumed for each configuration are discussed in the section DISCUSSION OF COMPUTED PERFORMANCE.

Hypothetical Compressor, Cases IV and V

Reference 1 suggested that improvements in part-speed performance of multistage compressors might be obtained by matching the stages so that at design speed the inlet stages operate at the high end and the rear stages at the low end of their flow-coefficient ranges. Case IV was, therefore, considered to evaluate the potential of such stage-matching compromises. Thus, the match-point flow coefficients for case IV were arbitrarily varied from 0.76 in the first stage to 0.63 in the twelfth stage, as compared with a constant value of 0.69 for cases I to III. The stage characteristics used were identical to those for case I. Inasmuch as the results of case IV indicated that this stage-matching compromise greatly reduced the complete-compressor-stall or surge margin at design speed, case V was considered, in which a thirteenth stage was added. The performance characteristics for this added stage were assumed identical to those for stages 9 to 12, and the match-point flow coefficient was taken as 0.626. As in previous cases, the compressor was assumed to have a constant tip diameter. 3357

Pertinent reference-point values for cases IV and V are as follows:

	Case IV	Case V
Number of stages	12	13
Over-all total-pressure ratio	7.73	9.10
Inlet specific weight flow, equivalent flow per sq ft of annulus area	35.96	35.96
Inlet corrected tip speed, ft/sec	950	950
Absolute inlet-air angle at pitch radius of each stage, deg	$22\frac{1}{2}$	$22\frac{1}{2}$

Individual stage parameters for these two cases are listed in table I(b).

Range of Calculations

For each case considered, calculations were made for a range of speeds of 50 to 110 percent of the reference value. The maximum flow considered at each speed was the estimated exit-vane choke flow. For these examples, choke flow was assumed to exist at a value of specific weight flow at the exit of the last stage of 41.4 pounds per second per square foot of annulus area. This value of specific flow is based on flow conditions at the exit of the last stage. The minimum flow considered at each speed was that

at which a discontinuity in the performance curve of any stage was encountered. As indicated in chapter XII, discontinuities in multistage-compressor performance at a given speed may lead to either compressor surge or complete compressor stall. In the computation of intermediate-speed performance for cases II and III, operation with the inlet stage stalled and unstalled was considered.

3357

DISCUSSION OF COMPUTED PERFORMANCE

Case I

The assumed stage performance curves for case I are presented in figure 2. The first four stages were assumed to have only a progressive stall, and the pressure coefficient and efficiency were taken as continuous functions of the flow coefficient, as shown in figure 2(a). Stages 5 to 8 were assumed to have an initial progressive stall and an abrupt stall at lower values of flow coefficient (fig. 2(b)). Stages 9 to 12 were assumed to have only an abrupt stall (fig. 2(c)). As noted in figures 2(b) and (c), a discontinuity of stage performance characteristics was considered to result from abrupt stall. The stage characteristics for stage pressure ratios below 1.00, which were the same for all stages, are given in figure 3. As noted in appendix B of reference 6, a modified computational procedure was used when stages operated at turbining pressure ratios. Interaction effects were considered negligible throughout the compressor.

Computed over-all performance. - The computed over-all performance map for case I is given in figure 4 as a plot of over-all total-pressure ratio against specific weight flow. The over-all total-pressure ratio, which is the ratio of total pressure at the exit of last stage to that at the compressor inlet, would not include an exit-vane or diffuser loss. The specific weight flow is the equivalent weight flow per square foot of annulus area at the compressor inlet. Also shown in figure 4 are contours of constant efficiency, the estimated choking-flow condition for the exit vanes, and the estimated complete-compressor-stall limit.

The computed maximum efficiencies for this case varied from slightly over 0.70 at 50 percent of reference speed to approximately 0.87 at 100-percent speed. The values of computed efficiency at the lowest speeds considered indicate that stage mismatching at low speeds will not completely explain the extremely low efficiencies obtained experimentally for some high-pressure-ratio multistage axial-flow compressors.

The exit-vane choke limit was the maximum flow considered at each speed. Further decreases in over-all pressure ratio would not alter the stage matching but would merely increase the losses downstream of the point of choking.

The complete compressor stall limit at each speed was the flow at which a discontinuity of performance occurred because of abrupt stall of some stage. Occurrence of abrupt stall in a stage results in very large flow fluctuations that could seriously affect the performance of all stages in the compressor. Therefore, the occurrence of abrupt stall in the multistage compressor can logically be taken as the lower limit of usable range at that speed. As pointed out in chapter XII, discontinuities in over-all performance of the compressor may result in compressor surge; and, thus, the complete-compressor-stall limit may also be considered to be the surge limit of the compressor. As noted in figure 4, this limit does not exhibit the customary dip or kink at intermediate speeds. If surge were assumed to occur at the maximum-pressure-ratio points as in reference 1, the general trends would be unchanged. 3357

Variation of stage flow coefficients. - In order to illustrate the stages that are stalled at various inlet flows and speeds, the stage flow coefficient is plotted against stage number (fig. 5) for several values of inlet flow at speeds of 100, 80, and 50 percent of the reference value. The heavily shaded area on these plots represents the range of progressive stall, and the lightly shaded area represents the range of abrupt stall with the associated discontinuity of stage pressure coefficient (fig. 2).

At 100 percent of reference speed (fig. 5(a)), flow-coefficient variations are shown for the reference-point specific flow of 33.5, the approximate exit-vane choke flow of 33.68, and the complete-compressor-stall flow of 33.06. The variation of flow coefficient in the front stages is small, and thus the specific-weight-flow range at this speed is also small. The maximum change in flow coefficient occurs in the last stage, and complete compressor stall results from abrupt stall of this stage.

As the speed is reduced to 80 percent of the reference value, the flow coefficients decrease for the entrance stage and increase for the exit stage, as shown in figure 5(b). At this speed, the first stage operates in the progressive-stall range even at the maximum specific weight flow of 23.40. Complete compressor stall results from stall of the ninth stage at a specific weight flow of 17.16. It should also be noted that the number of stages operating in the progressive-stall range increases from one to eight as the flow is decreased from the exit-vane choke value of 23.40 to the complete-compressor-stall value of 17.16.

As the speed is further decreased to 50 percent of the reference value (fig. 5(c)), the front stages move deeper into stall and the rear stages closer to choking flow. Complete compressor stall results from occurrence of abrupt stall in the fifth stage. From five to seven stages operate in the progressive-stall range at all flows.

A comparison of figures 5(a), (b), and (c) shows that at high speeds complete compressor stall results from abrupt stall of the rear stages; and,

as speed is reduced, earlier stages in the compressor instigate complete compressor stall. As shown by the variation of stage flow coefficient and by the assumed abrupt-stall limits (fig. 5), complete compressor stall will only be instigated by stages 5, 9, and 12 for this example.

In order to define more clearly the relation of stage stall to compressor speed and flow, the individual stage stall limits are cross-plotted on the computed performance map in figure 6. This figure shows that progressive stall exists in from one to eight stages for all speeds below 80 percent of the reference value and for the low-flow portion of the flow range at speeds of 85 and 90 percent. It should be noted that, near the complete-compressor-stall point at 90-percent speed (fig. 6), nearly all the stages stall at approximately the same value of specific weight flow. In fact, stages 2 to 5 stall at a slightly higher value of inlet flow than stage 1. As pointed out in chapter XI, rotating stall is a prevalent source of compressor blade vibration. Therefore, this range of operation where progressive stall exists is extremely important with respect to engine reliability.

3357

In general, the computed progressive-stall limits of this hypothetical compressor (fig. 6) are verified by experimental studies of rotating stall in multistage compressors. The speeds at which this type stall are encountered are somewhat higher than discussed in chapter XI. The speed at which inlet-stage stall first occurs, however, would be a function of stage characteristics as well as design-point matching. For this example, all stages were assumed to have identical characteristics up to the stall point and were matched at a constant value of flow coefficient of 0.69. Mach number effects, which were ignored in this analysis, may also vary the speed at which inlet-stage stall is first encountered. As can be seen from the stage curves of figure 1, a reduction in rotational speed, which corresponds to a reduction in stage-inlet Mach number, results in an increase in the maximum obtainable flow coefficient of the exit stage of a multistage compressor. Correspondingly, a decrease in inlet Mach number of the first stage would tend to decrease the flow coefficient at which stall of this stage is encountered. Both of these effects would tend to decrease the speed at which first-stage stall is encountered in the multistage compressor but would not alter the trends indicated by the computed compressor performance.

The lines of abrupt stall (fig. 6) show that, for speeds up to 70 percent of the reference value, complete compressor stall results from abrupt stall of the fifth stage; for speeds of 75 to 90 percent, from abrupt stall of the ninth stage; and for speeds of 95 percent and higher, from abrupt stall of the twelfth stage. The resulting complete-compressor-stall limit, however, is free of the normal dip or kink that is frequently encountered in high-pressure-ratio multistage compressors.

Case II

Case II was computed to evaluate the effects of small discontinuities resulting from interaction effects in the first few stages of a multistage compressor, and also to evaluate the effects of unstalling hysteresis of the inlet stage. Interaction effects were assumed to exist in the first four stages. The detailed flow studies of the 10-stage research compressor discussed in chapter XI reveal that flow fluctuations of rotating stall increased through the first four stages and then decreased through the remaining stages. Therefore, the assumption of interaction effects in four stages appeared reasonable. The magnitude of the decrease in performance was arbitrarily chosen. 3357

The stage characteristics used for stages 1 to 4 of case II are given in figure 7. These stage performance characteristics were obtained by arbitrarily modifying the pressure-coefficient characteristics used in case I and computing the modified efficiency curves assuming no change in the actual work input from that of case I. A small discontinuity in the performance of stage 1 was assumed as shown in figure 7(a). The unstalling hysteresis effect is also indicated in this figure. Stall recovery was assumed to occur at a flow coefficient of 0.60, whereas stall originally occurred at a flow coefficient of 0.565. To evaluate interaction effects, stages 1 to 4 were assumed to operate on the lower or stalled portions of their performance curves (fig. 7) whenever any of these stages encountered stall. The stage performance characteristics for stages 5 to 12 were identical to those of case I (figs. 2(b) and (c)).

Performance with front stages unstalled. - The calculated performance map for case II for the condition of no stall in the front stages is presented in figure 8(a). This performance map is identical to the high-speed part of the map for case I (figs. 4 and 6) except for the complete-compressor-stall limit at speeds below 95 percent of the reference value. In case II the stall of one of the front stages leads to a discontinuity of over-all performance because of the assumed interaction effects. Thus, an envelope of the progressive-stall limits for case I (fig. 6) represents the complete-compressor-stall limit for case II for speeds from 80 to approximately 95 percent of reference speed. No operation with the front stage unstalled is obtainable below 80-percent speed.

Performance with first stage stalled. - The computed performance for case II for the condition of stall in the first stage and interactions in stages 2 to 4 is shown in figure 8(b) for speeds of 50 to 95 percent of the reference speed. The upper limit of flow for speeds of 85, 90, and 95 percent of the reference value was determined by the unstalling flow coefficient for the first stage. At 95-percent speed, the front-stage unstalling limit intersects the ninth-stage stall-limit line (fig. 8(b)). Therefore, this was the maximum speed for which calculations of performance with the front stage stalled were made. Complete compressor stall

at speeds of 50 to 70 percent results from discontinuities due to the occurrence of abrupt stall of the fifth stage, and, at speeds of 75 to 95 percent, from abrupt stall of the ninth stage.

The efficiencies for case II at intermediate speeds are somewhat lower than for case I. This decrease in efficiency is a direct result of the decrease in pressure coefficient assumed for stages 1 to 4 for the condition of progressive stall and stage interaction effects in these stages.

3357

Complete performance map. - The complete performance map for case II is obtained by superimposing the performance maps for operation with the inlet stage unstalled and the performance map for operation with the inlet stage stalled and interactions in stages 2 to 4 (figs. 8(a) and (b)). The resulting performance in terms of pressure ratio against specific weight flow is given in figure 8(c) for a range of speeds from 50 to 110 percent of the reference value. For a range of speeds from 80 to 95 percent of the reference value, operation with both the inlet stage stalled and the inlet stage unstalled is possible. Thus, in this intermediate-speed range, the existence of double performance curves and two complete-compressor-stall or surge points at a given speed is indicated. The double curves of this analysis were obtained as a result of a small discontinuity in the performance characteristics of the first stage and interactions in stages 2 to 4. These results are verified by the multiple performance curves obtained in the experimental investigations reported in references 4 and 5.

CH-12

It should be noted that, for the computations of case II, a small discontinuity in the pressure-coefficient curve of stage 1 was assumed. Similar results would be obtained, however, if the performance of stage 1 were assumed to be continuous, provided discontinuities of stage performance as a result of interaction were assumed for any of the following stages.

Transition from stalled to unstalled operation of inlet stage. - Reference 5 indicates multiple values of surge-point performance for intermediate-speed operation. In these tests, the particular surge point obtained depended upon the schedule of speed and flow that preceded the occurrence of surge. The double-valued curves of figure 8(c) and the dependence of compressor performance on the manner in which a particular operating point is approached indicate the necessity of studying the transition from compressor operation with the inlet stage stalled to operation with the inlet stage unstalled.

The usual operating schedule in compressor-component testing is to start at maximum or choke flow for a given speed and increase the throttling in successive steps until surge is obtained. Inasmuch as compressor operation at maximum flow at low and intermediate speeds is normally set

by the choke of the exit vanes, transition from stalled to unstalled operation of the inlet stage can be considered to occur along the exit-vane choke limit of figure 8(c). Thus, as the compressor speed is increased, the choking limit of the exit vanes will prevent unstalling of the inlet stages for this case until a speed of 85 percent of the reference value is attained. Unstalling of the inlet stage and alleviation of the resulting interaction effects will result in a transient change of operation from the exit-vane choke point on the dashed speed curve to the exit-vane choke point on the solid speed curve. For this example, the specific weight flow increases from 26 to 26.3 and the pressure ratio from 4.23 to 4.30. The efficiency is not changed appreciably. For the purposes of this chapter, the transient conditions following unstalling of the inlet stage are not considered, and the compressor operation is assumed to change discontinuously from that for inlet stage stalled to that for inlet stage unstalled. 3357

The type of over-all performance map obtained from the normal compressor-component rating techniques described is given in figure 8(d). For speeds up to 85 percent of the reference value, the compressor would operate with the front stage stalled; and for speeds above 85 percent, with the front stage unstalled. Therefore, both branches of the performance curve are given at this crossover speed of 85 percent of the reference value.

Complete-compressor-stall limit. - The complete-compressor-stall limit will follow the discontinuity points of the dotted curves up to the crossover speed and the discontinuity point on the solid curves above this speed. Thus, a stall-limit line faired through these points exhibits the dip common to most high-pressure-ratio axial-flow compressors. As indicated by this analysis of case II, however, two discrete stall-limit lines exist, the low-speed stall limit representing the mode of operation with the front stages stalled and the high-speed stall limit representing the mode of operation with no stages stalled. Inasmuch as these two stall-limit lines may overlap in the intermediate-speed range where multiple performance characteristics may exist, a continuous stall-limit line should not be faired through the stall points for the complete range of speeds. In presentation of experimental data, however, the compressor stall or surge line is faired through a finite number of points and is generally considered a continuous function of flow, pressure ratio, and speed.

The analysis of case II shows that the dip in the compressor stall or surge limit that is experimentally found to exist for intermediate-speed operation of high-pressure-ratio multistage compressors can be simulated by assuming a small discontinuity in the performance characteristics of the inlet stage and interaction effects in stages 2 to 4. Similar results would be obtained from any combination of discontinuous performance characteristics of the inlet stages. For example, the performance characteristics of the first stage of the 16-stage compressor reported in

reference 2 were continuous, but discontinuities did exist in the characteristics of a few stages after the first. It should also be noted that relatively continuous stage characteristics will result in a fairly smooth surge or stall-limit line, as indicated in reference 3.

The transition from the complete-compressor-stall limit for operation with the inlet stage stalled to that for operation with the inlet unstalled depends on the manner in which this limit is approached. If the compressor-discharge throttling is sufficient to cause the compressor to operate appreciably above the exit-vane choke limit as speed is increased, unstalling of the front stage may not be achieved until a speed appreciably greater than 85 percent of the reference value is attained. In the range of speeds from 85 to 95 percent of the reference value, the complete-compressor-stall limit may follow that of figure 8(b). But, if the speed is first increased above the value for unstalling of the inlet stage and then reduced, complete compressor stall may occur on the limit of figure 8(a) for speeds of 80 to somewhat over 90 percent of the reference value. Thus, for case II, double-valued compressor stall points at a given speed may be obtained for the range of speeds from 80 to 95 percent of reference speed, as indicated in figure 8(c). As previously discussed, this phenomenon has been observed in experimental studies of multistage axial-flow-compressor performance. For cases where unstalling of groups of stages or alleviation of interaction effects occurs stepwise, even more than two compressor performance characteristic curves may be obtained at a given value of speed.

For maximum engine acceleration, the compressor operating line in an engine will be very close to the surge or stall limit at low and intermediate speeds. Thus, the intermediate-speed complete-compressor-stall limit obtained by normal compressor rating techniques may not be representative of the complete-compressor-stall or surge limit obtained during engine acceleration. Therefore, when multiple operating curves exist at any compressor speed, performance evaluations must include all possible operating conditions. This may be done by approaching a given operating point by varying compressor speed at each of several fixed system throttle settings, as well as by variation of throttle settings at a fixed speed. Speed changes must include both increases and decreases in rotational speed. An operating technique such as this will give performance maps of the type shown in figure 8(c) for those cases where multiple performance curves exist for a given compressor rotational speed. The data of reference 5 indicate six separate performance curves at approximately 75 percent of design speed. For this compressor, the performance characteristic that exhibited no stall in the inlet stages was easily duplicated. Points on the performance characteristics for the condition of stall in the inlet stages were in general duplicable, but minor variations in the method of approach to this particular speed would result in operation on different curves of the separate performance characteristics for the condition of stall in the inlet stages. Thus, estimation of the compressor

3357

CH-12 back

performance in the actual engine based on compressor-component tests may be difficult for this intermediate-speed range. During component testing of compressors, however, it is desirable to evaluate all possible performance characteristics in this intermediate-speed range where multiple characteristics may exist.

Effect of unstalling hysteresis. - For case II a hysteresis effect was assumed in the unstalling characteristic of the inlet stage. This had no effect on the general trend of complete-compressor-stall characteristics, except with respect to the speed at which transition from stalled to unstalled operation of the inlet stage was achieved. For no hysteresis effect, unstalling of the inlet stage along the exit-vane choke line (fig. 8(b)) would be achieved at 81.5 percent of reference speed rather than at 85 percent as for the case with hysteresis. Possible discontinuities in the complete-compressor-stall limit and the potential of double-valued points between speeds of 80 to 93 percent can be seen from figure 8(c). 3357

Part-speed efficiency. - At 85-percent speed, the transition speed, the maximum computed efficiency for operation with no stage stalled was 0.86; whereas the maximum efficiency was 0.84 at this speed for the condition of inlet stage stalled and interactions in stages 2 to 4. This small difference in computed efficiency simply reflects the small changes in stage performance that were assumed to result from inlet-stage stall and the attendant interactions (fig. 7). Thus, no conclusive results can be obtained from these computed efficiencies. Interaction effects or sharp decreases in stage efficiency as a result of stage stall will, however, affect compressor efficiency adversely.

Case III

In order to evaluate more serious interaction effects, calculations were made for case III that assumed the same conditions in stages 1 to 4 as for case II and, in addition, assumed large interaction effects in stages 5 to 8. The modified performance curves for these middle stages are given in figure 9. As for stages 1 to 4, the pressure-coefficient curve for stages 5 to 8 was arbitrarily modified and the efficiency curve was computed from the pressure coefficient by assuming no change in total work input for the stage. The magnitude of discontinuity of pressure coefficient is representative of that for an abrupt type of stage stall. When progressive stall existed in stage 1, stages 5 to 8 were assumed to operate on the dotted curves of figure 9. The performance of stages 9 to 12 was identical to that for case I.

The performance of this case for the condition of unstalled operation of the inlet stage is identical to that for case II (fig. 8(a)). For the condition of stall of the inlet stage, however, the performance is markedly changed (fig. 10(a)).

Complete performance map. - The complete computed compressor performance map for case III (fig. 10(b)) is obtained by superimposing figures 8(a) and 10(a). As in case II, the multiple performance curves at speeds above 80 percent of the reference value indicate the necessity of varying the mode of testing in component rating so that all possible compressor operating conditions can be evaluated.

3357

Transition from stalled to unstalled operation of inlet stage. - For case III, if compressor speed is increased along the exit-vane choke limit, inlet-stage unstalling will be effected at 94 percent of the reference speed. At this speed the transient change in computed pressure ratio would be from 4.85 to 5.2, the change in specific weight flow would be from 28.3 to 30.9, and the change in efficiency from 0.71 to 0.81. Thus, for large interaction effects, unstalling of the inlet stage is accompanied by relatively large increases in weight flow, pressure ratio, and efficiency. The transition speed of 94 percent is shown in figure 10(b) for both the condition of stall in the inlet stage and interactions in stages 2 to 8 and the condition of no stall in the inlet stage and no interactions. If interaction effects of the magnitude assumed for this case do exist and the compressor operating characteristic follows a throttling line close to the complete-compressor-stall limit, unstalling of the inlet stage may not be achieved even at design speed. By increasing the speed to a value above that for unstalling of the inlet stage and then decreasing the speed, stall-free operation might be obtained down to 80 percent of the reference speed at low values of pressure ratio.

Complete-compressor-stall limit. - For the high-speed portion of the compressor map where no stages are stalled (fig. 8(a)), at speeds above 95 percent of the reference value, complete compressor stall results from abrupt stall of the twelfth stage; and at speeds of 80 to approximately 95 percent, from stall of stages 1 to 4 and the attendant stage interactions. For the operating conditions where stall in the inlet stage and interactions in stages 2 to 8 exist (fig. 10(a)), complete compressor stall for speeds up to 95 percent of the reference value results from abrupt stall of the ninth stage, and for higher speeds, from abrupt stall of the twelfth stage.

The complete-compressor-stall-limit line indicated for case III for the normal component rating technique can be obtained from figure 10(b). This stall-limit line would follow the complete-compressor-stall-limit points for the dashed speed curves (fig. 10(a)) up to 94 percent of reference speed. In this speed range the compressor would operate with the first stage stalled and interactions in stages 2 to 8. For speeds above 94 percent, the stall-limit line will follow the complete-compressor-stall-limit points for the solid speed curves, which represent a condition of stall-free operation for all stages.

Effect of unstalling hysteresis. - If the hysteresis effect on unstalling of the inlet stage were neglected, the first stage in this case would become unstalled at 91.5 percent of reference speed for operation along the exit-vane choke limit. The general trend of performance and complete-compressor-stall limit would, however, be unchanged. The effect of inlet-stage unstalling hysteresis is to increase the speed at which the inlet stage becomes unstalled regardless of the throttling or compressor operating line.

Part-speed efficiency. - As can be seen from a comparison of figures 4 and 10(a), interactions of the magnitude assumed for case III result in large reductions in efficiency for operation with stall in the inlet stages. The computed values indicate a reduction in efficiency of about 15 percent compared with about 2 percent for case II. Thus, the low part-speed efficiencies exhibited by some multistage axial-flow compressors may result from severe interaction effects. 3357

Multiple-valued performance characteristics. - Both cases II and III indicate the potential of two separate curves in this general speed range. If at any given value of speed the potential of different degrees of deterioration of stage performance due to interactions is considered, then more than two performance curves may be obtained. For example, if the characteristics for 85-percent speed are considered for cases I to III, the performance characteristics shown in figure 11 are obtained. Curve I represents a condition of unstalled operation for all stages; curve II, a condition of stall in the inlet stages and interactions in stages 2 to 4 as obtained for case II; and curve III, a condition of stall in the inlet stages and interactions in stages 2 to 8 as obtained for case III. Such variations in performance may be a result of changes in the number of stages that exhibit this deterioration of performance or changes in the magnitude of the performance deterioration of each stage that is affected. Variations of stall interaction effects, therefore, will result in a multiplicity of over-all performance characteristics at a given speed; and the compressor flow, pressure ratio, and efficiency will increase with decreasing severity of stall and interaction effects. The particular performance obtained will depend on the previous history of speed and flow as well as the hysteresis effect accompanying changes of stall pattern in any given compressor. Needless to say, flow distortions at the compressor inlet can aggravate these adverse effects.

Case IV

Inasmuch as part-speed performance problems of high-pressure-ratio axial-flow compressors can be attributed to stalling of the inlet stages as a result of flow limitations of the rear stages, some improvement in part-speed performance may be expected by matching the front stages near their choking value of flow coefficient and the rear stages near their stalling value of flow coefficient. This stage-matching compromise is

equivalent to matching the compressor stages for some speed lower than the design value, as suggested in reference 1. In addition to improving part-speed performance, such compromises in stage matching may reduce the speed at which progressive stall is encountered and, thus, decrease the potential of blade vibrations excited by rotating stall. To evaluate these potentials, case IV was computed. In this case, the reference-point flow coefficients of the stages were varied as shown in table I(b) from a value of 0.760 in the inlet stage to a value of 0.630 in the twelfth stage. The principal purpose of this study was to investigate variations of stage operation with speed. Therefore, no interactions were considered. The stage characteristics used for the individual stages were identical to those for case I (fig. 2).

3357

Computed over-all performance. - The computed over-all performance map for case IV is given in figure 12(a) as a plot of over-all total-pressure ratio against specific weight flow. For this case as for case I, complete compressor stall was assumed to occur when abrupt stage stall was encountered in any stage. Complete compressor stall for case IV results from abrupt stall of the fifth stage for speeds of 50, 60, and 70 percent of the reference value, from abrupt stall of the ninth stage for speeds of 80 and 90 percent, and abrupt stall of the twelfth stage for 100 and 110 percent. These results are similar to those for case I.

The peak efficiencies calculated for case IV varied from approximately 0.74 at 50 percent of reference speed to a maximum of 0.87 at 90-percent speed, and decreased to 0.85 at the reference speed.

Stage progressive-stall limits. - In order to determine the speed at which various stages reach the flow coefficient for progressive stall (0.565), the progressive-stall limits for stages 1 to 8 are cross-plotted on the computed performance map in figure 12(b). This figure shows that the first stage is stalled over almost the entire flow range at 70 percent of reference speed, and over only the low-flow portion of the compressor flow range at 80-percent speed. The first-stage stall limit intersects the complete-compressor-stall limit at approximately 85 percent of reference speed. Consideration of the stall limits of stages 2 to 7 indicates that at 90-percent speed stage 7 is the first stage to encounter progressive stall. In the range of approximately 70- to 85-percent speed, several of the front stages approach stall almost simultaneously at a weight flow somewhat higher than that for first-stage stall. At the higher values of pressure ratio at intermediate speeds, the general effect of the stage-matching compromise was to transfer the progressive-stall problem from the front stages towards the middle stages of the compressor.

No interaction effects were considered in this analysis. However, as pointed out previously, stages operating near the stalling value of flow coefficient are very susceptible to deteriorations of performance induced by flow fluctuations resulting from stall of adjacent stages.

Therefore, serious interaction effects may be expected where simultaneous stall of several stages occurs (fig. 12(b)). Furthermore, the higher hub-tip ratio stages, such as stages 5 to 7 of case IV, are more apt to exhibit an abrupt stall than are low hub-tip ratio stages, such as stages 1 to 3. At speeds of 80 to 90 percent, therefore, interaction effects may instigate abrupt stall of one of the middle stages of the case IV compressor and thereby limit the flow range at these speeds.

Comparison of cases I and IV. - A comparison of the efficiencies of case I (fig. 4) and case IV (fig. 12(a)) indicates no appreciable variations of the over-all compressor efficiency due to the stage-matching compromises of case IV. It should be noted, however, that in case I the stages were not matched at the peak-efficiency points (see fig. 2). Compared with a compressor for which all stages were matched at the peak-efficiency points, the compromise of case IV would have decreased the over-all compressor efficiency at high speeds and increased it at low speeds. 3357

The increase in first-stage flow coefficient for case IV resulted in an increased specific weight flow from 33.5 for case I to 35.9 for case IV. Thus, for a given weight-flow requirement, the compromised matching would permit the use of a slightly smaller compressor diameter.

In order to compare the complete-compressor-stall limits and stage progressive-stall limits for cases I and IV, these performance maps are superimposed in figure 12(c). This figure is plotted as pressure ratio against percent of reference-point specific weight flow in order to compare compressors of equivalent flow capacities. Comparison of the complete-compressor-stall limits (fig. 12(c)) shows that the compromise of stage matching (case IV) gave a marked decrease in the attainable pressure ratio at all speeds. It can also be seen from figure 12(c) that the percentages of reference-point specific weight flow at the lower speeds are higher for case IV than for case I. At the overspeed condition, however, the condition is reversed and case I indicates the higher percentage of reference-point flow.

The progressive-stall limits shown in figure 12(c) represent the envelope of the progressive-stall limit for stages 1 to 8 as given in figures 4 and 12(b). A comparison of these limits for cases I and IV indicates that, along the exit-vane choke limit, the speed at which progressive stall is encountered is decreased from 80-percent speed for case I to slightly less than 70-percent speed for case IV. Along the complete-compressor-stall limit, however, progressive stall occurs at somewhat higher speeds for the compromise matching design (case IV) than for case I. During engine operation at part speed, the compressor will normally operate in the high-pressure-ratio range at any given speed. As shown in figure 12(c), the stage-matching compromise used for case IV gave no effective reduction in the speed at which progressive stall might be encountered during engine operation but merely transferred the instigation of this stall from the first stage to one of the middle stages of the compressor.

From the comparison of the computed performance of cases I and IV, it is obvious that the compromise in stage matching used in case IV does not improve the progressive-stall limit appreciably but decreases the complete-compressor-stall margin. Inasmuch as this compromise in stage matching does not result in a marked decrease in the speed at which rotating stall could be encountered, it would not appreciably alter the potential blade-vibration problem associated with rotating stall.

3357

Case V

Since the compromise matching of case IV indicated a severe decrease in the pressure ratio estimated for complete compressor stall, the effect of an additional stage was considered. This hypothetical compressor, designated case V, is identical to case IV except for the addition of a thirteenth stage. The stage characteristics assumed for this added stage were the same as for stages 9 to 12 (fig. 2(c)). As in case IV, no stage interaction effects were considered in case V. The details of the stage matching and stage reference-point performance characteristics for this case are given in table I(b).

CH-13

Computed over-all performance. - Figure 13(a) presents the computed over-all performance for case V as a plot of over-all total-pressure ratio against specific weight flow. The reference-point total-pressure ratio indicated in this figure is 9.1 as compared with 7.73 for case IV. Complete compressor stall at speeds of 50, 60, and 70 percent of the reference value results from abrupt stall of the fifth stage; at speeds of 80 and 90 percent, from abrupt stall of the ninth stage; and at speeds of 100 and 110 percent, from abrupt stall of the thirteenth stage.

The peak efficiencies computed for case V varied from 0.70 at 50 percent of reference speed to 0.85 at reference speed with a maximum of 0.87 at 90-percent speed.

Stage progressive-stall limits. - The stage progressive-stall limits for case V are cross-plotted on the over-all performance map in figure 13(b). Progressive-stall limits for stages 1 to 8 are shown in this figure, and the results are similar to those for case IV (fig. 12(b)). At 90 percent of reference speed for case V, the seventh stage encounters progressive stall at a flow only slightly higher than that for complete compressor stall. At 80-percent speed, stages 3 to 6 encounter progressive stall almost simultaneously at a flow about halfway between the exit-vane choke limit and the complete-compressor-stall limit; and at 70-percent speed, stages 1 to 4 are stalled at the exit-vane choke limit.

Comparison of cases I and V. - Comparison of the efficiencies of case I (fig. 4) and case V (fig. 13(a)) shows that the stage-matching compromise and the addition of a thirteenth stage have little effect on the computed over-all efficiency. The addition of the thirteenth stage resulted

in a higher reference-point pressure ratio (9.1 for case V compared with 7.75 for case I). Because the efficiency contours are displaced towards higher pressure ratios, the case V compressor indicates a computed efficiency of approximately 0.84 at a pressure ratio of 7.75 as compared with a value of 0.86 for case I at the same pressure ratio.

The comparison of complete-compressor-stall limits for cases I and V are presented in figure 13(c), which gives a plot of pressure ratio against percent of reference-point specific weight flow. As in case IV, the specific weight flow for case V was 35.9 pounds per second per square foot of annulus area as compared with 33.5 for case I. Figure 13(c) indicates that case I has a slightly better complete-compressor-stall margin at speeds of 50 to 70 percent of the reference value; the two compressors exhibit about the same complete-compressor-stall limit at speeds of 80 to 90 percent; and case V has a slightly better stall limit at 100- and 110-percent speed. 3357

The envelope lines of the stage progressive-stall limits for stages 1 to 8 are also plotted in figure 13(c). These limits indicate that along the exit-vane choke limit case I encounters progressive stall at 80 percent of reference speed, whereas case V encounters progressive stall at about 72-percent speed. Along the complete-compressor-stall limit, both cases I and V encounter progressive stall at somewhat over 90 percent of reference speed. Thus, the compromise of stage matching and the addition of a stage (case V) do not decrease the speed at which progressive stall is encountered in the vicinity of the complete-compressor-stall limit. Therefore, the potential of blade vibrations excited by progressive stall would be equally as critical for a compressor such as case V as for one such as case I.

Figure 13(c) also shows that the compromised compressor (case V) has a slightly higher percentage of reference-point flow at lower than reference speed and a slightly lower percentage at higher than reference speed than does the compressor of case I.

This comparison indicates that, with respect to complete-compressor-stall and progressive-stall limits, the original 12-stage hypothetical compressor (case I) is comparable with the 13-stage compressor with modified stage matching (case V). For a given design flow, the case V compressor would be slightly smaller than that for case I, but this advantage is offset by the necessity of an extra stage in order to maintain the complete-compressor-stall margin for the compressor with compromised stage matching.

CONCLUDING REMARKS

Part-Speed Performance Problems

The analysis reported herein was made to study the effects of various stage stall and interaction characteristics on the part-speed efficiency,

intermediate-speed complete-compressor-stall characteristics, and multiple-valued performance characteristics of high-pressure-ratio multistage axial-flow compressors. In addition, the range of conditions where progressive rotating stall exists was considered as a range of potential blade vibrations. Effects of compromising stage matching to favor part-speed performance have also been considered. Because of the simplifying assumptions used, the results obtained represent only a first approximation. The qualitative results, however, are generally in agreement with trends observed experimentally.

3357

This analysis indicates that multiple-valued multistage performance curves will be obtained if stall of the inlet stage results in discontinuities of that stage or of one or more of the succeeding stages. Discontinuities of these succeeding stages may be a result of interaction effects due to unsteady flow initiated by progressive stall of the first stage. The particular operating point of the compressor at the speeds where multiple curves exist depends on the manner in which that operating point is approached. More than two performance curves may be obtained at a given speed if the number of stages affected by interaction varies or if the severity of interactions varies.

CH-13 back

The dip obtained in the experimentally determined surge or complete-compressor-stall-limit lines of high-pressure-ratio axial-flow compressors apparently is merely a result of transition from compressor operation with the front stages stalled to operation with these stages unstalled. The intermediate-speed limit obtained by normal component test techniques may not be representative of that obtained in an engine at the same speed. Furthermore, the engine complete-compressor-stall limit obtained during accelerations may be different from that obtained during decelerations.

This analysis indicates that extremely poor part-speed efficiencies cannot be attributed entirely to stage mismatching but can to a large extent be attributed to stage interactions or deterioration of stage performance due to unsteady flow resulting from rotating stall originating in the inlet stages. The magnitude of interaction effects for each stage and the number of stages affected will determine the reductions in performance at low and intermediate speeds.

Hysteresis effects in the unstalling characteristics of the first stage do not alter the existence of double-valued performance curves at intermediate speeds. The existence of large unstalling hysteresis in combination with severe discontinuities in stage performance may prevent unstalling of the inlet stages until very high speeds are obtained.

With respect to part-speed efficiency and intermediate-speed complete compressor stall, this study indicates the desirability of stages having continuous characteristics at their stall points. It should be noted that these stage characteristics must be maintained when the stage is operating in the flow environment of the multistage compressor. Stages of this type generally have a progressive stall that originates at one end of the blade and gradually increases in severity as the flow coefficient is decreased. Design of such stages depends on a better knowledge of the effects of unsteady flow and of radial maldistribution of flow, which result from off-design operation of adjacent stages. The stage data and over-all compressor performance characteristics obtained from the 10-stage compressor of reference 3, however, indicate that these desirable stage characteristics can to a degree be achieved. Although the use of stages having progressive stall may alleviate the part-speed efficiency and complete-compressor-stall problems, it would not alleviate the potential of blade vibrations excited by rotating stall. 3357

Increasing the stall-free range of operation of the inlet stages would, of course, increase the range of stall-free operation of the multistage compressor. Inasmuch as the part-speed problem in the multistage compressor results from flow limitations of the exit stages, stage range with respect to off-design performance can best be evaluated on the basis of flow range at the discharge rather than that at the inlet of the stage. Therefore, devices or design improvements that would increase the stage-loading limit or flow range must be evaluated to determine the potential gains in effective stage range.

More complete data on effects of stage design and blading geometry on stage stall characteristics, as well as a better understanding of stage interactions due to radial maldistribution of flow and unsteady flow as encountered in multistage compressors, are required in order to obtain a more quantitative evaluation of part-speed performance.

Stage-Matching Compromises

One proposed technique of improving part-speed performance is to compromise stage matching to favor low-speed operation of the compressor. The analysis of this technique indicates that such compromises severely reduce the complete-compressor-stall margin unless additional stages are used. The higher flow coefficients of entrance stages may permit the use of a slightly smaller compressor for a given flow capacity, but this advantage would be offset by the necessity of an additional stage to obtain the required complete-compressor-stall margin. Furthermore, no gain in the range of speeds where no rotating stall exists is obtained except near the exit-vane choke limit. Stage compromises tend to result in progressive stall in the middle stages at speeds above that for stall of the inlet stage. Thus, the potential for abrupt stall, interaction effects, and poor intermediate-speed complete-compressor-stall

characteristics would be greater for the compromised design. No reduction in the potential of blade vibration excited by rotating stall is indicated. Furthermore, stage-matching compromises to favor part-speed performance would definitely restrict the obtainable overspeed performance of any compressor.

Variable Geometry

3357

Inlet baffles. - As indicated in chapter XI, the use of adjustable inlet blockage either in the form of baffles or ramps may disrupt the periodic nature of rotating stall and thus present a potential solution to the blade-vibration problem. Preliminary tests of a hub baffle (ref. 9) indicate that the use of such a baffle may also result in some improvement in the complete-compressor-stall or surge margin at low speeds. In addition, baffles may be used at high speeds to reduce the compressor mass flow and, therefore, to act as a thrust-spoiling device.

Adjustable blading. - Adjustable inlet guide vanes and adjustable stator blades have also been proposed as variable-geometry features for alleviation of part-speed performance problems and improvement of flexibility of engine operation. The satisfactory application of such adjustable blading, however, depends on a knowledge of the variations of stage matching and radial distribution of flows that result from blade adjustment. As indicated in references 10 and 11, closing the inlet guide vanes reduces both the flow coefficient and pressure coefficient of the first stage. This change in pressure coefficient tends to moderate the decrease in first-stage flow coefficient so that the flow coefficient of the second stage is not appreciable altered. The operation of middle and latter stages, therefore, tends to be primarily a function of compressor speed and throttling rather than of inlet-guide-vane position. Thus, closing the inlet guide vanes results in an appreciable reduction in flow but only a small reduction in over-all pressure ratio for the compressor. This, in general, improves the complete-compressor-stall-limit or surge-limit characteristics. Of course, when the guide vanes are opened, the converse is true. References 10 and 11 also point out that closing the inlet guide vanes alters the radial variation of loading of the first rotor as a result of the establishment of radial equilibrium of static pressure. This radial variation of loading is in the direction of increasing the value of flow coefficient at which tip stall is encountered and thus would tend to reduce the effectiveness of guide-vane adjustment in relieving the part-speed operating problem. Furthermore, alterations in radial distribution of flow and blade loading may affect the stalling characteristics of the individual stages. Adjustable inlet guide vanes have, however, been effectively used as a means of improving engine acceleration characteristics, and adjustable guide vanes and stators provide a potential technique for improving the flexibility of high-pressure-ratio compressor operation without sacrificing design-point performance. The added weight and complexity of the engine and its control system must be considered, however.

Compressor air bleed. - Compressor-discharge bleed has been used effectively to alter the matching of the compressor and turbine at part speed so as to avoid serious intermediate-speed complete-compressor-stall problems (ref. 12). This technique, however, does not eliminate the potential of blade vibrations instigated by rotating stall. Interstage air bleed in the multistage compressor has the potential of effectively altering the matching of the inlet and exit stages and, thus, appreciably reducing the speed at which rotating stall is encountered, as well as improving the complete-compressor-stall or surge margin at intermediate speeds. The computed effects of bleed on a 16-stage compressor (ref. 13) indicate improvements in efficiency at part speed even when the compressor is charged with the work added to the bleed air. Care must be exercised in design of bleed ports to avoid resonance with adjacent blades and to avoid serious distortions of flow distribution in the vicinity of the bleed ports. The use of interstage bleed will add some weight and complexity to the turbojet engine but, in general, offers improvement in regard to intermediate-speed complete-compressor-stall or surge margins and to blade-vibration problems resulting from rotating stall.

3357

REFERENCES

1. Finger, Harold B., and Dugan, James F., Jr.: Analysis of Stage Matching and Off-Design Performance of Multistage Axial-Flow Compressors. NACA RM E52D07, 1952.

2. Medeiros, Arthur A., Benser, William A., and Hatch, James E.: Analysis of Off-Design Performance of a 16-Stage Axial-Flow Compressor with Various Blade Modifications. NACA RM E52L03, 1953.

3. Budinger, Ray E., and Serovy, George K.: Investigation of a 10-Stage Subsonic Axial-Flow Research Compressor. IV - Individual Stage Performance Characteristics. NACA RM E53C11, 1953.

4. Foster, D. V.: The Performance of the 108 Compressor Fitted with Low Stagger Free Vortex Blading. Rep. No. R.116, British N.G.T.E., June 1952.

5. Lucas, James G., and Filippi, Richard E.: Multiple Over-All Performance and Rotating-Stall Characteristics of a 15-Stage Experimental Axial-Flow Compressor at an Intermediate Speed. NACA RM E54C29, 1954.

6. Benser, William A.: Analysis of Part-Speed Operation for High-Pressure-Ratio Multistage Axial-Flow Compressors. NACA RM E53I15, 1953.

7. Huppert, Merle C., and Benser, William A.: Some Stall and Surge Phenomena in Axial-Flow Compressors. Jour. Aero. Sci., vol. 20, no. 12, Dec. 1953, pp. 835-845.

8. Compressor and Turbine Research Division: Aerodynamic Design of Axial-Flow Compressors. Vol. II. NACA RM E56B03a, 1956.

9. Lucas, James G., Finger, Harold B., and Filippi, Richard E.: Effect of Inlet-Annulus Area Blockage on Over-All Performance and Stall Characteristics of an Experimental 15-Stage Axial-Flow Compressor. NACA RM E53L28, 1954.

10. Budinger, Ray E., and Serovy, George K.: Investigation of a 10-Stage Subsonic Axial-Flow Research Compressor. V - Effect of Reducing Inlet-Guide-Vane Turning on Over-All and Inlet-Stage Performance. NACA RM E53H10, 1954.

11. Budinger, Ray E., and Kaufman, Harold R.: Investigation of the Performance of a Turbojet Engine with Variable-Position Compressor Inlet Guide Vanes. NACA RM E54L23a, 1955.

12. Rebeske, John J., Jr., and Rohlik, Harold E.: Acceleration of High-Pressure-Ratio Single-Spool Turbojet Engine As Determined from Component Performance Characteristics. I - Effect of Air Bleed at Compressor Outlet. NACA RM E53A09, 1953.

13. Rebeske, John J., Jr., and Dugan, James F., Jr.: Acceleration of High-Pressure-Ratio Single-Spool Turbojet Engine As Determined from Component Performance Characteristics. II - Effect of Compressor Interstage Air Bleed. NACA RM E53E06, 1953.

3357

TABLE I. - REFERENCE-POINT VALUES

(a) Cases I, II, and III

Stage	Area ratio[a]	Mean-radius ratio[b]	Hub-tip radius ratio	Stage pressure ratio
1	0.8431	1.071	0.5000	1.179
2	.8510	1.046	.6063	1.196
3	.8547	1.033	.6795	1.203
4	.8580	1.025	.7348	1.204
5	.8630	1.019	.7779	1.202
6	.8695	1.015	.8120	1.198
7	.8720	1.012	.8389	1.192
8	.8780	1.010	.8613	1.186
9	.8835	1.008	.8794	1.179
10	.8875	1.007	.8943	1.172
11	.8920	1.0055	.9068	1.166
12	.8960	1.0045	.9173	1.159

3357

(b) Cases IV and V

Stage	Area ratio[a]	Mean-radius ratio[b]	Hub-tip radius ratio	Stage pressure ratio	Flow coefficient	Pressure coefficient
1	0.9009	1.046	0.5000	1.136	0.760	0.231
2	.8929	1.038	.5696	1.157	.741	.252
3	.8889	1.031	.6299	1.173	.723	.270
4	.8857	1.026	.6810	1.186	.705	.287
5	.8818	1.022	.7246	1.197	.686	.304
6	.8803	1.018	.7623	1.205	.668	.320
7	.8606	1.018	.7944	1.210	.650	.335
8	.8651	1.014	.8261	1.205	.650	.335
9	.8787	1.010	.8516	1.198	.650	.335
10	.8850	1.008	.8709	1.193	.643	.340
11	.8857	1.007	.8867	1.189	.636	.346
12	.8889	1.006	.9003	1.183	.630	.350
13	.8897	1.006	.9100	1.177	.626	.353

[a]Ratio of exit to inlet area for stage.
[b]Ratio of exit to inlet mean radius for stage.

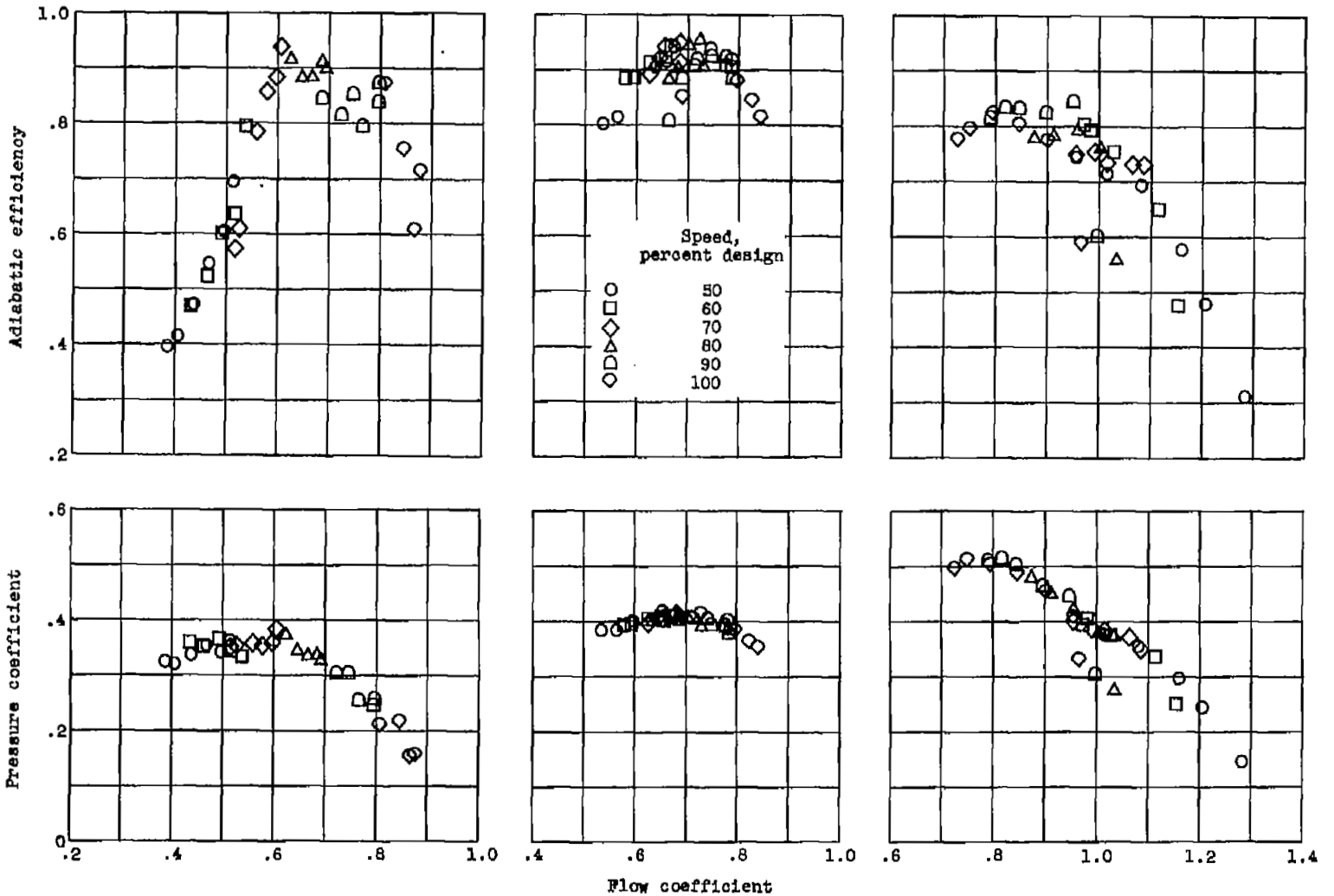

(a) Stage 1. (b) Stage 5. (c) Stage 10.

Figure 1. - Generalized stage performance for stages 1, 5, and 10 of reference 3.

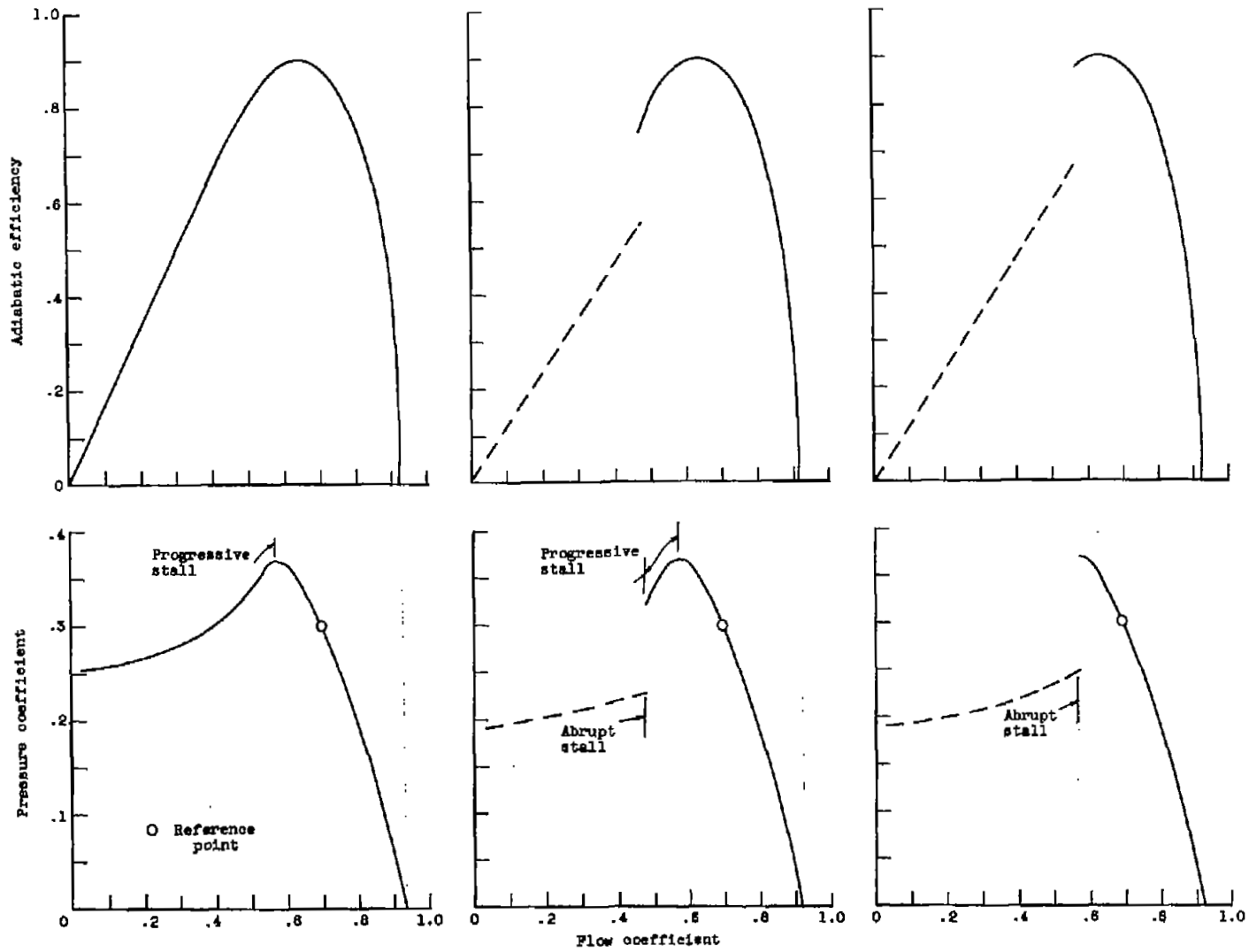

(a) Stages 1 to 4. (b) Stages 5 to 8. (c) Stages 9 to 12.

Figure 2. - Assumed stage performance characteristics for case I.

3357

CH-1, back

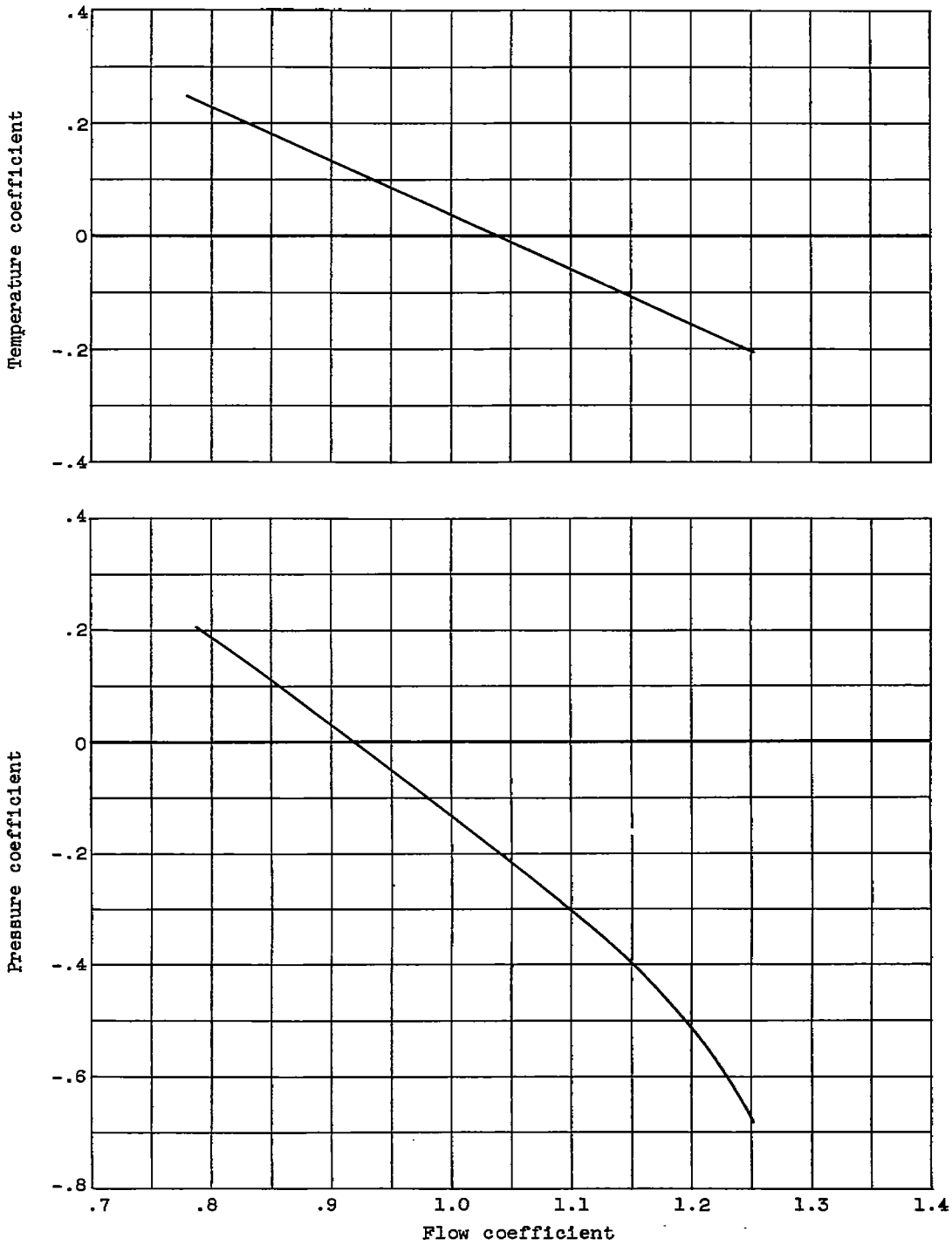

Figure 3. - Assumed performance characteristics for negative values of pressure coefficient for all stages.

[redacted]

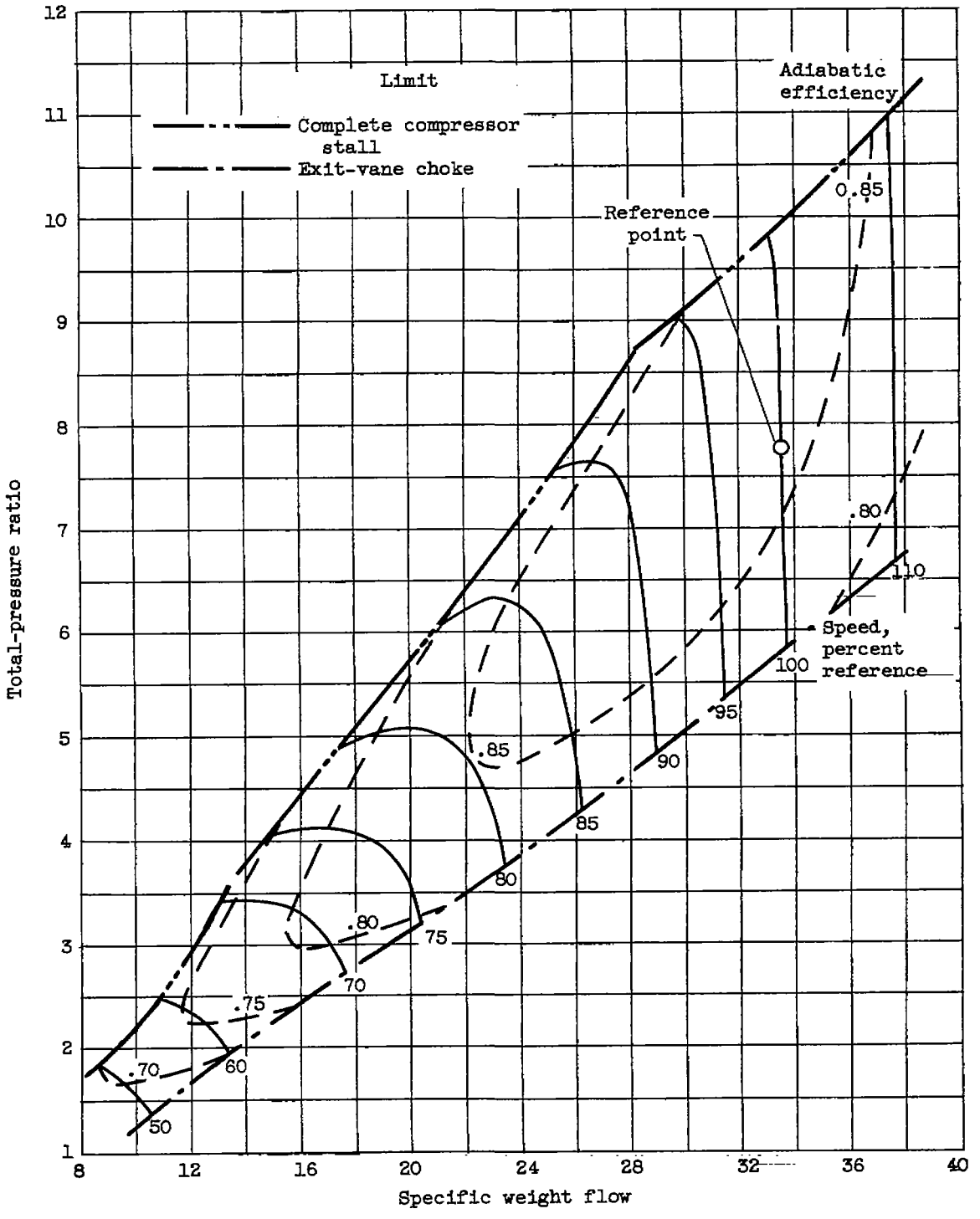

Figure 4. - Computed over-all performance for case I.

3357

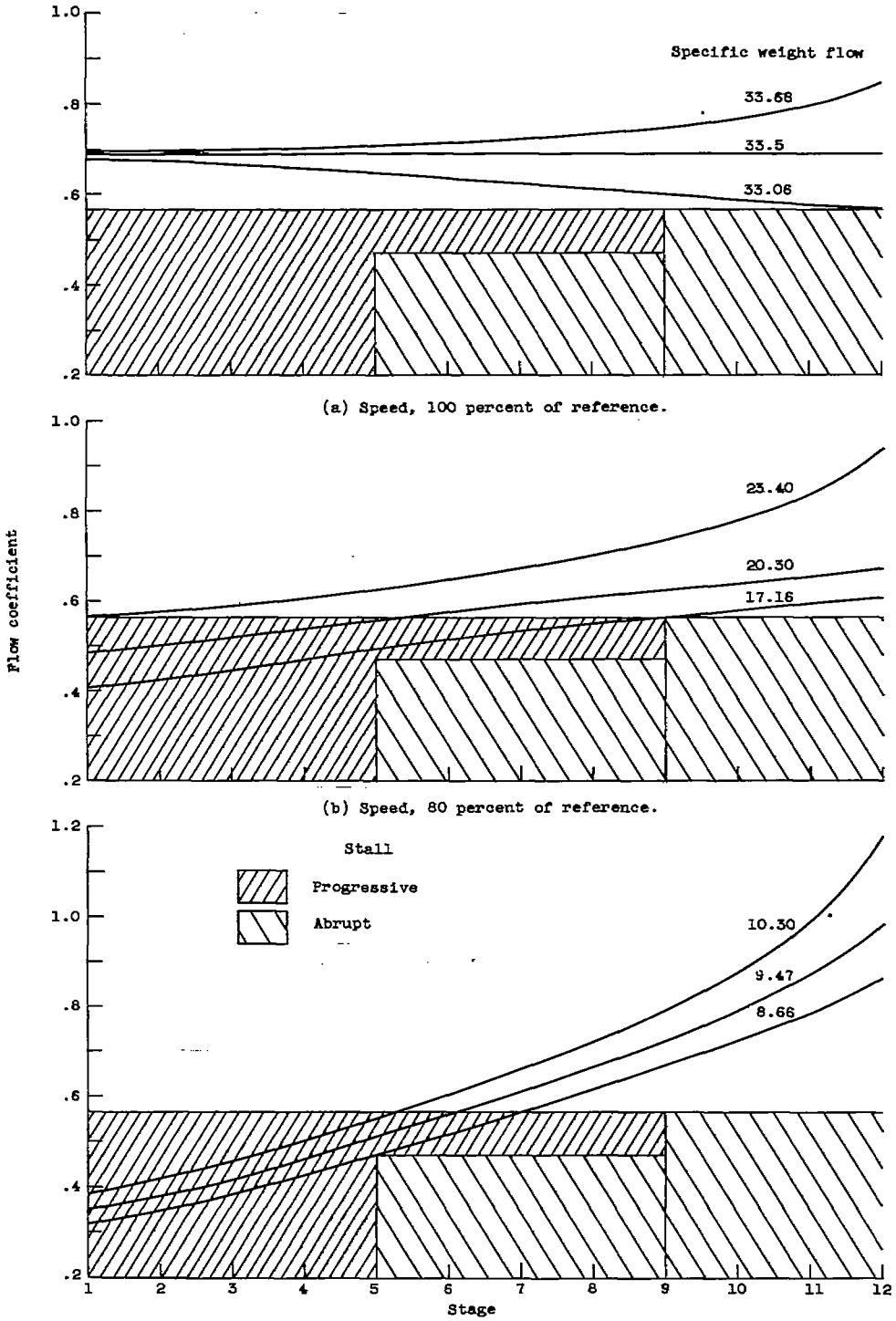

(a) Speed, 100 percent of reference.

(b) Speed, 80 percent of reference.

(c) Speed, 50 percent of reference.

Figure 5. - Stagewise variation of flow coefficient for case I.

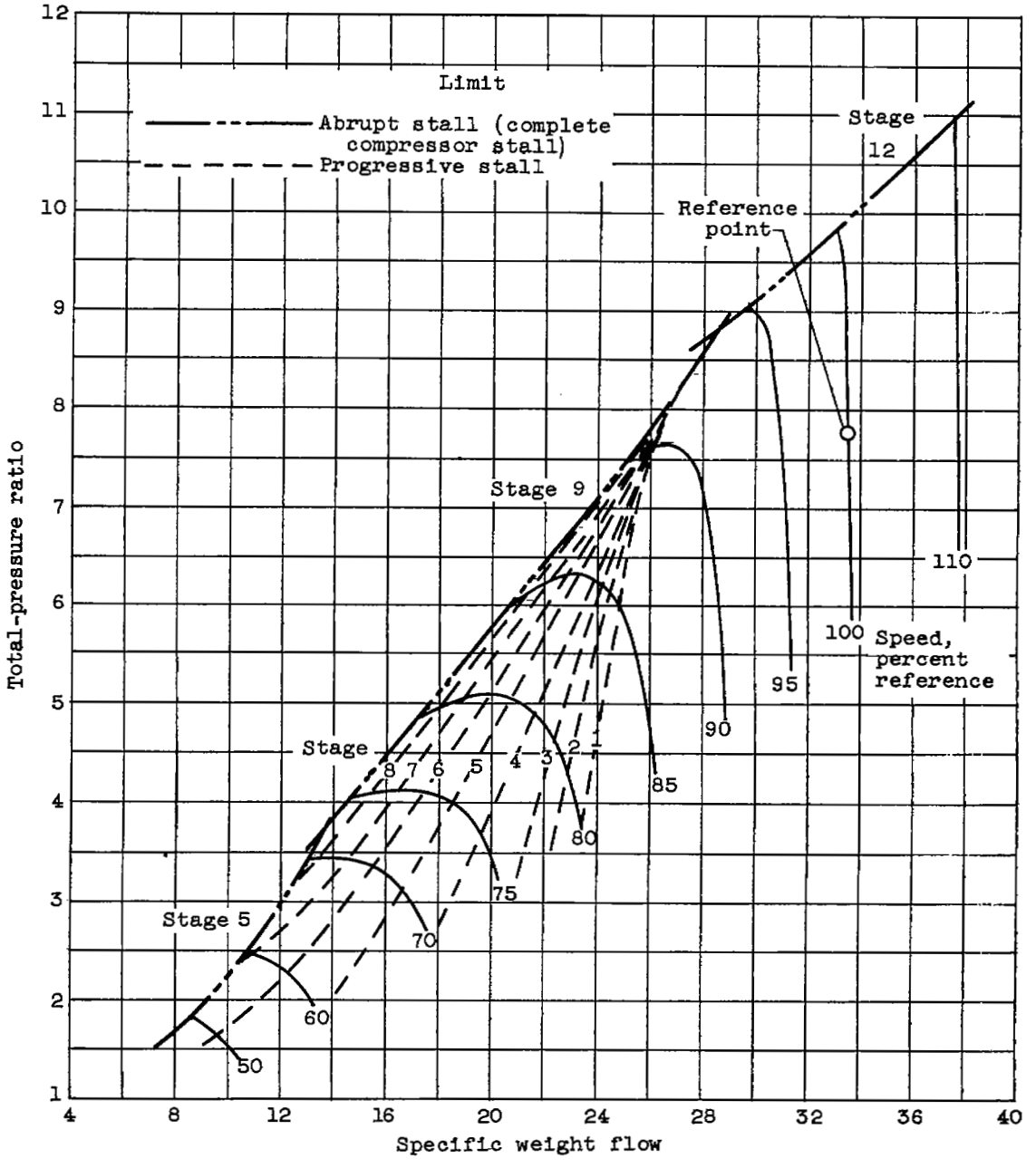

Figure 6. - Relation of stage stall and over-all compressor performance for case I.

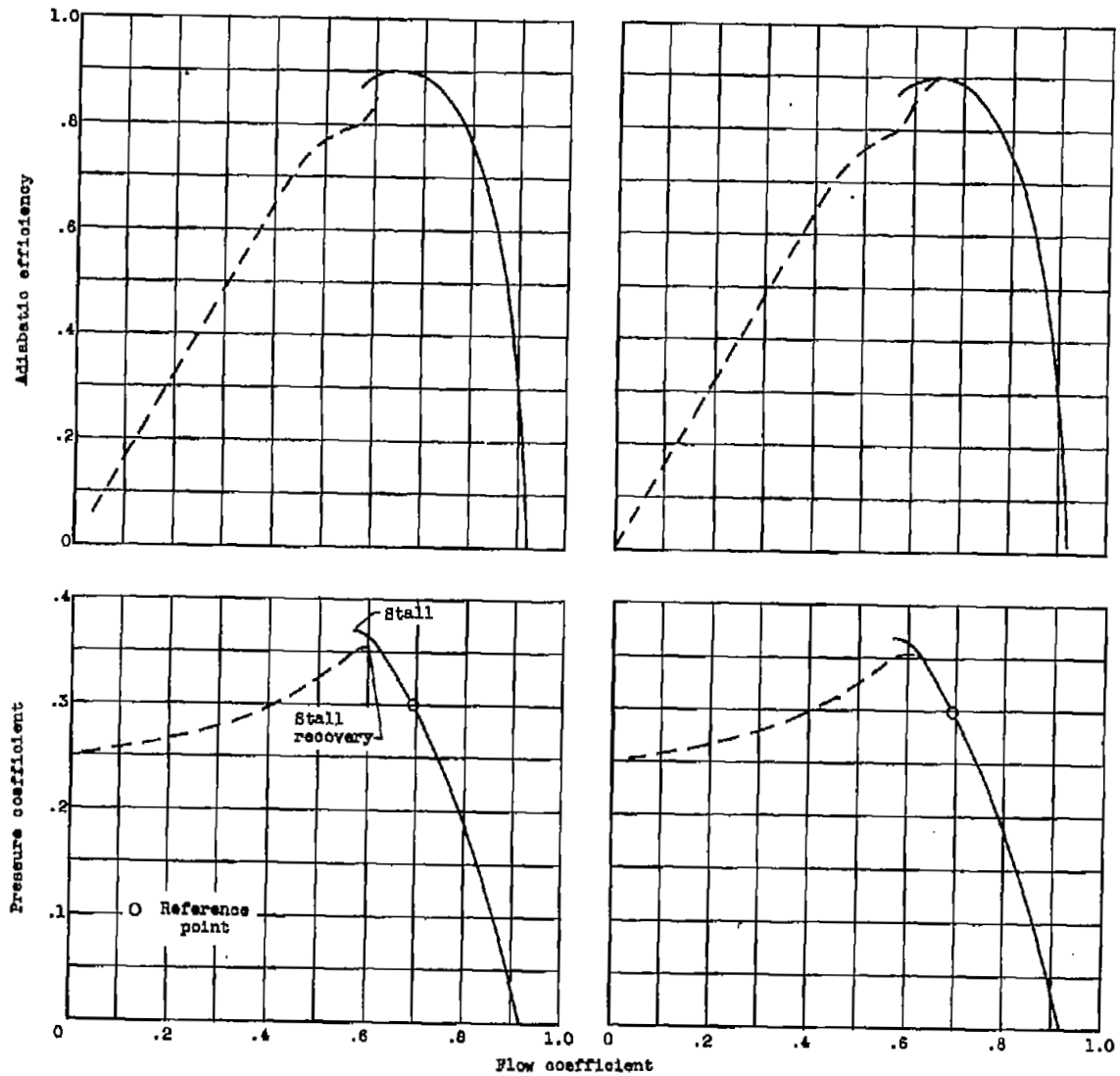

(a) Stage 1.

(b) Stages 2 to 4.

Figure 7. - Assumed performance characteristics for stages 1 to 4 for case II.

3357

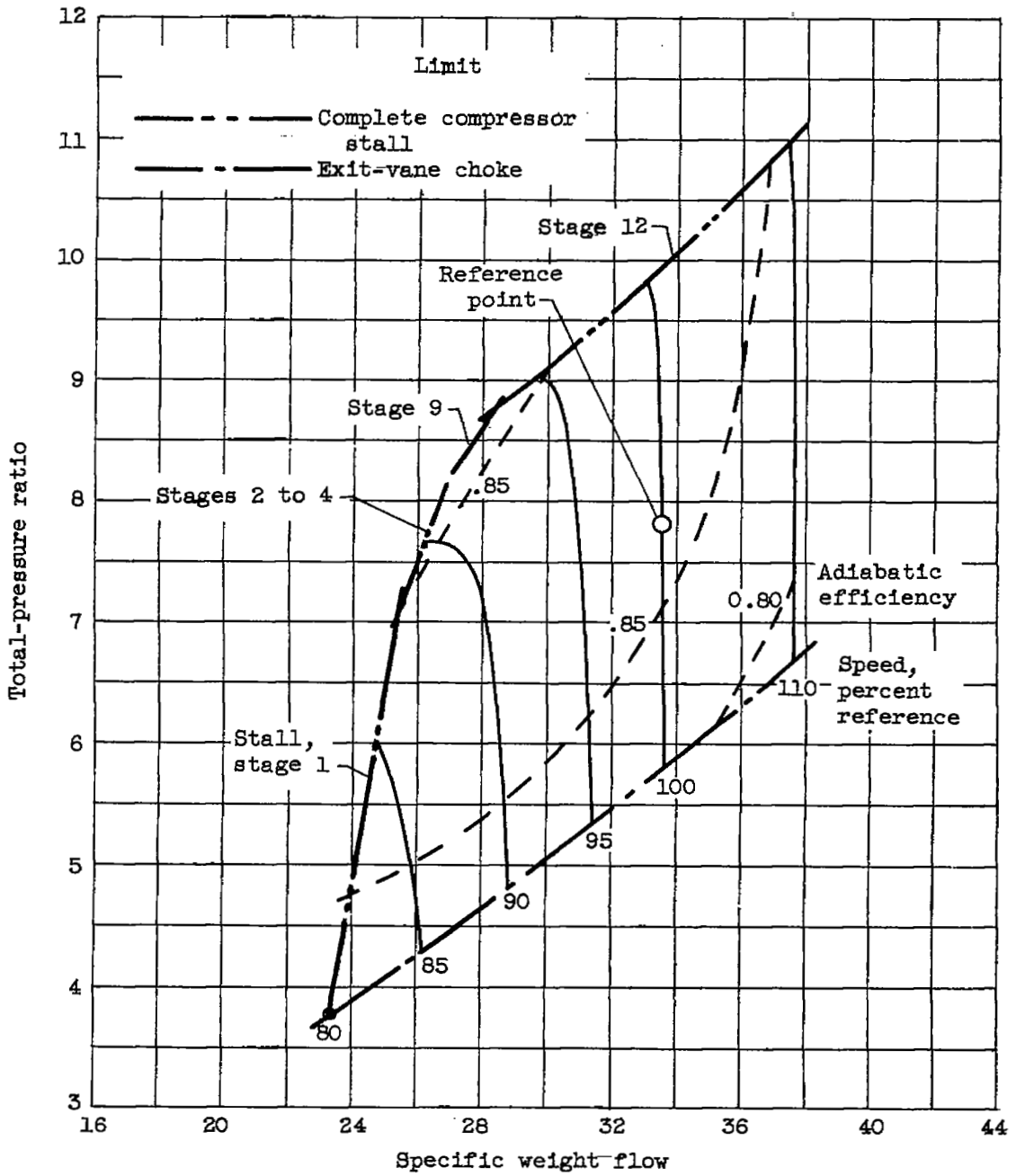

(a) Front stage unstalled.

Figure 8. - Computed over-all performance for case II.

3357

CH-15

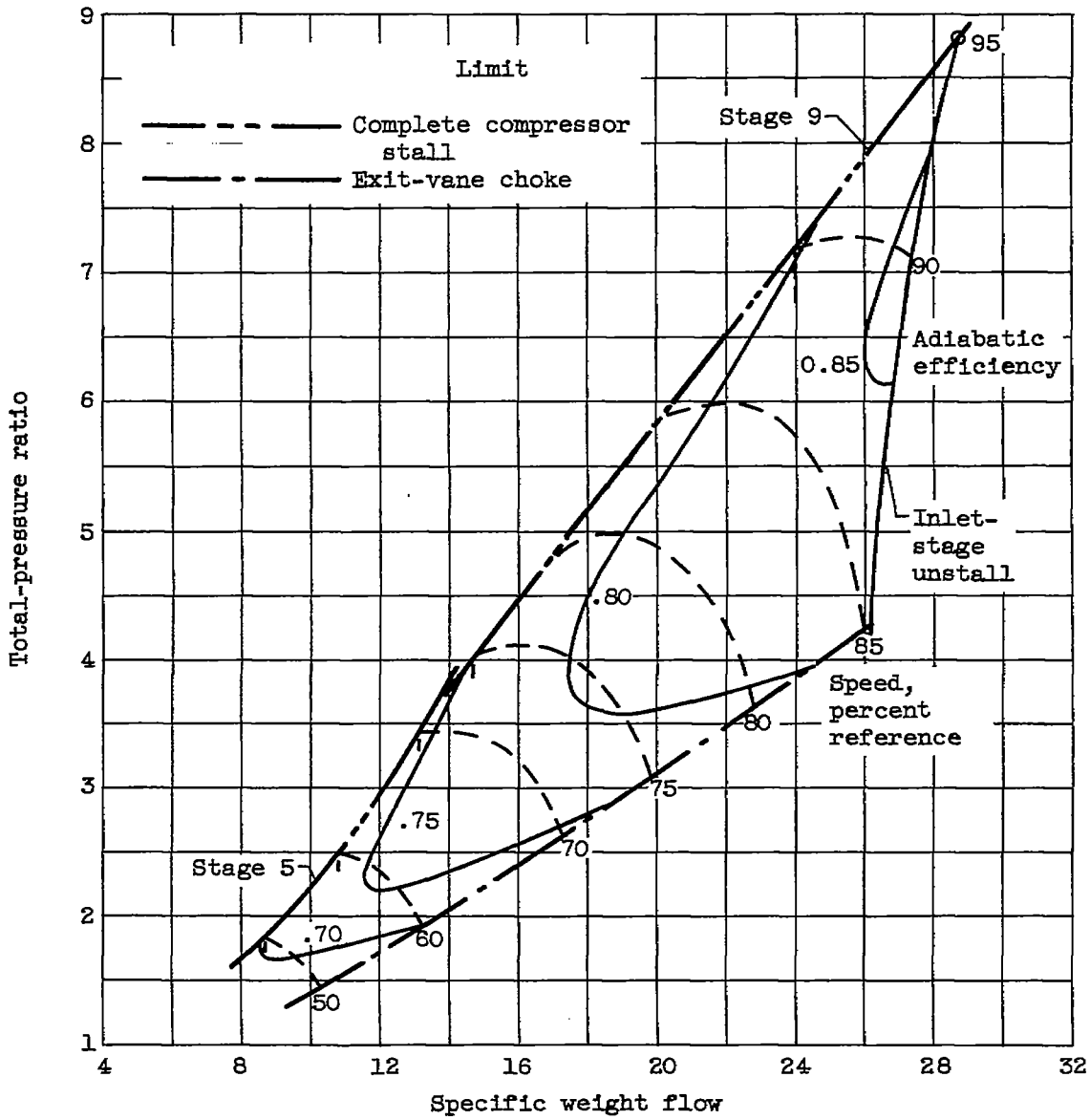

(b) Front stage stalled and interactions in stages 2 to 4.

Figure 8. - Continued. Computed over-all performance for case II.

[redacted]

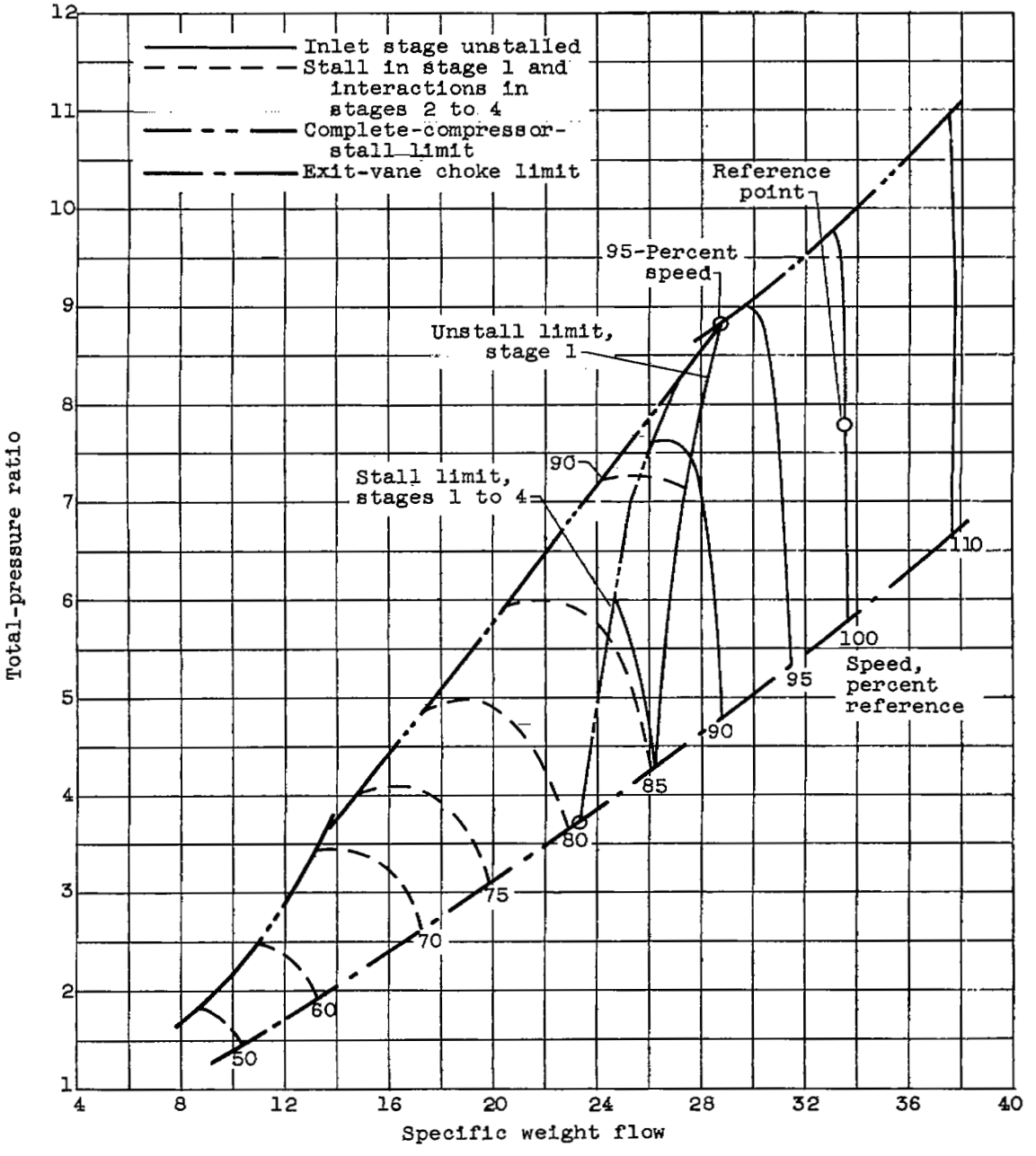

(c) Composite performance (superimposition of figs. 8(a) and (b)).

Figure 8. - Continued. Computed over-all performance for case II.

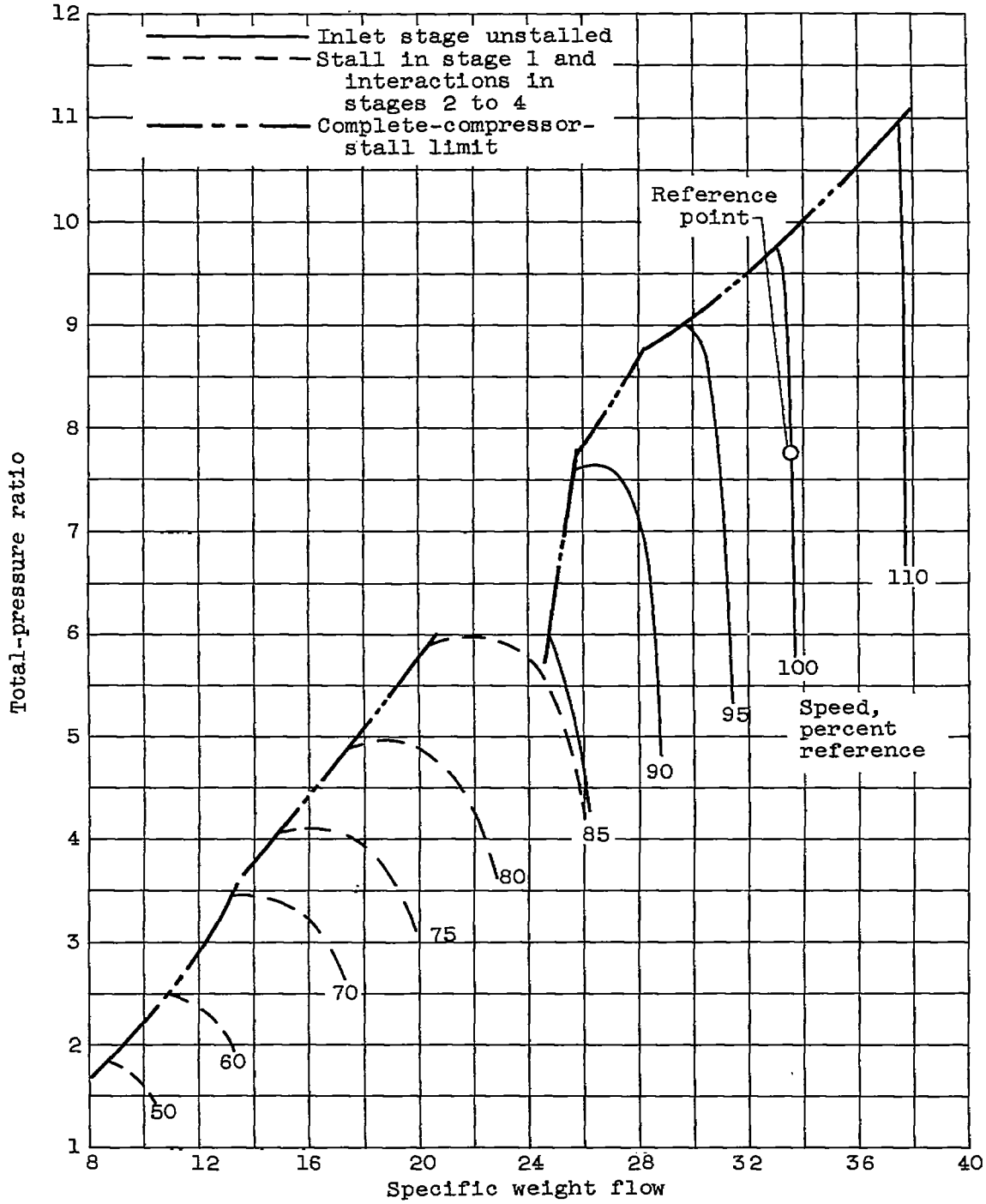

(d) Transition from stalled to unstalled inlet stage on exit-vane choke line.

Figure 8. - Concluded. Computed over-all performance for case II.

[redacted]

CH-15 back

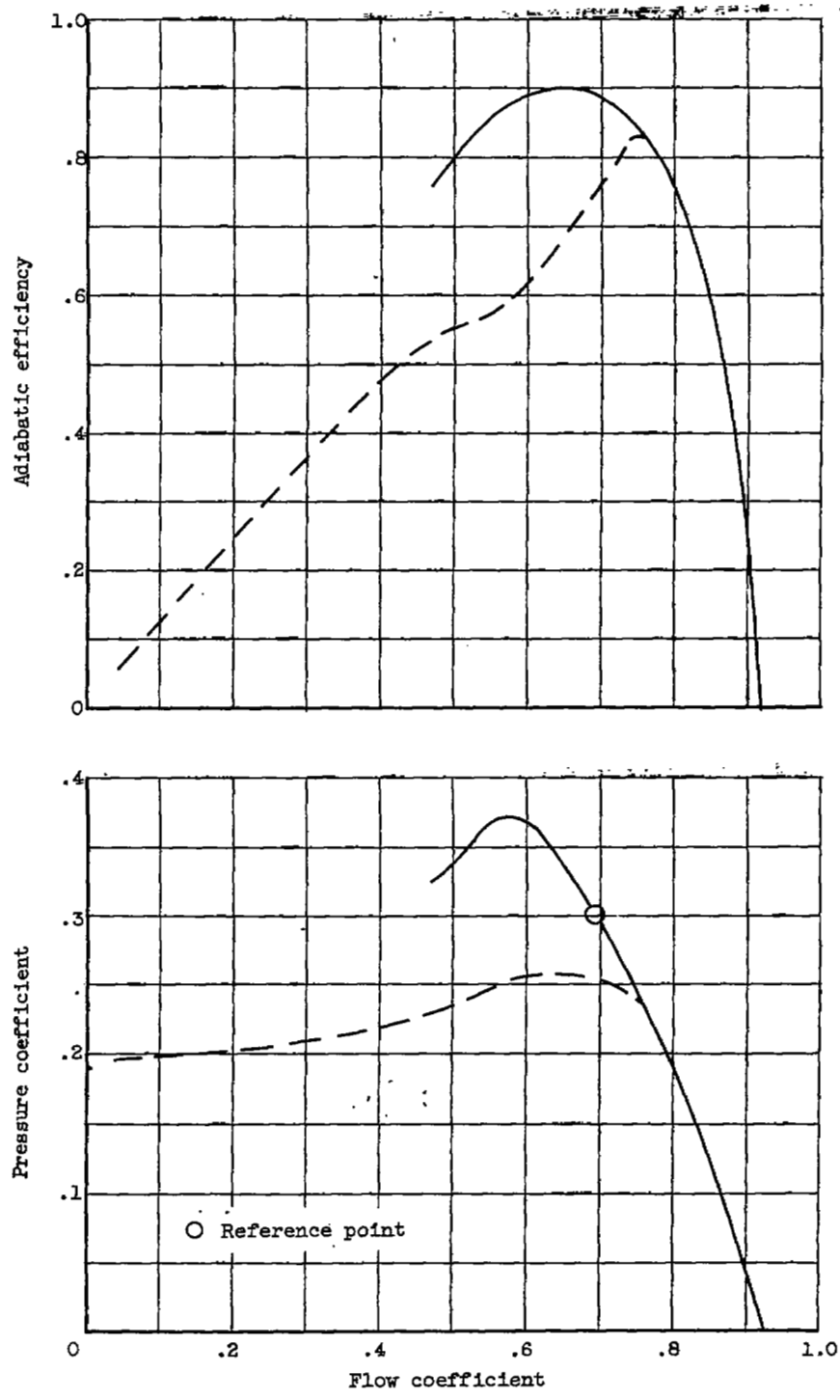

Figure 9. - Assumed performance characteristics for stages 5 to 8 for case III.

[redacted]

3357

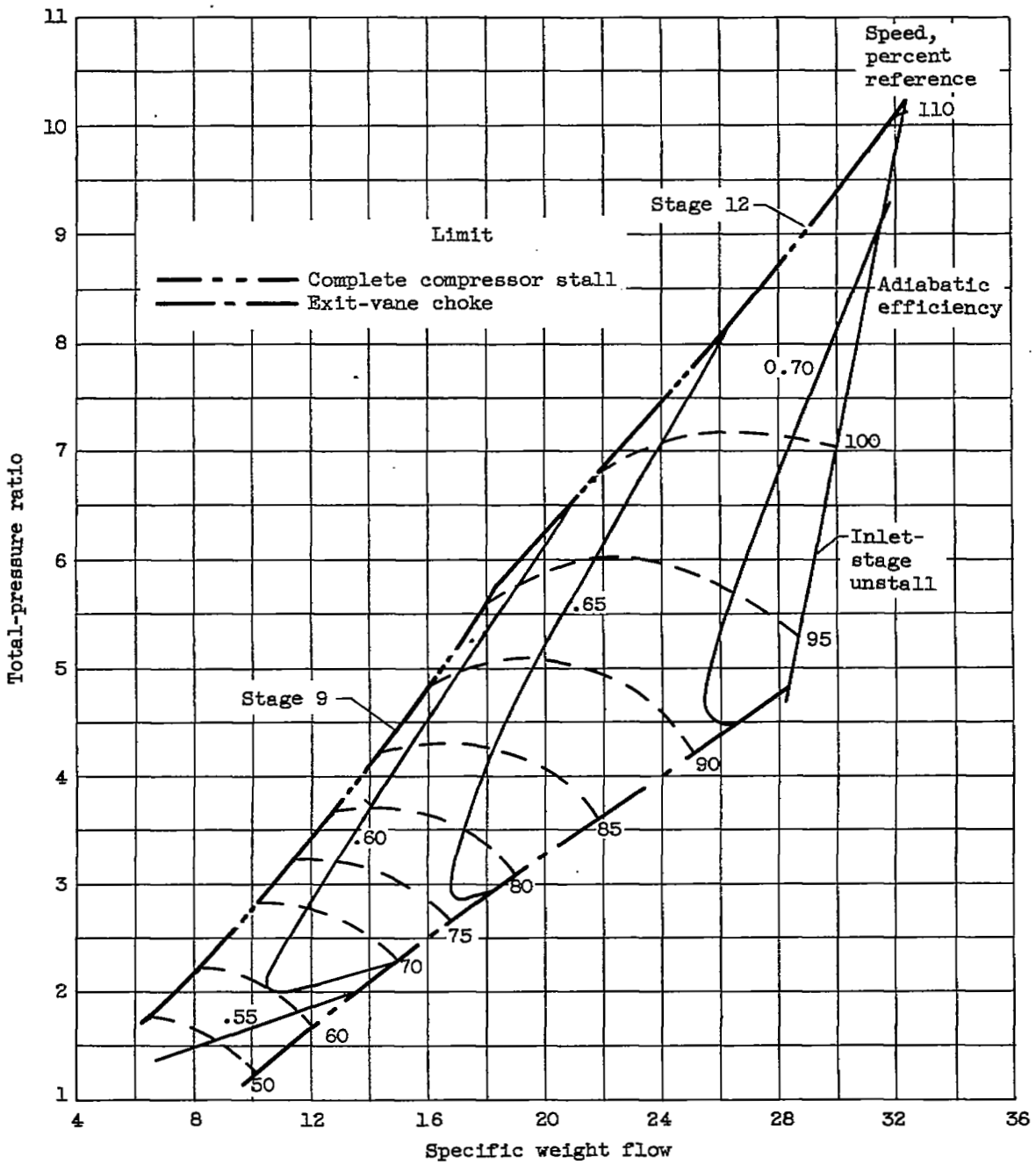

(a) Front stage stalled and interactions in stages 2 to 8.

Figure 10. - Computed over-all performance for case III.

3357

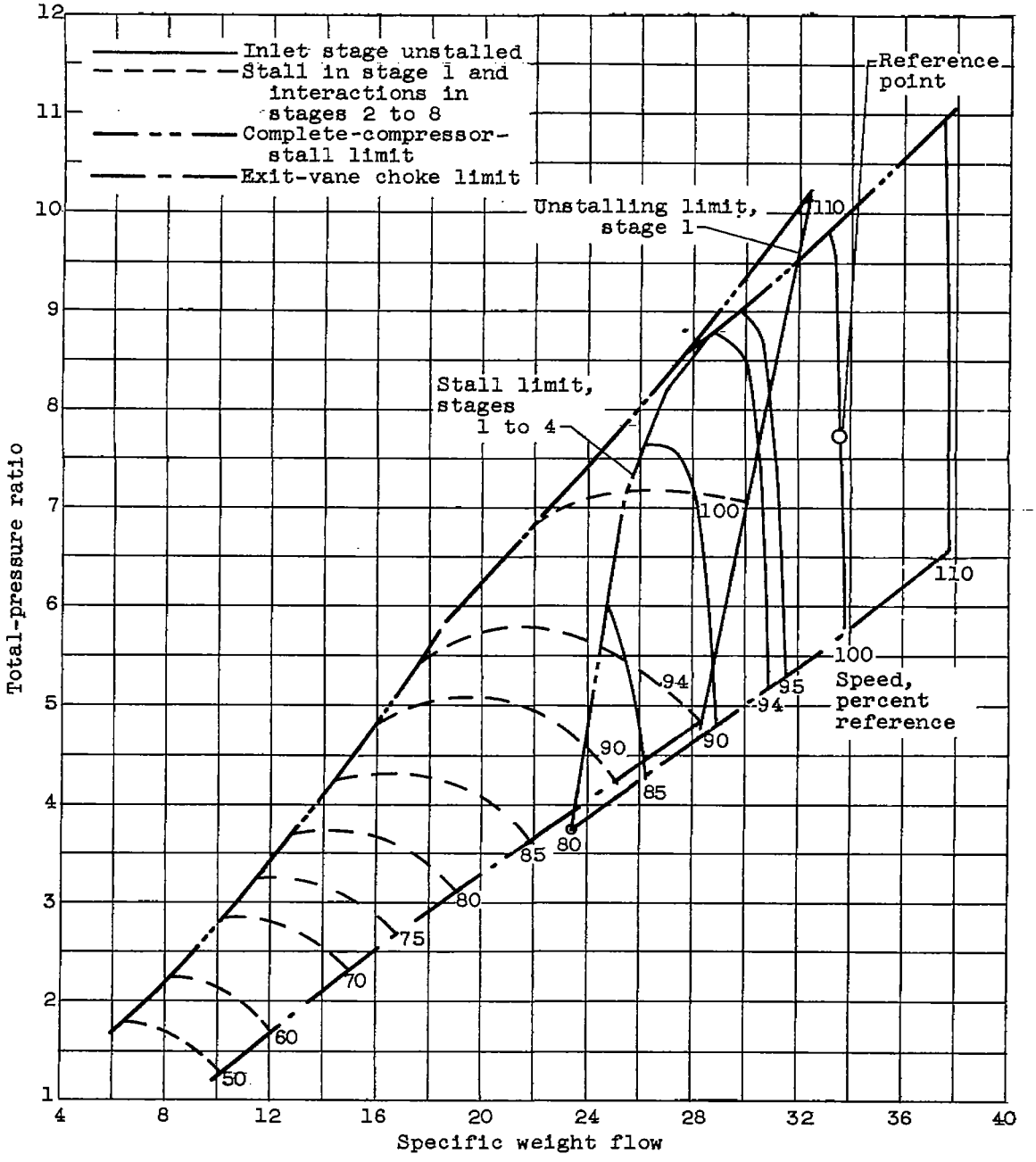

(b) Composite performance (superimposition of figs. 8(a) and 10(a)).

Figure 10. - Concluded. Computed over-all performance for case III.

3357,

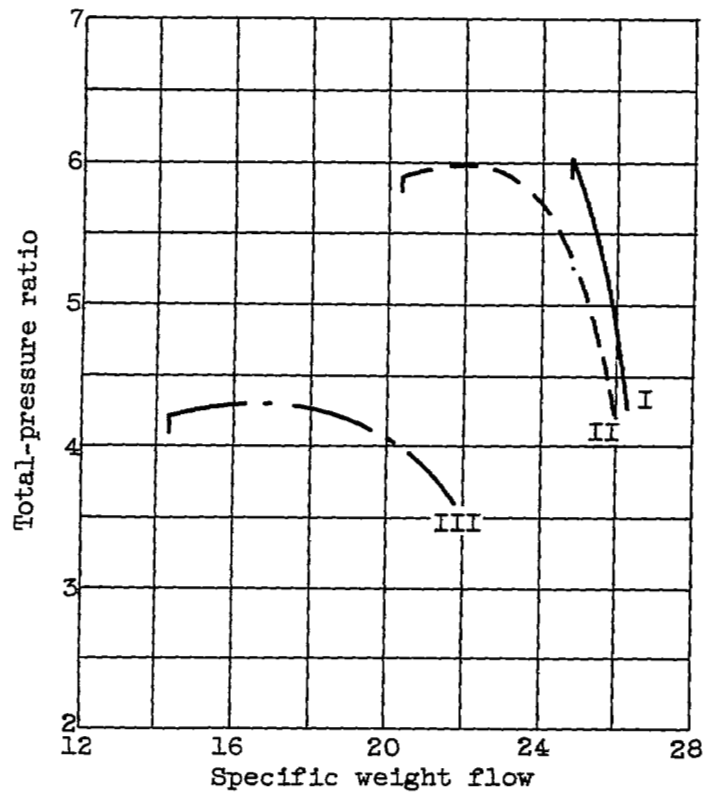

Figure 11. - Comparison of computed performance at 85-percent speed for cases I to III.

[redacted]

3357

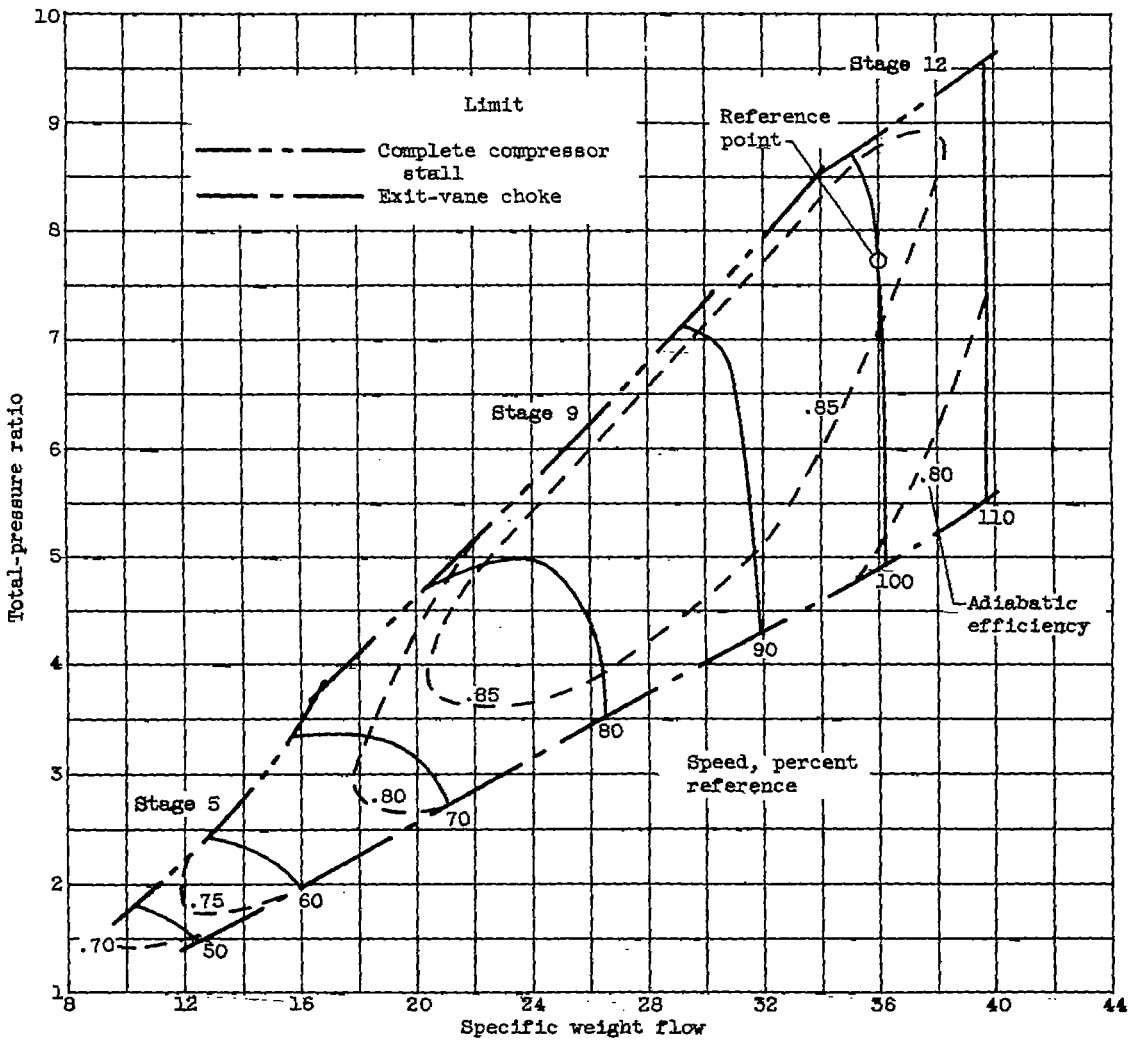

(a) Over-all performance.

Figure 12. - Computed over-all performance for case IV.

3357

CH-16

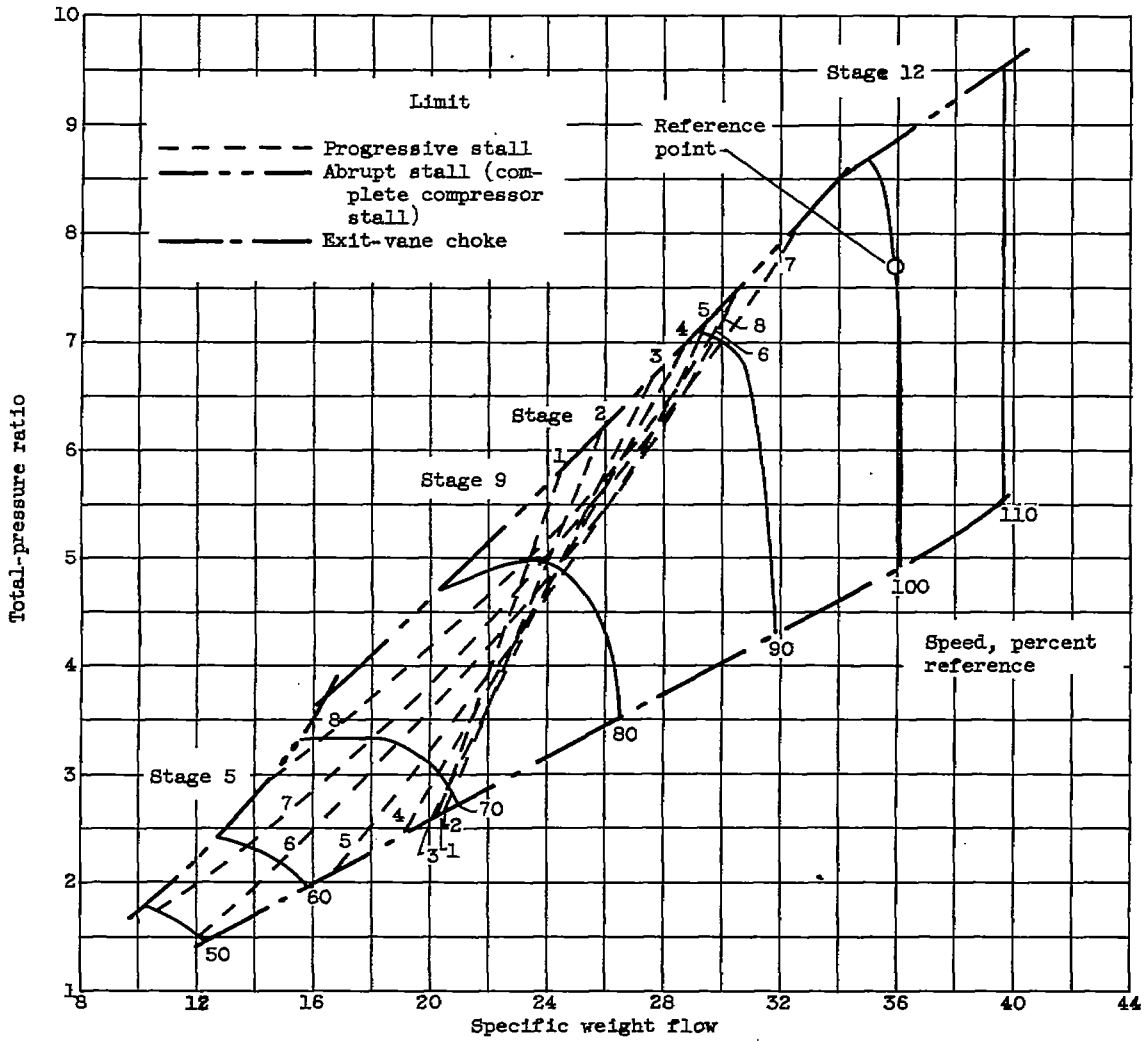

(b) Stage stall limits.

Figure 12. - Continued. Computed over-all performance for case IV,

[redacted]

3357

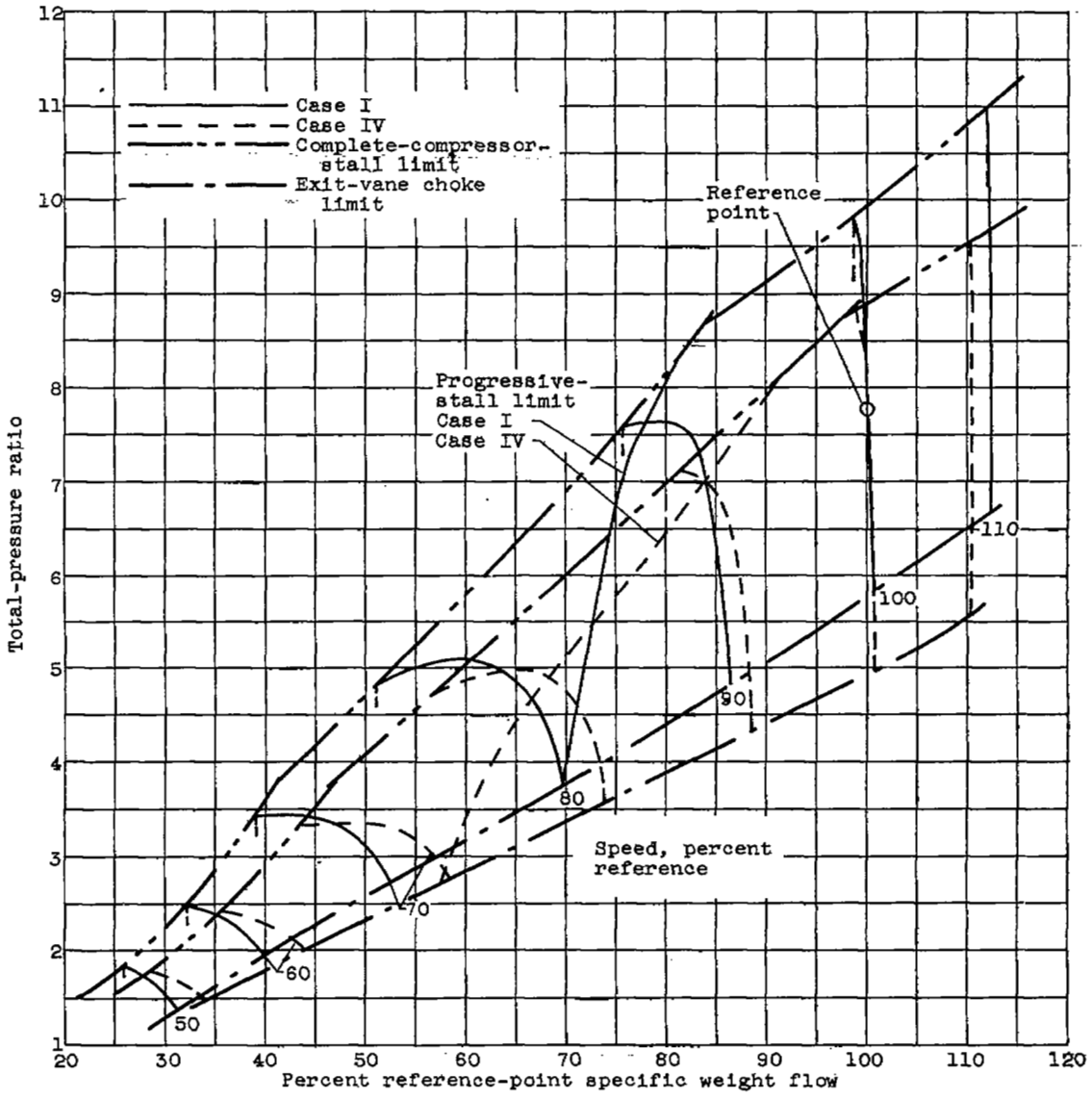

(c) Comparison of stall limits for cases I and IV.

Figure 12. - Concluded. Computed over-all performance for case IV.

3357

CH-16 back

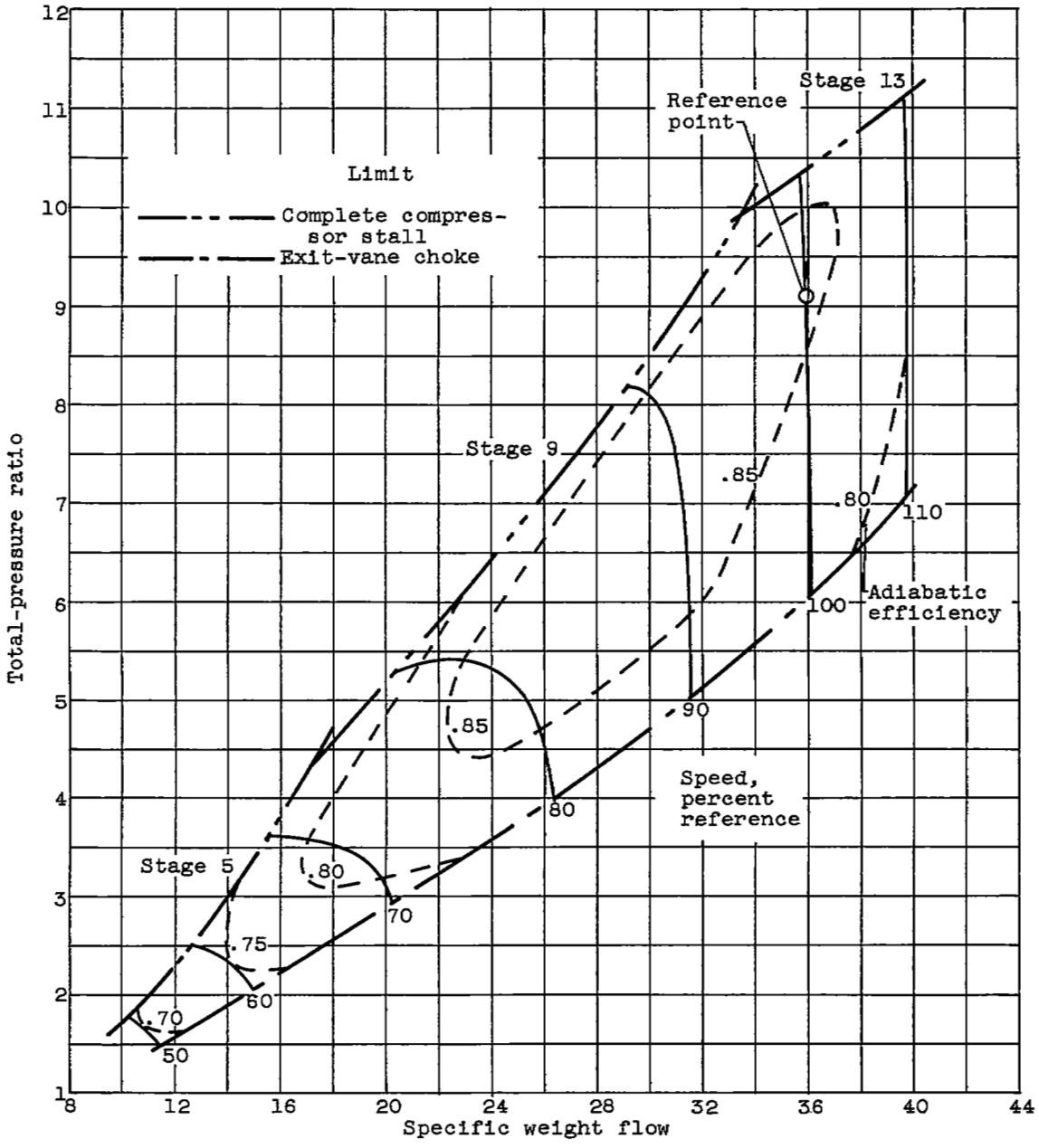

(a) Over-all performance.

Figure 13. - Computed over-all performance for case V.

3357

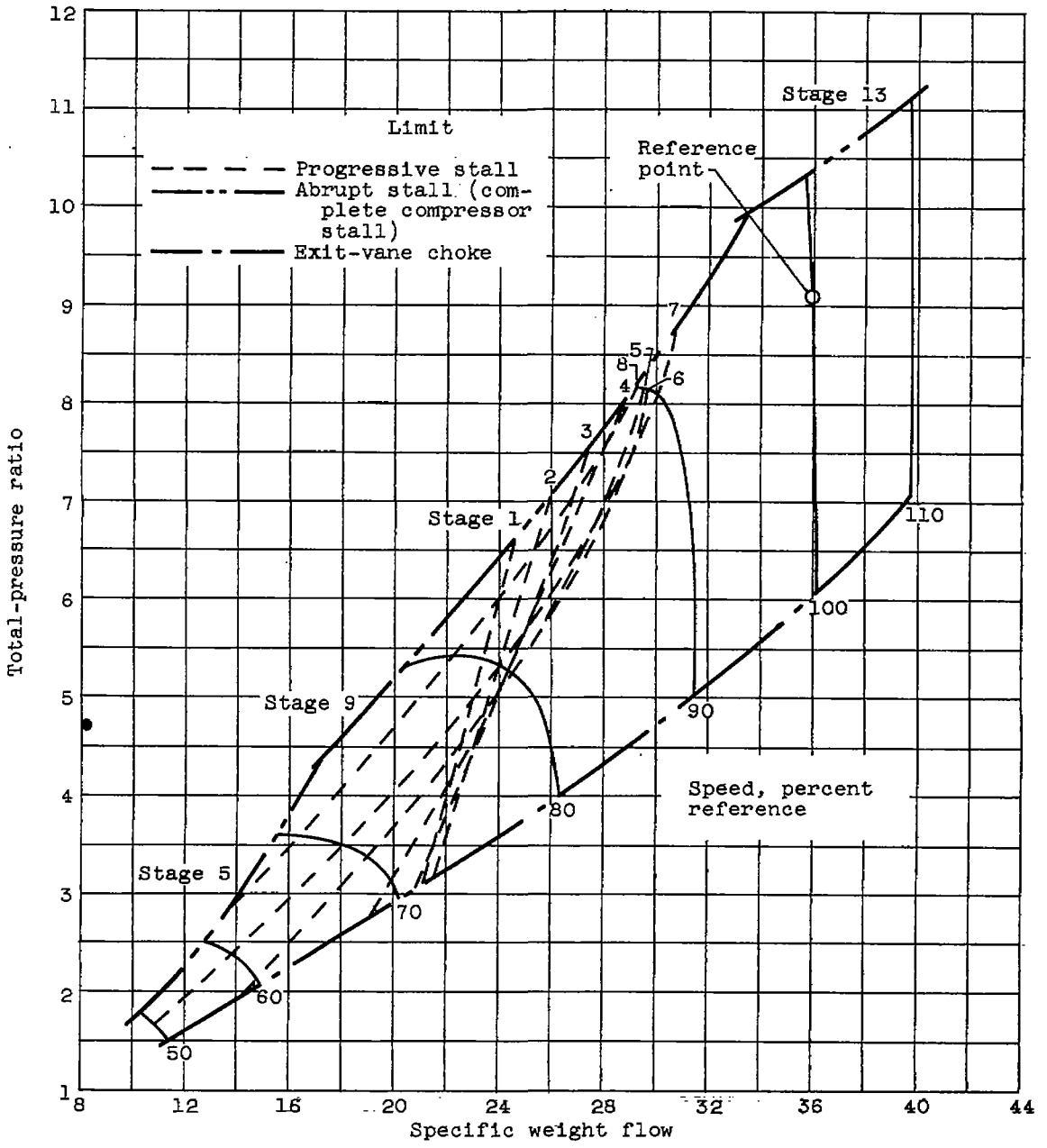

(b) Stage stall limits.

Figure 13. - Continued. Computed over-all performance for case V.

3357

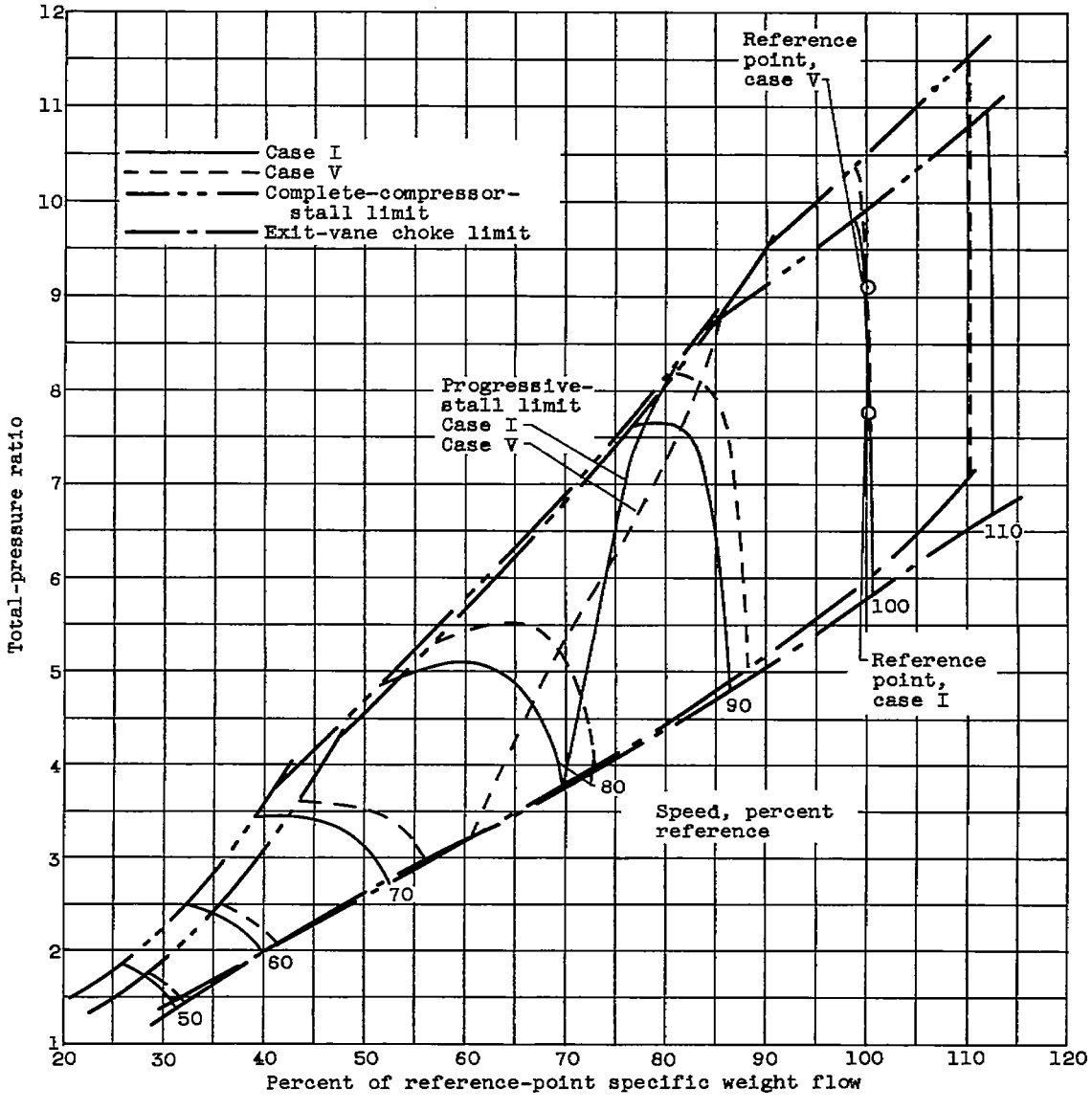

(c) Comparison of stall limits for cases I and V.

Figure 13. - Concluded. Computed over-all performance for case V.

3357

3452

CHAPTER XIV

THREE-DIMENSIONAL COMPRESSOR FLOW THEORY AND REAL FLOW EFFECTS

By Howard Z. Herzig and Arthur G. Hansen

SUMMARY

The discrepancies observed between the actual flows in an axial-flow compressor and theoretical simplified design flows increase in magnitude and diversity with the trend toward more compact compressors. The research into design procedures to reduce these discrepancies is reviewed and discussed. The improved design procedures are arbitrarily classified into two categories. One category includes investigations that successively extend the design procedures from the simplified-radial-equilibrium axially symmetric designs to the complex complete three-dimensional design. The second category includes individual studies of more restricted problems such as secondary flows, radial variation of circulation, entropy, or enthalpy. Such research leads to more adequate correction factors for use with simplified design procedures.

INTRODUCTION

One of the most important problems in the aerodynamic design of compressors is that of expressing the design flow equations in forms that are at once simple enough and accurate enough. The equations and their solutions should be simple enough that the designer can see the relative significance of the variables he is free to specify, and it must be possible to solve the relations quickly. The latter is important because it is frequently necessary to compute many compressor designs in order to select the one most suitable for a particular application. The equations and their solutions must represent the fluid motion accurately enough that the discrepancies between predicted and measured flow conditions are acceptably small.

The equations of motion for the flow of a real fluid in an axial-flow compressor are nonlinear three-dimensional equations and to date have proved mathematically intractable. Accordingly, designers have evolved the use of various assumptions to obtain reduced linear flow equations for which solutions can be obtained. Such procedures are necessarily conditional upon obtaining physically valid flow descriptions by their use.

In practice, the aerodynamic design of subsonic compressors has usually been based on two principal assumptions: (1) axially symmetric flow and (2) blade-element flow. The axially symmetric flow assumption is primarily a mathematical device which reduces the general flow equation from a three-dimensional to a two-dimensional system. In order to linearize and further simplify the flow equations, several auxiliary flow assumptions are made, such as considering the flow to be nonviscous and time-steady. Additional assumptions often made within the axial-symmetry approach include simple radial equilibrium and constant entropy radially.

The assumption of blade-element flow enables the designer to use the performance data (obtained chiefly from two-dimensional-cascade investigations, ch. VI (ref. 1)) in the compressor blading design. In fine, the over-all advanced compressor design requires a combined approach. It is necessary to simplify the mathematical problem in order to obtain solutions readily; and it is likewise necessary to use empirical information obtained in related investigations in order to correct, as far as possible, for the discrepancies between the real and the design flows in the compressor. 3452

In the past, suitable compressors have been designed by this simplified design procedure. Experience has taught that, by adhering to well-established limits on inlet relative flow Mach numbers, blade-turning and -loading parameters, wheel speeds, pressure ratios, and others, designers can consistently produce satisfactory compressors. From a practical point of view, these results justify the axial-symmetry and blade-element-flow approach to the design of such compressors (ch. III (ref. 2)), herein called "conservative compressors."

However, with the present requirements of compact engines, it becomes necessary to increase the air-flow-handling capacity and the stage pressure ratios while maintaining or even improving the efficiency if possible. Therefore, the Mach numbers, wheel speeds, and blade loading must be allowed to rise while the hub-tip radius ratio, the axial length per stage, and the number of stages must go down. Thus, the higher compressor performance requirements make it desirable to exceed the design limits earlier found advisable for conservative compressor design. In addition, such problems as blade-row interference, unsteady-flow phenomena, and off-design performance may become increasingly important.

Changing design conditions in order to meet increased compressor performance requirements, of course, requires corresponding adjustments in design techniques. These follow several courses. Particular flow problems may be attacked by intensive theoretical and experimental studies limited to the specific problem at hand. Such studies are directed toward learning enough about the nature of the flow process involved and the magnitudes of the effects to enable this information to be incorporated into the design approach. Results of such studies have made available modified theoretical design procedures in which one or more of the auxiliary simplifying assumptions (e.g., simplified radial equilibrium) can be avoided

(refs. 3 to 8). These have been called "improved" axially symmetric designs. Or, the information may take the form of new empirical design criteria or blade shapes, that is, new blade-loading and flow Mach number criteria. The diffusion factor is a pertinent example (ref. 9).

Eventually, the trend toward high power output with efficiency and compactness results in a condition wherein the discrepancies between the real and the design flows may no longer be encompassed by quantitative correction factors and improved axial-symmetry theories. In order to obtain physically valid descriptions of such real flows, further advanced design approaches must be found. The three-dimensional-flow theory of reference 10 is cited as an example.

In view of the importance to compressor designers of finding satisfactory solutions for these design problems, it is hardly surprising that there should exist an already extensive and now rapidly growing body of related literature. This paper summarizes and reviews some of this literature and includes examples of improved axisymmetric design theories as well as examples of further advanced design approaches. Because of increasing importance, blade-row interference effects and time-unsteady effects are also discussed, despite the fact that only crude beginnings have been made toward solutions of these complex problems.

SYMBOLS

The following symbols are used in this chapter:

$D/D\tau$ differentiation with respect to time following the motion

$\bar{\mathcal{F}}$ blade force acting on gas particles per unit mass of gas

$\mathcal{F}$ magnitude of $\bar{\mathcal{F}}$

H total or stagnation enthalpy per unit mass of gas, $h + (V^2/2)$

h static enthalpy per unit mass of gas, $u + (p/\rho)$

I modified total enthalpy, $h + \frac{(V')^2}{2} - \frac{U^2}{2} = H - \omega(rV_\theta)$

n polytropic compression exponent

p	static or stream pressure
Q	external heat added to gas per unit mass per unit time
R	gas constant
r	radius
S	entropy per unit mass of gas
t	static or stream temperature
U	magnitude of $\overline{U}$
$\overline{U}$	vector velocity of rotor blades at radius r
u	internal energy per unit mass of gas
V	magnitude of $\overline{V}$
$\overline{V}$	absolute vector velocity of gas
V'	magnitude of $\overline{V}'$
$\overline{V}'$	vector velocity of gas relative to rotor blade
z	coordinate along axis
Γ	circulation
γ	ratio of specific heats
$\overline{\zeta}$	absolute vorticity vector
η_p	polytropic efficiency

θ angular distance

μ viscosity

ν kinematic viscosity

ρ mass density

τ time

Φ viscous dissipation of energy per unit volume of gas per unit time

ω angular velocity of rotor

Subscripts:

r radial direction

z axial direction

θ tangential direction

DESIGN ASSUMPTIONS

The chief desideratum in compressor design is to perceive the most advantageous compromise between ease of obtaining possible design solutions and magnitude of the resulting inaccuracies. It is clear that the present trend toward higher-power-output, more compact, and yet more efficient compressors requires shifting the compromise point in the direction of fewer simplifying assumptions, despite the increased complexity of the calculation procedures involved. The first prerequisite, however, is a better understanding of the physical significance of the various design assumptions and their ranges of applicability.

Axial Symmetry

The assumption of axially symmetric flow is one of the two most important assumptions used in axial-flow-compressor design. By this assumption, all the partial derivatives of the gas properties with respect to the angular coordinate are taken equal to zero. The system of flow equations is thereby reduced to a two-dimensional system, in which the gas properties are functions of the axial and radial coordinates only. Basically, this is equivalent to assuming the three-dimensional flow through a blade row can be represented sufficiently accurately, at a measuring station between blade rows, by a circumferential average of the flow

3452

CH-17 back

conditions at each radial position. Symmetry about the axis of rotation does, of course, obtain for the limiting case of an infinite number of blades. Thus, one way of envisioning axially symmetric flow is to consider the flow as being restricted to hypothetical flow surfaces, as follows: Consider the number of blades in the blade row to increase without bound, in such fashion that the ratio of the spacing to blade thickness remains constant. Then the spacing between blades approaches zero, and the thickness of the blades approaches zero, so that the two blade surfaces and the space between them approach a mean surface. The streamlines are confined to such a mean surface.

3452

Mathematically, the assumption serves to simplify the calculation problems. Physically, the assumption of axial symmetry, at least between the blade rows, is somewhat justified, because in a compressor, where adjacent blade rows rotate relative to each other, the blade-row incidence angles can be correct only for an average exit flow from the preceding blade row. As to design, the assumption of axial symmetry enables the designer to fix his attention on the radial distribution of the gas properties at a station between blade rows by averaging out the gas-property variations in the circumferential direction.

Simple radial equilibrium. - An auxiliary simplifying assumption that has been found convenient is the assumption of simple radial equilibrium. The condition of simple radial equilibrium further simplifies the flow equations by considering radial accelerations due to curvature of the streamlines in the radial-axial plane equal to zero. Physically, this assumption does not mean that radial velocity components are zero, but that the acceleration due to curvature of the flow path is negligible.

As the trend shifts toward higher aspect ratios or toward transonic and supersonic compressors, this assumption becomes increasingly inappropriate for two reasons: (1) The requirement of high mass flow per unit frontal area in such compressors necessitates low hub-tip radius ratios in the first stages, with attendant high curvature of the annulus walls and large aspect ratios. High pressure ratios per stage generally mean tapered passages. (2) Main-flow radial displacement due to boundary-layer accumulations, especially in the stator hub regions, may assume sizable proportions at the higher Mach numbers as a result of secondary flows. These factors combine to qualify seriously the physical validity of the simple-radial-equilibrium condition.

Constant entropy radially. - Another auxiliary simplifying assumption often used for compressor design is that the radial variation of entropy is zero. Radial variation of entropy depends upon viscous dissipation of energy and upon radial variations of heat transfer to or from the compressor. In the absence of cooling, the heat transfer to or from a compressor is negligible. The entropy gradient can be considered negligible in the inlet stages at all radii except in the blade end regions.

In conservative compressors, therefore, the assumption of zero variation of entropy radially is reasonable, at least for the inlet stage (ref. 11 and ch. VIII (ref. 1)). Flow conditions that result in increased losses and corresponding entropy rises result in increased secondary-flow effects. The attendant redistribution of increased-entropy fluids leads to nonnegligible radial entropy variations. In general, this is the physical situation, at least in the rear stages of compressors. In these stages, if constant entropy radially is not assumed, agreement between design and actual flow conditions may be considerably improved.

3452

Blade-Element Flow

The assumption of blade-element flow is an important assumption used in conjunction with the axisymmetric approach. Both theoretical and experimental considerations are involved. Underlying the assumption of blade-element flow is the physical assumption that stream surfaces through a blade row are largely undistorted and that the fluid, by and large, remains on nearly conical surfaces, independent of the radial gradients. This assumption implies that the flow about any blade section or element remains the same regardless of whether the section is in a two-dimensional cascade or in an arbitrary rotor configuration.

The blade-element characteristics are obtained from measurements made on similar blade sections, usually in two-dimensional cascades (ch. VI (ref. 1)). Strong efforts are made to eliminate the distorting influences of the end-wall boundary layers by means of various devices such as porous-wall boundary-layer suction, and so forth. Empirical correlation formulas are thus obtained for the flows about the blade sections for wide ranges of blade-setting angles, solidities, and flow velocities. In recognition of the influence of three-dimensional flows and the wall boundary layers in annular configurations, experimental data are likewise taken from tests in such configurations (ch. VII (ref. 1)). Correlations are obtained for the performance of the blade sections at various radial positions spanwise. Empirical loss factors are thus developed to account for the viscous losses that arise in flow through a blade row. As a result of continuing experiments, there is a large growing body of such information and data on compressor blade rows available for use (chs. IV to VII (refs. 1 and 2)).

When large deviations from the physical assumption of flow on conical surfaces independent of radial gradients occur, the flow estimations based on blade-element flow become correspondingly more inaccurate. At higher inlet Mach numbers and increasing stage pressure ratios, stream surface distortions also increase, from secondary-flow boundary-layer displacement phenomena, for example. Under these conditions the combined assumptions of axial symmetry and blade-element theory may no longer give a satisfactory, physically valid flow picture at a given measuring station. Considerable research is being devoted at present to obtaining more insight

into the nature of the losses that result from flow through a blade row and to obtaining better methods of accounting for the losses than is afforded by current blade-element-flow theories.

Improved Design Theories

High-output compact axial-flow compressors, in order to outperform conventional compressors, must be designed to operate at higher relative flow Mach numbers, wheel speeds, and blade loading, with lower hub-tip radius ratios and axial length per stage, and with fewer stages. Experience indicates that under these conditions the real flows in compressor configurations are different locally from those predicted by the simplified design methods to an extent which suggests that the simplifying assumptions therein may be qualitatively as well as quantitatively wrong for such applications. The quantitative differences arise from augmented boundary-layer phenomena such as viscous losses, separation effects, clearance effects, secondary-flow effects, and others as well. The qualitative differences include large distortions in the mainstream flow surfaces. Near sonic velocities, the secondary-flow distribution may change drastically from that at subsonic flow conditions (ch. XV), with resulting large local accumulations of low-energy fluids that give rise to local blockage effects. Likewise, near sonic velocities, small changes in flow area mean large changes in flow Mach number. 3452

Thus, even minor deviations from predicted flow directions and expected boundary-layer behavior (due to secondary-flow effects or to three-dimensional effects, e.g.) can cause large deviations from design flow conditions. As a result of these deviations, measurements in compressors, particularly in the blade end regions, show the following major discrepancies from design predictions based on two-dimensional-cascade data (chs. VI and VII (ref. 1)): (1) Integrated total-pressure losses across the blade row are greater than predicted from blade-element theory, (2) flow directions deviate from those predicted at the blade-row exit, and (3) the operating range of angle of attack (without sharp rise in losses) is different from that predicted. The measurements further indicate that these blade end-region effects may account for half the observable losses.

To the designer seeking to achieve high-performance compressors, this increasing inability to approximate satisfactorily the real flows in actual compressors by means of idealized flows through simple configurations, with corrections for the anticipated differences between the real and the simulated cases, presents problems that must be solved. The importance of incorporating progressively more complete solutions of the flow equations into compressor design procedures has led to a series of experimental and theoretical investigations. The research toward improved compressor design procedures falls roughly into two categories. One phase of this research has been devoted to lifting the restrictions on the design flow calculations - that is, using a more exact basis for design.

The results of these investigations appear in reports for proposed design procedures such as improved axisymmetric, quasi-three-dimensional- and three-dimensional-flow solutions. Another phase of the research has been to make a series of individual studies of more restricted problems within a chosen over-all design approach.

The succeeding sections of this report present brief reviews and discussions of some of the investigations into both aspects of the compressor design problem. A brief section is devoted to the timewise variations of the gas properties in compressors exclusive of the surging and stalling phenomena (see chs. XI to XIII).

3452

COMPRESSOR DESIGN THEORIES

Basic Equations

Following reference 3, the state of a gas in motion may be specified in terms of its velocity $\overline{V}$ and two thermodynamic properties, enthalpy per unit mass H and entropy per unit mass S. These are defined by

$$H = h + \frac{V^2}{2} = u + \frac{p}{\rho} + \frac{V^2}{2} \tag{1}$$

and

$$t\ dS = du + p\ d\rho^{-1} \tag{2}$$

The equation of state for a perfect gas is

$$p = \rho R t \tag{3}$$

As given in reference 3, the Navier-Stokes equation of motion for a real fluid with constant viscosity is

$$\frac{D\overline{V}}{D\tau} = \overline{\mathcal{F}} - \frac{1}{\rho}\nabla p + \frac{\mu}{\rho}\left[\nabla^2\overline{V} + \frac{1}{3}\nabla(\nabla\cdot\overline{V})\right] \tag{4}$$

The energy equation is

$$\frac{Du}{D\tau} + p\frac{D\rho^{-1}}{D\tau} = Q + \frac{\Phi}{\rho} \tag{5}$$

The continuity equation is

$$\frac{\partial\rho}{\partial\tau} + \nabla\cdot(\rho\overline{V}) = 0 \tag{6}$$

Equations (1) to (6) are combined to give general flow equations (7) to (10).

Equilibrium equation. - The equilibrium equation

$$\nabla H = \bar{\mathscr{F}} + t\nabla S + \bar{V}\times(\nabla\times\bar{V}) - \frac{\partial\bar{V}}{\partial\tau} + \nu\left[\nabla^2\bar{V} + \frac{1}{3}\nabla(\nabla\cdot\bar{V})\right] \tag{7}$$

expresses the instantaneous gradient of total enthalpy at a measuring station in terms of blade force, viscous forces, velocity, entropy gradient, and so forth. For design purposes, the desired velocity diagram and thermodynamic properties of the gases are determined at measuring stations between successive blade rows. In such locations, the blade force $\bar{\mathscr{F}}$ is zero, and the flow is generally presumed time-steady; that is, $\partial\bar{V}/\partial\tau$ is zero. The last term in equation (7), in the brackets, represents the results of viscous action. In reasonably efficient flow, at least through the main flow except in thin boundary-layer regions, this term is small. Therefore, for design purposes, the last term is considered negligible. 3452

The flow at the measuring station is considered inviscid. Physically, this is equivalent to assuming that the variations in velocity caused by viscous effects in the fluid in the spaces between the blade rows are small compared with the variations in velocity at those stations which are the results of viscous dissipation within the blade rows upstream. This appears in general to be a reasonable assumption. At any rate, the correction factors used to account for boundary-layer effects can accommodate such viscous losses as may arise in the space between blade rows.

Equation (7) thus becomes

$$\nabla H = t\nabla S + \bar{V}\times(\nabla\times\bar{V}) \tag{7a}$$

where $\nabla\times\bar{V}$ is the absolute vorticity $\bar{\zeta}$ of the fluid. Thus, the modified equilibrium equation

$$\nabla H = t\nabla S + \bar{V}\times\bar{\zeta} \tag{7b}$$

shows how the gradient in total enthalpy at a measuring station is related to the gradient of entropy and the absolute vorticity of the fluid. The aerothermodynamic equations for rotating blade rows can be expressed more conveniently in terms of relative velocity vector $\bar{V}'$, entropy S, and a quantity I in place, respectively, of absolute velocity vector $\bar{V}$, entropy S, and total enthalpy H. The relative quantities I and $\bar{V}'$ are defined as follows (ref. 8):

$$I = h + \frac{(V')^2}{2} - \frac{U^2}{2} = H - \omega(rV_\theta) = H - UV_\theta$$

In cylindrical coordinates, with z-axis (of machine) parallel to $\overline{\omega}$,

$$\overline{V} = \overline{V}' + \overline{\omega}\times\overline{r}$$

The modified equilibrium equation for a rotating system can thus be written

$$\nabla I = t\nabla S + \overline{V}'\times\overline{\zeta} \tag{7c}$$

3452

Energy equation. - The energy equation is

$$\frac{DH}{D\tau} = Q + \frac{\Phi}{\rho} + \frac{1}{\rho}\frac{\partial p}{\partial \tau} + \overline{V}\cdot\left\{\overline{\mathscr{F}} + \nu\left[\nabla^2\overline{V} + \frac{1}{3}\nabla(\nabla\cdot\overline{V})\right]\right\} \tag{8}$$

The substantial derivative $D/D\tau$ indicates that the variation in total enthalpy of a particle along its streamline path from station to station is expressed by equation (8); whereas, equation (7) is used to define the variations in total enthalpy from streamline to streamline at a fixed station. The rate of change of total enthalpy per unit mass of fluid along a streamline is seen in equation (8) to be a function of the rate of external heat addition Q, the rate of viscous dissipation of useful energy along the path Φ/ρ, the rate of work done by the blades, measured by $\overline{V}\cdot\overline{\mathscr{F}}$, and the viscous effects on the velocity distributions as measured by the last term $\nu\left[\nabla^2\overline{V} + \frac{1}{3}\nabla(\nabla\cdot\overline{V})\right]$. In the case of steady real flow through a rotor, the $\overline{V}\cdot\overline{\mathscr{F}}$ is the predominating term on the right side of equation (8). For the real flow through a stator blade row, all the terms on the right side are usually small enough to be ignored.

CH-18

For nonviscous flow, the energy equation becomes

$$\frac{DH}{D\tau} = Q + \frac{1}{\rho}\frac{\partial p}{\partial \tau} + \overline{V}\cdot\overline{\mathscr{F}} \tag{8a}$$

and there is the additional relation that the blade force is normal to the blade surface (normal to the relative velocity of the fluid),

$$(\overline{V} - \overline{U})\cdot\overline{\mathscr{F}} = 0$$

Thus, the energy equation for nonviscous flow through a stator in absolute quantities is written

$$\frac{DH}{D\tau} = Q + \frac{1}{\rho}\frac{\partial p}{\partial \tau} \tag{8b}$$

Correspondingly, in terms of relative quantities, the energy equation for nonviscous flow through a rotor is written

$$\frac{DI}{D\tau} = Q + \frac{1}{\rho}\frac{\partial p}{\partial \tau} \tag{8c}$$

According to this equation, for steady adiabatic flow the entropy and the quantity I remain constant along relative streamlines through the rotor. For steady relative flow, the rate of change of I along a streamline is proportional to the change of Q along the streamline. In addition to their convenience mathematically in finding the flows through rotating blade rows, the relative quantities help greatly in clarifying physical occurrences in nonviscous fluid flows in rotating turbomachines. 3452

In compressors, the external heat exchange Q is small. If Q is neglected, for inviscid steady flow, equation (8) becomes

$$\frac{DH}{D\tau} = \bar{V}\cdot\bar{\mathcal{F}} \tag{8d}$$

which is equivalent to (ref. 3)

$$\frac{DH}{D\tau} = \omega\,\frac{D(rV_\theta)}{D\tau} \tag{8e}$$

that is, the rate of change of enthalpy along a streamline (work done on the gas) is equal to the angular speed of the blades multiplied by the rate of change of angular momentum about the compressor axis of the particle along the streamline. In terms of relative quantities,

$$\frac{DI}{D\tau} = \frac{DH}{D\tau} - \omega\,\frac{D(rV_\theta)}{D\tau} = 0 \tag{8f}$$

Maintaining the quantity I constant is a more concise but equivalent way of expressing that the rate of change of total enthalpy H along a streamline is equal to the angular speed of the blade multiplied by the rate of change of whirl of the gas streamline as it passes through the rotor. This is Euler's turbine equation.

For conventional compressors, the rotors are often designed to add the same amount of energy to the gas at all sections radially; that is, H is kept radially constant through the machine for design purposes. For free-vortex distribution and addition of whirl, I is radially constant throughout the machine.

Entropy equation. - The entropy equation

$$\frac{DS}{D\tau} = \frac{Q}{t} + R\,\frac{\Phi}{p} \tag{9}$$

indicates that the rate of change of entropy along a streamline depends only upon the rate of external heat addition and the rate of viscous dissipation of useful energy. As observed earlier, Q, the external heat-exchange rate, can be considered zero for compressors.

The first two terms in equation (8) are thus seen to be a measure of rate of entropy change along a streamline:

3452

$$t \frac{DS}{D\tau} = Q + \frac{\Phi}{\rho}$$

Continuity equation. - The continuity equation

$$\nabla \cdot \overline{V} + \frac{1}{\gamma - 1} \frac{D \ln t}{D\tau} - \frac{D}{D\tau}\left(\frac{S}{R}\right) = 0 \tag{10}$$

which is the last of the general flow equations presented herein, expresses the continuity relation in terms of divergence of velocity, rate of change of temperature function, and rate of change of entropy.

CH-18 back

Axisymmetric-Flow Theory

In order to simplify the analysis, the flow about the axis of rotation is usually assumed symmetrical. As has been discussed previously, this is often interpreted physically as assuming that the number of blades is allowed to increase without limit in such a way as to keep the total circulation constant, and accordingly the flow approaches the axisymmetric solution as a limit. Mathematically, the action of the blades can be computed by representing the blades by a volume distribution of forces in the flow equations. The magnitude of the force at a point is obtained by maintaining the product of the number of blades and the resultant force constant at any point on a blade as the number of blades is increased. The resultant force is the difference between the forces on the two sides of the blade. The flow follows stream surfaces, and the derivatives in the equations refer to changes of the fluid properties on the stream surfaces. This kind of solution, which gives average values in the circumferential direction, is usually valid when the departure from that average is small. For incompressible frictionless flow, when the blades are thin and the solidity fairly high, the solution can be considered as applying to the mean stream surface between two blades based on mass-flow considerations (ref. 12).

Equilibrium equation. - All partial derivatives of gas properties with respect to time and angular position are taken as zero for steady axisymmetric flow. With this simplification and neglecting the viscosity effects, the radial, tangential, and axial components of equation (7) become

$$\frac{\partial H}{\partial r} = \mathscr{F}_r + t\,\frac{\partial S}{\partial r} + \frac{V_\theta}{r}\,\frac{\partial(rV_\theta)}{\partial r} + V_z\,\frac{\partial V_z}{\partial r} - V_z\,\frac{\partial V_r}{\partial z} \tag{11a}$$

$$0 = \mathscr{F}_\theta - \frac{V_r}{r}\,\frac{\partial(rV_\theta)}{\partial r} - V_z\,\frac{\partial V_\theta}{\partial z} \tag{11b}$$

and

$$\frac{\partial H}{\partial z} = \mathscr{F}_z + t\,\frac{\partial S}{\partial z} + V_r\,\frac{\partial V_r}{\partial r} - V_r\,\frac{\partial V_z}{\partial r} + V_\theta\,\frac{\partial V_\theta}{\partial z} \tag{11c}$$

3452

Equation (11a) is the radial-equilibrium equation. At a station between blade rows, $\mathscr{F}_r$ is zero. For the usual assumption of constant entropy radially, the second term on the right side is taken to be zero. The fifth term represents the effect of radial motion on the condition of radial equilibrium and is neglected (ch. VIII (ref. 1)) for the assumption of simplified radial equilibrium. The simplified-radial-equilibrium equation is thus generally written as follows for design purposes:

$$\frac{\partial H}{\partial r} = \frac{V_\theta}{r}\,\frac{\partial(rV_\theta)}{\partial r} + V_z\,\frac{\partial V_z}{\partial r}$$

or, by differentiating and combining,

$$\frac{\partial H}{\partial r} = \frac{1}{2}\,\frac{\partial V_z^2}{\partial r} + \frac{1}{2}\,\frac{\partial V_\theta^2}{\partial r} + \frac{V_\theta^2}{r} \tag{11d}$$

Energy equation. - From equation (8) for steady axially symmetric viscous flow and the assumption that heat generated by frictional work remains in the stream, $DH/D\tau$ can be written as

$$\frac{DH}{D\tau} = Q + \omega\,\frac{D(rV_\theta)}{D\tau}$$

in which Q is generally considered zero. This same relation was previously derived for frictionless steady flow (eq. (8e)).

Entropy equation. - For axially symmetric flow, equation (9) becomes

$$\frac{DS}{D\tau} = \frac{Q}{t} + \frac{\nu}{t}\left\{2\left(\frac{\partial V_r}{\partial r}\right)^2 + 2\left(\frac{V_r}{r}\right)^2 + 2\left(\frac{\partial V_z}{\partial z}\right)^2 + \left(\frac{\partial V_\theta}{\partial z}\right)^2 + \left(\frac{\partial V_r}{\partial z} + \frac{\partial V_z}{\partial r}\right)^2 + \left[r\,\frac{\partial\left(\frac{V_\theta}{r}\right)}{\partial r}\right]^2 - \frac{2}{3}\left[\frac{1}{r}\,\frac{\partial(rV_r)}{\partial r} + \frac{\partial V_z}{\partial z}\right]^2\right\} \tag{12a}$$

For the frictionless case,

$$\frac{DS}{D\tau} = \frac{Q}{t} \tag{12b}$$

Continuity equation. - For axisymmetric flow, equation (10) becomes

$$\frac{1}{r}\frac{\partial(rV_r)}{\partial r} + \frac{\partial V_z}{\partial z} + \frac{1}{\gamma - 1}\left(V_r \frac{\partial \ln t}{\partial r} + V_z \frac{\partial \ln t}{\partial z}\right) - V_r \frac{\partial\left(\frac{S}{R}\right)}{\partial r} - V_z \frac{\partial\left(\frac{S}{R}\right)}{\partial z} = 0 \tag{13}$$

3452

Improved Flow Theories

Design theories have been presented that dispense with several of the flow assumptions made for the simplified axisymmetric designs. The first of these (ref. 3) used a modified equation (11a) for the radial-equilibrium condition (see ch. VIII (ref. 1) for details) in lieu of equation (11d), the simplified-radial-equilibrium condition. In succeeding reports (refs. 5 to 7), the theories are extended to finite numbers of blades. In reference 8, a through-flow theory is developed; and the effects of blade thickness are considered in references 13 and 14.

Radial-equilibrium condition. - The preceding analysis, as developed in reference 3, has led to the development of six equations with eight independent variables, namely V_θ, V_r, V_z, $\mathscr{F}_\theta$, $\mathscr{F}_r$, $\mathscr{F}_z$, H, and S. Of these equations ((8e), (11a), (11b), (11c), (12a), and (13)), five are independent. For nonviscous flow, the following relation must hold:

$$(\overline{V} - \overline{U})\cdot\overline{\mathscr{F}} = 0 \tag{14}$$

as discussed earlier. This provides a sixth independent equation to replace equation (8e). For this case, equation (12b) is used instead of equation (12a).

For viscous flow, a sixth independent relation is developed (ref. 3) for the rate of change of entropy along a streamline, in terms of n, the polytropic exponent of the flow process:

$$\frac{DS}{D\tau} = R\,\frac{n - \gamma}{(n - 1)(\gamma - 1)}\left(V_r \frac{\partial \ln t}{\partial r} + V_z \frac{\partial \ln t}{\partial z}\right) \tag{15}$$

where

$$n = \frac{1}{1 - \frac{1}{\eta_p}\frac{\gamma - 1}{\gamma}}$$

and η_p is the assumed design polytropic efficiency.

For the design problem, two degrees of freedom are thus available. Accordingly, the desirable variation of two of the gas properties, one of which is usually V_θ, can be specified; and the variation of the other gas properties and the blade force can then be determined theoretically.

Current design procedure is to specify desired gas conditions at stations in the gaps between blade rows only, where the blade-force terms are zero. One of the two available degrees of freedom in going from one such station to the next is taken up by the blade section selected. Accordingly, except at the first-stage inlet, there is only one condition at each station which the designer can specify. 3452

No general analytical solution is presented in reference 3, but two numerical methods of solution are suggested. In one method, the design equations are written as finite-difference equations and applied to successive closely spaced axial stations. The second method employs only three stations per stage but assumes the shape of the radial-flow paths between stations. This method is considerably simpler to apply than the first. In reference 3, with assumed sinusoidal radial-flow paths, a form of the radial-equilibrium equation is developed which shows that the effects of radial motion are functions of the radial displacement, the square of the axial velocity, and the square of the blade-row aspect ratio.

Summarizing briefly the results and conclusions of reference 3, an investigation was conducted into the radial motion of the flow in a turbomachine by means of an axial-symmetry theory that does not assume simplified radial equilibrium. Blade aspect ratio had an important effect on the radial motion. The amount of radial motion depended also upon the passage taper, hub-tip ratio, speed of the main flow and design type (velocity diagram). Thus, for large blade-row aspect ratio or high axial velocity even with a small amount of radial displacement, the effect of radial motion may be large (i.e., a large oscillatory radial motion may be expected within the blade row). In reference 3, radial entropy gradients were neglected. Under certain conditions (ref. 11), these gradients have been shown to be important.

The results of a simplified analysis by the methods of reference 3, assuming sinusoidal flow paths through the blade row, are found in reference 15 to compare favorably with the results obtained by improved axisymmetric and three-dimensional analyses.

The analysis presented in reference 3, while it gives much useful information concerning the flow within blade rows, does not readily yield information concerning the flow just upstream or just downstream of such blade rows. The distribution of flow properties near a blade row is considered as an individual study in references 16 and 17. The problem is treated as an investigation into the matter of the flow near a blade row rather than with regard to design, and therefore is discussed in this report in the section SOME ASPECTS OF THREE-DIMENSIONAL FLOWS.

3452

Finite blade spacing. - The design theories are extended from the blade systems with infinitesimal blade spacing (i.e., axially symmetric) to systems with finite blade spacing in an interesting series of reports (refs. 5 to 7). The procedure requires the axisymmetric solution for the flow as a first step. Reference 5 first presents the axisymmetric solution for the complete inverse (design) problem; that is, neither the blade shapes nor the wall geometry is specified in advance. The axial-flow-compressor designer starting with a reference streamline does specify the desired radial variation of the axial velocity component V_z (as in ref. 5) and an enthalpy function $\int dp/\rho$. By integration of the continuity equation (for isentropic flow in refs. 5 and 6), the radial velocity component V_r is obtained. The tangential velocity component V_θ is next obtained from the energy equation. The continuous force field that replaces the blade system in axially symmetric solutions can then be calculated from the Euler dynamic equations for axially symmetric flow. The infinitesimally spaced blades (stream surfaces) can be computed by use of the streamline equations

$$\frac{\partial r}{\partial z} = \frac{V_r}{V_z}$$

$$\frac{r\partial\theta}{\partial r} = \frac{V_\theta}{V_r}$$

$$\frac{r\partial\theta}{\partial z} = \frac{V_\theta}{V_z}$$

and the inlet conditions. Thus, the compression ratio, the form of the airfoils, and the flow around them can be determined.

When the cascade of blades with infinitesimal spacing and axially symmetric flow is replaced by a cascade of blades with finite spacing, the flow can no longer be considered circumferentially uniform. The uniform force field, which in the equations replaced the effects of the blades in the axially symmetric case, is in turn replaced in the equations by the asymmetric inertia and pressure terms, the $\partial/\partial\theta$ terms, that had earlier been neglected. Changing the force field and adding circumferentially asymmetric terms means that the streamlines of flow must change as well. One set of "mean" stream surfaces, considered to be halfway between the finite-spacing blades, is assumed "frozen," that is, unchanged. All the other streamlines shift and deform. This means the velocity and pressure terms must also change.

Corrective terms are to be found, which are to be added to the axisymmetric flow in order to obtain the asymmetric flow in the spaces

between blades. These corrective terms are obtained as a power-series development for the flow-variable changes in terms of a spacing parameter ψ, the angular distance from the frozen streamline surfaces. Recurrence formulas are developed for these corrective terms, and an iteration process is set up for the desired solution. For simplicity, it is assumed that the changes in the flow variables are small enough that only terms linear in ψ need be kept. This is equivalent to assuming a linear pressure variation across each passage.

Thus, when the radial variations of a velocity component and of an enthalpy (pressure) function are prescribed, the steady, nonviscous three-dimensional flow through a cascade of blades with finite spacing can be found. For the two-dimensional solution (ref. 7), only the enthalpy function need be prescribed. While airfoils of finite thickness can be designed in this way, the numerical example of reference 7 is actually for a cascade of line (zero-thickness) airfoils with shapes approximating closely the streamlines found for the axisymmetric solution and with small lift coefficients. A further extension to the viscous-flow case is made in the appendix of reference 7. The methods developed in references 5 to 7 are instructive, as they indicate that the blade-to-blade variations with finite numbers of blades of finite thickness can be treated as perturbations on a mean, "frozen" streamline. However, in the nonviscous case (e.g., ref. 7), the Bauersfeld condition that, for a nonviscous fluid, the force field must be perpendicular to the streamlines defining the blade surfaces was not considered. And in the treatment of the viscous-flow case (appendix of ref. 7), it was not possible in the one-step perturbation method to satisfy some boundary conditions and obtain closure of the nose and trailing edges of the blades. 3452

In a series of reports (refs. 18 to 20), a treatment of the viscous flow through infinitely many thin blades is developed and extended, using the frozen-streamline notion, to develop the theory for an iteration process for the viscous, laminar, incompressible flow through blade rows with a finite number of blades of finite thickness. The application of this considerably more complex procedure greatly improves the solutions and makes possible the closure of the blade surface at the nose and trailing edge. Even with this procedure, however, it is necessary to relax the boundary condition of zero velocity (no slip) at the blade surfaces in order to linearize the problem sufficiently for possible solutions.

Through-flow theory. - A further generalization beyond the simplified axisymmetric-flow approach, the through-flow theory (ref. 8), considers the flow along an arbitrary surface $S(r,\theta,z) = C$. Retaining the blade force terms $\bar{\mathcal{F}}$ in the equations of motion partially takes into account the circumferential variations of pressure (enthalpy) and density. The development of the analysis presents a unified theory; that is, the direct and inverse problems are solved for compressible flow, either subsonic or supersonic, for arbitrary blade and wall shapes, and for high-

solidity, thin blades. A principal equation is developed from the continuity equation, the equation of motion in the radial direction, and through use of a stream function. Two main groups of designs are considered. In the first group the designer prescribes the variation of the angular momentum. This group includes the free-vortex type, the wheel type, the symmetrical-velocity-diagram type, and so forth. In the second group of designs a relation between the tangential and axial velocities is prescribed. This group includes such radial-blade-element configurations as are found in high-speed centrifugal and mixed-flow impellers.

3452

Criteria are established for both groups to determine whether the principal equation is elliptic or hyperbolic, roughly whether the flow is subsonic or supersonic. Two methods are presented for solving the elliptic case. In one method the equations can be expressed in difference form and solved either by relaxation procedures or by a suggested iterative procedure if a high-speed large-scale digital computing machine is available. The relaxation procedure, for which the machine can also be used, is preferred. The other method suggested, machine solution of the set of simultaneous equations by a matrix process, is much quicker, especially when a number of solutions is to be found. The details of this matrix method are given in reference 21.

CH-19

Blade thickness. - In standard design procedures, the axisymmetric solutions provide "mean-line" information that can then be corrected for the effects of blade thickness by use of experimental data. A simple extension of the through-flow theory (ref. 8) incorporates some of the blade-thickness effects directly in the design procedure. For blades that are not thin, an approximate blade thickness factor b is included in the definition of the stream function. Better physical understanding of the significance of such a blade thickness-correction factor is obtained (refs. 13 and 14) by analyses of the effects of blade thickness on flow along a mean streamline on a blade-to-blade flow surface.

In a thick-bladed turbine configuration (in order to emphasize the effects) with subsonic incompressible flows, the mean streamline based on mass flow in the channel has less curvature than either the mean channel line or the mean camber line. The variation in the axial component of flow is nonlinear across the channel; the specific mass flow $\rho V_z'$ along the mean streamline was about 4 percent higher than that obtained by a one-dimensional calculation based on channel-width reduction. Furthermore, the influence of blade thickness extends a short distance upstream and downstream of the channel. The tangential velocity on the mean streamline rises above its inlet value before the leading edge and decreases rapidly at first through the channel and then more slowly to a value below its exit value for some distance downstream of the trailing edge.

For compressible flows, the mean streamline approximates the position of the mean channel line better than for incompressible flows but still has a lower curvature. The effects of blade thickness on tangential velocities of the mean stream and on specific mass flow are similar to, albeit somewhat larger than, the corresponding effects in the incompressible case. The variation in specific mass flow was higher than that given by the one-dimensional calculations based on channel width, and the effect was observed outside the channel.

For supersonic flows (ref. 14) in a configuration with higher solidity and thinner blades, the mean streamline conformed more closely to the mean camber line than for the other cascade with lower solidity and thicker blades. The analysis using the thickness-correction factor b shows that the specific mass flow along the mean streamline increased an average of 9 percent more than anticipated from a one-dimensional calculation. Comparison of the specific mass flow in the axial direction with the variation in channel width likewise showed a 9-percent increase on the average in specific mass flow axially over the area reduction. This increase, it will be noted, is more than twice the value obtained for the previous subsonic cases. The variations of axial and tangential velocity components on the mean streamline are correspondingly increased.

For the symmetrical nozzle configurations (no turning), the increase in specific mass flow along the mean streamline at supersonic flow conditions was about 8 percent higher than expected from a one-dimensional calculation.

Three-Dimensional Theory

A general three-dimensional, nonviscous, compressible-flow theory is developed in reference 10 for subsonic and supersonic turbomachines with finite numbers of blades of finite thickness. The theory is applicable to axial-, radial-, or mixed-flow turbomachines for both the direct and inverse problems. Such a theory may be required for the case of low hub-tip radius ratios and for highly loaded stages with high inlet Mach numbers, where two-dimensional solutions may be inadequate.

As in earlier reports, the equations of motion, energy, and continuity are expressed in terms of the velocity components, entropy, and the quantity I (a modified total enthalpy). Estimated entropy changes due to shock waves, heat transfer (turbine cooling), and viscous effects can be accommodated in the calculations.

Analysis. - A three-dimensional-flow solution is obtained by combining solutions for mathematically two-dimensional flows on two different kinds of intersecting relative stream surfaces (fig. 1). A stream surface S_1 of the first kind is one traced out by fluid particles initially, at some axial position, on a circumferential circular arc of fixed

radius about the axis of the machine. The blade-to-blade variations of flow can be computed on such surfaces (which extend from the suction surface of one blade to the pressure surface of the adjacent blade) in an essentially two-dimensional fashion. Suitable stream functions are defined that facilitate the solutions.

These S_1 surfaces will in general be twisted (fig. 2); that is, the flows are not restricted to surfaces of revolution as in quasi-three-dimensional solutions developed elsewhere. The S_1 surfaces can be modified and redefined in order to cope with the large circumferential derivatives that result from cases of large surface twist. Complications arise in regions where, because of secondary flows, for example, particles leave the walls and flow onto the blade surface, or, as is more likely, leave the blade surface and flow onto the wall or even out into the passage. In these regions it is necessary to approximate a solution by assuming that the flow follows the hub and casing walls.

A relative stream surface of the second kind S_2 is one traced out by fluid particles which, at some axial position, were initially along a radial or nearly radial line. The most important S_2 surface is the one that starts midway between two blades (fig. 1) and divides the mass flow in the channel between the blades into two approximately equal parts. The through-flow solution obtained for large numbers of thin blades is a special case of S_2 stream surface solution. The problems of surface twist and complications near the boundaries for S_2 surfaces are similar to those already described for S_1 surfaces.

In general, the three-dimensional solutions for both the direct and inverse problems employ the solutions on both these two kinds of surfaces. The correct solution on one kind of surface often requires information obtained from solutions of the other kind. For example, determination of flow on S_1 surfaces requires information concerning the radial variation of the velocity components that is obtained from solutions along the S_2 surfaces. Consequently, iterative solutions between the two kinds of surfaces may be required. However, the computations are essentially two-dimensional and can be handled by present computational techniques. A general method is provided for solving the flow equations manually or by high-speed digital machine computations.

In the direct problem, the solution starts with an assumed flow surface and proceeds with successive alternate solutions on the two kinds of flow surfaces until a satisfactory approximation is obtained. The better the first approximation, the shorter the computation.

3452

CH-19 back

The process is usually shorter for the inverse problem. The calculation begins on the mean S_2 surface on which the designer has one degree of freedom and an estimated blade thickness distribution B to specify. After the solution on this S_2 surface has been obtained, the blade coordinates are determined by extending the solution circumferentially.

Initial approximations. - The computations of the general theory for three-dimensional flows can be shortened materially by starting the iteration procedure with a reasonably good first approximation of the detailed flow variation. Reference 22 presents a quick approximate solution for the two-dimensional, compressible, subsonic, nonviscous flow past arbitrary turbomachine blades on arbitrary surfaces of revolution.

The first step in this particular solution is to estimate a mean streamline shape and the specific mass flow (product of velocity and density) along it. (For alternate methods, see ch. IV (ref. 2).) Equations for the flow along stream filaments of revolution are then solved to obtain values of the density and velocity components separately and of their derivatives in the circumferential direction. Next a Taylor series expansion in the circumferential direction using these values, together with mass-flow integrations, provides calculated blade shapes. Finally, an iteration procedure is set up in which the variance between the calculated blade shapes and the actual blade shapes provides the information required as a starting point for the second cycle. According to reference 22, depending upon the configuration and the original estimates, the detailed flow variations can be suitably obtained in two to four computation cycles.

Solutions on flow surfaces S_1 and S_2. - The three-dimensional analysis of reference 10 can provide a clearer understanding of the flows uncomplicated by viscous, secondary-flow effects than was obtainable from the simplified solutions. More complete knowledge about the effects of the main stream on the development of viscous boundary layers may then aid in understanding the secondary-flow behavior in the turbomachines.

The practical utility of the more accurate flow representation of reference 10 depends, of course, upon its susceptibility to accurate and quick computation. Reference 23 is an investigation of the mechanics of obtaining solutions for the principal flow equations of the general three-dimensional-flow theory.

It will be recalled that the three-dimensional solution was obtained by combinations of mathematically two-dimensional solutions on two kinds of intersecting relative stream surfaces, designated S_1 and S_2. The principal flow equations for both kinds of surfaces are similar, and the methods of successive approximations used for their solution are similar.

If it can be shown that the solution on one of the surfaces converges readily, the solution on the other should converge as well. Reference 23 evaluates three methods for obtaining solutions on the S_2 surfaces: (1) a relaxation method using hand-operated desk calculator, (2) a matrix method on an IBM card-programmed electronic calculator, and (3) a matrix method on a Univac. The actual machine analyzed was a single-stage axial-flow turbine, but the results are equally meaningful to compressor design. Free-vortex variation in tangential velocity and cylindrical bounding walls were specified to reduce radial-flow effects. The blades are quite long, however, with hub-tip radius ratio of 0.6.

3452

For both relaxation and matrix solutions, the nonlinear partial differential principal equation is replaced by a number of finite-difference equations representing the principal equation at the number of grid points in the flow region. The equations are solved by a method of successive approximations. The accuracy of such solutions depends upon the grid size (number of points), the degree of the polynomial representation used, the size of the residuals accepted, and the number of successive cycles completed for convergence.

Convergence was readily obtained in all cases of the investigation. The indications are that the matrix methods were quicker and somewhat more accurate than the relaxation solutions. In any event, the calculations were feasible and not overly difficult for the solution of the flow on a flow surface, one step in the over-all three-dimensional-flow solution.

Information concerning the detailed flow distribution (ref. 22) and particularly concerning the relations of the pressure gradients and blade shape to radial-flow components (ref. 23) is discussed in the next main section of this chapter.

Evaluation and relation to previous methods. - Because of the complexity of the over-all three-dimensional design theory, very little has been recorded about experience in its use. Little information is available concerning the convergence of the iteration procedures or the magnitudes of the random errors of the computational methods. At present, this three-dimensional theory may serve best as a useful guide for evaluating experimental data.

As noted in reference 10, the through-flow solution (ref. 8) can be considered as a limiting case for the more general three-dimensional solution. It may be regarded, for example, as the solution for the flow along the S_2 mean stream surface that divides the mass flow equally when the circumferential variation of the velocity components approaches zero. Thus, the through-flow solution serves to indicate trends when the effects resulting from having a finite number of blades are small or constant.

In this connection, the use of a blade thickness factor, based on information about blade thickness effects such as obtained, for example, in references 13 and 14, should improve the solutions considerably.

The effects of compressibility, spanwise variation of circulation $V_\theta r$, and radial components $\mathcal{F}_r$ or distributed-force vector $\bar{\mathcal{F}}$ upon the radial variations of gas state in a single-stage and in a seven-stage subsonic compressor with symmetrical velocity diagram are studied in reference 15. The results of these studies are presented briefly in the next main section. The investigation includes a brief discussion of the comparison between simplified-radial-equilibrium solutions and the solutions according to reference 3, while employing solutions obtained by means of the through-flow and three-dimensional theories (refs. 8 and 10, respectively) as criteria for accuracy. In this comparison, at axial stations in front of and behind the rotor of the single-stage compressor the simplified-equilibrium solution and the limiting solutions of reference 3 (zero and infinite aspect ratios) produced rather poor approximations to more complete solutions. The simple approximation to the streamline path suggested in reference 3, with an assumed sinusoidal path through the rotor, gave a good approximation to the three-dimensional solution in the case investigated in reference 17. 3452

SOME ASPECTS OF THREE-DIMENSIONAL FLOWS

The formidability of the complete three-dimensional design theory makes its application to compressor design somewhat impractical at this time. Nevertheless, considerable information about the three-dimensional aspects of the actual fluid behavior in compressors is required for design purposes. Such information has been obtained most successfully from many experimental and theoretical studies, each directed and confined to a particular phase of the real flow. By restricting the scope of a particular study, the investigator can make sweeping assumptions which simplify his solutions greatly. He need only be careful that his assumptions do not qualify the particular aspects of the flow being investigated. In the following subsections, several such phases of the over-all three-dimensional-flow behavior are described briefly, such as the effects of radial variations of circulation and of blade loading, radial components of flow within and between the blade rows, the effects of compressibility and of blade-force components, and some secondary-flow effects. Only steady-flow phenomena are considered here. The time-unsteady flows are considered in the next main section of this chapter.

Radial-Flow Variations

In order to facilitate the investigations of the effects of radial variation of circulation, the flows are generally assumed axially

symmetric and nonviscous, with constant entropy and enthalpy radially at the inlet. Even for these conditions, the solutions for the governing equations are simple only for the incompressible case of vortex distribution of the tangential velocity component, that is, constant circulation spanwise. For this condition only, the flow is two-dimensional and the streamlines all lie on cylindrical surfaces. For conditions of inconstant circulation radially, according to Prandtl's theory, vortices trail from the blades with their vorticity vectors downstream in the flow direction. The flow equations are then nonlinear, nonhomogeneous partial differential equations; and the flow itself is no longer confined radially to cylindrical surfaces. The aerodynamic advantages to be gained by use of nonvortex designs (i.e., lower relative velocities in the case of solid-body rotation design) must be weighed against the radial-flow components which arise and which can be calculated only with difficulty. Nevertheless, the aerodynamic advantages associated with nonvortex designs have frequently been beneficial enough to outweigh any detrimental effects.

3452

Radial-flow shifts. - The radial-flow displacement that occurs within blade rows, both rotating and stationary, is discussed in reference 3. Here the use of a sinusoidal approximation to the probable flow path was suggested in a calculation procedure based on this kind of assumed curve. For a subsonic single-stage and a subsonic seven-stage compressor designed for symmetrical velocity diagram at all radii, reference 15 compares the simplified-radial-equilibrium solution, the assumed sinusoidal-flow-path solution (single stage only)(ref. 3), the through-flow solution (ref. 8), and the three-dimensional solution (ref. 10). Using references 8 and 10 as criteria, reference 15 found that, in the single-stage compressor, the sinusoidal-flow-path assumption gave answers that agreed closely with the more complete solutions. The simplified-radial-equilibrium solution did not agree well.

One conclusion reached in reference 15 is that, while compressibility does not change the streamline shapes very much, it does affect the velocity components a great deal. Another conclusion is that the gas undergoes an oscillatory radial motion in passing through the compressor. The period of the oscillatory motion is equal to the length of a stage. The gas (e.g., ref. 15) shifts inward through the inlet guide vanes and the first rotor and then outward in the first stator, the effects of this oscillatory motion being greatest in high-aspect-ratio stages. In general, the shift through the guide vanes, if present, is always inward. The shift through the rotor depends upon the particular velocity diagram and may be inward (for velocity distribution that is wheel type in the direction of the rotor rotation), may not shift (free vortex), or may be outward (wheel type in opposite direction to rotor rotation). In a velocity-diagram analysis, reference 24 shows that for inward radial shift in a rotor the negative radial gradients of the axial velocity components behind the rotor lead to undesirable diffusion factors at the rotor tip and high stator-inlet Mach numbers.

By choosing a wheel-type flow distribution at the rotor inlet counter to the rotor direction with vortex distribution in the rotor, a radially outward shift in mass flow may be obtained. This should lead to more favorable diffusion-factor and Mach number distributions.

Reference 23 points out that the axial component of velocity is constant radially for free-vortex blading only for the case of simplified radial equilibrium. In the more general case, including, for example, the effects of radial variation of entropy and enthalpy, considerable radial variation of the axial velocity components results for both incompressible and compressible flows. In all such cases described in reference 23 (turbine configurations), there was a negative radial gradient of axial velocity ahead of the rotor. 3452

Reference 23 indicates that the actual path within the blade row may be far from sinusoidal and depends upon such factors as radial twist of the stream (due to $\mathcal{F}_r$, radial component of the distributed-force term) and compressibility of the gas.

Flow near blade rows. - Reference 16 provides information about the flow near a blade row, just upstream or just downstream. It is first noted in reference 16 that the three-dimensional nonviscous incompressible-flow solution is simple only for the case of vortex distribution of the tangential velocity component. For this condition, the blade circulation spanwise is constant and there are no radial components or axial variations. For varying circulation spanwise, it is still possible to calculate the difference between the axial velocity profiles far upstream and far downstream of the blade row fairly readily by neglecting radial transport of vorticity shed from the blades. But to determine the velocity distribution of the flow field near the blade rows is a more difficult problem, involving nonlinear, nonhomogeneous, partial differential equations.

In reference 16, the flow is considered nonviscous, incompressible, and axially symmetric, with no inner- or outer-shroud taper. It is further assumed that there is no self-transport of vorticity; that is, the vorticity is transported only by the mean velocity and not by its own induced velocity. This last qualification reduces the problem to the solution of a linear, nonhomogeneous, partial differential flow equation. The solutions thus obtained provide an approximation to the velocity field for any blade-loading distribution. The results are useful, then, for such conditions in which self-transport is negligible - that is, for moderate-turning, high-solidity configurations.

For the particular case where the blade chord approaches zero (actuator disk), the linearized partial differential equation describing the tangential velocity component becomes homogeneous as well and can be solved directly by using the given boundary conditions. Physically, this

assumption is equivalent to requiring the change in mean tangential component through a blade row to occur as a discontinuity (the actuator disk) in a plane normal to the axis at a chosen axial location. By appropriately choosing the location for the discontinuous jump in tangential velocity (the axial and radial velocity components remaining continuous throughout), the direct solution for the homogeneous case is shown to be a useful approximation to the more exact solution for the case of finite nonzero blade chord, except near the lifting line, where large radial velocities and axial velocity gradients are generated.

3452

For both the finite blade chord and the discontinuous approximation, the linearized flow equations make possible the attainment of the incompressible solution for a multistage turbomachine by superposition of the flows for the individual blade rows. Exponential approximations are developed for rapid estimations of the velocity-component distributions, which provide an even simpler method of approximating the flow through a turbomachine. These approximations were sufficient for the particular case calculated in reference 16 to estimate the general order of the velocity components and were sufficiently simple to make these relations useful in estimating the interference of adjacent blade rows.

CH-20

An illustrative example is calculated in reference 16, which assumes a linearly increasing circulation distribution from root to tip. The calculations indicate sizable changes in axial velocity profile both upstream and downstream of the blade row. The linearized approximation used (with the blade loading similar at all radii and assuming no radial force components) makes possible the separation of the velocity components into the series of terms associated with the blades considered stationary and the additional terms due to rotation effects. Thus, the radial velocity disturbances, important principally as they affect the axial and tangential velocity components, are analyzed. An interesting asymmetrical behavior is observed. The induced effects associated with the stationary blade attain their maximum downstream of the blade midchord position axially; the disturbances associated with rotation, upstream.

Reference 25 describes two physically possible types of nonviscous incompressible flow for a special case of the "actuator-disk" theory, the limiting case of a cascade of blades with negligible chord, discussed as an approximation to the more exact solution of reference 16. As before, only the tangential velocity components have a discontinuity at the actuator-disk section, the radial and axial components being continuous throughout. Axial symmetry, negligible heat transfer, and isentropic flow are assumed. The basic equations employed are Euler's equation of motion, the continuity equation, and the thermodynamic entropy and energy equations. As shown by a numerical example, the exact solutions to the problems as formulated here may match desired turbomachine flow conditions sufficiently closely to provide useful approximations of interest to designers. [Note that ξ and ζ should be interchanged in equations (9) to (11) in ref. 25.]

Radial adjustment and blade-row interference. - The shape of a stream surface as it passes through the stages of an axial turbomachine is investigated in reference 17 with the use of the exponential approximation to the linearized flow solution developed in reference 16. Attention is directed to the flow near the blade row and the manner in which the transition is made from the far-upstream to the far-downstream velocity profile. For the configuration investigated in reference 15, it was found that the radial velocity requires more than two axial chord lengths upstream of the inlet guide vanes and downstream of the stator before becoming negligible. Reference 17 establishes a relation between the aspect ratio of the blades and the rate of radial adjustment. The radial adjustment ranges from nearly complete by the time the trailing edge of low-aspect-ratio blades (≈ 1.0) is reached, to almost negligible radial adjustment at the trailing edges of high-aspect-ratio blades (≈ 3.0). This information is then brought to bear on the dual problems of the mutual interference of neighboring blade rows and the three-dimensional flows in an axial turbomachine at off-design conditions. Briefly, for blade aspect ratios of 1.0 or less, the effects on the velocity distribution of interference between adjacent blade rows are negligible, and distortion of the design axial velocity profile at off-design operation is small. The effects of off-design operation may increase considerably with higher blade aspect ratio, while the interference between adjacent blade rows may become a predominant influence for aspect ratios over 3.0.

3452

Secondary-Flow Effects

General discussion. - The three-dimensional behavior of a real fluid is intimately associated with the three-dimensional boundary-layer behavior of that fluid. The tendencies of the boundary layers to accumulate locally, to develop large radial and cross-channel flows in a complex of motions generally termed secondary flows, are discussed in chapter XV. Detailed experimental information on secondary-flow patterns is presented in chapter XV, together with the results of the more important theoretical developments. The present report is concerned chiefly with the overall flow picture; only the broad aspects of secondary flows are considered here.

The flow through a blade grid is considered as flow through individual channels or curved ducts in reference 26, and three distinct boundary-layer phenomena are discussed: (1) the cross-channel displacement leading to thickened boundary-layer regions at the suction surface of the passage, (2) the different behavior of boundary layer when adhering to a solid surface as contrasted with detached boundary layers such as wakes, and (3) the effect of centrifugal acceleration inducing radial components of motion affecting especially the boundary layers of moving blade rows. A criterion of radial stability is developed indicating that "stability of compressible flow depends not only upon the radial distribution of

total energy, as is the case for incompressible flow, but also upon the temperature distribution." With this criterion, the radial displacement of boundary layer in turbomachines is analyzed for various conditions of flow circulation and boundary-layer distribution.

In reference 27, the secondary flows are attributed largely to trailing-edge vortices shed as a result of spanwise variation of circulation along the blades and nonuniform inlet approach velocities (see ch. XV for discussion of passage vortices). Reasonable orders of magnitude of three-dimensional losses are estimated by the methods of reference 27 for the very conservative flow conditions assumed. A practical extension of this investigation is provided in the guide-vane analysis of reference 28. End-wall boundary layers are shown to cause deviations of the real flow from blade-element-flow considerations. Some of the effects noted are first underturning and then overturning in the boundary layer as the end wall is approached, a general decrease in circulation and turning angle along the blade in the boundary-layer regions, and large induced losses in the guide-vane end regions. A calculation procedure for quantitative estimations of the mean flow variations induced by the end-wall boundary-layer effects is set up in which the distribution along the blades is represented by a system of vortices, the effects of which are calculated by the method of images, with use of an empirical correlation factor. The closing section of reference 28 considers several aspects of the secondary-flow problem, from the designer's viewpoint, in some detail.

The more complex flow situation in rotor blading is considered in reference 27. Tip-clearance and relative blade- to wall-motion effects are discussed in very general terms, as is boundary-layer displacement of the type noted in reference 26. The action of secondary flows under certain conditions to prevent stalling and to enable blades to operate above the two-dimensional stalling limit is brought out. The work-done factor and the induced-drag coefficient are connected on the basis of these secondary-flow considerations. Finally, the conclusion is reached that ordinarily (conservative, subsonic turbomachines) the primary flow conditions and primary losses are still due to two-dimensional blade-section performance. Experimental evidence (ch. XV and ref. 29) indicates that the secondary-flow-induced losses assume considerably more importance with higher flow velocities and larger turning angles.

An interesting analysis is developed in reference 30 of the relation between the secondary flows and the main flow characterized by radially varying blade circulation and rotational incoming flow. References 30 and 4 present a clear, understandable physical picture of three-dimensional flows in turbomachines.

Commentary. - Despite the great amount of research already devoted to the study of secondary flows in turbomachinery, empirical information,

3452

CH-20 back

useful to designers, concerning the actual flows within the blade rows themselves is still largely lacking. Most analyses to date provide information and devise design procedures about the flows encountered at stations between the blade rows. For design purposes, the nature of the flows in the blade rows themselves is almost invariably assumed. References 14 and 18 give evidence that the flow patterns within the blade rows are quite complex, that large stream surface distortions can and do exist. These results must be considered to qualify the conclusions reached from analyses (i.e., ref. 4) based on assumed simple flow configurations in the passages between stations. 3452

TIME-UNSTEADY FLOW

A theory of nonstationary motion around airfoils is presented in reference 31. The purpose of the paper is to present the theory originally developed by Birnbaum, Wagner, Küssner, Glauert, and Theodorsen in relatively uncomplicated mathematical forms. A remarkably clear exposition of the fundamental conceptions of the two-dimensional circulation theory of airfoils is presented first. The report shows how a "wake of vorticity" is produced if the circulation around the airfoil is a timewise variable. The induced vorticity distributions over a thin airfoil are presented for such wake vortices at various distances in the wake ξ from the midpoint of the airfoil.

Formulas for the lift and momentum are next obtained for the thin airfoil, and here it is seen that the simple Joukowski formula $L = \rho V \Gamma$ no longer will do. Instead, the expression for the lift consists of three parts:

$$L = L_0 + L_1 + L_2$$

where

$$L_0 = \rho u \Gamma_0$$

$$L_1 = -\rho \frac{d}{d\tau} \int_{-1}^{1} \gamma_0(x) x \, dx$$

$$L_2 = \rho u \int_{1}^{\infty} \gamma(\xi) d\xi / \sqrt{\xi^2 - 1}$$

and

u velocity of motion of airfoil (or of gust of wind past airfoil)

Γ_0 circulation resulting from vorticity $\gamma_0(x)$

$\gamma_0(x)$ vorticity bound to airfoil that would be produced by airfoil motion (or by gust) if instantaneous velocity were maintained permanently

x coordinate along blade rearward from midchord position

$\gamma(\xi)$ vorticity in wake

3452

The quasi-steady lift L_0 is that which would be produced if the instantaneous velocity and angle of attack were permanently maintained. The lift L_1 represents the forces acting on a body in an ideal fluid when no circulation is produced because of the reaction of the accelerated fluid masses. It is obtained by integrating over the surface the "impulsive pressures" $\rho \frac{\partial \varphi}{\partial \tau}$ (where φ is the instantaneous potential function). The lift L_2 represents the contributions to the lift from the wake itself, and contains the wake effects. A corresponding formulation is obtained for the moment:

$$M = M_0 + M_1 + M_2$$

In these formulas, L_0 and M_0 as well as L_1 and M_1 require only solutions of steady-state problems by usual methods. The wake contributions L_2 and M_2 can be interpreted physically as the differences between the instantaneous and the final values of lift and moment for a case in which the quasi-steady lift and moment undergo a sudden change. Hence, L_2 and M_2 can be called the "deficiencies" caused by the nonuniformity of the motion of the airfoil or of the fluid velocity.

These general results were then applied to an oscillating airfoil and to an airfoil entering a vertical gust with various velocity profiles. The general expressions for the lift and moment developed by von Kármán and Sears (ref. 31) are applied in reference 32 to a series of alternating up and down gusts, sinusoidally distributed. The magnitude of the lift decreases as the frequency of the gusts increases. As in reference 31, the lift is shown to act, always, at the quarter-chord point of the airfoil. These results are applied to a wind-tunnel fan blade operating just downstream of a set of prerotation vanes. The vanes produce periodical disturbances through which the fan blades pass, which in turn give rise to periodical forces on the blades and perhaps vibrations of dangerous amplitudes. An approximate calculation is made in order to apply the results obtained, in which it is necessary to take the two-dimensional flow across some mean cross section representative of the blade and to

consider that this mean section encounters flow conditions in its path that can be approximated by superimposing a sinusoidal variation of axial velocity on a uniform mean axial velocity. No dangerously large vibration amplitudes were calculated in the example given in reference 32.

The results derived in reference 32 for an airfoil moving through a stationary gust pattern are extended in references 33 and 34 by means of a simple generalization to provide formulas for calculating the unsteady aerodynamic quantities for a single stator row followed by a single rotor row. Because the blades are thin, slightly cambered, and lightly loaded, this configuration resembles a compressor more closely than a turbine. The flow is assumed incompressible and inviscid; the blade rows are represented by infinite cascades of two-dimensional blades. Each airfoil (ref. 33) is considered "to be acting in a velocity field induced by (a) its own wake, (b) the (variable) bound vortices of fellow members of its own blade row, (c) their wakes, (d) the (variable) bound vortices of members of the other blade row, and (e) their wakes." 3452

In order to obtain a solution with reasonable ease, a scheme of successive approximations is followed:

(1) Assume first that the unsteady effect on the circulation of a blade is small compared with the steady circulation ordinarily considered by a designer.

(2) The first approximation to the unsteady effects on a typical stator blade ${}_{\tau}\Gamma^{s}(\tau)$ is calculated on the assumption that the only significant contribution arises from the steady circulation on the rotor blades ${}_{0}\Gamma^{r}$. For this first approximation, the unsteady rotor circulation ${}_{\tau}\Gamma^{r}(\tau)$ and the unsteady parts of the circulation of all the other stator blades and of all the vortex wakes except that of the chosen stator blade are neglected. "(Presumably this approximation breaks down for stator cascades of extremely large solidity, in which the adjacent blades are so close that their nonsteady circulation components induce large effects.)"

(3) In order to calculate the unsteady effects on a rotor blade, in this same first approximation process, the significant contributions are assumed to arise from the steady circulation about the stator blades ${}_{0}\Gamma^{s}$ and from the effects of the rotor blades passing through the vortex wakes shed by the stator blades.

The procedure thus far can be considered as the first of a series of successive approximations. The second step might consider the additional effects of ${}_{0}\Gamma^{r}$ but, as noted in reference 33, would very likely be extremely difficult to calculate.

On the basis of this first-approximation scheme, then, a calculation is made for the unsteady velocity at a rotor or stator blade induced by the steady circulation distribution on the blades of the other row in motion relative to the blade in question. From this the unsteady lift and moment of a stator or rotor blade can likewise be calculated. Investigations of numerical examples were made for configurations of thin, small-turning airfoils, with rotor and stator solidities fixed at unity, with a 50-percent reaction stage, and with the stagger angles $\alpha_r = \alpha_s = 45^\circ$. The calculations were made for a range of the parameter b'/c_r (ratio of axial separation between trailing edge of stator row and leading edge of rotor row to rotor half-chord) and over a range of d_n/d_s (ratio of pitch of rotor blades to pitch of stator blades).

3452

The results showed large increase of unsteady lift with decreasing b'/c_r, and appreciable change of lift with variation of d_n/d_s. In one case the unsteady part of the lift was as much as 18 percent of the steady lift and, for this approximation, is accordingly of practical importance. Also, the contribution of the stator wakes to the unsteady lift of the rotor blades was comparable in magnitude to the effects induced by the bound circulation of the stators themselves. The assumption made for the first approximation, namely that the unsteady effect on the circulation of a blade is much less than the steady circulation $|_\tau\Gamma| << |_0\Gamma|$, was checked and found to be reasonable. In addition, the authors find the power in the vortex wakes quite small. (The power is expressed as the ratio of the energy transferred to the wakes per unit time to the steady power required to turn the rotor.)

A further result is that the energy in the stator wake for the present cases is about 100 times as large as the energy in the rotor wake. Because the kinetic energy transferred to the vortex wakes due to periodic variation in circulation is proportional to $|_\tau\Gamma|^2$ (ref. 35), the squared amplitude of variation of circulation, and therefore the unsteady circulation on the stator blades, is about 10 times as large as that on the rotor blades. The unsteady lift on both was about the same, however, for the example in reference 34 because of the differences in chordwise velocity distributions on the stator and rotor. In general, then, according to references 33 and 34, the induced circulation on a blade row due to the relative motion of an adjacent downstream row is considerably greater than that due to the effects of an adjacent upstream row.

REFERENCES

1. Compressor and Turbine Research Division: Aerodynamic Design of Axial-Flow Compressors. Vol. II. NACA RM E56B03a, 1956.

2. Compressor and Turbine Research Division: Aerodynamic Design of Axial-Flow Compressors. Vol. I. NACA RM E56B03, 1956.

3. Wu, Chung-Hua, and Wolfenstein, Lincoln: Application of Radial-Equilibrium Condition to Axial-Flow Compressor and Turbine Design. NACA Rep. 955, 1950. (Supersedes NACA TN 1795.)

4. Smith, L. H., Jr., Traugott, S. C., and Wislicenus, G. F.: A Practical Solution of a Three-Dimensional Flow Problem of Axial-Flow Turbomachinery. Trans. A.S.M.E., vol. 75, no. 5, July 1953, pp. 789-803.

5. Reissner, Hans: Blade Systems of Circular Arrangement in Steady, Compressible Flow. Studies and Essays. Courant Anniversary Vol., Interscience Pub., Inc. (New York), 1948, pp. 307-327.

6. Reissner, H. J., and Meyerhoff, L.: Analysis of an Axial Compressor Stage with Infinitesimal and Finite Blade Spacing. NACA TN 2493, 1951.

7. Reissner, Hans J., Meyerhoff, L., and Bloom, Martin: Two-Dimensional Steady Nonviscous and Viscous Compressible Flow through a System of Equidistant Blades. NACA TN 2718, 1952.

8. Wu, Chung-Hua: A General Through-Flow Theory of Fluid Flow with Subsonic or Supersonic Velocity in Turbomachines of Arbitrary Hub and Casing Shapes. NACA TN 2302, 1951.

9. Lieblein, Seymour, Schwenk, Francis C., and Broderick, Robert L.: Diffusion Factor for Estimating Losses and Limiting Blade Loadings in Axial-Flow-Compressor Blade Elements. NACA RM E53D01, 1953.

10. Wu, Chung-Hua: A General Theory of Three-Dimensional Flow in Subsonic and Supersonic Turbomachines of Axial-, Radial-, and Mixed-Flow Types. NACA TN 2604, 1952.

11. Hatch, James E., Giamati, Charles C., and Jackson, Robert J.: Application of Radial-Equilibrium Condition to Axial-Flow Turbomachine Design Including Consideration of Change of Entropy with Radius Downstream of Blade Row. NACA RM E54A20, 1954.

12. Ruden, P.: Investigation of Single Stage Axial Fans. NACA TM 1062, 1944.

13. Wu, Chung-Hua, and Brown, Curtis A.: Method of Analysis for Compressible Flow Past Arbitrary Turbomachine Blades on General Surface of Revolution. NACA TN 2407, 1951.

14. Wu, Chung-Hua, and Costilow, Eleanor L.: A Method of Solving the Direct and Inverse Problem of Supersonic Flow along Arbitrary Stream Filaments of Revolution in Turbomachines. NACA TN 2492, 1951.

15. Wu, Chung-Hua: Subsonic Flow of Air through a Single-Stage and a Seven-Stage Compressor. NACA TN 2961, 1953.

16. Marble, Frank E.: The Flow of a Perfect Fluid through an Axial Turbomachine with Prescribed Blade Loading. Jour. Aero. Sci., vol. 15, no. 8, Aug. 1948, pp. 473-485.

17. Marble, Frank E.: Some Problems Concerning the Three-Dimensional Flow in Axial Turbomachines. Preprint No. 182, Inst. Aero. Sci., 1949.

18. Torda, T. P., Hilton, H. H., and Hall, F. C.: Analysis of Viscous Laminar Incompressible Flow through Axial Flow Turbomachines with Infinitesimal Blade Spacing. Rep. No. C-TR-1, Eng. Exp. Station, Aero. Eng. Dept., Univ. Ill., Feb. 24, 1953. (Contract AF 33(616)-52, E.O. No. R-467-3 BR-1.)

19. Born, P. W., Hall, F. C., Hilton, H. H., and Torda, T. P.: Analysis of Viscous Laminar Incompressible Flow through Axial Flow Turbomachines with Finite Blade Spacing. Rep. No. C-TR-2, Eng. Exp. Station, Aero. Eng. Dept., Univ. Ill., Mar. 18, 1953. (Contract AF 33(616)-52, E.O. No. R-467-3 BR-1.)

20. Torda, T. P.: Analysis of Viscous Laminar Incompressible Flow through Axial Flow Turbomachines. Annual Summary Rep. No. C-TR-3, Eng. Exp. Station, Aero. Eng. Dept., Univ. Ill., July 15, 1953. (Contract AF 33(616)-52, E.O. No. R-467-3 BR-1.)

21. Wu, Chung-Hua: Formulas and Tables of Coefficients for Numerical Differentiation with Function Values Given at Unequally Spaced Points and Application to Solution of Partial Differential Equations. NACA TN 2214, 1950.

22. Wu, Chung-Hua, Brown, Curtis A., and Prian, Vasily D.: An Approximate Method of Determining the Subsonic Flow in an Arbitrary Stream Filament of Revolution Cut by Arbitrary Turbomachine Blades. NACA TN 2702, 1952.

23. Wu, Chung-Hua: Matrix and Relaxation Solutions That Determine Subsonic Through Flow in an Axial-Flow Gas Turbine. NACA TN 2750, 1952.

24. Lieblein, Seymour: Review of High-Performance Axial-Flow-Compressor Blade-Element Theory. NACA RM E53L22, 1954.

25. Bragg, Stephen L., and Hawthorne, William R.: Some Exact Solutions of the Flow through Annular Cascade Actuator Discs. Jour. Aero. Sci., vol. 17, no. 4, Apr. 1950, pp. 243-249.

26. Weske, John R.: Fluid Dynamic Aspects of Axial-Flow Compressors and Turbines. Jour. Aero. Sci., vol. 14, no. 11, Nov. 1947, pp. 651-656.

27. Carter, A. D. S.: Three-Dimensional-Flow Theories for Axial Compressors and Turbines. War Emergency Issue No. 41 pub. by Inst. Mech. Eng. (London). (Reprinted in U.S. by A.S.M.E., Apr. 1949, pp. 255-268.)

28. Lieblein, Seymour, and Ackley, Richard H.: Secondary Flows in Annular Cascades and Effects on Flow in Inlet Guide Vanes. NACA RM E51G27, 1951.

29. Rohlik, Harold E., Kofskey, Milton G., Allen, Hubert W., and Herzig, Howard Z.: Secondary Flows and Boundary-Layer Accumulations in Turbine Nozzles. NACA Rep. 1168, 1954. (Supersedes NACA TN's 2871, 2909, and 2989.)

30. Smith, Leroy H., Jr.: Three-Dimensional Flow in Axial-Flow Turbomachinery. Pt. I - Theoretical Determination of Secondary Flow. Rep. 1-14, Mech. Eng. Dept. Internal Flow Res., The Johns Hopkins Univ., Nov. 1953. (Air Force Contract AF-33(616)-152.)

31. von Kármán, Th., and Sears, W. R.: Airfoil Theory for Non-Uniform Motion. Jour. Aero. Sci., vol. 5, no. 10, Aug. 1938, pp. 379-390.

32. Sears, William R.: Some Aspects of Non-Stationary Airfoil Theory and Its Practical Application. Jour. Aero. Sci., vol. 8, no. 3, Jan. 1941, pp. 104-108.

33. Kemp, Nelson H., and Sears, W. R.: Aerodynamic Interference between Moving Blade Rows. Jour. Aero. Sci., vol. 20, no. 9, Sept. 1953, pp. 585-597.

34. Kemp, Nelson H., and Sears, W. R.: Aerodynamic Interference between Moving Blade Rows. Grad. School Aero. Eng., Cornell Univ., Dec. 1, 1952. (Contract AF 33(038)-21406.)

35. Keller, C.: Kinetic Energy Losses Behind Blade Grids As a Result of Periodic Variation in the Circulation. Rep. Inst. Aero., Tech. Hochschule (Zurich), 1934, pp. 167-187. (Available as R.T.P. Trans. No. 1883, British M.A.P.)

3452

CH-21 back

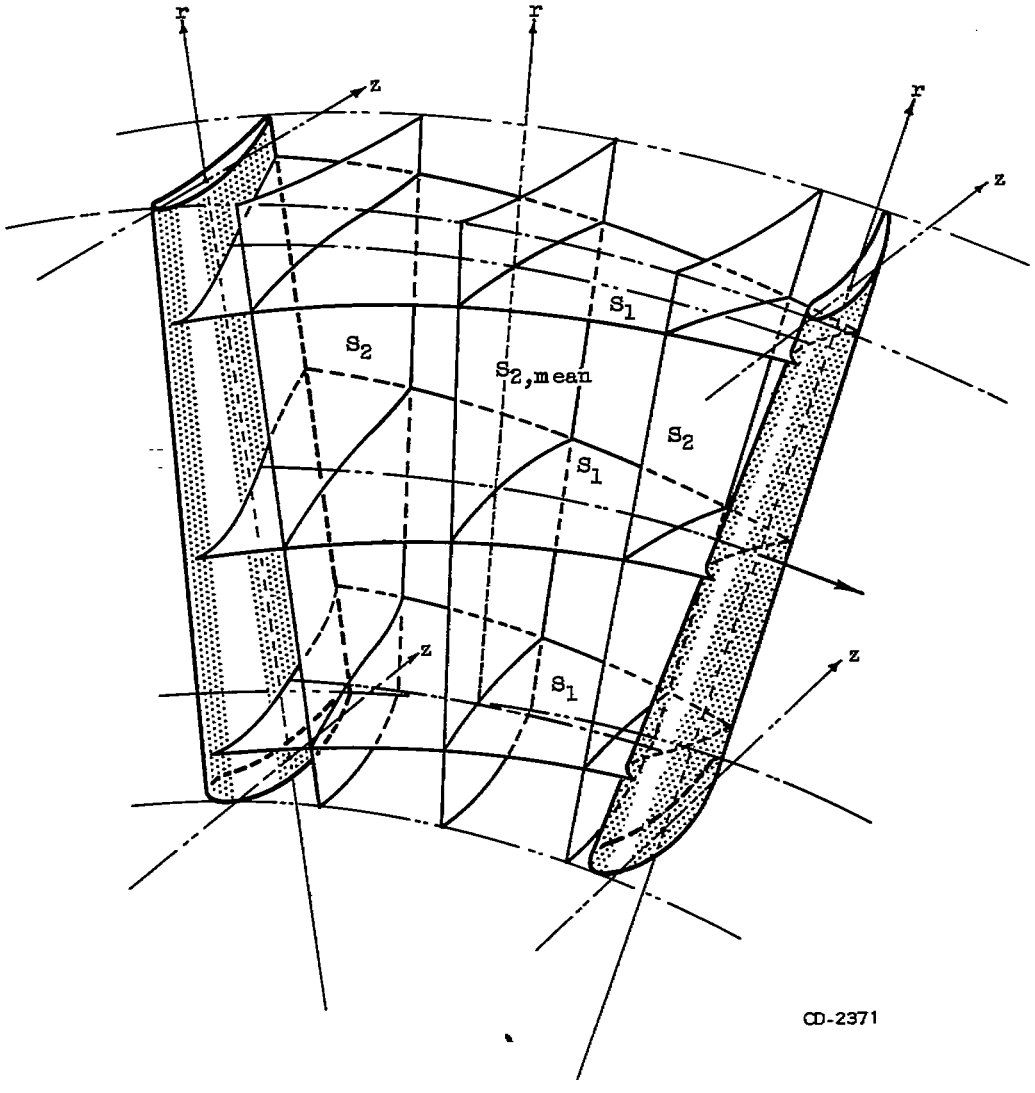

Figure 1. -Intersecting S_1 and S_2 surfaces in blade row.

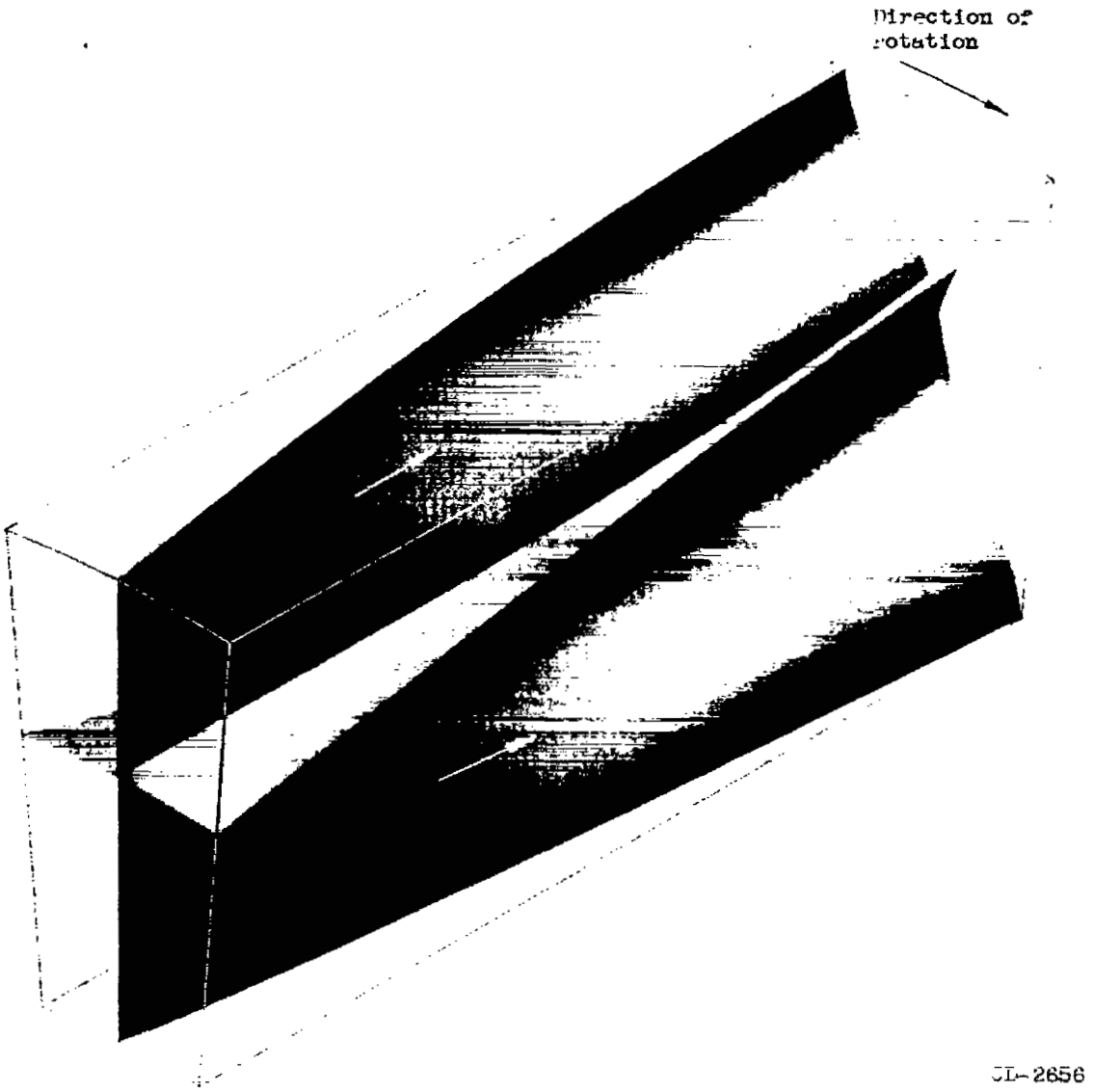

Figure 2. -Twist of flow surfaces in axial-flow channel.

3475

CHAPTER XV

SECONDARY FLOWS AND THREE-DIMENSIONAL BOUNDARY-LAYER EFFECTS

By Arthur G. Hansen and Howard Z. Herzig

SUMMARY

A survey of experimental and theoretical research on secondary flows and three-dimensional boundary-layer flows as applicable to compressor flow phenomena is presented. The results of experimental research are used to construct a simple model of secondary flow in compressor blade rows.

The limitations of the application of present research on secondary flows to flow in a multistage compressor and indications of ways this research might be applied to current design considerations are also presented.

INTRODUCTION

The importance of boundary-layer development in relation to compressor design procedures is discussed in chapter III (ref. 1) and reference 2. As these references point out, there are no simple techniques that accurately account for viscous effects in current design systems. Instead, the effects of boundary layers are taken into account only by introducing some gross correction factors into calculations derived from nonviscous-flow theory. These correction factors, moreover, are based on empirical data and give only rough estimates of boundary-layer development. Nevertheless, this method of accounting for viscous-flow effects has proved relatively adequate for the design of compressors of the type currently in use. With the trend toward high-speed and high-mass-flow turbomachines, however, the influence of boundary layers becomes increasingly critical in design calculations. This is simply illustrated by noting the sensitivity of flow velocities in the transonic range to slight changes in boundary-layer-flow blockage.

It is important to recognize that a more satisfactory description of boundary-layer flow cannot come from refinements of the two-dimensional

boundary-layer theory currently in use (ch. V (ref. 1)). The reason is that boundary-layer behavior in blade rows of an actual turbomachine exhibits certain irreconcilable differences from boundary-layer behavior predicted by two-dimensional theory. Two-dimensional boundary-layer theory predicts characteristics of a boundary layer resulting from a mainstream flow that has no variation in its lateral direction. In an actual blade row, however, lateral variations of the main stream and the associated boundary layer cannot be ignored. The occurrence of secondary flows - that is, boundary-layer flows having components normal to the mainstream direction - often results in sizable displacements and accumulations of boundary-layer material. These flows arise principally from blade end clearance, blade-to-blade and radial pressure gradients, centrifugal-force effects, and relative motion between blade ends and annulus walls (refs. 2 and 3). Flows of this type have no counterpart in two-dimensional theory. 3475

Losses occurring in blade end regions of compressor blade rows account for a sizable portion of the total measured loss (ch. VII (ref. 4)). As blade end losses are principally the result of boundary-layer displacements and accumulations, it may be stated that future improvement of compressor efficiencies will depend significantly upon understanding the nature and causes of these boundary-layer phenomena and upon finding more realistic and accurate methods of accounting for them in design procedures.

For these reasons, the analysis of secondary flows has become the major problem associated with research on boundary-layer behavior in compressors. While many important aspects of secondary-flow phenomena have not as yet been investigated, considerable research progress has been made. This chapter presents an over-all review of both experimental and theoretical research and indicates its relevancy to compressor design.

At the present time, research on secondary flows has two immediate goals: (1) to find methods of reducing the magnitude of undesirable secondary-flow disturbances in blade rows, and (2) to develop practical theories of secondary-flow behavior that the compressor designer can incorporate into design methods. In attaining these goals, three basic problems can be recognized: (1) isolating the factors that may cause secondary flows, (2) analyzing the types of secondary-flow components resulting from these factors, and (3) determining the contribution of these components to the total flow behavior. The factors that cause secondary flows are fairly well-known and have been indicated previously. The state of knowledge concerning the characteristics of the associated secondary-flow components, however, leaves much to be desired. As will be evident from the discussions presented, most of the current knowledge is qualitative in nature. Adequate theories furnishing the quantitative information necessary for improving compressor designs are still to be formulated.

EXPERIMENTAL INVESTIGATION OF SECONDARY FLOWS

Because of the importance of the problem, many experimental and theoretical investigations of secondary flow in turbomachines are presented in current literature (surveys 212 to 240, ref. 5). In experimental research carried out at the NACA Lewis laboratory, flow-visualization techniques as well as total-pressure and flow-angle measurements were used in order to obtain an insight into the three-dimensional boundary-layer-flow patterns in typical axial-flow turbomachines. The results of the investigations (refs. 2 and 3) are presented here only for the over-all physical understanding of secondary-flow processes in turbomachines that they afford rather than for detailed compressor flow information.

The following discussion attempts to build up a concept of secondary-flow behavior in compressor blade rows by separate descriptions of the various types of secondary-flow components that can occur. In this regard, an analysis of secondary flows arising from cross-channel pressure gradients is first discussed. Next, the influence of radial pressure gradients that contribute to the local accumulation of boundary-layer material is analyzed. The size and locations of these accumulations depend upon the character of blade boundary layers, which are, in turn, a function of profile shapes; hence, some indication of the effect of blade profile shapes on secondary flows is also included in the discussions. This is followed by a discussion of blade tip clearance and relative motion between blades and annulus walls. Finally, the influence of rotor-stator interaction on flow behavior is presented. Comprehensive descriptions of the methods employed to obtain the results can be found in references 2, 3, and 6.

The section is concluded with consideration of a model of the complete secondary-flow pattern as indicated by the experimental results and a discussion of ways certain aspects of secondary-flow theory might be applied to compressor design.

Cross-Channel Flows and Passage Vortex Formation

Apparatus and procedure. - For simplicity, the study of secondary-flow components resulting from cross-channel pressure gradients was begun by visualization of the end-wall inlet boundary layer of a two-dimensional cascade at low airspeeds. It was intended, by using a smoke flow-visualization method (ref. 2), to isolate and to evaluate the effects of cross-channel gradients upon the wall boundary layer while eliminating such complicating considerations as radial flows and possible shock phenomena.

A sketch of the two-dimensional cascade rig is shown in figure 1. The cascade section was so designed that the solidity, angle of attack, aspect ratio, turning angle, and blade stagger angle could be varied

quite readily. The two-dimensional cascades were used for tests at Mach numbers below 0.4. The boundary-layer flow was visualized by means of smoke introduced through a probe. The smoke flow-visualization method was used only at low mainstream velocities (about 30 ft/sec). At higher velocities, dispersion of the smoke due to turbulence made the method impracticable.

Passage vortex formation. - The overturning in the end-wall boundary layer of a two-dimensional cascade with no tip clearance is illustrated in figure 2. The overturning results from imposition of the mainstream static-pressure gradients upon the low-momentum boundary-layer fluid. The smoke used to trace out the flow patterns was introduced at the wall by means of the probe. A downstream view of a boundary-layer streamline crossing a channel (fig. 3) shows that, as the streamline approaches the suction surface, it deflects spanwise and then rolls up into a vortex-type flow. (The insert shows the entire streamline pattern schematically.) Probe surveys showed that all the streamlines in the wall boundary layer converged to approximately the same region and rolled up into the flow vortex (fig. 4(a)). The pattern of vortex formation was such that, as the point of smoke introduction was shifted toward the suction side, the streamlines along the end wall exhibited increased spanwise deflection as they approached the region of convergence, where they rolled up into the central portions of the vortex, as shown schematically in figure 4(b). 3475

This secondary-flow vortex is called the "passage vortex" in order to emphasize the fact that it is a passage wall and not a blade trailing-edge vortex due to circulation changes along the blade. The size and vorticity of the passage vortex increase with increasing main-flow turning. When the turning is large enough (fig. 5), the outermost layer of the vortex may come from boundary-layer flow on the pressure surface that deflects onto the end wall and flows all the way across the channel until it reaches the suction surface.

At low airspeeds where smoke could be used, passage vortex formation was observed for other configurations, including cascades of NACA 65-(12)10 blades. At higher Mach numbers, surface indications, obtained by use of hydrogen sulphide traces on white lead paint, show that the cross-channel deflection pattern remains unchanged (ref. 2).

It should be noted that the cross-channel component of boundary-layer flow can be considered as a "double" boundary layer (fig. 6). The component normal to the main stream must have zero velocity at the wall, rise to some maximum value, and then fall to zero again in the main stream. The outer portion of this cross-channel boundary layer rolls up to form the passage vortex. The "sub-layer" next to the wall has vorticity of the opposite sign to the outer portion, and when it rolls up produces vortices opposite in direction to passage vortices. Under these

test conditions, the diffusion of vorticity forces from this sub-layer was rapid enough to cause this portion of the boundary-layer vorticity to disappear rapidly. Photographs of this sub-layer roll-up are found in reference 6 and in the motion-picture supplement to that report.

Passage vortex behavior and effects. - Once the passage vortex has been formed, it tends to resist turning and does not follow subsequent mainstream turnings as it proceeds downstream. Figure 7 shows how in tandem cascades a vortex formed in the upstream cascade resists the turning in the downstream cascade. Test observers could see the passage vortex ricochet off a pressure surface of the downstream cascade and cause flow separation in the region of impact. The phenomenon has been observed in accelerating as well as decelerating cascades.

3475

Thus, the accumulation of low-energy material near the suction surface of a turbomachine passage causes flow disturbances and losses leading to flow-angle deviations and poor angles of attack in subsequent blade rows. Furthermore, the vortex behavior as it passes downstream can lead to flow disturbances on the blade surfaces that it impinges upon and to additional losses there. This behavior may account for a large part of the losses variously attributed to secondary flows. The mixing action of the vortex behavior likewise represents a large deviation from the kind of simplified boundary-layer behavior assumed in design procedure.

CH-22

Radial Secondary Flows in Stators

Just as the cross-channel pressure gradient imposed by the main stream causes cross-channel secondary flows, so the radial pressure gradient causes radial boundary-layer flows. Given a boundary-layer region extending from the inner to the outer shroud in a stator row, radial transport from the tip to the root regions can occur. The quantity of such transport depends upon the thickness of the radial boundary-layer region or flow path and the magnitude of the radial pressure gradient (a function of mainstream turning and velocity).

In rotors, the flow picture is further complicated by the centrifugal forces on the rotor blade boundary layers. In general, for compressors where the blade speeds are higher than the mainstream tangential velocity component, the boundary layer will be forced radially outward (see ref. 5, section II-F).

Apparatus and procedure. - The effects of radial pressure gradients and higher flow Mach numbers were studied in an annular-cascade test unit, shown schematically in figure 8. The cascade blades investigated therein were of several types (ref. 3). However, attention is confined initially to the tests in a cascade of high-turning vortex blades

designed for smooth two-dimensional blade surface velocity profiles. While these blades are not typical of those found in compressor units, the tests conducted provide sufficient information to formulate theories that apply to annular blade rows in general.

The annular cascade was used for a range of hub discharge Mach numbers up to about 1.5. As mentioned previously, smoke flow-visualization tests were unsatisfactory for flow velocities much in excess of 30 feet per second. Consequently, for high speeds, two other flow-visualization techniques were employed. In the first, the surfaces of the blade passages were painted with a lead carbonate base paint. Hydrogen sulfide gas (which has a density comparable to air) was then introduced into the boundary-layer region, and boundary-layer motion was indicated by the brown trace made by the reaction of the hydrogen sulfide with the paint. Unfortunately, this method provides indications of flows along boundaries only; and, because of the turbulence at higher Mach numbers, the traces indicate the flow paths of a region of the boundary layer instead of individual streamline paths. The second flow-visualization method was based on paint flow traces. The paint used was a lead carbonate paint deliberately made nondrying and capable of flowing with the surface flow gradients at the higher Mach numbers investigated. 3475

Since hydrogen sulfide and paint traces can at best give indications of boundary flows directly on blade surfaces and annulus walls, the significance of these traces is interpreted only on the basis of previous information obtained either by the smoke visualization method or by quantitative measurements.

It should also be noted that total pressures, flow angles, and wall static pressures were measured at a discharge measuring station in the annular-cascade investigations. The measurements were made on three sets of blades and at two flow conditions for each set of blades. These flow conditions are designated, respectively, "lower Mach number" (high subsonic flow) and "higher Mach number" (supersonic flow). The measuring probes and hot-wire anemometers used are described in reference 3. Great care was taken in the fabrication and use of these instruments in order to make the results as reliable and accurate as possible. Nevertheless, because of the large pressure and angle gradients involved in the flow regions of chief interest in this report, the results are discussed in qualitative terms only.

Indications of radial flows based on downstream measurements. - Contours of loss in inlet kinetic energy for the annular cascade of vortex blades are presented in figure 9. The hub loss accumulation is much larger than the outer-shroud loss accumulation for both the subsonic and supersonic flow conditions, despite the fact that the "wetted" area is greater in the outer half of the passages. This fact indicates radial flow of boundary-layer material. The decrease in outer-shroud loss core

and the increase in inner-shroud core with increasing Mach number indicate the development of additional or larger paths for radial transport of low-energy fluid at the higher flow Mach number.

Visual indications of radial flows. - In the presence of a radial pressure gradient in the annular cascade, the radial transport of sizable quantities of low-energy material can be expected in blade boundary-layer regions having low viscous shear forces along the blade span. Such a path, for example, might be provided by the blade trailing-edge regions. Another possible radial pathway might be provided on the suction surface of each blade at supersonic flow conditions when a shock exists across the passage to cause thickening of the blade suction-surface boundary layer.

3475

One method used to detect such paths was to apply narrow bands of paint on the suction surfaces of certain blades in the cascade. The paint traces found after a test then indicated paths along which low-energy material might be transported radially. Such traces are shown in figure 10. For this photograph, bands were painted on the suction surfaces of blades 1, 2, and 3 at the inner-shroud, midspan, and outer-shroud radial positions, respectively. Two such paths are shown in the figure, one at about midchord on the suction surface and the other along the blade trailing edge.

CH-22 back

Evaluation of radial components of secondary flow. - The existence of radial flow of low-energy material as indicated in the previous section was proved and the quantity of such flows at the supersonic flow condition was evaluated by the following rather simple device (ref. 3). Flow fences were fastened to the blades at the midspan position as in figure 11. The full flow fence (fig. 11(a)) was intended to interrupt radial flows both along the trailing edge and in the thickened boundary-layer region indicated in figure 10. The reduced flow fence (fig. 11(b)) was modified by being cut back so that it now affected only the trailing-edge radial flows. The results are presented in figure 12. Because of possible losses due to the fences themselves, the reduction in inner-shroud loss core is used to measure the quantities of radial transport. At the supersonic flow condition for this set of vortex blades, radial transport of boundary layer accounted for 65 percent of the low-energy material in the inner-shroud loss core at the blade-exit station. Of this 65 percent, 35 percent came through along the trailing edge, and 30 percent through the thickened boundary-layer paths on the suction surfaces. Thus, radial transport of boundary-layer material may be considerable under certain conditions.

Loss accumulations and passage vortices. - Briefly, measurements downstream of a cascade of vortex blades at a high subsonic flow Mach number (fig. 9(b)) indicate the presence at the measuring plane of (1) a large accumulation of boundary-layer material near the hub corner, (2) a much smaller accumulation near the outer shroud, and (3) a

well-defined wake between. The interpretation (ref. 3) is straightforward. Radially inward flow of boundary-layer material originating either on the outer shroud both upstream and within the cascade or on the blades themselves must, of necessity, take place somewhere upstream of the measuring plane. Most likely, radial-flow regions are on the suction surfaces of the blades and behind the trailing edges. At higher flow Mach numbers, the measured outer-shroud losses decrease further, the wake between remains nearly unchanged, and the inner-shroud loss core increases further. There being little reason to assume smaller outer-shroud losses at the higher Mach numbers, it is concluded that increased radial flows must occur at the higher Mach numbers for these vortex blades. Judging from the relative sizes of the inner- and outer-shroud loss cores and the total absolute values of the losses, the radial-flow mechanism must serve to transport sizable quantities of boundary-layer material. The flow-fence tests on the vortex blades proved that this is the case and located the radial-flow paths behind the blade trailing edges and in a shock-thickened boundary-layer region along the blade suction surface. 3475

The loss measurements at any position do not indicate the losses that actually develop at that radial position on the blade. Presumably, even in the radial-transport regions, through-flow components of the boundary-layer flow exist, and some of this material is shed and appears in the measured wakes at all radial positions. Since there is no apparent increase in the measured wakes when the shock-thickened suction-surface radial-flow path is established, it might be speculated that little of the boundary-layer material from this radial-flow path is shed to contribute to the measured wakes.

For comparison with the preceding results obtained on vortex blades, tests were conducted on two sets of constant-discharge-angle blades at comparable flow conditions. For one set of these blades, designated set A, the measured results (fig. 13) indicate very closely the same kind of radial-flow mechanism as for the vortex blades for both the lower and higher flow Mach numbers. Thus, the differences in the circulation distribution of the vortex blades and the constant-discharge-angle blades are not potent factors affecting the over-all secondary-flow picture. There are no indications from measurements on either of these sets of blades that outer-shroud passage vortices are ever formed. For the other set of constant-discharge-angle blades, designated set B, the measured loss distributions (fig. 14) appear quite different. At the lower flow Mach number in particular (fig. 14(a)), the measured loss pattern near the outer shroud certainly implies the existence of a passage vortex. The different kind of loss pattern here requires further consideration to establish possible reasons for the differences.

The flow Mach numbers and inlet Reynolds numbers are the same for all three sets of blades. The over-all apparatus setup is the same.

This means that the boundary-layer conditions at the inlets are the same, and measurements show that this is so (ref. 3). The main-flow turning is nearly the same for all three blades. As mentioned, the circulation variation between the two types does not appear to be a significant factor.

One particular difference noted in reference 3, however, is that at the tip section there were definite peaks in the blade suction-surface velocity profile for set B. The other vortex blades and set A had fairly smooth suction-surface velocity profiles at the tips. All three sets of blades had fairly smooth suction-surface velocity profiles at midspan and near the hub. According to boundary-layer theory, velocity peaks and subsequent decelerations on a blade suction surface lead to relatively thick and perhaps even to separated boundary layers on the blades downstream of these peaks. By comparison, smooth velocity profiles are more likely to lead to thinner blade boundary layers. Smoke flow tests on the blades in question substantiated this predicted boundary-layer behavior, albeit at low Mach numbers.

3475

Thus, it is a fair assumption that, all other things being equal, the boundary layer on the suction surface in the tip region for set B is likely to be thicker than for the other blades. On this account, reference 3 proposes that, when the cross-channel boundary-layer flow on the outer shroud encounters the relatively thicker blade boundary layer, roll-up and passage vortex formation occur. The boundary-layer material on and near the annulus outer wall becomes entrained in this passage vortex. Judging from the size of the measured tip loss region, the passage vortex formation in this manner reduces the material available for secondary-flow radial transport. For the subsonic case (fig. 14(a)), the occurrence of this phenomenon could conceivably account for all the measured loss patterns observed: that is, (1) a large tip loss region, (2) a small hub loss region as compared with both the tip region of this blade and the hub regions of the other two blades (figs. 12(a) and 13(a)), and (3) smaller measured wakes in between.

At the higher Mach number, once again the shock-thickened radial-flow path is formed, providing an additional path for boundary-layer removal to the inner-shroud region. This path is formed well up on the blade suction surface, nearer the point of passage vortex formation than is the blade trailing-edge region. This additional flow path may serve (ref. 3) to drain off some of the tip-region boundary-layer material before (or despite the fact that) it rolls up into the passage vortex. This criterion is somewhat borne out by the reduction in measured tip loss region at the higher flow Mach number and the great increase in measured hub loss region (fig. 14(b)). Again, if this criterion is correct, the radial flows through the thickened boundary-layer region on the blade suction surface appear to contribute little to the measured wake losses.

Flow in Blade End Regions with Clearance

In the blade passages of turbines and axial-flow compressors, large flow disturbances tend to occur in blade end regions. Furthermore, in passages having blade end clearance, the magnitude of the clearance has a direct influence on losses and flow behavior in the blade tip regions. In order to understand better the manner in which tip clearance influences flow behavior, flow-visualization studies were made in two-dimensional cascades provided with tip clearance and in a two-dimensional cascade modified to provide relative motion between the blades and an end wall (ref. 2). This latter case was chosen to approximate more closely conditions that exist in an actual compressor or turbine. 3475

Tip clearance. - The initial studies of blade tip-clearance regions were made in two-dimensional cascades having 0.060- and 0.014-inch tip clearances (1.7- and 0.4-percent span, respectively). These studies disclosed that flow along the blade pressure surface in the tip vicinity and in the wall boundary layer near the pressure surface deflected under the tip and formed a vortex lying against the suction surface (shown in fig. 15 for 0.060-in. clearance). Figure 16 shows that the passage vortex previously described still exists; however, it has been displaced by the tip-clearance vortex. These two vortices rotate side by side in opposite directions with little apparent mixing. Furthermore, the formation of the tip-clearance vortex appeared to influence the magnitude of the passage vortex only to the extent that some of the flow on or near the blade pressure surface, which in the case of no tip clearance would have flowed into the passage vortex region, now becomes part of the tip-clearance vortex. Consequently, the formation of the two vortices, when tip clearance exists, constitutes a much larger flow disturbance in the blade end region than would exist with no clearance.

Relative motion between blades and wall. - In order to study flow in a blade end region when relative motion exists between the blades and an end wall, one of the end walls of a two-dimensional cascade was replaced by an endless moving belt (fig. 17), the direction and speed of which could be varied at will (see ref. 2). Smoke flow-visualization tests were conducted in this modified cascade for various wall speeds.

The test disclosed two interesting phenomena. The first was that a blade surface which was "leading" relative to the wall motion exerted a scraping effect on boundary layer entrained on the moving wall. One effect of this phenomenon was to impart a rolling motion to the boundary layer as it is piled up near the pressure surface (fig. 18). Another consequence of this scraping action in a compressor is that flow along the pressure surface that would normally have deflected under the blade tip with a stationary wall is deflected away from the wall when relative motion exists. This flow deflection is shown for a stationary wall in figure 19(a) and for a wall moving at moderate speed (approximately equal to airspeed) in figure 19(b). The second result of interest

was that the motion of the wall exerted an "aspirating" effect on low-momentum air on the blade surface that was trailing relative to the wall motion and deflected this air toward the moving wall. Figure 20 depicts the significant increase in flow deflection toward the wall caused by aspiration on the suction surface.

For both the stationary and moving wall, smoke tests indicated that the flow over the blade surface at midspan showed no spanwise deflections on either the pressure or the suction surface. Therefore, if it is assumed that the midspan conditions have not changed much, the deflection off the pressure surface near the tip (fig. 19(a)) indicates the static pressure to be lower there than at midspan. Smoke tests on the blade suction surface showing a deflection of the blade tip surface flows toward midspan indicate an increased static pressure at the blade suction-surface tip region as compared with midspan. Thus, tip-clearance effects can result in a smaller pressure differential across the blade tip section than at the midspan section - in effect, reduced blade tip loading. The scraping and aspirating effects of relative motion (figs. 19(b) and 20(b)), which show that these tip streamline deflections can be prevented or reversed, indicate that the relative-motion secondary-flow effects may even benefit a compressor by increasing the blade tip loading.

Rotor-Stator Interaction Effects

The interference effects of a rotating blade row upon a stationary row upstream are shown by high-speed flash in figure 21. (While the blade rows depicted are more typical of a turbine configuration, the effects should be qualitatively the same for compressor blade rows.) Figure 21(a) shows that the pressure field associated with the rotor blading at certain rotor positions causes thickening of the boundary layer on the suction surface and along the trailing edge of the upstream blades, and increased radial flow results. At the second rotor position (fig. 21(b)), this thickening does not occur. Further tests indicate that these effects depend on the blade stagger angles, pressure distribution, rotor speed, and mainstream Mach number. The motion-picture supplement to reference 6 shows these effects very clearly, as well as blade boundary-layer development and shedding in annular-cascade configurations, radial boundary-layer flows, secondary-flow double-boundary-layer roll-up, and others.

A Model of Secondary Flow in Compressor Blade Rows

On the basis of the experimental results presented herein, it is possible to construct a model of secondary flow in compressor blade rows. However, two important factors are not accounted for in the experimental tests: (1) the effect of centrifugal forces on flow in a

rotor, and (2) the effect of upstream stages on flow in either stators or rotors. Therefore, before such a secondary-flow model can be assumed realistic, further knowledge of these factors is required.

Insight into the influence of both of these factors can be obtained from tests conducted on a multistage compressor (ref. 7). The results presented give indications of outward radial flow of boundary-layer material in rotor blade passages and subsequent accumulation of this material in the blade tip region. In stators, inward radial flow is indicated. As boundary-layer air flows through the various stages, the comparatively large secondary-flow displacements produce a mixing of this boundary-layer air with the main stream. This mixing action prevents continuous boundary-layer buildup on flow surfaces and tends to make the mainstream velocity more uniform. It also makes possible more direct application of the secondary-flow studies in cascades to flow analyses of multistage compressors. If continuous boundary-layer growth took place on compressor annulus walls, a situation would occur in which flow conditions would be significantly different from those occurring in the cascade studies. Theories of compressor flow behavior based on cascade studies would then be of doubtful validity even in a qualitative sense.

The above-mentioned factors, along with the experimental results previously presented, are used to predict the probable secondary-flow patterns in the various types of blade rows of axial-flow compressors.

Flow in shrouded stators. - Pressure gradients in inlet guide vanes or in a shrouded stator transport wall boundary layers toward the suction-surface side of blade passages and transport blade surface boundary layer and boundary layer that accumulates near blade tips radially inward. Radial transport of boundary layer takes place in regions where viscous shear forces are low; for example, in blade wakes. The paths by which the secondary-flow mechanism transports boundary layer are indicated in figure 22.

Boundary layer that accumulates near a blade suction surface at the hub generally rolls up into a pair of flow vortices rotating side by side in opposite directions. In physical extent, this vortex pair is dominated by the passage vortex. On the outer annulus walls, vortices may or may not form. As indicated by these experiments, a vortex is likely to form if the boundary layer on the suction surface is either separated or relatively thick - a condition associated with "poor" suction-surface velocity profiles. If suction-surface boundary layers are thin and unseparated, cross-channel boundary layers tend to flow radially inward in the wake region rather than to roll up at the blade tip.

Because of the pressure rise through a given stage, there may be flow leakage around a shroud ring causing local disturbances at the inlet to a stage. This would tend to qualify to some degree the secondary-flow model presented.

Flow in unshrouded stators. - In unshrouded stator passages, two secondary-flow components exist in addition to those noted previously: (1) tip-clearance flow through the gap between the blade ends and the hub, and (2) flow caused by the relative motion between the blades and the rotating hub. The effect of this relative motion appears to be aspiration of boundary-layer material from the blade suction surface with attendant transport of this boundary-layer air in the direction of the rotating hub. As these two flow components oppose the motion of cross-channel secondary-flow components, the resultant flow pattern is a function of the respective magnitudes of the various components. As such, the resultant flow depends upon such factors as the size of the blade end-clearance space, blade end loading, magnitude of cross-channel pressure gradient, boundary-layer accumulation on blade surfaces, and speed of the rotor relative to the blades. Because of the motion of the hub, accumulations of boundary-layer material that would occur near a blade suction surface for a stationary hub will now occur nearer the pressure-surface side of a passage. As indicated in the tests of the two-dimensional cascade with a moving wall, boundary-layer material may be swept completely across a blade passage and roll up against the pressure-surface side.

Flow in rotors. - Experimental information concerning secondary flow in rotors indicates that radially outward flow of boundary-layer material will probably take place because of the predominance of centrifugal-force effects over radial pressure gradients. At present, details of flow behavior in the blade tip region must be inferred from knowledge of secondary flows in other types of configurations. On this basis, it is highly probable that flow behavior in the tip regions should not differ markedly from the behavior predicted in the hub region of unshrouded stators.

THEORETICAL INVESTIGATION OF SECONDARY FLOWS

The limitations inherent in the types of experimental analysis of secondary flows considered leave several important problems to be investigated. One of these problems is quantitative prediction of variations in thermodynamic properties of the fluid that result from the development of secondary flows. Another problem is the establishment of the physical basis or underlying causes for certain observed phenomena (e.g., vortex roll-up near a blade suction surface). Problems of this nature are perhaps best attacked by means of theoretical investigations.

To date, theoretical research on secondary flows has been limited because of mathematical complexities. However, certain special aspects of secondary-flow behavior have been treated analytically by use of simplified theories. A fair amount of progress, for example, has been made on the calculation of boundary-layer crossflows and on the calculation of vorticity components associated with secondary flows in two-dimensional cascades and channels. While much of the work has been restricted in scope, important groundwork has been provided for more extended investigations.

In the following sections a review of representative analyses from the body of current theoretical research is presented and discussed. It is the purpose of this review to provide insight into methods of analytically attacking secondary-flow problems, to illustrate the nature of the mathematical theory involved, to indicate application of solutions to specific problems, and to point out possible bases for further research.

As will be noted, the analyses discussed are categorized on the basis of assumptions made in current secondary-flow theory regarding the nature of the fluid analyzed. The two major categories are (1) nonviscous-flow analysis and (2) boundary-layer-flow analysis. The analyses are discussed in this way because particular analyses in one of these categories are necessarily restricted to the consideration of specific types of physical flow phenomena. As a consequence, only certain special aspects of secondary flows observed experimentally can be treated within the framework of the theory. A division of the discussion into "analysis types" is therefore equivalent, in a sense, to a division into specific types of problems having certain common characteristics.

Discussion of Methods

With only minor exceptions, the theoretical research on secondary flows has been concerned with steady, incompressible flows. Such flows are described in their most general form by the Navier-Stokes equations along with the equation of continuity. This system of four equations in rectangular coordinates is as follows:

$$u\frac{\partial u}{\partial x} + v\frac{\partial u}{\partial y} + w\frac{\partial u}{\partial z} = -\frac{1}{\rho}\frac{\partial p}{\partial x} + \nu\left(\frac{\partial^2 u}{\partial x^2} + \frac{\partial^2 u}{\partial y^2} + \frac{\partial^2 u}{\partial z^2}\right) \tag{1a}$$

$$u\frac{\partial v}{\partial x} + v\frac{\partial v}{\partial y} + w\frac{\partial v}{\partial z} = -\frac{1}{\rho}\frac{\partial p}{\partial y} + \nu\left(\frac{\partial^2 v}{\partial x^2} + \frac{\partial^2 v}{\partial y^2} + \frac{\partial^2 v}{\partial z^2}\right) \tag{1b}$$

$$u\frac{\partial w}{\partial x} + v\frac{\partial w}{\partial y} + w\frac{\partial w}{\partial z} = -\frac{1}{\rho}\frac{\partial p}{\partial z} + \nu\left(\frac{\partial^2 w}{\partial x^2} + \frac{\partial^2 w}{\partial y^2} + \frac{\partial^2 w}{\partial z^2}\right) \tag{1c}$$

$$\frac{\partial u}{\partial x} + \frac{\partial v}{\partial y} + \frac{\partial w}{\partial z} = 0 \tag{2}$$

where u, v, and w are components in the x, y, and z directions, ρ is the density, p the static pressure, and ν the kinematic viscosity.

Solutions to the complete set of equations are almost impossible to obtain for boundary conditions of the type usually occurring in aerodynamic problems. In general, it is necessary to make such simplifying assumptions concerning the nature of the flow problems that the corresponding simplifications in the equations make them mathematically tractable. Two typical simplifying assumptions occurring in secondary-flow research are now considered.

3475

One of the ways to simplify the Navier-Stokes equations greatly is to assume a nonviscous flow, that is, $\nu = 0$. Although secondary flows are almost always a result of viscous action in a fluid, the assumption of nonviscous fluid flow is considered reasonable in certain instances. One of the most common is the case where the flow paths under consideration are not large in extent (e.g., flow in cascade passage) and where viscous shear forces are not likely to be high. The flow crossing the boundary of this region is considered to have a velocity gradient, and hence vorticity, by virtue of viscous action upstream of the boundary. Within the region, however, the basic assumption is that the effects of viscosity over the short flow path are negligible compared with effects of the vorticity associated with the flow.

CH-23 back

It should be noted at this point that, with the assumption $\nu = 0$, the flow equations are reduced to first-order equations and it is no longer possible to satisfy the two boundary conditions for a real flow; that is, that the normal and tangential components of the flow at a surface be zero. The single boundary condition specified is that the flow normal to the surface is zero and hence the condition of "no-slip" at the surface is not assured. In actual application of nonviscous-flow analyses, this defect is generally of secondary importance.

In flow problems where viscous shear forces near bounding surfaces are likely to be high, it is desirable to retain the friction terms ($\nu \neq 0$) in the Navier-Stokes equations. One of the ways in which this is done, while still simplifying the general form of the equations, is by use of boundary-layer theory. The principal physical assumption made here is that the effects of viscosity are predominant only in a very thin region (the boundary layer) in the neighborhood of the fluid boundaries, while the rest of the flow is regarded as frictionless. Furthermore, the pressures associated with the frictionless region of the flow are assumed known and are superimposed on the boundary-layer flow. Mathematically, the governing equations for the boundary layer can be obtained in several ways, with the various derivations stressing either intuitive physical considerations or rigorous mathematical theory. (See ref. 8 ch. 4 for the physical approach and ref. 9 ch. 18 for the mathematical approach.) To illustrate the simplifications in the

Navier-Stokes equations that result from boundary-layer hypotheses, the boundary-layer equations for flow on a nonrotating, flat (or slightly curved) surface are given:

$$u \frac{\partial u}{\partial x} + v \frac{\partial u}{\partial y} + w \frac{\partial u}{\partial z} = \nu \frac{\partial^2 u}{\partial y^2} + U \frac{\partial U}{\partial x} + V \frac{\partial U}{\partial y} + W \frac{\partial U}{\partial z} \tag{3a}$$

$$u \frac{\partial w}{\partial x} + v \frac{\partial w}{\partial y} + w \frac{\partial w}{\partial z} = \nu \frac{\partial^2 w}{\partial y^2} + U \frac{\partial W}{\partial x} + V \frac{\partial W}{\partial y} + W \frac{\partial W}{\partial z} \tag{3b}$$

3475

where x, y, and z are rectangular coordinates with x and z parallel to the bounding surface and y normal to the surface; u, v, and w are boundary-layer velocity components in the x, y, and z directions, respectively; and U, V, and W are the velocity components of the nonviscous region of the flow in the x, y, and z directions, respectively. These velocity components of the nonviscous region are assumed known. The third equation necessary for solution (the continuity equation) has the same form as equation (2).

Although equations (3a) and (3b) indicate that the Navier-Stokes equations have been greatly simplified, solutions for the system of equations (2) and (3) are difficult to obtain for even relatively simple three-dimensional configurations. In fact, almost all existing analyses require the application of numerical methods to obtain solutions.

The boundary-layer approach to secondary-flow behavior should be satisfactory for flow problems where frictional effects or energy gradients are confined to the neighborhood of the fluid boundaries and flow separation does not exist.

It might be noted that a few investigations of secondary flows have dealt directly with the Navier-Stokes equations without assuming any special properties for the flow. This approach is practical only if the aerodynamic configuration is simple in form. At the present time, analyses of completely viscous flow that might have had significance for secondary-flow research in turbomachines have been confined to the study of flows in pipes and channels (refs. 10 to 13). Unfortunately, the solutions presented in these references have been achieved only for very low Reynolds numbers and for the case of fully developed flow; that is, flow in which the effects of the centrifugal forces acting on the energy particles and the effects of viscous dissipation in the fluid are in balance. In turbomachine blade rows, this condition of equilibrium is generally not achieved; and, hence, the secondary flow is a function of the turning. Although theoretical studies of viscous flows of this type are of great interest in their own right, further discussion of these studies will not be undertaken in the present chapter.

Nonviscous-Secondary-Flow Theory

The study of secondary flows through application of incompressible nonviscous-flow theory has been principally restricted to investigations of flows in pipes or rectangular channels such as formed by airfoils in cascades. The fairly large number of reports dealing with this topic make a complete review of the theoretical literature prohibitive. Consequently, the review is restricted to four reports (refs. 14 to 17) which are closely associated with flow through cascades and which incorporate basic notions common to most nonviscous-flow analyses.

3475

Flows in channels and two-dimensional cascades. - Two reports (refs. 14 and 15) have become classical references in nonviscous-secondary-flow research. Both papers consider, in general, secondary flow in a guiding passage (pipe, channel, blade row, etc.) which results from a nonuniform total-pressure distribution upstream of the passage inlet. Mathematically, the analyses are based upon three governing equations for flow of a steady, incompressible, inviscid fluid. These equations are

$$\text{curl}\ (V \times \Omega) = 0, \text{ the equation of motion} \tag{4}$$

$$\text{div}\ \Omega = 0, \text{ the conservation of vorticity} \tag{5}$$

$$\text{div}\ V = 0, \text{ the continuity equation} \tag{6}$$

where V and Ω are, respectively, the velocity and vorticity vectors of the flow.

From equations (4) to (6), reference 14 derives an expression for the vorticity component in the through-flow direction downstream of a two-dimensional cascade. Knowing the magnitude of this vorticity component, it is then possible to obtain an approximation to the secondary-flow velocities. This derivation is based upon a perturbation analysis that considers the two-dimensional potential flow through the cascade as a first approximation to the actual flow. Consequently, the applicability of the analysis is restricted to a class of flows for which the perturbation assumptions are reasonable.

The expression for the vorticity component in the through-flow direction was actually evaluated for flow in a circular-arc channel in which the basic flow was given as that of a free vortex. Before the calculations were completed, however, a further assumption was made which is physically equivalent to assuming that the channel is very narrow. This leads to the following expression for the vorticity component:

$$\xi_1 = -2\varepsilon \frac{\partial U}{\partial z}$$

where

ξ_1 magnitude of vorticity component in through-flow direction at cascade exit ($\xi = 0$ at inlet)

ε total turning of channel

U inlet flow velocity

z distance measured normal to base of channel

3475

From the expression for ξ_1, the secondary-flow velocity components were obtained and a plot of secondary-flow streamlines calculated (ref. 14). These theoretical results were compared with experimental data taken in a circular-arc turning section. The flow in the experimental tests had an induced inlet velocity variation of the type required in the analysis; that is, small velocity gradient. For the velocity profile shown in figure 23, agreement between theory and experiment was fairly good.

Reference 15 differs from reference 14 in that the former analysis begins with equations (4) to (6) and develops a general expression for the change in "secondary circulation" along a streamline in a perfect, incompressible fluid. The secondary circulation is proportional to ξ/q where ξ is the component of vorticity in the direction of fluid flow and q is the magnitude of the flow velocity vector.

The expression for the change in secondary circulation along a streamline is obtained from equations (4) to (6) by applying certain well-known results from vector analysis and differential geometry. The final form of the expression is given by

$$\left(\frac{\xi}{q}\right)_2 - \left(\frac{\xi}{q}\right)_1 = -2\int_{s_1}^{s_2}\left|\operatorname{grad}\left(\frac{p_0}{\rho}\right)\right| \frac{\sin\varphi}{R}\,\frac{ds}{q^2} \tag{7}$$

where

s streamline arc length

p_0 total pressure

ρ density

φ angle between direction of principal normal to streamline and normal to Bernoulli surface (surface of constant total pressure) on which streamline lies

R radius of curvature of streamline

and the subscripts 1 and 2 indicate arbitrary points on the streamline. It follows at once that, if $\varphi = 0$ $(R \neq 0)$, then $(\xi/q)_2 = (\xi/q)_1$; that is, there is no change in secondary circulation along the streamline. Furthermore, from differential-geometric considerations, $1/R_g = \sin \varphi/R$ where $1/R_g$ is the geodesic curvature of the streamline on the Bernoulli surface. Therefore, $\varphi = 0$ $(R \neq 0)$ implies that $1/R_g = 0$. Reference 15 summarizes these results by stating, "Hence streamlines along which the secondary circulation remains unchanged are geodesics on the Bernoulli surface."

3475

It is pointed out that the simplest examples to which the general theory may be applied are those in which the initial flow has a uniform static pressure and a velocity varying in one direction only. Such flows may exist in the boundary layer of a large straight duct or in an open channel whose width is large compared with its depth.

From a physical standpoint, when a stream enters a bend whose plane is parallel to the Bernoulli surfaces, a secondary circulation is created and the ensuing secondary flow will eventually distort the Bernoulli surfaces so that all semblance to the original velocity and total-pressure distribution may be lost. However, if the distortion of the Bernoulli surfaces is assumed small, $|\text{grad}\ (p_0/\rho)|$ and φ in equation (7) can be considered constant and a first-order solution obtained for the secondary circulation. As an illustration, the method (with these assumptions) is applied to the problem posed in reference 14. The resulting equation for change in the vorticity component in the through-flow direction is identical to that obtained in reference 14.

Even though nonviscous-flow analyses represent a simplified approach to secondary-flow problems, solutions of the governing equations still are difficult to obtain. A question always exists as to the meaningfulness of results obtained by introducing further simplifying assumptions in the flow model to obtain solutions. A partial answer to this question is found in reference 16, which considers secondary flow in a 90° bend of rectangular cross section. The secondary flow is first calculated by means of a perturbation analysis and then compared with a "simplified solution." Theoretical results are finally compared with experimental data.

In carrying out the perturbation analysis, the stagnation pressure is assumed to vary in a direction perpendicular to the plane of the bend, and the secondary-flow velocities are assumed small compared with the main-flow velocities. The basic flow is defined, as in reference 14, to be the flow in a free vortex. The perturbation velocities are then shown to be determinable from the solution of a Poisson equation. This solution is expressed as an infinite series involving Bessel functions. The series, however, converges slowly, and a great deal of calculation is required to obtain answers of reasonable accuracy.

The simplified analysis presented incorporates further assumptions than those made in the perturbation analysis, and the problem is finally made comparable to the one considered in reference 14. A particular solution to the problem is then calculated by assuming a linear variation in stagnation pressure at the entrance of a bend having the geometry of the author's test apparatus. The velocities obtained by the simplified method are compared with the more exact perturbation solution mentioned earlier, and the agreement is found to be good for this particular case.

The theoretical results are then compared with experimental results in a 90° bend (ref. 16). For a turning angle in the bend comparable to that found in compressor cascades, a comparison of the theoretical and experimental radial velocities falls within the limits of experimental accuracy. Therefore, for the types of nonviscous-flow analysis under consideration, the extra labor involved in improving the solutions to secondary flow in a channel by the more exact calculations would appear to be unwarranted as long as the secondary-flow velocities are assumed small.

A few attempts have been made to develop methods which are extensions of the type of analysis initiated in references 14 and 15 and which potentially are capable of yielding more exact solutions to secondary-flow problems. One such method is outlined in reference 17. In this report the secondary flow in channels and cascades of airfoils is considered calculable by a successive-approximation technique. The flow is assumed to become asymptotically parallel and nonuniform at upstream infinity. A velocity field is postulated for the region to be investigated which has zero normal velocities on the flow boundaries and which assumes the given asymptotic values at upstream infinity. This velocity field is chosen to satisfy the continuity equation though not necessarily the momentum equations. From the prescribed velocities, a vortex field is calculated by means of the Cauchy vorticity equations. The vortex field is then integrated to give a new velocity field, and the process is repeated until discrepancies between successively calculated velocity fields are small.

Reference 17 points out, however, that the computational labor involved in the approximation scheme makes more than one step unlikely. A realistic choice of the initial velocity field is required, and usually enough is known about the desired solution to make this possible.

Evaluation and conclusions. - The various analyses discussed outline approximate methods for predicting secondary flows in channels and two-dimensional cascades. The principal restriction applying to these analyses is that they assume a variation in inlet velocity that extends well into the flow passage (see fig. 23). In most two-dimensional-cascade investigations, the variation is likely to be confined to a thin

boundary layer. Tests in such cascades indicate a pronounced cross-channel flow and a concentration of vorticity near the suction-surface side of the passage. As would be expected, none of the examples worked out by nonviscous-flow methods predict such a phenomenon. There are indications, however, that this type of approach may be a first step in treating secondary flow in the final stages of a compressor where variations in velocity are of the type required and viscous effects on the primary flow pattern are of secondary importance. A complete analysis, of course, would have to include the effects of tip clearance and radial pressure gradients. It might also be possible to combine nonviscous-flow theory and boundary-layer theory in a manner that would allow for calculation of secondary flows in the inlet stages of a compressor.

3475

Reference 15 is of particular interest, in that the equations derived are general in form. However, it should be noted that the formula for secondary circulation

$$\left(\frac{\xi}{q}\right)_2 - \left(\frac{\xi}{q}\right)_1 = -2\int_{s_1}^{s_2}\left|\operatorname{grad}\left(\frac{p_0}{\rho}\right)\right| \frac{\sin\varphi}{R}\,\frac{ds}{q^2} \tag{7}$$

CH-24

is not an explicit relation for the change in secondary circulation. This follows from the fact that the velocity q is affected by ξ, and hence the integrand is in turn a function of ξ. Consequently, equation (7) is actually an integral equation for the secondary circulation or the vorticity component ξ. The cases where the formula for a change in secondary circulation can be readily simplified are those in which it is assumed that the Bernoulli surfaces remain flat. The formula then becomes

$$\left(\frac{\xi}{q}\right)_2 - \left(\frac{\xi}{q}\right)_1 = -2\left|\operatorname{grad}\frac{p_0}{\rho}\right|\int_{s_1}^{s_2}\frac{ds}{q^2 R}$$

Experimental studies have shown, however, that this assumption (without further modifications) will be invalid for many problems of practical interest (see experimental section of the present chapter). This fact is recognized by the author of reference 15 in a discussion of flow in bent circular pipes. In this case, simplification was achieved by considering only the path of a particle of maximum total pressure near the outside wall of the pipe and assuming that the velocity and $|\operatorname{grad}(p_0/\rho)|$ remain constant on a streamline.

References 16 and 17 emphasize the mathematical difficulties involved when more exact methods are used in calculating secondary flows by use of nonviscous-flow theory. However, the reports also indicate that the simplified solutions give fairly adequate results for the type of problem under consideration.

Three-Dimensional Boundary-Layer Flows

One of the early theoretical papers on three-dimensional boundary layers is reference 18, which points out two effects in three-dimensional boundary-layer flows that are not present in the two-dimensional case. The first effect is the result of lateral expansion or convergence of streamlines in the "potential flow region" that are parallel to the bounding wall. This convergence causes changes in boundary-layer thickness and profile shape. The second effect is the displacement of the boundary layer toward the concave side of the potential stream as a result of lateral curvature of that stream. This results in boundary-layer crossflows such as shown in figure 2. As indicated in reference 18, theoretical calculation of such flows entails difficulties not present in two-dimensional boundary-layer studies.

3475

The theoretical investigation of secondary flows in blade passages through application of boundary-layer theory has, in the past, been restricted in scope. Almost all analyses bearing on compressor secondary-flow problems have been confined to the study of boundary-layer crossflows of the type noted in the experimental section. Because of the assumptions generally made in classical boundary-layer theory, investigation of such phenomena as vortex roll-up and tip-clearance flows is, of necessity, severely limited.

In the following sections, reports dealing with basic boundary-layer theory and the application of this theory to secondary-flow problems are discussed. Although reports that employ momentum-integral concepts play an important part in the study of boundary layers in turbomachines, this class of reports is excluded from the discussion. This restriction is made because momentum-integral methods require a priori assumptions concerning the character of the velocity profiles in the boundary layer, and at present some important questions remain as to how to make these assumptions realistically for three-dimensional flows (ref. 19). Consequently, reports that evolve basic concepts and determine fundamental flow characteristics are considered principally.

All the reports that give solutions to specific secondary-flow problems assume that the boundary layer under investigation is laminar, as a result of general inability to apply current mathematical techniques to the vastly more complicated problems of turbulent viscous-flow phenomena. However, as boundary layers in turbomachines are not likely to be laminar but rather turbulent, the question may arise as to the significance of laminar-flow studies in relation to turbomachines. In this regard, past experience indicates that the factors having an important influence on laminar-boundary-layer flow behavior are qualitatively the same for turbulent flow.

3475

CH-24 back

Investigations of three-dimensional boundary-layer equations. - Because of the complexity of the boundary-layer equations, it has been profitable to examine the nature of the equations without actually carrying out solutions of specific problems. Several reports, for example, give derivations of the boundary-layer equations in various curvilinear coordinate systems followed by detailed examination of the equations in these systems to determine their important characteristics. Some of the basic reports of this type that can be considered ultimately applicable to secondary-flow analysis in turbomachines are summarized briefly.

The equations in reference 20 are derived for incompressible boundary-layer flow in a general orthogonal curvilinear coordinate system, and the influence of curvature of the main flow on boundary-layer behavior is discussed. Compressible boundary-layer equations in orthogonal curvilinear coordinates are developed in reference 21, along with the energy equation. The results of reference 21 are, therefore, more widely applicable than those of reference 20. Following the general development, the boundary-layer equations are derived for various special cases and the nature of the equations is discussed. The special cases include flow over a body of revolution, cylindrical flow, and conical flow. For treatment of more general cases, the equations are derived for an orthogonal coordinate system determined by the external flow streamlines, the orthogonal trajectories of those streamlines, and a line mutually perpendicular to the streamlines and their trajectories.

In the discussion of the boundary-layer equations in the system designated, reference 21 shows that, in the absence of a lateral body force, external stream curvature is needed to produce crossflow. Therefore, if the curvature is small and the flow unseparated, the crossflow velocity will probably be small. This then suggests that it might be possible to simplify the boundary equations by considering a "small-crossflow" approximation. In such an approximation, the terms of higher order than unity in the crossflow velocity or lateral derivatives would be neglected. This approximation is carried out, and it is shown that the equations for the flow velocity in the streamline direction (the "principal velocity") can be put into the precise form of the two-dimensional boundary-layer equations and independently solved. Once such a solution has been achieved, it is possible to solve for the crossflow component. Solving for this component, however, is difficult, and it is suggested that the boundary layer be considered as divided into two parts. One part would consist of the outer region of the boundary layer where viscous forces are not large. By setting the viscous terms in the governing equation equal to zero, a "stripwise" solution for this region can be obtained along a given external streamline. The other part of the boundary layer, termed the "boundary sub-layer" would consist of the region adjacent to the surface where viscous forces are large. By assuming that the principal velocity component is linear in

this region, an approximate solution for the crossflow component can be obtained that is valid in the region close to the wall. This sub-layer solution can then be joined to the solution obtained for the upper region of the boundary layer to give a result valid for the entire boundary layer.

The equations for steady, compressible three-dimensional boundary-layer flow in Cartesian coordinates and in an "implicit" orthogonal coordinate system applicable to flow over bodies of revolution and conical bodies are derived in reference 22. A discussion of the energy equation, along with a simplification of the energy equation for a Prandtl number of 1, is then presented. By introducing a vector potential, the number of dependent variables in the boundary-layer equation can be reduced by one. This is accomplished by properly defining the boundary-layer velocity components in terms of the components of the vector potential. The boundary-layer equations and the energy equation are then transformed to a system of equations including the components of the vector potential as dependent variables. In incompressible flows, these components are the only two dependent variables.

3475

Various applications of the equations to specific types of problems are also discussed in reference 22. Among the conclusions reached are the following: (1) For flow with plane or axially symmetric boundary conditions, the three-dimensional equations reduce to two-dimensional form by Mangler's transformation; and (2) in cases of flow over flat plates at zero angle of attack, when the leading edge is some arbitrary curve, the flow viewed in planes parallel to the stream and perpendicular to the plate is given by the plane Blasius solution.

The effect of angular rotation of the coordinate system on the boundary-layer equations is considered in references 23 and 24. The boundary-layer equations are obtained in reference 23 for a Cartesian coordinate system rotating with a constant angular velocity about a fixed axis in space. In this report the additional forces caused by rotation of the system and the influence of blade rows in a turbomachine on the boundary layer are qualitatively discussed. In reference 24 the boundary-layer equations are derived for an orthogonal coordinate system rotating with a constant angular velocity. Both the laminar and the turbulent forms are given. These equations are then used to develop generalized momentum-integral equations.

Boundary-layer crossflow over flat plate with leading edge. - Initial research on boundary-layer crossflow on flat or slightly curved surfaces was principally concerned with calculations of two special types of boundary-layer flow over an infinite flat plate. The first was the result of rotating the plate about an axis normal to its surface in a uniform stream (ref. 25). The second was the result of imposing a

flow having circular streamline (e.g., a free-vortex type flow) on the plate surface (ref. 26). In neither of these cases, however, is there any variation of boundary-layer properties with mainstream turning, nor is there any concept that allows boundary-layer development in the direction of the mainstream flow relative to the plate. The results obtained, therefore, do not directly apply to the type of crossflow observed in two-dimensional cascades and channels (fig. 2). As a first approximation to the latter type of secondary flow, several investigators have calculated boundary-layer crossflows over flat plates having a leading edge. In this type of problem, both the variation of the boundary layer with mainstream turning and the development of the boundary layer in the mainstream direction can be studied.

3475

One of the early papers dealing with this problem is reference 27. This analysis considers laminar-boundary-layer development over a semi-infinite flat plate placed in a flow with concentric circular streamlines. Both incompressible flow and a compressible flow with Prandtl number of 1 are investigated. The method of solution for the incompressible case is similar to that employed in two-dimensional boundary-layer theory. The boundary-layer equations are first expressed in a curvilinear system of the type outlined in reference 24. A "similarity parameter" η is then defined; and, with suitable definitions for the boundary-layer velocity components in terms of unknown functions $F(\eta)$ and $G(\eta)$, the boundary-layer equations are simplified to two simultaneous total differential equations for F and G. However, certain terms in these equations have as a coefficient the square of the total turning of the main flow from the plate leading edge. The analysis is then restricted to apply to the region of the flow where the total turning is small, and all terms containing the square of the total turning are discarded. This approximation simplifies greatly the equations for the unknown functions F and G, and solutions are obtained for the special case of a mainstream flow of the free-vortex type. The results show that the velocity component u in the direction of the main flow and the component w normal to the main flow direction and parallel to the plate surface can be expressed by

$$u = U_1 F'(\eta)$$

and

$$w = \theta U_1 G'(\eta)$$

where U_1 is the mainstream velocity and θ is the total turning of the flow.

Typical velocity profiles are shown in figure 24. The analysis of reference 27 also discloses that there is a limiting deflection of the

boundary layer at the plate surface, which for the particular case discussed is a function of the total mainstream turning. Limiting deflection has also been noted in visualization studies of crossflows.

Further progress in the investigation of crossflow phenomena is made in references 28 and 29. Both analyses treat a flow over a flat plate which is of a type that makes possible the exact solution of the boundary-layer equations. Their solutions, therefore, are not subject to the restrictions inherent in reference 27 because of the assumption of small mainstream turning made in that reference. The special two-dimensional mainstream flow considered in references 28 and 29 is defined by 3475

$$U = \text{constant}$$

$$W = a + bx$$

where

U mainstream component normal to plate leading edge

W mainstream component parallel to leading edge

a,b constants

x distance from leading edge measured along plate surface

This rotational flow has streamlines that are parabolic in form. Furthermore, the entire streamline pattern can be obtained by simply translating a given streamline in a direction parallel to the plane leading edge (fig. 25).

The solutions of the boundary-layer equations in this problem are obtained in the usual way of defining a similarity variable and reducing the boundary-layer equations to ordinary differential equations. In both reference 25 and reference 29, solutions are obtained for the case where the mainstream flow has 0° inclination to a line perpendicular to the plate leading edge. Reference 28 also considers two other cases where the inclinations are 60° and -60°. The streamline patterns for these flows are obtained by merely shifting the parabolas in figure 25 to the left or to the right.

In the three cases discussed in reference 28, regions exist in the flow field for which the total pressure in the boundary layer exceeds that in the mainstream. The reason that particles in the boundary layer can have a larger total pressure than those in the mainstream follows the postulation of a total-pressure gradient for the main flow parallel to the leading edge of the plate. Consequently, boundary-layer

streamlines (which curve more sharply than those in the main stream, fig. 25) may transport particles of high total pressure underneath main-flow streamlines of lower total pressure.

Reference 28 also discusses the problem of "three-dimensional separation" (i.e., separation of the actual flow profile as distinguished from separation of a single velocity-component profile that may not indicate separation of the total flow). The reference shows that such three-dimensional separation does not occur, because the crossflow prevents separation (in the example presented) by transporting fluid with high energy to the "critical" regions.

3475

In addition to the research mentioned, there is one other publication known to the authors that includes detailed treatment of crossflow over flat plates, namely, reference 19. In this report a group of problems for which the mainstream flow has small curvature in the lateral direction are analyzed. The velocity components of the mainstream are characterized by

$$U = U_0 + U^*(x,z)$$

$$W = W^*(x,z)$$

where U is the velocity component in the direction normal to the leading edge of the plate (the x-direction), and W is the velocity component parallel to the leading edge of the plate (the z-direction, fig. 26). It is also assumed that

$$U_0 = \text{constant}$$

$$W^* << U_0$$

$$U^* << U_0$$

By a perturbation method, the velocity profiles of the crossflow in the x- and z-directions are calculated for a variety of incompressible mainstream flows for which U^* and W^* are expressible as

$$U^* = bx^m z^i$$

and

$$W^* = ax^n z^k$$

In this analysis, the boundary-layer velocities u, w, and v in the x, z, and y directions, respectively, are then considered to be of the form

$$u = u_0 + u^*$$

$$w = w^*$$

$$v = v_0 + v^*$$

where u_0 and v_0 are the boundary-layer velocity components in the well-known Blasius solution for a uniform flow of velocity U_0 over a flat plate. The quantities u^*, w^*, and v^* are the perturbation velocities on this basic boundary-layer flow. 3475

It can be seen that one of the flows considered in references 28 and 29 is a special case of the family of flows investigated here; for example, $U^* = 0$, $W^* = ax$. This special case is worked out with the use of the perturbation analysis; and, in this instance, the perturbation analysis is equivalent to the type of analysis employed in references 28 and 29.

By considering a range of values of the exponents m, i, n, and k, the effect of various flow patterns on velocity profiles and boundary-layer displacement thickness is investigated at some length. As in references 28 and 29, certain rotational flows give rise to boundary-layer velocites that exceed mainstream values. The effects of angular rotation of the coordinate system and compressibility on crossflow velocities are briefly analyzed. The results of the analysis of angular rotation are applied to flow on surfaces of compressor blades. It is concluded that, if the main flow deflects toward the blade tip near the suction-surface side and toward the hub near the pressure-surface side, then the effect of angular rotation is to increase the crossflow on the suction surface and decrease the crossflow on the pressure surface.

The effect of compressibility is discussed for the flow defined by $W^* = ax$ and $U^* = bx$. The conclusion reached is that compressibility has the over-all effect of increasing the boundary-layer perturbation velocities.

Flow over flat plate with thick boundary layer. - In the previous discussion of boundary-layer flow over a flat plate, the boundary layer developed from a definite leading edge and was immediately subjected to lateral pressure gradients that gave rise to secondary flows. For flow in turbomachine configurations, this is usually not the case. Generally, the boundary layer develops for a distance in the absence of lateral pressure gradients before secondary flows develop. This is true, for example, in flow through the inlet of a channel or cascade or along the casing of a compressor between blade rows. Reference 30 attempts to gain some insight into the effect of this boundary-layer growth on secondary-flow behavior. The problem analyzed is that of a thick

boundary-layer flow over a flat plate where the boundary layer is subjected to a sudden lateral perturbation caused either by a pressure gradient or a sudden movement of a part of the plate surface over which the flow develops.

The analysis presented is a small-crossflow perturbation analysis of the type employed in reference 19. In obtaining solutions for boundary-layer velocities, an approximate but rapid method of solution is employed. This method is based on the assumption that the flow can be considered to be composed of a nonviscous outer region and a viscous inner region adjacent to the wall. In view of this assumption, separate solutions are obtained for these two regions. These solutions are then joined at a distance from the wall that is determined from the analysis.

As most of the report is devoted to the development of methods, only two simple applications are given. In the first, a boundary layer flowing two-dimensionally from the leading edge of a plate encounters at some fixed distance from the edge a surface moving laterally with a constant velocity. At a given distance from the edge of the moving surface, the crossflow velocity is a function of the Blasius similarity variable η. Near the leading edge of the moving plate, these functions have a steep slope, which indicates rapid rise of velocity from the plate surface to the main stream. Farther downstream, they approach the well-known Blasius solution for flow over a flat plate with zero pressure gradient.

The second example given is the case of a thick boundary layer which, at a given reference line parallel to the leading edge, encounters a pressure field arising from a "parabolic" mainstream flow; for example, a flow having a lateral velocity component that varies as the nth power of the distance from the fixed reference line. Solutions are carried out for various values of these powers and for various distances from the reference line. Near the point where the pressure perturbation is first felt, the solutions indicate that the thick boundary layer develops greater crossflow velocities than in the case where the boundary develops from the leading edge. It is possible in this analysis to compare the solutions obtained for flow at a great distance from the reference line with the more exact solutions worked out in reference 19, for here the two theoretically must agree. Progressively better agreement results from taking larger values of the powers defining the mainstream lateral velocity.

Boundary-layer flow in corners. - One of the important problems mentioned earlier was that of analyzing secondary flows in the corner formed by the side of a channel or blade row and the end wall of the flow passage. As outlined in the experimental section of this report, a fair amount of information on boundary-layer behavior in corners has

been obtained in visualization studies. Theoretically, however, the analysis of boundary-layer behavior in corner regions is still in a very preliminary stage of development.

Early analyses of flow in corner regions (e.g., refs. 31 and 32) are generally confined to special cases in which there is no pressure gradient in the main flow and the corner region is formed by the intersection of plane walls. Reference 19 considers flows over surfaces with very sharply varying lateral curvature (equivalent to a corner with a fillet). Perturbation assumptions of the type employed in the analysis of flow over a flat plate in the same reference are employed in this case. In particular, the mainstream velocity is considered to be the resultant of a constant "axial" velocity and superimposed perturbation velocities of very small magnitude in the axial and lateral directions. 3475

The boundary-layer equations in reference 19 are solved numerically for two choices of mainstream flow in a corner having a hyperbolic cross section. For the first flow analyzed, the axial perturbation velocity is assumed zero and the lateral perturbation velocity is assumed constant. In the second case, the axial perturbation velocity is again assumed zero, but the lateral perturbation velocity is assumed to vary as the first power of the axial distance. Plots of velocity profiles and deflections of the crossflow from the mainstream direction are presented. The results indicate that, for the case of constant lateral perturbation velocity, the corner establishes a crosswise pressure gradient that causes boundary-layer air to flow from the upper part of the wall into the corner region. For the second example, the results indicate that the external flow possesses a crosswise pressure gradient before it reaches the corner and that this pressure gradient not only opposes the one established in the corner but also causes a strong crossflow from the corner region up onto the side of the wall.

Evaluation and conclusions. - Application of boundary-layer theory to the analysis of secondary flow in turbomachines has the advantage of accounting for viscosity in the fluid and thereby allowing the computation of secondary flows that are principally the result of viscous action, for example, cross-channel flows. However, the application of the boundary-layer studies outlined in this chapter to compressor flows is severely limited. For example, the theories in general have assumed steady, incompressible, laminar-boundary-layer flow. In compressor blade rows, such flows will be primarily unsteady, compressible, and turbulent. (To date, of course, it has not been possible to give an adequate mathematical treatment of flows of this type.) Furthermore, the present state of boundary-layer theory does not allow the ready computation of flows in the presence of blade rows. Although some progress has been made in this direction (ref. 19), the computations of secondary flows arising from lateral pressure variations in the main stream are principally confined to flows over surfaces that are essentially flat.

In spite of these restrictions, several advantages can be gained from present boundary-layer analyses. As mentioned earlier, they can serve as the first step in a more comprehensive study of secondary flows and can possibly be combined with analyses treating other aspects of the flow. Secondly, they can be used in their present form to explain and interpret experimental findings in relatively simple flow configurations. (The "limiting crossflow" phenomenon found in both experimental and theoretical studies is an example.) Finally, calculations of velocity-profile shapes and basic parameters are useful in the application of more general theoretical treatments that presently exist (such as the momentum-integral methods). The determination of profile shapes, in fact, was one of the principal motivations for the analysis presented in reference 19.

3475

CONCLUDING REMARKS

The survey of experimental and theoretical research on secondary flows and three-dimensional boundary-layer effects indicates in broad outline the present state of knowledge in this field. It is evident from the work discussed that, at best, only an elementary understanding of the basic flow behavior has been achieved.

CH-25 back

The experimental work indicates how such phenomena as flow disturbances caused by relative motion between blade ends and annulus walls, cross-channel and radial flows, and vortex formation in blade passages may occur in simple compressor configurations. In a multistage unit, however, the pattern of flow is greatly complicated by the interaction of these effects and the influence of other compressor phenomena (e.g., rotating stall) that have not been considered in conjunction with these studies. The experimental studies, therefore, are best used as a guide for interpretation of experimental findings in multistage compressors and as a basis for constructing more comprehensive models of the actual flow behavior. With proper caution, however, the results can be used in their present form to guide certain design considerations. In the past, for example, shrouding of blade rows has at times been advocated for the reduction of losses in blade end regions (ref. 33). The tests concerning relative motion between blade ends and annulus wall, however, indicate that smaller flow disturbances and better performance are likely to occur in unshrouded blade passages (with due regard for clearance, of course) than in shrouded passages.

Theoretical research on secondary flows and three-dimensional boundary-layer effects has been severely handicapped by the mathematical complexity associated with even the simplest types of problems. It is probably sufficient to hope that present theories can be used to predict

"orders of magnitude" of various quantitative aspects of the flow and to provide a better physical understanding of the mechanisms that give rise to observable flow patterns.

REFERENCES

1. Compressor and Turbine Research Division: Aerodynamic Design of Axial-Flow Compressors. Vol. I. NACA RM E56B03, 1956.

2. Herzig, Howard Z., Hansen, Arthur G., and Costello, George R.: A Visualization Study of Secondary Flows in Cascades. NACA Rep. 1163, 1954. (Supersedes NACA TN 2947.)

3. Rohlik, Harold E., Kofskey, Milton G., Allen, Hubert W., and Herzig, Howard Z.: Secondary Flows and Boundary-Layer Accumulations in Turbine Nozzles. NACA Rep. 1168, 1954. (Supersedes NACA TN's 2871, 2909, and 2989.)

4. Compressor and Turbine Research Division: Aerodynamic Design of Axial-Flow Compressors. Vol. II. NACA RM E56B03a, 1956.

5. Herzig, Howard Z., and Hansen, Arthur G.: A Survey of Unclassified Axial-Flow-Compressor Literature. NACA RM E55H11, 1955.

6. Kofskey, Milton G., and Allen, Hubert W.: Smoke Study of Nozzle Secondary Flows in a Low-Speed Turbine. NACA TN 3260, 1954.

7. Briggs, William B., and Giamati, Charles C.: Interstage Surveys and Analysis of Viscous Action in Latter Stages of a Multistage Axial-Flow Compressor. NACA RM E52I12, 1953.

8. Goldstein, Sydney, ed.: Modern Developments in Fluid Dynamics. Vol. I. Clarendon Press (Oxford), 1938.

9. Michal, Aristotle D.: Matrix and Tensor Calculus. John Wiley & Sons, Inc., 1947.

10. Dean, W. R.: Note on the Motion of Fluid in a Curved Pipe. Phil. Mag., ser, 7, vol. 4, no. XX, July 1927, pp. 208-223.

11. Dean, W. R.: The Stream-line Motion of Fluid in a Curved Pipe. Phil. Mag., ser. 7, vol. 5, no. XXX, April 1928, pp. 673-695.

3475

12. Kito, Fumiki: On the Secondary Vortex Generated in a Bent-Pipe of Elliptical Cross-Section. Jour. Japan Soc. Appl. Mech., 1950, pp. 73-75.

13. Itō, Hidesato: Theory of Laminar Flows through Curved Pipes of Elliptic and Rectangular Cross Sections. Inst. High Speed Mech., Tôhoku Univ., Sendai (Japan), vol. I, 1951, pp. 1-16.

14. Squire, H. B., and Winter, K. G.: The Secondary Flow in a Cascade of Airfoils in a Nonuniform Stream. Jour. Aero. Sci., vol. 18, no. 4, Apr. 1951, pp. 271-277.

15. Hawthorne, William R.: Secondary Circulation in Fluid Flow. Proc. Roy. Soc. (London), ser. A, vol. 206, no. A1086, May 7, 1951, pp. 374-387.

16. Eichenberger, Hans P.: Shear Flow in Bends. Tech. Rep. No. 2, Office Naval Res., Gas Turbine Lab., M.I.T., Apr. 15, 1952. (Contract N5ori07848.)

17. Kronauer, Richard E.: Secondary Flows in Fluid Dynamics. Pratt and Whitney Res. Rep. No. 132, Gordon McKay Lab., Harvard Univ., Apr. 1951.

18. Prandtl, L.: On Boundary Layers in Three Dimensional Flow. Rep. and Trans. No. 64, British R.A.E., May 1, 1946.

19. Mager, Artur: Laminar Boundary Layer Problems Associated with Flow through Turbomachines. Tech. Rep. No. 2, GALCIT, June 1953. (Contract AF 18(600)178.)

20. Howarth, L.: The Boundary Layer in Three Dimensional Flow. I - Derivation of the Equations for Flow along a General Curved Surface. Phil. Mag., ser. 7, vol. 42, no. 326, Mar. 1951, pp. 239-243.

21. Hayes, Wallace D.: The Three-Dimensional Boundary Layer. NAVORD Rep. 1313, NOTS 384, U. S. Naval Ord. Test Station (Inyokern), May 9, 1951. (Bur. Ord. Task Assignment NOTS-36-Re3d-441-3.)

22. Moore, Franklin K.: Three-Dimensional Compressible Laminar Boundary-Layer Flow. NACA TN 2279, 1951.

23. Burgers, J. M.: Some Considerations on the Development of Boundary Layers in the Case of Flows Having a Rotational Component. Nederl. Akad. van Wetenschappen, vol. XLIV, nos. 1-5, 1941, pp. 12-25.

3475

24. Mager, Artur: Generalization of Boundary-Layer Momentum-Integral Equations to Three-Dimensional Flows Including Those of Rotating System. NACA Rep. 1067, 1952. (Supersedes NACA TN 2310.)

25. von Kármán, Th.: On Laminar and Turbulent Friction. NACA TM 1092, 1946.

26. Bödewadt, U. T.: Die Drehströmung über festem Grunde. Z.a.M.M., Bd. 20, Heft 5, Oct. 1940, pp. 241-253.

27. Mager, Artur, and Hansen, Arthur G.: Laminar Boundary Layer over Flat Plate in a Flow Having Circular Streamlines. NACA TN 2658, 1952.

28. Loos, H. G.: A Simple Laminar Boundary Layer with Secondary Flow. Tech. Rep. No. 1, GALCIT, June 1953. (Contract AF 18(600)-178.)

29. Sowerby, L.: Secondary Flow in a Boundary Layer. Rep. No. AERO. 2512, British R.A.E., Mar. 1954.

30. Mager, A.: Thick Laminar Boundary Layer Under Sudden Lateral Perturbation. Tech. Rep. No. 5, GALCIT, Apr. 1954. (Contract AF 18(600)-178.)

31. Carrier, G. F.: The Boundary Layer in a Corner. Quart. Appl. Math., vol. IV, no. 4, Jan. 1947, pp. 367-370.

32. Loitsianskii, L. G., and Bolshakov, V. P.: On Motion of Fluid in Boundary Layer Near Line of Intersection of Two Planes. NACA TM 1308, 1951.

33. Ainley, D. G., and Jeffs, R. A.: Analysis of the Air Flow through Four Stages of Half-Vortex Blading in Axial Compressors. R. & M. No. 2383, British A.R.C., Apr. 1946.

3475

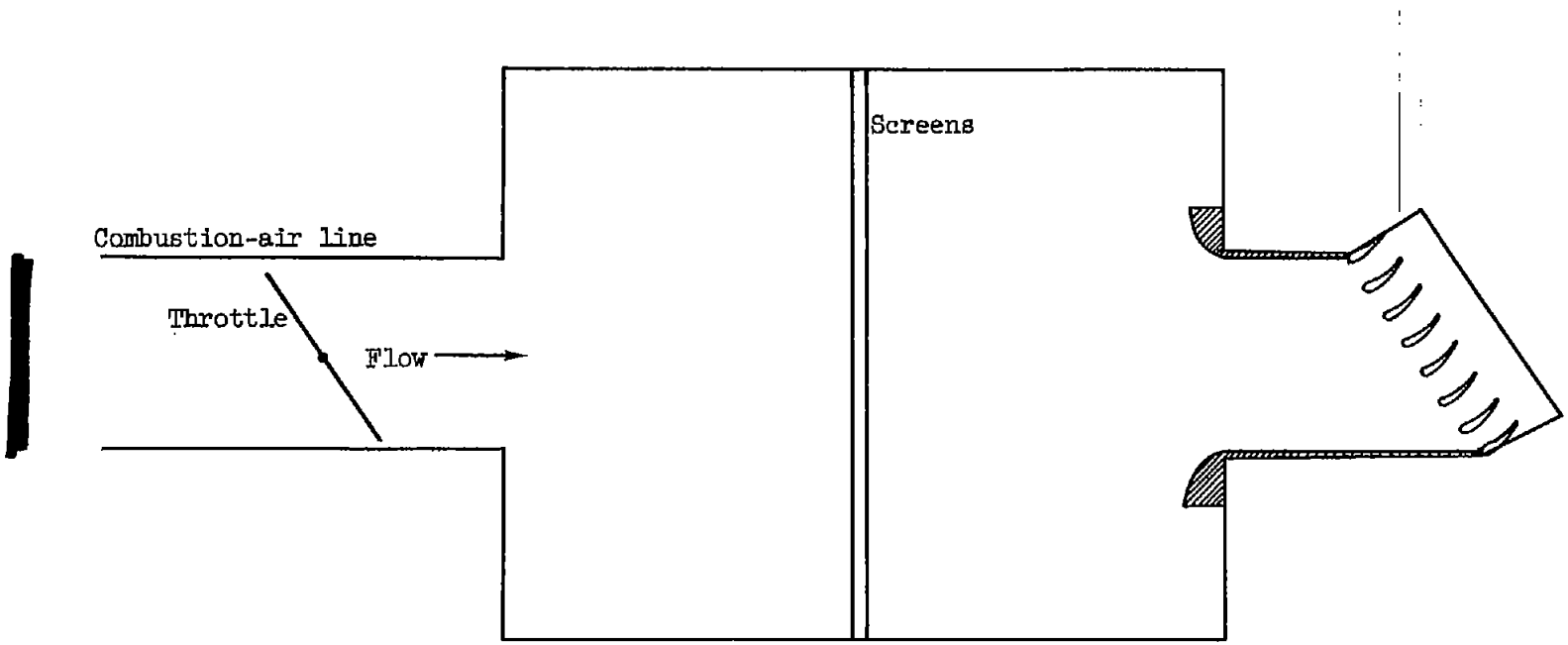

Figure 1. - Two-dimensional steady-flow cascade (ref. 2).

Figure 2. - Overturning in end-wall boundary layer due to secondary flow. Smoke introduced through probe on wall in passage at inlet (ref. 2).

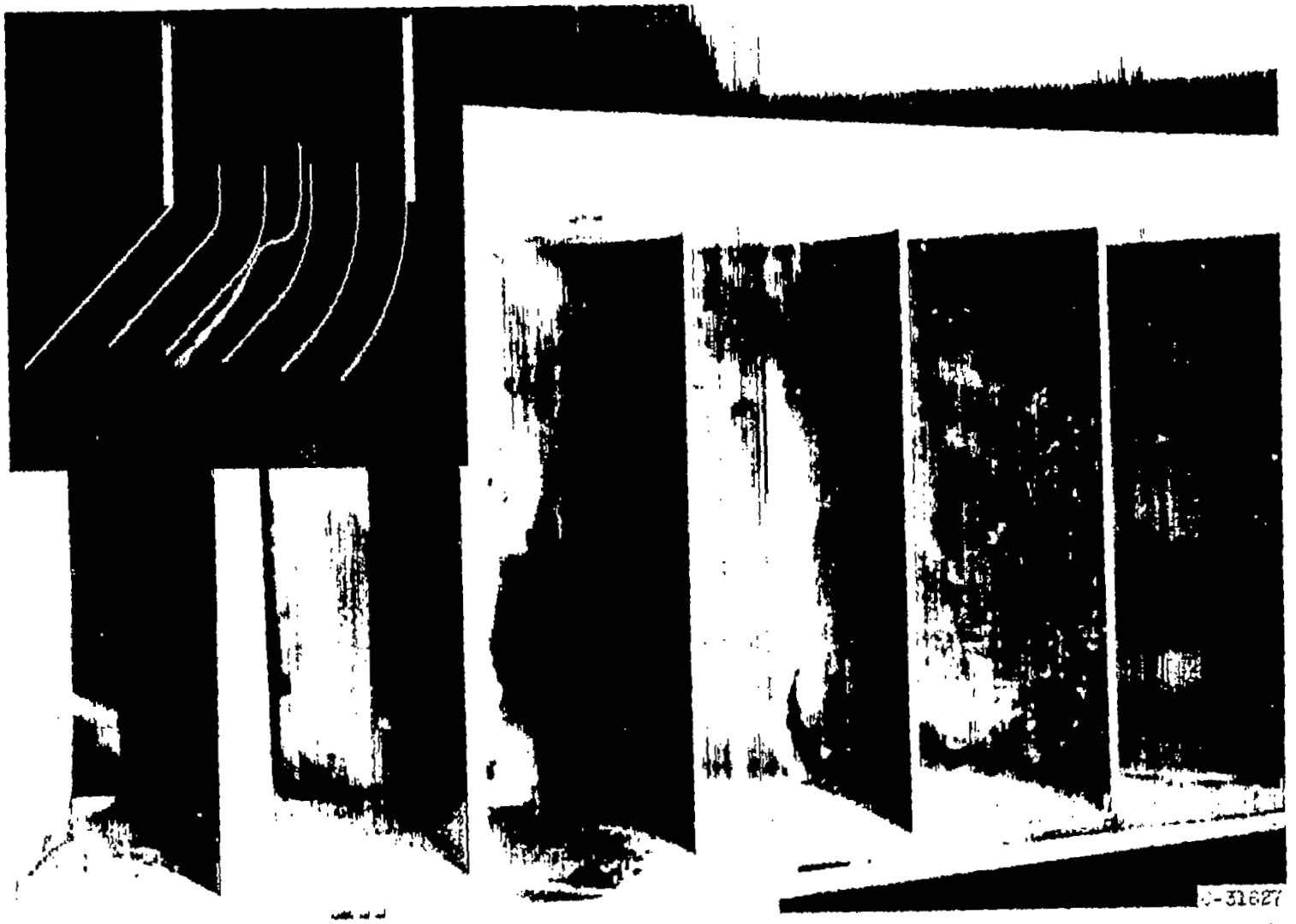

Figure 3. - Downstream view showing vortex formation resulting from roll-up of end-wall boundary layer. Smoke introduced on wall near blade pressure surface (ref. 2).

3475

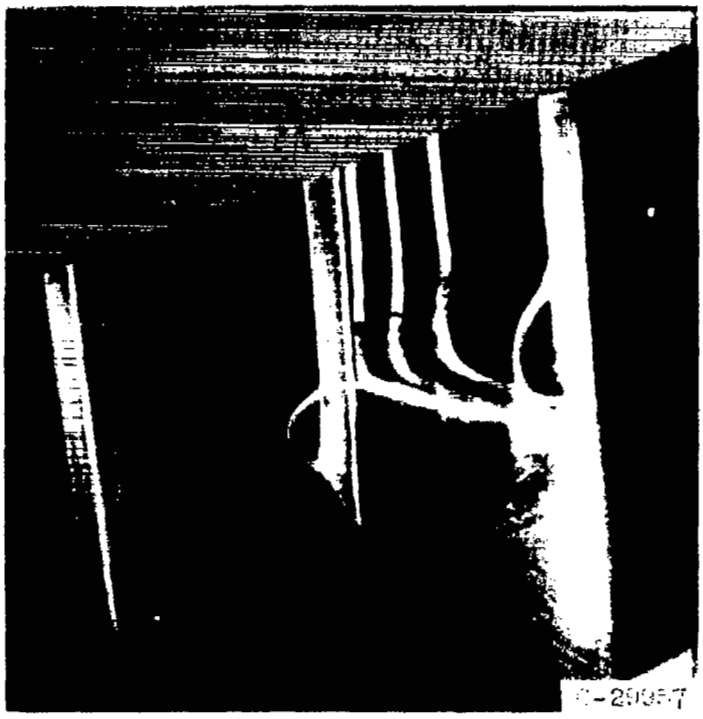

(a) Convergence of streamlines (ref. 2).

Figure 4. - Passage vortex formation.

3475

CH-26 back

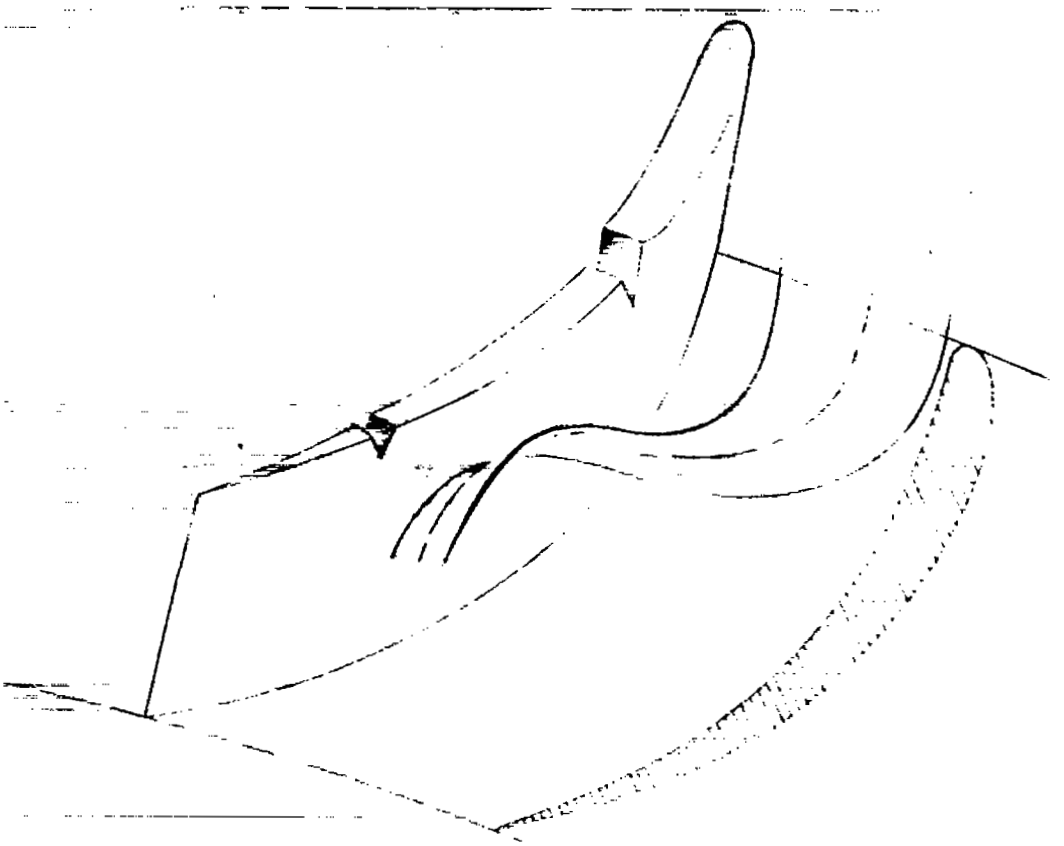

CD-4324

(b) Spanwise deflection and vortex roll-up.

Figure 4. - Concluded. Passage vortex formation.

[redacted]

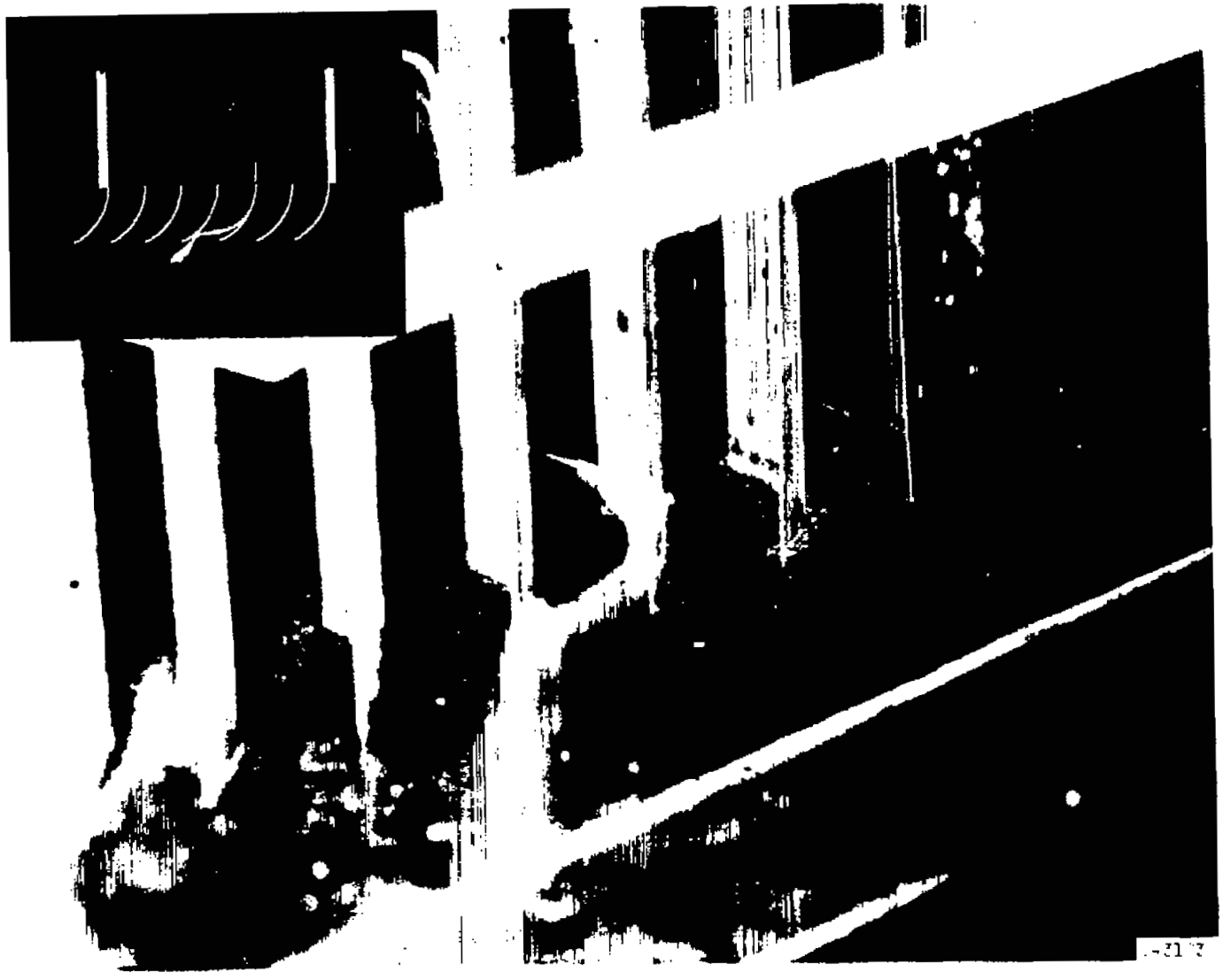

Figure 5. - Deflection of flow off blade pressure surface and across passage to roll up into outer layers of passage vorter (ref. 2).

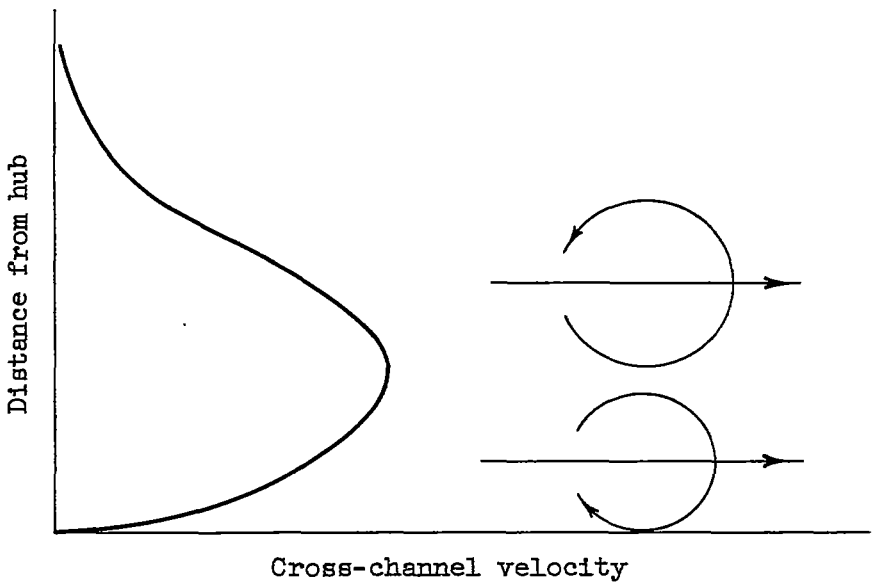

Figure 6. - Boundary-layer velocity and vorticity profiles for cross-channel component of boundary-layer flow (ref. 6).

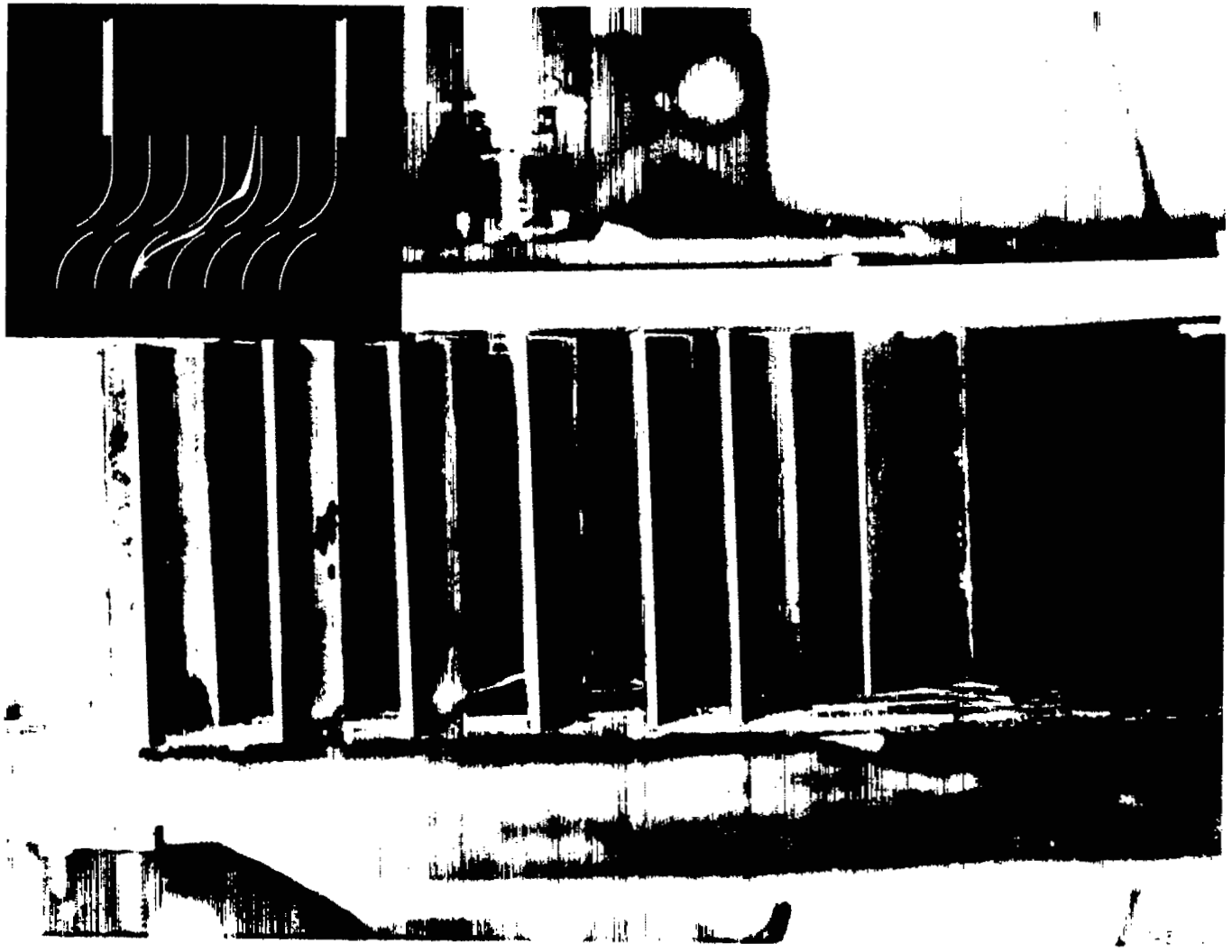

Figure 7. - Resistance to turning of passage vortex generated by upstream cascade causes it to strike pressure surface of blade in downstream cascade. Smoke introduced through probe on wall at inlet to upstream cascade (ref. 2).

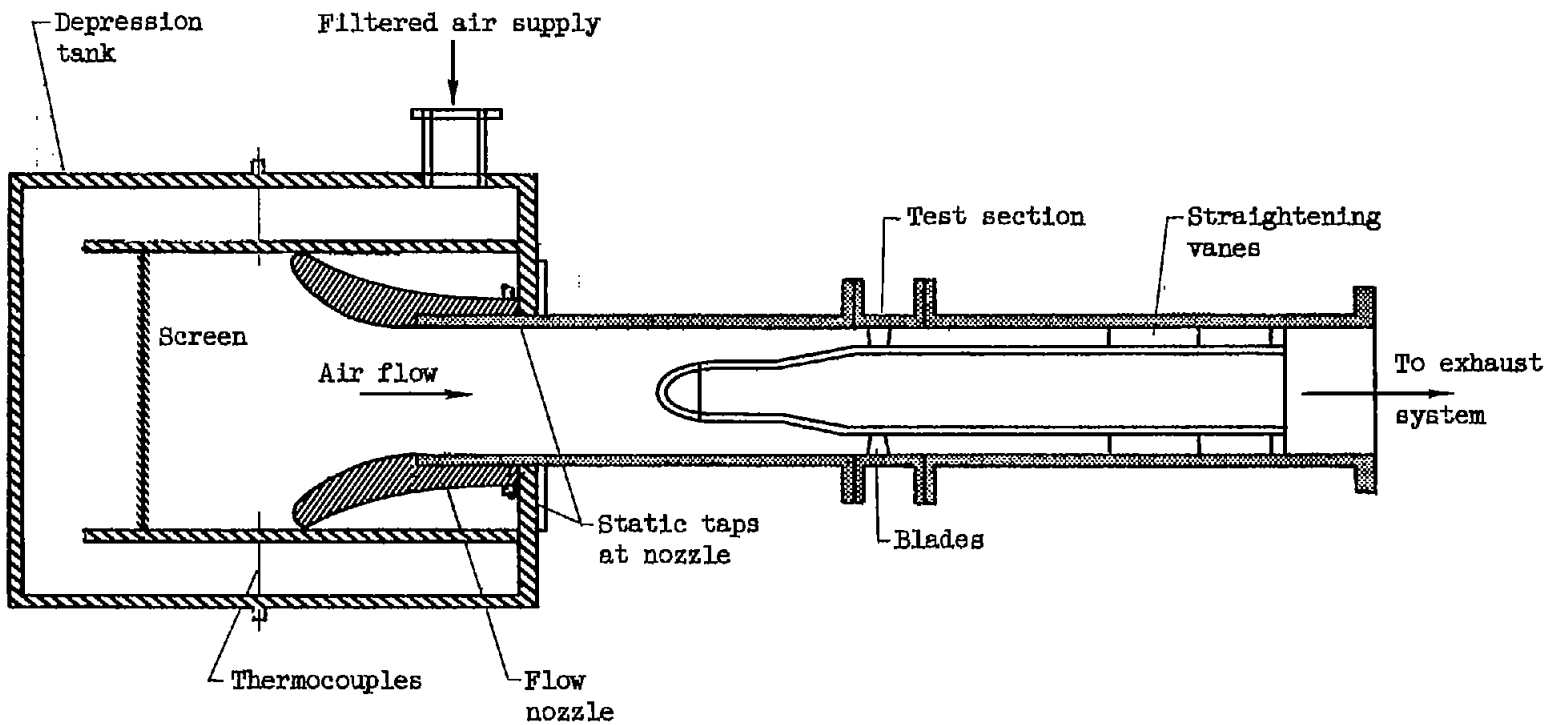

Figure 8. - Schematic view of annular-cascade test unit (refs. 2 and 3).

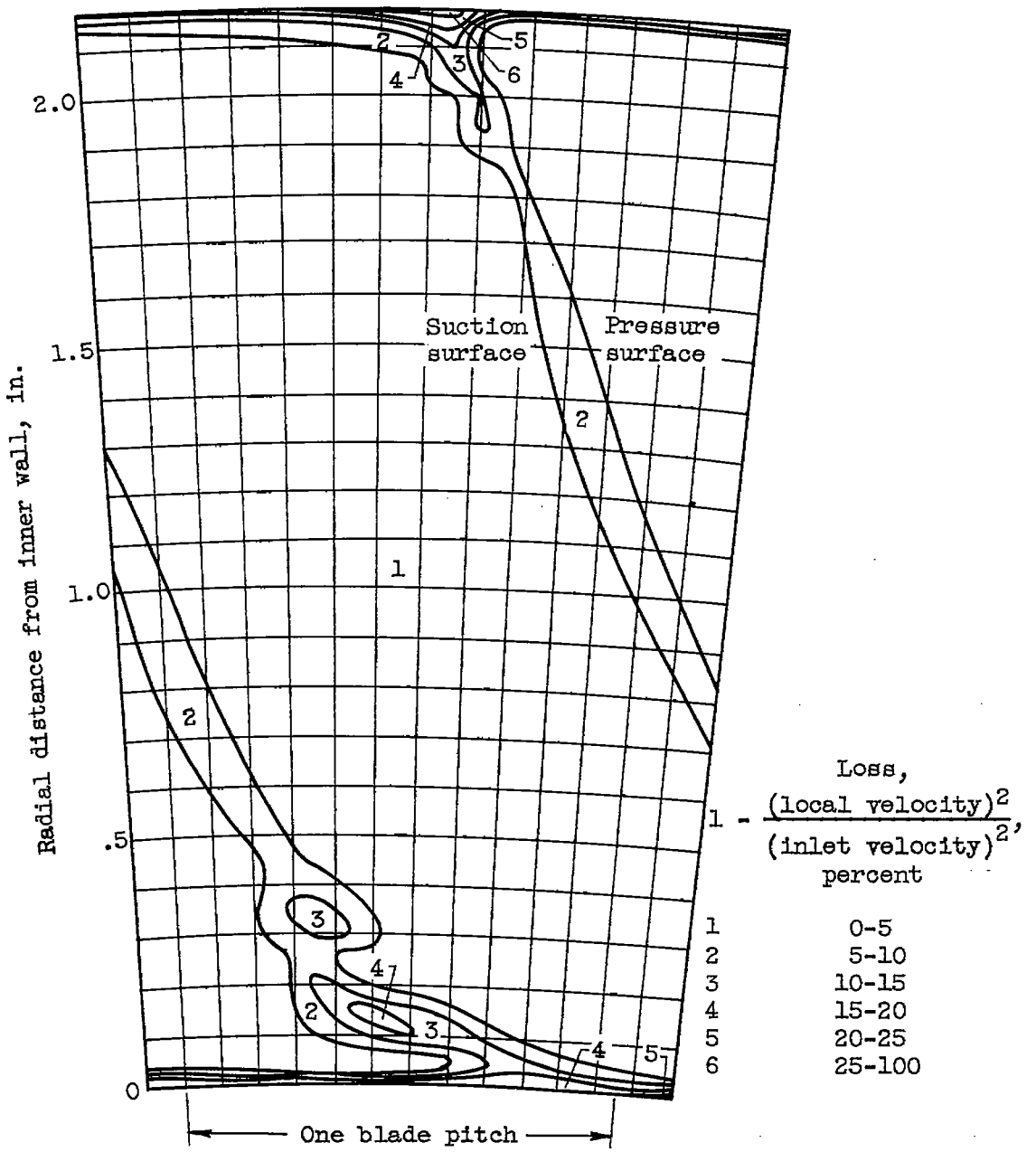

(a) Subsonic flow condition (lower Mach number).

Figure 9. - Contours of kinetic-energy loss at exit measuring station of vortex blades (ref. 3).

3475

CH-27

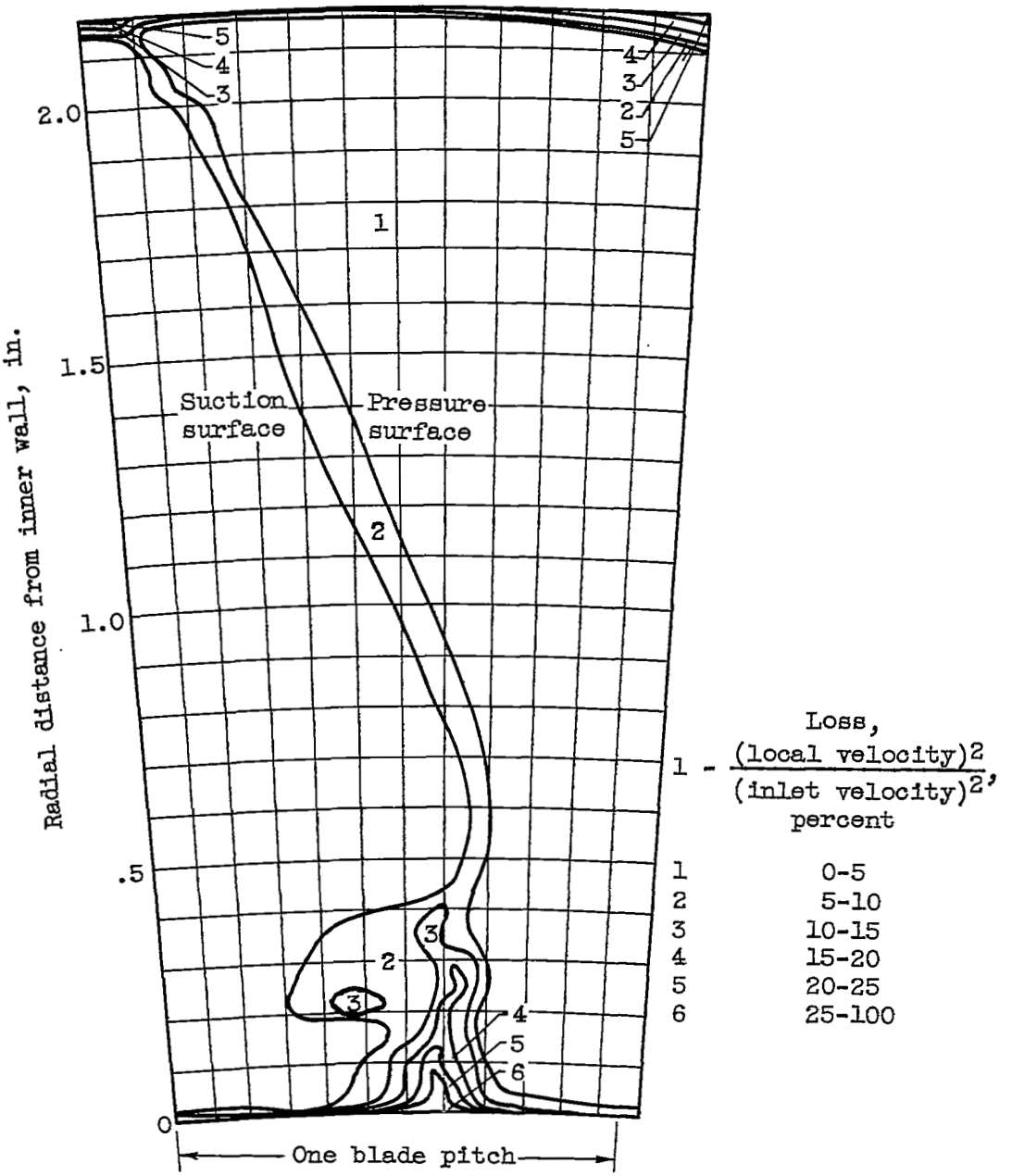

(b) Supersonic flow condition (higher Mach number).

Figure 9. - Concluded. Contours of kinetic-energy loss at exit measuring station of vortex blades (ref. 3).

3475

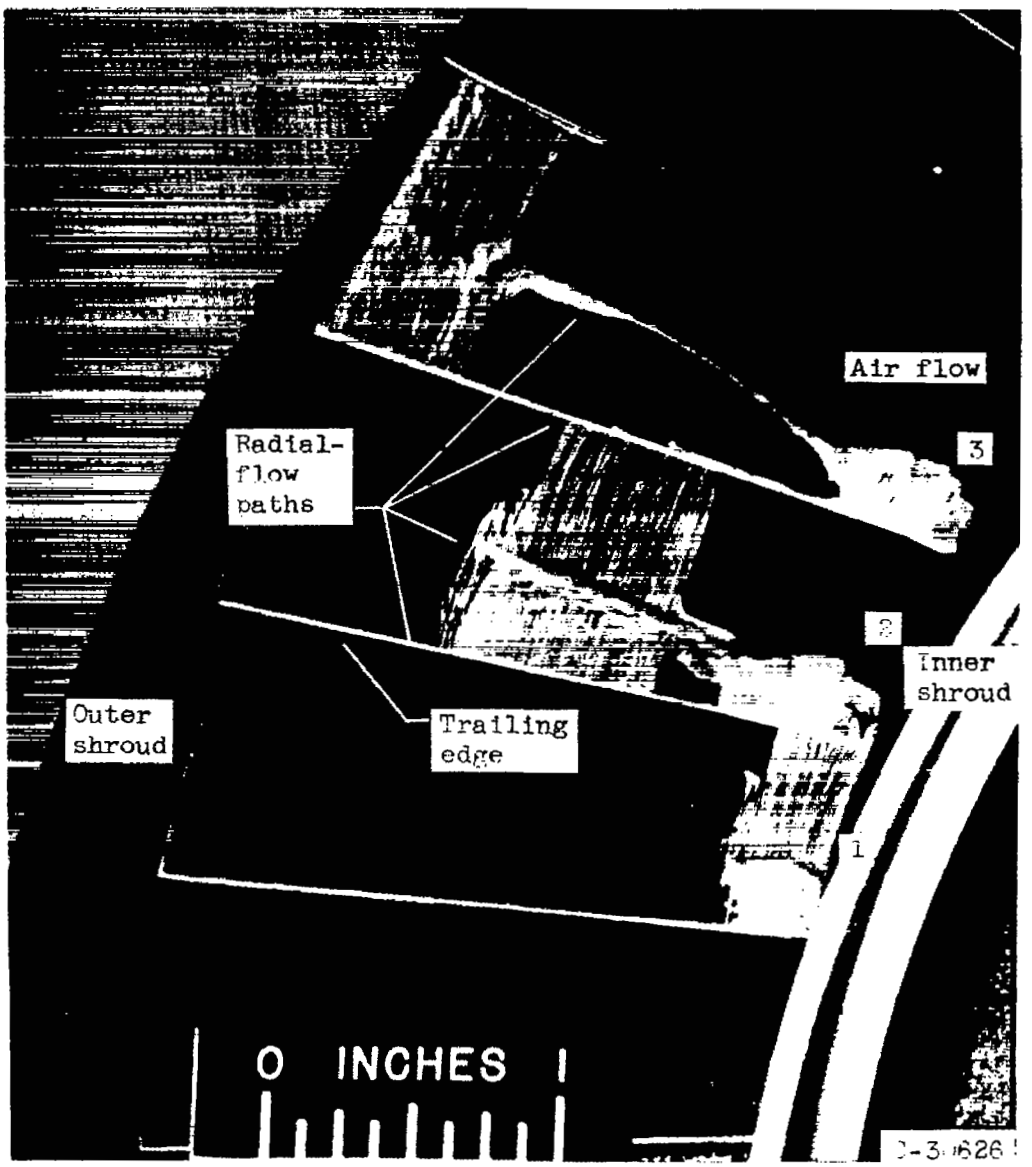

Figure 10. - Paint traces showing location of shock and radial flow in thickened boundary regions on suction surfaces of vortex blades (ref. 3).

[redacted]

3475

CH-27 back

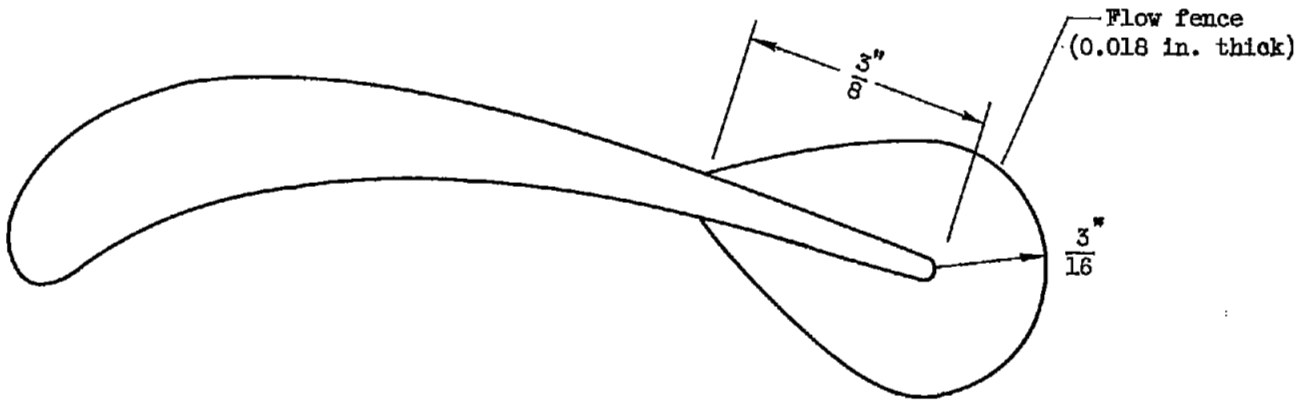

(a) Flow fence to interrupt radial flow along blade trailing edge and in thickened boundary-layer region.

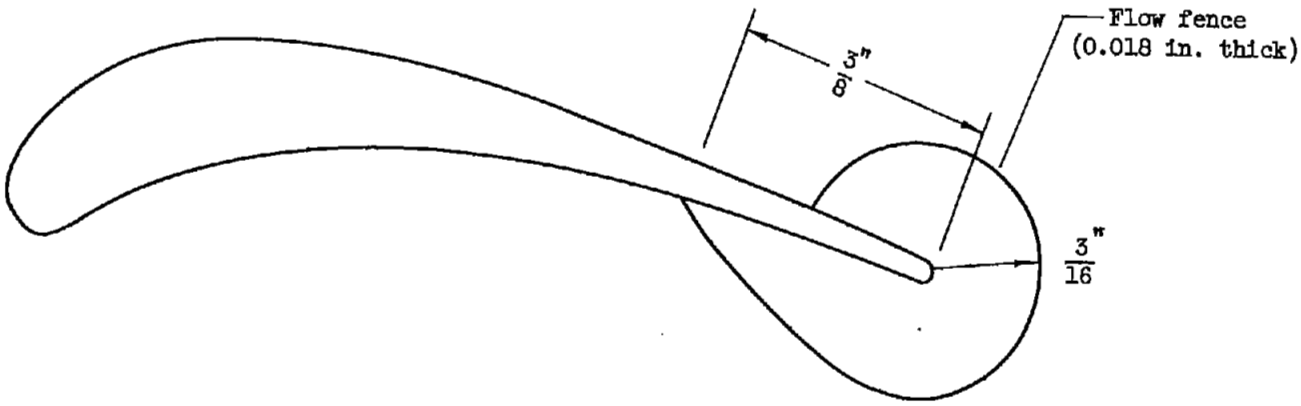

(b) Modified flow fence to interrupt radial flow along blade trailing edge only.

Figure 11. - Sketches of flow fences located on blades at midspan position (ref. 3).

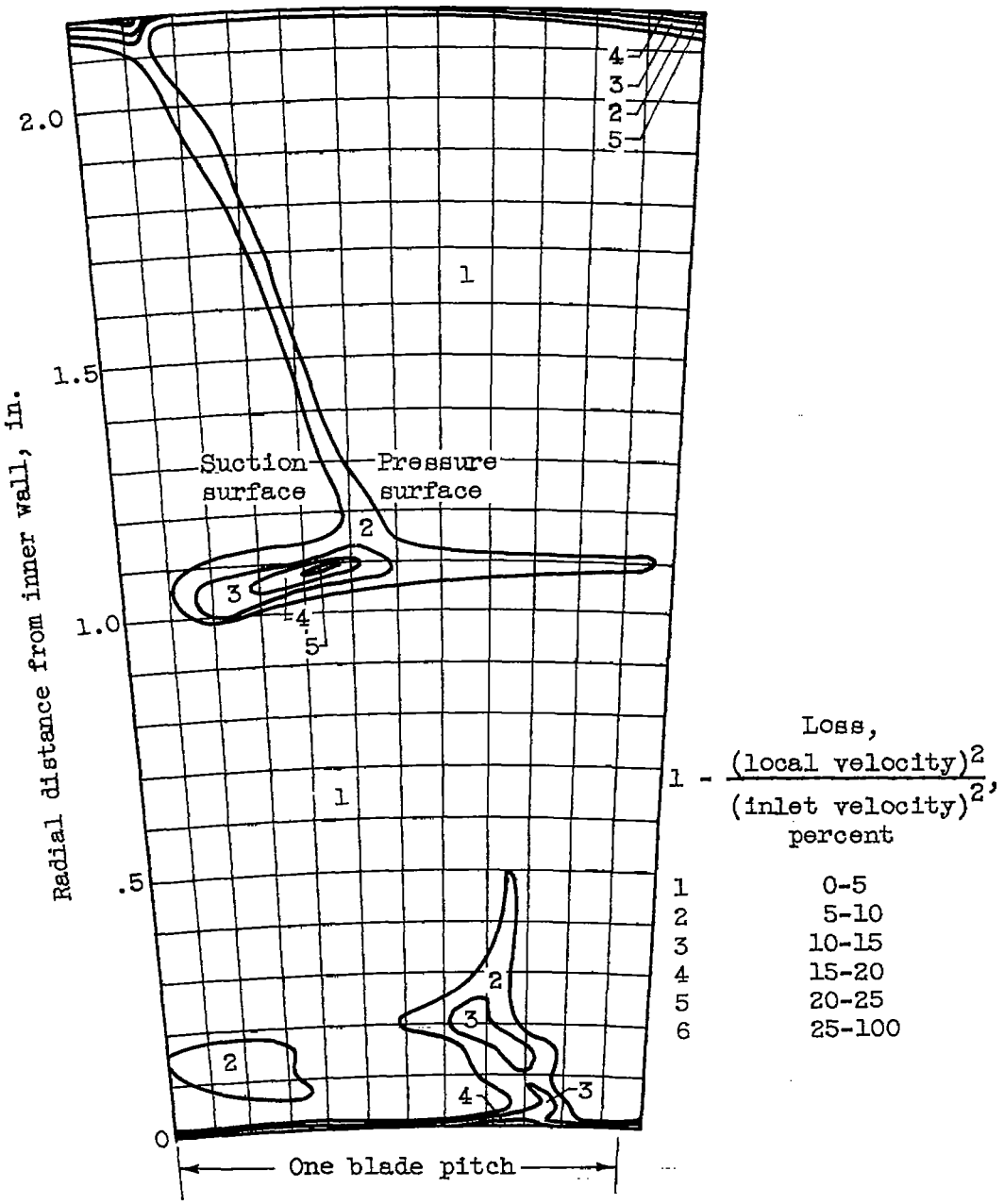

(a) Full flow fence interrupts radial flow along trailing edge and along suction surface.

Figure 12. - Contours of kinetic-energy loss at exit of vortex blades, showing results of radial-flow fences. Higher Mach number (ref. 3).

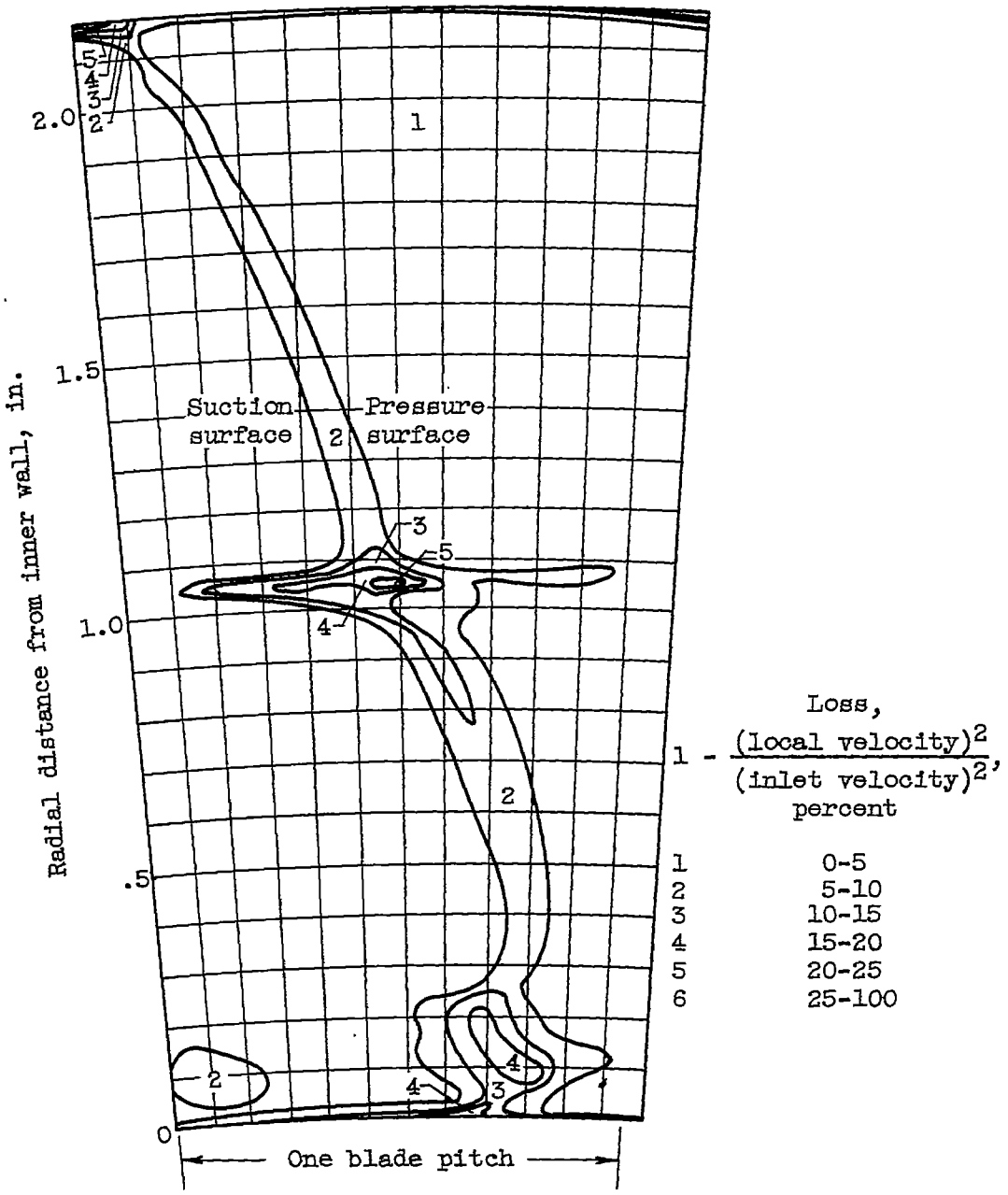

(b) Modified flow fence interrupts radial flow along trailing edge only.

Figure 12. - Concluded. Contours of kinetic-energy loss at exit of vortex blades, showing results of radial-flow fences. Higher Mach number (ref. 3).

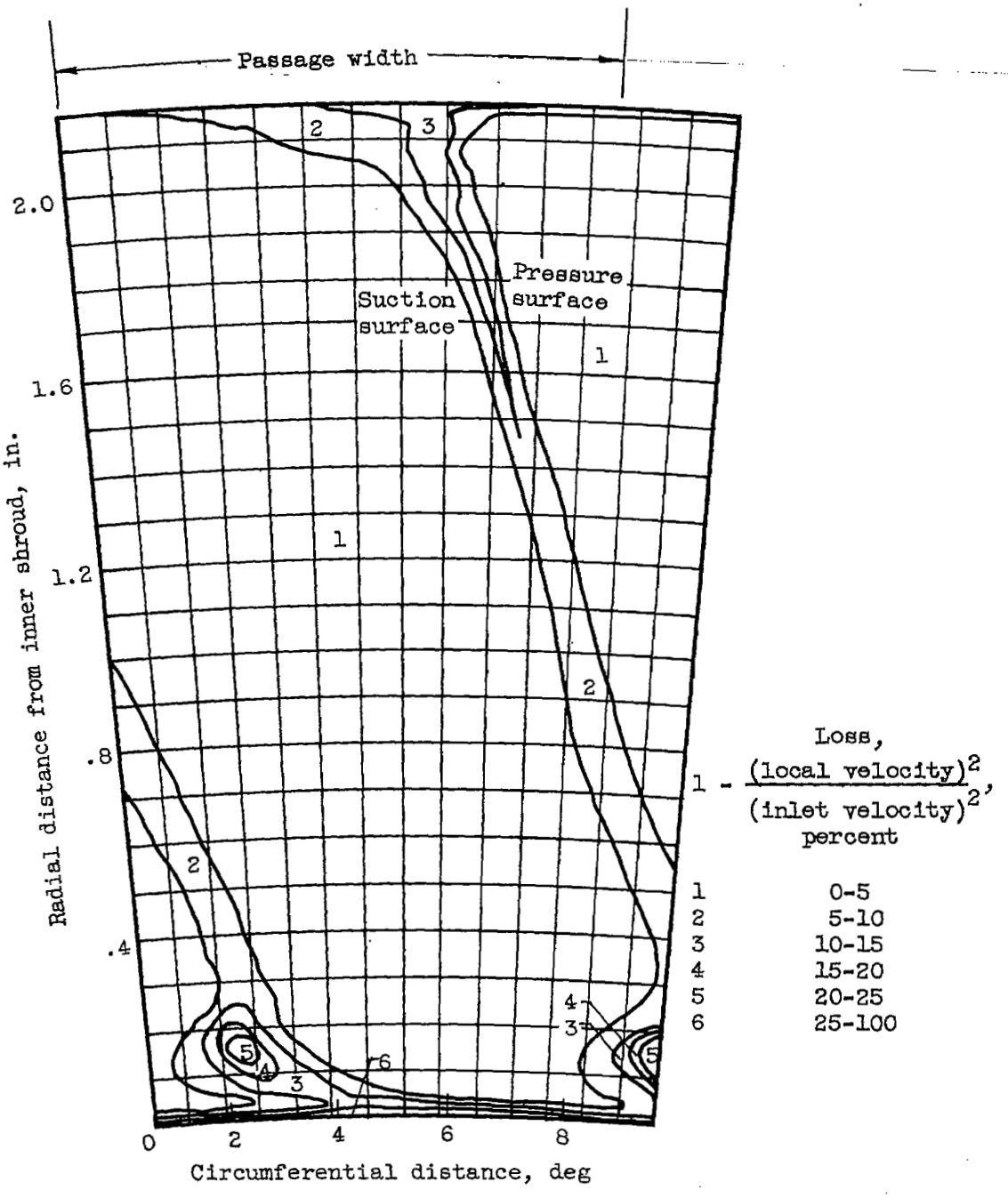

(a) Lower Mach number.

Figure 13. - Contours of kinetic-energy loss at exit measuring station of constant-discharge-angle blades, set A (ref. 3).

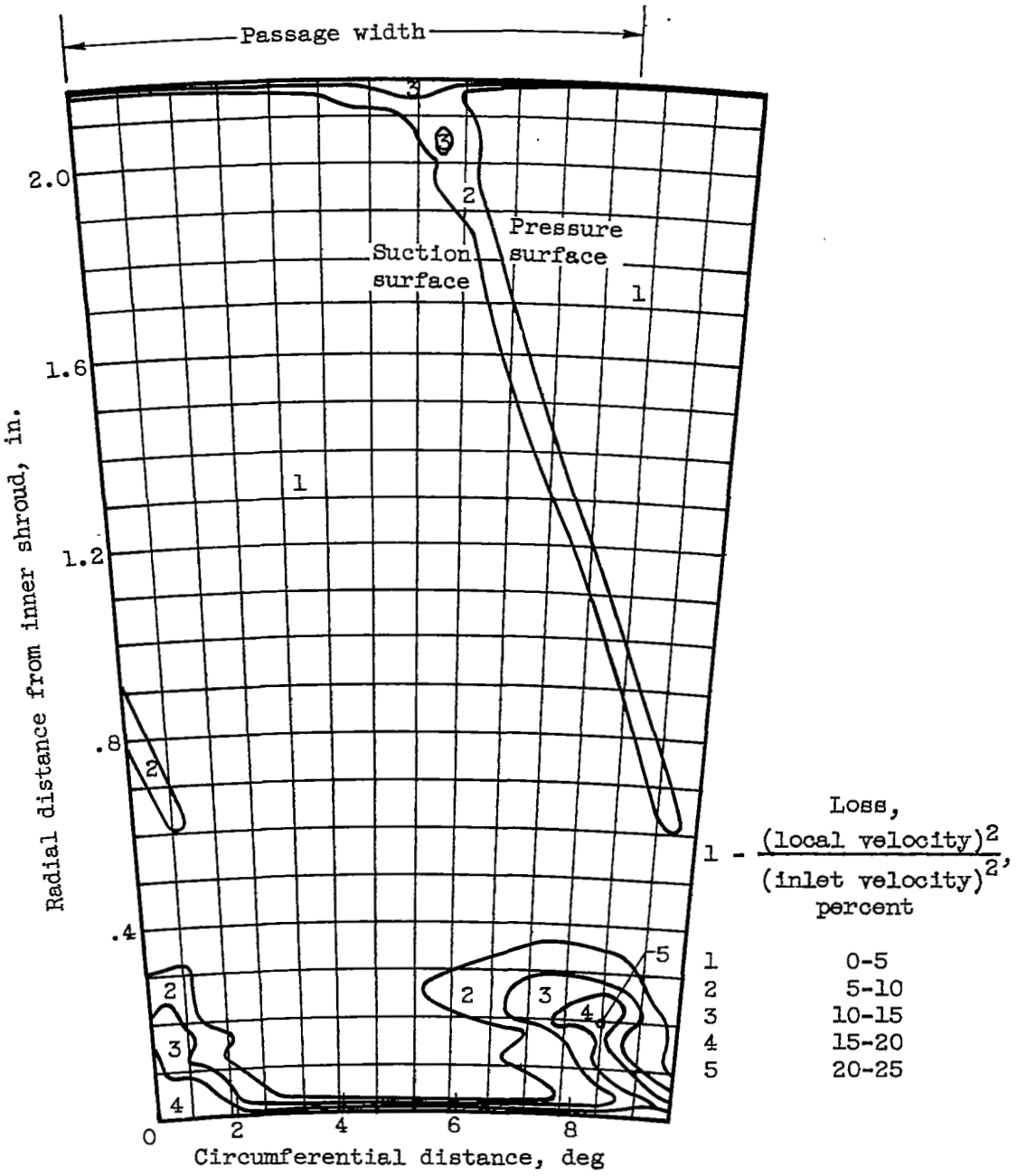

(b) Higher Mach number.

Figure 13. - Concluded. Contours of kinetic-energy loss at exit measuring station of constant-discharge-angle blades, set A (ref. 3).

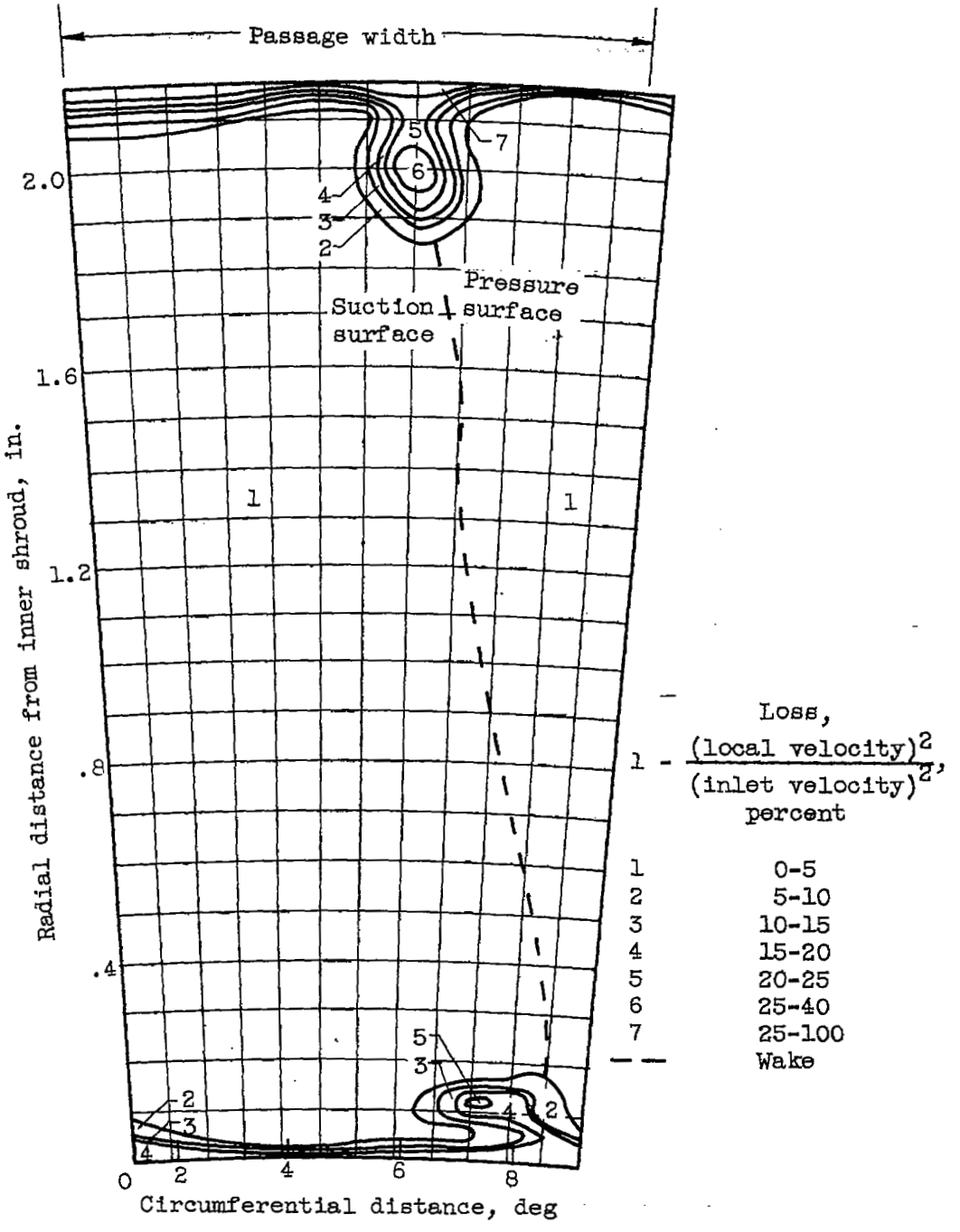

(a) Lower Mach number.

Figure 14. - Contours of kinetic-energy loss at exit measuring station of constant-discharge-angle blades, set B (ref. 3).

3475

CH-28

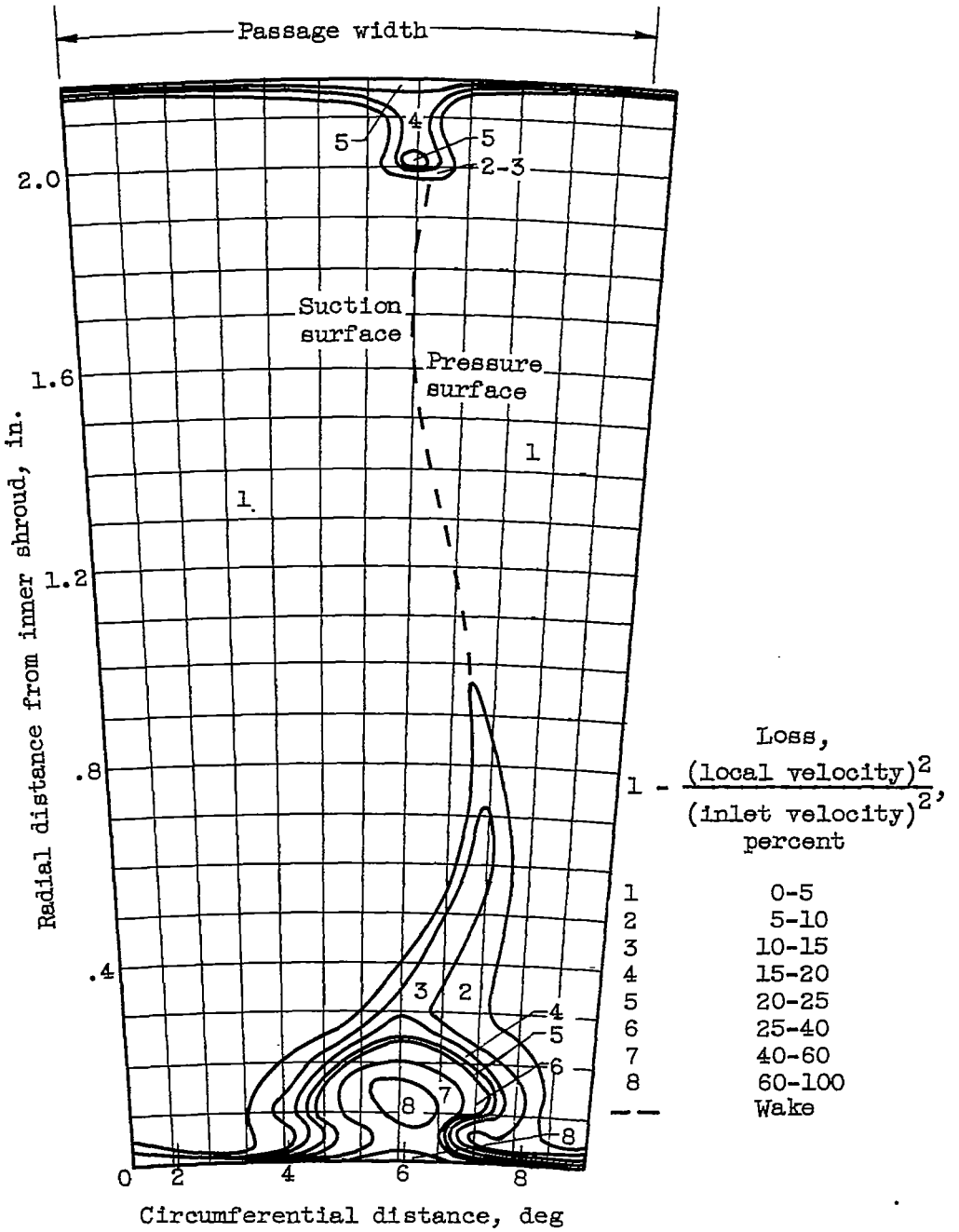

(b) Higher Mach number.

Figure 14. - Concluded. Contours of kinetic-energy loss at exit measuring station of constant-discharge-angle blades, set B (ref. 3).

Figure 15. - Deflection of flow off pressure surface at blade end and through tip-clearance region to roll up as vortex near suction surface (ref. 2).

Figure 16. - Displacement of passage vortex by tip-clearance vortex (ref. 2).

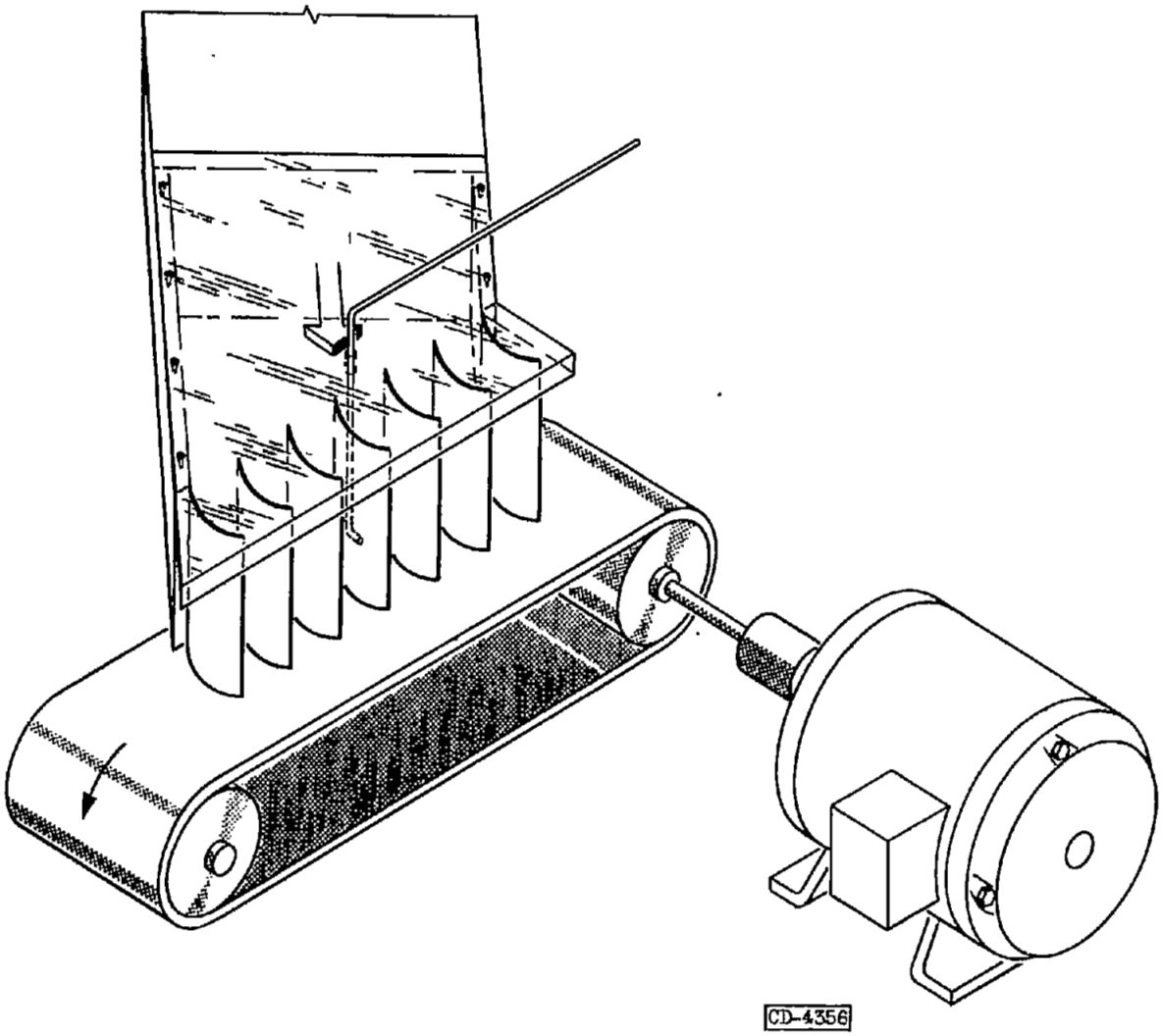

Figure 17. - Schematic diagram of apparatus used for studying tip-clearance effects with relative motion between wall and blades (ref. 2).

3475

Figure 18. - Streamline pattern showing scraping effects at leading surfaces of blades with relative motion between blades and wall (ref. 2).

[redacted]

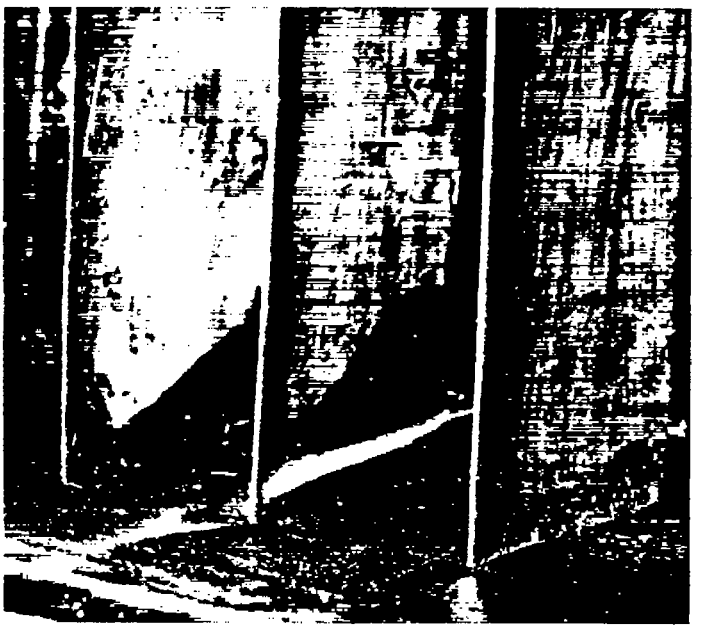

(a) Stationary wall.

(b) Moderate-speed wall.

Figure 19. - Effects of scraping action on streamline deflections on pressure surface of blade for "compressor configuration." Probe on nose of blade (ref. 2).

3475

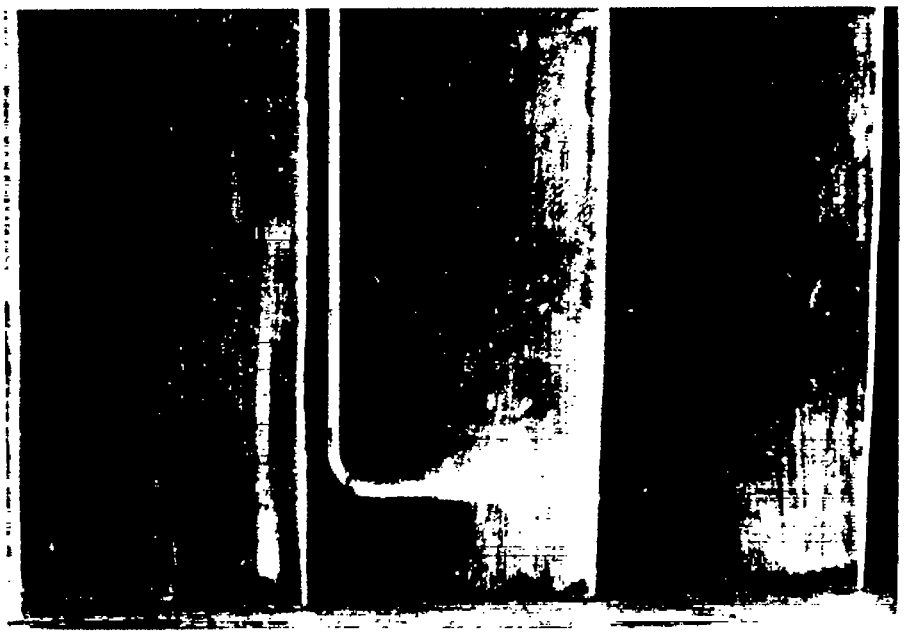

(a) Stationary wall.

(b) Moderate-speed wall.

Figure 20. - Aspirating effects on streamline deflections on suction surface of blades. Probe on nose of blade (ref. 2).

3475

(a) First rotor position.

(b) Second rotor position.

Figure 21. - Effect of rotor blade position on radial flow (ref. 6).

[redacted]

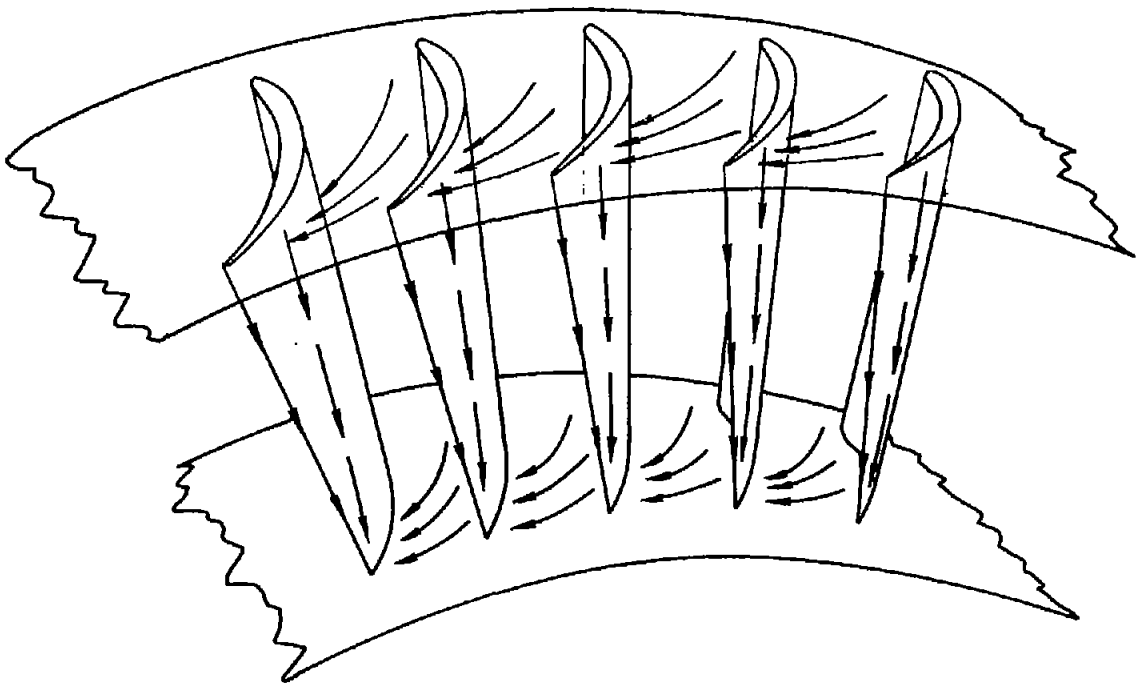

Figure 22. - Schematic sketch of secondary-flow paths in annular-nozzle cascade (ref. 3).

3475

CH-29

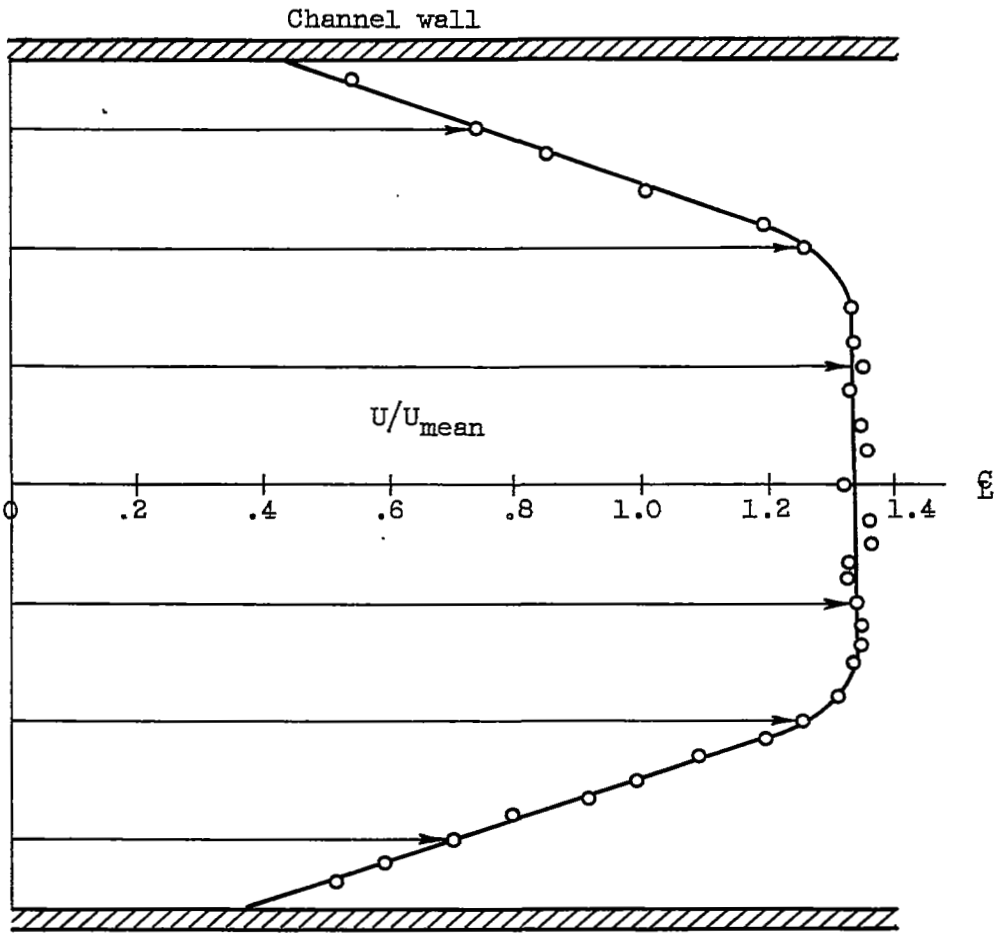

Figure 23. - Velocity variation at inlet to channel (ref. 14).

[redacted]

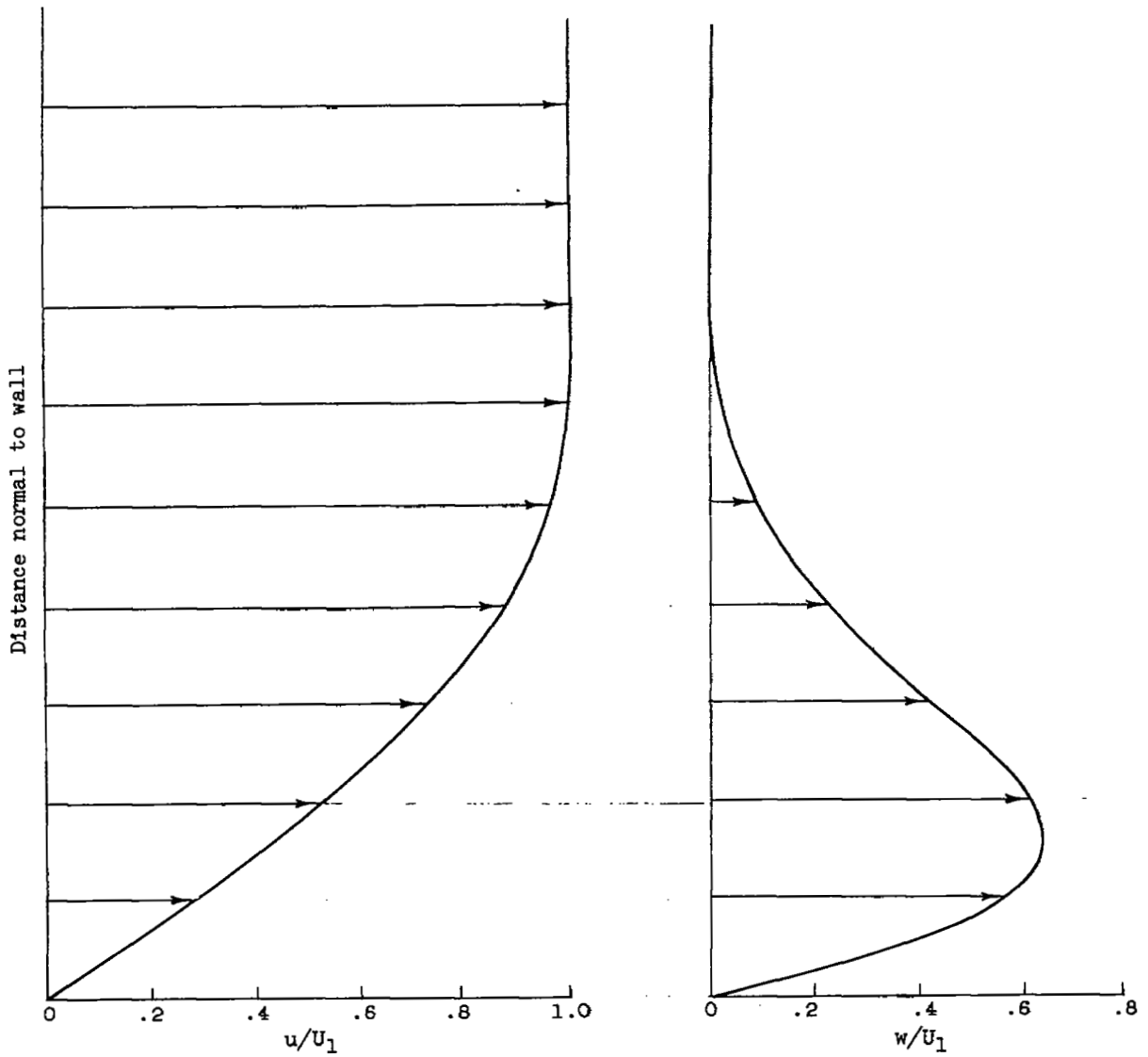

(a) Mainstream direction.

(b) Cross-channel direction.

Figure 24. - Typical boundary-layer velocity profiles (ref. 27).

5473

CH-29 back

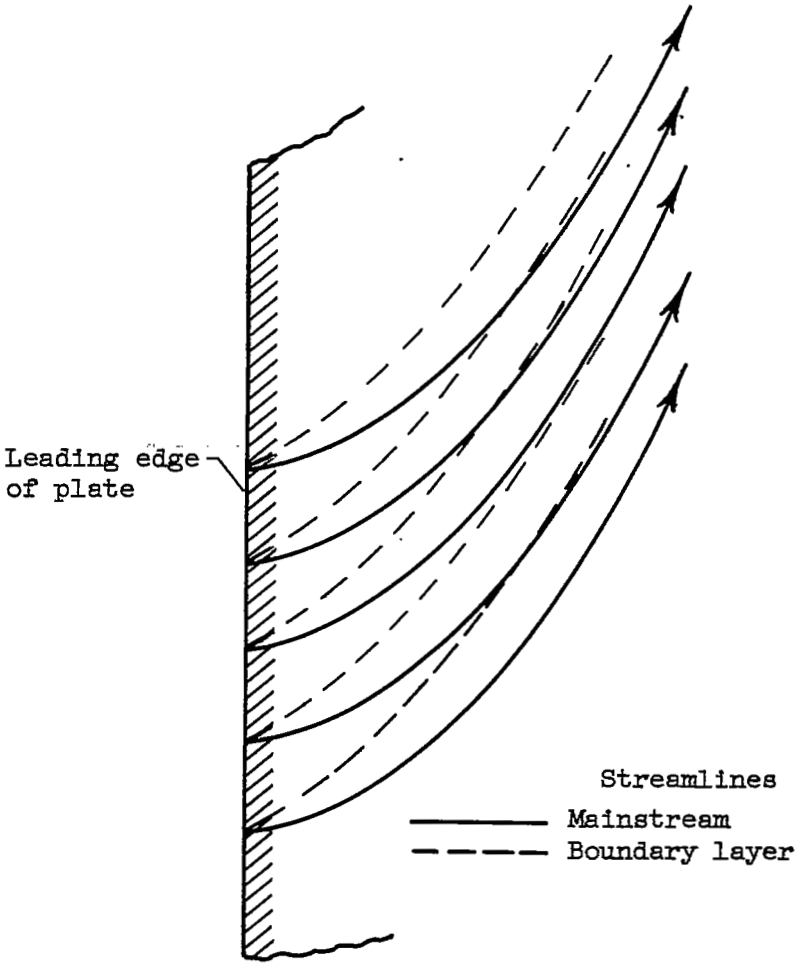

Figure 25. - Parabolic mainstream flow over flat plate with crossflow in boundary layer (refs. 28 and 29).

3475

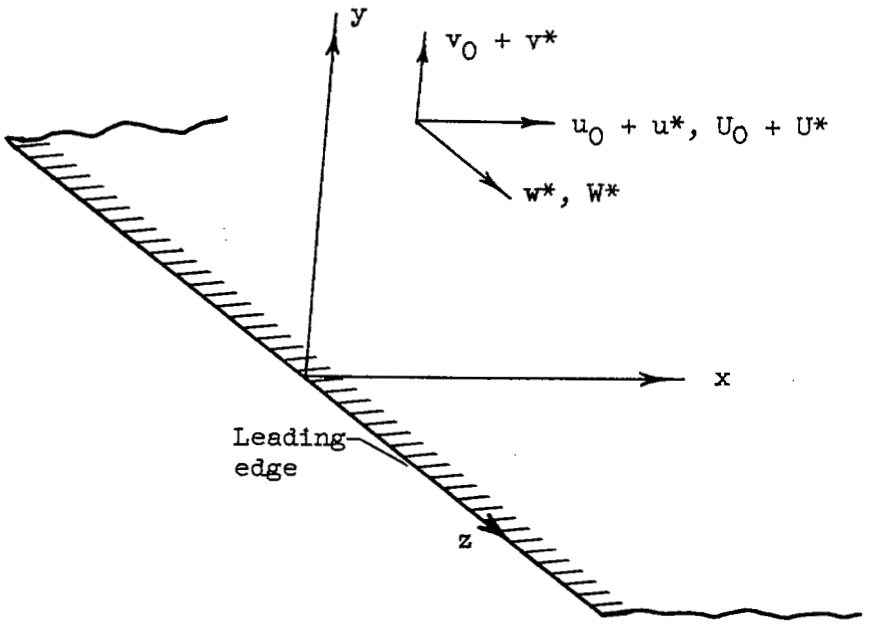

Figure 26. - Coordinate system for flow along semi-infinite flat plate (ref. 19).

CHAPTER XVI

EFFECTS OF DESIGN AND MEASUREMENT ERRORS ON COMPRESSOR PERFORMANCE

By Robert J. Jackson and Peggy L. Yohner

SUMMARY

Effects of design errors on compressor performance parameters and of measurement errors on calculated values of performance parameters are analyzed. Formulas and charts are presented from which the changes in blade-element performance and calculated parameters due to the design and measurement errors can be determined.

The use of the design-error charts during the design calculations and in the analysis and interpretation of data is discussed. The charts can be used to evaluate the sensitivity of a given velocity diagram to design errors and to determine whether iterations of design calculations are warranted. To a limited extent, the uncertainty intervals in blade-element performance can be calculated from the charts.

The measurement-error charts can be employed along with the procedure devised at the Gas Turbine Laboratory of the Massachusetts Institute of Technology for the estimation of uncertainty intervals in calculated performance and can also be of assistance in the evaluation of data and in the planning of instrumentation for research or development.

INTRODUCTION

The attainment of design rotor pressure ratio for an axial-flow-compressor stage depends upon the correct prediction of blade-element turning angle and loss, upon an accurate design distribution radially of the local specific mass flow downstream of the rotor, and upon the agreement between the actual and design rotor-inlet flow distribution. Rotor blade-element design errors can result from the approximate nature of available design-data correlations, from blade manufacturing tolerances, and from the necessary simplifications in the design equations. Discrepancies between the actual and design rotor-inlet flow distribution can result from the foregoing types of design errors in preceding blade rows. (The design variables and their sources of error are identified and discussed in the section ANALYTICAL APPROACH.)

A means for estimating the error in a performance parameter due to an assumed error in a blade-element design variable or to an error in the inlet flow conditions is useful to both the compressor designer and to the research worker. Therefore, an analysis of this problem was made, the results of which are presented in this chapter. From the available equations relating blade-element performance parameters to the design variables, differential formulas were calculated that relate a small change in a design variable to the consequent change in the performance parameter. The formulas are presented in this chapter in the form of carpet plots, and the significant trends are discussed.

3479

An analysis of this type may be expected to indicate the degree of design control required for a given velocity diagram as evidenced by its sensitivity to design errors. Among a group of suitable design velocity diagrams, the analysis may show that one diagram is relatively insensitive to design errors, thus indicating that it would be the best choice for the design. The charts can also be employed to determine, in certain cases, whether an iteration of the design calculations is warranted.

The interpretation of experimental data requires some consideration of measurement errors. This problem is particularly relevant to the work of the researcher and also to the compressor designer, since correlations of design variables are based on experimental data, and compressor development programs depend on the interpretation and application of experimental data. Differential formulas were calculated that give the error in a performance parameter caused by a measurement error in one of the flow properties. These formulas are presented in this chapter in the form of carpet plots. A method for combining the effects of several measurement errors is outlined.

SYMBOLS

The following symbols are used in this chapter:

a	speed of sound
D	diffusion factor
H	total or stagnation enthalpy
H_M	total enthalpy calculated from change of moment of momentum
h	static enthalpy
M	Mach number
P	total or stagnation pressure

3479

p	static or stream pressure
R	gas constant
r	radius
T	total or stagnation temperature
U	rotor speed
V	air velocity
β	air angle, angle between air velocity and axial direction, deg
γ	ratio of specific heats
δ°	deviation angle, angle between outlet-air direction and tangent to blade mean camber line at trailing edge, deg
η_{ad}	adiabatic efficiency
ρ	density
σ	solidity, ratio of chord to spacing
Ω	quantity $\frac{P'_{2,id}}{P'_2} - 1$
$\bar{\omega}$	total-pressure-loss coefficient

Subscripts:

d	design value
h	hub
id	ideal
l	lower limit of uncertainty interval
sys	denotes systematic error
t	tip
u	upper limit of uncertainty interval
z	axial direction

0	station ahead of guide vanes or stators
1	station at rotor inlet or stator exit
2	station at rotor exit
i . . . viii	denotes variable in error

Superscript:

'	indicates quantity relative to rotor

3479

ANALYTICAL APPROACH

Consider a function of several variables $f(x_1,x_2, \ldots x_n)$. The change in f caused by a given set of small changes in $x_1,x_2, \ldots x_n$ is given approximately by the following formula (ref. I, ch. IV):

$$\Delta f = \frac{\partial f}{\partial x_1} \Delta x_1 + \frac{\partial f}{\partial x_2} \Delta x_2 + \ldots + \frac{\partial f}{\partial x_n} \Delta x_n \tag{1}$$

The nth term of formula (1)

$$\Delta f_n = \frac{\partial f}{\partial x_n} \Delta x_n \tag{2}$$

can be directly calculated (for an assumed value of Δx_n) and plotted as a function of the parameters that fix the value of $\partial f/\partial x_n$. This procedure is used in the present report.

The degree of approximation of formula (2) depends upon the way f varies with x_n and upon the magnitude of Δx_n. The accuracy of the formulas presented in this report for reasonable magnitudes of design errors was spot-checked by means of sample calculations and plots. The results of these calculations are given in appendix A. These checks do not constitute a general proof of the accuracy of the formulas, but do verify their applicability for certain conditions of flow and velocity diagram.

Design Errors

A brief outline of the blade-element approach to single-stage-compressor design follows in order to clarify the application of formula (1) to the analysis of design errors.

For given design values of pressure ratio, mass flow, rotational speed, and tip diameter, the hub profile and the preliminary velocity diagrams are calculated by methods discussed in chapter VIII (ref. 2). These preliminary velocity diagrams determine approximate values of diffusion factor and other blade-loading and blade-configuration parameters. This information permits the estimation of the radial distribution of the relative total-pressure-loss coefficient $\bar{\omega}$ (or $\bar{\omega}'$) for each blade row as discussed in chapter VII (ref. 2). The velocity-diagram calculations (including the radial-equilibrium calculation) are then repeated in order to incorporate the effects of the loss estimation. Finally, the methods of chapter VII (ref. 2) can be employed for the selection of blade-section cambers, incidence angles, and deviation angles.

3479

The employment of blade elements in this design procedure (as discussed in ch. III (ref. 3)) requires the estimation or calculation of the radii to each blade element at the axial stations upstream and downstream of the rotor. Thus, since r_1 is assigned by the designer, r_2 is identified as a design variable. For a rotor, the design method outlined in the preceding paragraph requires predictions of relative stagnation-pressure loss (in terms of $\bar{\omega}'$) and of deviation angle. The radial-equilibrium calculation and the condition of continuity determine the values of axial velocity or local specific mass flow downstream of the rotor for each blade element. Three additional design variables are, therefore, $\bar{\omega}'$, β_2', and $(\rho V_z)_2$. (The use of the local specific mass flow $(\rho V_z)_2$ was found to be more convenient in this analysis than the axial velocity $V_{z,2}$.)

CH-30

Errors in the design rotor-inlet flow distribution can be caused by design or blade manufacturing tolerances or errors in any of the upstream blade rows. At the design mass flow, these errors can lead to off-design values of rotor-inlet stagnation pressure P_1, absolute air angle β_1, local specific mass flow $(\rho V_z)_1$, and stagnation enthalpy H_1.

In summary, then, the design variables for rotor blade elements are identified as P_1, β_1, $(\rho V_z)_1$, H_1, $\bar{\omega}'$, β_2', $(\rho V_z)_2$, and r_2. Instead of the general design variable P_1, the loss parameter $\bar{\omega}$ for the adjacent upstream stationary blade row can be used. The agreement between the actual and design values of a performance parameter (such as P_2) depends, within the limitations of the design system, on the agreement between the actual and design values of these design variables.

In the following discussion, the foregoing design variables are identified by the lower-case Roman numerals i to viii as follows:

P_1 or $\bar{\omega}$	β_1	$(\rho V_z)_1$	H_1	$\bar{\omega}'$	β_2'	$(\rho V_z)_2$	r_2
i or (i)	ii	iii	iv	v	vi	vii	viii

The symbol denoting the error in a performance parameter due to a design error in any one variable (assuming for the moment that all other variables are correct) is identified by the appropriate lower-case Roman numeral subscript. For instance, $(\Delta H_2/H_2)_i$ denotes the error in H_2 due to an error solely in P_1. The stator (or guide-vane) loss parameter $\bar{\omega}$ is not an independent design variable; an error in $\bar{\omega}$ is one of many sources of error in P_1, and it is denoted by parentheses around its identifying number.

Some sources of errors in the variables are as follows:

Design variable	Some sources of error
$\bar{\omega}'$	(1) Accuracy of loss parameter and incidence-angle correlation system (ch. VII (ref. 2))
β_2'	(2) Accuracy of deviation-angle correlation system (3) Blade-fabrication tolerances
$(\rho V_z)_2$	(4) Degree of simplification of radial-equilibrium equation (5) Effects of errors in $\bar{\omega}'$ and β_2' on radial-equilibrium calculation (6) Inaccurate allowance for wall boundary-layer development
r_2	(7) Same as (4), (5), and (6) if r_2 is calculated (8) If r_2 is assumed, error depends on degree of radial shift in flow as gas crosses rotor

The foregoing types of design errors in blade rows upstream of a given rotor contribute to discrepancies between actual and design values of P_1, β_1, $(\rho V_z)_1$, and H_1. For the inlet stage of a compressor, an additional source of such errors lies in the performance of the inlet diffuser section.

A basic source of disagreement between actual and design performance is contained in certain simplifications to the equations of motion as applied to the blade-element design method (e.g., the assumptions of axial symmetry and steady flow). This source of error is not amenable to analytical investigation and is not considered in this chapter.

The design variables P_1, β_1, $(\rho V_z)_1$, H_1, $\bar{\omega}'$, β_2', $(\rho V_z)_2$, and r_2, in conjunction with known inlet conditions, determine the value of a compressor blade-element performance parameter. For the purposes of this investigation, then, any of the blade-element performance parameters can be designated as a function of these eight design variables:

$$f = f\left[P_1,\ \beta_1,\ (\rho V_z)_1,\ H_1,\ \bar{\omega}',\ \beta_2',\ (\rho V_z)_2,\ r_2\right] \tag{3}$$

3479

Formula (1) (the total differential of f) is particularized as follows for application to the analysis of design errors:

$$\Delta f = \frac{\partial f}{\partial P_1}\Delta P_1 + \frac{\partial f}{\partial \beta_1}\Delta\beta_1 + \frac{\partial f}{\partial (\rho V_z)_1}\Delta(\rho V_z)_1 + \frac{\partial f}{\partial H_1}\Delta H_1 +$$

$$\frac{\partial f}{\partial \bar{\omega}'}\Delta\bar{\omega}' + \frac{\partial f}{\partial \beta_2'}\Delta\beta_2' + \frac{\partial f}{\partial (\rho V_z)_2}\Delta(\rho V_z)_2 + \frac{\partial f}{\partial r_2}\Delta r_2 \tag{1a}$$

CH-30 back

The partial-derivative coefficients of formula (1a) can be calculated from the available blade-element performance equations. Each individual term $\left(\text{such as } \frac{\partial f}{\partial P_1}\Delta P_1\right)$ represents the contribution to the total error in f caused by a design error in one variable only (ΔP_1, e.g.), with all other design variables assumed correct.

For the calculations and the plotting of the results, it is convenient to make all terms of formula (1a) dimensionless in order to reduce the number of parameters determining the value of each error term. Formula (1a) is modified as follows:

$$\frac{\Delta f}{f} = \frac{P_1}{f}\frac{\partial f}{\partial P_1}\frac{\Delta P_1}{P_1} + \frac{1}{f}\frac{\partial f}{\partial \beta_1}\Delta\beta_1 + \frac{(\rho V_z)_1}{f}\frac{\partial f}{\partial (\rho V_z)_1}\frac{\Delta(\rho V_z)_1}{(\rho V_z)_1} + \frac{H_1}{f}\frac{\partial f}{\partial H_1}\frac{\Delta H_1}{H_1} +$$

$$\frac{1}{f}\frac{\partial f}{\partial \bar{\omega}'}\Delta\bar{\omega}' + \frac{1}{f}\frac{\partial f}{\partial \beta_2'}\Delta\beta_2' + \frac{(\rho V_z)_2}{f}\frac{\partial f}{\partial (\rho V_z)_2}\frac{\Delta(\rho V_z)_2}{(\rho V_z)_2} + \frac{r_2}{f}\frac{\partial f}{\partial r_2}\frac{\Delta r_2}{r_2} \tag{1b}$$

For cases where a performance parameter is associated with axial station 2 (f_2), any one of the first four terms might contain as many as eight design variables. A degree of further simplification in the plotting of some of these formulas is achieved by the use of certain performance-parameter error terms as intermediate variables. In certain cases the formula for one term of (1b) takes the following form:

$$\left(\frac{\Delta f_2}{f_2}\right)_i = Y\left[\bar{\omega}',\ \beta_2',\ (\rho V_z)_2,\ r_2\right]\ Z\left[P_1,\ \beta_1,\ (\rho V_z)_1,\ H_1\right]\frac{\Delta P_1}{P_1} \tag{4}$$

A formula for error in a performance parameter associated with axial station 1 might be

$$\left(\frac{\Delta f_1}{f_1}\right)_i = Z\left[P_1,\ \beta_1,\ (\rho V_z)_1,\ H_1\right]\frac{\Delta P_1}{P_1} \tag{5}$$

In this case, formula (4) can be expressed in terms of the intermediate variable f_1 as follows:

$$\left(\frac{\Delta f_2}{f_2}\right)_i = Y\left[\bar{\omega}',\ \beta_2',\ (\rho V_z)_2,\ r_2\right]\left(\frac{\Delta f_1}{f_1}\right)_i \tag{4a}$$

3479

Formula (1b) can be written as follows:

$$\frac{\Delta f}{f} = \left(\frac{\Delta f}{f}\right)_i + \left(\frac{\Delta f}{f}\right)_{ii} + \ldots + \left(\frac{\Delta f}{f}\right)_{viii} \tag{1c}$$

Each term of formula (1c) represents the contribution to the relative error in f of an error in the particular design variable identified by the subscript.

Formula (1c) gives a value of relative error in f caused by a given set of errors in the design variables. The only case for which a set of errors in design variables is known is the case of analysis of experimental data. For this case, formula (1c) can be applied to determine, at least approximately, what design errors may have caused a measured discrepancy between the actual and design values of a performance parameter. This use of the design-error charts is outlined in a later section.

The estimation of a probable discrepancy between the actual and design values of a performance parameter requires that the design errors be identified as either random errors or as systematic errors. For the purposes of this investigation, random errors are defined as errors that are unpredictably positive or negative. Systematic errors are predictable in sign, and in some cases an approximate estimate of their magnitudes can be made. An example of a systematic design error is the error in local specific mass flow (or axial velocity) caused by neglect of the entropy gradient during the radial-equilibrium calculation. This type of design error depends on the design flow distribution and the radial distribution of blade losses.

The approximate nature of the available correlations of design data (deviation angle and loss) leads to random design errors. The actual causes of such discrepancies are not known; their influence cannot, at present, be correlated with the various combinations of velocity-diagram parameters.

For the analysis of random errors, an uncertainty interval in a design variable can be estimated on the basis of past experience. An uncertainty interval in β_1, for instance, can be defined as a finite interval in β_1, such as $\beta_{1,u} - \beta_{1,l}$, for which a definite statistical probability exists that the value of β_1 will lie. For example, if, for a design value of $\beta_1 = 30^\circ$, 80 percent of the actual values of β_1 for different design cases fall in the interval from $\beta_1 = 29^\circ$ to $\beta_1 = 31^\circ$, then the uncertainty interval corresponding to odds of 4 to 1 is 2°. The term $\frac{1}{f}\frac{\partial f}{\partial \beta_1}\Delta\beta_1 = \left(\frac{\Delta f}{f}\right)_{ii}$ represents the corresponding uncertainty interval in f due to that in β_1 only. For the uncertainty interval in f due to the uncertainty intervals corresponding to the same odds in all the design variables, the second-power formula of reference 4 can be employed:

3479

$$\left(\frac{\Delta f}{f}\right)^2 = \left(\frac{\Delta f}{f}\right)_i^2 + \cdot \cdot \cdot + \left(\frac{\Delta f}{f}\right)_{viii}^2 \tag{6}$$

The uncertainty interval in f due to the uncertainty intervals in all of the design variables for a given probability can be calculated approximately for a mean-radius condition only. The reasons for this limitation are given in the section entitled Use of Design-Error Charts (p. 258). As an example of the use of formula (6), uncertainty intervals in $\bar{\omega}'$ and β_2' would be combined as follows to give the corresponding interval in the performance parameter f:

$$\frac{\Delta f}{f} = \sqrt{\left(\frac{1}{f}\frac{\partial f}{\partial \bar{\omega}'}\Delta\bar{\omega}'\right)^2 + \left(\frac{1}{f}\frac{\partial f}{\partial \beta_2'}\Delta\beta_2'\right)^2}$$

If all the uncertainty intervals of the design variables are estimated on the basis of the best available information so that the same odds (say b to 1) can be quoted that the value of each variable will lie within its interval, then, according to reference 4, statistical analysis shows that the odds will be b to 1 that the actual value of the performance parameter f will fall within the uncertainty interval given by formula (6).

The errors in axial velocity caused by neglect of the entropy gradient in the radial-equilibrium calculation cannot be interpreted as uncertainty intervals but as estimated corrections to the design values. An investigation of these errors (wherein the error is discussed in terms of axial velocity rather than the local specific mass flow) and a method of making the corrections are reported in reference 5. These estimated corrections and uncertainty intervals can be combined as follows:

$$f_{u,l} = f_d \left\{ 1 + \left[\left(\frac{\Delta f}{f}\right)_i + \cdot \cdot \cdot + \left(\frac{\Delta f}{f}\right)_{viii} \right]_{sys} \pm \frac{1}{2}\sqrt{\left(\frac{\Delta f}{f}\right)_i^2 + \cdot \cdot \cdot + \left(\frac{\Delta f}{f}\right)_{viii}^2} \right\} \tag{7}$$

The second term of formula (7) constitutes the estimated corrections to the design value of f for the systematic design errors, and the last term represents half the uncertainty interval in f due to the uncertainty intervals in each of the design variables.

3479

The eight terms of formula (1b) were calculated (where applicable) for each of the following blade-element performance parameters: axial velocities $V_{z,1}$ and $V_{z,2}$, relative stagnation enthalpies H_1' and H_2', stagnation enthalpy H_2, stagnation pressures P_1 and P_2, relative air angle β_1', absolute air angle β_2, and diffusion factor D. The stagnation pressure P_1, which is one of the rotor design variables, is a performance parameter only in the specialized sense that is affected by design errors in stationary-blade-row loss parameter $\bar{\omega}$. The resulting formulas are presented in this report in the form of carpet and lattice plots. For the purpose of preparing the charts, unit errors were assigned to the design variables (1 percent, 0.01, or 1°, as applicable). The technique of preparing plots of two or more independent parameters (carpet and lattice plots) is discussed in reference 6.

The analysis was made for a rotor of any stage of a compressor. The results are given for blade-element performance parameters only; the estimation of uncertainty intervals in the radially averaged over-all performance of a stage is not discussed in this report. This problem involves considerations of statistical and probability theory that are beyond the scope of the present investigation.

Measurement Errors

For the analysis of measurement errors, formula (1) assumes the following form:

$$\Delta f = \frac{\partial f}{\partial P_1}\Delta P_1 + \frac{\partial f}{\partial p_1}\Delta p_1 + \frac{\partial f}{\partial \beta_1}\Delta \beta_1 + \frac{\partial f}{\partial T_1}\Delta T_1 + \frac{\partial f}{\partial P_2}\Delta P_2 + \frac{\partial f}{\partial p_2}\Delta p_2 + \frac{\partial f}{\partial \beta_2}\Delta \beta_2 + \frac{\partial f}{\partial T_2}\Delta T_2 \tag{1d}$$

Formula (1d) can be applied directly only in cases where, for a specific experiment, each of the error terms is known. This situation, of course, is never realized. When the best methods of calibration are used, measurement errors are considered as random errors and can only be

estimated; thus, the statistical approach outlined in the preceding section was applied also to the analysis of measurement errors. The terms of formula (1d) are interpreted as uncertainty intervals for the function f due to uncertainty intervals for the same prescribed odds in each variable. The uncertainty interval in f due to all the estimated errors can be calculated from the following formula (in dimensionless form):

3479

$$\left(\frac{\Delta f}{f}\right)^2 = \left(\frac{P_1}{f}\frac{\partial f}{\partial P_1}\frac{\Delta P_1}{P_1}\right)^2 + \left(\frac{p_1}{f}\frac{\partial f}{\partial p_1}\frac{\Delta p_1}{p_1}\right)^2 + \left(\frac{1}{f}\frac{\partial f}{\partial \beta_1}\Delta\beta_1\right)^2 + \left(\frac{T_1}{f}\frac{\partial f}{\partial T_1}\frac{\Delta T_1}{T_1}\right)^2 + \left(\frac{P_2}{f}\frac{\partial f}{\partial P_2}\frac{\Delta P_2}{P_2}\right)^2 + \left(\frac{p_2}{f}\frac{\partial f}{\partial p_2}\frac{\Delta p_2}{p_2}\right)^2 + \left(\frac{1}{f}\frac{\partial f}{\partial \beta_2}\Delta\beta_2\right)^2 + \left(\frac{T_2}{f}\frac{\partial f}{\partial T_2}\frac{\Delta T_2}{T_2}\right)^2 \tag{8}$$

Formula (8) is valid only for the estimation of uncertainty intervals due to random errors. That is, as the number of observations of each variable approaches infinity, the mean of all observations should approach the true value of the variable.

The error terms of formula (8) were calculated, and the results are presented in chart form for the following performance parameters: ρV_z, β', $\overline{\omega}$, $\overline{\omega}'$, η_{ad}, $H_{M,2}$, and D.

CALCULATION AND PRESENTATION OF FORMULAS

In the following presentation, all formulas are designated by a lower-case letter, a capital letter, and a lower-case Roman numeral. The letters d and m denote, respectively, the analysis of design and measurement errors. The capital letter identifies the performance parameter under analysis, and the lower-case Roman numeral identifies the variable in error. The following tables provide this identification:

Case d - Design-error performance parameters										
Performance parameter	P_1	$V_{z,1}$	H_1'	β_1'	H_2'	$V_{z,2}$	H_2	P_2	β_2	D
Formula symbol	A	B	C	D	E	F	G	H	J	K

Case d - Design variables								
Design variable	P_1 or $\bar{\omega}$	β_1	$(\rho V_z)_1$	H_1	$\bar{\omega}'$	β_2'	$(\rho V_z)_2$	r_2
Formula numeral	i or (i)	ii	iii	iv	v	vi	vii	viii

Case m - Measurement-error performance parameters							
Performance parameter	(ρV_z)	β'	$\bar{\omega}$	$\bar{\omega}'$	η_{ad}	$H_{M,2}$	D
Formula symbol	A	B	C	D	E	F	G

Case m - Flow variables								
Flow variable	p_1	P_1	T_1	β_1	p_2	P_2	T_2	β_2
Formula numeral	i	ii	iii	iv	v	vi	vii	viii

3479

The symbol for the error in the performance parameter under consideration is given a subscript to identify the source of error. This subscript is the lower case Roman numeral of the appropriate table.

Design-Error Formulas

The design-error differential formulas were calculated from the following equations:

$$P_1 = P_0 \left\{ 1 - \bar{\omega} \left[1 - \left(\frac{h_0}{H_1} \right)^{\frac{\gamma}{\gamma-1}} \right] \right\} \tag{9}$$

$$V_{z,1} = \sqrt{2}\,(H_1 - h_1)^{1/2} \cos \beta_1 \tag{10}$$

$$H_1' = H_1 + \frac{1}{2} U_1^2 - U_1 V_{z,1} \tan \beta_1 \tag{11}$$

$$\tan \beta_1' = \frac{U_1}{V_{z,1}} - \tan \beta_1 \tag{12}$$

$$H_2' = H_1' + \frac{1}{2} U_1^2 \left[\left(\frac{r_2}{r_1}\right)^2 - 1\right] \tag{13}$$

$$V_{z,2} = \sqrt{2}\,(H_2' - h_2)^{1/2} \cos \beta_2' \tag{14}$$

3479

$$H_2 = H_1 + U_1^2 \left(\frac{r_2}{r_1}\right)^2 - U_1 \frac{r_2}{r_1} V_{z,2} \tan \beta_2' - U_1 V_{z,1} \tan \beta_1 \tag{15}$$

$$\frac{P_2}{P_1} = \left(\frac{H_2}{H_1}\right)^{\frac{\gamma}{\gamma-1}} \left\{1 - \bar{\omega}' \left(\frac{P_1'}{P_2'}\right)_{id} \left[1 - \left(\frac{h_1}{H_1'}\right)^{\frac{\gamma}{\gamma-1}}\right]\right\} \tag{16}$$

$$\tan \beta_2 = \frac{r_2}{r_1} \frac{U_1}{V_{z,2}} - \tan \beta_2' \tag{17}$$

CH-31

$$D = 1 + \frac{\sin \beta_1'}{2\sigma} - \left(1 + \frac{\sin \beta_2'}{2\sigma}\right) \frac{V_{z,2} \cos \beta_1'}{V_{z,1} \cos \beta_2'} \tag{18}$$

$$(\rho V_z)_1 = \frac{\sqrt{2}\,\gamma}{\gamma - 1} \frac{P_1}{H_1} \left(\frac{h_1}{H_1}\right)^{\frac{1}{\gamma-1}} (H_1 - h_1)^{1/2} \cos \beta_1 \tag{19}$$

$$(\rho V_z)_2 = \frac{\sqrt{2}\,\gamma}{\gamma - 1} \frac{P_2'}{H_2'} \left(\frac{h_2}{H_2'}\right)^{\frac{1}{\gamma-1}} (H_2' - h_2)^{1/2} \cos \beta_2' \tag{20}$$

$$\left(\frac{P_2'}{P_1'}\right)_{id} = \left(\frac{H_2'}{H_1'}\right)^{\frac{\gamma}{\gamma-1}} \tag{21}$$

(Formula (18) was obtained from the form given in ref. 7 by rearranging terms.) Some of the resulting differential formulas included terms which were considered sufficiently small that they could be neglected. Two specific examples of the general procedure used in deriving the differential formulas are presented in appendix B.

The design-error formulas contain certain parameters that are presented in the form of carpet and lattice plots. The formulas for these parameters are as follows:

$$\frac{H_2'}{H_1'} = \frac{1}{1 - \frac{\gamma - 1}{2} \frac{\left(M_2'\right)^2}{1 + \frac{\gamma - 1}{2}\left(M_2'\right)^2} \left[1 - \left(\frac{r_1}{r_2}\right)^2\right] \cos^2\beta_2' \left(\tan\beta_2 + \tan\beta_2'\right)^2}$$

(22)
(fig. 1)

3479

$$\Omega = \frac{P_{2,id}'}{P_2'} - 1 = \frac{\bar{\omega}' \left\{1 - \left[1 + \frac{\gamma - 1}{2}\left(M_1'\right)^2\right]^{-\frac{\gamma}{\gamma-1}}\right\}}{\left(\frac{H_2'}{H_1'}\right)^{\frac{\gamma}{\gamma-1}} - \bar{\omega}' \left\{1 - \left[1 + \frac{\gamma - 1}{2}\left(M_1'\right)^2\right]^{-\frac{\gamma}{\gamma-1}}\right\}}$$

(23)
(fig. 2)

The following differential formulas were obtained from the analysis of errors in design variables:

$$\left(\frac{\Delta P_1}{P_1}\right)_{(i)} = -\frac{1 - \left(1 + \frac{\gamma - 1}{2} M_0^2\right)^{-\frac{\gamma}{\gamma-1}}}{1 - \bar{\omega}\left[1 - \left(1 + \frac{\gamma - 1}{2} M_0^2\right)^{-\frac{\gamma}{\gamma-1}}\right]} \Delta\bar{\omega}$$

(dA-(i))
(fig. 3)

$$\left(\frac{\Delta V_{z,1}}{V_{z,1}}\right)_i = -\frac{1}{1 - M_1^2} \frac{\Delta P_1}{P_1}$$

(dB-i)
(fig. 4(a))

$$\left(\frac{\Delta V_{z,1}}{V_{z,1}}\right)_{ii} = \frac{\pi M_1^2 \tan\beta_1}{180\left(1 - M_1^2\right)} \Delta\beta_1$$

(dB-ii)
(fig. 4(b))

$$\left(\frac{\Delta V_{z,1}}{V_{z,1}}\right)_{iii} = \frac{1}{1 - M_1^2} \frac{\Delta(\rho V_z)_1}{(\rho V_z)_1}$$

(dB-iii)
(fig. 4(a), substitute ρV_z for P, multiply result by -1)

$$\left(\frac{\Delta V_{z,1}}{V_{z,1}}\right)_{iv} = \frac{1 - \frac{1}{2} M_1^2}{1 - M_1^2} \frac{\Delta H_1}{H_1}$$

(dB-iv)
(fig. 4(c))

$$\left(\frac{\Delta H_1'}{H_1'}\right)_{i,iii} = -(\gamma - 1) \frac{M_1^2 \sin \beta_1 \cos \beta_1 (\tan \beta_1 + \tan \beta_1')}{1 + \frac{\gamma - 1}{2} M_1^2 \cos^2\beta_1 \sec^2\beta_1'} \cdot \left(\frac{\Delta V_{z,1}}{V_{z,1}}\right)_{i,iii}$$

(dC-i,iii)
(fig. 5(a))

$$\left(\frac{\Delta H_1'}{H_1'}\right)_{ii} = \frac{\pi(\gamma - 1) M_1^2 (\sec^2\beta_1 - M_1^2) \cos^2\beta_1 (\tan \beta_1 + \tan \beta_1')}{180 (1 - M_1^2)\left(1 + \frac{\gamma - 1}{2} M_1^2 \cos^2\beta_1 \sec^2\beta_1'\right)} \Delta\beta_1$$

(dC-ii)
(fig. 5(b))

$$\left(\frac{\Delta H_1'}{H_1'}\right)_{iv} = \frac{1 + \frac{\gamma - 1}{2} M_1^2}{\left(1 + \frac{\gamma - 1}{2} M_1^2 \cos^2\beta_1 \sec^2\beta_1'\right)(1 - M_1^2)} \times$$

$$\left[1 - M_1^2 \cos^2\beta_1 (1 - \tan \beta_1 \tan \beta_1') - \frac{\gamma M_1^2}{1 + \frac{\gamma - 1}{2} M_1^2} \sin \beta_1 \cos \beta_1 (\tan \beta_1 + \tan \beta_1')\right] \frac{\Delta H_1}{H_1}$$

(dC-iv)
(fig. 5(c))

$$(\Delta\beta_1')_{i,iii,iv} = \frac{180}{\pi} \cos^2\beta_1' (\tan \beta_1 + \tan \beta_1')\left(\frac{\Delta V_{z,1}}{V_{z,1}}\right)_{i,iii,iv}$$

(dD-i,iii,iv)
(fig. 6(a))

$$(\Delta\beta_1')_{ii} = \frac{\cos^2\beta_1'}{\cos^2\beta_1}\left[1 + \frac{M_1^2}{1 - M_1^2} \sin \beta_1 \cos \beta_1 (\tan \beta_1 + \tan \beta_1')\right] \Delta\beta_1$$

(dD-ii)
(fig. 6(b))

$$\left(\frac{\Delta H_2'}{H_2'}\right)_{i-iv} = \frac{H_1'}{H_2'}\left(\frac{\Delta H_1'}{H_1'}\right)_{i-iv}$$

(dE-i-iv)
(No fig. necessary)

$$\left(\frac{\Delta H_2'}{H_2'}\right)_{viii} = (\gamma - 1) \frac{(M_2')^2}{1 + \frac{\gamma - 1}{2} (M_2')^2} \cos^2\beta_2' (\tan \beta_2 + \tan \beta_2')^2 \frac{\Delta r_2}{r_2}$$

(dE-viii)
(fig. 7)

3479

CH-31 back

$$\left(\frac{\Delta V_{z,2}}{V_{z,2}}\right)_{i} = -\frac{1}{\gamma - 1}\,\frac{1 + \frac{\gamma - 1}{2}\left(M_2'\right)^2}{1 - \left(M_2'\right)^2}\left(\frac{\Delta H_2'}{H_2'}\right)_{i} - \frac{1}{1 - \left(M_2'\right)^2}\,\frac{\Delta P_1}{P_1} \qquad \begin{matrix}\text{(dF-i)}\\ \text{(fig. 8(a))}\end{matrix}$$

$$\left(\frac{\Delta V_{z,2}}{V_{z,2}}\right)_{ii,iii} = -\frac{1}{\gamma - 1}\,\frac{1 + \frac{\gamma - 1}{2}\left(M_2'\right)^2}{1 - \left(M_2'\right)^2}\left(\frac{\Delta H_2'}{H_2'}\right)_{ii,iii} \qquad \begin{matrix}\text{(dF-ii,iii)}\\ \text{(fig. 8(b))}\end{matrix}$$

3479

$$\left(\frac{\Delta V_{z,2}}{V_{z,2}}\right)_{iv} = \frac{\gamma}{(\gamma - 1)\left[1 - \left(M_2'\right)^2\right]}\,\frac{\Delta H_1}{H_1} - \frac{1 + \frac{\gamma - 1}{2}\left(M_2'\right)^2}{(\gamma - 1)\left[1 - \left(M_2'\right)^2\right]}\left(\frac{\Delta H_2'}{H_2'}\right)_{iv}$$

$$\begin{matrix}\text{(dF-iv)}\\ \text{(fig. 8(c))}\end{matrix}$$

$$\left(\frac{\Delta V_{z,2}}{V_{z,2}}\right)_{v} = \frac{\Omega}{\bar{\omega}'\left[1 - \left(M_2'\right)^2\right]}\,\Delta\bar{\omega}' \qquad \begin{matrix}\text{(dF-v)}\\ \text{(fig. 8(d))}\end{matrix}$$

$$\left(\frac{\Delta V_{z,2}}{V_{z,2}}\right)_{vi} = \frac{\pi\left(M_2'\right)^2}{180\left[1 - \left(M_2'\right)^2\right]}\tan\beta_2'\,\Delta\beta_2' \qquad \begin{matrix}\text{(dF-vi)}\\ \text{(fig. 4(b), substitute}\\ M_2',\ \beta_2' \text{ for } M_1,\ \beta_1,\\ \text{respectively)}\end{matrix}$$

$$\left(\frac{\Delta V_{z,2}}{V_{z,2}}\right)_{vii} = \frac{1}{1 - \left(M_2'\right)^2}\,\frac{\Delta(\rho V_z)_2}{(\rho V_z)_2} \qquad \begin{matrix}\text{(dF-vii)}\\ \text{(fig. 4(a), substitute}\\ M_2',\ (\rho V_z)_2 \text{ for } M_1,\\ P_1, \text{ respectively,}\\ \text{multiply result by -1)}\end{matrix}$$

$$\left(\frac{\Delta V_{z,2}}{V_{z,2}}\right)_{viii} = \frac{1}{(\gamma - 1)\left[1 - \left(M_2'\right)^2\right]}\left\{\gamma\Omega - \left[1 + \frac{\gamma - 1}{2}\left(M_2'\right)^2\right]\right\}\left(\frac{\Delta H_2'}{H_2'}\right)_{viii}$$

$$\begin{matrix}\text{(dF-viii)}\\ \text{(fig. 8(e))}\end{matrix}$$

$$\left(\frac{\Delta H_2}{H_2}\right)_{i,iv} = \varphi\left(\frac{\Delta H_2'}{H_2'}\right)_{i,iv} + \psi\left(\frac{\Delta V_{z,2}}{V_{z,2}}\right)_{i,iv} \qquad \text{(dG-i,iv)}$$

where

$$\varphi = \frac{1 + \frac{\gamma - 1}{2}\left(M_2'\right)^2}{1 + \frac{\gamma - 1}{2}\left(M_2'\right)^2\cos^2\beta_2'\,\sec^2\beta_2} \qquad \begin{matrix}(24)\\ \text{(fig. 9(a))}\end{matrix}$$

and

$$\psi = -\frac{(\gamma - 1)(M_2')^2 \sin \beta_2' \cos \beta_2' (\tan \beta_2 + \tan \beta_2')}{1 + \frac{\gamma - 1}{2} (M_2')^2 \cos^2\beta_2' \sec^2\beta_2} \qquad \begin{matrix}(25)\\ (\text{fig. } 9(b))\end{matrix}$$

$$\left(\frac{\Delta H_2}{H_2}\right)_{ii,iii} = \frac{1 + \frac{\gamma - 1}{2} (M_2')^2}{1 + \frac{\gamma - 1}{2} (M_2')^2 \cos^2\beta_2' \sec^2\beta_2} \times$$

$$\left[1 + \frac{(M_2')^2}{1 - (M_2')^2} \sin \beta_2' \cos \beta_2' (\tan \beta_2 + \tan \beta_2')\right]\left(\frac{\Delta H_2'}{H_2'}\right)_{ii,iii}$$

(dG-ii,iii)
(fig. 10)

$$\left(\frac{\Delta H_2}{H_2}\right)_{v,vii} = \psi\left(\frac{\Delta V_{z,2}}{V_{z,2}}\right)_{v,vii} \qquad \begin{matrix}(dG\text{-}v,vii)\\ (\text{No fig. necessary})\end{matrix}$$

$$\left(\frac{\Delta H_2}{H_2}\right)_{vi} = -\frac{\pi(\gamma - 1)(M_2')^2 \left[\sec^2\beta_2' - (M_2')^2\right] \cos^2\beta_2' (\tan \beta_2 + \tan \beta_2')}{180 \left[1 - (M_2')^2\right] \left[1 + \frac{\gamma - 1}{2} (M_2')^2 \cos^2\beta_2' \sec^2\beta_2\right]} \Delta\beta_2'$$

(dG-vi)
(fig. 5(b), substitute M_2', β_2', β_2 for M_1, β_1, β_1', respectively)

$$\left(\frac{\Delta H_2}{H_2}\right)_{viii} = \xi \frac{\Delta r_2}{r_2} + \psi\left(\frac{\Delta V_{z,2}}{V_{z,2}}\right)_{viii} \qquad (dG\text{-}viii)$$

where

$$\xi = \frac{(\gamma - 1)(M_2')^2 \cos^2\beta_2' (\tan \beta_2 + \tan \beta_2')(2 \tan \beta_2 + \tan \beta_2')}{1 + \frac{\gamma - 1}{2} (M_2')^2 \cos^2\beta_2' \sec^2\beta_2} \qquad \begin{matrix}(26)\\ (\text{fig. } 9(c))\end{matrix}$$

$$\left(\frac{\Delta P_2}{P_2}\right)_i = \frac{\Delta P_1}{P_1} + \frac{\gamma}{\gamma - 1}\left(\frac{\Delta H_2}{H_2}\right)_i \qquad \begin{matrix}(dH\text{-}i)\\ (\text{No fig. necessary})\end{matrix}$$

$$\left(\frac{\Delta P_2}{P_2}\right)_{ii,iii,vi\text{-}viii} = \frac{\gamma}{\gamma - 1}\left(\frac{\Delta H_2}{H_2}\right)_{ii,iii,vi\text{-}viii}$$

(dH-ii,iii,vi-viii)
(No fig. necessary)

$$\left(\frac{\Delta P_2}{P_2}\right)_{iv} = \frac{\gamma}{\gamma - 1}\left[\left(\frac{\Delta H_2}{H_2}\right)_{iv} - \frac{\Delta H_1}{H_1}\right] \qquad \begin{matrix}(dH\text{-}iv)\\ (\text{No fig. necessary})\end{matrix}$$

[redacted]

3479

$$\left(\frac{\Delta P_2}{P_2}\right)_v = -\left\{\left[1 - (M_2')^2\right] + \frac{\gamma(M_2')^2 \sin\beta_2' \cos\beta_2' (\tan\beta_2 + \tan\beta_2')}{1 + \frac{\gamma - 1}{2}(M_2')^2 \cos^2\beta_2' \sec^2\beta_2}\right\}\left(\frac{\Delta V_{z,2}}{V_{z,2}}\right)_v$$

(dH-v)
(fig. 11)

$$(\Delta\beta_2)_{i-v,vii} = -\frac{180}{\pi}\cos^2\beta_2 (\tan\beta_2 + \tan\beta_2')\left(\frac{\Delta V_{z,2}}{V_{z,2}}\right)_{i-v,vii}$$

(dJ-i-v,vii)
(fig. 6(a), substitute β_2, β_2', $V_{z,2}$ for β_1', β_1, $V_{z,1}$, respectively)

$$(\Delta\beta_2)_{vi} = -\frac{\cos^2\beta_2}{\cos^2\beta_2'}\left[1 + \frac{(M_2')^2}{1 - (M_2')^2}\sin\beta_2'\cos\beta_2'(\tan\beta_2 + \tan\beta_2')\right]\Delta\beta_2'$$

(dJ-vi)
(fig. 6(b), substitute M_2', β_2', β_2 for M_1, β_1, β_1', respectively)

$$(\Delta\beta_2)_{viii} = \frac{180}{\pi}\cos^2\beta_2 (\tan\beta_2 + \tan\beta_2')\left[1 + \frac{(M_2')^2}{1 - (M_2')^2}\cos^2\beta_2'(\tan\beta_2 + \tan\beta_2')^2\right]\frac{\Delta r_2}{r_2}$$

(dJ-viii)
(fig. 12)

$$(\Delta D)_{i-iv} = A(\Delta\beta_1')_{i-iv} + \Gamma\left(\frac{\Delta V_{z,2}}{V_{z,2}} - \frac{\Delta V_{z,1}}{V_{z,1}}\right)_{i-iv} \qquad \text{(dK-i-iv)}$$

where

$$A = \frac{1}{2\sigma\cos\beta_1'} + (1 - D)\tan\beta_1' \qquad \begin{matrix}(27)\\ \text{(fig. 13(a))}\end{matrix}$$

and

$$\Gamma = -\left[\frac{\sin\beta_1'}{2\sigma} + (1 - D)\right] \qquad \begin{matrix}(28)\\ \text{(fig. 13(b))}\end{matrix}$$

$$(\Delta D)_{v,vii,viii} = \Gamma\left(\frac{\Delta V_{z,2}}{V_{z,2}}\right)_{v,vii,viii} \qquad \begin{matrix}\text{(dK-v,vii,viii)}\\ \text{(No fig. necessary)}\end{matrix}$$

3479

$$\frac{V_1'}{V_2'}(\Delta D)_{vi} = -\frac{\pi}{180}\left[\left(1 + \frac{\sin\beta_2'}{2\sigma}\right)\frac{\tan\beta_2'}{1 - (M_2')^2} + \frac{\cos\beta_2'}{2\sigma}\right]\Delta\beta_2' \qquad \begin{matrix}(dK\text{-}vi)\\(fig.\ 14)\end{matrix}$$

Measurement-Error Formulas

Measured quantities include the rotational speed, the inlet pressure and temperature, and the following flow properties: static pressure p, stagnation pressure P, absolute air angle β, and stagnation temperature T. In the following table, the calculated performance parameters are listed in the left column, and the flow properties of which they are explicit functions are listed in the right column:

3479

ρV_z	p,P,T,β
β'	p,P,T,β
$\bar{\omega}$	p_0,P_0,P_1
$\bar{\omega}'$	$p_1,P_1,T_1,\beta_1,P_2,T_2$
η_{ad}	P_1,T_1,P_2,T_2
H_M	$p_1,P_1,T_1,\beta_1,p_2,P_2,T_2,\beta_2$
D	$p_1,P_1,T_1,\beta_1,p_2,P_2,T_2,\beta_2$

The equations for the performance parameters in the foregoing table, as explicit functions of the measured flow properties, are as follows (for convenience in writing, some of the functions are given in terms of absolute velocity V):

$$\rho V_z = \left[\frac{2\gamma}{(\gamma - 1)\ RT}\right]^{\frac{1}{2}} P\left(\frac{p}{P}\right)^{\frac{1}{\gamma}}\left[1 - \left(\frac{p}{P}\right)^{\frac{\gamma-1}{\gamma}}\right]^{\frac{1}{2}}\cos\beta \tag{19a}$$

$$\tan\beta' = \left(\frac{\gamma - 1}{2\gamma RT}\right)^{\frac{1}{2}}\frac{U}{\left[1 - \left(\frac{p}{P}\right)^{\frac{\gamma-1}{\gamma}}\right]^{\frac{1}{2}}\cos\beta} - \tan\beta \tag{12a}$$

$$\bar{\omega} = \frac{P_0 - P_1}{P_0 - p_0} \tag{9a}$$

$$\bar{\omega}' = \left(\frac{P_2'}{P_1'}\right)_{id}\frac{1 - \dfrac{\frac{P_2}{P_1}}{\left(\frac{T_2}{T_1}\right)^{\frac{\gamma}{\gamma-1}}}}{1 - \dfrac{p_1}{P_1}\left(\dfrac{H_1}{H_1 + \frac{1}{2}U_1^2 - U_1V_1\sin\beta_1}\right)^{\frac{\gamma}{\gamma-1}}} \tag{16a}$$

$$\eta_{ad} = \frac{\left(\frac{P_2}{P_1}\right)^{\frac{\gamma-1}{\gamma}} - 1}{\frac{T_2}{T_1} - 1} \tag{29}$$

$$H_{M,2} = H_1 + U_2V_2 \sin \beta_2 - U_1V_1 \sin \beta_1 \tag{15a}$$

$$D = 1 - \left(\frac{U_2^2 + V_2^2 - 2U_2V_2 \sin \beta_2}{U_1^2 + V_1^2 - 2U_1V_1 \sin \beta_1}\right)^{1/2} + \frac{U_1 - U_2 + V_2 \sin \beta_2 - V_1 \sin \beta_1}{2\sigma \left(U_1^2 + V_1^2 - 2U_1V_1 \sin \beta_1\right)^{1/2}} \tag{18a}$$

3479

The analysis of measurement errors yielded the following formulas, which give the relative uncertainty interval in a performance parameter due to the corresponding uncertainty interval in the measurement of one flow property:

$$\left[\frac{\Delta(\rho V_z)}{\rho V_z}\right]_{i,v} = \frac{1}{\gamma}\left(1 - \frac{1}{M^2}\right)\frac{\Delta p}{p}$$ (mA-i,v) (fig. 15(a))

$$\left[\frac{\Delta(\rho V_z)}{\rho V_z}\right]_{ii,vi} = \frac{1}{\gamma}\left(\frac{1}{M^2} + \gamma - 1\right)\frac{\Delta P}{P}$$ (mA-ii,vi) (fig. 15(b))

$$\left[\frac{\Delta(\rho V_z)}{\rho V_z}\right]_{iii,vii} = -\frac{1}{2}\frac{\Delta T}{T}$$ (mA-iii,vii) (No fig. necessary)

$$\left[\frac{\Delta(\rho V_z)}{\rho V_z}\right]_{iv,viii} = -\frac{\pi}{180} \tan \beta \, \Delta\beta$$ (mA-iv,viii) (fig. 15(c))

$$(\Delta\beta')_{i,v} = \frac{180}{\pi} \frac{\cos^2\beta' \, (\tan \beta + \tan \beta')}{\gamma M^2} \frac{\Delta p}{p}$$ (mB-i,v) (fig. 16(a))

$$(\Delta\beta')_{ii,vi} = -\frac{180}{\pi} \frac{\cos^2\beta' \, (\tan \beta + \tan \beta')}{\gamma M^2} \frac{\Delta P}{P}$$ (mB-ii,vi) (fig. 16(a), prefix minus sign to result, substitute P for p)

$$(\Delta\beta')_{iii,vii} = -\frac{90}{\pi} \cos^2\beta' \, (\tan \beta + \tan \beta') \frac{\Delta T}{T}$$ (mB-iii,vii) (fig. 16(b))

$$(\Delta\beta')_{iv,viii} = -\cos^2\beta' \, (1 - \tan \beta \tan \beta') \, \Delta\beta$$ (mB-iv,viii) (fig. 16(c))

$$(\Delta\bar{\omega})_{ii} = -\left[\frac{1}{1 - \left(1 + \frac{\gamma - 1}{2} M_0^2\right)^{-\frac{\gamma}{\gamma-1}}} - \bar{\omega}\right]\frac{\Delta P_1}{P_1}$$ (mC-ii) (fig. 17)

$$(\Delta\bar{\omega}')_{ii} = \frac{\bar{\omega}'}{\omega}\frac{\Delta P_1}{P_1}$$ (mD-ii) (fig. 18)

$$(\Delta\bar{\omega}')_{iii} = -\frac{\gamma}{\gamma - 1}\frac{\bar{\omega}'}{\omega}\frac{\Delta T_1}{T_1}$$ (mD-iii) (fig. 18, multiply result by $-\frac{\gamma}{\gamma-1}$, substitute T_1 for P_1)

$$(\Delta\bar{\omega}')_{vi} = -\frac{\bar{\omega}'}{\omega}\frac{\Delta P_2}{P_2}$$ (mD-vi) (fig. 18, prefix minus sign to result, substitute P_2 for P_1)

$$(\Delta\bar{\omega}')_{vii} = \frac{\gamma}{\gamma - 1}\frac{\bar{\omega}'}{\omega}\frac{\Delta T_2}{T_2}$$ (mD-vii) (fig. 18, multiply result by $\frac{\gamma}{\gamma-1}$, substitute T_2 for P_1)

$$(\Delta\eta_{ad})_{ii} = -\frac{\gamma - 1}{\gamma}\frac{\eta_{ad}\left(\frac{P_2}{P_1}\right)^{\frac{\gamma-1}{\gamma}}}{\left(\frac{P_2}{P_1}\right)^{\frac{\gamma-1}{\gamma}} - 1}\frac{\Delta P_1}{P_1}$$ (mE-ii) (fig. 19(a))

$$(\Delta\eta_{ad})_{iii} = \frac{\eta_{ad}\frac{T_2}{T_1}}{\frac{T_2}{T_1} - 1}\frac{\Delta T_1}{T_1}$$ (mE-iii) (fig. 19(b))

$$(\Delta\eta_{ad})_{vi} = \frac{\gamma - 1}{\gamma}\frac{\eta_{ad}\left(\frac{P_2}{P_1}\right)^{\frac{\gamma-1}{\gamma}}}{\left(\frac{P_2}{P_1}\right)^{\frac{\gamma-1}{\gamma}} - 1}\frac{\Delta P_2}{P_2}$$ (mE-vi) (fig. 19(a), multiply result by -1, substitute $\Delta P_2/P_2$ for $\Delta P_1/P_1$)

3479

CH-32

$$(\Delta\eta_{ad})_{vii} = -\frac{\eta_{ad}\,\frac{T_2}{T_1}}{\frac{T_2}{T_1} - 1}\,\frac{\Delta T_2}{T_2}$$

(mE-vii)
(fig. 19(b), prefix minus sign to result, substitute $\Delta T_2/T_2$ for $\Delta T_1/T_1$)

$$\left(\frac{\Delta H_{M,2}}{H_1}\right)_i = \frac{\gamma - 1}{\gamma}\,\frac{\sin\beta_1\cos\beta_1\,(\tan\beta_1 + \tan\beta_1')}{1 + \frac{\gamma - 1}{2}M_1^2}\,\frac{\Delta p_1}{p_1}$$

(mF-i)
(fig. 20(a))

$$\left(\frac{\Delta H_{M,2}}{H_1}\right)_{ii} = -\frac{\gamma - 1}{\gamma}\,\frac{\sin\beta_1\cos\beta_1\,(\tan\beta_1 + \tan\beta_1')}{1 + \frac{\gamma - 1}{2}M_1^2}\,\frac{\Delta P_1}{P_1}$$

(mF-ii)
(fig. 20(a), prefix minus sign to result, substitute P_1 for p_1)

$$\left(\frac{\Delta H_{M,2}}{H_1}\right)_{iii} = \left[1 - \frac{\frac{\gamma - 1}{2}M_1^2\sin\beta_1\cos\beta_1\,(\tan\beta_1 + \tan\beta_1')}{1 + \frac{\gamma - 1}{2}M_1^2}\right]\frac{\Delta T_1}{T_1}$$

(mF-iii)
(fig. 20(c), substitute subscript 1 for 2 and subtract from 1)

$$\left(\frac{\Delta H_{M,2}}{H_1}\right)_{iv} = -\frac{\pi(\gamma - 1)\,M_1^2\cos^2\beta_1\,(\tan\beta_1 + \tan\beta_1')}{180\left(1 + \frac{\gamma - 1}{2}M_1^2\right)}\,\Delta\beta_1$$

(mF-iv)
(fig. 20(b))

$$\left(\frac{\Delta H_{M,2}}{H_{M,2}}\right)_v = -\frac{\gamma - 1}{\gamma}\,\frac{\sin\beta_2\cos\beta_2\,(\tan\beta_2 + \tan\beta_2')}{1 + \frac{\gamma - 1}{2}M_2^2}\,\frac{\Delta p_2}{p_2}$$

(mF-v)
(fig. 20(a), substitute subscript 2 for 1 and prefix minus sign)

$$\left(\frac{\Delta H_{M,2}}{H_{M,2}}\right)_{vi} = \frac{\gamma - 1}{\gamma}\,\frac{\sin\beta_2\cos\beta_2\,(\tan\beta_2 + \tan\beta_2')}{1 + \frac{\gamma - 1}{2}M_2^2}\,\frac{\Delta P_2}{P_2}$$

(mF-vi)
(fig. 20(a), substitute subscript 2 for 1, and P_2 for p_1)

3479

$$\left(\frac{\Delta H_{M,2}}{H_{M,2}}\right)_{vii} = \frac{\gamma - 1}{2} \frac{M_2^2 \sin \beta_2 \cos \beta_2 (\tan \beta_2 + \tan \beta_2')}{1 + \frac{\gamma - 1}{2} M_2^2} \frac{\Delta T_2}{T_2}$$

(mF-vii)
(fig. 20(c))

$$\left(\frac{\Delta H_{M,2}}{H_{M,2}}\right)_{viii} = \frac{\pi(\gamma - 1) M_2^2 \cos^2\beta_2 (\tan \beta_2 + \tan \beta_2')}{180 \left(1 + \frac{\gamma - 1}{2} M_2^2\right)} \Delta\beta_2$$

(mF-viii)
(fig. 20(b), substitute subscript 2 for 1 and multiply result by -1)

$$M_1^2 (\Delta D)_i = \frac{\cos^2\beta_1'}{\gamma} \left[\frac{\cos \beta_1' (\tan \beta_1 + \tan \beta_1')}{2\sigma} - \left(\frac{\sin \beta_1'}{2\sigma} + 1 - D\right)(1 - \tan \beta_1 \tan \beta_1')\right] \frac{\Delta p_1}{p_1}$$

(mG-i)
(fig. 21(a))

$$M_1^2 (\Delta D)_{ii} = -\frac{\cos^2\beta_1'}{\gamma} \left[\frac{\cos \beta_1' (\tan \beta_1 + \tan \beta_1')}{2\sigma} - \left(\frac{\sin \beta_1'}{2\sigma} + 1 - D\right)(1 - \tan \beta_1 \tan \beta_1')\right] \frac{\Delta P_1}{P_1}$$

(mG-ii)
(fig. 21(a), prefix minus sign to result, substitute P_1 for p_1)

$$(\Delta D)_{iii} = -\frac{\cos^2\beta_1'}{2} \left[\frac{\cos \beta_1' (\tan \beta_1 + \tan \beta_1')}{2\sigma} - \left(\frac{\sin \beta_1'}{2\sigma} + 1 - D\right)(1 - \tan \beta_1 \tan \beta_1')\right] \frac{\Delta T_1}{T_1}$$

(mG-iii)
(fig. 21(a), multiply result by $-\gamma/2$, substitute T_1 for p_1)

$$(\Delta D)_{iv} = -\frac{\pi}{180} \cos^2\beta_1' \left[\frac{\cos \beta_1' (1 - \tan \beta_1 \tan \beta_1')}{2\sigma} + \left(\frac{\sin \beta_1'}{2\sigma} + 1 - D\right)(\tan \beta_1 + \tan \beta_1')\right] \Delta\beta_1$$

(mG-iv)
(fig. 21(b))

$$M_2^2 \frac{V_1'}{V_2'} (\Delta D)_v = \frac{\cos^2\beta_2'}{\gamma} \left[\left(1 + \frac{\sin \beta_2'}{2\sigma}\right)(1 - \tan \beta_2 \tan \beta_2') - \frac{\cos \beta_2'}{2\sigma} (\tan \beta_2 + \tan \beta_2')\right] \frac{\Delta p_2}{p_2}$$

(mG-v)
(fig. 21(c))

3479

CH-32 back

$$M_2^2 \frac{V_1'}{V_2'} (\Delta D)_{vi} = -\frac{\cos^2\beta_2'}{\gamma} \left[\left(1+\frac{\sin\beta_2'}{2\sigma}\right)(1-\tan\beta_2 \tan\beta_2') - \frac{\cos\beta_2'}{2\sigma}(\tan\beta_2+\tan\beta_2')\right]\frac{\Delta P_2}{P_2}$$

(mG-vi)
(fig. 21(c), prefix minus sign to result, substitute P_2 for p_2)

$$\frac{V_1'}{V_2'} (\Delta D)_{vii} = -\frac{\cos^2\beta_2'}{2} \left[\left(1+\frac{\sin\beta_2'}{2\sigma}\right)(1-\tan\beta_2 \tan\beta_2') - \frac{\cos\beta_2'}{2\sigma}(\tan\beta_2+\tan\beta_2')\right]\frac{\Delta T_2}{T_2}$$

(mG-vii)
(fig. 21(c), multiply result by $-\gamma/2$, substitute T_2 for p_2)

$$\frac{V_1'}{V_2'} (\Delta D)_{viii} = \frac{\pi}{180}\cos^2\beta_2' \left[\left(1+\frac{\sin\beta_2'}{2\sigma}\right)(\tan\beta_2+\tan\beta_2') + \frac{\cos\beta_2'}{2\sigma}(1-\tan\beta_2 \tan\beta_2')\right]\Delta\beta_2$$

(mG-viii)
(fig. 21(d))

The measurement-error formulas give the effects of independent measurement errors. For instance, formula (mE-ii) gives the error in calculated value of blade-element efficiency due to a measurement error solely in P_1. However, in many experimental compressors, the measured value of P_2 depends on the measured value of P_1, such as when P_2 is obtained by adding a measured pressure rise to the value of P_1. For such cases $\Delta P_2 = \Delta P_1$, and the effects of ΔP_1 on $\bar{\omega}'$ and η_{ad} become quite small because of the similarity, except for sign, of the -ii and -vi formulas. The same situation prevails for measurements of T_2 that depend upon T_1.

Reading of Carpet Plots

As discussed in reference 6, carpet and lattice plots permit the charting of two or three independent variables and provide a means for interpolation among these variables. A fourth variable can also be charted by the use of an ordinate scale that is a function of the dependent variable and the fourth independent variable. An example of a four-variable chart is figure 1, the plot of the formula for relative stagnation enthalpy ratio (formula (22)), for which the independent variables are β_2, β_2', M_2', and r_2/r_1. The chart consists of nine carpets in β_2 and β_2', each of which corresponds to a given value of M_2' and r_2/r_1. The carpets for different values of M_2' are displaced horizontally by distances proportional to the changes in M_2', thus forming three lattices for three values of r_2/r_1. In order to provide a means for interpolation of r_2/r_1, these lattices are displaced horizontally by distances proportional to the changes in r_2/r_1. It is then necessary, for clear reading of the charts, to displace the lattices vertically and to incorporate r_2/r_1 into the ordinate function. A value of H_2'/H_1' for given values of β_2, β_2',

M_2', and r_2/r_1 is obtained in principle from the chart as follows (in practice, many of the steps illustrated here can be omitted).

The first step is to locate on each of the nine carpets a point corresponding to the given values of β_2 and β_2' as follows: It will be observed that each curve, in effect, has its own abscissa scale. On each of the curves for constant β_2', the given value of β_2 can be located; a curve sketched through these points will yield a curve for varying β_2' at the given value of β_2, whereupon the desired point on each carpet can be located. Appropriate points on the nine carpets are then connected by curves so as to form three curves of varying M_2', each having its own constant value of r_2/r_1. The three points corresponding to the given M_2' are then located. This is done by marking off a proportional horizontal distance along each curve from a known reference point. The three points thus obtained determine a curve of given β_2, β_2', M_2', and varying r_2/r_1. It will be noted that the carpets are staggered horizontally two major grid divisions for a change of 0.2 in r_2/r_1; therefore, the point corresponding to the given r_2/r_1 can be located and the value of the ordinate scale obtained. The final step is to equate this value to the ordinate function $(H_2'/H_1') + \left[(r_2/r_1) - 0.9\right]$ and solve for H_2'/H_1'.

The foregoing procedure appears to be laborious, but in practice not all the various points need actually to be joined by curves; the interpolations can be made by an appropriate placing of French curves or splines on the charts and the desired points located directly. The work involved is, of course, much greater for the four-variable charts than for the three- or two-variable charts. For some formulas (formula (dG-i,iv), e.g.), two charts are employed, and the values obtained from each chart are combined to obtain the desired value of the dependent variable.

DISCUSSION OF FORMULAS AND CHARTS

In order to facilitate discussion of the formulas and charts, values of design and measurement errors were obtained from the charts for four velocity diagrams. These velocity diagrams are representative of inlet-stage rotor tip and hub operation at two Mach number levels. The velocity-diagram specifications are as follows:

	Case 1 (tip condition)		Case 2 (hub condition)	
	Design (a)	Design (b)	Design (a)	Design (b)
M_1'	1.15	1.00	0.81	0.70
M_1	.58	.50	.58	.50
β_1'	60°	60°	45°	45°
β_1	0°	0°	0°	0°
M_2'	.90	.75	.60	.50
M_2	.64	.55	.73	.63
β_2'	50°	50°	15°	15°
β_2	24.6°	28.2°	38.3°	40.1°
$\bar{\omega}'$	.080	.080	.050	.050
σ	.80	.80	1.5	1.5
D	.34	.43	.41	.44
r_2/r_1	1.00	1.00	1.1	1.1
P_2/P_1	1.35	1.30	1.42	1.32
T_2/T_1	1.10	1.09	1.11	1.09
η_{ad}	.86	.87	.95	.95

3479

Sample Design and Measurement Errors

Values of design errors and measurement errors for the foregoing velocity-diagram cases were read from the charts. For each case, an arbitrary assumption of 1-percent error in independent variable was made (except that the assumed error in flow angle was 1° and that in $\bar{\omega}$ or $\bar{\omega}'$ was 0.01). Design errors in $V_{z,1}$, β_1', $V_{z,2}$, H_2, P_2, β_2, and D, and measurement errors in ρV_z, β', $\bar{\omega}'$, η_{ad}, H_M, and D were obtained as follows:

3479

Error term	Design errors, case number			
	1(a)	1(b)	2(a)	2(b)
$(\Delta V_{z,1}/V_{z,1})_{i}$	-0.0150	-0.0133	-0.0150	-0.0133
ii	0	0	0	0
iii	.0150	.0133	.0150	.0133
iv	.0125	.0118	.0125	.0118
$(\Delta\beta_1')_{i}$	0.38	0.33	0.44	0.39
ii	.25	.25	.60	.60
iii	-.38	-.33	-.44	-.39
iv	-.31	-.30	-.36	-.34
$(\Delta V_{z,2}/V_{z,2})_{i}$	-0.0520	-0.0220	-0.0150	-0.0140
ii	.0460	.0166	.0079	.0052
iii	0	0	0	0
iv	.0550	.0240	.0150	.0140
v	.0310	.0110	.0050	.0037
vi	.0885	.0270	.0028	.0015
vii	.0525	.0230	.0155	.0133
viii	-.0447	-.0140	-.0049	-.0037
$(\Delta H_2/H_2)_{i}$	0.0124	0.0038	0.0006	0.0004
ii	-.0143	-.0056	-.0021	-.0016
iii	0	0	0	0
iv	-.0041	.0051	.0085	.0088
v	-.0074	-.0019	-.0002	-.0001
vi	-.0303	-.0112	-.0025	-.0018
vii	-.0125	-.0040	-.0006	-.0004
viii	.0150	.0059	.0026	.0020
$(\Delta P_2/P_2)_{i}$	0.0534	0.0233	0.0119	0.0113
ii	-.0500	-.0196	-.0074	-.0056
iii	0	0	0	0
iv	-.0494	-.0171	-.0058	-.0039
v	-.0326	-.0117	-.0039	-.0031
vi	-.1060	-.0392	-.0088	-.0063
vii	-.0437	-.0140	-.0020	-.0013
viii	.0525	.0206	.0091	.0070
$(\Delta\beta_2)_{i}$	4.05	1.69	0.56	0.52
ii	-3.59	-1.26	-.29	-.19
iii	0	0	0	0
iv	-4.29	-1.84	-.56	-.52
v	-3.42	-.84	-.20	-.14
vi	-8.90	-3.90	-.70	-.70
vii	-4.10	-1.76	-.57	-.49
viii	4.60	2.00	.63	.52
$(\Delta D)_{i}$	0.0583	0.0244	0.0078	0.0045
ii	-.0410	-.0078	.0045	.0067
iii	.0005	.0004	.0042	.0028
iv	-.0618	-.0268	-.0085	-.0079
v	-.0350	-.0124	-.0040	-.0030
$(V_1'/V_2')(\Delta D)_{vi}$	-.1790	-.0815	-.0130	-.0120
$(\Delta D)_{vii}$	-.0594	-.0260	-.0124	-.0106
viii	.0505	.0158	.0049	.0030

[redacted]

Error term	Measurement errors, case number			
	1(a)	1(b)	2(a)	2(b)
$\left[\frac{\Delta(\rho V_z)}{\rho V_z}\right]_i$	-0.0150	-0.0220	-0.0150	-0.0220
ii	-.0250	-.0310	.0250	.0310
iii	-.0050	-.0050	-.0050	-.0050
iv	0	0	0	0
v	-.0110	-.0170	-.0070	-.0115
vi	.0210	.0270	.0160	.0210
vii	-.0050	-.0050	-.0050	-.0050
viii	-.0080	-.0090	-.0130	-.0140
$(\Delta\beta')_i$	0.58	0.71	0.67	0.82
ii	-.58	-.71	-.67	-.82
iii	-.13	-.13	-.15	-.15
iv	-.25	-.25	-.50	-.50
v	.73	1.16	.74	1.13
vi	-.73	-1.16	-.74	-1.13
vii	-.20	-.20	-.30	-.30
viii	-.19	-.15	-.76	-.72
$(\Delta\bar{\omega}')_{ii}$	0.0170	0.0205	0.030	0.036
iii	-.0595	-.0717	-.105	-.126
vi	-0.0170	-.0205	-.030	-.036
vii	.0595	.0717	-.105	-.126
$(\Delta\eta_{ad})_{ii}$	-0.030	-0.034	-0.028	-0.038
iii	.094	.106	.096	.118
vi	.030	.034	.028	.038
vii	-.094	-.106	-.096	-.118
$(\Delta H_{M,2}/H_1)_i$	0	0	0	0
ii	0	0	0	0
iii	.0100	.0100	.0100	.0100
iv	-.0038	-.0029	-.0020	-.0016
v	-.0016	-.0019	-.0014	-.0015
vi	.0016	.0019	.0014	.0015
vii	.0007	.0005	.0005	.0005
viii	.0038	.0028	.0037	.0016
$M_1^2\ (\Delta D)_i$	-0.0010	-0.0010	-0.0017	-0.0017
ii	.0010	.0010	.0017	.0017
$(\Delta D)_{iii}$	.0007	.0007	.0012	.0012
iv	-.0105	-.0105	-.0136	-.0136
$M_2^2\ \frac{V_1'}{V_2'}\ (\Delta D)_v$	.0017	.0017	.0039	.0039
vi	-.0017	-.0017	-.0039	-.0039
$\frac{V_1'}{V_2'}\ (\Delta D)_{vii}$	-.0012	-.0012	-.0027	-.0027
viii	.0138	.0138	.0127	.0127

The foregoing sample values of error terms provide data for the discussions of the following sections.

Interpretation of numerical values. - The numerical values of error terms obtained from the design-error charts must be carefully interpreted. Their main utility is in an evaluation of the sensitivity to design errors of one velocity diagram as compared with another. Secondarily, for a mean-radius condition where the local specific mass flow $(\rho V_z)_2$ can reasonably be assumed constant at a given annular mass flow, the values obtained from the charts can be combined to yield uncertainty intervals in blade-element performance.

3479

The precautions concerning the interpretation of numerical values of error terms, such as those listed in the table, are partly involved with the fact that some of the design variables can be considered independent only for blade-element flow. In actual compressor operation, the conditions of radial equilibrium and continuity impose a dependence between local specific mass flow and deviation angle and loss. Therefore, sweeping conclusions cannot be drawn from any one chart (one chart represents only one term of formula (7)).

CH-33

An example of the dependence of local specific mass flow on deviation angle occurs for the case $M_2' = 0.90$. At this Mach number, the local specific mass flow is very near its maximum value. A quite small increase in β_2' can cause a choking-flow condition, and any additional increase in β_2' will necessarily be accompanied by a decrease in the value of $(\rho V_z)_2$. The tabulated values of error terms show that the effects of an increase in β_2' and decrease in $(\rho V_z)_2$ are opposite in sign and therefore tend to nullify each other to some extent.

If the value of β_2' is smaller than expected, the choking-flow condition will not arise, but, even in this case, the value of $(\rho V_z)_2$ will probably change because of the effect of the error in β_2' on the radial-equilibrium condition. No method is available for estimating this effect without recomputing the entire flow field for a specified set of errors at all radii.

The foregoing discussion indicates that, to ensure the achievement of design mass flow, deviation angles near the upper limit of their uncertainty intervals should be employed for high Mach number designs.

Trends exhibited by sample design errors. - The trend most apparent from an examination of the tabulated values of design error is that, for case 1 (the tip operating condition), a Mach number level of $M_2' = 0.90$ is accompanied by error terms much greater in magnitude than those for

$M_2' = 0.75$. This difference in magnitude is a consequence of the term $1/\left[1 - (M_2')^2\right]$, which appears in many formulas. It is possible that the various errors would tend to cancel out; but it would apparently be advantageous, in the design of transonic rotors, to hold the value of M_2' as low as is consistent with reasonable values of diffusion factor D and, of course, to employ the highest possible degree of design control in the choice of the design variables. It would probably be warranted to employ the continuity condition in the design calculations for the choice of r_2 because of the large effects indicated in the table for an assumed error in r_2 of 1 percent. The results also indicate no error in performance parameters at station 2 due to error in inlet local specific mass flow $(\rho V_z)_1$ for the case $\beta_1 = 0$, except for a very small effect on diffusion factor D. However, errors in $(\rho V_z)_1$ do cause errors in β_1', hence in incidence angle. For high Mach numbers where the low-loss range of incidence angle might be narrow, this effect can lead to design errors in $\bar{\omega}'$ and deviation angle.

3479

Trends exhibited by sample measurement errors. - For many of the parameters, the effects of measurement errors are greatest at low Mach numbers. This trend is especially evident for the loss parameter $\bar{\omega}'$ and is caused by terms like $1/M^2$ and $\dfrac{1}{1 - \dfrac{p_1}{P_1'}}$ in the measurement-error formulas. Case 2(b), for an inlet Mach number M_1' of 0.70, shows an error in $\bar{\omega}'$ of -0.036 due to an assumed error of 1 percent in the measurement of stagnation pressure P_2. This trend shows that the accurate determination of $\bar{\omega}'$ from low-speed data requires very precise measurement of stagnation pressure (and temperature).

Use of Design-Error Charts

Suggested uses of the formulas and charts which were obtained from the analyses of design and measurement errors are outlined in this section.

For the preliminary velocity-diagram calculations, a common practice is to assign r_2 at the same proportion of the passage depth as the corresponding r_1; or, perhaps, r_2 is located so that the same proportion of flow area is contained between r_2 and the hub as between the corresponding r_1 and the hub. After the calculations are made, r_2 can

easily be determined as a function of r_1 by application of the continuity condition. The charts of the formulas for design errors in r_2 can then be employed to determine whether an iteration with the new values of r_2 is warranted.

Similarly, the preliminary radial-equilibrium calculations may neglect the effects of entropy gradient on the radial distribution of axial velocity. The order of magnitude of the consequent design errors in axial velocity can be estimated from the results of the investigation reported in reference 5. The design-error charts can then be consulted to determine whether the blade-element losses should be included in the radial-equilibrium calculation.

3479

Certain refinements in the design calculations (such as the inclusion of blade-element losses in the radial-equilibrium calculation) may appreciably change the values of D factor. These new D factors will lead to changes in the design values of $\bar{\omega}'$, and, again, the charts can be consulted to determine whether an iteration is warranted with the new values of $\bar{\omega}'$.

CH-33 back

For any general blade element, the formulas and charts can be employed as a test of the sensitivity of a particular velocity diagram to design errors and manufacturing tolerances. Thus, the appropriate degree of design control can be applied to the problem, and, in some cases, the sensitivity to design errors and manufacturing tolerances can be employed as one of the criteria by which choice among several otherwise suitable velocity diagrams can be made.

The charts can be employed by the research worker in the analysis of data. Discrepancies between actual and design performance of an experimental compressor that cannot reasonably be accounted for by measurement errors are caused mainly by design errors of the type herein analyzed. (Some of these discrepancies are undoubtedly caused by simplifications introduced into the equations of motion on which the design system is based, such as the assumption of axial symmetry.) The approximate contribution of the design error in each design variable to the measured discrepancy in a performance parameter can be obtained from the charts. The sum of these terms (formula (1b)) can be compared with the measured discrepancy between actual and design values of a performance parameter.

Such comparisons may serve as an additional means of evaluating measurement errors and may indicate just which phase of the design problem requires the highest degree of design control.

Within certain limitations, the design-error charts can be employed by the compressor designer to estimate an interval about the design point within which the performance of a given blade element should lie. The limitations on this procedure are involved with the estimation of uncertainty intervals in local specific mass flow.

Estimation of uncertainty intervals. - Local specific mass flow: The uncertainty intervals in local specific mass flow are caused by blade-element design errors. As evidenced by the radial-equilibrium equation, the radial distribution of flow is a function of flow angles and blade losses at all blade elements. Discrepancies between actual and design values of these quantities lead, therefore, to discrepancies between actual and design values of local specific mass flow.

Unfortunately, no method is known for relating uncertainty intervals in local specific mass flow to uncertainty intervals in blade-element design data. This fact restricts the applicability of formula (7). However, at the design mass flow, the actual and design values of local specific mass flow must necessarily agree for at least one blade element. It would appear reasonable to assume that this blade element would be near the mean radius. 3479

Loss parameter: A set of mean-radius loss data reported in chapter VII (ref. 2) was employed in an investigation of the uncertainty intervals in loss parameter $\overline{\omega}'$. The design values of loss parameter $\overline{\omega}_d'$ for each observation were obtained by the use of the loss-correlation method of chapter VII, and the quantities $(\overline{\omega}' - \overline{\omega}_d')$ were calculated. Frequency ratios for increments in $(\overline{\omega}' - \overline{\omega}_d')$ of 0.02 were calculated and are plotted in figure 22 as an approximate frequency-distribution curve. The frequency ratio plotted in figure 22 is the ratio of the number of observations within an increment in $(\overline{\omega}' - \overline{\omega}_d')$ of 0.02 to the total number of observations. For instance, the value of 0.132 plotted at $(\overline{\omega}' - \overline{\omega}_d')$ equal to -0.02 denotes that 13.2 percent of the values of $(\overline{\omega}' - \overline{\omega}_d')$ fall within limits of from -0.03 to -0.01. The total number of observations for this set of mean-radius loss data was 68.

The curve of figure 22 indicates that the discrepancies between the design and measured values of $\overline{\omega}'$ plot in a rough approximation of a random distribution, although there is some bias in the direction of positive errors. These mean-radius data indicate that an interval of from -0.03 to 0.03 in $(\overline{\omega}' - \overline{\omega}_d')$ (an uncertainty interval of 0.06) contains 82.4 percent of the observations; the corresponding odds for this interval are 4.7 to 1.0.

The data of figure 22 represent a combination of measurement errors and design errors; thus, the uncertainty interval for design errors only corresponding to odds of 4.7 to 1.0 would be less than the value of 0.06 obtained from these data.

Deviation angle: An approximate frequency-distribution curve for mean-radius design errors in deviation angle was prepared in the same way

as the corresponding curve for loss parameter. The resulting curve, which was prepared for intervals of 1°, is plotted in figure 23. For these data, 89.1 percent of the observations were within an interval in $(\delta^{\circ} - \delta_d^{\circ})$ of 3° $(-1.5^{\circ}$ to $1.5^{\circ})$, which corresponds to odds of 8.2 to 1.0. As was the case for design error in loss parameter, this interval for the quoted odds in design error only would be smaller than 3°.

3479

Radius to blade element: Design errors in the choice of r_2 as a function of r_1 are involved with the radial-equilibrium condition and are mainly systematic errors that depend on the design flow distribution and the compressor configuration. It can probably be assumed, therefore, that the uncertainty interval for random errors in r_2 is negligible compared with the other errors introduced.

Calculation of uncertainty intervals in performance. - For the estimation of the limits in blade-element performance near the mean radius, formula (7) is employed.

Use of Measurement-Error Charts

The charts for the analysis of measurement errors can be employed in several ways: (1) for the calculation of uncertainty intervals in performance parameters corresponding to estimated uncertainty intervals in the measured data, (2) for the evaluation of measured data based on the consistency evidenced by plots of performance parameters, and (3) as an aid in planning instrumentation.

Uncertainty intervals in performance. - For measurement errors of the random type, the procedure outlined in reference 4 can be followed. Intervals are estimated for each measured datum within which the same odds (b) can be quoted that the true value will lie. The uncertainty intervals in a performance parameter due to errors in each measured variable are then obtained from the charts and are combined by means of formula (6). The final result will be an interval in the performance parameter for which the odds are b that the value of the performance parameter will lie.

Evaluation of data. - Plots of performance parameters against mass flow or incidence angle can sometimes be employed, along with the charts, to evaluate the accuracy of measured data. For instance, figure 18 shows that the calculated values of $\bar{\omega}'$ are very sensitive to errors in P and T. If, therefore, a plot of rotor $\bar{\omega}'$ against incidence shows only a slight scatter from a smooth curve, the measured values of P and T can be considered very consistent. Also, figure 20(b) shows that the calculated values of stagnation enthalpy (or stagnation temperature) by

change of moment of momentum are sensitive at high Mach numbers to measurement errors in flow angle β. Even if a discrepancy of 2° F were observed between the measured stagnation temperature and the value obtained by change of moment of momentum, this could be accounted for by a measurement error of less than 1° in flow angle (for the conditions $M_2 = 0.64$, $\beta_2 = 25^{\circ}$, $\beta_2' = 50^{\circ}$). This example illustrates the difficulty of checking the measurement of temperature at high Mach numbers by the temperature calculated from the change of moment of momentum across a rotor. At a Mach number of 0.5, the effects of errors in flow angle and static pressure on change of moment of momentum would be approximately the same; at lower Mach numbers, the static-pressure errors would have the greater effect (figs. 20(a) and (b)). For many conditions of velocity diagram, an error of 1 percent in static pressure would cause an error in change of moment of momentum equivalent to approximately 1° F in temperature rise. Since 1° F is also a reasonable error to be expected in the direct measurement of temperature, no advantage in accuracy is indicated either for the direct measurement of temperature or for the calculation of change of moment of momentum at low Mach numbers.

Instrumentation. - The charts can be used as a guide in choosing instrumentation of sufficient accuracy for the expected test conditions and combinations of flow parameters. The relative air angle β_1' or β_2' is an important parameter in the correlation of data, since these flow angles determine incidence, deviation, and turning angles. Figures 16(a) and (c) show that measurement errors in static pressure (or stagnation pressure) can cause greater error in the calculated value of β' than would a reasonable error in the measurement of absolute air angle β, especially at low Mach numbers. Thus, the necessity for careful design and calibration of static-pressure probes is emphasized.

CONCLUDING REMARKS

An analysis was performed of effects of design errors on compressor performance parameters, and of effects of measurement errors on calculated values of performance parameters. The following results were obtained:

1. Formulas and charts were prepared and presented from which the changes in blade-element performance parameters caused by design errors and the errors in calculated performance parameters due to measurement errors can be determined.

2. The use of the design-error charts during the design calculations and in the analysis and interpretation of data is discussed. The charts can be used to evaluate the sensitivity of a given velocity diagram to design errors, to determine whether iterations of design calculations are warranted, and, to a limited extent, to calculate the uncertainty intervals in blade-element performance.

3. The measurement-error charts can be employed along with the procedure devised at the Gas Turbine Laboratory of the Massachusetts Institute of Technology for the estimation of uncertainty intervals in calculated performance and can also be of assistance in the evaluation of data and in the planning of instrumentation.

3479

APPENDIX A

ACCURACY OF FORMULAS

The accuracy of the design-error and measurement-error formulas for reasonable magnitudes of errors was spot-checked by means of sample calculations for various combinations of Mach number and absolute and relative flow angles.

3479

Design-Error Formulas

A sample calculation of the actual effects (within the limitations of the design system) of certain assumed design errors was made as follows: A transonic-inlet-stage rotor design was calculated. The rotor-outlet air angles β_2' were then increased by 1° and a direct-problem calculation of the rotor performance was made. The consequent changes in various performance parameters were then compared with the corresponding results obtained from the charts. Similarly, the design values of rotor $\bar{\omega}'$ were increased by 25 percent, the rotor performance was again calculated, and appropriate comparisons were made between the changes in performance and the predictions of the charts.

It should be pointed out that, in a direct-problem calculation of this type, the specified error in β_2' is propagated through the radial-equilibrium calculation and causes changes in local specific mass flow. Thus, the calculation yields the combined effects of errors in β_2' and $(\rho V_z)_2$ on the performance parameters. These combined effects cannot be obtained from the charts alone; the charts provide no means for obtaining $\Delta(\rho V_z)_2$ as a function of $\Delta\beta_2'$, because in blade-element flow β_2' and $(\rho V_z)_2$ are treated as if they were independent. The values of $\Delta(\rho V_z)_2$ obtained from the calculation were therefore employed along with the specified error of 1° in β_2' to obtain the chart predictions of changes in performance. The values obtained from the charts for effects of errors in β_2' and from the charts for effects of errors in $(\rho V_z)_2$ were added algebraically, as specified by formula (1c).

The design assumptions were as follows:

(1) $M_1' = 1.10$ at rotor tip.

(2) $\beta_1' = 60^\circ$ at rotor tip, $\beta_1 = 0^\circ$ at all radii.

(3) $(r_1/r_t)_h = 0.5$.

(4) $H_2 - H_1$ varied linearly from 300,000 ft-lb/slug at hub to 400,000 ft-lb/slug at tip.

An approximate calculation of density ratio was made to determine the annular-area ratio for no change in average axial velocity. This calculation yielded a value for $(r_2/r_t)_h$ of 0.6.

The radial-equilibrium calculation was based on simplified radial equilibrium including entropy gradient (ref. 5). An arbitrary assumption of $\bar{\omega}'$ was made, varying from 0.040 at the hub to 0.100 at the tip (nonlinearly).

3479

The following table lists values of performance parameters obtained; the range given is the variation from hub to tip:

β_2'	13.61° - 48.52°
β_2	40.94° - 34.19°
M_2'	0.512 - 0.752
M_2	0.659 - 0.603
H_2/H_1	1.096 - 1.128
P_2/P_1	1.363 - 1.445

CH-34

The direct-problem calculation, employing values of β_2' increased by 1° at all radii, resulted in small changes in the local specific mass flow at the different radii of from -1.2 to 0.8 percent because of the propagation of the assumed error in β_2' through the radial-equilibrium calculation.

The changes in blade-element stagnation-pressure ratio were analyzed. The pressure ratio was reduced by the assumed decrease in turning angle, together with the consequent changes in $(\rho V_z)_2$, and the net decrement in pressure ratio obtained from the charts agreed very closely with the calculated values, as follows:

Radius ratio, r_1/r_t	Net $\Delta(P_2/P_1)$ due to $\Delta\beta_2' = 1^\circ$ and to consequent $\Delta(\rho V_z)_2$	
	Calculated	From charts
0.5	-0.0104	-0.0103
.6	-.0145	-.0141
.7	-.0186	-.0185
.8	-.0236	-.0233
.9	-.0278	-.0278
1.0	-.0316	-.0318

The assumed increase in $\bar{\omega}'$ for the second phase of the check calculation also caused small changes in local values of $(\rho V_z)_2$ of from

-1.6 to 1.2 percent. The net effect of these changes was a general decrease in pressure ratio, and good agreement between the calculated values and those obtained from the charts was observed:

Radius ratio, r_1/r_t	Net $\Delta(P_2/P_1)$ due to $\Delta\bar{\omega}'/\bar{\omega}' = 0.25$ and to consequent $\Delta(\rho V_z)_2$	
	Calculated	From charts
0.5	-0.0061	-0.0065
.6	-.0093	-.0096
.7	-.0118	-.0125
.8	-.0146	-.0137
.9	-.0168	-.0159
1.0	-.0181	-.0189

3479

It is believed that the foregoing calculation verifies the applicability of the design-error formulas, for the given range of Mach numbers and flow angles, to the uses suggested in the text.

A limitation of the design-error formulas containing the term $1 - M^2$ in their denominators is that they are inaccurate for Mach numbers in the neighborhood of 1.0. Sample calculations indicate that the accuracy of such formulas is good for Mach numbers up to at least 0.75.

Measurement-Error Formulas

The measurement-error formulas were checked by means of sample calculations and, in a few cases, by comparison with the exact formula.

Local specific mass flow. - Calculations were made to compare the actual and chart values of $\Delta(\rho V_z)$ caused by changes in static or stagnation pressure of 1 percent. The following values were obtained:

M	Percent change in ρV_z for $\Delta p/p = 0.01$	
	Calculated	From charts
0.5	-2.63	-2.14
.7	-.83	-.74

M	Percent change in ρV_z for $\Delta P/P = 0.01$	
	Calculated	From charts
0.5	2.88	3.15
.7	1.67	1.74

Formula (mA-iii,vii), which gives the effect on ρV_z of a measurement error in T, contains the approximation that

$$\frac{1}{\left(1 + \frac{\Delta T}{T}\right)^{1/2}} - 1 \cong -\frac{1}{2}\frac{\Delta T}{T}$$

Substitution of $\Delta T/T = 0.01$ into the left side yields a value of -0.00496. Thus, for $\Delta T/T = 0.01$, formula (mA-iii,vii) yields a result only 1.009 times the correct value.

3479 Similarly, formula (mA-iv,viii), which gives the error in ρV_z due to a measurement error in β, contains the following approximation:

$$(\tan \beta)\Delta\beta \cong \frac{\cos \beta - \cos(\beta + \Delta\beta)}{\cos \beta}$$

CH-34 back For the range $0^\circ \leqslant \beta \leqslant 60^\circ$, the degree of approximation decreases as β increases. For the worst case ($\beta = 0^\circ$), where formula (mA-iv,viii) indicates no error in ρV_z, a measurement error of $\Delta\beta = 1^\circ$ would actually cause an error of 0.015 percent in ρV_z. This discrepancy is clearly negligible. For $\beta = 60^\circ$, the discrepancy between the values of $\Delta(\rho V_z)$ obtained from formula (mA-iv,viii) and from the exact calculation is only 0.0013 percent of ρV_z.

Relative air angle. - The following table presents a sample comparison of calculated magnitudes of changes in β' with the corresponding values obtained from the charts (formulas (mB-i,v) to (mB-iv,viii)) for the specified assumed measurement errors:

M ($\beta = 30^\circ$, $\beta' = 40^\circ$)	$\lvert\Delta\beta'\rvert$, deg					
	$\frac{\Delta p}{p}$ or $\frac{\Delta P}{P} = 0.01$		$\frac{\Delta T}{T} = 0.002$		$\Delta\beta = 1^\circ$	
	Actual	From charts	Actual	From charts	Actual	From charts
0.5	1.33	1.36	0.05	0.06	0.32	0.31
.7	.69	.71				

APPENDIX B

DERIVATION OF FORMULAS

Design-Error Formulas

The derivation of formula (dF-v) is presented here as an example of the general procedure. The error in axial velocity $V_{z,2}$ due to an error in the rotor loss parameter must be found for the condition of unchanging local specific mass flow. A formula for $V_{z,2}$ is as follows: 3479

$$V_{z,2} = \sqrt{2}\,(H_2' - h_2)^{1/2} \cos \beta_2' \tag{14}$$

The relative stagnation enthalpy H_2' is not affected by an error in $\bar{\omega}'$; and, for this derivation, β_2' is held constant:

$$\frac{\partial V_{z,2}}{\partial \bar{\omega}'} = \frac{\sqrt{2}}{2}\,(H_2' - h_2)^{-1/2} \cos \beta_2' \left(-\frac{\partial h_2}{\partial \bar{\omega}'}\right) \tag{B1}$$

The condition of constant $(\rho V_z)_2$ provides a means for evaluation of $(\partial h_2/\partial \bar{\omega}')$:

$$(\rho V_z)_2 = \frac{\gamma}{\gamma - 1} \frac{P_2'}{H_2'} \left(\frac{h_2}{H_2'}\right)^{\frac{1}{\gamma-1}} \sqrt{2}\,(H_2' - h_2)^{1/2} \cos \beta_2' \tag{20}$$

Differentiation of formula (20) with respect to $\bar{\omega}'$ yields the following:

$$0 = \frac{\gamma}{\gamma - 1} \frac{1}{H_2'} \frac{\partial P_2'}{\partial \bar{\omega}'} \left(\frac{h_2}{H_2'}\right)^{\frac{1}{\gamma-1}} \sqrt{2}\,(H_2' - h_2)^{1/2} \cos \beta_2' +$$

$$\frac{\gamma}{\gamma - 1} \frac{P_2'}{H_2'} \frac{1}{\gamma - 1} \left(\frac{h_2}{H_2'}\right)^{\frac{1}{\gamma-1} - 1} \frac{1}{H_2'} \frac{\partial h_2}{\partial \bar{\omega}'} \sqrt{2}\,(H_2' - h_2)^{1/2} \cos \beta_2' +$$

$$\frac{\gamma}{\gamma - 1} \frac{P_2'}{H_2'} \left(\frac{h_2}{H_2'}\right)^{\frac{1}{\gamma-1}} \frac{\sqrt{2}}{2}\,(H_2' - h_2)^{-1/2} \left(-\frac{\partial h_2}{\partial \bar{\omega}'}\right) \cos \beta_2' \tag{B2}$$

Rearrangement of (B2) yields

$$0 = (\rho V_z)_2 \frac{1}{P_2'} \frac{\partial P_2'}{\partial \bar{\omega}'} + \frac{1}{\gamma - 1} (\rho V_z)_2 \frac{1}{h_2} \frac{\partial h_2}{\partial \bar{\omega}'} - \frac{(\rho V_z)_2}{V'^2} \frac{\partial h_2}{\partial \bar{\omega}'}$$

$$= \frac{1}{P_2'} \frac{\partial P_2'}{\partial \bar{\omega}'} + \left(\frac{1}{a_2^2} - \frac{1}{V'^2}\right) \frac{\partial h_2}{\partial \bar{\omega}'} \tag{B3}$$

3479

The relative stagnation pressure P_2' is a function of P_1', $\bar{\omega}'$, the relative enthalpy ratio H_2'/H_1', and p_1/P_1' (or M_1'):

$$P_2' = P_1' \left(\frac{H_2'}{H_1'}\right)^{\frac{\gamma}{\gamma-1}} \left[1 - \bar{\omega}' \left(\frac{H_1'}{H_2'}\right)^{\frac{\gamma}{\gamma-1}} \left(1 - \frac{p_1}{P_1'}\right)\right] \tag{B4}$$

$$\frac{\partial P_2'}{\partial \bar{\omega}'} = - P_1' \left(1 - \frac{p_1}{P_1'}\right) \tag{B5}$$

Substitution of (B5) into (B3) and rearrangement yield

$$\frac{\partial h_2}{\partial \bar{\omega}'} = - (V_2')^2 \frac{\frac{P_1'}{P_2'}\left(1 - \frac{p_1}{P_1'}\right)}{1 - (M_2')^2} \tag{B6}$$

Finally, (B6), (B4), and (B1) yield the following:

$$\frac{\partial V_{z,2}}{\partial \bar{\omega}'} = \frac{\cos \beta_2'}{V_2'} (V_2')^2 \frac{1 - \frac{p_1}{P_1'}}{\left[\left(\frac{H_2'}{H_1'}\right)^{\frac{\gamma}{\gamma-1}} - \bar{\omega}' \left(1 - \frac{p_1}{P_1'}\right)\right]\left[1 - (M_2')^2\right]}$$

$$= \frac{V_{z,2}\left\{1 - \left[1 + \frac{\gamma - 1}{2} (M_1')^2\right]^{-\frac{\gamma}{\gamma-1}}\right\}}{\left(\left(\frac{H_2'}{H_1'}\right)^{\frac{\gamma}{\gamma-1}} - \bar{\omega}' \left\{1 - \left[1 + \frac{\gamma - 1}{2} (M_1')^2\right]^{-\frac{\gamma}{\gamma-1}}\right\}\right)\left[1 - (M_2')^2\right]}$$

[redacted]

Therefore,

$$\left(\frac{\Delta V_{z,2}}{V_{z,2}}\right)_v = \frac{\Omega}{\bar{\omega}'\left[1 - (M_2')^2\right]}\Delta\bar{\omega}' \tag{dF-v}$$

where

$$\Omega = \frac{P_{2,id}'}{P_2'} - 1 = \frac{\bar{\omega}'\left\{1 - \left[1 + \frac{\gamma - 1}{2}(M_1')^2\right]^{-\frac{\gamma}{\gamma-1}}\right\}}{\left(\frac{H_2'}{H_1'}\right)^{\frac{\gamma}{\gamma-1}} - \bar{\omega}'\left\{1 - \left[1 + \frac{\gamma - 1}{2}(M_1')^2\right]^{-\frac{\gamma}{\gamma-1}}\right\}} \tag{23}$$

3479

For some of the subsequent formulas of series d, $V_{z,2}$ was used as an intermediate variable. The derivation of the formula for error in P_2 is presented as an example:

$$P_2 = P_1\left(\frac{H_2}{H_1}\right)^{\frac{\gamma}{\gamma-1}}\left[1 - \bar{\omega}'\left(\frac{P_1'}{P_2'}\right)_{id}\left(1 - \frac{p_1}{P_1'}\right)\right] \tag{B7}$$

$$\frac{\partial P_2}{\partial\bar{\omega}'} = P_1\frac{\gamma}{\gamma-1}\left(\frac{H_2}{H_1}\right)^{\frac{\gamma-1}{\gamma}-1}\frac{1}{H_1}\frac{\partial H_2}{\partial\bar{\omega}'}\left[1 - \bar{\omega}'\left(\frac{P_1'}{P_2'}\right)_{id}\left(1 - \frac{p_1}{P_1'}\right)\right] + P_1\left(\frac{H_2}{H_1}\right)^{\frac{\gamma}{\gamma-1}}\left[-\left(\frac{P_1'}{P_2'}\right)_{id}\left(1 - \frac{p_1}{P_1'}\right)\right]$$

$$= \frac{\gamma}{\gamma-1}P_2\frac{1}{H_2}\frac{\partial H_2}{\partial\bar{\omega}'} - P_2\frac{\left(\frac{P_2'}{P_1'}\right)_{id}}{\frac{P_2'}{P_1'}}\left[\left(\frac{P_1'}{P_2'}\right)_{id}\left(1 - \frac{p_1}{P_1'}\right)\right]$$

Therefore,

$$\left(\frac{\Delta P_2}{P_2}\right)_v = \frac{\gamma}{\gamma - 1}\left(\frac{\Delta H_2}{H_2}\right)_v - \frac{1 - \frac{p_1}{P_1'}}{\left(\frac{P_2'}{P_1'}\right)_{id} - \bar{\omega}'\left(1 - \frac{p_1}{P_1'}\right)}\Delta\bar{\omega}' \tag{B8}$$

The term $(\Delta H_2/H_2)_v$ is obtained as follows:

$$H_2 = H_1 + U_2^2 - U_2V_{z,2} \tan \beta_2' - U_1V_{z,1} \tan \beta_1 \quad , \tag{B9}$$

$$\frac{\partial H_2}{\partial \varpi'} = - U_2 \tan \beta_2' \frac{\partial V_{z,2}}{\partial \varpi'}$$

Therefore,

$$\left(\frac{\Delta H_2}{H_2}\right)_v = - \frac{U_2V_{z,2}}{H_2} \tan \beta_2' \left(\frac{\Delta V_{z,2}}{V_{z,2}}\right) \tag{B10}$$

Combination of (B10), (B8), and (dF-v) yields the following:

$$\left(\frac{\Delta P_2}{P_2}\right)_v = - \frac{\gamma}{\gamma - 1} \frac{U_2V_2' \sin \beta_2'}{H_2} \left(\frac{\Delta V_{z,2}}{V_{z,2}}\right)_v - \left[1 - (M_2')^2\right]\left(\frac{\Delta V_{z,2}}{V_{z,2}}\right)_v$$

$$= - \gamma \frac{M_2' \sin \beta_2' \cos \beta_2'(\tan \beta_2 + \tan \beta_2')}{1 + \frac{\gamma - 1}{2} M_2^2} \left(\frac{\Delta V_{z,2}}{V_{z,2}}\right)_v - \left[1 - (M_2')^2\right]\left(\frac{\Delta V_{z,2}}{V_{z,2}}\right)_v$$

$$\left(\frac{\Delta P_2}{P_2}\right)_v = -\left\{\left[1 - (M_2')^2\right] + \frac{\gamma(M_2')^2 \sin \beta_2' \cos \beta_2'(\tan \beta_2 + \tan \beta_2')}{1 + \frac{\gamma - 1}{2} (M_2')^2 \cos^2\beta_2' \sec^2\beta_2}\right\}\left(\frac{\Delta V_{z,2}}{V_{z,2}}\right)_v \tag{dH-v}$$

Measurement-Error Formulas

The derivation of formula (mA-i) is presented to illustrate the calculation of the series m formulas. Formula (mA-i) gives the error in ρV_z caused by a measurement error in p_1:

$$\rho V_z = \frac{\sqrt{2}\gamma}{\gamma - 1} \frac{P}{H^{1/2}} \left(\frac{p}{P}\right)^{\frac{1}{\gamma}} \left[1 - \left(\frac{p}{P}\right)^{\frac{\gamma-1}{\gamma}}\right]^{1/2} \cos \beta \tag{B11}$$

$$\frac{\partial(\rho V_z)}{\partial p} = \frac{\sqrt{2}\gamma}{\gamma - 1} \frac{P \cos \beta}{H^{1/2}} \left\{\frac{1}{\gamma}\left(\frac{p}{P}\right)^{\frac{1}{\gamma} - 1} \frac{1}{P}\left[1 - \left(\frac{p}{P}\right)^{\frac{\gamma-1}{\gamma}}\right]^{1/2} + \left(\frac{p}{P}\right)^{\frac{1}{\gamma}} \frac{1}{2}\left[1 - \left(\frac{p}{P}\right)^{\frac{\gamma-1}{\gamma}}\right]^{-1/2}\left[- \frac{\gamma - 1}{\gamma}\left(\frac{p}{P}\right)^{\frac{\gamma-1}{\gamma} - 1} \frac{1}{P}\right]\right\}$$

$$= \frac{1}{\gamma p}(\rho V_z) - \frac{1}{\gamma p} \frac{\rho V_z}{\frac{2}{\gamma - 1}\left[\left(\frac{p}{P}\right)^{-\frac{\gamma-1}{\gamma}} - 1\right]}$$

$$\left[\frac{\Delta(\rho V_z)}{\rho V_z}\right]_i = \frac{1}{\gamma}\left(1 - \frac{1}{M^2}\right) \frac{\Delta p_1}{p_1} \tag{mA-i}$$

REFERENCES

1. Wilson, Edwin Bidwell: Advanced Calculus. Ginn and Co., 1912.

2. Compressor and Turbine Research Division: Aerodynamic Design of Axial-Flow Compressors. Vol. II. NACA RM E56B03a, 1956.

3. Compressor and Turbine Research Division: Aerodynamic Design of Axial-Flow Compressors. Vol. I. NACA RM E56B03, 1956.

4. Dean, Robert C., Jr.: Aerodynamic Measurements. Gas Turbine Lab., M.I.T., 1953.

5. Hatch, James E., Giamati, Charles C., and Jackson, Robert J.: Application of Radial-Equilibrium Condition to Axial-Flow Turbomachine Design Including Consideration of Change of Entropy with Radius Downstream of Blade Row. NACA RM E54A20, 1954.

6. Yates, A. H.: 'Carpets' and 'Lattices.' Aircraft Eng., vol. XVIII, no. 203, Jan. 1946, pp. 8-9.

7. Lieblein, Seymour, Schwenk, Francis C., and Broderick, Robert L.: Diffusion Factor for Estimating Losses and Limiting Blade Loadings in Axial-Flow-Compressor Blade Elements. NACA RM E53D01, 1953.

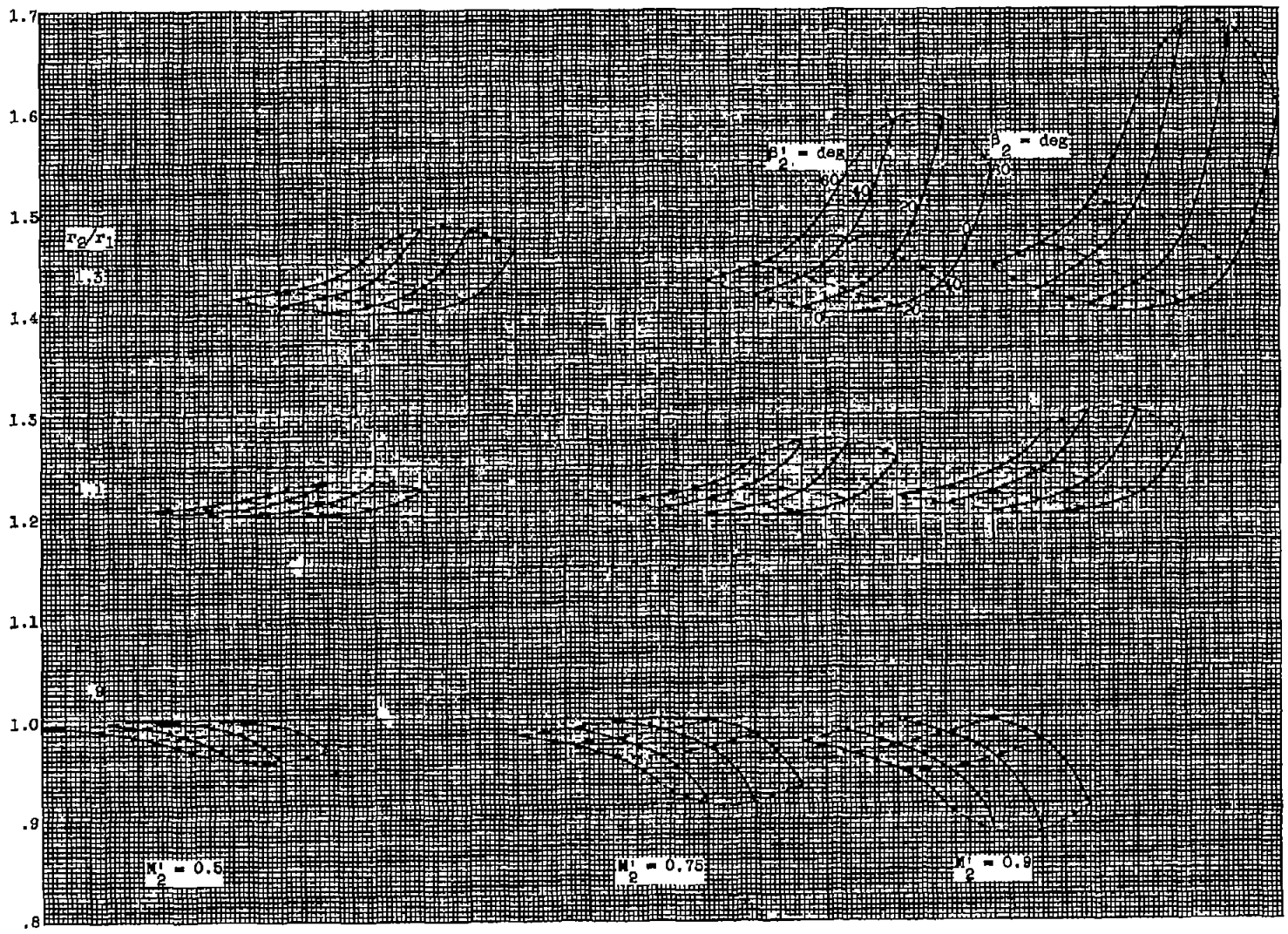

Figure 1. - Relative stagnation-enthalpy ratio as function of velocity-diagram parameters (eq. (22)). (A large working copy of this figure may be obtained by using the request card bound in the back of the report.)

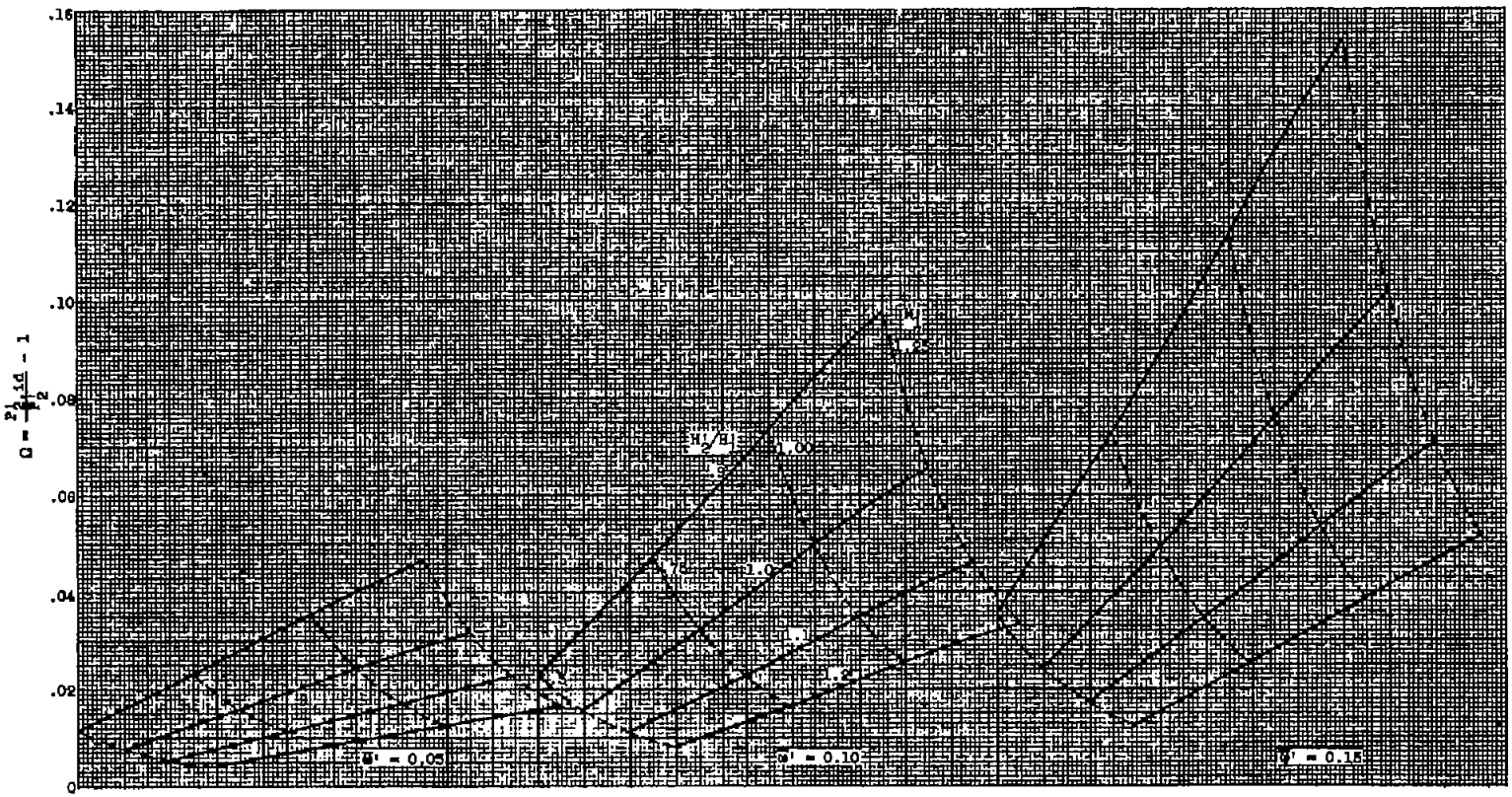

Figure 2. - Relative stagnation-pressure-ratio term Ω (eq. (23)) as function of relative stagnation-pressure-loss parameter, relative stagnation-enthalpy ratio, and relative Mach number. (A large working copy of this figure may be obtained by using the request card bound in the back of the report.)

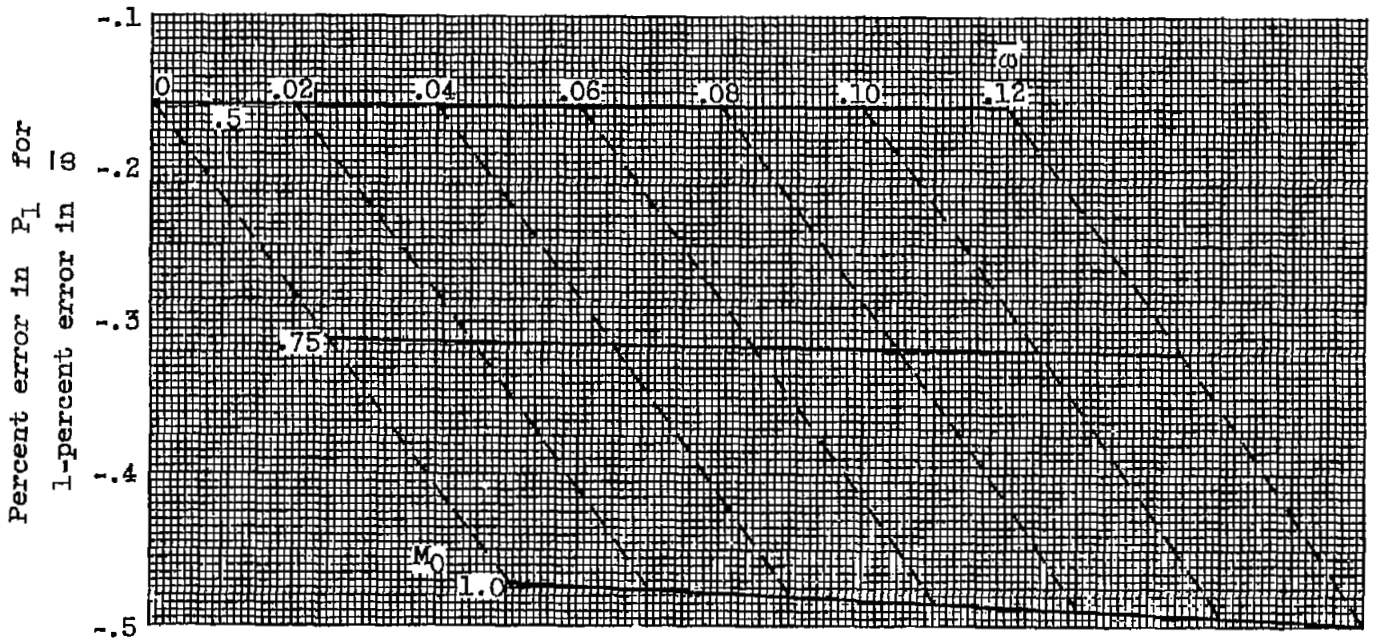

Figure 3. - Effect of design error in stagnation-pressure-loss parameter on stagnation pressure [eq. (dA-(i))].

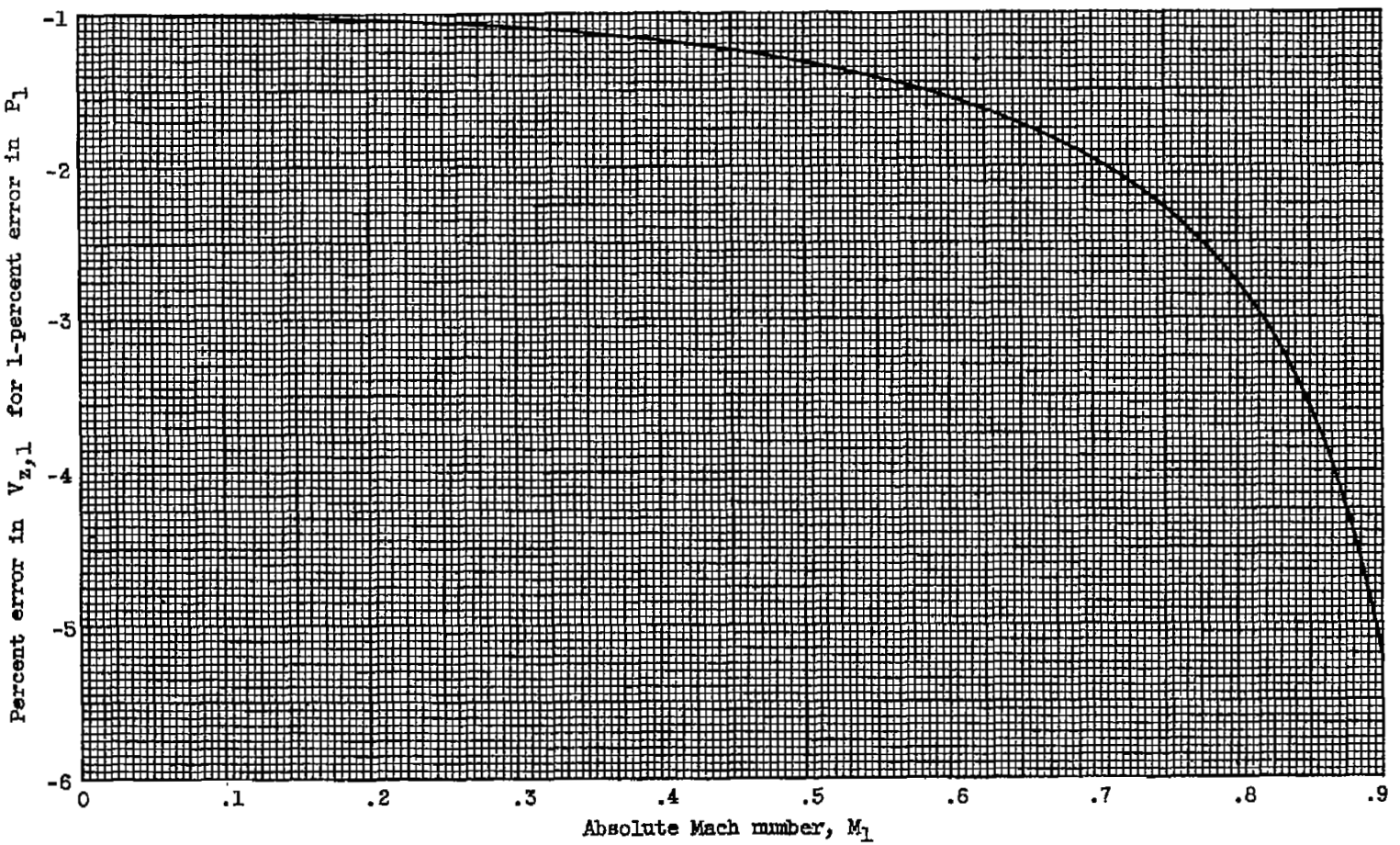

(a) Stagnation pressure (eq. (dB-1)).

Figure 4. - Effect of design errors on axial velocity upstream of rotor.

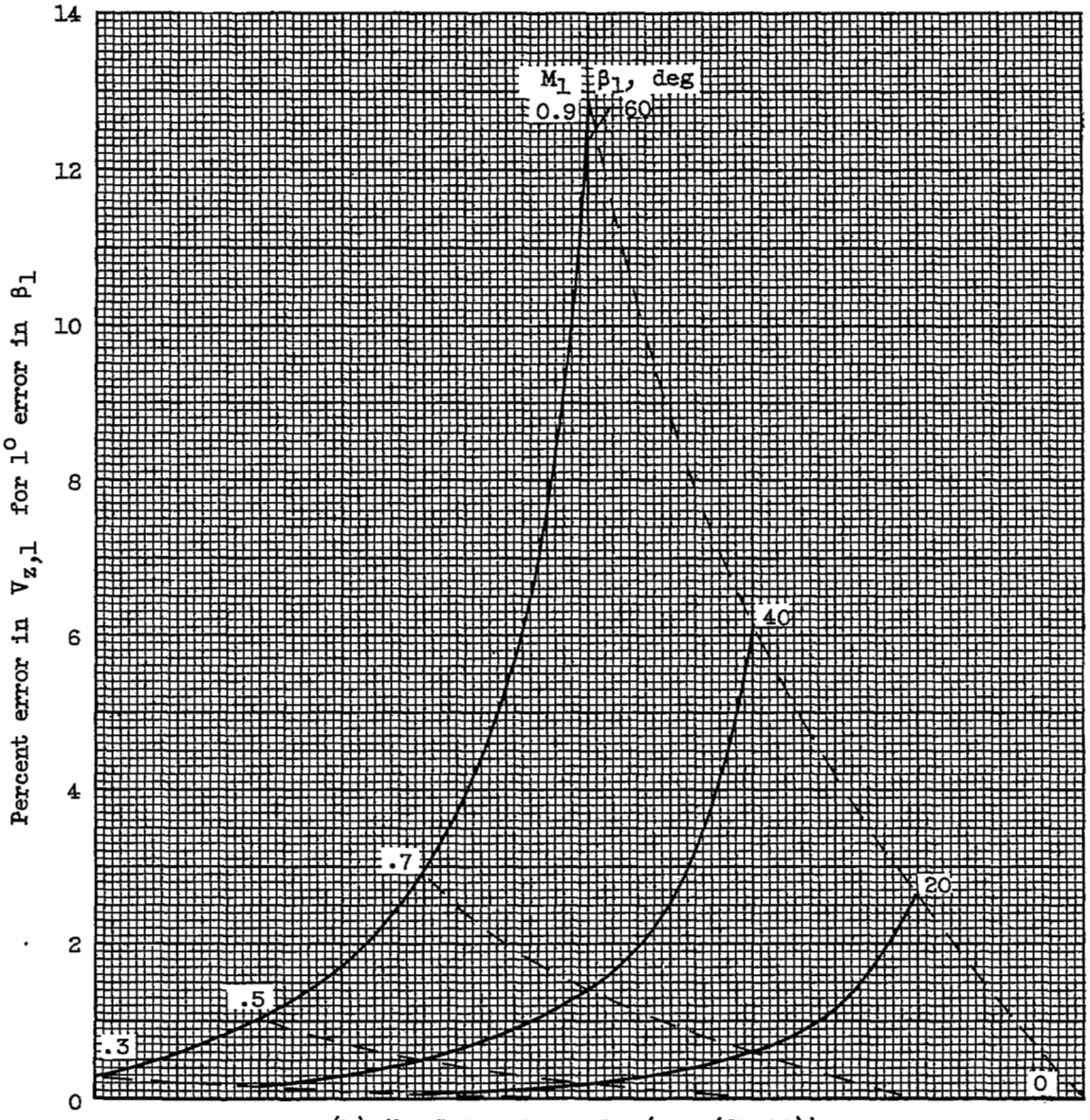

(b) Absolute air angle (eq. (dB-11)).

Figure 4. - Continued. Effect of design errors on axial velocity upstream of rotor.

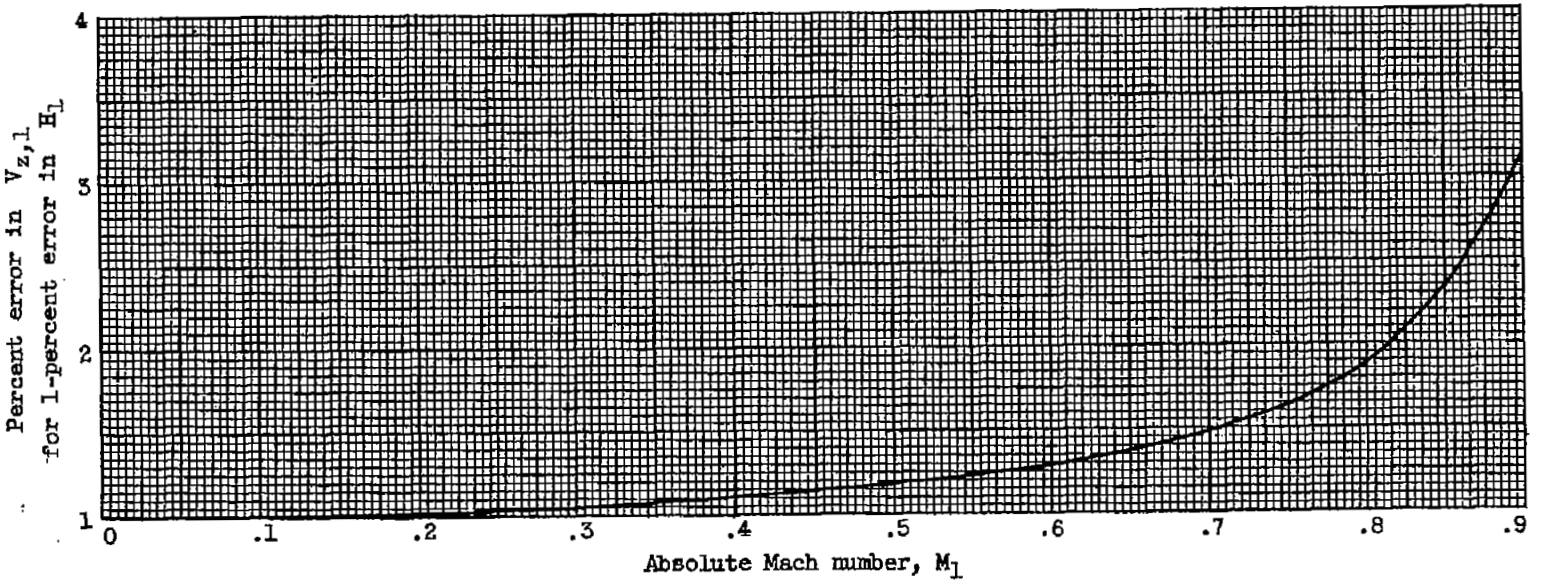

(c) Stagnation enthalpy (eq. (dB-iv)).

Figure 4. - Concluded. Effect of design errors on axial velocity upstream of rotor.

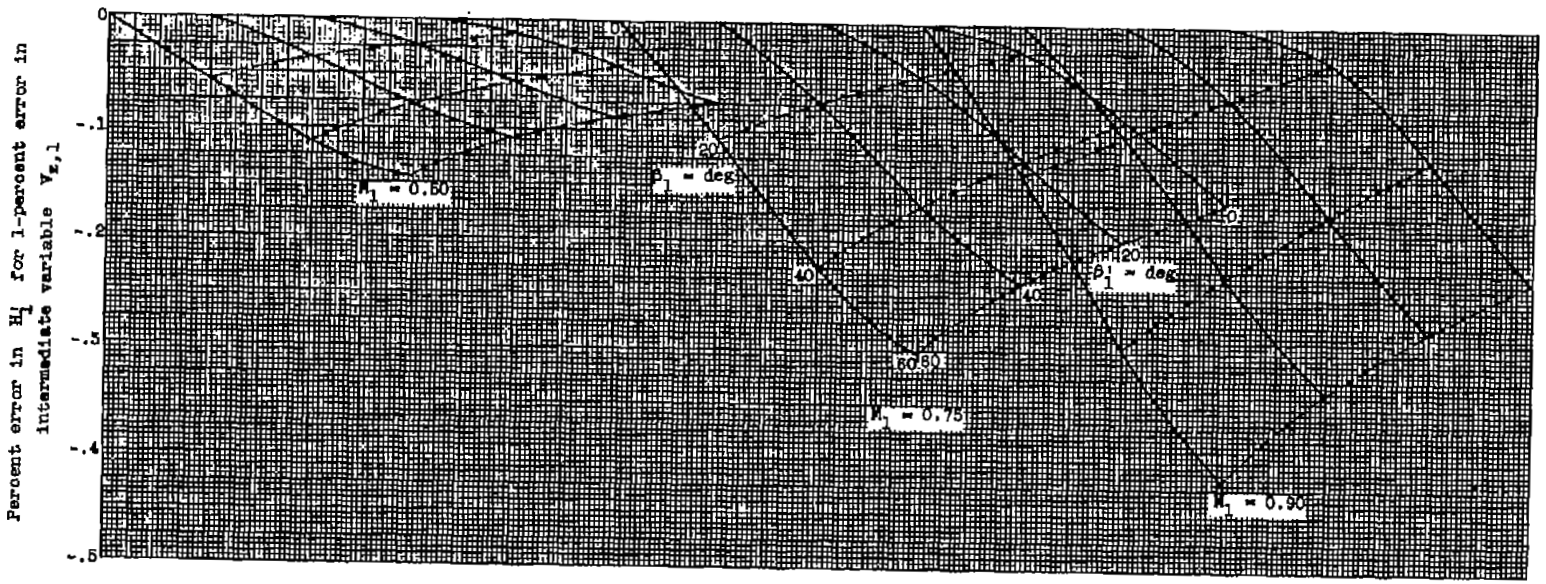

(a) Stagnation pressure or local specific mass flow (eq. (dC-i,iii)).

Figure 5. - Effect of design errors on relative stagnation enthalpy. (A large working copy of this figure may be obtained by using the request card bound in the back of the report.)

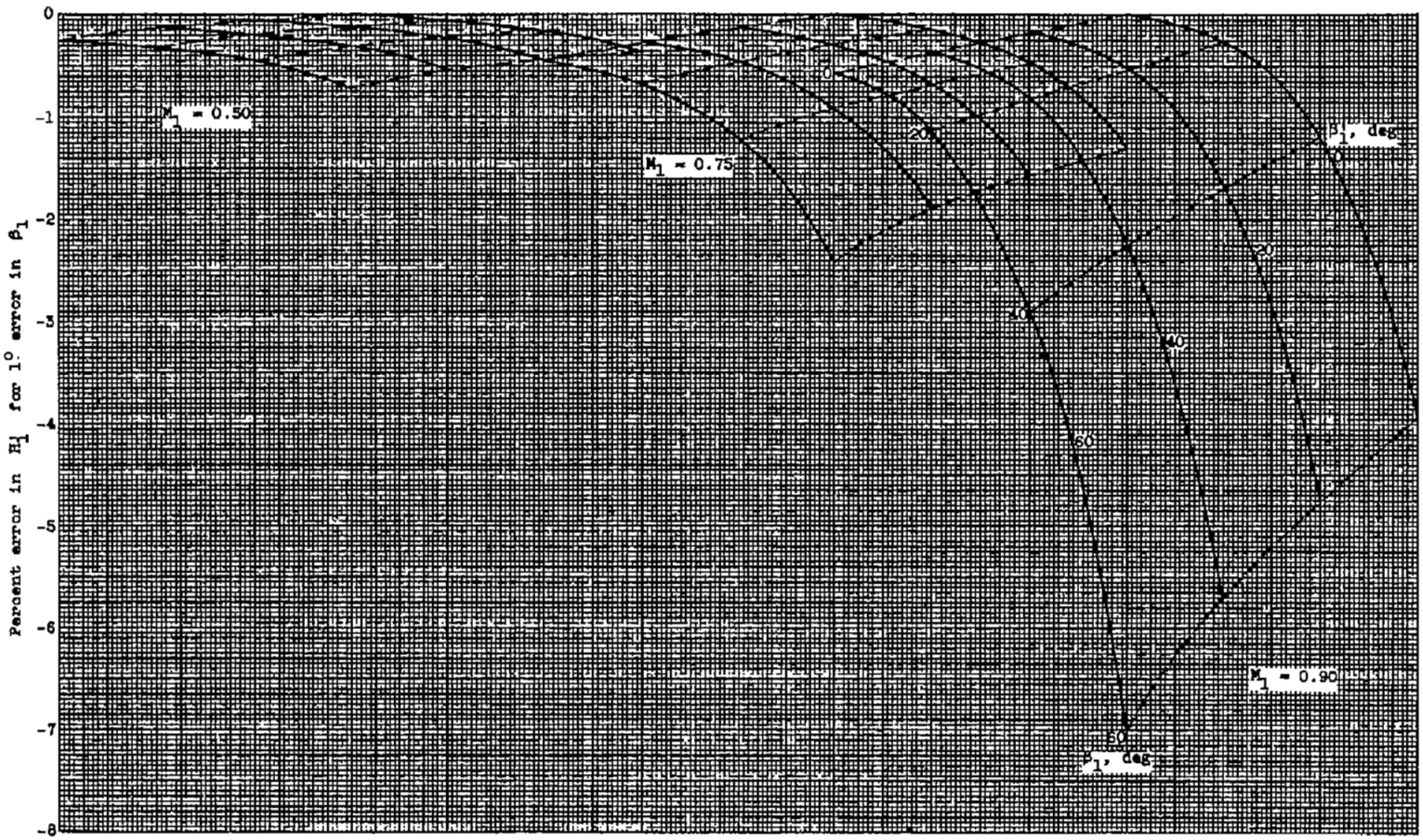

(b) Absolute air angle (eq. (dC-11)).

Figure 5. - Continued. Effect of design errors on relative stagnation enthalpy. (A large working copy of this figure may be obtained by using the request card bound in the back of the report.)

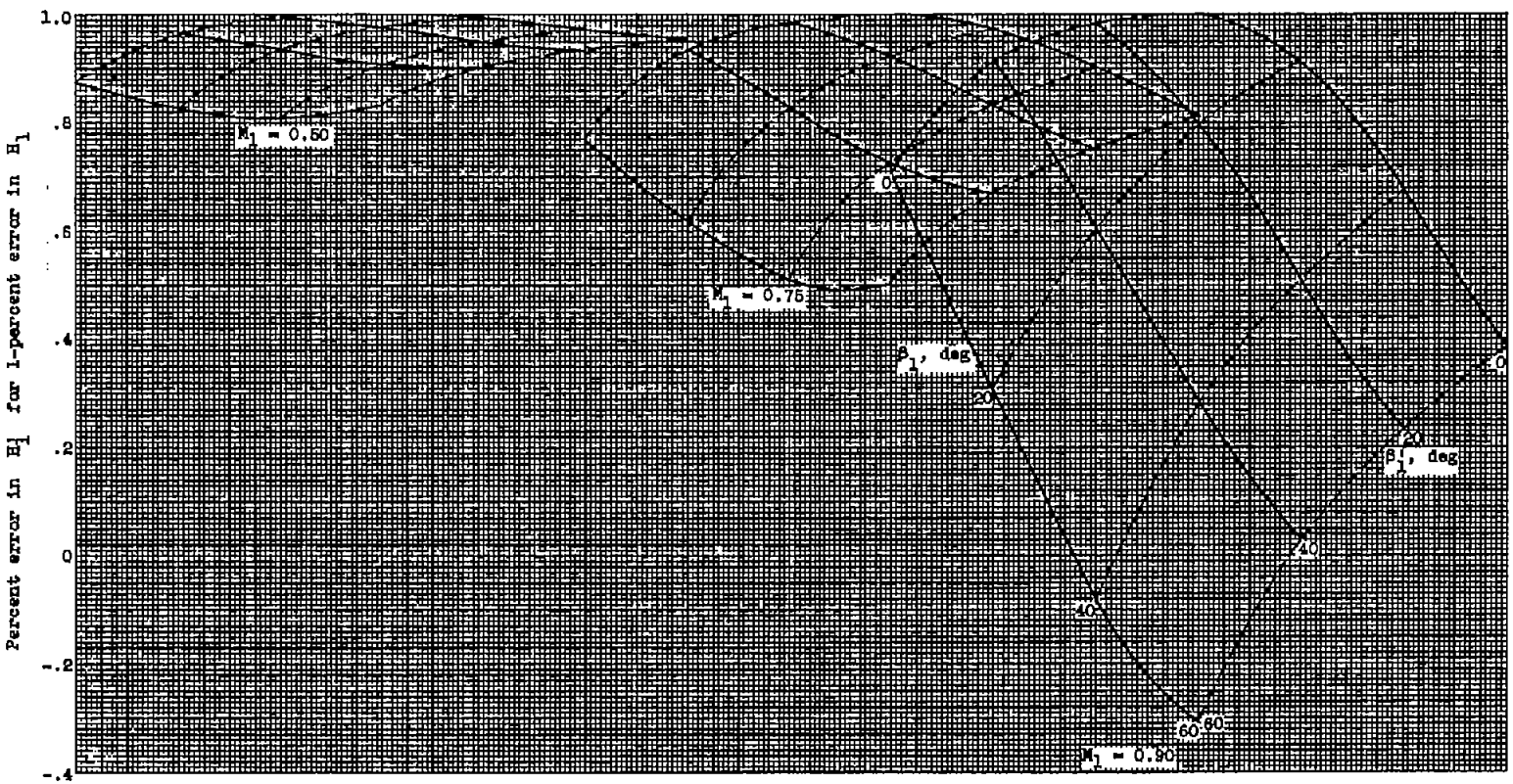

(c) Stagnation enthalpy (eq. (dC-iv)).

Figure 5. - Concluded. Effect of design errors on relative stagnation enthalpy. (A large working copy of this figure may be obtained by using the request card bound in the back of the report.)

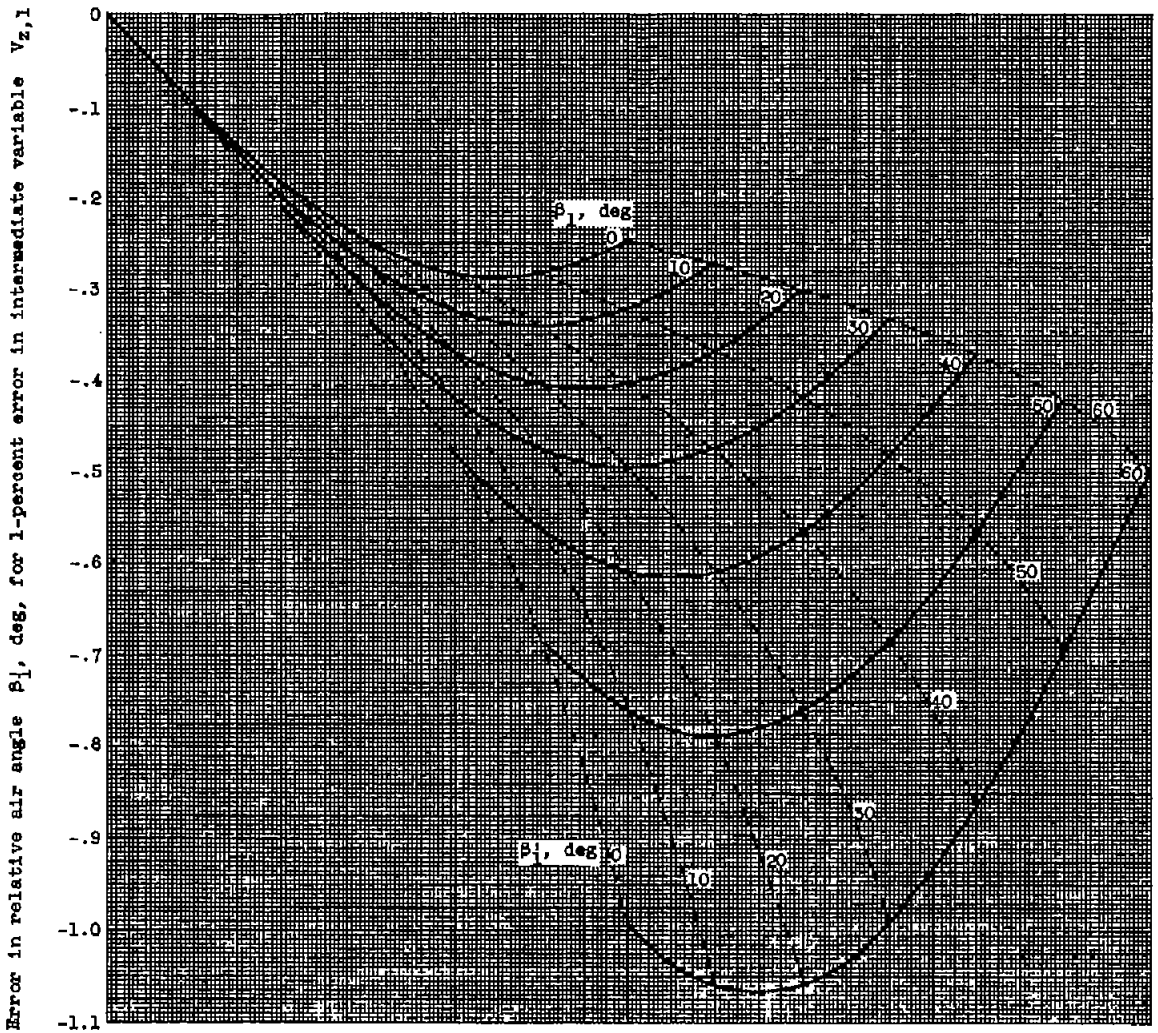

(a) Stagnation pressure, local specific mass flow, or stagnation enthalpy (eq. (dD-i,iii,iv)).

Figure 6. - Effect of design errors on relative air angle. (A large working copy of this figure may be obtained by using the request card bound in the back of the report.)

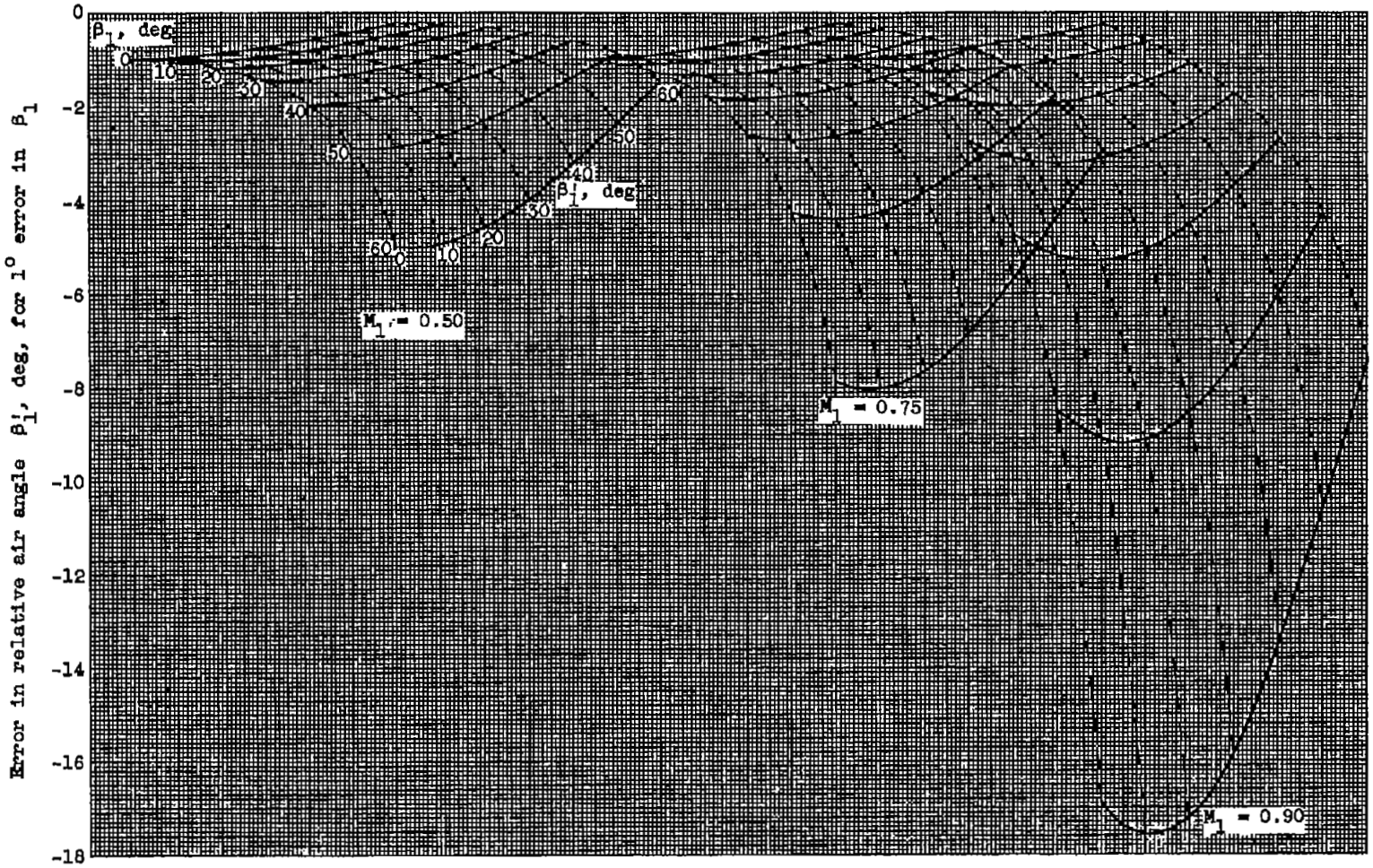

(b) Absolute air angle (eq. (dD-11)).

Figure 6. - Concluded. Effect of design errors on relative air angle. (A large working copy of this figure may be obtained by using the request card bound in the back of the report.)

3479

CH-36 back

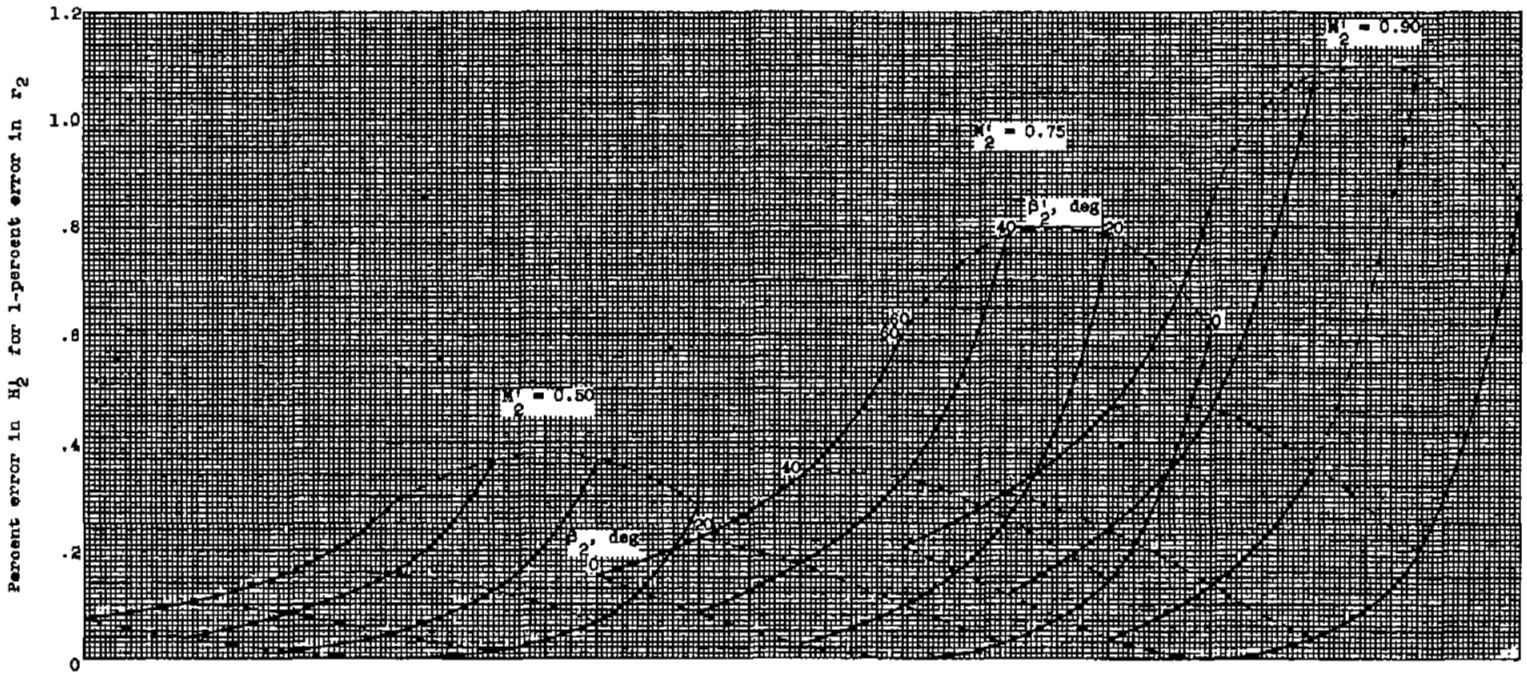

Figure 7. - Effect of design error in radius to blade element on relative stagnation enthalpy (eq. (dE-viii)). (A large working copy of this figure may be obtained by using the request card bound in the back of the report.)

3479

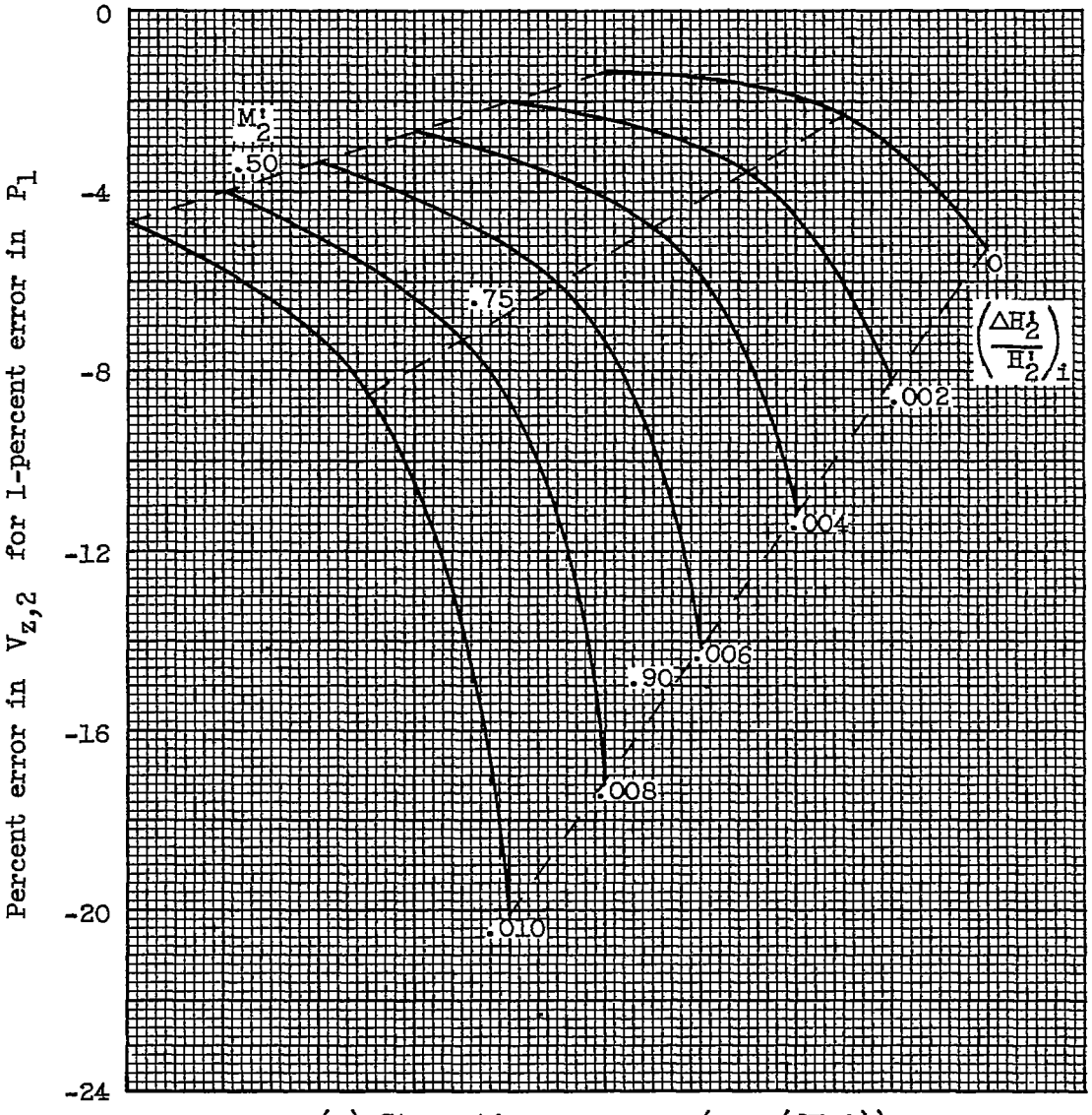

(a) Stagnation pressure (eq. (dF-i)).

Figure 8. - Effect of design errors on axial velocity downstream of rotor.

[redacted]

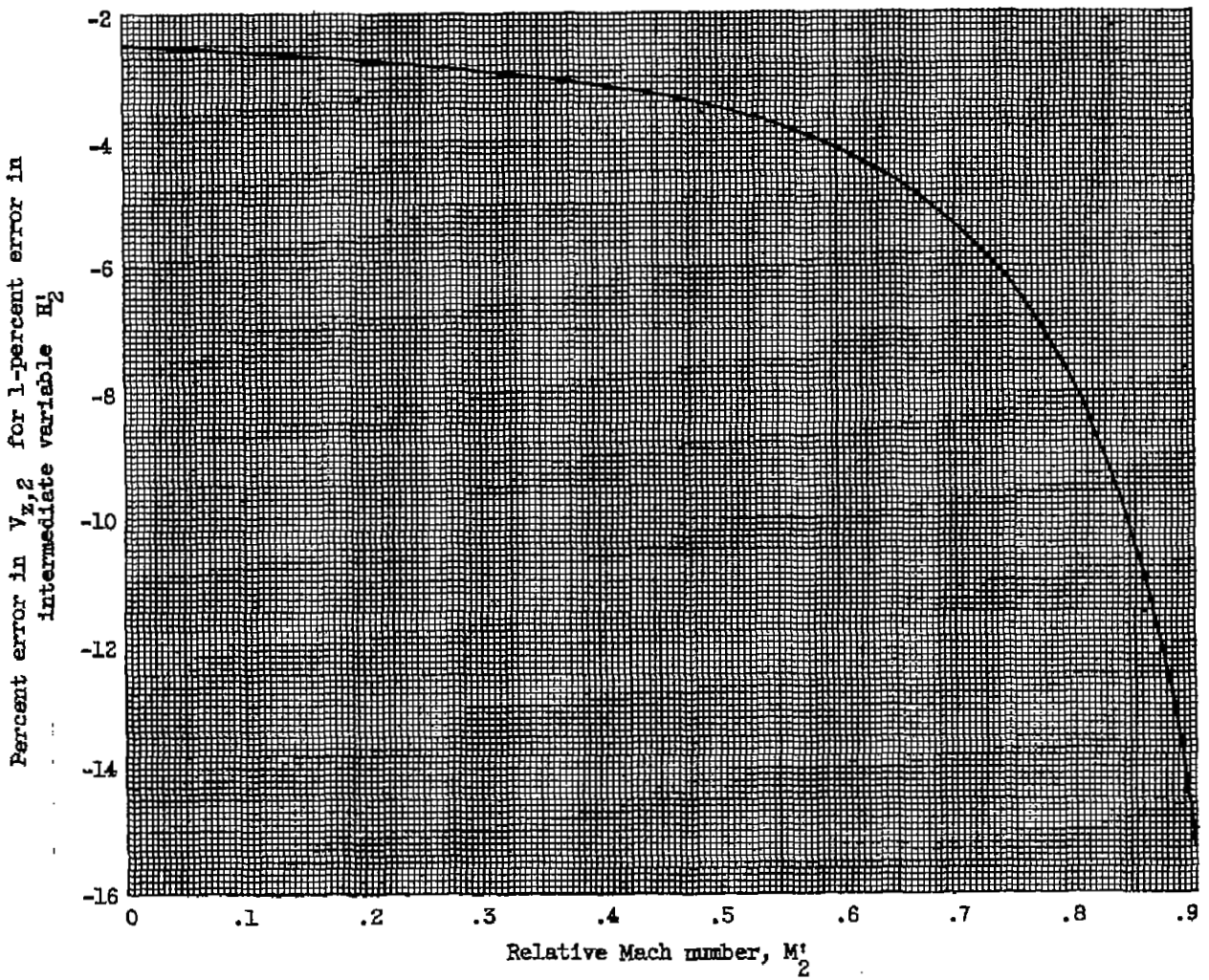

(b) Absolute air angle or local specific mass flow (eq. (dF-ii,iii)).

Figure 8. - Continued. Effect of design errors on axial velocity downstream of rotor.

3479

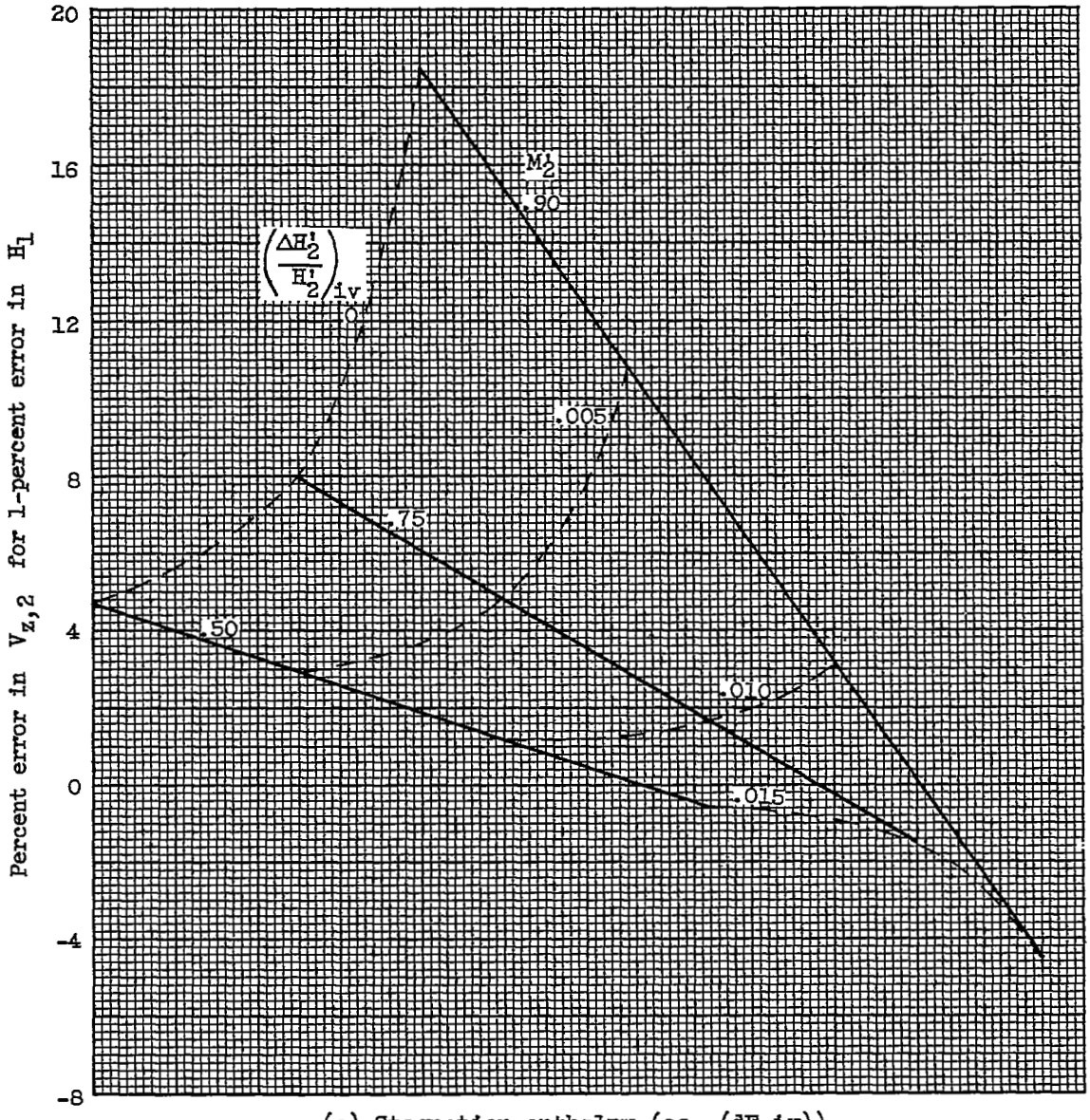

(c) Stagnation enthalpy (eq. (dF-iv)).

Figure 8. - Continued. Effect of design errors on axial velocity downstream of rotor.

[redacted]

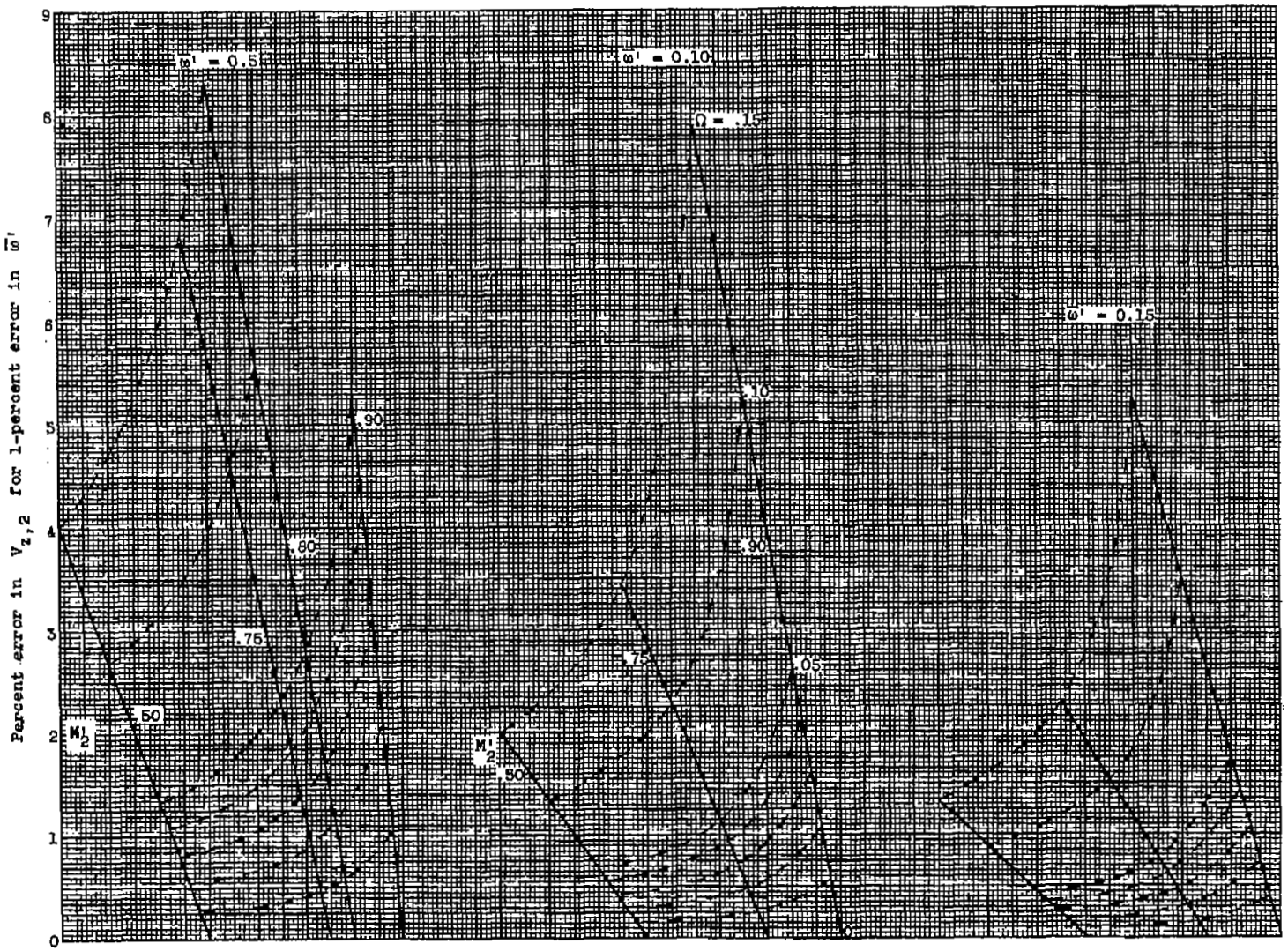

(d) Relative stagnation-pressure-loss parameter (eq. (dF-v)).

Figure 8. - Continued. Effect of design errors on axial velocity downstream of rotor. (A large working copy of this figure may be obtained by using the request card bound in the back of the report.)

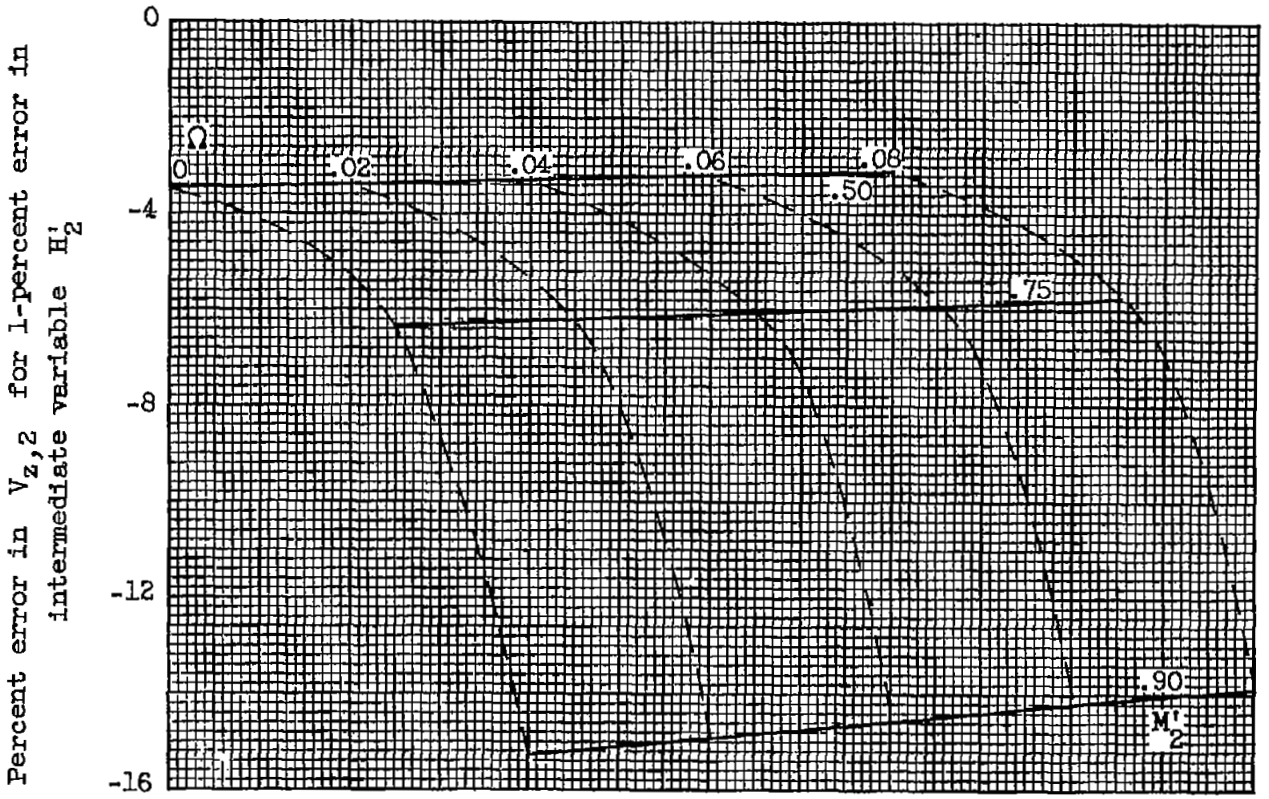

(e) Radius to blade element (eq. (dF-viii)).

Figure 8. - Concluded. Effect of design errors on axial velocity downstream of rotor.

3479

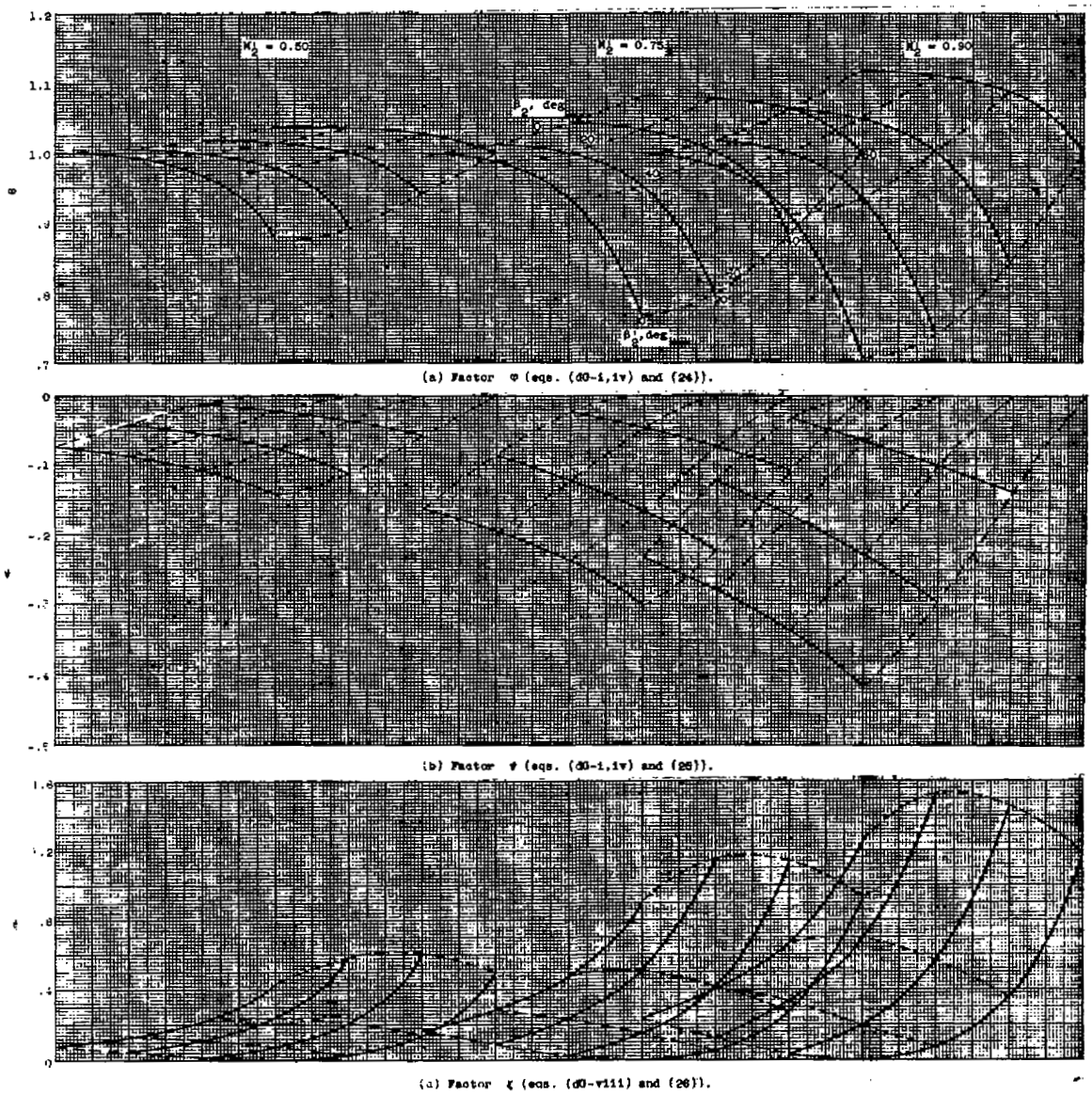

Figure 9. - Factors φ, ψ, and ξ as functions of relative Mach number, relative air angle, and absolute air angle. (A large working copy of this fig. may be obtained by using the request card bound in the back of the report.)

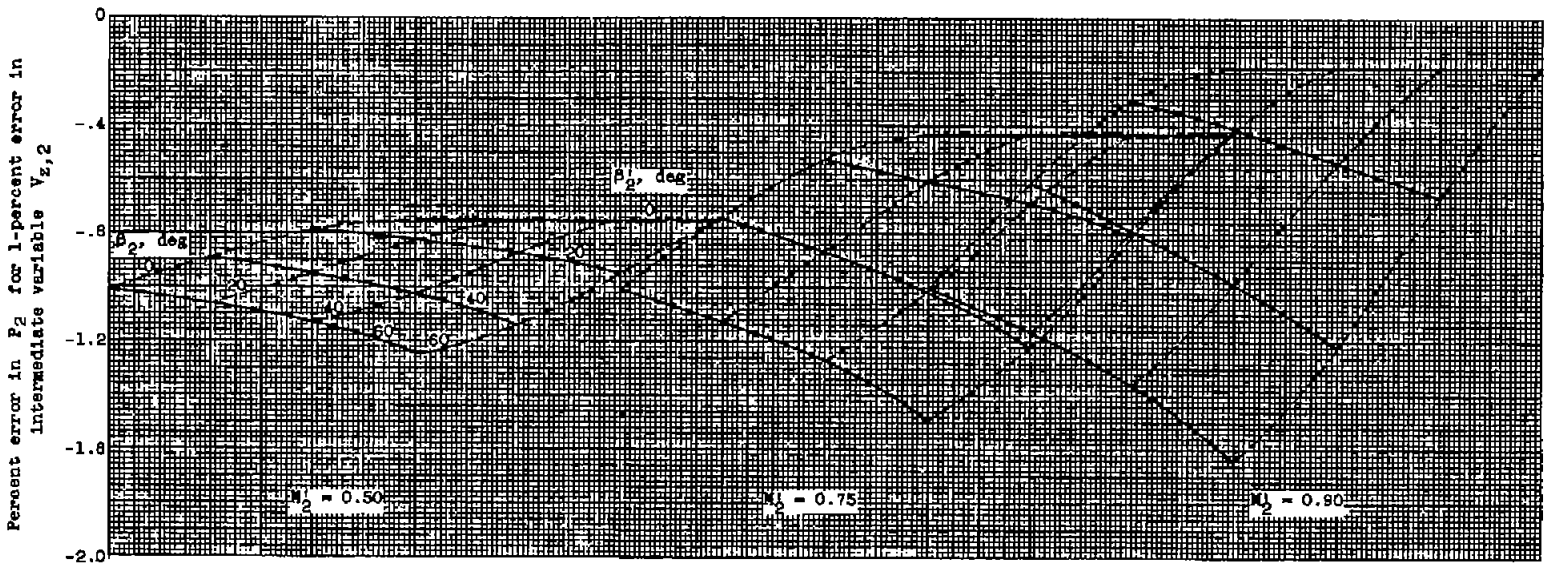

Figure 11. - Effect of design error in relative stagnation-pressure-loss parameter on stagnation pressure (eq. (dH-v)). (A large working copy of this figure may be obtained by using the request card bound in the back of the report.)

NACA – Digidocs

Document processing error

Unreadable tiff image

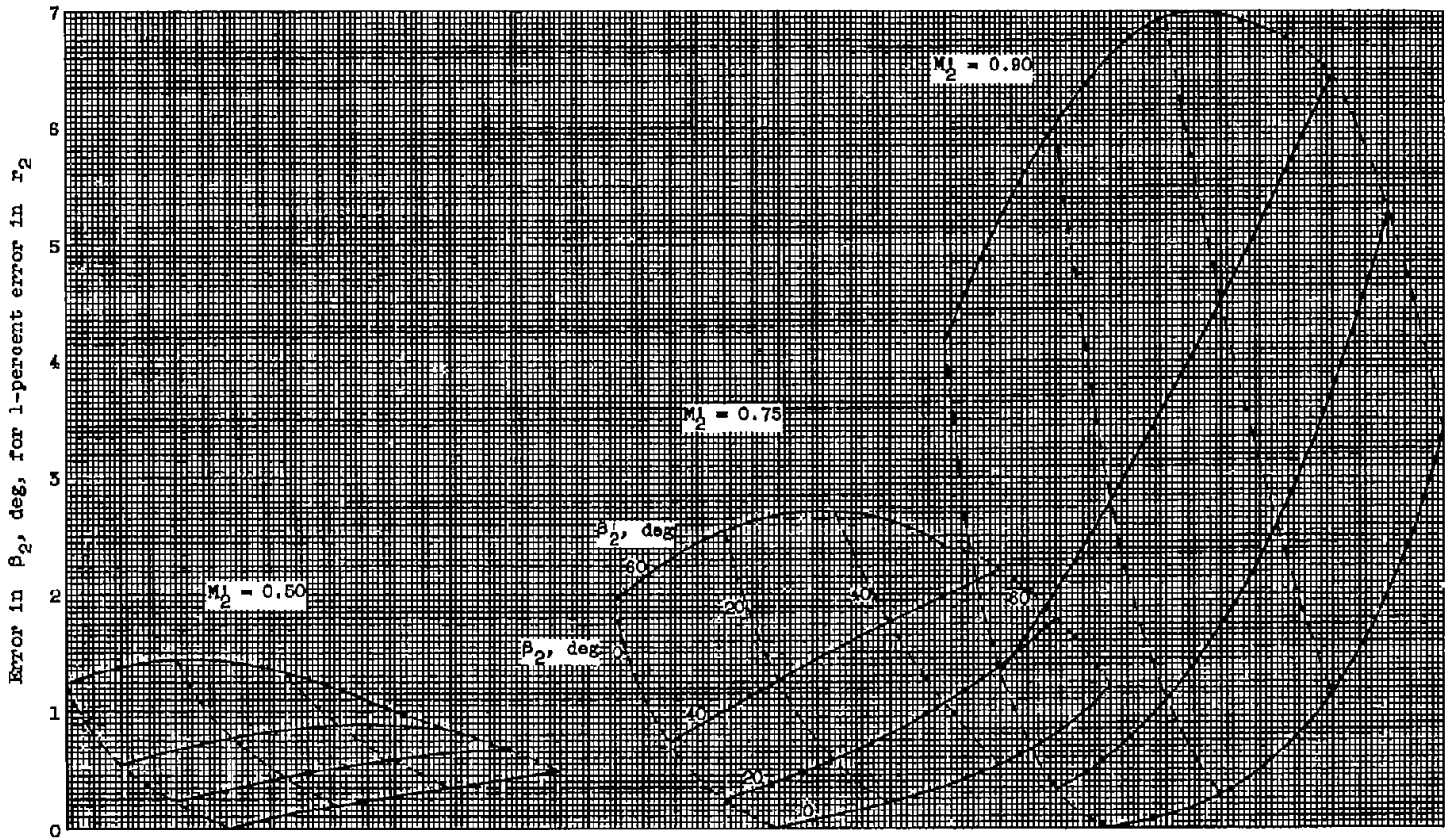

Figure 12. - Effect of design error in radius to blade element on absolute air angle (eq. (dJ-viii)). (A large working copy of this figure may be obtained by using the request card bound in the back of the report.)

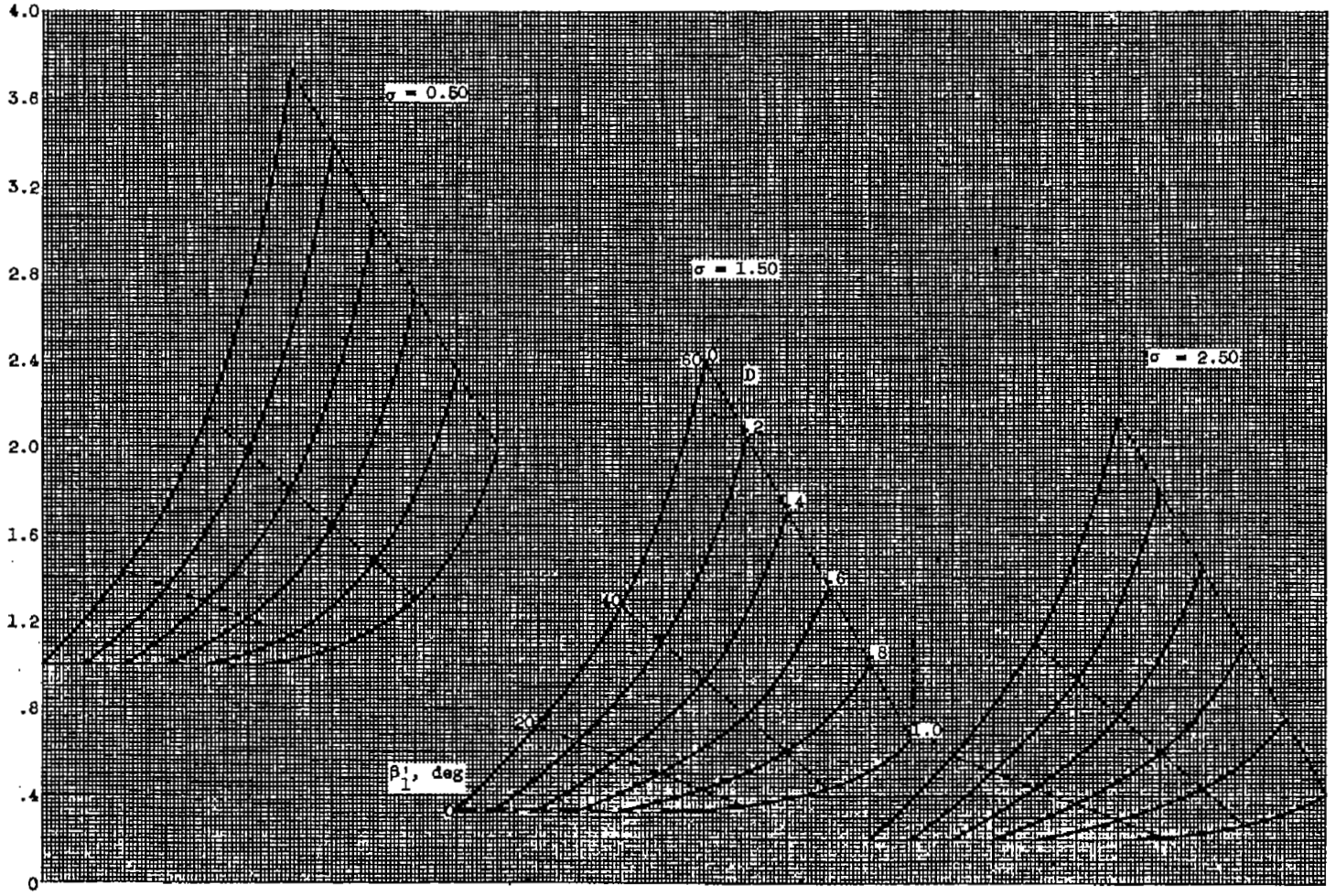

(a) Factor A (eqs. (dK-i-iv) and (27)).

Figure 13. - Factors A and Γ as functions of relative air angle, solidity, and diffusion factor. (A large working copy of this figure may be obtained by using the request card bound in the back of the report.)

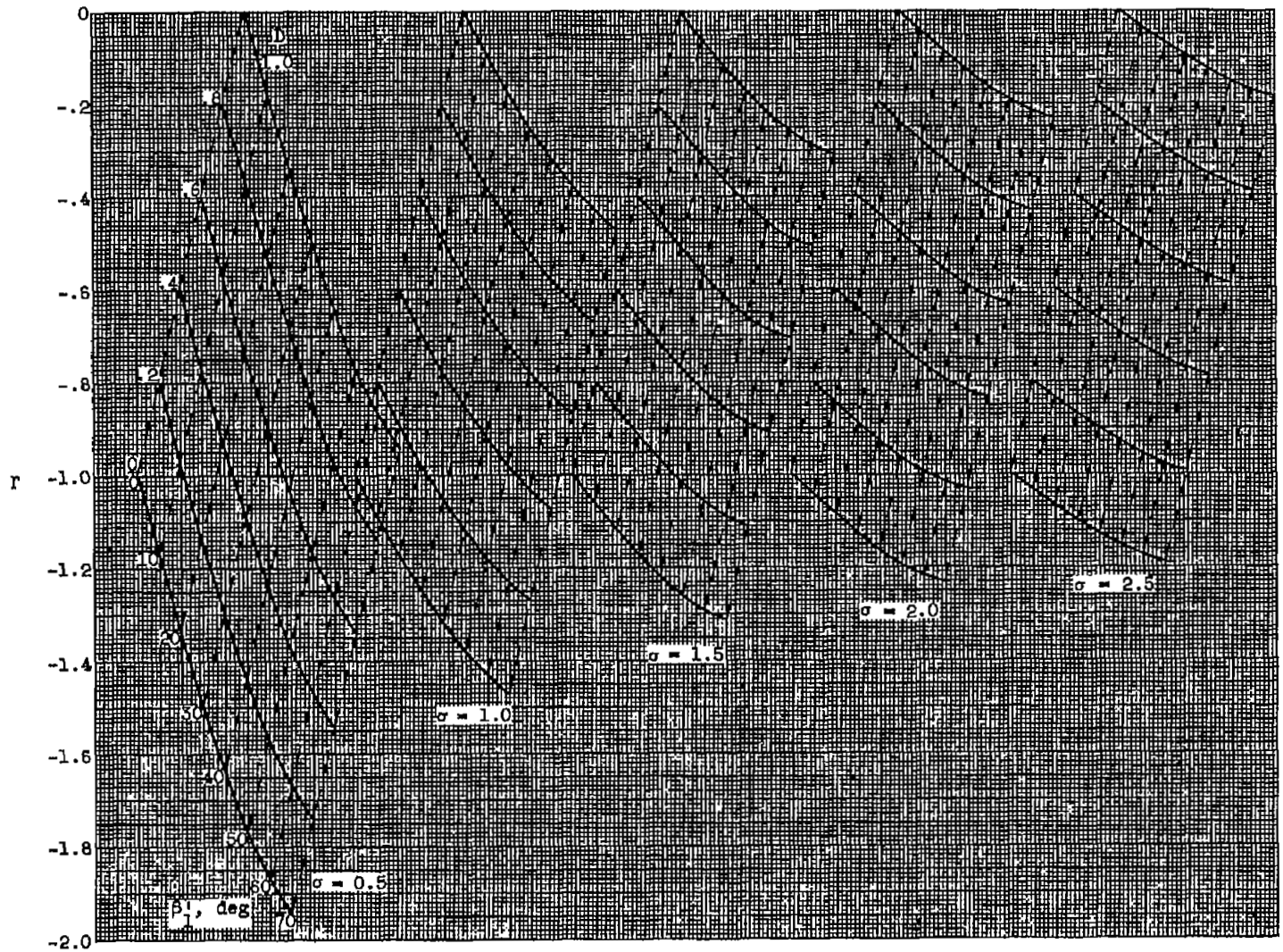

(b) Factor Γ (eqs. (dK-i-iv) and (28)).

Figure 13. - Concluded. Factors A and Γ as functions of relative air angle, solidity, and diffusion factor. (A large working copy of this figure may be obtained by using the request card bound in the back of the report.)

3479

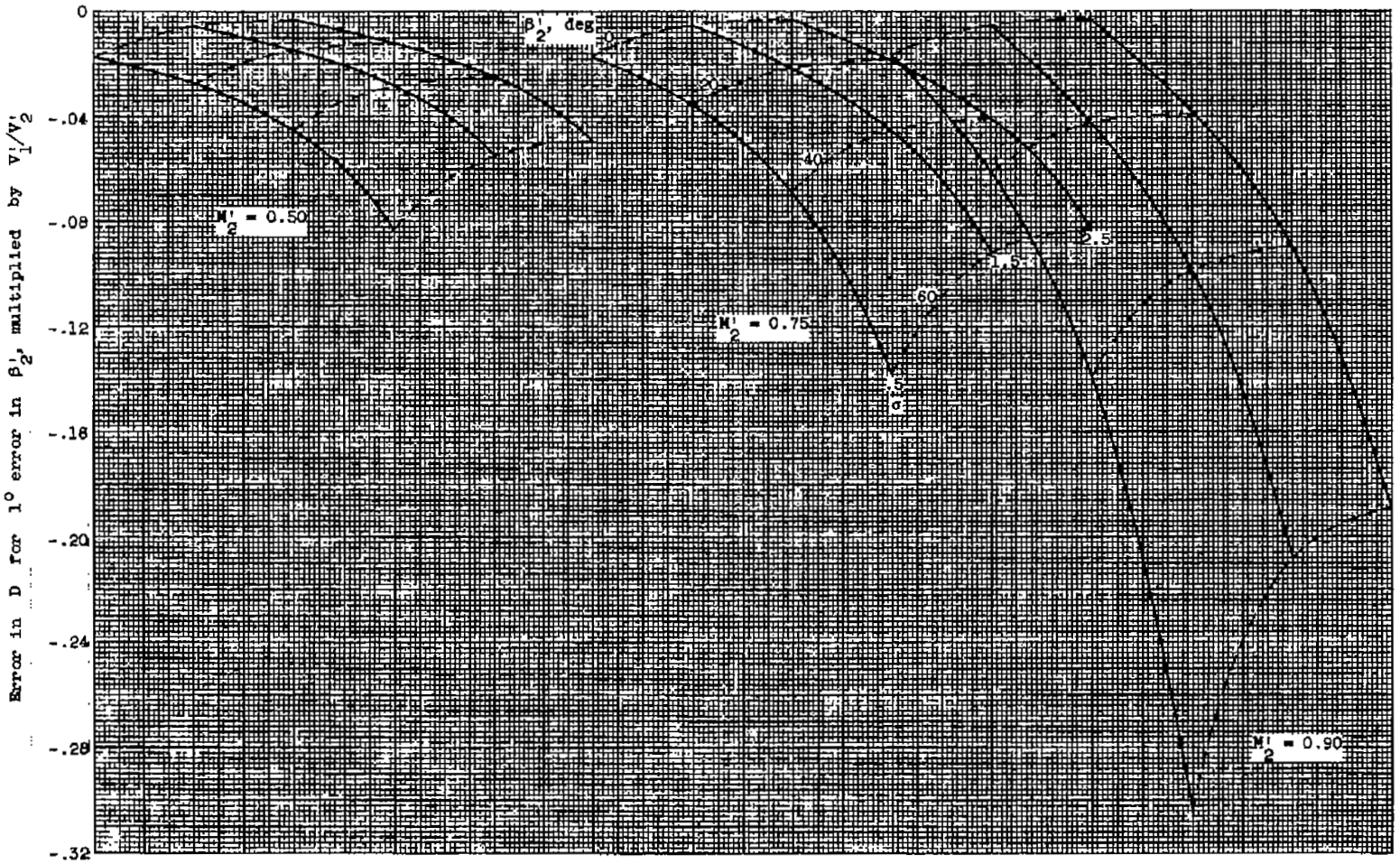

Figure 14. - Effect of design error in relative air angle on diffusion factor (eq. (dK-vi)). (A large working copy of this figure may be obtained by using the request card bound in the back of the report.)

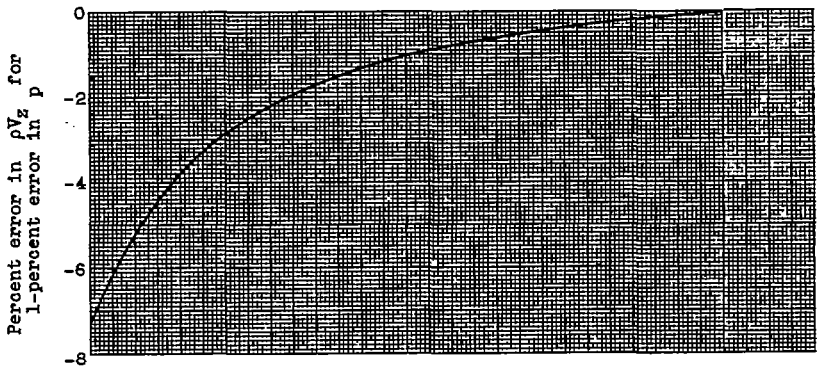

(a) Static pressure (eq. (mA-i,v)).

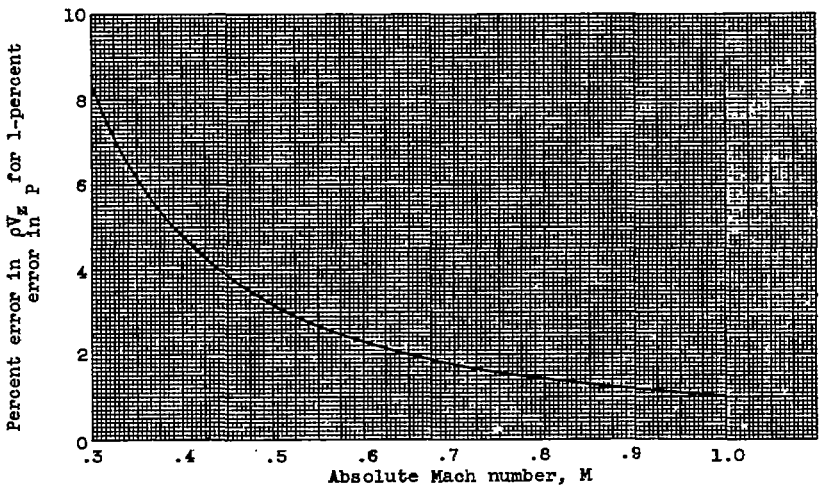

(b) Stagnation pressure (eq. (mA-ii,vi)).

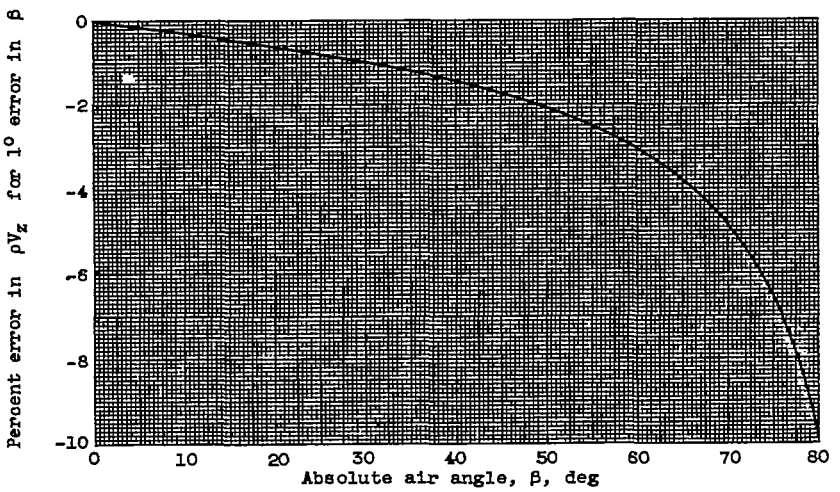

(c) Absolute air angle (eq. (mA-iv,viii)).

Figure 15. - Effect of measurement errors on calculated value of local specific mass flow. (A large working copy of this figure may be obtained by using the request card bound in the back of the report.)

[redacted]

3479

CH-38

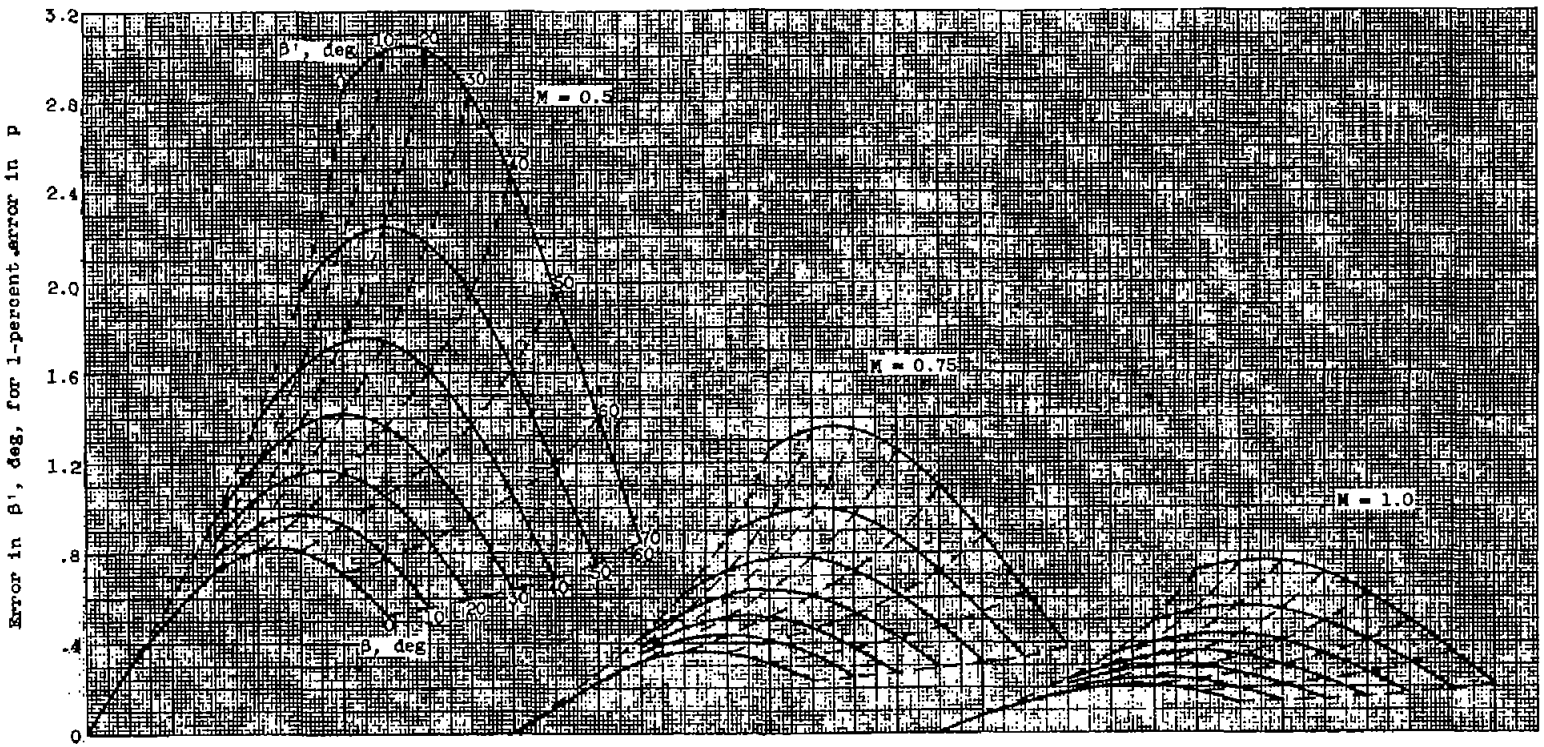

(a) Static pressure (eq. (mB-1,v)).

Figure 16. - Effect of measurement errors on calculated value of relative air angle. (A large working copy of this figure may be obtained by using the request card bound in the back of the report.)

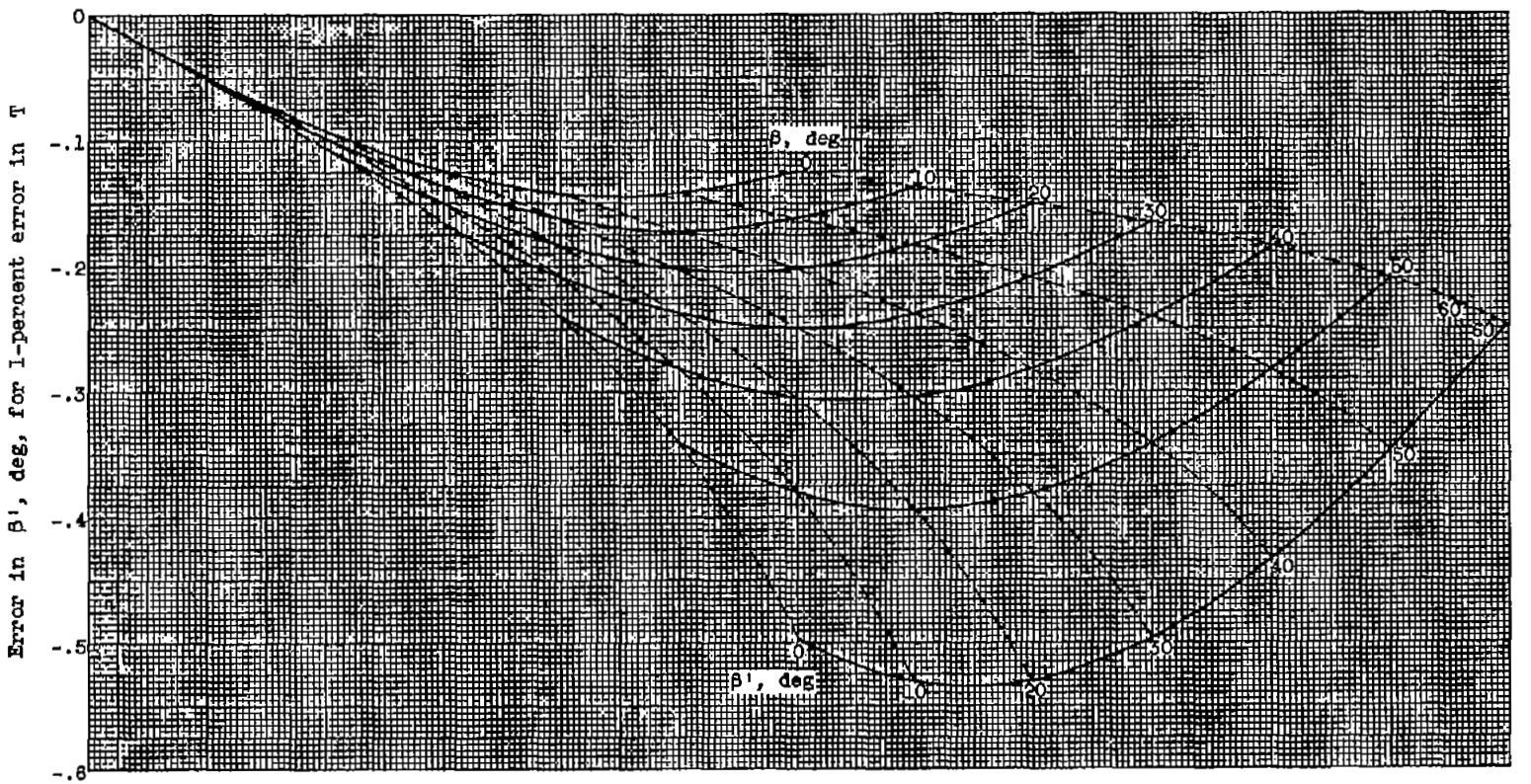

(b) Stagnation temperature (eq. (mB-iii,vii)).

Figure 16. - Continued. Effect of measurement errors on calculated value of relative air angle. (A large working copy of this figure may be obtained by using the request card bound in the back of the report.)

3479

CH-38 back

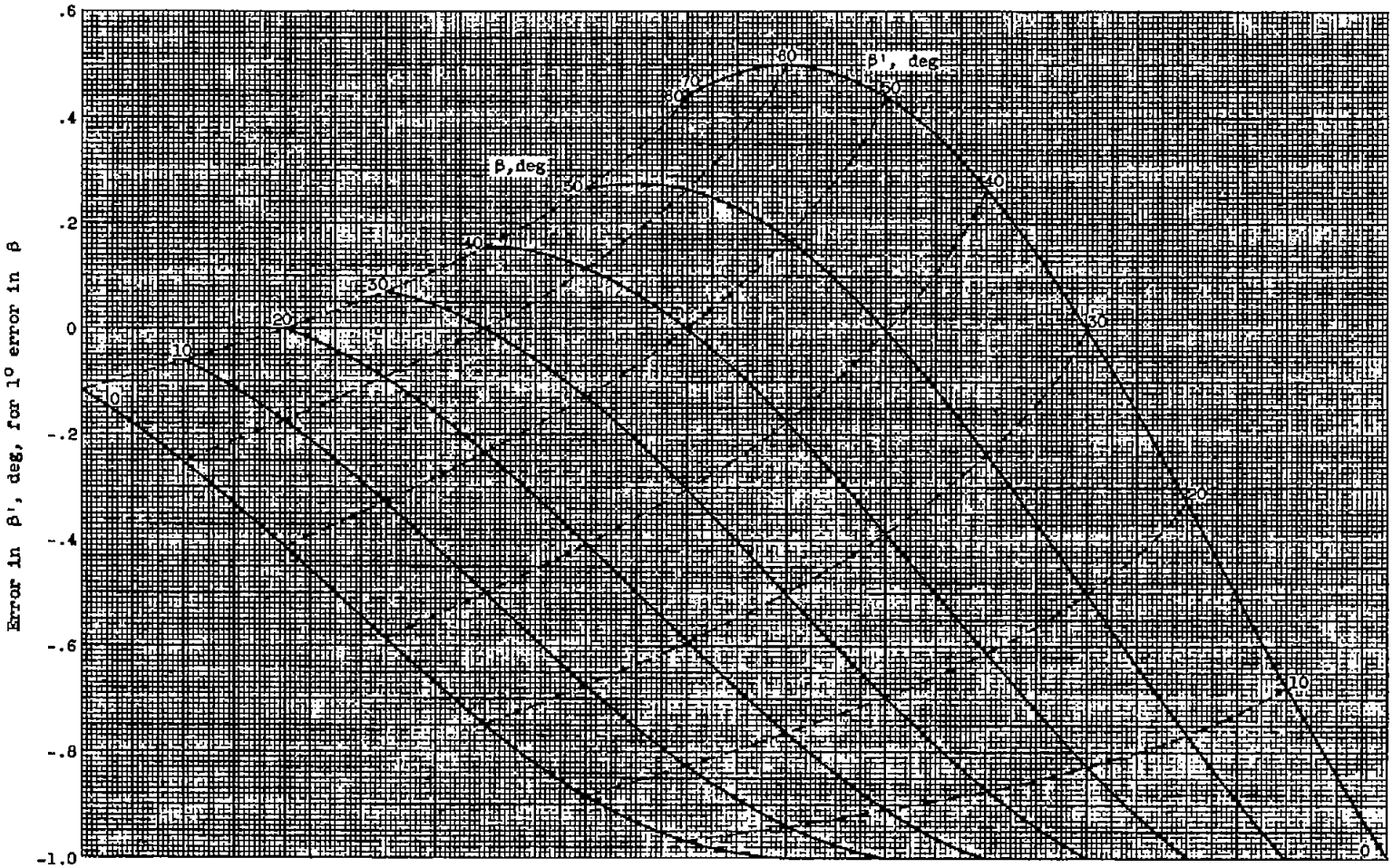

(c) Absolute air angle (eq. (mB-iv,viii)).

Figure 16. - Concluded. Effect of measurement errors on calculated value of relative air angle. (A large working copy of this figure may be obtained by using the request card bound in the back of the report.)

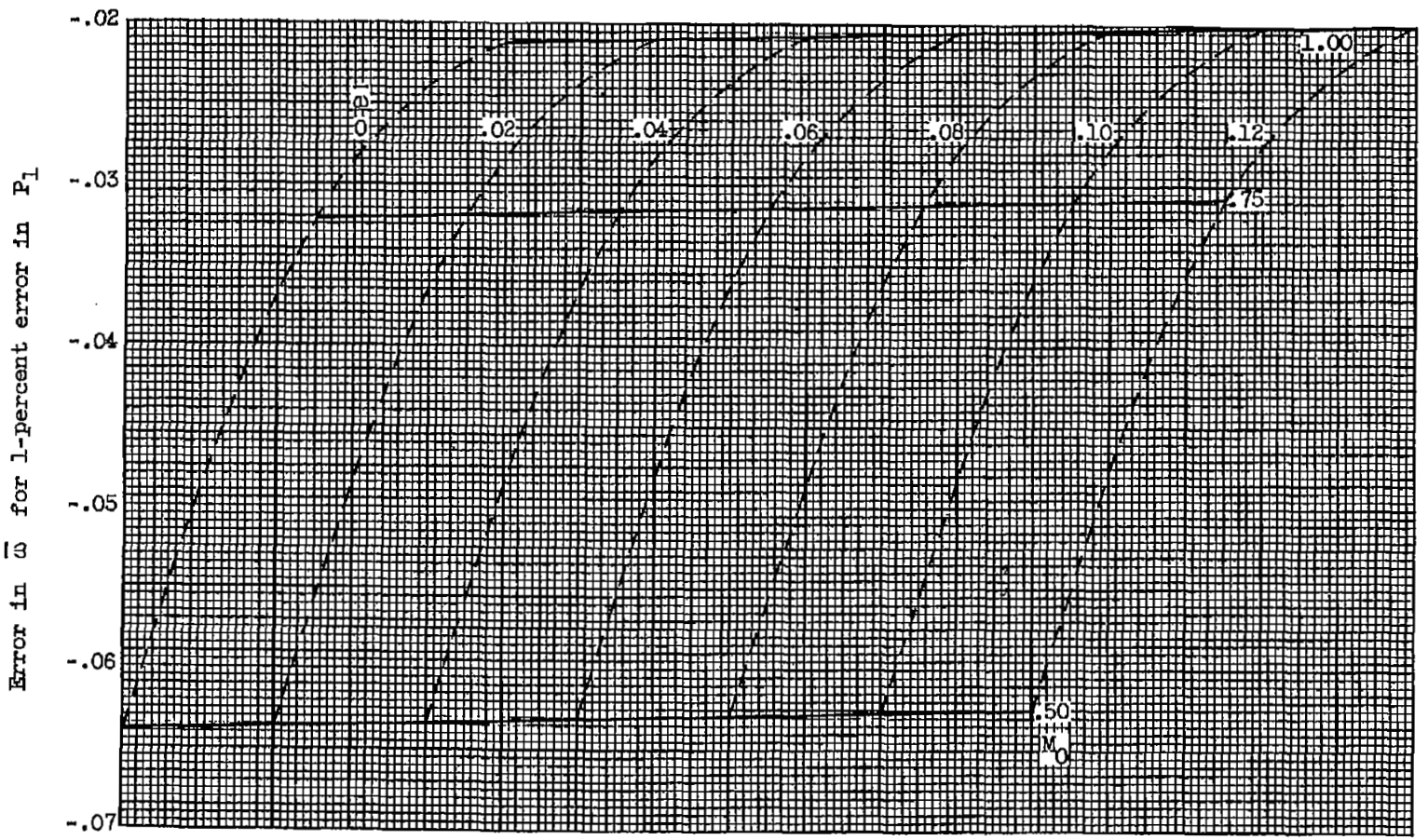

Figure 17. - Effect of measurement error in stagnation pressure on calculated value of absolute stagnation-pressure-loss parameter (eq. (mC-ii)).

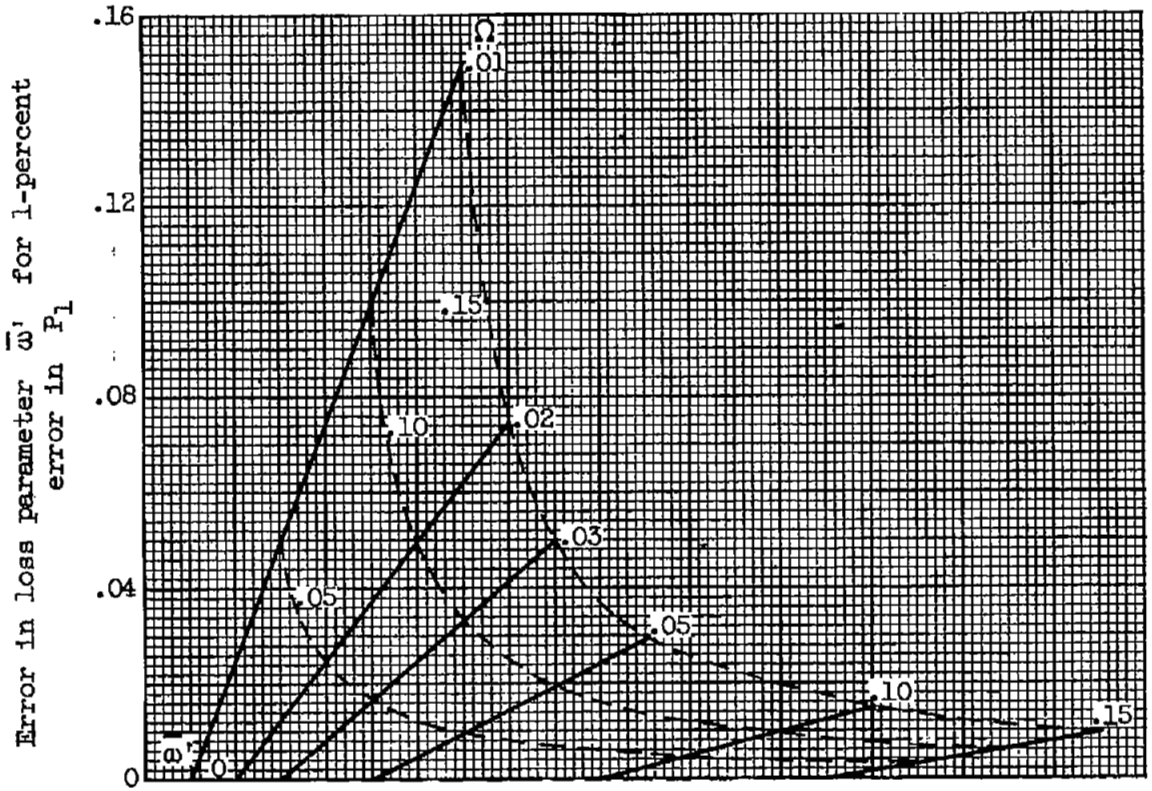

Figure 18. - Effect of measurement error in stagnation pressure on calculated value of relative stagnation-pressure-loss parameter (eq. (mD-ii)).

2479

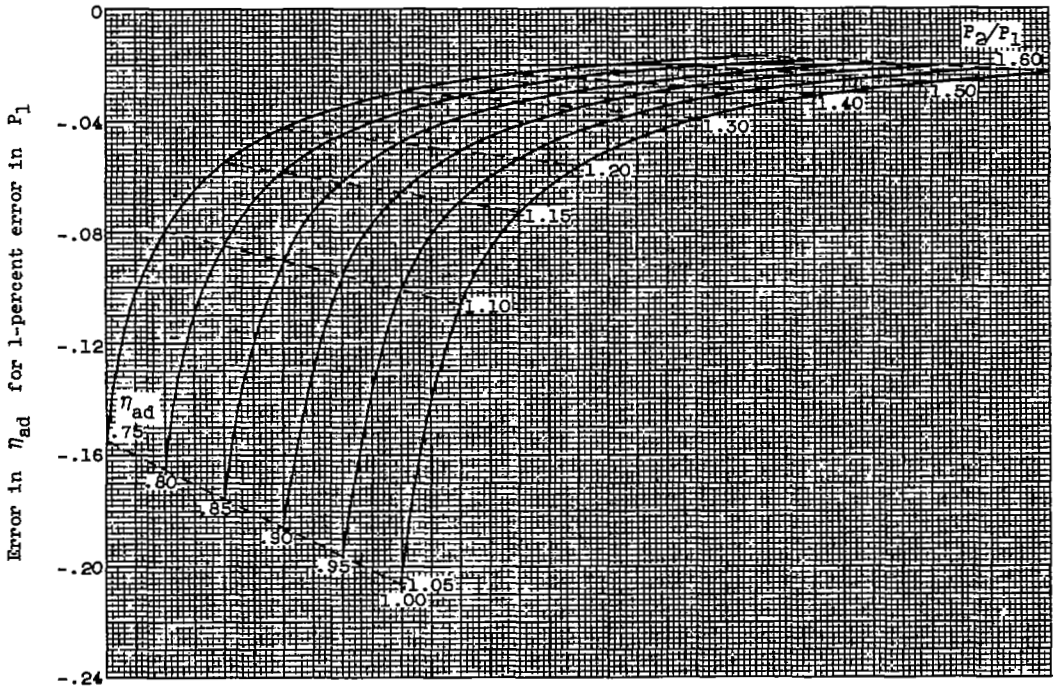

(a) Stagnation pressure (eq. (mE-ii)).

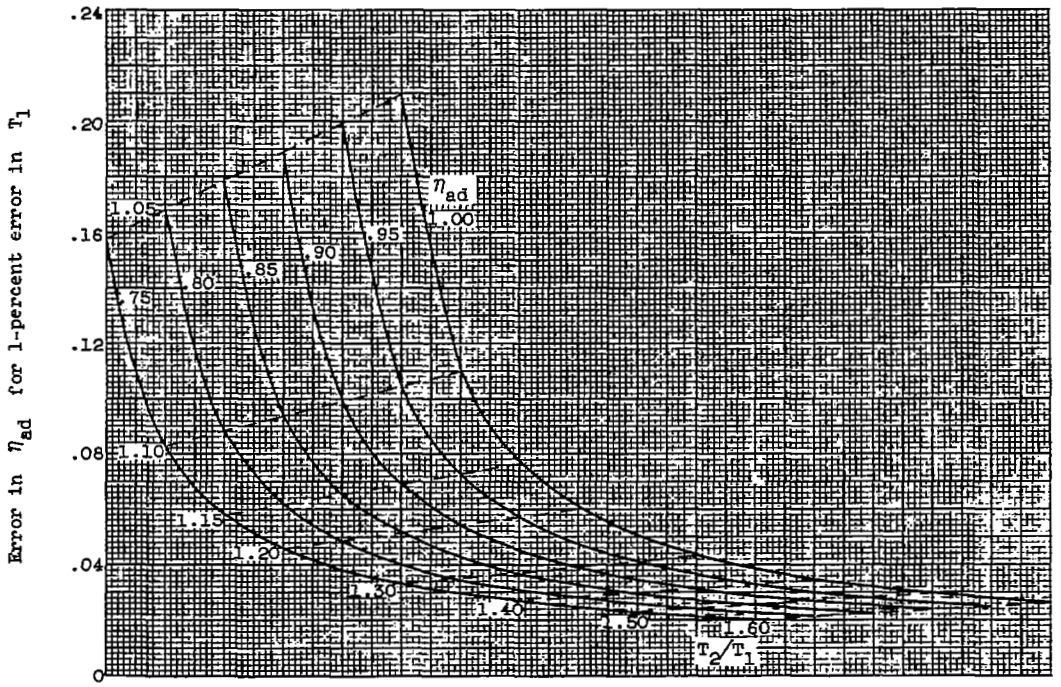

(b) Stagnation temperature (eq. (mE-iii)).

Figure 19. - Effect of measurement errors on calculated value of blade-element efficiency. (A large working copy of this figure may be obtained by using the request card bound in the back of the report.)

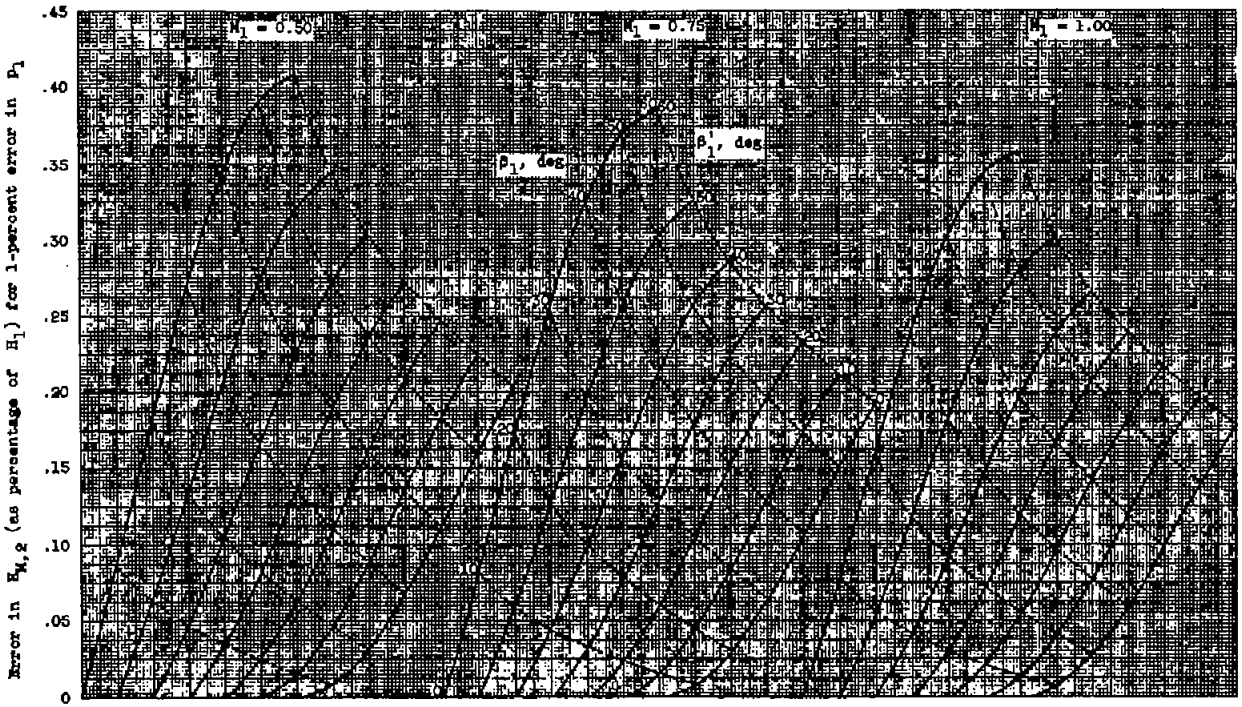

(a) Static pressure (eq. (mF-i)).

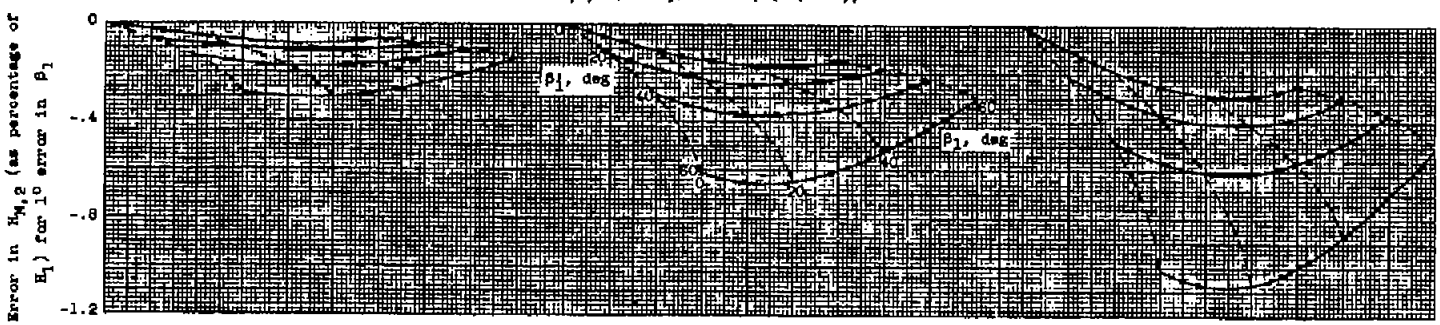

(b) Absolute air angle (eq. (mF-iv)).

Figure 20. - Effect of measurement errors on stagnation enthalpy calculated from change of moment of momentum. (A large working copy of this figure may be obtained by using the request card bound in the back of the report.)

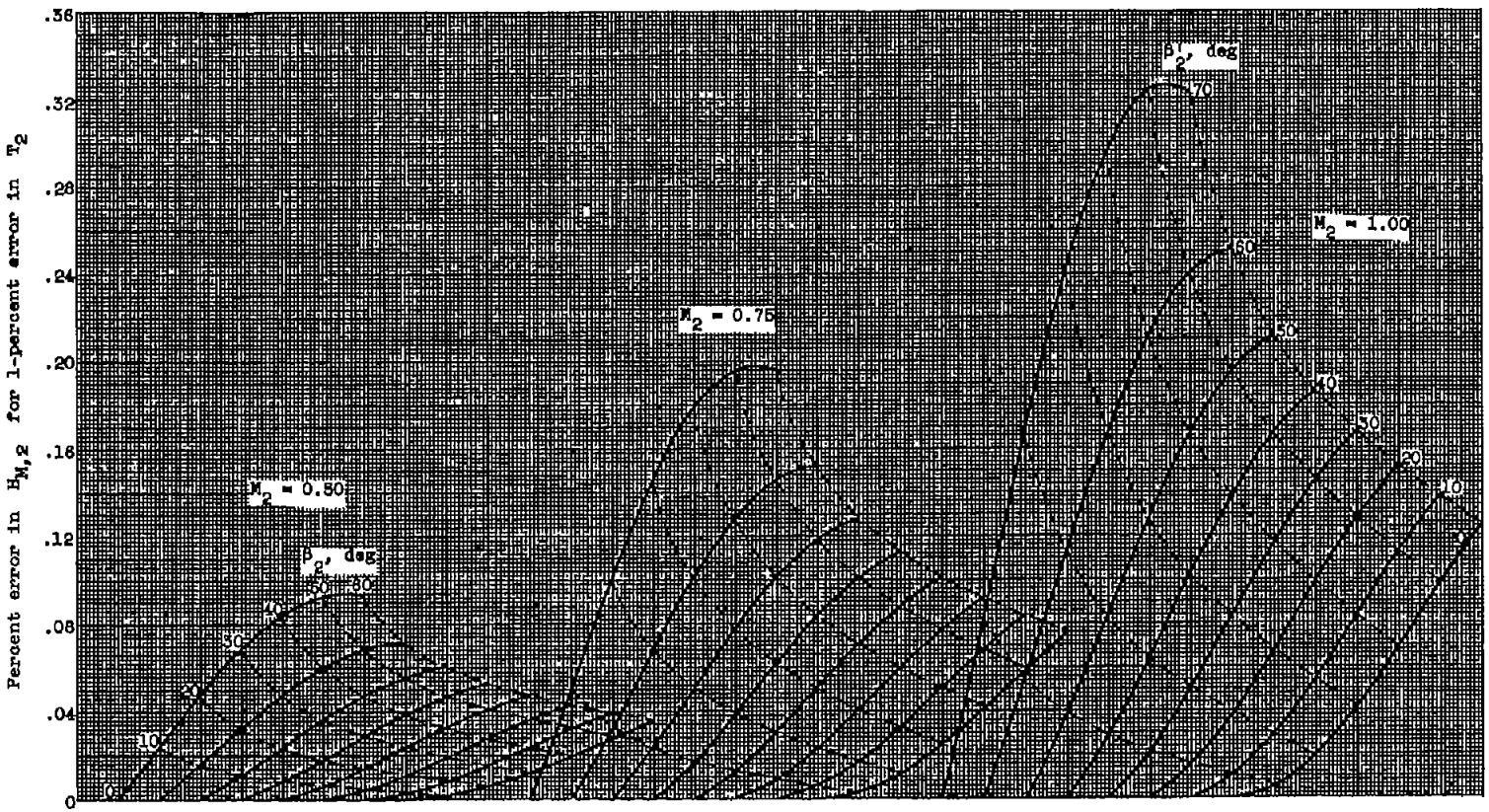

(c) Stagnation temperature (eq. (mF-vii)).

Figure 20. - Concluded. Effect of measurement errors on stagnation enthalpy calculated from change of moment of momentum. (A large working copy of this figure may be obtained by using the request card bound in the back of the report.)

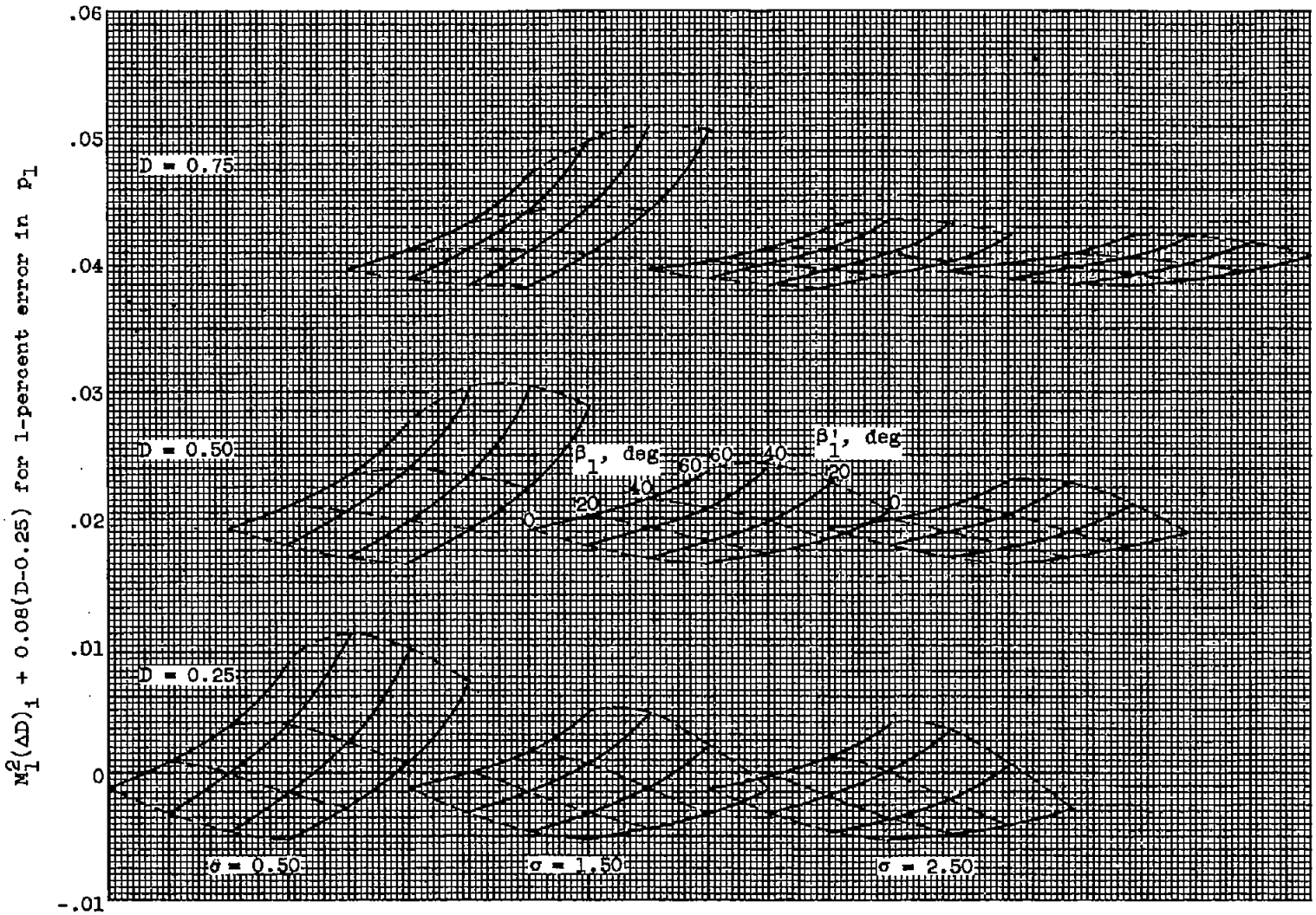

(a) Static pressure upstream of rotor (eq. (mG-1)).

Figure 21. - Effect of measurement errors on calculated value of diffusion factor. (A large working copy of this figure may be obtained by using the request card bound in the back of the report.)

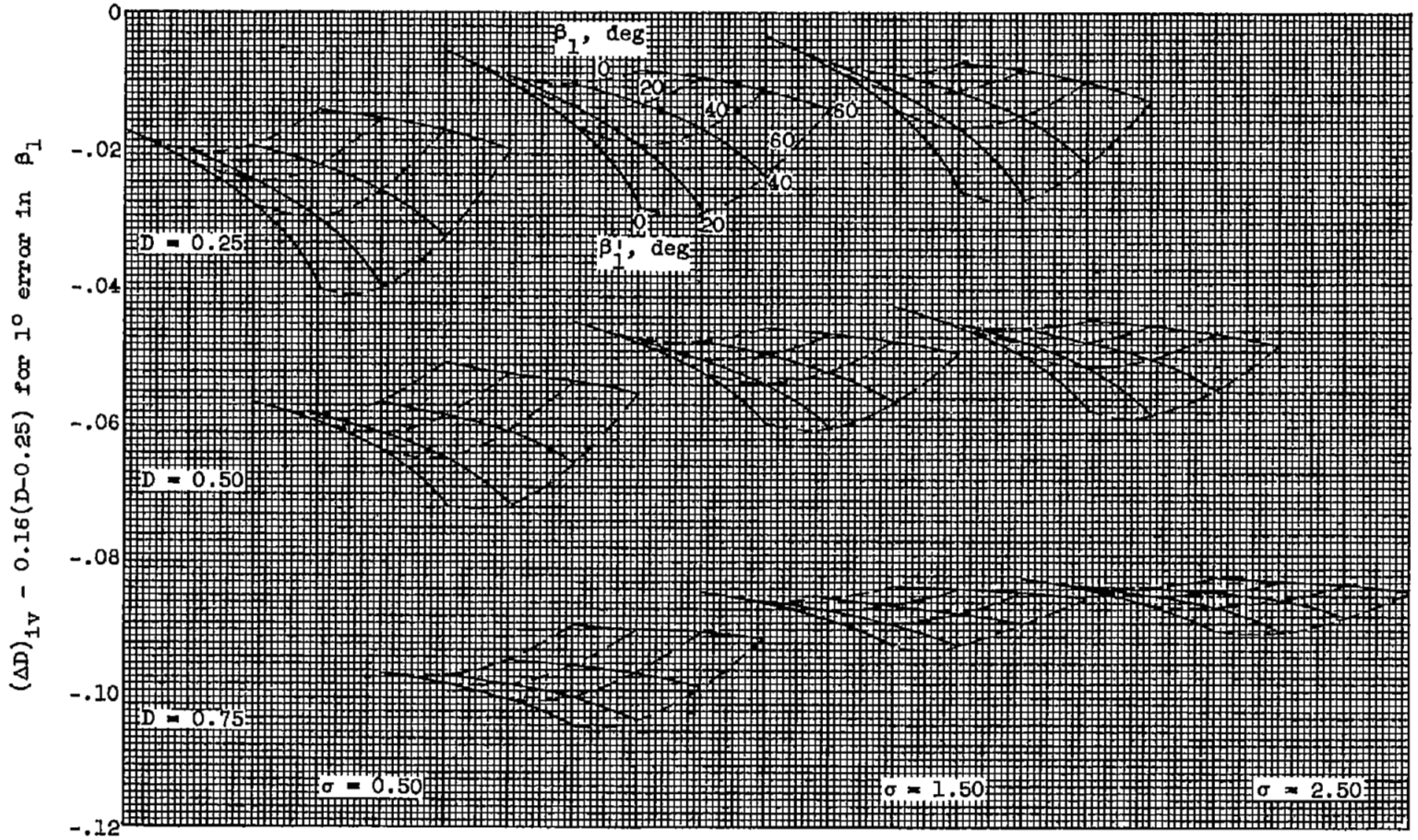

(b) Absolute air angle upstream of rotor (eq. (mG-iv)).

Figure 21. - Continued. Effect of measurement errors on calculated value of diffusion factor. (A large working copy of this figure may be obtained by using the request card bound in the back of the report.)

3479 CH-39 back

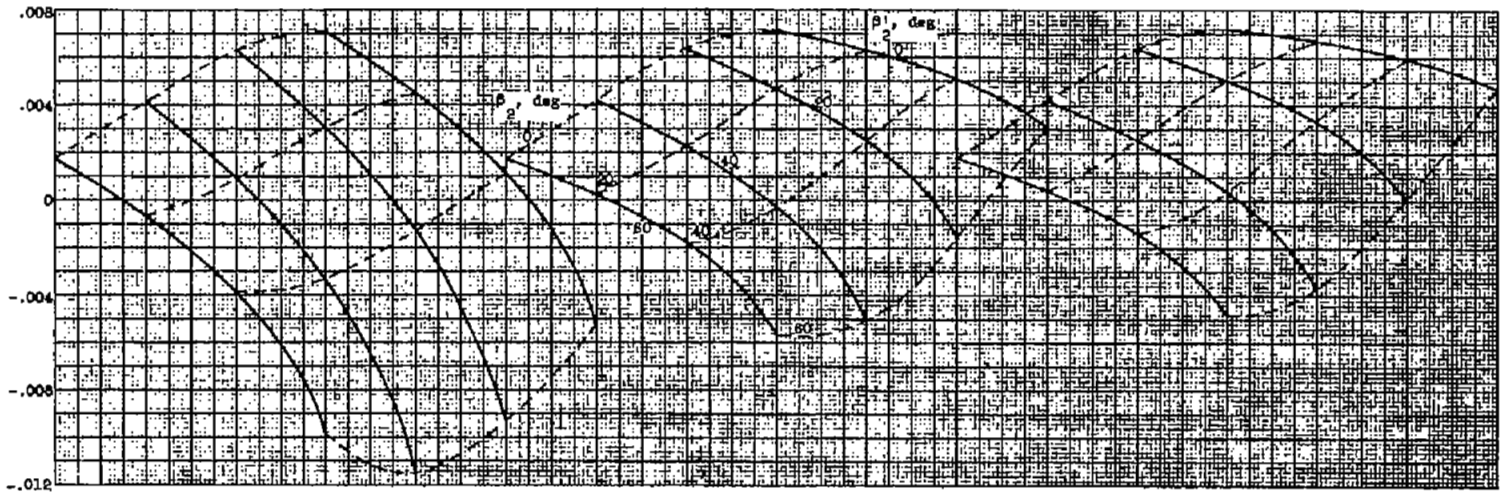

(c) Static pressure downstream of rotor (eq. (mG-v)).

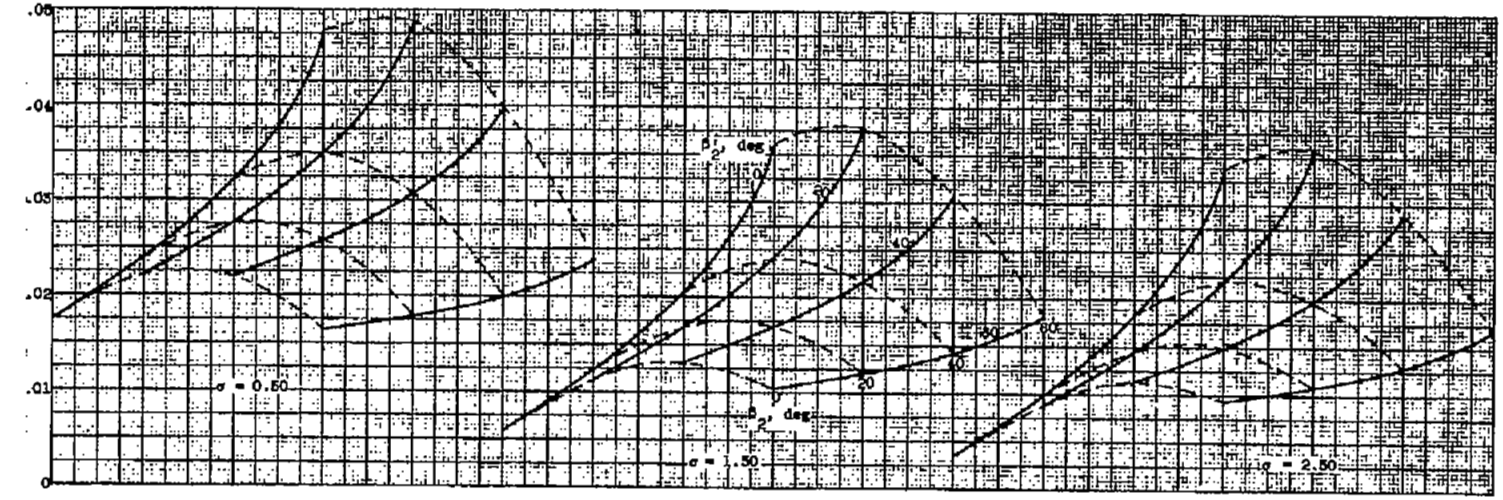

(d) Absolute air angle downstream of rotor (eq. (mG-viii)).

Figure 21. - Concluded. Effect of measurement errors on calculated value of diffusion factor. (A large working copy of this figure may be obtained by using the request card bound in the back of the report.)

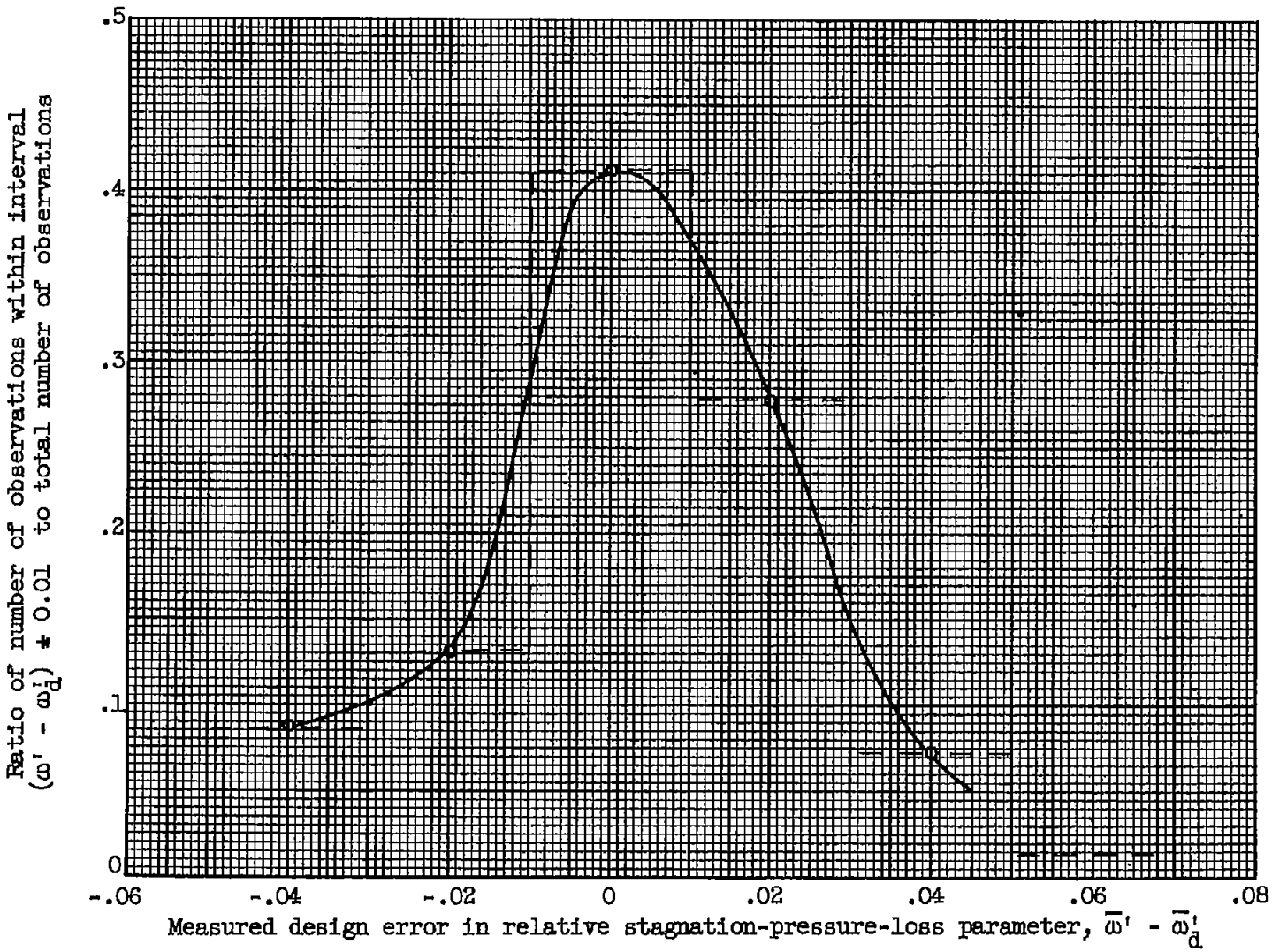

Figure 22. - Approximate frequency distribution for set of measured design errors in relative stagnation-pressure-loss parameter.

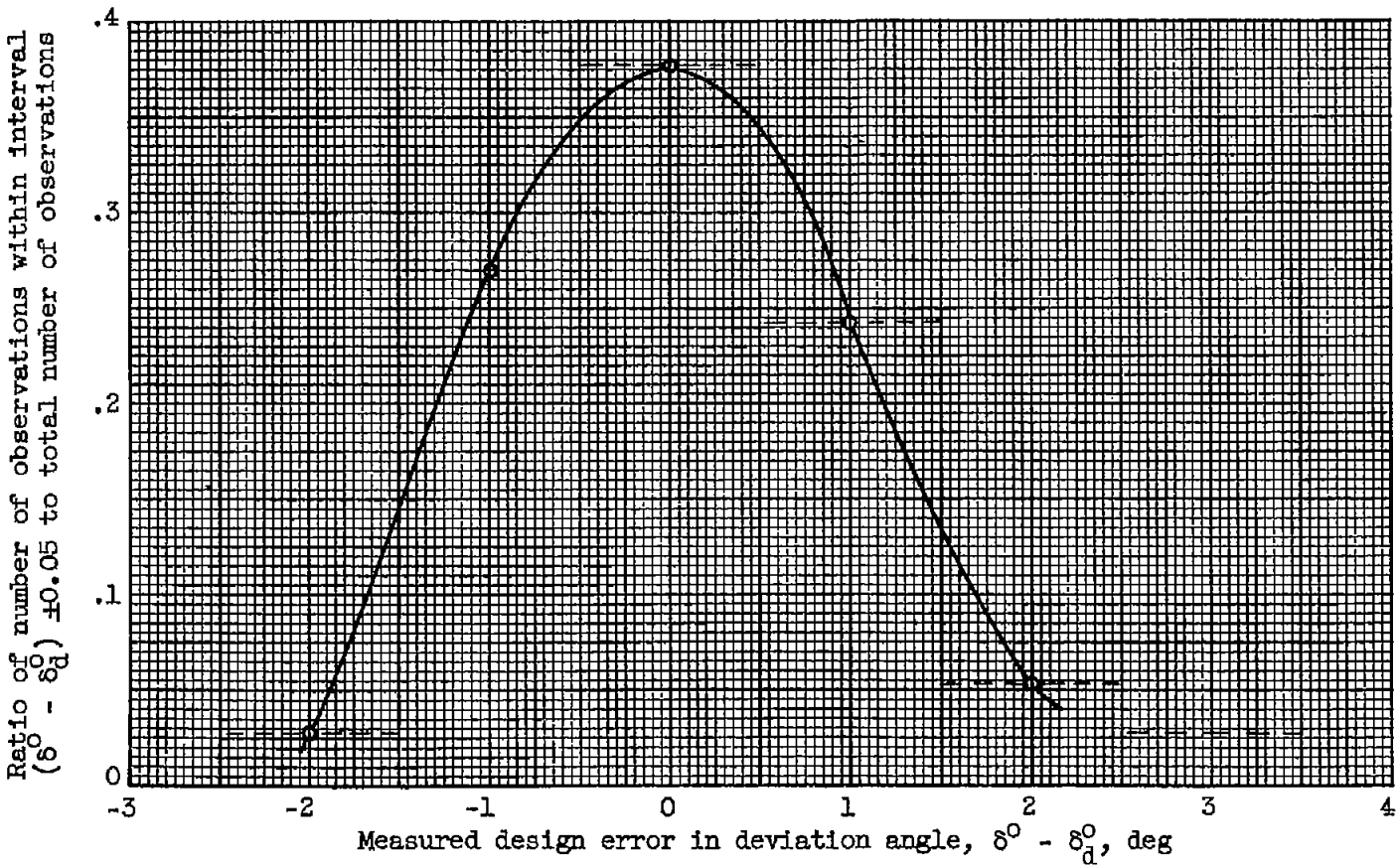

Figure 23. - Approximate frequency distribution for set of measured design errors in deviation angle.

3556

CHAPTER XVII

COMPRESSOR AND TURBINE MATCHING

By James F. Dugan, Jr.

SUMMARY

In order that compressor operation can be found for specified flight conditions and a mode of engine operation, methods are presented for relating the compressor to the other components of four types of gas-turbine engines - the simple turbojet, the afterburning turbojet, the turboprop with coupled power turbine, and the turboprop with free-wheeling power turbine.

The method of superposing component matching maps to obtain one- and two-spool gas-generator performance is discussed, as well as simplified methods for obtaining gas-generator performance. The simplification results from assuming constant turbine-inlet equivalent weight flow and an approximate relation for turbine efficiency. Compressor operation can be found from the gas-generator performance alone for a range of flight conditions when the mode of engine operation is specified by assigning values of mechanical speed and turbine-inlet temperature.

Procedures are also discussed for (1) combining the gas generator with the other components of gas-turbine engines so that compressor operation can be found for a range of flight conditions when the operating mode is specified by assigning values of mechanical speed and exhaust-nozzle area; (2) locating a constant-exhaust-nozzle-area equilibrium operating line on the compressor performance map of a one-spool nonafterburning turbojet engine operated at static sea-level conditions; (3) matching the components of a one-spool simple turbojet engine during transient operation for a specified flight condition, a specified transient path on the compressor map, and a fixed exhaust-nozzle area; (4) finding the compressor paths during a transient for a nonafterburning two-spool turbojet for which the exhaust-nozzle area and inner-turbine-inlet temperature are maintained constant; and (5) calculating the time required to accelerate to a higher engine speed for both one- and two-spool turbojet engines.

INTRODUCTION

An axial-flow compressor is designed so that at a specific rotative speed and weight flow the desired value of total-pressure ratio is achieved at a high level of efficiency. As a component of a gas-turbine engine, the compressor is required to operate over a range of pressure ratios, weight flows, and rotational speeds during steady-state and transient engine operation. To illustrate this point, engine operation is related to the compressor performance map of pressure ratio plotted against equivalent weight flow with equivalent rotational speed as a parameter. During engine acceleration prior to takeoff when the compressor speed increases from zero to the takeoff value, the compressor may operate in a region characterized by severe blade vibrations caused by rotating stall. Acceleration may even be prevented by compressor operation outside the stable operating region bounded by the compressor surge- or stall-limit line. For subsonic flight in the stratosphere, the compressor may operate in a low-efficiency region at high values of compressor equivalent speed. At supersonic flight speeds, the compressor surge- or stall-limit line may be encountered or operation may be required in a region characterized by low compressor efficiency or dangerous blade vibrations.

The purpose of this chapter is to present matching procedures so that compressor operation can be found for specified flight conditions and a mode of engine operation. (The matching procedures also yield the operating points of all the other engine components and data from which engine performance can be calculated.) Such methods are useful in selecting engine design values for compressor pressure ratio and weight flow. After the compressor performance map is estimated (see ch. X (ref. 1)), it may be evaluated by employing matching procedures to find the region over which the compressor will be required to operate for the desired mode of operation and range of flight conditions. Besides permitting an evaluation of compressor performance maps, the matching methods presented herein permit calculation of the effects of compressor changes on engine performance. The methods of chapter X may be used to estimate the effect on compressor performance of changes involving interstage bleed, passage flow area, or blade-setting angles. With the new compressor performance map and the matching procedures, the effect of the compressor change on engine performance may be found.

In order to find where on its performance map a compressor will operate as part of an engine for a specified flight condition and mode of engine operation, the engine components must be matched. The following three approaches may be used to accomplish component matching. Regardless of the approach, four relations involving continuity of flow, power balance, speed of rotation, and pressure ratio are available.

In one approach, the conventional compressor and turbine performance maps are employed. For an operating point assigned to one of the component maps, the corresponding points on the other component maps are found by satisfying the four matching relations. Such an approach is discussed in reference 2 for the turbojet engine and in reference 3 for the turboprop engine.

In a second approach, the performances of the turbine, tailpipe, and exhaust nozzle are combined. The conventional compressor performance map is retained; and, for an operating point on this map, the corresponding operating points of the other components are found through the use of the combined performance of the turbine, tailpipe, and exhaust nozzle. This approach is used in reference 4 for the one-spool turboprop with coupled power turbine and in reference 5 for the one-spool turbojet without afterburning.

In a third approach, the combined performance of the compressor, combustor, and turbine is found. In place of the conventional compressor and turbine performance maps, matching maps are used. All possible match points are determined by the superposition of these matching maps. When the operating mode is such that the mechanical speed and turbine-inlet temperature are specified, this approach is especially useful. For this type of problem, the compressor operation can be found from the combined performance of the compressor, combustor, and turbine, independent of the inlet, tailpipe, or exhaust-nozzle performance. The idea of superposition of component maps to achieve matching is used in references 6 to 8 for one-spool gas-turbine engines and in references 9 and 10 for two-spool gas-turbine engines.

Procedures for matching the components of one- and two-spool turbojet engines during transients are presented in references 11 and 12, respectively. The equations and procedures in reference 13 facilitate the computation of part-load and off-design-point internal performance by the use of automatic computing machinery.

Much of the material in this chapter is derived from references 5, 8, and 10 to 12. General and simplified methods are given for matching compressor and turbine components of one- and two-spool jet engines for equilibrium operation (refs. 8 and 10). Procedures for combining the performances of the compressor, combustor, and turbine components to yield gas-generator performance are explained, as well as the way compressor operation can be found from the gas-generator performance for a range of flight conditions when the mode of engine operation is specified by assigning values of mechanical speed and turbine temperature. In order that compressor operation can be found when the exhaust-nozzle area is specified, procedures are discussed for combining the gas-generator performance with that of other components such as an inlet, a propeller, an afterburner, a free-wheeling power turbine, and an exhaust nozzle. A simplified method for locating a constant-exhaust-nozzle-area

3656

CH-40

equilibrium operating line on the compressor performance map of a one-spool turbojet engine operated at static sea-level conditions is discussed (ref. 5). The combined performance of the turbine, tailpipe, and exhaust nozzle is related to compressor pressure ratio and weight flow in several charts. Desired operating lines can be located on specific compressor performance maps through the use of the charts. A method is discussed whereby the compressor and turbine of a one-spool turbojet engine may be matched for a specified flight condition, a specified transient path on the compressor map, and a fixed exhaust-nozzle area (ref. 11). For a two-spool turbojet engine (ref. 12), procedures are discussed for finding the compressor paths during a transient for which the exhaust-nozzle area and inner-turbine-inlet temperature are held constant. 3656

SYMBOLS

The following symbols are used in this chapter:

A	area, sq ft
$\bar{A}$	area parameter equal to $\frac{A_8}{A_4}\left(\frac{w^*}{w}\right)_4 \frac{w_4}{w_8}$
B	ratio of bleed weight flow to weight flow at compressor inlet
c_p	specific heat at constant pressure, Btu/(lb)(°R)
F_j	jet thrust, lb
f	fuel-air ratio at combustor inlet
g	acceleration due to gravity, 32.17 ft/sec^2
H	total or stagnation enthalpy, Btu/lb
I	moment of inertia, (lb)(ft)(sec^2)
J	mechanical equivalent of heat, 778.2 ft-lb/Btu
K	constant
M	Mach number
N	rotational speed, rps
P	total or stagnation pressure, lb/sq ft

$\overline{P}$ pressure-ratio parameter equal to $\frac{P_3}{P_1}\frac{P_4}{P_3}\frac{P_1}{p_0}\frac{p_0}{p_8}$

$\mathscr{P}$ power for propeller and/or accessories, Btu/sec

p static or stream pressure, lb/sq ft

Q_{xs} excess torque, lb-ft

R gas constant, 53.35 ft-lb/(lb)(°R)

T total or stagnation temperature, °R

$\overline{T}$ temperature parameter equal to $(1 - B_3)(1 + f)\frac{T_4}{T_1}\eta_{ad,C}\eta_{ad,T}$

U rotor speed, ft/sec

V air velocity, ft/sec

w weight flow, lb/sec

$\overline{w}$ weight-flow parameter equal to $\sqrt{\frac{(1 - B_3)(1 + f)}{\eta_{ad,C}\eta_{ad,T}}}\frac{w_8}{w_4}\frac{A_1}{A_8}\frac{w_1\sqrt{\theta_1}}{\delta_1 A_1}$

β air angle, angle between air velocity and axial direction, deg

γ ratio of specific heats

δ ratio of total pressure to NACA standard sea-level pressure of 2116 lb/sq ft

η_{ad} adiabatic efficiency

θ ratio of total temperature to NACA standard sea-level temperature of 518.7° R

ρ density, lb/cu ft

τ time, sec

ψ turbine pressure coefficient, $(V \sin \beta)/U$

Subscripts:

C compressor

3656

CH-40 back

i inner spool

o outer spool

PT power turbine

T turbine

Station numbers shown in figs. 1 and 2:

	Two-spool notation	One-spool notation
0	ambient conditions	
1	outer-compressor inlet	compressor inlet
2	outer-compressor exit, inner-compressor inlet	
3	inner-compressor exit, combustor inlet	compressor exit, combustor inlet
4	combustor exit, inner-turbine inlet	combustor exit, turbine inlet
5	inner-turbine exit, outer-turbine inlet	
6	outer-turbine exit	turbine exit
6a	uncoupled power-turbine exit	
7	exhaust-nozzle inlet	
8	exhaust-nozzle exit	exhaust-nozzle exit

Superscript:

* critical flow conditions

GENERAL DISCUSSION

The four types of gas-turbine engines discussed in this report are the simple turbojet, the afterburning turbojet, the turboprop with coupled power turbine, and the turboprop with free-wheeling power turbine (fig. 1). Common to all four engines is the gas generator, which may be either the one- or two-spool type (fig. 2). This chapter is

chiefly concerned with the compressor of a one-spool gas generator and the outer and inner compressors of a two-spool gas generator when operated as components of any of the four gas-turbine engines.

In the section GENERAL METHODS FOR EQUILIBRIUM OPERATION, a matching technique for the superposition of component maps is employed. A procedure for obtaining the performance of a one-spool gas generator is followed by an explanation of the way compressor operating points for various flight conditions may be found from the gas-generator performance alone when engine operation is defined by setting values of mechanical speed and turbine-inlet temperature. The discussion of the two-spool gas generator parallels that for the one-spool. In order that compressor operation may be determined when engine operation is defined by setting values of exhaust-nozzle area and rotative speed, methods are discussed for matching the gas generator with the other components for each of the four engine types shown in figure 1.

3656

In the SIMPLIFIED METHODS FOR EQUILIBRIUM OPERATION, turbine-inlet equivalent weight flow is assumed to be constant for all operating conditions and turbine efficiency is assumed to be a function only of the ratio of the rotative speed to the square root of the enthalpy drop. Methods for obtaining the performance of one- and two-spool gas generators are discussed.

A matching technique involving the use of the combined performance of the turbine, tailpipe, and exhaust nozzle is used in the section EQUILIBRIUM OPERATING LINE OF ONE-SPOOL TURBOJET. An approximate method is discussed for locating a constant-exhaust-nozzle-area equilibrium operating line on the performance map of a compressor that is part of a one-spool turbojet engine operated at static sea-level conditions. The charts of reference 5, which are needed to accomplish this, are included.

In the section METHODS FOR TRANSIENT OPERATION, conventional compressor and turbine maps are used, and matching is achieved by satisfying the thermodynamic relations and the imposed conditions. A method is discussed whereby the compressor and turbine of a one-spool turbojet engine may be matched for a specified flight condition, a specified transient path on the compressor map, and a fixed exhaust-nozzle area. For a two-spool turbojet engine, procedures are discussed for finding the compressor paths during a transient for which the exhaust-nozzle area and inner-turbine-inlet temperature are held constant.

GENERAL METHODS FOR EQUILIBRIUM OPERATION

In this and the following main section, which discusses simplified methods for equilibrium operation, it is convenient to think of a

gas-turbine engine as composed of a gas generator and other components. Sketches of one- and two-spool gas generators are shown in figure 2. The addition of other components such as an inlet, a propeller, an afterburner, a free-wheeling power turbine, and an exhaust nozzle results in either a turboprop or a turbojet engine (fig. 1).

In the discussion of the one-spool gas generator, the component performances are plotted in such a way that the maps may be superposed to satisfy the matching relations of continuity, power balance, and rotational speed. A similar discussion appears in references 6 to 8. In the discussion of the two-spool gas generator, two procedures are presented for matching the inner spool with the outer compressor and turbine, the inner-spool performance having been found by the procedures for the one-spool gas generator. Two-spool matching methods are discussed in references 9 and 10. The sections on compressor operation from gas-generator performance discuss the procedure for finding compressor operating points when engine operation is specified by assigning values of mechanical speed and turbine-inlet temperature. When exhaust-nozzle area and mechanical speed are assigned, compressor operation can be found for turbojet and turboprop engines as discussed in the section Matching Gas Generator with Other Engine Components. 3656

One-Spool Gas Generator

In order to match the compressor and turbine of a particular gas generator, the performance of the compressor, combustor, and turbine must be known. Typical compressor and turbine performance maps are shown in figures 3(a) and (b), respectively. In figure 3(a), compressor total-pressure ratio is plotted against equivalent weight flow with equivalent speed and adiabatic efficiency as parameters. In figure 3(b), turbine equivalent specific work is plotted against a flow parameter with equivalent speed, total-pressure ratio, and adiabatic efficiency as parameters. The performance of a typical combustor is nearly constant for a wide range of operation. In this chapter the combustor total-pressure ratio P_4/P_3 is taken equal to a constant. When fuel-air ratios are calculated, combustor efficiency is also taken to be a constant.

Matching relations. - In matching the compressor and turbine, three of the four matching relations are available:

(1) The air weight flow into the compressor minus the air weight flow bled from the compressor exit plus the fuel weight flow added in the combustor equal the gas weight flow into the turbine.

(2) The power output of the turbine is absorbed by the compressor and the accessories.

(3) The mechanical speeds of the compressor and its driving turbine are the same.

For simplicity, the three matching relations are expressed in terms of equivalent performance parameters as follows:

3656

Continuity:

$$\frac{(1 - B_3)(1 + f)\ w_1 N}{\frac{P_3}{P_1}\ \frac{P_4}{P_3}\ \delta_1} = \frac{w_4 N}{\delta_4} \tag{1}$$

Power:

$$\frac{H_3 - H_1}{(1 - B_3)(1 + f)\ N^2} + \frac{\mathscr{P}}{(1 - B_3)(1 + f)\ w_1 N^2} = \frac{H_4 - H_6}{N^2} \tag{2}$$

Speed:

$$\frac{T_4}{T_1} = \left(\frac{\frac{N}{\sqrt{\theta_1}}}{\frac{N}{\sqrt{\theta_4}}}\right)^2 \tag{3}$$

Matching maps and their superposition. - Compressor and turbine matching is achieved by graphically satisfying equations (1) to (3). The performance of the compressor is plotted as $(H_3-H_1)/N^2(1-B_3)(1+f)$ against w_4N/δ_4 for constant values of $N/\sqrt{\theta_1}$ (fig. 4(a)). The compressor variables are computed from

$$\frac{w_4 N}{\delta_4} = \frac{(1 - B_3)(1 + f)}{\frac{P_3}{P_1}\frac{P_4}{P_3}} \frac{w_1\sqrt{\theta_1}}{\delta_1} \frac{N}{\sqrt{\theta_1}} \tag{4}$$

$$\frac{H_3 - H_1}{(1 - B_3)(1 + f)N^2} = \frac{518.7\ c_{p,C}\left[\left(\frac{P_3}{P_1}\right)^{\frac{\gamma_C - 1}{\gamma_C}} - 1\right]}{\eta_{ad,C}(1 - B_3)(1 + f)\left(\frac{N}{\sqrt{\theta_1}}\right)^2} \tag{5}$$

3656

For the purpose of this conversion, it is usually sufficient to assume constant values of fuel-air ratio f, compressor-exit-bleed ratio B_3, specific heat at constant pressure $c_{p,C}$, combustor pressure ratio P_4/P_3, and γ_C. (The variation of $c_{p,C}$ and γ_C with total temperature may be accounted for by using charts such as those presented in ref. 14.)

The turbine performance is plotted as $(H_4 - H_6)/N^2$ against w_4N/δ_4 for constant values of $N/\sqrt{\theta_4}$ as in figure 4(b). The ordinate is computed from

$$\frac{H_4 - H_6}{N^2} = \frac{\frac{H_4 - H_6}{\theta_4}}{\left(\frac{N}{\sqrt{\theta_4}}\right)^2} \tag{6}$$

The components are matched by superposing figures 4(a) and (b) so as to satisfy the continuity and power relations (eqs. (1) and (2)). The abscissas are superposed directly, while the ordinates are offset by the value of the accessory power term in equation (2). In many instances the accessory power term is so small that it can be neglected. Sometimes the value of the accessory power term computed for one engine operating condition is assumed to prevail for all other operating conditions. With the compressor and turbine matching maps overlaid, each

point common to both maps is a possible match point for the gas generator. At each such point, the turbine-inlet to compressor-inlet temperature ratio T_4/T_1 may be calculated by using equation (3) and the values of equivalent speed read from the overlaid maps.

Component parameters. - For each match point, the pressure and temperature ratios across the compressor and turbine may be calculated or read from appropriate component maps. The compressor pressure ratio and temperature ratio could be read from plots of these variables against w_4N/δ_4 with $N/\sqrt{\theta_1}$ as a parameter. After the turbine equivalent specific work is calculated from the values of $(H_4 - H_6)/N^2$ and $N/\sqrt{\theta_4}$, the turbine pressure ratio can be read from the conventional performance map (fig. 3(b)). The turbine temperature ratio may be calculated from

$$\frac{T_6}{T_4} = 1 - \frac{H_4 - H_6}{\theta_4} \frac{1}{c_{p,T}\ 518.7} \tag{7}$$

The value of $c_{p,T}$ can be calculated from

$$c_p = \frac{\gamma}{\gamma - 1} \frac{R}{J} \tag{8}$$

The value of γ is usually based on the design values of fuel-air ratio and the arithmetic average of the turbine-inlet and -outlet temperatures. If more precise calculations are warranted, the charts of reference 14 may be used to find values of T_6/T_4.

For matching purposes, the value of f is usually assumed to be a constant (its design value). Once the compressor and turbine are matched, however, the equivalent fuel-air ratio f/θ_1 at each match point may be found by using the values of T_3/T_1 and T_4/T_1, an assumed fuel, a combustor efficiency, and combustion charts such as those presented in reference 14. There is no need to rematch the compressor and turbine, because the term $(1 + f)$ changes only slightly. The compressor equivalent weight flow $w_1\sqrt{\theta_1}/\delta_1$ may be calculated by using equation (4). The turbine-outlet equivalent weight flow may be calculated from

$$\frac{w_6\sqrt{\theta_6}}{\delta_6} = (1 - B_3)(1 + f)\ \frac{w_1\sqrt{\theta_1}}{\delta_1}\ \frac{\sqrt{\dfrac{T_4}{T_1}\ \dfrac{T_6}{T_4}}}{\dfrac{P_3}{P_1}\ \dfrac{P_4}{P_3}\ \dfrac{P_6}{P_4}} \tag{9}$$

[redacted]

The performance of the one-spool gas generator may be presented as plots of T_4/T_1, P_6/P_1, T_6/T_1, f/θ_1, P_3/P_1, and $w_1\sqrt{\theta_1}/\delta_1$ against $w_6\sqrt{\theta_6}/\delta_6$ with $N/\sqrt{\theta_1}$ as a parameter (fig. 5).

Compressor operation from gas-generator performance. - Compressor operating points for various flight conditions may be found from the gas-generator performance alone if engine operation is defined by setting values of mechanical speed N and turbine-inlet temperature T_4. For a particular flight condition (altitude and Mach number), values of T_1 and θ_1 can be found. From figure 5 and values of T_4/T_1 and $N/\sqrt{\theta_1}$, a value of $w_6\sqrt{\theta_6}/\delta_6$ is read. Then, from values of $w_6\sqrt{\theta_6}/\delta_6$ and $N/\sqrt{\theta_1}$, values of P_3/P_1 and $w_1\sqrt{\theta_1}/\delta_1$ are read. Thus, for each flight condition the compressor operating point can be located.

One-spool matching methods are applied to specific equilibrium problems in references 15 to 19.

Two-Spool Gas Generator

A schematic of a two-spool gas generator is shown in figure 2(b). The outer compressor and outer turbine are mounted on a common shaft. Hereafter, these components are called the outer spool. The inner compressor and the inner turbine are mounted on a second shaft which is not coupled mechanically to the shaft of the outer spool. In airplane engines, the outer-spool shaft is inside of and concentric with the hollow shaft of the inner spool. Between the inner compressor and inner turbine is the combustor; taken together, these components comprise the inner spool.

In matching the components of a two-spool gas generator, it is convenient to match the components of the inner spool and then match the inner-spool with the outer-spool components. The inner-spool components are matched according to the procedures for matching the components of a one-spool gas generator. Notice that engine stations 1, 3, 4, and 6 for the one-spool gas generator are replaced by 2, 3, 4, and 5 for the inner spool of a two-spool gas generator (fig. 2). The manner in which inner-spool performance is presented is determined by the method employed to match the outer-spool components. Two procedures are discussed for matching the outer- and inner-spool components. In the first procedure, an inner-spool operating point is assigned and matching with the outer compressor and outer turbine is achieved directly. In the second procedure, which involves a trial-and-error step, an outer-compressor operating point is assigned so that the gas-generator performance for constant values of outer-spool equivalent speed results.

Direct method of matching outer and inner spools. - The two-spool matching problem becomes one of matching the outer spool with the inner spool. Because of the aerodynamic coupling between the two spools, specifying two independent conditions determines the operating points of all the components. If an operating point is assigned to the inner spool, outer-spool matching is achieved directly. For this approach it is convenient to express the power and continuity relations with regard to the outer compressor and outer turbine, respectively, as

$$\frac{H_2 - H_1}{N_o^2} \frac{1}{(1 - B_2)(1 - B_3)(1 + f)} + \frac{\mathscr{P}}{w_1(1 - B_2)(1 - B_3)(1 + f)\, N_o^2} = \frac{H_5 - H_6}{N_o^2} \tag{10}$$

$$\log \frac{w_1 N_o}{\delta_2} = \log \left[\frac{\frac{P_5}{P_2}}{(1 - B_2)(1 - B_3)(1 + f)}\right] + \log \frac{w_5 N_o}{\delta_5} \tag{11}$$

Constant values of compressor bleed at stations 2 and 3 and fuel-air ratio may be chosen. The matching map for the outer compressor is shown in figure 6(a). Here $\frac{H_2 - H_1}{N_o^2(1 - B_2)(1 - B_3)(1 + f)}$ is plotted against $\log (w_1 N_o/\delta_2)$ for lines of constant equivalent speed $N_o/\sqrt{\theta_1}$ and constant equivalent weight flow $w_2\sqrt{\theta_2}/\delta_2$. For the matching map of the outer turbine, $(H_5 - H_6)/N_o^2$ is plotted against $\log (w_5 N_o/\delta_5)$ with $w_5\sqrt{\theta_5}/\delta_5$ and $N_o/\sqrt{\theta_5}$ as parameters (fig. 6(b)). In order to match the outer-spool components with the inner spool, the matching map of the inner spool is plotted as in figure 6(c). Here, inlet equivalent weight flow $w_2\sqrt{\theta_2}/\delta_2$ is plotted against outlet equivalent weight flow $w_5\sqrt{\theta_5}/\delta_5$ with $N_1/\sqrt{\theta_2}$ and P_5/P_2 as parameters. Inner-spool operation is, of course, limited by the equivalent flow that can be passed by the outer turbine.

With these three matching maps (fig. 6), the match points of the two-spool gas generator can be found. An inner-spool operating point is assigned on figure 6(c). The values of $w_2\sqrt{\theta_2}/\delta_2$, $w_5\sqrt{\theta_5}/\delta_5$, and $\frac{P_5}{P_2}$ are noted, and the value of $\log\left[\frac{P_5/P_2}{(1 - B_2)(1 - B_3)(1 + f)}\right]$ is calculated. The outer-compressor and outer-turbine matching maps (figs. 6(a) and (b)) are superposed so as to satisfy equations (10) and (11). The ordinates of figures 6(a) and (b) are offset by the value of the accessory power term in equation (10), and the abscissas are offset by the

calculated value of the term $\log\left[\frac{P_5/P_2}{(1 - B_2)(1 - B_3)(1 + f)}\right]$. The operating points of the outer compressor and the outer turbine corresponding to the assigned inner-spool operating point are at the intersection of the appropriate lines of constant $w_2\sqrt{\theta_2}/\delta_2$ and $w_5\sqrt{\theta_5}/\delta_5$. In using this procedure, it has been found convenient to assign several values of $w_5\sqrt{\theta_5}/\delta_5$ for each selected value of $w_2\sqrt{\theta_2}/\delta_2$ in figure 6(c). Choosing pairs of values for $w_2\sqrt{\theta_2}/\delta_2$ and $w_5\sqrt{\theta_5}/\delta_5$ in this way dictates the values of these parameters to be used in plotting lines of constant equivalent weight flow in figures 6(a) and (b). Use of this direct method of matching outer and inner spools or of the iterative method, which is described in the following paragraphs, is a matter of personal preference.

3696

Iterative method of matching outer and inner spools. - An alternative procedure for matching the outer-spool components with the inner spool may be employed by assigning the outer-compressor operating point rather than that of the inner spool. For this procedure, the matching maps of figure 7 are used. The outer-compressor performance is plotted as $(H_2 - H_1)/N_o^2$ against $w_2\sqrt{\theta_2}/\delta_2$ with $N_o/\sqrt{\theta_1}$ as a parameter (fig. 7(a)); the performance of the outer turbine is plotted as $(H_5 - H_6)/N_o^2$ against w_5N_o/δ_5 with $N_o/\sqrt{\theta_5}$ as parameter (fig. 7(b)); and inner-spool performance is plotted as $w_2\sqrt{\theta_2}/\delta_2$ against $w_5\sqrt{\theta_5}/\delta_5$ for constant values of $N_i/\sqrt{\theta_2}$ and T_5/T_2 (fig. 7(c)).

The inner- and outer-spool components may be matched by employing an iterative procedure in conjunction with the matching maps of figure 7:

(1) An operating point is assigned on the outer-compressor map (fig. 7(a)) from which values of $w_2\sqrt{\theta_2}/\delta_2$, $N_o/\sqrt{\theta_1}$, and $(H_2 - H_1)/N_o^2$ are read.

(2) The value of $(H_5 - H_6)/N_o^2$ is calculated from equation (10).

(3) The value of T_2/T_1 is calculated from

$$\frac{T_2}{T_1} = 1 + \frac{H_2 - H_1}{N_o^2}\left(\frac{N_o}{\sqrt{\theta_1}}\right)^2 \frac{1}{518.7\ c_{p,oC}} \tag{12}$$

(4) A trial value of $N_o/\sqrt{\theta_5}$ is assigned.

Because assigning the outer-compressor operating point determines the operating points of all the other components, assuming a value of $N_o/\sqrt{\theta_5}$ is an overspecification and will lead to a contradiction if an incorrect value is assumed.

(5) A value of w_5N_o/δ_5 is read from figure 7(b) for the values of $(H_5 - H_6)/N_o^2$ and $N_o/\sqrt{\theta_5}$.

3652

(6) A value of $w_5\sqrt{\theta_5}/\delta_5$ is calculated from the values of w_5N_o/δ_5 and $N_o/\sqrt{\theta_5}$.

(7) A value of T_5/T_2, which depends on the inner-spool performance, is read from figure 7(c) for the values of $w_2\sqrt{\theta_2}/\delta_2$ and $w_5\sqrt{\theta_5}/\delta_5$.

(8) A second value of T_5/T_2, which depends on the relation between the outer compressor and outer turbine, is calculated from

$$\frac{T_5}{T_2} = \left(\frac{\dfrac{N_o}{\sqrt{\theta_1}}}{\dfrac{N_o}{\sqrt{\theta_5}}}\right)^2 \frac{1}{\dfrac{T_2}{T_1}} \tag{13}$$

If this does not equal the value from step (7), steps (4) to (8) are repeated until agreement is reached. In using this procedure, it has been found convenient to assign outer-compressor operating points along lines of constant outer-spool speed and to first calculate the match points for the higher values of $w_2\sqrt{\theta_2}/\delta_2$. As lower values of $w_2\sqrt{\theta_2}/\delta_2$ are assigned at a fixed speed $N_o/\sqrt{\theta_1}$, higher values of $w_5\sqrt{\theta_5}/\delta_5$ will result until the critical value is reached. From this point on, all lower selected values of $w_2\sqrt{\theta_2}/\delta_2$ will be accompanied by the critical value of $w_5\sqrt{\theta_5}/\delta_5$.

Variable pressure losses in primary combustor. - The matching procedure for the two-spool gas generator may also be applied for the case of either a one-spool generator or the inner spool of a two-spool generator when large, variable pressure losses occur in the primary burner. For these conditions, curves analogous to figure 6(c) would represent the combustor characteristics.

Component parameters. - For each match point of a two-spool gas generator, the pressure and temperature ratios across the components may be calculated or read from appropriate component maps. If the iterative procedure is used for matching the inner spool with the outer components, the following values are known for each match point: $N_o/\sqrt{\theta_1}$, $w_2\sqrt{\theta_2}/\delta_2$, $(H_5 - H_6)/N_o^2$, T_2/T_1, $w_5\sqrt{\theta_5}/\delta_5$, T_5/T_2, and $N_o/\sqrt{\theta_5}$.

The outer-compressor pressure ratio may be read from a plot of P_2/P_1 against $w_2\sqrt{\theta_2}/\delta_2$ with $N_o/\sqrt{\theta_1}$ as parameter. Inner-compressor equivalent speed $N_i/\sqrt{\theta_2}$ may be read from figure 7(c). The values of P_3/P_2, T_3/T_2, T_4/T_2, and P_5/P_2 may be read from plots of these variables against $w_5\sqrt{\theta_5}/\delta_5$ with $N_i/\sqrt{\theta_2}$ as a parameter. The outer-turbine pressure ratio may be read from a plot of P_5/P_6 against $(H_5 - H_6)/N_o^2$ with $N_o/\sqrt{\theta_5}$ as a parameter. Outer-turbine temperature ratio may be calculated from

$$\frac{T_6}{T_5} = 1 - \frac{H_5 - H_6}{N_o^2}\left(\frac{N_o}{\sqrt{\theta_5}}\right)^2 \frac{1}{518.7\ c_{p,oT}} \tag{14}$$

The equivalent fuel-air ratio f/θ_1 at each match point may be found by using the values of T_4/T_1 and T_3/T_1, an assumed fuel, a combustor efficiency, and combustion charts such as those presented in reference 14.

The performance of the two-spool gas generator may be presented as plots of T_4/T_1, P_6/P_1, T_6/T_1, f/θ_1, and $w_1\sqrt{\theta_1}/\delta_1$ against $w_6\sqrt{\theta_6}/\delta_6$ with $N_o/\sqrt{\theta_1}$ as a parameter and a plot of $N_i/\sqrt{\theta_1}$ against T_4/T_1 with $N_o/\sqrt{\theta_1}$ as a parameter (fig. 8).

Compressor operation from gas-generator performance. - The outer- and inner-compressor operating points at an assigned flight condition may be found from the gas-generator performance if engine operation is specified by assigning values of outer- or inner-spool mechanical speed and inner-turbine-inlet temperature. From the assigned flight condition are found values of θ_1 and T_1. From the assigned engine operation, values of $N_o/\sqrt{\theta_1}$ or $N_i/\sqrt{\theta_1}$ and T_4/T_1 are calculated. If $N_o/\sqrt{\theta_1}$ and T_4/T_1 are known, a value of $w_6\sqrt{\theta_6}/\delta_6$ is read from figure 8(a). If $N_i/\sqrt{\theta_1}$ and T_4/T_1 are known, a value of $N_o/\sqrt{\theta_1}$ is read from figure 8(d); and then, using the values of $N_o/\sqrt{\theta_1}$ and T_4/T_1, a value of $w_6\sqrt{\theta_6}/\delta_6$ is read from figure 8(a). Values of

P_2/P_1, $w_1\sqrt{\theta_1}/\delta_1$, P_3/P_2, and $w_2\sqrt{\theta_2}/\delta_2$ are read from plots of these variables against $w_6\sqrt{\theta_6}/\delta_6$ with $N_o/\sqrt{\theta_1}$ as a parameter. Thus, for each flight condition, the outer- and inner-compressor operating points may be found. In reference 20, two-spool matching methods are used to investigate the effect of design over-all compressor pressure ratio division on two-spool turbojet-engine performance and geometry.

Matching Gas Generator with Other Engine Components

To determine compressor operation when exhaust-nozzle area and mechanical speed are assigned, the gas generator must be matched with the other engine components. For either the one- or the two-spool gas generator, the following gas-turbine engine configurations are possible:

(1) Simple turbojet, where gas generator is preceded by inlet diffuser and followed by tailpipe and exhaust nozzle (fig. 1(a))

(2) Afterburning turbojet, where afterburner replaces tailpipe of simple turbojet (fig. 1(b))

(3) Turboprop with coupled power turbine, where propeller is geared to gas-generator shaft (fig. 1(c))

(4) Turboprop with free-wheeling power turbine, where propeller is geared to shaft of free-wheeling power turbine (fig. 1(d))

Methods for matching the gas generator with the other engine components for each of these engine configurations are discussed. By using these methods, compressor operation can be determined for various flight conditions when engine operation is specified by assigning values of exhaust-nozzle area and mechanical speed.

Simple turbojet. - The gas generator of a simple turbojet may be matched with the other components by using three plots, one each for the inlet and the gas generator and a combined map for the tailpipe and exhaust nozzle. The performance of a fixed-geometry diffuser inlet is shown in figure 9(a), where pressure ratio P_1/p_0 is plotted against equivalent weight flow $w_1\sqrt{\theta_1}/\delta_1$ with free-stream Mach number M_0 as parameter. Gas-generator performance is plotted as $\log (P_6/P_1)$ against $w_6\sqrt{\theta_6}/\delta_6$ with $N_o/\sqrt{\theta_1}$ as parameter (fig. 9(b)). The combined map for the tailpipe and exhaust nozzle is shown in figure 9(c), where $\log (P_6/p_0)$ is plotted against $w_6\sqrt{\theta_6}/\delta_6$ for a fixed exhaust-nozzle area.

From figure 9(a), trial values of P_1/p_0 and $w_1\sqrt{\theta_1}/\delta_1$ are read for the assigned flight Mach number. Figures 9(b) and (c) are superposed: the ordinates are offset by the value of $\log (P_1/p_0)$, while the abscissas are superposed directly. The value of $w_6\sqrt{\theta_6}/\delta_6$ is read from the overlaid maps at the intersection of the fixed-exhaust-nozzle-area curve and the appropriate constant-speed line. (The value of $N_o/\sqrt{\theta_1}$ may be calculated from the assigned values of M_0, altitude, and N_o.) A gas-generator plot of $w_1\sqrt{\theta_1}/\delta_1$ against $w_6\sqrt{\theta_6}/\delta_6$ with $N_o/\sqrt{\theta_1}$ as a parameter yields a value of $w_1\sqrt{\theta_1}/\delta_1$. If this value of $w_1\sqrt{\theta_1}/\delta_1$ is not equal to the trial value, the process is repeated. When the two values of $w_1\sqrt{\theta_1}/\delta_1$ agree, the gas generator is matched with the other engine components for the assigned flight condition and mode of engine operation. The outer- and inner-compressor operating points may now be found by reading values of P_2/P_1, P_3/P_2, and $w_2\sqrt{\theta_2}/\delta_2$ from plots of these variables against $w_6\sqrt{\theta_6}/\delta_6$ with $N_o/\sqrt{\theta_1}$ as a parameter.

3656

Afterburning turbojet. - The procedures for the afterburning turbojet are the same as for the simple turbojet. The combined map for the tailpipe and exhaust nozzle is replaced by the combined map for the afterburner and exhaust nozzle.

Turboprop with coupled power turbine. - When the propeller is geared to the compressor shaft of a one-spool gas generator or to the outer-spool shaft of a two-spool engine, the propeller power must be added to the accessory power in equation (2) or (10) before the gas-generator performance is obtained. For each value of propeller power, a distinct set of gas-generator performance curves will be obtained. Compressor operation can be found by assigning values of flight Mach number, altitude, mechanical speed, exhaust-nozzle area, and propeller power. The procedures for matching and for obtaining the compressor operating points are the same as those for a simple turbojet. One-spool turboprop problems are discussed in references 21 to 23.

Turboprop with free-wheeling power turbine. - For a turboprop with a free-wheeling power turbine, a procedure is discussed for finding the compressor operating points when the following are assigned: flight Mach number and altitude, propeller power $\mathscr{P}$, shaft speed of power turbine N_{PT}, and exhaust-nozzle area. The discussion is for a turboprop having a two-spool gas generator; the procedure is essentially the same for a turboprop having a one-spool gas generator.

(1) Values of T_1, θ_1, and p_0 are found for the assigned M_0 and altitude.

(2) A trial point is assigned in figure 9(a) for the assigned M_0, and values of P_1/p_0 and $w_1\sqrt{\theta_1}/\delta_1$ are read at this point.

(3) A value of $w_6\sqrt{\theta_6}/\delta_6$ is assumed. Over much of its operating range, the power turbine operates at a fixed value of $w_6\sqrt{\theta_6}/\delta_6$.

(4) A value of $N_o/\sqrt{\theta_1}$ is read from figure 8(f) for the values of $w_6\sqrt{\theta_6}/\delta_6$ and $w_1\sqrt{\theta_1}/\delta_1$.

(5) Values of P_6/P_1 and T_6/T_1 are read from figures 8(c) and (e) for the values of $w_6\sqrt{\theta_6}/\delta_6$ and $N_o/\sqrt{\theta_1}$.

(6) The power-turbine equivalent speed $N_{PT}/\sqrt{\theta_6}$ is calculated from

$$\frac{N_{PT}}{\sqrt{\theta_6}} = N_{PT}\frac{1}{\sqrt{\theta_1}}\frac{1}{\sqrt{\frac{T_6}{T_1}}} \tag{15}$$

(7) The power-turbine equivalent specific work is calculated from

$$\frac{H_6 - H_{6a}}{\theta_6} = \frac{\mathscr{P}}{\frac{w_6\sqrt{\theta_6}}{\delta_6}\frac{P_6}{P_1}\frac{P_1}{p_0}\frac{p_0}{2116}\sqrt{\theta_1}\sqrt{\frac{T_6}{T_1}}} \tag{16}$$

(8) A value of w_6N_{PT}/δ_6 is read from figure 10(a) for the values of $N_{PT}/\sqrt{\theta_6}$ and $(H_6 - H_{6a})/\theta_6$.

(9) A value of $w_6\sqrt{\theta_6}/\delta_6$ is calculated from

$$\frac{w_6\sqrt{\theta_6}}{\delta_6} = \frac{w_6N_{PT}}{\delta_6}\frac{1}{\frac{N_{PT}}{\sqrt{\theta_6}}} \tag{17}$$

If this does not equal the assumed value of $w_6\sqrt{\theta_6}/\delta_6$ (step (3)), steps (3) to (9) are repeated until the two values do agree.

(10) A value of P_6/P_{6a} is read from figure 10(a) for the values of $N_{PT}/\sqrt{\theta_6}$ and $(H_6 - H_{6a})/\theta_6$.

(11) A value of T_{6a}/T_6 is calculated from

$$\frac{T_{6a}}{T_6} = 1 - \frac{(H_6 - H_{6a})}{\theta_6} \frac{1}{518.7\ c_{p,PT}} \tag{18}$$

(12) A value of P_{6a}/p_0 is calculated from

$$\frac{P_{6a}}{p_0} = \frac{P_1}{p_0} \frac{P_6}{P_1} \frac{P_{6a}}{P_6} \tag{19}$$

3656

(13) A value of $(w\sqrt{\theta}/\delta)_{6a}$ is calculated from

$$\left(\frac{w\sqrt{\theta}}{\delta}\right)_{6a} = \left(\frac{w\sqrt{\theta}}{\delta}\right)_6 \frac{\sqrt{\frac{T_{6a}}{T_6}}}{\frac{P_{6a}}{P_6}} \tag{20}$$

(14) A value of $(w\sqrt{\theta}/\delta)_{6a}$ is read from figure 10(b) for the calculated value of P_{6a}/p_0 (step (12)). If this does not equal the value from step (13), steps (2) to (14) are repeated until agreement is reached.

(15) The compressor operating points can be found by reading values of P_2/P_1, P_3/P_2, and $w_2\sqrt{\theta_2}$ from gas-generator plots of these variables against $w_6\sqrt{\theta_6}/\delta_6$ for constant values of $N_o/\sqrt{\theta_1}$.

Turbojet- and turboprop-engine performance. - After the gas generator has been matched with the other turbojet-engine components, the air flow, the pressure, and the temperature at the exhaust nozzle are known. The jet thrust F_j can be found from the following equations (ref. 24), which relate F_j/w to P_8/p_0:

$$\frac{F_j}{\frac{w}{g}} = K_2\sqrt{T_8}\ (1 + f) \tag{21}$$

For a complete-expansion nozzle,

$$K_2 = \sqrt{2gJc_p}\sqrt{1 - \left(\frac{p_0}{P_8}\right)^{\frac{\gamma-1}{\gamma}}} \tag{22}$$

and for the convergent nozzle at supercritical pressures,

$$K_2 = \sqrt{2gJc_p}\left\{\sqrt{\frac{\gamma - 1}{\gamma + 1}} + \left(\frac{\gamma + 1}{2}\right)^{\frac{\gamma+1}{2(\gamma-1)}} \frac{\sqrt{\frac{\gamma - 1}{2}}}{\gamma}\left[\left(\frac{2}{\gamma + 1}\right)^{\frac{\gamma}{\gamma-1}} - \frac{p_0}{P_8}\right]\right\} \tag{23}$$

A graph relating K_2 to the nozzle pressure ratio is given in figure 11 of reference 24. Net thrust is found by deducting the momentum of the inlet air from the jet thrust.

Fuel flow can be computed by multiplying air flow by fuel-air ratio. The fuel economy expressed as thrust specific fuel consumption is simply the ratio of fuel flow to thrust.

After the gas generator has been matched with the other turboprop-engine components, the shaft power, jet thrust, and specific fuel consumption can be calculated from the equations derived in appendix D of reference 4.

SIMPLIFIED METHODS FOR EQUILIBRIUM OPERATION

In this section, simplified methods are presented for obtaining the performance of one- and two-spool gas generators. The simplification consists in making several assumptions regarding turbine performance. The equivalent weight flow at the turbine inlet is assumed constant for all operating conditions. This implies that the turbine nozzles are choked. Most one-stage turbines operate at nearly constant equivalent weight flow for all turbine pressure ratios greater than 2.0, while many multistage turbines operate at nearly constant equivalent weight flow for all turbine pressure ratios greater than 2.5. Only during starting conditions are turbines normally required to operate at pressure ratios less than 2.0 or 2.5. The accessory power is assumed to be zero. Normally it is so small that negligible error is introduced by considering it to be zero. The turbine efficiency is assumed to vary according to the following equation:

$$\eta_{ad} = a + b\left(\frac{N}{\sqrt{\Delta H}} - c\right)^2 \tag{24}$$

where

a design value of turbine efficiency

b $-a/c^2$

3657

CH-42 back

c design value of $\left(\frac{N/\sqrt{\theta}}{\sqrt{\Delta H/\theta}}\right)_T$

This approximation is quite good over much of the turbine performance map. Near limiting loading, however, actual turbine efficiencies are much lower than those calculated from equation (24). Once the gas-generator performance is obtained, the matching with the other engine components is achieved as described in the preceding section.

One-Spool Gas Generator

Design point. - From a given compressor performance map, the compressor operating point for the engine design conditions is selected. The design value of turbine efficiency is specified as well as the design value of turbine to compressor temperature ratio T_4/T_1. Design values of $w_4\sqrt{\theta_4}/\delta_4$ and $N/\sqrt{H_4 - H_6}$ are calculated from

$$\frac{w_4\sqrt{\theta_4}}{\delta_4} = \frac{w_1\sqrt{\theta_1}}{\delta_1}\,\frac{(1 - B_3)(1 + f)\sqrt{\frac{T_4}{T_1}}}{\frac{P_3}{P_1}\,\frac{P_4}{P_3}} \tag{25}$$

$$\frac{N}{\sqrt{H_4 - H_6}} = \frac{\frac{N}{\sqrt{\theta_1}}\sqrt{(1 - B_3)(1 + f)}}{\sqrt{c_{p,C}\,518.7\left(\frac{T_3}{T_1} - 1\right)}} \tag{26}$$

Constant values of B_3, f, and P_4/P_3 are usually adequate. The $w_4\sqrt{\theta_4}/\delta_4$ value from equation (25) is assumed to be constant for all operating conditions. The $N/\sqrt{H_4 - H_6}$ value from equation (26) is equal to the constant c in equation (24).

Off-design points. - For each compressor operating point, the corresponding turbine operating point may be found by the following steps:

(1) A value of T_4/T_1 is calculated from equation (25).

(2) The turbine temperature ratio is calculated from

$$\frac{T_6}{T_4} = 1 - \frac{c_{p,C}\left(\frac{T_3}{T_1} - 1\right)}{c_{p,T}\,(1 + f)(1 - B_3)\,\frac{T_4}{T_1}} \tag{27}$$

(3) A value of $N/\sqrt{H_4 - H_6}$ is calculated from equation (26).

(4) A value of $\eta_{ad,T}$ is calculated from equation (24).

(5) The turbine pressure ratio is calculated from

$$\frac{P_6}{P_4} = \left(1 - \frac{1 - \frac{T_6}{T_4}}{\eta_{ad,T}}\right)^{\frac{\gamma_T}{\gamma_T - 1}} \tag{28}$$

The gas-generator parameters $w_6\sqrt{\theta_6}/\delta_6$, P_6/P_1, and T_6/T_1 are calculated from

$$\frac{w_6\sqrt{\theta_6}}{\delta_6} = \frac{w_4\sqrt{\theta_4}}{\delta_4}\,\frac{\sqrt{\frac{T_6}{T_4}}}{\frac{P_6}{P_4}} \tag{29}$$

$$\frac{P_6}{P_1} = \frac{P_3}{P_1}\,\frac{P_4}{P_3}\,\frac{P_6}{P_4} \tag{30}$$

$$\frac{T_6}{T_1} = \frac{T_4}{T_1}\,\frac{T_6}{T_4} \tag{31}$$

As discussed previously, the equivalent fuel-air ratio f/θ_1 may be found from values of T_3/T_1 and T_4/T_1, an assumed fuel, a combustor efficiency, and combustion charts such as those presented in reference 14.

Thus, for a range of weight flow $w_1\sqrt{\theta_1}/\delta_1$ at each compressor speed $N/\sqrt{\theta_1}$, the values of $w_6\sqrt{\theta_6}/\delta_6$, T_4/T_1, T_6/T_1, P_6/P_1, P_3/P_1, and f/θ_1 may be found. The gas-generator performance can be represented by plots of $w_1\sqrt{\theta_1}/\delta_1$, T_4/T_1, T_6/T_1, P_6/P_1, P_3/P_1, and f/θ_1 against $w_6\sqrt{\theta_6}/\delta_6$ for constant values of $N/\sqrt{\theta_1}$ (fig. 5).

Two-Spool Gas Generator

The outer- and inner-compressor performance maps are given, and the compressor operating points for the engine design conditions are selected.

The design value of turbine to compressor temperature ratio T_4/T_1 is specified as well as the design values of outer- and inner-turbine efficiency.

Inner-spool matching. - The performance of the inner spool is obtained as described previously; engine stations 1, 3, 4, and 6 for the one-spool gas generator are replaced by stations 2, 3, 4, and 5 for the inner spool of the two-spool gas generator. The design value of $w_5\sqrt{\theta_5}/\delta_5$ is read from the inner-spool performance plot for the design value of P_3/P_2 and $N_i/\sqrt{\theta_2}$. This value of $w_5\sqrt{\theta_5}/\delta_5$ is assumed to to be constant for all operating conditions.

Because the inner-spool-outlet equivalent weight flow $w_5\sqrt{\theta_5}/\delta_5$ is assumed constant, inner-spool performance may be presented as plots of $w_2\sqrt{\theta_2}/\delta_2$, P_3/P_2, P_5/P_2, T_5/T_2, and T_4/T_2 against $N_i/\sqrt{\theta_2}$ for the design value of $w_5\sqrt{\theta_5}/\delta_5$.

Outer-spool matching. - The outer-spool components are matched with the inner-spool performance by first assigning values of $w_1\sqrt{\theta_1}/\delta_1$ at each speed $N_o/\sqrt{\theta_1}$. At each point, the outer-compressor performance is known. The equivalent weight flow $w_2\sqrt{\theta_2}/\delta_2$, which is common to the outer compressor and inner spool, is calculated from

$$\frac{w_2\sqrt{\theta_2}}{\delta_2} = (1 - B_2)\frac{w_1\sqrt{\theta_1}}{\delta_1}\frac{\sqrt{\frac{T_2}{T_1}}}{\frac{P_2}{P_1}} \tag{32}$$

From the inner-spool performance curves, values of $N_i/\sqrt{\theta_2}$ and T_5/T_2 are read.

The outer-turbine temperature ratio T_6/T_5 is calculated from

$$\frac{T_6}{T_5} = 1 - \frac{w_1 c_{p,oC}\left(\frac{T_2}{T_1} - 1\right)}{w_5 c_{p,oT}\frac{T_5}{T_2}\frac{T_2}{T_1}} \tag{33}$$

where $w_5 = w_1(1 - B_2)(1 - B_3)(1 + f)$. From the design value of $\eta_{ad,oT}$ and the design value of $N_o/\sqrt{H_5 - H_6}$, which is calculated from

$$\frac{N_o}{\sqrt{H_5 - H_6}} = \frac{\frac{N_o}{\sqrt{\theta_1}}\sqrt{(1 - B_2)(1 - B_3)(1 + f)}}{\sqrt{c_{p,oC}\ 518.7\left(\frac{T_2}{T_1} - 1\right)}} \tag{34}$$

the constants of equation (24) can be evaluated for use with the outer turbine. Outer-turbine efficiency may be calculated from equation (24) after $N_o/\sqrt{H_5 - H_6}$ is calculated from equation (34). Outer-turbine pressure ratio is calculated from

$$\frac{P_6}{P_5} = \left(1 - \frac{1 - \frac{T_6}{T_5}}{\eta_{ad,oT}}\right)^{\frac{\gamma_{oT}}{\gamma_{oT}-1}} \tag{35}$$

From the component operating points, the two-spool gas-generator performance may be calculated and plotted as in figure 8.

If the assumption that outer-turbine-inlet equivalent weight flow is constant for all engine operation does not appear to be valid, an approximation such as that described in EQUILIBRIUM OPERATING LINE OF ONE-SPOOL TURBOJET may be used. One of the curves representing the variation of turbine-inlet flow with turbine total-pressure ratio is selected. The value of equivalent weight flow at the outer-turbine inlet that is used in the matching procedures must agree with the value read from the selected curve and the calculated turbine pressure ratio. If this approximation is used for the outer turbine, then the inner-spool performance must be presented as plots of $w_2\sqrt{\theta_2}/\delta_2$, P_3/P_2, P_5/P_2, T_5/T_2, and T_4/T_2 against $N_i/\sqrt{\theta_2}$ for constant values of $w_5\sqrt{\theta_5}/\delta_5$.

EQUILIBRIUM OPERATING LINE OF ONE-SPOOL TURBOJET

A method is given in reference 5 for locating a constant-exhaust-nozzle-area equilibrium operating line on the performance map of a compressor that is part of a one-spool turbojet engine operated at static sea-level conditions. In this method the performance characteristics of the combustor, turbine, and exhaust nozzle are simplified in order to obtain charts from which an equilibrium operating line can be obtained for specified design conditions and the compressor map.

The charts of reference 5 are shown in figures 11 to 14. In figure 11, turbine pressure ratio P_4/P_6 is plotted against $(P_3/P_1)(P_4/P_3)(P_1/p_0)(p_0/p_8)$ with P_8/p_8 and $(A_8/A_4)(w^*/w)_4(w_4/w_8)$ as parameters. This represents the combined performance of the turbine, tailpipe, and simple convergent exhaust nozzle. For this chart a turbine polytropic efficiency of 0.85 was assumed, and the total-pressure drop in the tailpipe was assumed to vary according to

$$P_6 - P_8 = K \frac{\rho_8 V_8^2}{2g} \tag{36}$$

The value of K was set by assigning $P_6/P_8 = 1.05$ for sonic velocity at the exhaust-nozzle exit. A constant value of $4/3$ was assigned to γ_4 and γ_8.

In figure 12, which relates the compressor with the rest of the engine, $(1 - B_3)(1 + f)(T_4/T_1)\eta_{ad,C}\eta_{ad,T}$ is plotted against compressor pressure ratio P_3/P_1 with $(A_8/A_4)(w^*/w)_4(w_4/w_8)$, P_8/p_8, and P_4/P_6 as parameters. The bearing losses and accessory power are assumed to be negligible. The pressure ratio P_1/p_0 was taken equal to unity, and the combustor pressure ratio P_4/P_3 was taken equal to 0.97.

The compressor weight flow is related to the compressor pressure ratio and the performance of the combustor, turbine, tailpipe, and exhaust nozzle in figure 13, where P_3/P_1 is plotted against $\sqrt{(1 - B_3)(1 + f)/\eta_{ad,C}\eta_{ad,T}}\,(w_8/w_4)(A_1/A_8)(w_1\sqrt{\theta_1}/\delta_1 A_1)$ with $(1 - B_3)(1 + f)(T_4/T_1)\eta_{ad,C}\eta_{ad,T}$, A_8/A_4 $(w^*/w)_4(w_4 w_8)$, P_4/P_6, and P_8/p_8 as parameters.

In order to establish the compressor equilibrium operating line at pressure ratios less than design, it is necessary to estimate the variation in $(w/w^*)_4$ with turbine pressure ratio P_4/P_6. If actual turbine data are available, a good approximation to the variation in $(w/w^*)_4$ with turbine pressure ratio P_4/P_6 can be obtained by computing the value of $(w/w^*)_4$ for each value of P_4/P_6 at the best efficiency point. If turbine data are not available, a reasonably good approximation can be obtained from the curves of figure 14. The multistage curve represents the equation

$$\left(\frac{w}{w^*}\right)_4 = \sqrt{1 - \left(\frac{P_6}{P_4}\right)^2} \tag{37}$$

The two single-stage curves are theoretical variations computed for two values of the turbine parameter $\psi_T \eta_{ad,T}/\sin^2\beta_4$ of 1.5 and 2.0. Operating lines for two- or three-stage turbines would be between those for the single-stage turbine and that for the multistage turbine.

Use of Charts for Design Point

3656

The following procedure may be used to find the design values of A_8/A_4 and A_8 once the design conditions are specified:

(1) Design values are selected for P_3/P_1, $w_1\sqrt{\theta_1}/\delta_1$, T_4/T_1, w_4/w_8, $\eta_{ad,T}$, B_3, and f.

(2) Compressor efficiency $\eta_{ad,C}$ is read from the compressor map.

(3) The design value of $\overline{T} = (1 - B_3)(1 + f)(T_4/T_1)\eta_{ad,C}\eta_{ad,T}$ is calculated.

CH-43

(4) The design value of $\overline{A} = A_8/A_4\ (w^*/w)_4(w_4/w_8)$ is read from figure 12 for the known values of $\overline{T}$ and P_3/P_1.

(5) The design value of $\overline{w} = \sqrt{(1 - B_3)(1 + f)/\eta_{ad,C}\eta_{ad,T}}\ (w_8/w_4)$ $(A_1/A_8)\ (w_1\sqrt{\theta_1}/\delta_1 A_1)$ is read from figure 13 for the known values of $\overline{A}$ and P_3/P_1.

(6) A value of $\overline{P}$ is calculated assuming $p_0/p_8 = 1.0$.

(7) If the point read from figure 11 for the known values of $\overline{A}$ and $\overline{P}$ lies to the left of the line $P_8/p_8 = 1.85$, a value of P_4/P_6 is read at this point.

If the point read from figure 11 for the known values of $\overline{A}$ and $\overline{P}$ lies to the right or on the line $P_8/p_8 = 1.85$, a value of P_4/P_6 is read for the design value of $\overline{A}$ along the line $P_8/p_8 = 1.85$.

(8) The design value of $(w/w^*)_4$ is read from the proper curve in figure 14 for the design value of P_4/P_6.

(9) The design value of A_8/A_4 is calculated from known values of $\overline{A}$, $(w/w^*)_4$, and w_4/w_8.

(10) The design value of A_8 is calculated from known values of $\overline{w}$, $[(1 - B_3)(1 + f)]$, $\eta_{ad,C}\eta_{ad,T}$, (w_8/w_4), and $w_1\sqrt{\theta_1}/\delta_1$.

Use of Charts for Off-Design Points

The following procedure may be used to locate equilibrium operating points on the compressor map for operation with the design values of A_8 and A_8/A_4 at compressor pressure ratios higher or lower than design:

(1) A value of P_3/P_1 is selected.

(2) A trial value of $\overline{A}$ is chosen. Although the values of A_8/A_4 and w_4/w_8 are known, the value of $(w/w^*)_4$ is not known.

(3) A value of $\overline{P}$ is calculated assuming $p_0/p_8 = 1.0$.

(4) If the point read from figure 11 for the values of $\overline{A}$ and $\overline{P}$ lies to the left of the line $P_8/p_8 = 1.85$, a value of P_4/P_6 is read at this point.

If the point read from figure 11 for the values of $\overline{A}$ and $\overline{P}$ lies to the right or on the line $P_8/p_8 = 1.85$, a value of P_4/P_6 is read for the value of $\overline{A}$ along the line $P_8/p_8 = 1.85$.

(5) A value of $(w/w^*)_4$ is read from figure 14 for the value of P_4/P_6.

(6) A value of $\overline{A}$ is calculated from the values of A_8/A_4, w_4/w_8, and $(w/w^*)_4$. If the calculated $\overline{A}$ does not equal the trial value of $\overline{A}$ from step (2), steps (2) to (6) are repeated until agreement is reached.

(7) The weight-flow parameter $\overline{w}$ is read from figure 13 for the known values of P_3/P_1 and $\overline{A}$.

(8) A value of $\eta_{ad,C}$ is estimated from the compressor map for the known value of P_3/P_1.

(9) The compressor weight flow $w_1\sqrt{\theta_1}/\delta_1$ is calculated from values of $\overline{w}$, $[(1 - B_3)(1 + f)]$, $\eta_{ad,C}\eta_{ad,T}$, (w_8/w_4), and A_8.

(10) A value of $\eta_{ad,C}$ is read from the compressor map for the values of P_3/P_1 and $w_1\sqrt{\theta_1}/\delta_1$. If this does not equal the estimated value of $\eta_{ad,C}$ from step (8), steps (8) to (10) are repeated until agreement is reached.

(11) The desired equilibrium operating point can be located on the compressor map from the values of P_3/P_1 (step (1)), and $w_1\sqrt{\theta_1}/\delta_1$ (step (9)).

METHODS FOR TRANSIENT OPERATION

Two problems are treated in this section. A method is discussed whereby the compressor and turbine of a one-spool turbojet engine may be matched for a specified flight condition, a specified transient path on the compressor map, and a fixed exhaust-nozzle area (ref. 11). For a two-spool turbojet engine, procedures are discussed for finding the compressor paths during a transient for which the exhaust-nozzle area and inner-turbine-inlet temperature are held constant (ref. 12).

One-Spool Turbojet

Up until now, compressor operation has been found for a specified flight condition and mode of engine operation. For a given flight condition, the compressor equilibrium operating point was fixed by assigning two quantities such as mechanical speed and turbine-inlet temperature or mechanical speed and exhaust-nozzle area. Now, compressor operation is scheduled. During a transient, the power-balance relation no longer is valid, so that three quantities must be assigned. For a given flight condition, the desired transient path on the compressor map is specified by assigning values for mechanical speed and compressor pressure ratio. The exhaust-nozzle area is assigned to be constant during the transient; this accounts for the third quantity.

At each speed, the excess torque is calculated after the turbine operating point has been found for the assigned compressor operating point. For known values of moment of inertia and excess torque at each speed, the time required to accelerate (or decelerate) along the specified path may be calculated. Such calculations indicate whether the specified path on the compressor map is acceptable with respect to transient operation. If, for a given engine configuration, the time to accelerate is found to be excessive, various schemes may be tried to improve the engine accelerating characteristics. These schemes will involve changes in component performance or a rematching between the compressor and turbine, or both. The effect of these changes on the engine accelerating characteristics may be calculated by rematching the compressor and turbine.

Compressor operation. - The steady-state compressor and turbine maps are assumed to be valid during transient operation. The aerodynamic adjustments are assumed to occur much faster than the mechanical adjustments. An acceleration is considered such that the compressor operates along the path abcd shown in figure 15. At a given speed $N/\sqrt{\theta_1}$, the compressor operating point is known, so that the value of w_4N/δ_4 may be calculated from

$$\frac{w_4N}{\delta_4} = \frac{w_1\sqrt{\theta_1}}{\delta_1}\frac{N}{\sqrt{\theta_1}}\frac{(1 + f)(1 - B_3)}{\frac{P_3}{P_1}\frac{P_4}{P_3}} \tag{38}$$

3656

where the fuel-air ratio and combustor pressure ratio are usually assumed constant.

Turbine operation. - At this point in the procedure, one turbine parameter is known. The second turbine parameter required to define turbine operation is found in an indirect manner. At the known value of w_4N/δ_4, several values of turbine pressure ratio P_4/P_6 are selected from the turbine performance map (fig. 16). For each P_4/P_6 selection, values of $N/\sqrt{\theta_4}$ and $(H_4 - H_6)/\theta_4$ are read. The following calculations are made:

$$\frac{T_6}{T_4} = 1 - \frac{\frac{H_4 - H_6}{\theta_4}}{c_{p,T}\ 518.7} \tag{39}$$

$$\frac{w_4\sqrt{\theta_4}}{\delta_4} = \frac{\frac{w_4N}{\delta_4}}{\frac{N}{\sqrt{\theta_4}}} \tag{40}$$

$$\frac{T_4}{T_1} = \left(\frac{\frac{N}{\sqrt{\theta_1}}}{\frac{N}{\sqrt{\theta_4}}}\right)^2 \tag{41}$$

The nozzle equivalent weight flow is calculated from

$$\frac{w_8\sqrt{\theta_8}}{\delta_8} = \frac{w_4\sqrt{\theta_4}}{\delta_4}\frac{\sqrt{\frac{T_6}{T_4}}\sqrt{\frac{T_8}{T_6}}\frac{P_4}{P_6}}{\frac{P_8}{P_6}} \tag{42}$$

The values of T_8/T_6 and P_8/P_6 depend on the performance characteristics of the tailpipe and exhaust nozzle. A simplification that is satisfactory for many applications results from taking $T_8/T_6 = 1$ and $P_8/P_6 = 0.95$.

The exhaust-nozzle pressure ratio is calculated from

$$\frac{P_8}{p_0} = \frac{P_0}{p_0}\frac{P_1}{P_0}\frac{P_3}{P_1}\frac{P_4}{P_3}\frac{P_6}{P_4}\frac{P_8}{P_6} \tag{43}$$

The value of P_0/p_0 is known from the specified flight Mach number. Inlet performance yields a value of P_1/P_0. For all values of P_8/p_0 less than or equal to the critical value $\left[\left(\frac{P}{p}\right)^* = \left(\frac{\gamma + 1}{2}\right)^{\frac{\gamma}{\gamma-1}}\right]$, $\frac{P_8}{p_0} = \frac{P_8}{p_8}$;

and the effective area of the convergent exhaust nozzle A_8 is found as follows:

(1) M_8 is found from

$$\frac{P}{p} = \left(1 + \frac{\gamma - 1}{2} M^2\right)^{\frac{\gamma}{\gamma-1}} \tag{44}$$

(2) $(w\sqrt{\theta}/\delta A)_8$ is found from

$$\frac{w\sqrt{\theta}}{\delta A} = 2116 \cos \beta \sqrt{\frac{\gamma g}{R\ 518.7}}\, M \left(1 + \frac{\gamma - 1}{2} M^2\right)^{-\frac{(\gamma+1)}{2(\gamma-1)}} \tag{45}$$

(3) Exhaust-nozzle area is calculated from

$$A_8 = \frac{\left(\frac{w\sqrt{\theta}}{\delta}\right)_8}{\left(\frac{w\sqrt{\theta}}{\delta A}\right)_8} \tag{46}$$

When P_8/p_0 is greater than critical, the critical value of $w\sqrt{\theta}/\delta A$ is used in step (3). Nozzle area is plotted against turbine pressure ratio, and the value of P_4/P_6 for the assigned A_8 is read. Thus, the turbine operating point can be found for each compressor operating point along the assigned acceleration path.

Time to accelerate. - At each point along the assigned acceleration path, the excess torque available for acceleration may be calculated from

$$Q_{xs} = \frac{778.2w_1}{2\pi N}\left[(1 + f)(1 - B_3)\ c_{p,T}T_4\left(1 - \frac{T_6}{T_4}\right) - c_{p,C}T_1\left(\frac{T_3}{T_1} - 1\right)\right] \quad (47)$$

The actual values of weight flow and speed are obtained from the equivalent values and the values of θ_1 and δ_1, which are known for the assigned flight condition and inlet performance.

3656

The time to accelerate along the path b to c (fig. 15) is found from

$$\tau_c - \tau_b = 2\pi I \int_{N_b}^{N_c} \frac{1}{Q_{xs}}\, dN \quad (48)$$

where the moment of inertia I is a physical constant of the engine. The acceleration of a high-pressure-ratio one-spool turbojet engine as determined from component performance characteristics is investigated in references 11, 25, and 26.

Two-Spool Turbojet

For a two-spool turbojet engine, procedures are discussed for finding the compressor paths during a transient for which the exhaust-nozzle area and inner-turbine-inlet temperature are held constant. The component performance maps for equilibrium operation are assumed to be valid for transient operation. For equilibrium operation of a two-spool turbojet, the specification of two quantities fixes its operation. For transient operation, four quantities are required, as the power-balance condition for each spool is no longer valid. At the beginning of a transient, the outer- and inner-spool equivalent speeds are assumed to be the equilibrium values. These values of speed, together with the assigned values of inner-turbine-inlet temperature and exhaust-nozzle area, fix the operation of each of the components. The excess torque acting on each spool can then be calculated. The outer- and inner-spool speed increments occurring during a small time interval are found from the excess torque and moment of inertia for each spool. The new values of outer- and inner-spool speed, together with the constant values of inner-turbine-inlet temperature and exhaust-nozzle area, determine the operation of each of the components at the new time. The process is repeated until the desired end value of outer-spool speed is attained. It is a step-by-step procedure, then, and iterations are part of each step.

Thus, for a specified flight condition and assigned values of inner-turbine-inlet temperature and exhaust-nozzle area, the transient

paths on the compressor maps and the time required to traverse these paths may be calculated. From such calculations one can estimate whether or not an acceptable compromise can be reached between surge-free operation and time to accelerate for a given two-spool turbojet engine.

Compressor operation. - For a specified flight condition, initial values of $N_o/\sqrt{\theta_1}$, $N_i/\sqrt{\theta_1}$, T_4, and A_8, and the specification that T_4 and A_8 are maintained constant during an acceleration, the following procedures may be used to find the outer- and inner-compressor operating paths and the time required to accelerate to a higher engine speed:

(1) Values of $N_o/\sqrt{\theta_1}$, $N_i/\sqrt{\theta_1}$, T_4, and A_8 are specified.

(2) A trial value of $w_2\sqrt{\theta_2}/\delta_2$ is selected.

(3) A value of T_2/T_1 is read from a plot of T_2/T_1 against $w_2\sqrt{\theta_2}/\delta_2$ for constant values of $N_o/\sqrt{\theta_1}$.

(4) A value of $N_i/\sqrt{\theta_2}$ is calculated from values of $N_i/\sqrt{\theta_1}$ and T_2/T_1.

(5) A value of P_3/P_2 is read from a plot P_3/P_2 against $w_2\sqrt{\theta_2}/\delta_2$ for constant values of $N_i/\sqrt{\theta_2}$.

(6) A value of T_4 is calculated from

$$T_4 = T_1\left[\frac{w_4\sqrt{\theta_4}}{\delta_4}\,\frac{\dfrac{P_3}{P_2}\,\dfrac{P_4}{P_3}\sqrt{\dfrac{T_2}{T_1}}}{(1 - B_3)(1 + f)\,\dfrac{w_2\sqrt{\theta_2}}{\delta_2}}\right]^2 \tag{49}$$

The value of T_1 is found from the specified flight condition. The assumption of constant values for B_3, f, and P_4/P_3 is usually adequate. The value of $w_4\sqrt{\theta_4}/\delta_4$ is assumed to be the design value. (The validity of this assumption may be checked when the inner-turbine operating point is found.) If the value of T_4 calculated from equation (49) does not equal the assigned T_4 value (step (1)), steps (2) to (6) are repeated until agreement is reached.

Turbine operation. -

(7) A value of $N_i/\sqrt{\theta_4}$ is calculated from values of $N_i/\sqrt{\theta_1}$ and T_4/T_1.

(8) A trial value of P_4/P_6 is selected. If the proper value is chosen, the value of exhaust-nozzle area calculated later in the procedure will check with the specified value of A_8.

(9) A trial value of P_4/P_5 is selected.

(10) A value of T_4/T_5 is read from a plot of T_4/T_5 against $N_i/\sqrt{\theta_4}$ for constant values of P_4/P_5.

(11) A value of $N_o/\sqrt{\theta_5}$ is calculated from

$$\frac{N_o}{\sqrt{\theta_5}} = \frac{N_o}{\sqrt{\theta_1}} \frac{\sqrt{\frac{T_4}{T_5}}}{\sqrt{\frac{T_4}{T_1}}} \tag{50}$$

(12) A value of P_5/P_6 is calculated from

$$\frac{P_5}{P_6} = \frac{\frac{P_4}{P_6}}{\frac{P_4}{P_5}} \tag{51}$$

(13) A value of w_5N_o/δ_5 is calculated from

$$\frac{w_5N_o}{\delta_5} = \frac{w_2\sqrt{\theta_2}}{\delta_2} \frac{N_o}{\sqrt{\theta_1}} \frac{(1 - B_3)(1 + f)}{\sqrt{\frac{T_2}{T_1}} \frac{P_3}{P_2} \frac{P_4}{P_3} \frac{P_5}{P_4}} \tag{52}$$

(14) A value of w_5N_o/δ_5 is read from a plot of w_5N_o/δ_5 against $N_o/\sqrt{\theta_5}$ for constant values of P_5/P_6. If this does not equal the value of flow parameter calculated from equation (52) in step (13), steps (9) to (14) are repeated until agreement is reached.

(15) A value of T_6/T_5 is read from a plot of T_6/T_5 against $N_o/\sqrt{\theta_5}$ for constant values of P_5/P_6.

[redacted]

(16) A value of exhaust-nozzle area is found from the values of nozzle equivalent weight flow and nozzle equivalent specific weight flow as discussed for the one-spool turbojet. If the calculated value of A_8 does not equal the specified value, steps (8) to (16) are repeated until agreement is reached. When the selection of P_4/P_6 is found to be compatible with the specified exhaust-nozzle area, the operating point of each of the two-spool components is known at the initial time.

Time to accelerate. - From the component operating points, the excess torques available for accelerating the outer and inner spools can be calculated. The specified flight condition and inlet performance yield values of θ_1 and δ_1 which can be used to convert equivalent-speed and equivalent-weight-flow values to actual values. Outer- and inner-spool excess torque are calculated from

$$Q_{xs,o} = \frac{778.2w_1}{2\pi N_o}\left[(1 + f)(1 - B_2)(1 - B_3)c_{p,oT}T_5\left(1 - \frac{T_6}{T_5}\right) - c_{p,oC}T_1\left(\frac{T_2}{T_1} - 1\right)\right] \tag{53}$$

$$Q_{xs,i} = \frac{778.2w_2}{2\pi N_i}\left[(1 + f)(1 - B_3)c_{p,iT}T_4\left(1 - \frac{T_5}{T_4}\right) - c_{p,iC}T_2\left(\frac{T_3}{T_2} - 1\right)\right] \tag{54}$$

Speed increments in N_o and N_i for a specified time interval are defined by

$$\Delta N_o = (N_o)_b - (N_o)_a = \frac{1}{2\pi I_o}\int_{\tau_a}^{\tau_b} Q_{xs,o}\, d\tau \tag{55}$$

$$\Delta N_i = (N_i)_b - (N_i)_a = \frac{1}{2\pi I_i}\int_{\tau_a}^{\tau_b} Q_{xs,i}\, d\tau \tag{56}$$

Because the continuous variations of $Q_{xs,o}$ and $Q_{xs,i}$ with time are not known, an approximation is introduced. Trial increments in N_o and N_i are defined by

$$\Delta N_o = \frac{Q_{xs,o}}{2\pi I_o}\Delta\tau \tag{57}$$

$$\Delta N_i = \frac{Q_{xs,i}}{2\pi I_i}\Delta\tau \tag{58}$$

The time increment $\Delta\tau$ is selected so as to result in reasonable speed increments. If $\Delta\tau$ is made too large, the procedure becomes inaccurate as evidenced by large irregularities in the points that define the transient paths on the compressor maps. If $\Delta\tau$ is made too small, more points will be calculated than are necessary to define the transient paths. In reference 12, time increments of 0.1 and 0.2 second were used. At the new time (the initial time plus the time increment), trial values of N_o and N_i are defined to be equal to the initial values of N_o and N_i plus the incremental values calculated from the initial values of $Q_{xs,o}$ and $Q_{xs,i}$ and equations (57) and (58). For these trial values of N_o and N_i and the specified values of T_4 and A_8, the matching procedures are repeated to yield component operating points and excess-torque values. The actual increments in N_o and N_i occurring during the time interval are approximated by substituting in equations (57) and (58) average values of $Q_{xs,o}$ and $Q_{xs,i}$, which are defined to be the arithmetic means of the values corresponding to the initial and trial values of N_o and N_i. The actual values of N_o and N_i at the new time are equal to the initial values plus the actual speed increments. 3656

The transient paths on the outer- and inner-compressor performance maps are found by repeating the matching procedures until the end value of engine speed is attained. The time required to reach this speed is found by summing up the time increments considered. In reference 12, the component operating trends during acceleration and deceleration of two hypothetical two-spool turbojet engines are discussed.

REFERENCES

1. Compressor and Turbine Research Division: Aerodynamic Design of Axial-Flow Compressors. Vol. II. NACA RM E56B03a, 1956.

2. Pinkel, Benjamin, and Karp, Irving M.: A Thermodynamic Study of the Turbojet Engine. NACA Rep. 891, 1947. (Supersedes NACA WR E-241.)

3. Pinkel, Benjamin, and Karp, Irving M.: A Thermodynamic Study of the Turbine-Propeller Engine. NACA Rep. 1114, 1953. (Supersedes NACA TN 2653.)

4. Sutor, Alois T., and Zipkin, Morris A.: Method of Matching Components and Predicting Performance of a Turbine-Propeller Engine. NACA TN 2450, 1951.

5. Huppert, Merle C.: Approximate Method for Determining Equilibrium Operation of Compressor Component of Turbojet Engine. NACA TN 3517, 1955.

6. Goldstein, Arthur W.: Analysis of Performance of a Jet Engine from Characteristics of Components. I - Aerodynamic and Matching Characteristics of the Turbine Component Determined with Cold Air. NACA Rep. 878, 1947. (Supersedes NACA TN 1459.)

7. Goldstein, Arthur W., Alpert, Sumner, Beede, William, and Kovach, Karl: Analysis of Performance of Jet Engine from Characteristics of Components. II - Interaction of Components As Determined from Engine Operation. NACA Rep. 928, 1949. (Supersedes NACA TN 1701.)

8. Goldstein, Arthur W.: Interaction of Components of Gas Turbines for Aircraft. Paper presented at A.S.M.E. meeting, New London (Conn.), Apr. 28-May 5, 1949.

9. Woodworth, L. R.: Performance Analysis Methods for the Twin-Spool, High Pressure Ratio, Turbojet Engine. RM 1039, U. S. Air Force Proj. RAND, the RAND Corp., Oct. 15, 1952.

10. Dugan, James F., Jr.: Two-Spool Matching Procedures and Equilibrium Characteristics of a Two-Spool Turbojet Engine. NACA RM E54F09, 1954.

11. Rebeske, John J., Jr., and Rohlik, Harold E.: Acceleration of High-Pressure-Ratio Single-Spool Turbojet Engine As Determined from Component Performance Characteristics. I - Effect of Air Bleed at Compressor Outlet. NACA RM E53A09, 1953.

12. Dugan, James F., Jr.: Component Operating Trends during Acceleration and Deceleration of Two Hypothetical Two-Spool Turbojet Engines. NACA RM E54L28, 1955.

13. Gist, W. B., and Woodworth, L. R.: Approximate Methods for Determining the Performance of Gas Turbine Engines at Off-Design Conditions. RM 1205, U. S. Air Force Proj. RAND, the RAND Corp., Mar. 5, 1954.

14. Esgar, Jack B., and Ziemer, Robert R.: Methods for Rapid Graphical Evaluation of Cooled or Uncooled Turbojet and Turboprop Engine or Component Performance (Effects of Variable Specific Heat Included). NACA TN 3335, 1955.

3656

CH A. back

15. Hensley, Reece V., Rom, Frank E., and Koutz, Stanley L.: Effect of Heat and Power Extraction on Turbojet-Engine Performance. I - Analytical Method of Performance Evaluation with Compressor-Outlet Air Bleed. NACA TN 2053, 1950.

16. Rom, Frank E., and Koutz, Stanley L.: Effect of Heat and Power Extraction on Turbojet-Engine Performance. II - Effect of Compressor-Outlet Air Bleed for Specific Modes of Engine Operation. NACA TN 2166, 1950.

17. Koutz, Stanley L., Hensley, Reece V., and Rom, Frank E.: Effect of Heat and Power Extraction on Turbojet-Engine Performance. III - Analytical Determination of Effects of Shaft-Power Extraction. NACA TN 2202, 1950.

18. Koutz, Stanley L.: Effect of Heat and Power Extraction on Turbojet-Engine Performance. IV - Analytical Determination of Effects of Hot-Gas Bleed. NACA TN 2304, 1951.

19. Rebeske, John J., Jr., and Dugan, James F., Jr.: Matched Performance Characteristics of a 16-Stage Axial-Flow Compressor and a 3-Stage Turbine. NACA RM E52H18, 1953.

20. Dugan, James F., Jr.: Effect of Design Over-All Compressor Pressure Ratio Division on Two-Spool Turbojet-Engine Performance and Geometry. NACA RM E54F24a, 1954.

21. Davison, Elmer H.: Turbine Design Considerations for Turbine-Propeller Engine Operating over a Range of Flight Conditions. NACA RM E53D16, 1953.

22. Davison, Elmer H.: Turboprop-Engine Design Considerations. I - Effect of Mode of Engine Operation on Performance of Turboprop Engine with Current Compressor Pressure Ratio. NACA RM E54D19, 1955.

23. Davison, Elmer H., and Stalla, Margaret C.: Turboprop-Engine Design Considerations. II - Design Requirements and Performance of Turboprop Engines with a Single-Spool High-Pressure-Ratio Compressor. NACA RM E55B18, 1955.

24. Sanders, Newell D., and Behun, Michael: Generalization of Turbojet-Engine Performance in Terms of Pumping Characteristics. NACA TN 1927, 1949.

3656

25. Rebeske, John J., Jr., and Dugan, James, F., Jr.: Acceleration of High-Pressure-Ratio Single-Spool Turbojet Engine As Determined from Component Performance Characteristics. II - Effect of Compressor Interstage Air Bleed. NACA RM E53E06, 1953.

26. Rohlik, Harold E., and Rebeske, John J.: Acceleration of High-Pressure-Ratio Single-Spool Turbojet Engine As Determined from Component Performance Characteristics. III - Effect of Turbine Stator Adjustment. NACA RM E54F04, 1954.

3656

3656

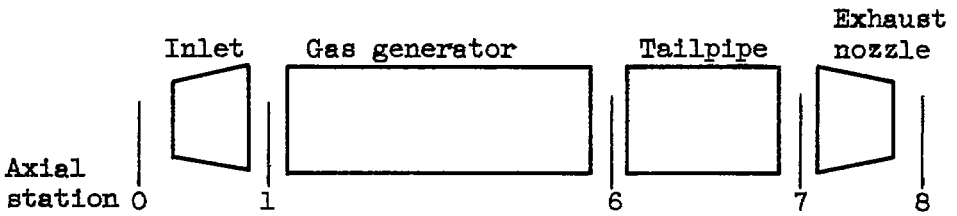

(a) Simple turbojet.

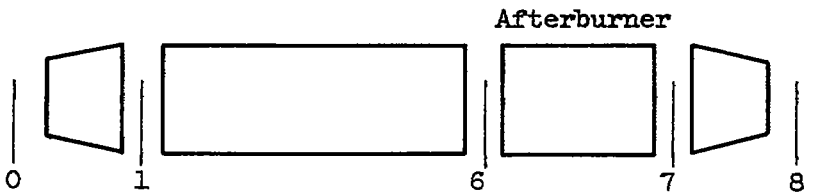

(b) Afterburning turbojet.

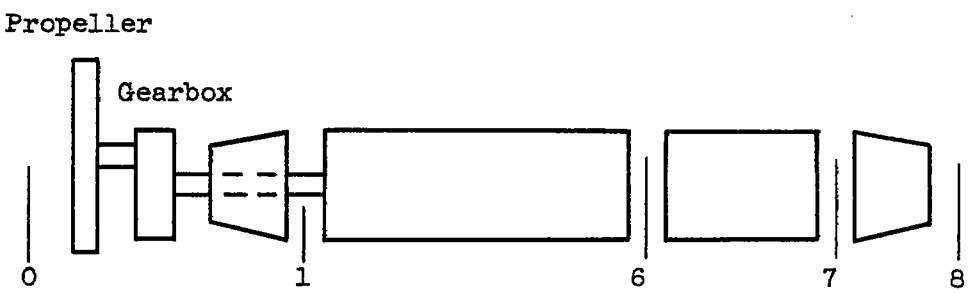

(c) Turboprop with coupled power turbine.

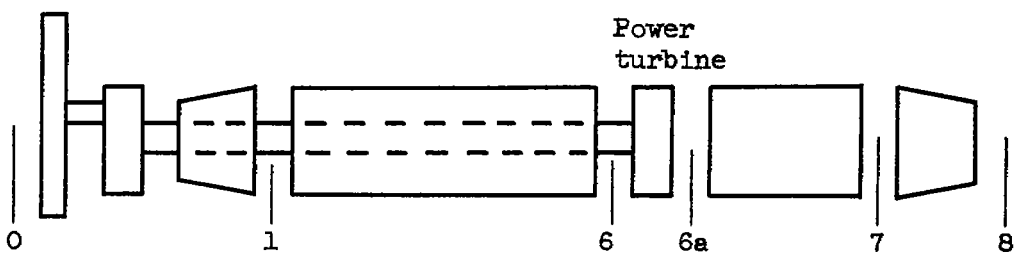

(d) Turboprop with free-wheeling power turbine.

Figure 1. - Gas-turbine engines.

3656

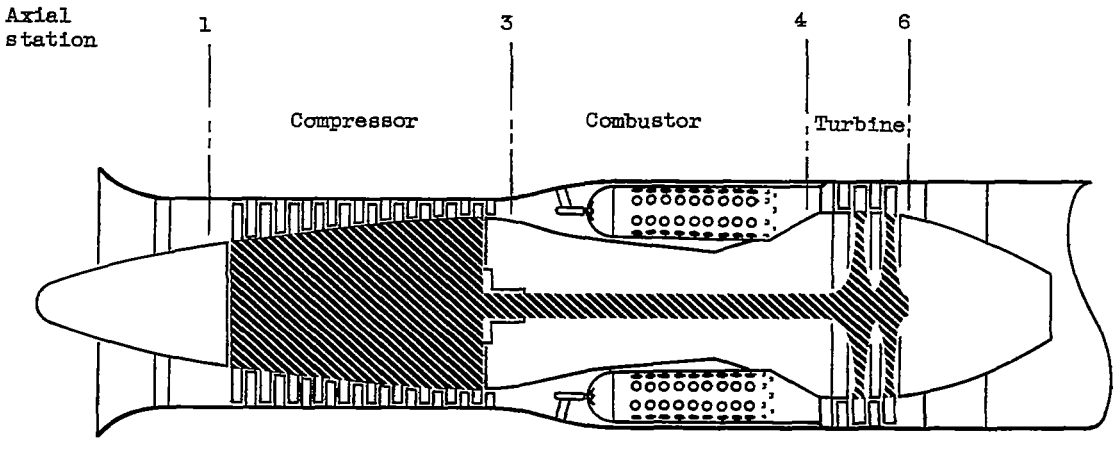

(a) One-spool.

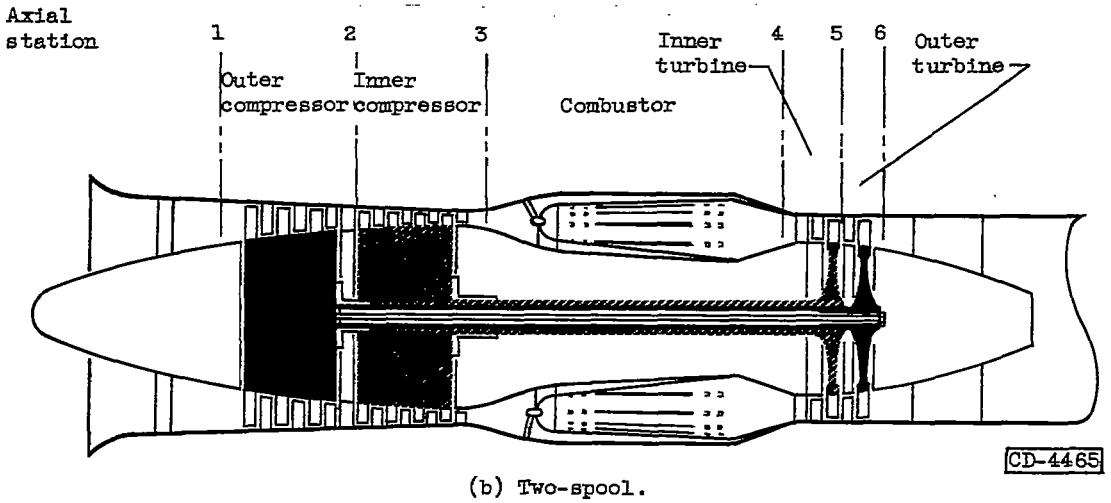

(b) Two-spool.

Figure 2. - Schematic diagrams of gas generators.

3656

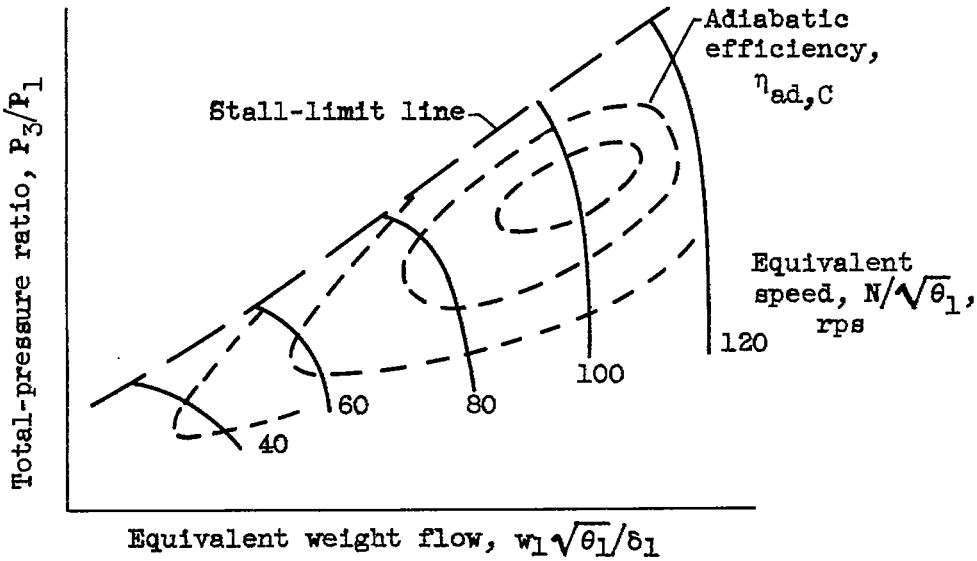

(a) Compressor performance map.

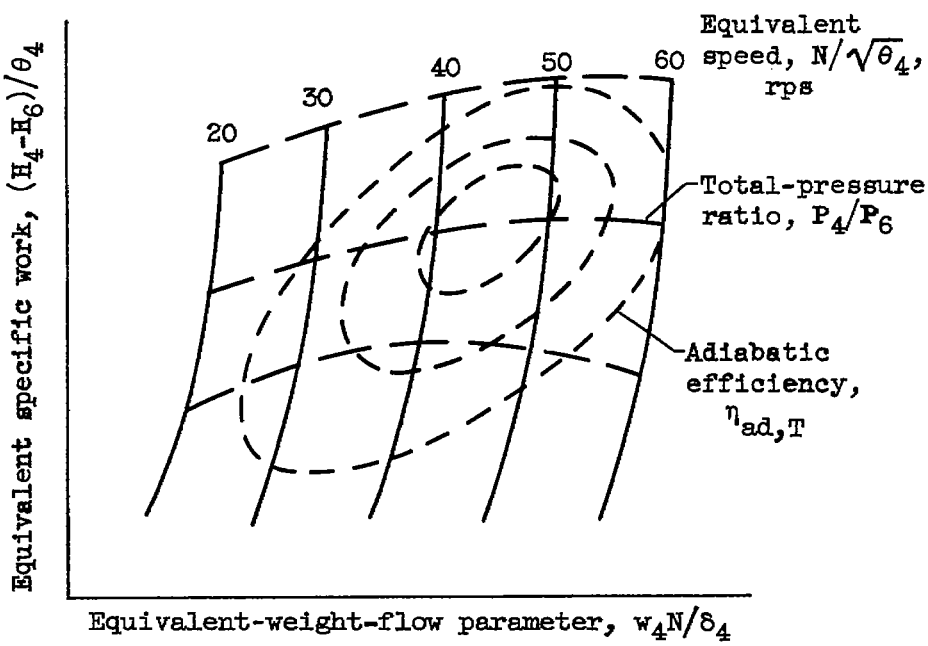

(b) Turbine performance map.

Figure 3. - Performance maps.

3656

CH-45

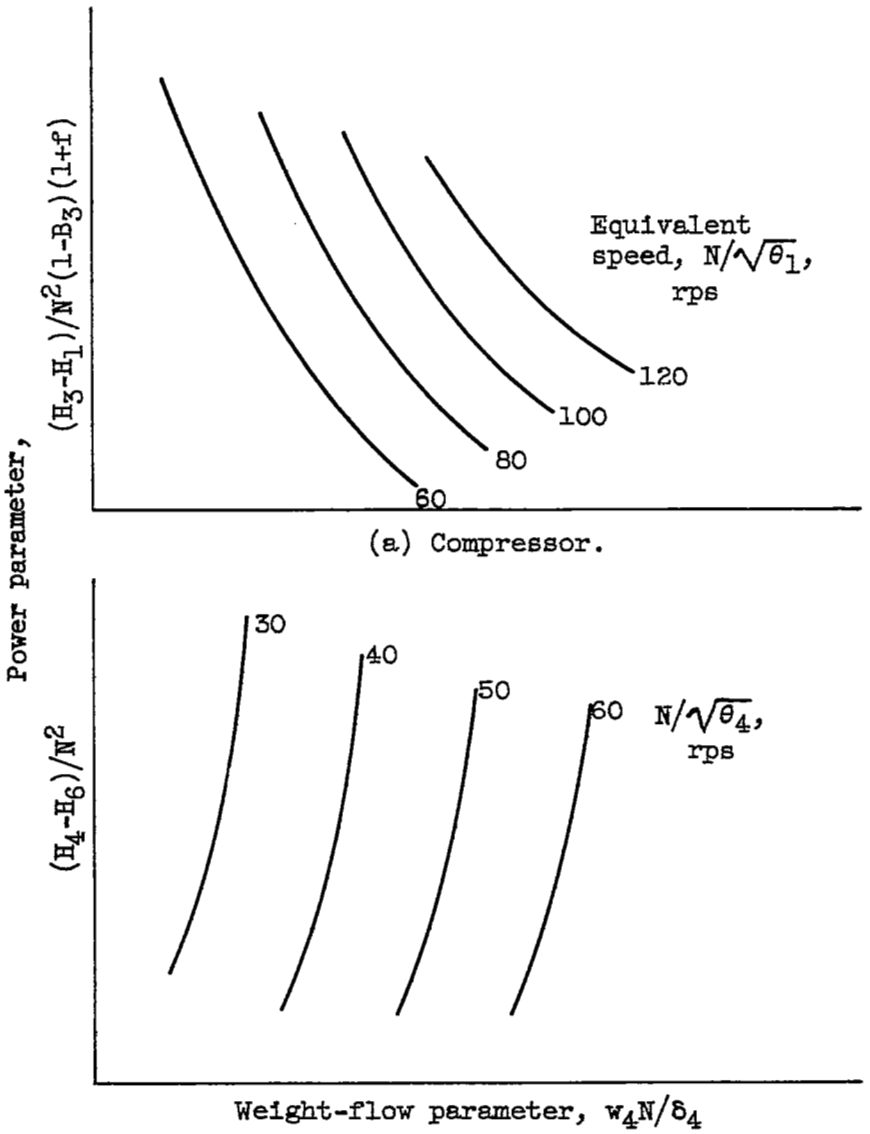

(b) Turbine.

Figure 4. - Matching maps for one-spool gas generator.

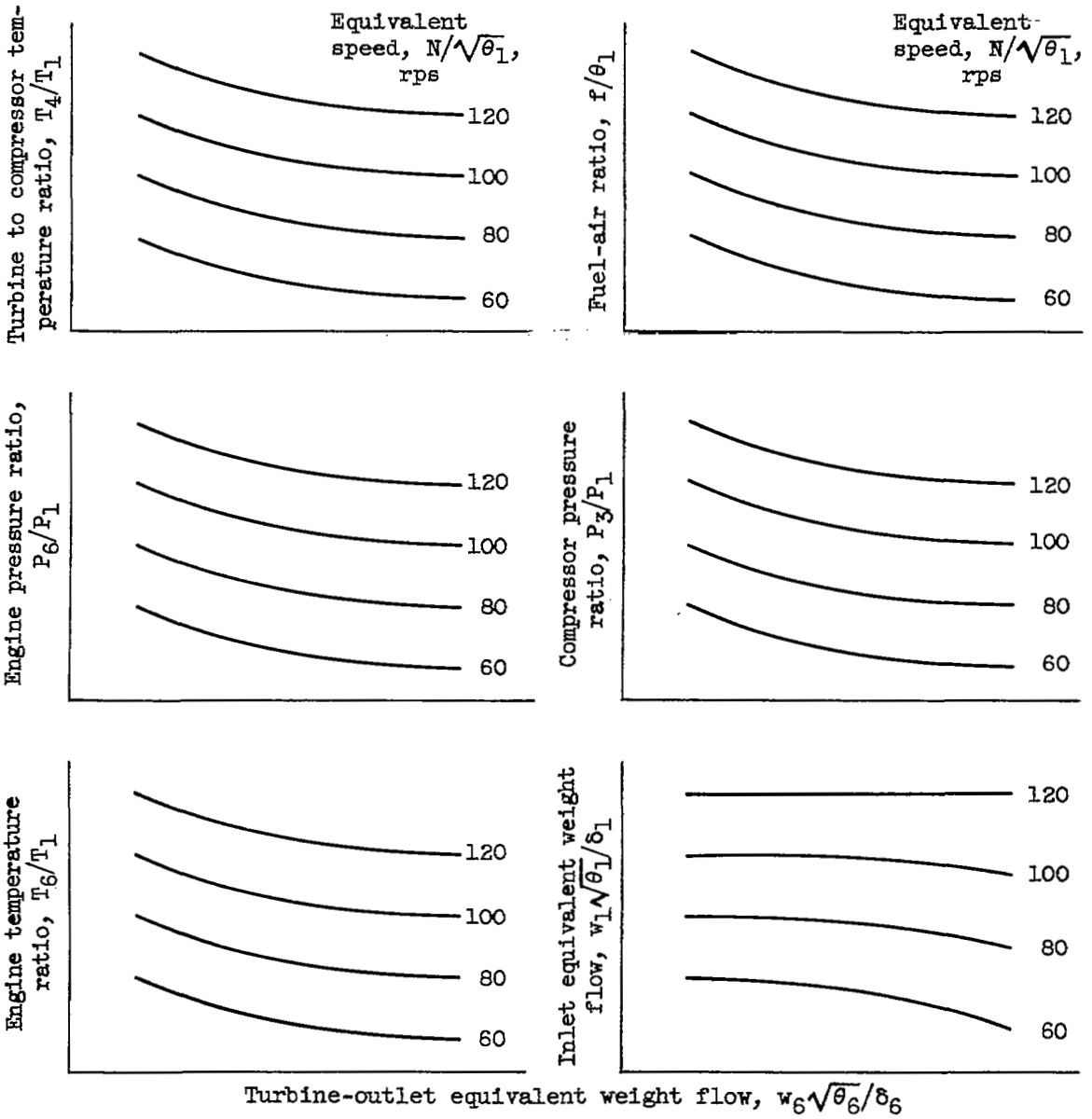

3656

Figure 5. - One-spool gas-generator performance.

3656

CH-45 back

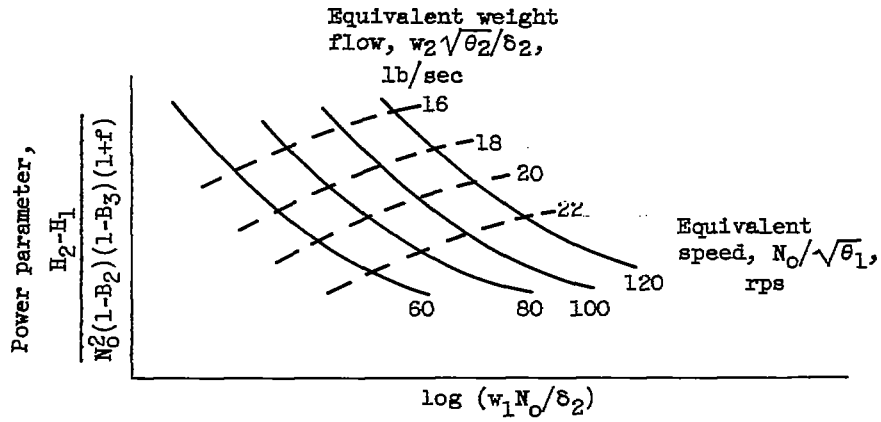

(a) Outer compressor.

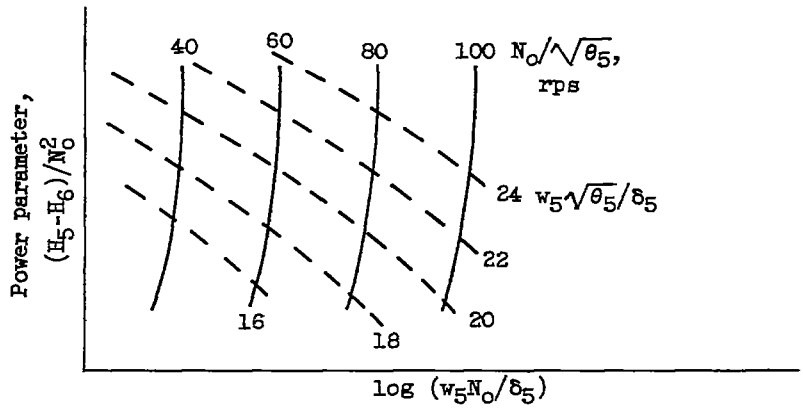

(b) Outer turbine.

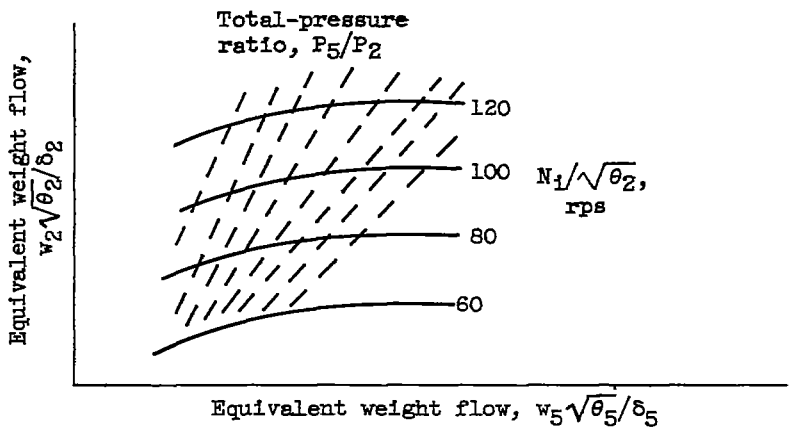

(c) Inner spool.

Figure 6. - Matching maps for direct method of matching outer and inner spools of two-spool gas generator.

3656

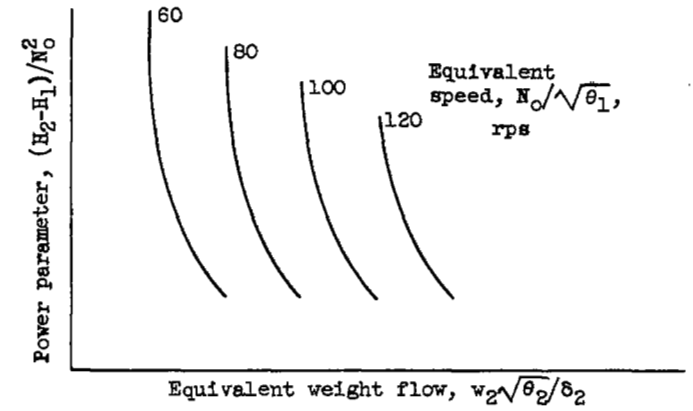

(a) Outer compressor.

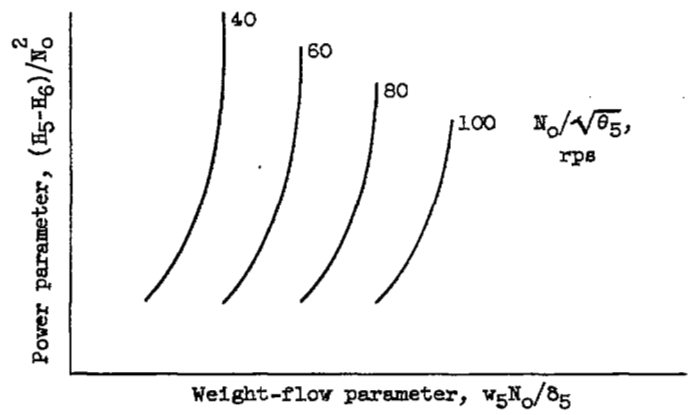

(b) Outer turbine.

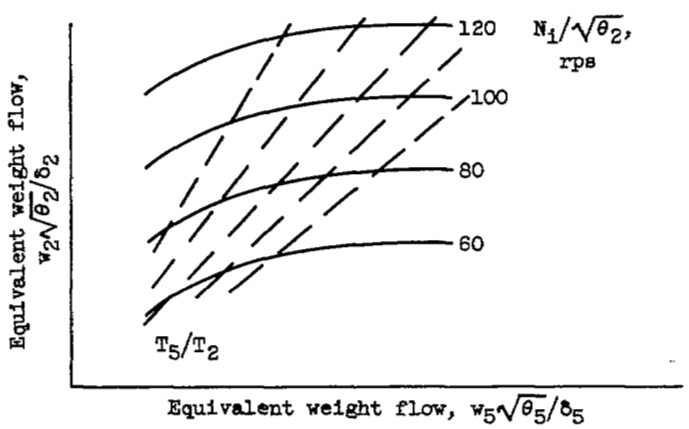

(c) Inner spool.

Figure 7. - Matching maps for iterative method of matching outer and inner spools of two-spool gas generator.

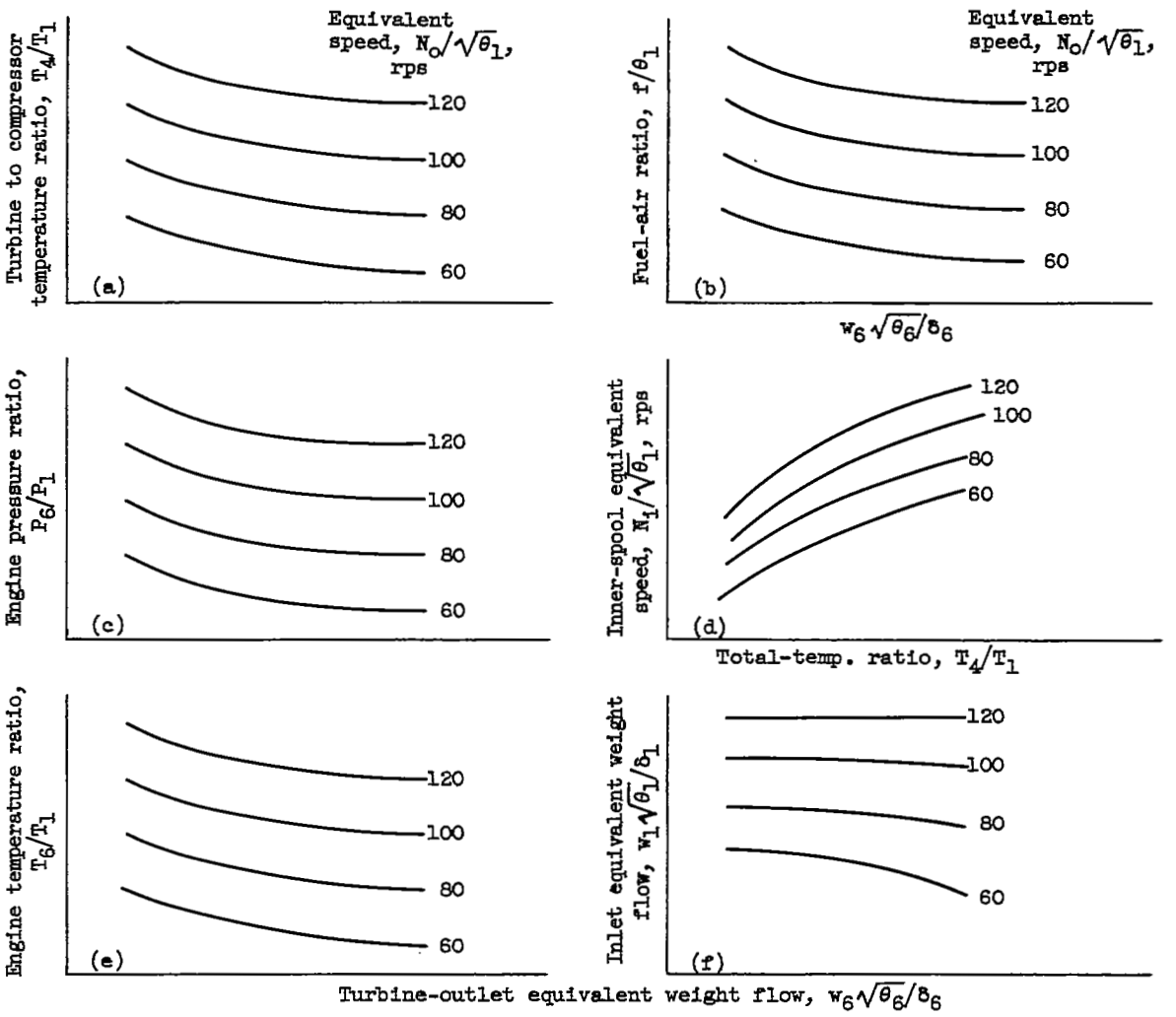

Figure 8. - Two-spool gas-generator performance.

3656

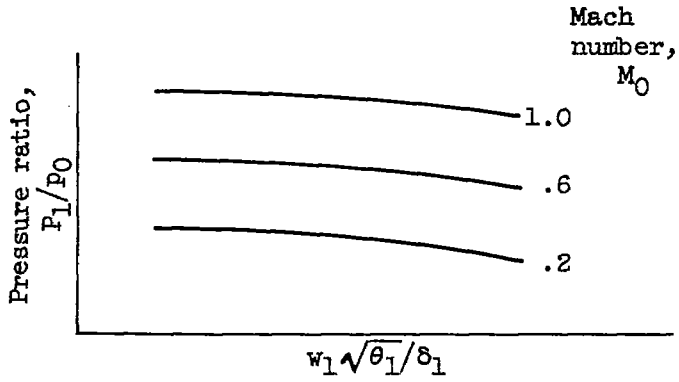

(a) Fixed-geometry inlet.

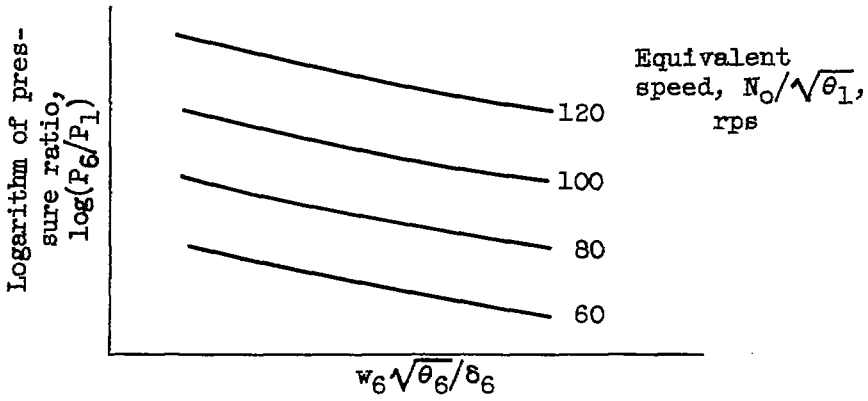

(b) Gas generator.

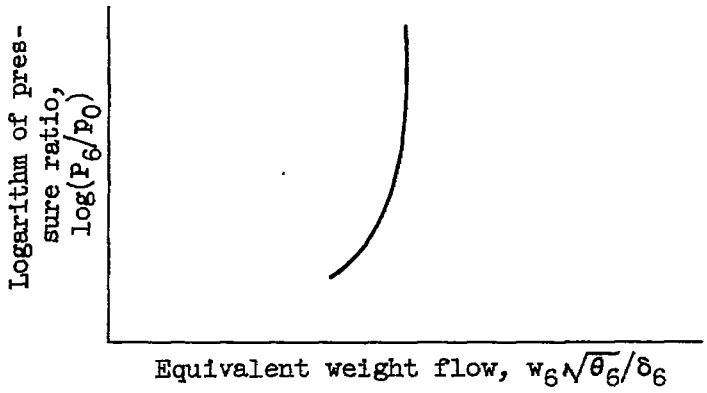

(c) Combined map for tailpipe and exhaust nozzle.

Figure 9. - Matching maps for simple turbojet.

[redacted]

3656

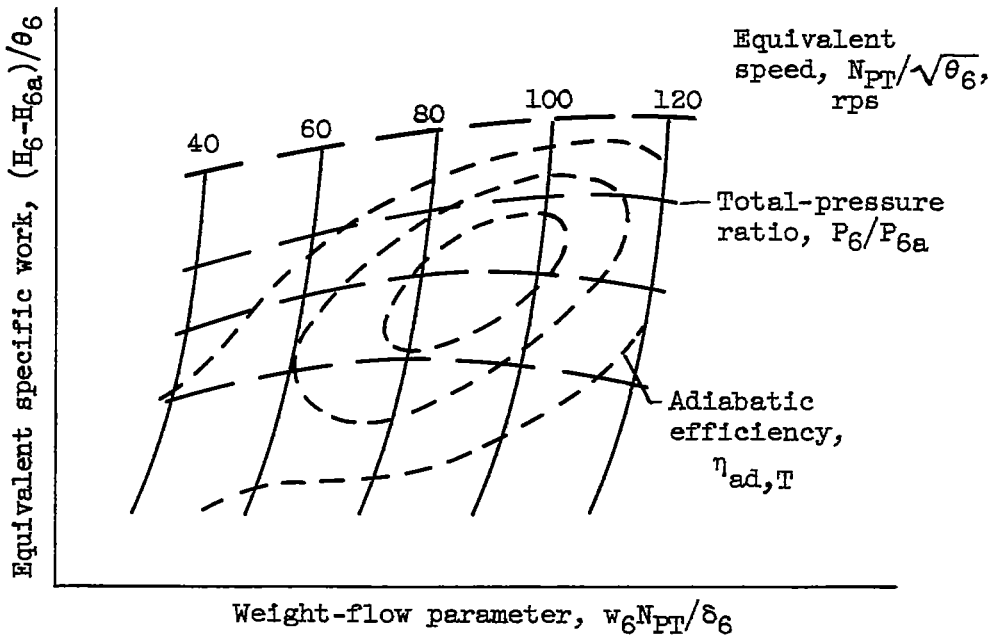

(a) Power-turbine performance.

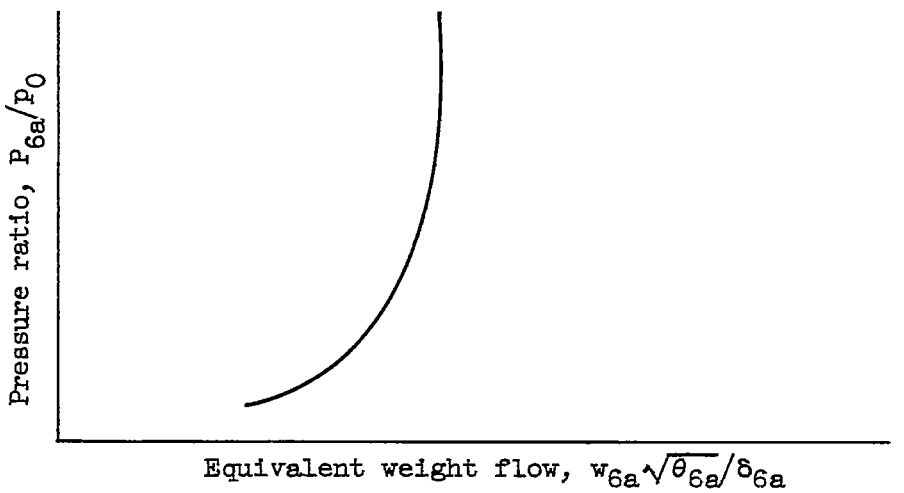

(b) Combined performance of tailpipe and exhaust nozzle.

Figure 10. - Matching maps for turboprop with free-wheeling power turbine.

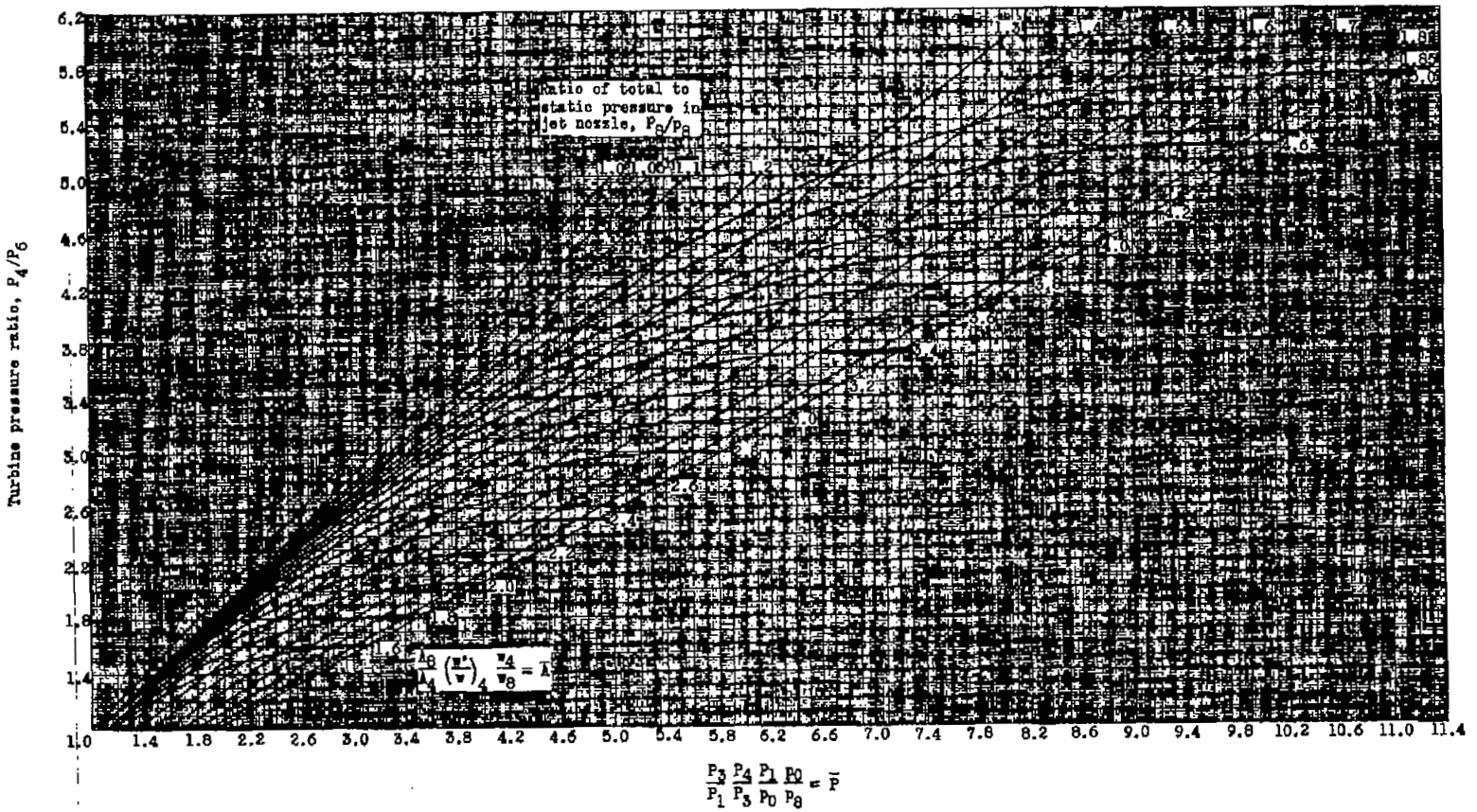

Figure 11. - Chart for estimating turbine pressure ratio. Turbine polytropic efficiency, 0.85; $\gamma_4 = \gamma_8 = 4/3$ (ref. 5). (A large working copy of this chart may be obtained by using the request card bound in the back of the report.)

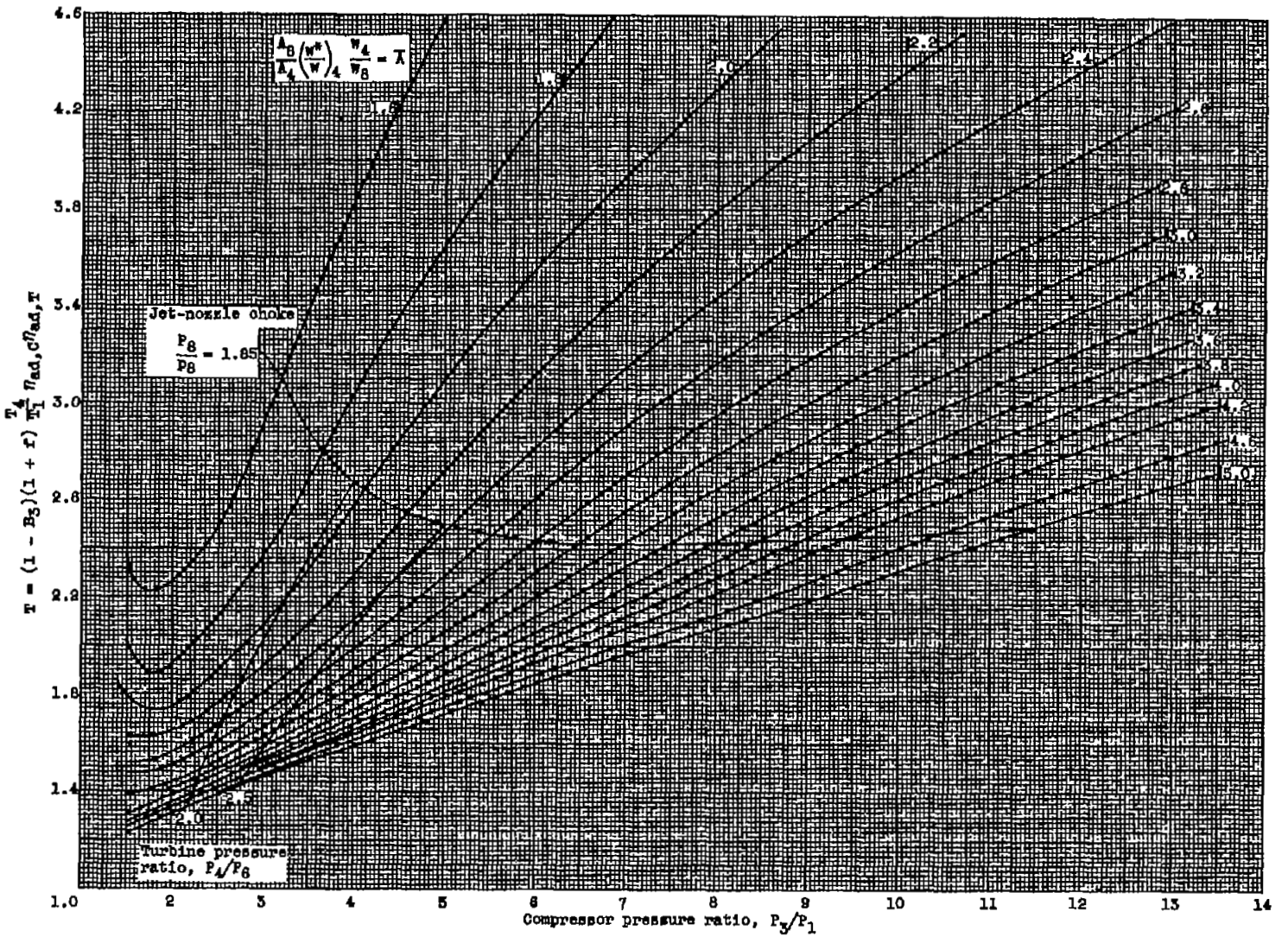

Figure 12. - Chart for estimating turbine-inlet temperature. Ram pressure ratio, P_1/p_0, 1; combustor pressure ratio, P_4/P_3, 0.97 (ref. 5). (A large working copy of this chart may be obtained by using the request card bound in the back of the report.)

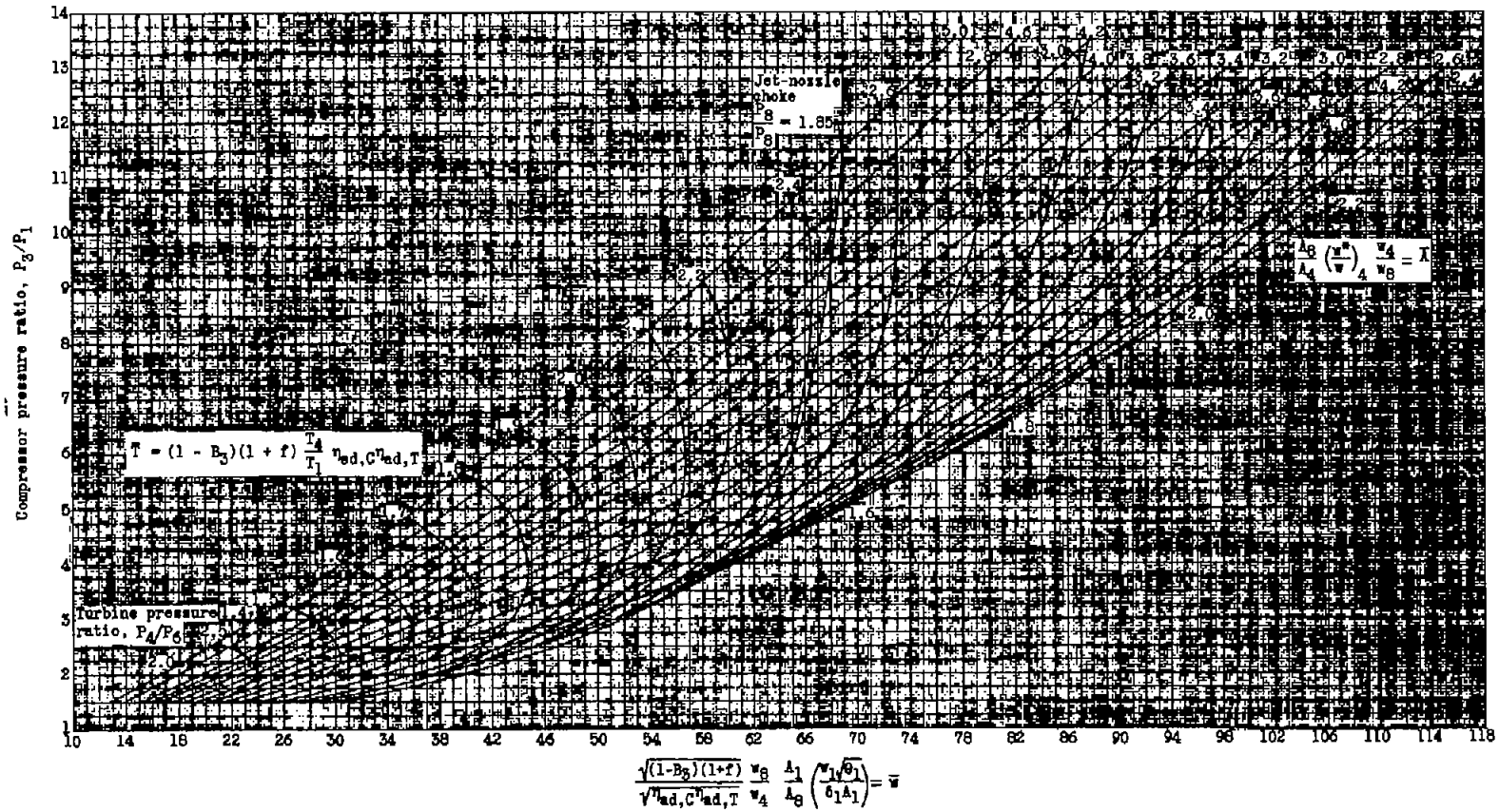

Figure 13. - Chart for estimating compressor equilibrium operating line. Ram pressure ratio, P_1/p_0, 1; combustor pressure ratio, P_4/P_3, 0.97; $\gamma_4 = \gamma_8 = 4/3$ (ref. 5). (A large working copy of this chart may be obtained by using the request card bound in the back of the report.)

3656

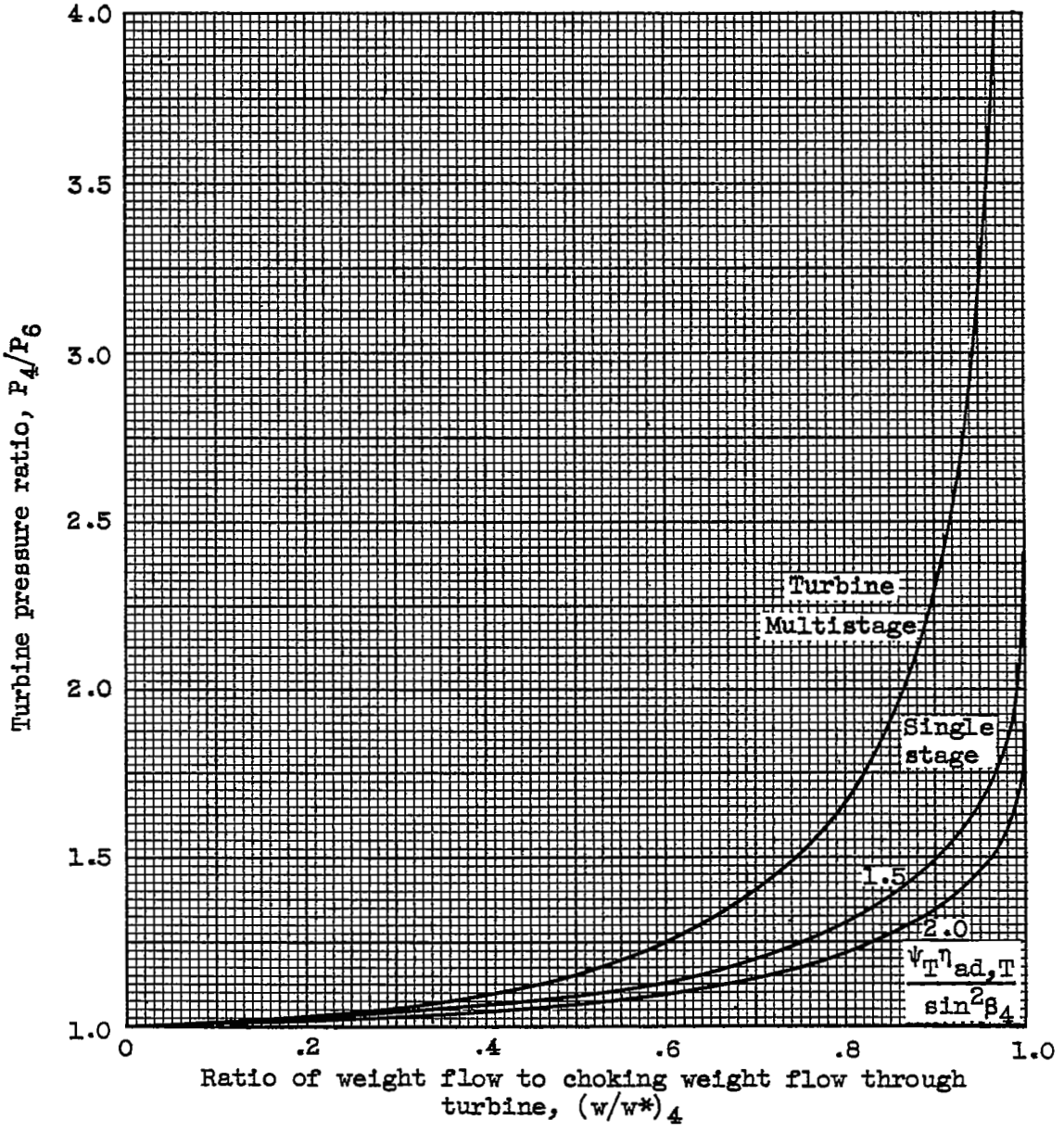

Figure 14. - Effect of turbine pressure ratio on weight flow (ref. 5).

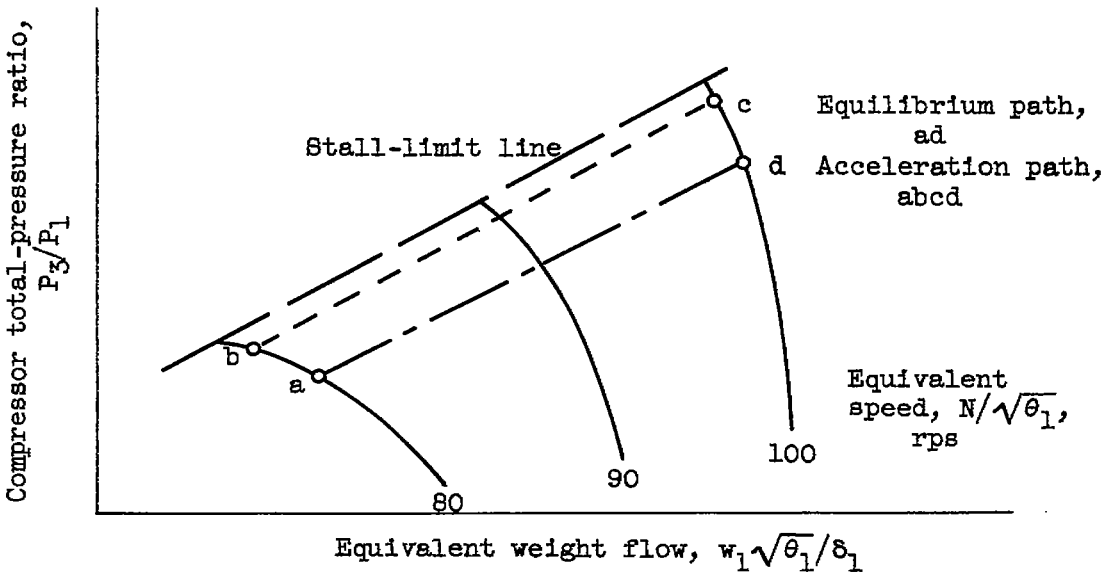

Figure 15. - Equilibrium and acceleration paths on compressor map.

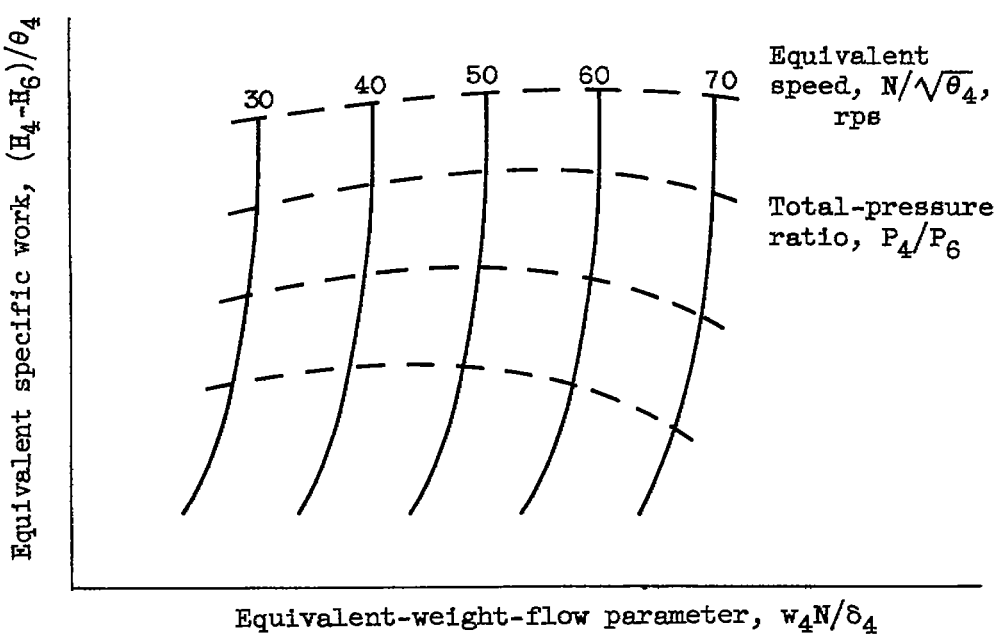

Figure 16. - Turbine performance map.

NACA - Langley Field, Va.

NASA Technical Library
3 1176 01435 4774